FLUX-PINNED DYNAMICAL SYSTEMS WITH APPLICATION TO SPACEFLIGHT

A Dissertation

Presented to the Faculty of the Graduate School

of Cornell University

in Partial Fulfillment of the Requirements

for the Degree of Doctor of Philosophy

by

Frances Zhu

May 2019

FLUX-PINNED DYNAMICAL SYSTEMS
WITH APPLICATION TO SPACEFLIGHT

Frances Zhu, Ph. D.

Cornell University 2019

Technology enables space exploration and scientific discovery. At this amazing intersection of time, new software and hardware capabilities give rise to daring robotic exploration and autonomy. Close-proximity operations for spacecraft is a particularly critical portion of any robotic mission that enables many types of maneuvers, such as docking and capture, formation flying, and on-orbit assembly. These dynamic maneuvers then enable different missions, like sample return, spacecraft construction larger than a single rocket faring, and deep-space operations. Commonly, spacecraft dynamic control uses thrusters for position and attitude control, which rely on active sensing and consumable propellant. The development of other dynamic control techniques opens new capabilities and system advantages, and further offers a more diverse technological trade space for system optimization.

This research comprehensively investigates the utilization of flux-pinning physics to manipulate spacecraft dynamics. Flux-pinned interfaces differ from conventional dynamic control through its passive and compliant behavior. These unique characteristics are extremely attractive for certain applications, but flux-pinned technology must mature considerably before adoption for spaceflight missions. A dynamic capture and docking maneuver in an upcoming mission concept,

Mars Sample Return, motivates the technology design. This body of work as much as possible follows a progression from cradle to grave.

A flux-pinning theoretical dynamics model and a system architecture are presented to specify general capabilities of such a spacecraft system. Different analyses on stability, state sensitivity, backwards reachability result from a physics-based dynamics model. An extensive literature review and basic science experiments inform a theoretical dynamics model about the incorporation of physical parameters when simulating realistic dynamics.

A series of testbeds enable experimentation and precise investigation of flux-pinned interface capabilities in the context of docking and capture. The testbeds ranged from the simplest expression of dynamics, in a single degree of freedom, to a flight traceable expression, in all six degrees of freedom. Experiments from these testbeds define and characterize system level capabilities specific to flux-pinned capture. Data collected from these experiments then supports development of a predictive dynamics model of the hardware system.

Various system identification methods aid in creating a dynamics model that accurately predicts the dynamics observed during experiments. Several objective metrics are considered to evaluate the model fidelity. The types of system identification methods are separated into analytical methods and numerical methods. The analytical method involves parameter estimation in a physics-based model. Numerical methods involve Taylor expansion, bag of functions, symbolic regression, and neural networks. Theoretical extensions towards verification further develops neural network approximation methods, driving at safe, real-time system identification.

BIOGRAPHICAL SKETCH

Frances Zhu was born in Austin, Texas. She grew up in part in Boston, Massachusetts and in part in Overland Park, Kansas. After her high school graduation in 2010, she attended Cornell University where she obtained the degree of Bachelor of Science in Mechanical Engineering in 2014. A serendipitous encounter in the second year of her undergraduate degree led Frances to conduct research with Dr. Mason Peck through his graduate student Laura Jones, which led to other opportunities like leading the attitude, controls, and sensing subsystem for the Violet satellite. In 2015, Frances joined Dr. Peck's Space Systems Design Studio and received the NASA Space Technology Research Fellowship (NSTRF). Her research focuses on developing spacecraft interfaces that leverage unique physical phenomena and extending machine learning techniques to aerospace applications. Frances graduated in the spring of 2019 with her Ph.D. in Aerospace Engineering, with a concentration in Dynamics and Controls and a minor in Computer Science.

ACKNOWLEDGEMENTS

I am eternally grateful to my advisor of nearly a decade, Dr. Mason Peck. No, I've not had a nine-year PhD, but a prolonged stay since sophomore year of my undergraduate degree, when I first started working with Mason. I stayed to work with him through a PhD because of his drive, his ideas, and his never-ending generous support. He has an everlasting impact on my research and mentorship vision. I would like to thank my committee, consisting of Dr. Hadas Kress-Gazit and Dr. Silvia Ferrari, a duo of fiercely accomplished and supportive role models. Their separate lines of research have inspired threads of this thesis and my future interests.

I'd also like to express gratitude to my mentors at other agencies. To Dr. Laura Jones-Wilson, who is my professional big sister and fearless leader of the flux pinning crew. To Dr. Alvin G. Yew, who first gave me a chance to work with him at Goddard Spaceflight Center and since selflessly dedicated immense support throughout all my career endeavors. To Joe Parrish, a first-class microgravity flyer, program manager, and humble wise sage who continues to be a vocal sponsor for me. To Dr. Fred Leve, who graciously makes time and energy to talk about our machine learning research despite having a full-time job as a program manager.

I appreciate and have had an immense amount of fun with the flux pinning team over the years. Of the JPL team led by Laura and Joe, I'd like to recognize William Jones-Wilson, Ian McKinley, Chris Hummel, and Paulo Younse. Of the Cornell team that I've had the pleasure of leading, I thank Eric Fiegel, Ty Burney, Steven Liu, Harley Dietz, Adler Smith, Kate Zhou, Reggie Lin, Somrita Banjeree, Mitch Dominguez, Bhavi Jagatia, Wesley Dixon, Joyce Cao, Sofya Calvin, Alexa Ditonto, and Michelle Zhou.

Many thanks go to the lovely alumni, staff, and current students in the Space System Design Studio. Marcia Sawyer, Patti Wojcik, Leon Stoll, and Don are the reasons I can navigate

logistics, can handle money, and have a nice working environment. To Rodrigo Zeledon, Zac Manchester, and Lorraine Weis, the space cadets sorely miss you and are so proud of you. To the current space cadets, Sawyer Elliott, Doga Yucalan, Kyle Doyle, Hunter Adams, Matt Walsh, Katherine Wilson, Kalani Rivera, Aneesh Heintz, and Aaron Zucherman, thank you for your daily presence, support, and shenanigans. I'd like to acknowledge the other students who I've worked with on various side projects: Hailee Hettrick, Dongheng Jing, David Levine, Haoyuan Zheng, and ZhiDi Yang.

I am so grateful to my family and friends. My mother, for being my original role model and fire. My father, for being my sensibility. My brother, for being my humor and compatriot. Ben, for being my platonic soulmate. My friends, for being my sanity. My partner, for being my joy.

Finally, I'd like to thank the organizations that have provided funding for me and for my project. My gratitude goes to Cornell University Next-Gen Professors and Colman Leadership Program for providing me professional guidance and opportunities. I would like to thank NASA for awarding me the Space Technology Research Fellowship and NASA JPL for funding the hardware development under a strategic research grant.

TABLE OF CONTENTS

LIST OF FIGURES

LIST OF ABBREVIATIONS

ABA	Avionics Bench Assembly
CAD	Computer-Aided Drawing
CG	Center of Gravity
CLS	Commanding Laptop Station
CO	Computer Operator
COM	Center of Mass
COTS	Commercial-Off-the-Shelf
DAQ	Data Acquisition
DARPA	Defense Advanced Research Projects Agency
DOF	Degree of Freedom
EM	Experiment Manager
FA	Frame Assembly
FC	field-cooled
FCT	Formation Control Testbed
FFT	Fast Fourier Transform
FM	Frame Manager
FPI	Flux-Pinned Interface
FPOS	Flux Pinning Orbiting Sample
FPS	Frames per Second
GA	Genetic Algorithm
GPTIPS	Genetic Programming and Symbolic Data Mining Platform
GUI	Graphical User Interface
IA	Initiator Assembly
IFA	Integrated Frame Assembly
IMU	Inertial Measurement Unit
ISS	International Space Station
JPL	Jet Propulsion Lab
MMMS	Multiple-Magnet and Multiple-Superconductor system
MSR	Mars Sample Return

NASA	National Aeronautics and Space Administration
NdFeB	Neodymium
NI	National Instruments
NN	Neural Network
NRMS	Normalized Root-mean-squared
OM	OSA Manager
OS	Orbiting Sample
OSA	Orbiting Sample Analogue
RMS	Root-mean-squared
SBA	SROA Bench Assembly
SMSS	Single-Magnet and Single-Superconductor system
SPECTRE	Sample Pinning Experiment for Capture Technology in a Reduced-gravity Environment
SR	Symbolic Regression
SRO	Sample Return Orbiter
SROA	Sample Return Orbiter Analogue
TRL	Technology Readiness Level
TRR	Test Readiness Review
YBCO	Yttrium Barium Copper Oxide

LIST OF SYMBOLS

L_{OFF}	lateral offset of the OS at the capture plane
V_{OS}	velocity magnitude of the OS at the capture plane
θ_V	direction of velocity vector from capture boresight axis
$\boldsymbol{m_p}$	magnetic-moment dipole or a physical magnetic field source
B	magnetic field
$\boldsymbol{r}$	position vector
$\boldsymbol{m}$	magnetic-moment dipole vector
$\boldsymbol{\rho}$	distance between two magnetic sources
$(\cdot)_{mag}$	subscript for physical magnet
$(\cdot)_{FC}$	subscript for field-cooled magnet
$(\cdot)_f$	subscript for frozen image
$(\cdot)_m$	subscript for mobile image
$(\cdot)_e$	subscript for equilibrium
$(\cdot)_l$	subscript for lateral
h	height
θ	angle
k	stiffness
$\dot{\blacksquare}$	derivative operator
$\hat{\blacksquare}$	direction vector or normalization operator
$\delta(\cdot)$	change in variable
$\boldsymbol{H_z}$	External magnetic field of permanent magnet
$\hat{\boldsymbol{m}}_{\boldsymbol{s}}$	unit direction normal to the surface of the superconductor
$\boldsymbol{O_s}$	reference point on the superconductor surface
$\boldsymbol{F}$	force
$\boldsymbol{\tau}$	torque
$\boldsymbol{\omega}$	angular velocity
$\boldsymbol{v}$	translational velocity
q	quaternion
M	mass tensor or matrix

I	inertia tensor or matrix
U	potential energy
μ_0	magnetic constant or the permeability of free space
s	state
A	state transition matrix
J	Jacobian
λ	eigenvalue
x	x position tied to a coordinate frame
y	y position tied to a coordinate frame
z	z position tied to a coordinate frame
c_F	scalar reduction in magnitude of magnetic field due to finite-dimension effect
T	temperature
c_t	scaling factor in magnitude of magnetic field due to temperature variation
$\mathbb{R}$	real space
t	time
V	viability kernel
S	state space
$T(\cdot)$	kinetic energy
$D(\cdot)$	dissipative energy
$E(\cdot)$	total energy
α	path angle
ϕ	yaw angle
${}^{VO}(\cdot)$	Vicon frame attached to the OSA body
${}^{VF}(\cdot)$	Vicon frame attached to the frame body
${}^{IO}(\cdot)$	IMU frame attached to the OSA body
$E(\cdot)$	expected value of distribution
$\sigma(\cdot)$	standard deviation of distribution
γ	time constant associated with energy dissipation
K	stiffness matrix
C	damping matrix

e	error
$P(\cdot)$	power curve of timeseries
$p(\cdot)$	peaks of power spectrum
ζ	damping ratio

CHAPTER 1: Introduction

Flux pinning was first observed three decades ago in which a magnetic phenomenon seemed to contradict Earnshaw's theorem about stable magnetic systems. Flux-pinning fundamental principles developed as a result of dedicated basic science. As understanding grew, material scientists began manipulating and refining the components that comprise of a flux-pinned interface to achieve stronger, more efficient systems. Engineers began finding applications and utility for this unexploited physics, as flux-pinned interfaces carry many advantages, like contactless, compliance, and passivity. The Space Systems Design Studio here at Cornell first looked at flux-pinning spacecraft more than a decade ago. Less than five years ago, the Mars Directorate at JPL started considering numerous technologies in a Mars Sample Return concept trade study, comparing docking and capture mechanisms from which flux-pinned interfaces became a candidate technology. The preliminary Mars Sample Return mission concept requirements specify the expected capabilities of a potential docking and capture system but retain flexibility to accommodate slight design modifications. This chapter reviews the origins and space applications of magnetic flux pinning, along with the specific motivating mission concept, and the approach in the subsequent technology development.

I. Context for Flux Pinning

a. *History*

Earnshaw's theorem states there is no stable stationary equilibrium for point charges that are solely held together by electrostatic forces [1]. Because they are also divergenceless, magnetic fields offer no stable equilibria except at the origin or at infinity. Flux-pinned magnets appear contradictory for which a stable equilibrium can exist for any number of magnets at arbitrary

relative positions and orientations. Seen as a magnet levitating above a superconductor, flux pinning was first observed by a series of scientists, Williams, Davis, and Matey, in 1988 [2], [3]. In early empirical studies of flux pinning, Williams measured potential curves that resemble a volcano, with a minimum at the center of the disk and a maximum near the edge [3]. To conceptualize and explain the levitating phenomenon, Kordyuk then proposed a model consisting of a repulsive magnetic field source (the mobile image) superimposed upon an attractive magnetic field source (the frozen image). The potential energy landscape generated from Kordyuk's theory generally matches the measured potential curves from Williams, validating a physical and theoretical self-stabilizing system.

Scientists are continuously refining and creating materials that emphasize certain aspects of superconductivity to improve the performance of all flux-pinning applications. Some efforts involved in improving superconducting performance include minimizing hysteresis, increasing levitation force, and improving the manufacturing process to generate larger bulk [4]. Generally, cost to manufacture and ability to cool superconductors impede widespread use of superconducting technologies [5]. Since the dawn of the superconductivity field, the community has dreamt of the existence or creation of a room-temperature superconductor of which a recent 2018 breakthrough seems to promise this capability shortly in the horizon [6]. The counterpart of materials development is technological development utilizing superconductors, which pushes forth science by motivating an application.

Flux-pinned interfaces stabilize passively, act contactlessly, and exhibit compliance. The engineering community draws excitement from the potential applications, such as frictionless joints and transportation [7]. Frictionless joints include magnetic bearings that dissipate magnitudes less energy, creating more efficient bearings for actuation and energy storage [8]–[12].

A seismometer that incorporates flux pinning exploits the contactless and frictionless interaction to measure rotational motions [13]. Transportation applications include high speed trains already operating today in Japan, South Korea, and China, utilizing a sister technology, magnetic levitation technology [14]–[16]. Preliminary work extends the use of flux pinning for high speed trains [17]. Numerous extensions can be made between a ground system utilizing magnetic flux pinning and a space system, as well as applications that are unique to spaceflight.

b. *Application to Space Systems*

When a type–II superconductor is cooled below its critical temperature in the presence of the magnetic field (~88K for Yttrium Barium Copper Oxide), the shielding currents within the superconductor persist even after the magnetic field source has been removed [2], [18]. Natural impurities in the crystal lattice structure of the material prevent the superconductor from completely negating an internal magnetic field, as is otherwise seen in Type-I superconductors and described by the Meissner Effect. The lack of electrical resistance in a cooled superconductor generate eddy currents inside the material around localized sites of magnetic field penetration. These currents are formed by induction and counteract changes in the ambient magnetic field outside the superconductor. In this manner, the magnet is said to be pinned to the superconductor.

Flux pinning a magnet to a superconductor creates an equilibrium, or minimum potential energy well, that stabilizes the magnet's position and orientation by up to six degrees of freedom without mechanical contact or active control [3] [2]. Passive forces and torques in six degrees of freedom minimize the difference between the magnetic field of an external magnetic moment object and the field in which the superconductor was initially cooled. The system thus exhibits a stiffness, which passively returns the pinned magnet to the same position and orientation in 6 DOF at which it was during field cooling. This stiffness is highly non-linear, and its influence diminishes

by a factor of distance to the fourth power. The flux-pinning effect influences the dynamics of kilogram-scale bodies out to about 10 cm of separation distance. The magnetic potential energy from the pinned field is the practical limit in which flux-pinning physics dominates all other physics, like friction, drag, or solar radiation pressure.

Figure 1: A Neodymium magnet (bottom) flux pinned to a YBCO superconductor disc (top). The YBCO was cooled below its critical temperature (~88K) in a bath of liquid nitrogen

In space-system applications, a flux-pinned interface (FPI) is formed between a spacecraft with an imprinted superconductor and another spacecraft with a corresponding set of magnets. This interface allows the flux-pinning physics to dominate the close-proximity relative motion between the vehicles, providing a robust solid-state docking interface where the passive physics – without active control – can correct misalignment and mitigate impact risk [19], [20]. If flux-pinning physics is paired with active magnetic field manipulation, then both the final equilibrium and the configuration of the FPI can be tuned to maneuver one spacecraft relative to the other without any contact between the vehicles [21]. This short-range "tractor beam" effect has many applications and unique benefits that distinguish it from most other rendezvous, capture, or relative-manipulation technologies currently available.

These unique traits make flux-pinned interfaces a technology candidate for applications such as spacecraft capture and docking [20] [20] [21], assembly of modular systems [17] [22],

formation flying [25] [26] [27]–[29], kinematic mechanisms [24] [28] [31], and station-keeping [29] [30]. Figure 2 illustrates a selection of applications. These capabilities trace to a range of future missions including on-orbit satellite servicing, telescope assembly [27], and precision pointing. Flux-pinned systems can be actively manipulated to control the orientation and position of close-proximity vehicles, while remaining contactless and compliant [21]. Research both in laboratory [33]–[35] and microgravity environments [31], [36] have led to a broad understanding of the design principles that govern this technology as well as its expected performance under a variety of circumstances.

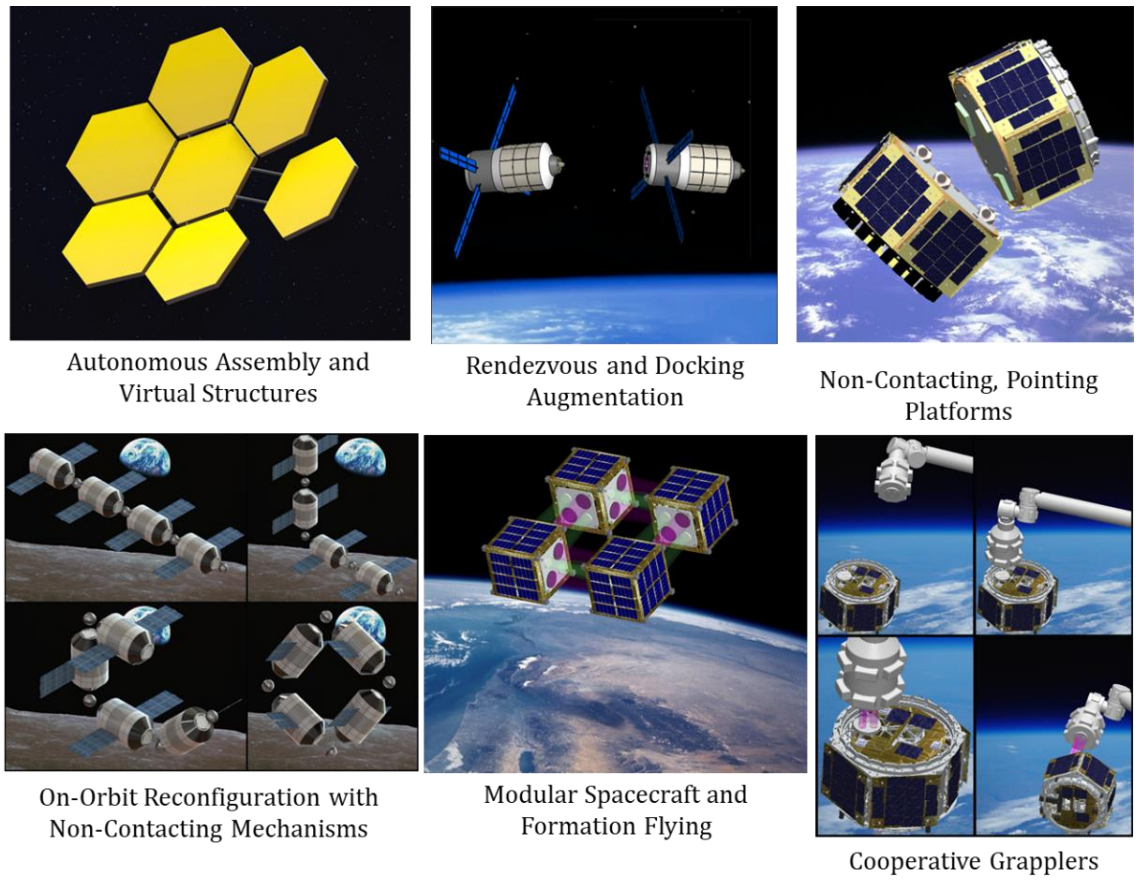

Figure 2: Potential applications for flux-pinned interfaces [37]

Dr. Mason Peck at Cornell University first proposed close-proximity spacecraft operations manipulation with magnetic flux-pinning physics. His Space Systems Design Studio has been

studying flux-pinning space technology for more than a decade with support from organizations such as the NASA Institute for Advanced Concepts, DARPA, Northrop Grumman Aerospace Systems, and through partnerships with other institutions such as UCDavis and JPL. Cornell has also laid the key technological groundwork for flux-pinned, non-contacting interfaces and electromagnetic actuation and manipulation. This research has involved a series of small planar air-bearing tests on the Cornell FloatCube testbed [33], [34] and two microgravity tests through the NASA FAST program. Figure 3 shows the progression from air-bearing test units to the microgravity results for the 2009 and 2010 test campaigns. These relatively simple tests successfully demonstrated a functioning revolute joint from an FPI [31] and the contactless flux pinning of a magnet in microgravity with a cryocooler-based thermal solution [38]. This collective effort has built a body of research spanning basic FPI physical principles to application-specific mission design work. Much of the modeling and characterization research, along with the technology development efforts, can be leveraged for all FPI applications.

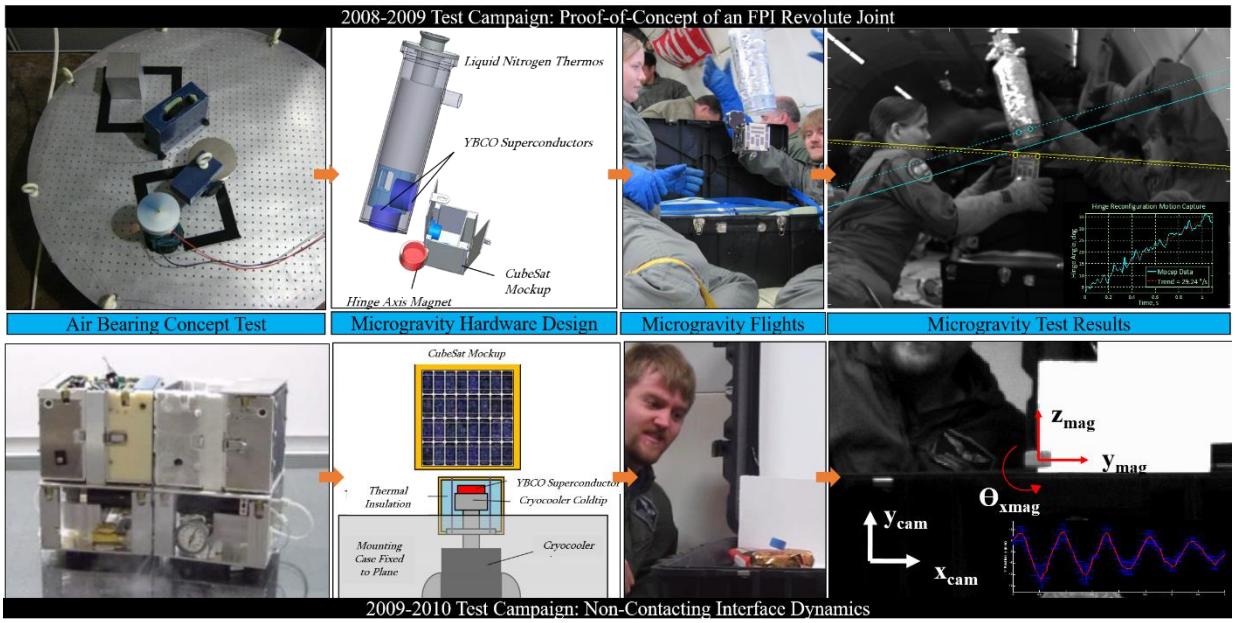

Figure 3: A progression of ground test campaigns to microgravity demonstrations for early technology raising efforts for non-contacting interfaces and revolute joints.

Outside Cornell, other research labs have gained interested in incorporating flux pinning for spacecraft applications. To enable the vast amount of possibilities, various efforts also lie in characterizing the fundamental properties of a flux-pinned interface agnostic to application, including space radiation on the efficacy and dynamic force characteristics [39], [40]. Lu of Harbin Institute of Technology, China focuses on flux-pinned interfaces in the context of docking spacecraft systems [42]–[49]. Lee of Korea Advanced Institute of Science & Technology initially developed general superconductor-magnet bearings, but then specified applications for energy storage and attitude control on spacecraft [50]–[53], along with other authors in China [54]. Other applications of superconducting magnets include spacecraft radiation shielding [55], electromagnetic deployment and support structures [56], and vibration isolation [57]–[59].

II. Mars Sample Return Mission Concept

a. *Proposed Mission Concept*

Humanity's profound search for life continues on by bringing samples back from Mars, as rock samples may reveal possible past organic activity [60]. Although rovers with embedded scientific laboratories are currently exploring the Martian surface, Mars Science Laboratory and the Mars Exploration Rovers were intended for different science objectives with instruments that were not designed to look for signs of life [61], [62]. The only successful example of sample return is the Apollo mission campaign in which 2200 samples summing 382 kilograms was brought back to Earth [63]. From these lunar samples, scientists better understand the geophysical interaction and formation of the moon in space, and even debunked a myth that the moon is devoid of water [64], [65]. Possession of samples on Earth enable complex and prolonged analyses with changing state-of-the-art equipment that is not possible in situ.

The Mars Sample Return Mission has been revisited many times over the decades, dating back to at least 1975 in which the Soviet Union proposed and cancelled their Mars sample-return due to rocket failure [66]. Since then, NASA has proposed to return samples from Mars through the Mars Exploration Program, which began in 1992 and aimed to have samples back on Earth by 2008 [67]. Although the previous effort was discontinued in 1999, continuous technological efforts progressed the feasibility and realizability of such a mission until a public declaration in 2012 demonstrated fiscal and institutional commitment [68]. In 2011, NASA JPL presented a concept of a Mars Sample Return mission and shortly after, the Planetary Science Decadal Survey: 2013-2022 listed Mars Sample Return as one of the highest priority science objectives [69], [70]. Thus, serious engineering efforts began to bring Mars samples back to Earth.

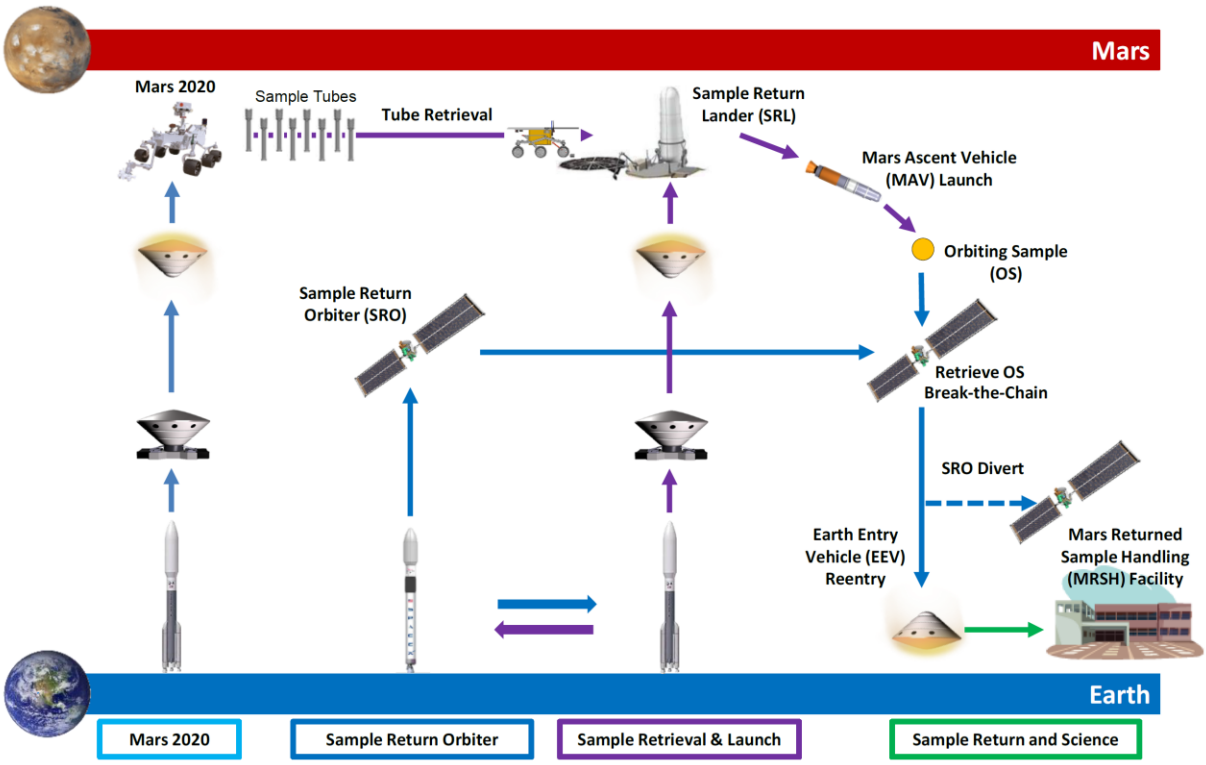

Figure 4: Notional Mars Sample Return architecture. Note that all elements beyond Mars 2020 are conceptual. (Credit: P. Younse)

The mission concept can be broken down into three spacecraft that work together like a relay team. An overall mission architecture is depicted in Figure 4. The first rover, Mars 2020, touches down on the Mars surface, drills into interesting rocks, and stashes the samples in sealed tubes [71]. Once the samples are collected, the first rover places these samples on the surface for the next rover to retrieve. This follow-up rover fetches the samples, load them into a container, and bring them to a small rocket [72]. This rocket brings the samples from the surface of Mars to orbit for pick up [73]. The third spacecraft, an orbiter, captures the sample cache and bring it back to Earth [74]. The docking and capture operational phase, shown in Figure 5, is a particularly dangerous and critical phase of the mission in which several technologies are in consideration for the spaceflight implementation.

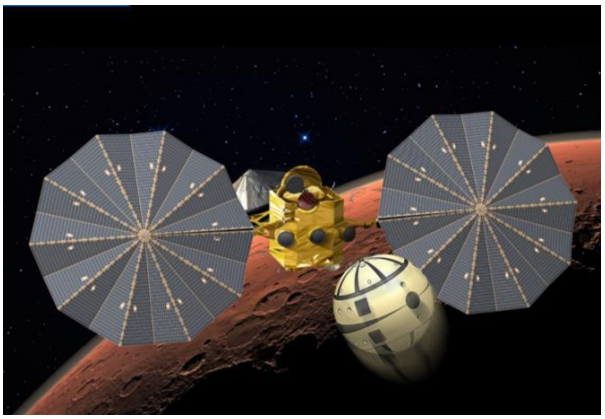

Figure 5: Artist's concept of docking and capturing an orbiting sample by a sample return orbiter. (Credit: D. Hinkle 2018)

Understanding the sample capture scenario concept under consideration is first necessary to understand the potential solutions. In the original 2015 concept, a cache of planetary samples is already in orbit around Mars. Although many different concepts exist for the size, shape, and other properties of this cache (called an orbiting sample, or OS), for the purpose of this study, the OS is a small, passive sphere with a diameter of approximately 20 cm and a mass of less than 6 kg. (Since the beginning of this study, the mass has increased to 12.5 kg and the diameter to 28 cm [74].) Without its own propulsive or maneuvering capabilities, the OS must be captured, stabilized, and manipulated into an appropriate orientation by a sample return orbiter (SRO) for the return trip to Earth. The SRO is considered a large (> 1000 kg, ~10 meters in body length) spacecraft with the

full set of maneuvering capabilities, thermal control, and other resources available to traditional spacecraft.

The assumed initial conditions of the OS at the onset of capture are based on spacecraft Monte Carlo simulations during rendezvous with the OS, with all relevant variables defined in Figure 6. The OS must tolerate any entrance attitude, enabling axially symmetric capture scenarios. The maximum lateral offset of the OS at the capture plane (L_{off}) is 10 cm in any direction off the capture boresight axis. The velocity magnitude (V_{os}) of the OS at the capture plane ranges from 2 to 10 cm/s. The maximum angular rate of the OS is initially 3 revolutions per minute, or 18 deg/sec. The maximum radial component of velocity results in a max angle θ_V of 5° in any radial direction. These initial conditions drive the design and capabilities of the capture and docking solution.

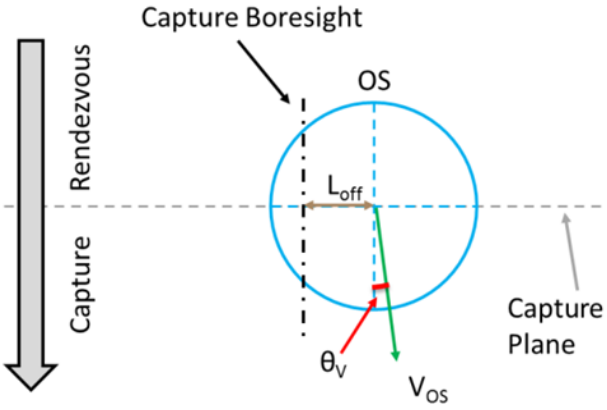

Figure 6: Assumed OS rendezvous initial conditions

b. *Spacecraft Capture and Docking Methods*

A critical operation in many missions with cooperative spacecraft is capture and docking. A capture operation occurs after rendezvous between two spacecraft in close-proximity, closing the separation gap within the last meter. Some missions do not distinguish between rendezvous and capture, as the capture sequence is an extension of the rendezvous phase [75]. To dock the spacecraft, the two bodies must reduce relative velocity to avoid collision and potential damage. This capture and docking operation has been critically dangerous and detrimental. An example of a critical failure occurred when Progress M-34 collided with Mir, sending Progress into Spektr's

solar panels, causing the first on-orbit decompression [76]. Spacecraft are huge financial investments and are intentionally designed to mitigate any risk of failure or damage.

Current capture technologies involve a human teleoperator or active sensing and control in autonomous operations. Historically, teleoperators rendezvous and dock spacecraft, like the space shuttle and the ISS [77]–[79]. Although teleoperation may be simpler and more reliable for humans directly deposited in the space environment, such as Low Earth Orbit, teleoperation separated by far distances incur time delay of signal transfer, greatly reducing the effectiveness of teleoperation. Autonomous capture methods utilize sensors and actuators in conjunction with a form of relative navigation control. Common sensors include video guidance sensors and the global positioning system, although advances in solid-state electronics and photonics have led to a suite of other modern options [80]. The most common form of relative position and attitude control involves coordination of thrusters, seen on spacecraft intending to dock with the ISS [81]. After successful rendezvous and capture, the docking operation initiates.

Autonomous docking techniques use either a mechanism (such as a robotic arm) or actuators in conjunction with a mechanical capture cone or locking feature to secure the final mate [82][83]. These mechanisms have high complexity designs [84]–[86]. A recent US Navy patented demountable docking interface touts simplicity, scalability to CubeSat size, and the ability to transfer fluid [87]. Other studies have examined the use of magnetic docking solutions that use actively controlled magnets to augment (or completely control) the docking sequence [88], [89].

None of these techniques can generate the passive equilibrium in six degrees of freedom that FPIs offer, and all of them ultimately require mechanical contact between the bodies to work. In the context of Mars Sample Return, any abrupt mechanical contact between a notional return vehicle to Earth and a spacecraft contaminated with surface material could bring a measure of

uncertainty and risk into the sequence. Furthermore, these traditional docking solutions often depend on lighting conditions or other sensor conditioning and are vulnerable to errors in the control system. FPIs are based on passive physics. The interfaces are robust to these kinds of risk. The interface can be solid-state, for example, and does not require the use of sensors at all once the two spacecraft are within the FPI effective range.

Finally, if a specific orientation is required for the mate, many traditional solutions require mechanical keying features on the target surface and mechanisms to achieve this state. Because an FPI acts on magnetic field shape, rather than mechanical shape, an FPI design can be independent of the mechanical configuration of the target. Once the capture and reorientation are complete, the interaction can be removed by warming the superconductors, simplifying subsequent maneuvers.

In addition to these advantages, FPIs also carry a unique set of risks. Specific to potential sample capture applications, exposure to magnetic fields can adversely impact the sample science. Additional shielding would be necessary to avoid this exposure. Also, FPIs require a proper field-cooling configuration to set up the interface for capture- this critical event introduces a set of risks that must be addressed (albeit prior to the capture phase itself). Similarly, thermal failures can lead to the loss of the interaction and docking scenarios with significant amounts of energy may not stay within the potential well and not make a successful capture on the first attempt. These risks must be understood and addressed in the FPI technology development efforts for docking and capture applications if the technology is ever to become a viable alternative to other more traditional solutions.

c. *Proposed Flux Pinning Solution for Docking and Capture*

The Mars Sample Return docking and capture operational phase, shown in Figure 7, motivates the technological development of a flux-pinned interface. The proposed approach to

achieving Mars orbiting sample capture involves an array of permanent magnets on an orbiting sample (OS) and an imprinted superconductor on the sample return orbiter (SRO) to create an FPI [68]. The resulting flux-pinned interface enables the non-contacting attraction and manipulation of the OS by the SRO when they are within tens of centimeters of each other. This solution is powerful for a number of reasons: 1) the OS is required to accommodate only an array of unpowered permanent magnets, rather than specialized mechanical keying, powered sensors, or unique surface preparation, 2) an FPI can achieve a passively stable non-contacting capture of the OS, which may minimize contamination of the SRO with Martian material as compared to an approach that allows the OS to mechanically contact the capture device, 3) the passive stability of an FPI makes the system robust to control failures, and 4) the FPI can enable the SRO to enforce

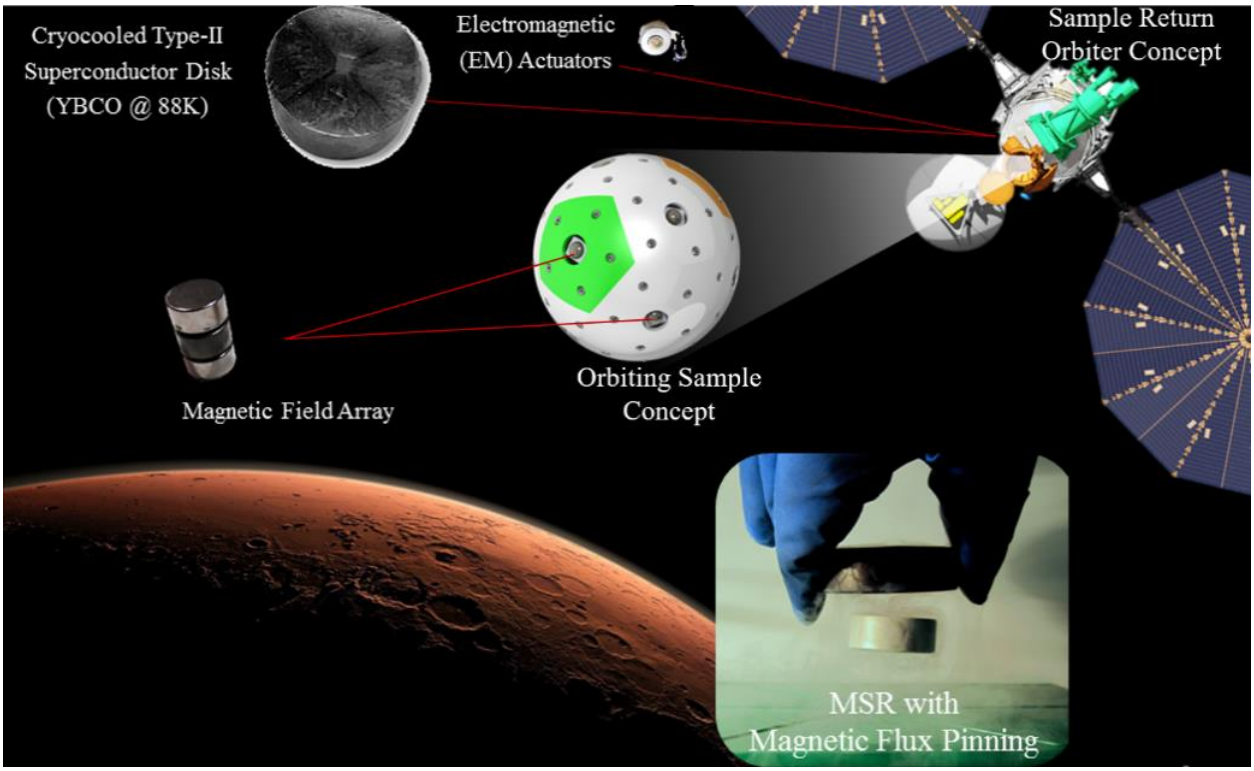

Figure 7: A conceptual sample-capture flux-pinned interface, where an orbiting sample containing a sample cache and populated with surface permanent magnets must be collected by a sample return orbiter containing field-cooled superconductors and electromagnets. Illustration created 2015

the orientation of the OS without contact, facilitating cleaning solutions to limit SRO contamination while conditioning the OS for ingestion into the SRO.

When outfitted with an FPI, the highly capable SRO cools down the superconductors as the SRO approaches the OS orbit prior to capture operations, generating the appropriate field-cooled equilibrium with surrogate training magnets. This set of magnets can be jettisoned or removed via mechanism once the cooling process is complete. Once properly configured, the SRO then navigates to within range of the FPI, where the OS is drawn into its passively stable, non-contacting equilibrium. This soft-capture maneuver can benefit from the misalignment correction and impact-attenuation properties offered by an FPI. Similarly, once captured, the OS can be reoriented with electromagnets to support cleaning or containment operations and to achieve the proper ingestion orientation, all without contacting the SRO. Once the OS is ingested into the SRO, the purpose of the FPI is complete and the thermal control of the superconductors can be powered off.

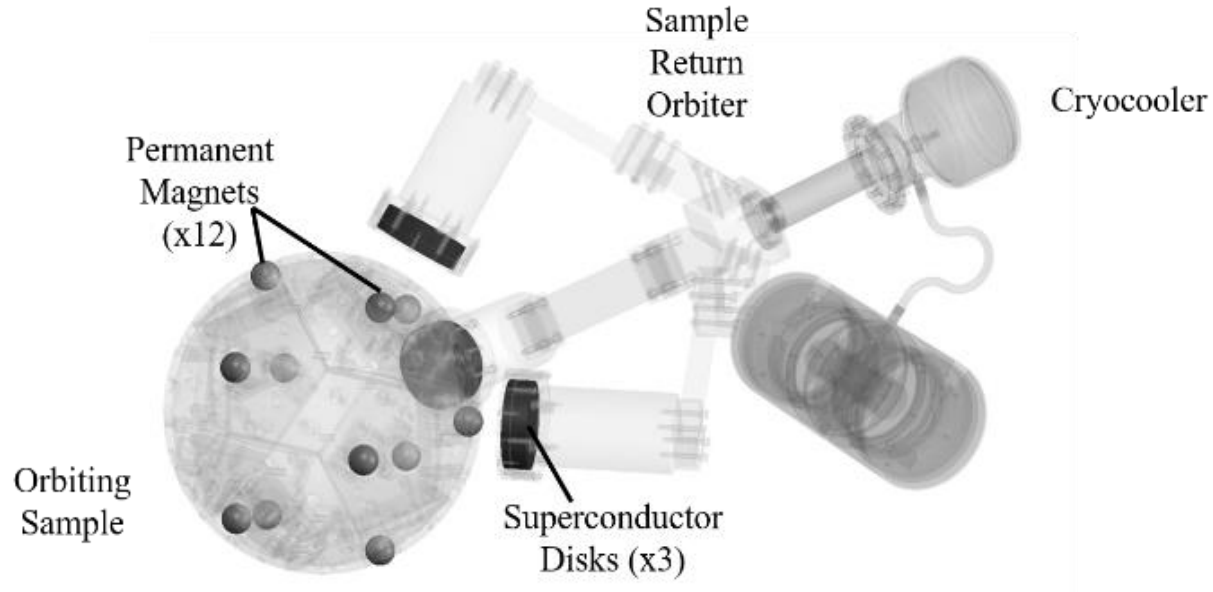

Figure 8: An FPI design for a sample capture concept where a cryocooler maintains three superconductors below their critical temperature so that they can capture an OS prepared with permanent magnets.

To achieve these objectives, the OS's surface is populated with an array of spherical 1.9 cm diameter Neodymium permanent magnets, placed evenly on the points of an icosahedron with the magnetic dipoles all facing radially outward, as shown in Figure 8. This configuration ensures that each plane of the OS is identical to the next, enabling the system to use the same field-cooled superconductors to capture any given face. Similarly, this design enables the system to achieve an orientation where any plane can face the SRO, to ensure that all faces of the OS can be cleaned, and the system can be ingested in the proper orientation.

The other half of the interface, mounted to the SRO, contains an array of three single-grain YBCO superconductor disks 1.6 cm thick and 5.6 cm in diameter. The superconductor YBCO was selected because of its relatively high critical temperature of 88K (making it easily achievable in laboratory conditions) and its well-characterized flux-pinning behavior. This material also exhibits flux-pinning effects across a large range of magnetic field strengths, making it particularly tailorable to many applications. These disks were selected because of their low propensity for hysteresis and their commercial availability. Other superconductor types or disk sizes may be optimal for this application and should be studied in future work.

Each of these disks are mounted such that one magnet can be centered over each superconductor surface at the equilibrium with a separation distance to the closest tangent point on the magnet of 1.6 cm. The planes of each superconductor disk are parallel to three adjacent planes on the OS icosahedron mounting surface, as shown in Figure 3. Any trio of equidistant magnets form a stable joint with the trio of superconductors, allowing many relative equilibria. This superconductor arrangement provides redundancy, greater capture stiffness due to the three interfaces (to avoid OS-SRO collisions), and clocking stiffness to maintain a stable equilibrium between the OS and SRO in all six degrees of freedom.

A flux-pinned interface offers many advantages over conventional mechanical docking solutions [68]. The flux-pinned interface primarily provides a non-contacting, passive linkage between two interacting spacecraft and automatic misalignment correction during docking or capture rendezvous. In particular, contactless interaction reduces risk of damaging the spacecraft through collision mitigation [18]. Impact attenuation is present due to the magnetic stiffness of the interface.

An FPI also provides a method of breaking-the-chain regarding planetary protection because the interface does not rely on physical manipulation of a captured body. The OS can be cleaned or contained prior to ingestion into the SRO sample-handling system. This approach may limit the contamination of the SRO during the rendezvous, which would enable the MSR team to "break-the-chain" of Martian material at the SRO. Additionally, the solid-state nature of an FPI has the potential to relax mechanical design requirements by removing a need for mechanical keying interfaces on the surfaces of the interacting satellites.

FPIs tolerate misalignments and the permanent magnets on the OS can provide eddy-current damping with the aluminum in an SRO structure to slow a spinning OS as the SRO approaches. Misalignments are automatically handled because the magnets on one side of the interface passively restore into a known equilibrium configuration with respect to the superconductors on the other side of the interface. No additional energy needs to be expended other than that required to keep the superconductors below their critical temperatures. While FPIs do have capture limits (relative velocity, capture range, capture cone), these limits may prove to be more forgiving than the state-of-the-art solutions. Electromagnetic actuators can further enhance an FPI by enabling contactless manipulation during close-proximity maneuvers [21].

Finally, the passivity and the stability of flux-pinned interfaces reduce the sensing and actuation requirements but necessitates more stringent thermal requirements on the spacecraft system to cryogenically cool the superconductors [2] [23]. The system requires no close-range sensors such as LIDAR or cameras to successfully close the distance with the OS. This benefit means that FPIs may be able to relax some of the SRO guidance and control requirements in the close-proximity rendezvous phase. The passive stability of the system enables the FPI to be robust to many different mission-ending failure scenarios (such as poor lighting conditions or sensor outages). However, in order to weigh the advantages of the FPI solution relative to alternatives, the technology must be sufficiently mature to realistically assess the resources required and performance offered by an FPI. This project bridges a critical TRL gap needed to make these assessments.

III. Contributions and Approach of Thesis

Flux pinning, stemming from the field of superconductivity, is an exciting physical phenomenon that shows great potential for space applications but lacks the technological maturity for spaceflight mission adoption. Before this magnetic levitation effect was observed, docking technologies had to use different physical methods, such as a combination of thrusters and mechanical adapters from the Apollo era. Today, the ISS performs capture with Canadarm2, a mobile manipulator driven by a human operator. Although effective, both docking procedures require human involvement and mechanical contact to establish docking. Flux-pinned capture and docking interfaces enable passive, contactless, and compliant behavior, doing away with the human-in-the-loop requirement and reducing hardware damage due to mechanical contact. Autonomous robotic technologies, like flux-pinned interfaces, fundamentally change the way future spacecraft missions are design and operated. But to achieve these capabilities, flux-pinned

technology must undergo rigorous study in system design architecture, in engineering solutions for hardware implementation, and in modeling the system dynamics accurately.

Due to a close collaboration with JPL, the technology design was motivated by an upcoming mission concept, Mars Sample Return, and the development process guided by a NASA standard, Technology Readiness Level, TRL [90]. The research approach to increase the maturity of a technology follows the TRL ladder depicted in Figure 9 from the bottom, TRL 1, to the top, TRL 9. This research effort is a primarily designed to advance FPIs for sample capture to the point where it can be properly considered in Mars Sample Return trade studies, but the theory and process generalize to other FPI configurations and spacecraft operations.

Starting at TRL 1, Chapter 1 discusses the discovery and utilization of flux pinning for spacecraft systems. Previous work demonstrates understanding of basic principles and a flux-pinned concept is developed for the docking and capture dynamic maneuver in the Mars Sample Return mission, satisfying TRL 2. Chapter 2 details the progression of a general flux-pinned system dynamics model by exploring the assumptions of the baseline model, refining the model with basic science experiments, and adding higher-order effects detailed

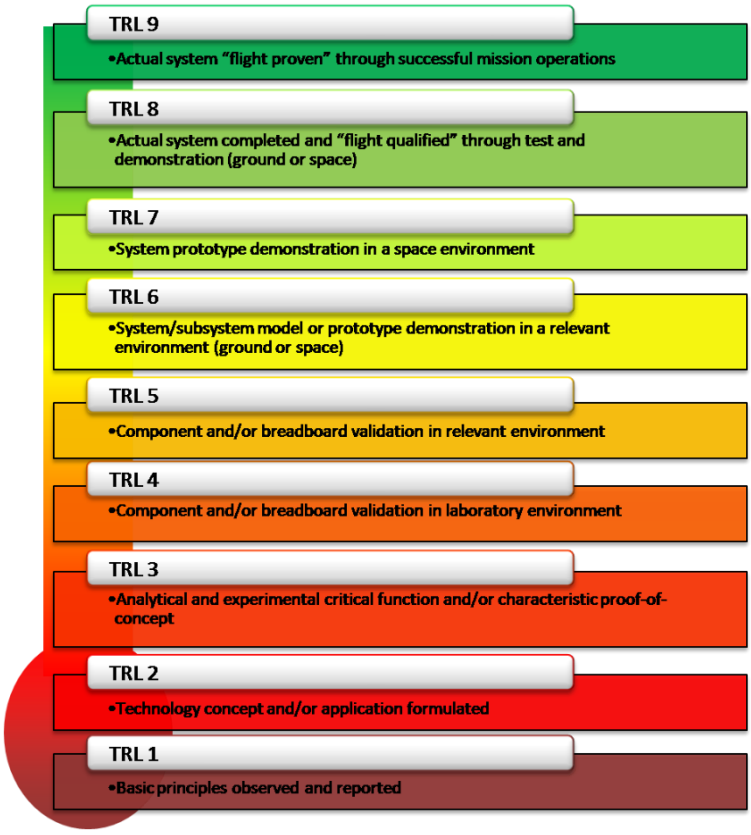

Figure 9: Technology readiness level (TRL) ladder defined by NASA to assess maturity of technology

in scientific literature. The model development contributes two-fold to the overall effort: system level design architecture and high-fidelity dynamic state prediction. Transitioning the system design to physical test articles, Chapter 3 begins with a description a proof-of-concept experiment to fulfill TRL 3. The chapter continues with a progression of more representative testbeds, which mature the hardware technology from a laboratory environment, TRL 4, to a relevant environment, TRL 5. The testbed experiments produce a wealth of data that is used to mature the dynamics model. Chapter 4 analyzes the experiment data with a suite of system identification methods in hopes of generating precise state predictions from a representative dynamics model, the criteria for achieving TRL 6. Chapter 5 extends machine learning techniques further than offline system identification to real-time and more interpretable system identification. Chapter 6 summarizes the overall contributions from this body of work, suggesting a research path forward to bring this technology ever closer to impacting the way humans explore space.

CHAPTER 2: Flux-Pinning Dynamics

Flux-pinned technology is driven by the underlying dynamic behavior, which exhibits nonlinearities and coupled dynamics. This chapter establishes the basis for simulating flux-pinned dynamics with a physics-based model, building upon electromagnetism theory and rigid-body dynamics. From the baseline dynamics model, a potential energy landscape derivation yields intuition as to the stability and energetic movement of an object in space. Another result from the baseline model is the linearized dynamics derivation, which informs control design and offers sensitivity to state perturbation. To refine the dynamics model, a central assumption from the baseline dynamics model is tested in an experiment measuring the variation in amount of embedded magnetic flux due to field-cooling separation distance. Further efforts in refining the dynamics model include a comprehensive literature review of physical parameters that affect flux-pinning interactions, which capture higher-order effects not encapsulated in the baseline model. This chapter closes with the application of potential energy in conjunction with the full dynamics model to formulate a formal method reporting backwards reachability without requiring dynamic prediction. With the incorporation of experiment data from Chapter 3, the full dynamics model may be refined and produce a high-fidelity predictive dynamics model, discussed in Chapter 4.

I. Flux-Pinning Theoretical Dynamics Model

The critical state model and the advanced frozen-image model are two conventional methods of modeling magnetization behavior for a system of magnets and type–II superconductors. Both models macroscopically represent changes in the superconductor's embedded magnetic field as external field changes but differ in magnetization expression, complexity, and scope of modeling a superconducting system. Valid for an arbitrary superconductor geometry and magnetic field gradient, the critical-state model increases in

accuracy and fidelity as the resolution of magnetization loops is refined, but is also more numerically intensive [91] [92]. Kordyuk's frozen-image model geometrically maps a magnetic field source as a dipole into paramagnetic and diamagnetic image reflected across the superconductor boundary and moving virtually within the superconductor volume for each independent magnet and superconductor interaction [93]. For a system of *M* superconductors and *N* magnets, the critical state model not only compounds across every superconductor and magnet, but also across every mesh node *P* of each object at an order of $\mathcal{O}(MP_M^2N^2P_N^4)$, an immense amount of computation. Kordyuk's two closed-form analytical image representations drastically simplify the macroscopic behavior, especially for a system of multiple magnets and superconductors, computing processes at an order of $\mathcal{O}(MN^2)$. The computational intensity of the critical-state model is restrictive for real-time applications and systems of many magnets and superconductors. Whereas, the frozen-image model is simple enough to simulate real-time dynamics, which have natural modes as fast as hundreds of Hertz. The trade-off in simplicity permeates into assumptions about the superconducting system, which reduces the model's fidelity.

The frozen-image model omits the effects from physical parameters like temperature, material, and geometry, but they may be accounted for in a modified frozen-image model [94]. For simplicity, the following assumptions are made. Critical current density is assumed to be infinite. For familiar problems, this limitation has no practical effect. The induced magnetic field is greater than the first critical magnetic field− again, an issue that rarely arises in practical applications. The temperature is low enough that scaling and hysteretic effects are negligible, although Yang offers a method to incorporate elastic hysteresis [95]. These assumptions, as well as the previous ones, are readily accommodated in systems designed for analyzability. Kordyuk's

model and the magnetic-dipole model provide the foundation for many subsequent analytical assessments of flux-pinned dynamics and is the basis for the rest of this paper [96], [97].

Kordyuk created an analytical model to explain image effects of flux pinning, known as the frozen-image model [93]. Kordyuk's geometric relation between magnet parameters and image parameters is graphically depicted in Figure 10. Other authors (Alqadi [98], Cansiz [99], Suguira [100], etc.) have written primarily about finding the potential fields of magnet/superconductor arrangements or the equilibria of magnet/superconductor arrangements in three or less degrees of freedom. This section derives the most general case in six degrees of freedom by reviewing magnetic field sources, relating Kordyuk's frozen-image model, applying Villani's magnetic-dipole model, and tying all components together with a rigid-body dynamics model.

a. *Magnetic Field Sources*

The general expression for magnetic field strength at distance $\boldsymbol{\rho}$ from the field source is given in Eq. (1) [10]. $\boldsymbol{m}$ is the magnetic moment of the dipole of interest. From Eq. (1), the magnetic field strength decreases with distance cubed. The expression for magnetic field strength can be related to a flux-pinned mobile image, flux-pinned frozen image, electromagnet, or permanent magnet. The magnetic field is a function of two variables: $\boldsymbol{m}$ the magnetic-moment dipole and $\boldsymbol{\rho}$ the distance from the field source. $\boldsymbol{m}$ is a parameter determined by the physical nature of the source. $\boldsymbol{\rho}$ can be defined or measured in the physical system. The expression for magnetic-moment dipoles differs for each type magnetic field source.

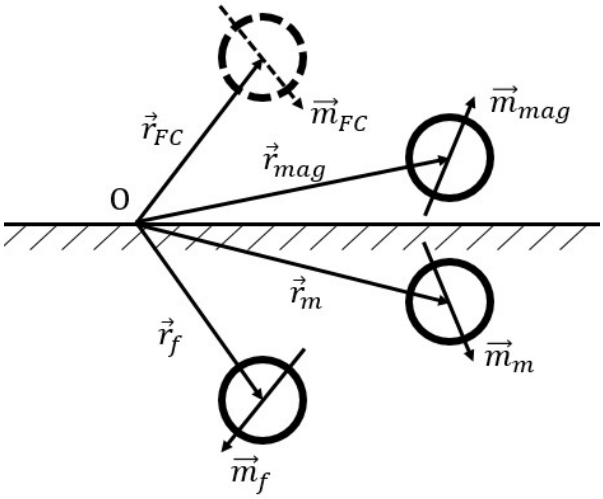

Figure 10: Geometric relationship between the equilibrium, frozen image, mobile image, superconductor and magnet. [4]

$$\boldsymbol{B}(\boldsymbol{\rho}) = \frac{\mu_0}{4\pi|\boldsymbol{\rho}|^3}(3(\boldsymbol{m}\cdot\hat{\boldsymbol{\rho}})\hat{\boldsymbol{\rho}} - \hat{\boldsymbol{m}}) \quad (1)$$

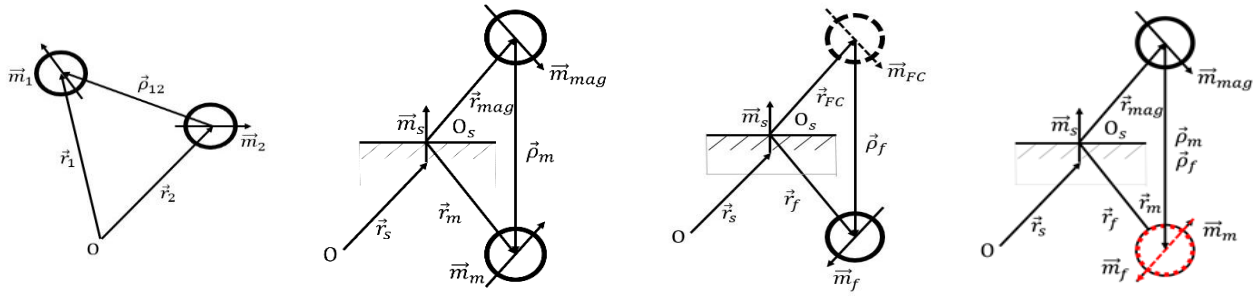

Figure 11: Different types of magnetic field interactions.
(a) Geometric representation of permanent magnet or electromagnet magnetic field source positions.
(b) Geometric representation of mobile image magnetic field source positions.
(c) Geometric representation of frozen image magnetic field source positions.
(d) Geometric representation of frozen image and mobile image overlaid at field-cooled position.

Physical Magnet

There are two types of physical magnetic field sources: permanent magnets and electromagnets. The magnetic-moment dipole of a permanent magnet is purely defined by physical characteristics in Eq. (2). The manufacturer's measurement of the magnetic field at the surface of the magnet is B_0. The distance from the center of dipole to the surface is d. The unit direction of the magnetic-moment dipole is $\hat{\boldsymbol{m}}_{\boldsymbol{p}}$. The electromagnetic-moment dipole is represented by Eq. (3), where V (t) is the voltage potential of the electromagnet, A is the area enclosed by the electromagnet's coil of wire, T is the number of turns of the electromagnet, and R is the resistance of the electromagnet. Besides their physical differences, they mathematically represent a physical magnetic-moment dipole $\boldsymbol{m}_{\boldsymbol{p}}$. For a graphic depiction of how to relate the variables, refer to Figure 3.a. The two physical sources of magnetic field differ in the physical parameters that make up the magnetic-moment dipole expression.

$$\boldsymbol{m}_{\boldsymbol{p}} = \frac{2\pi B_0 d^3}{\mu_0}\hat{\boldsymbol{m}}_{\boldsymbol{p}} \quad (2)$$

$$\boldsymbol{m}_{\boldsymbol{E}} = \frac{VAT}{R}\hat{\boldsymbol{m}}_{\boldsymbol{E}} \quad (3)$$

b. *Kordyuk's Frozen-Image model*

This subsection follows Kordyuk's derivation of the frozen-image model and test the assumptions laid out in his derivation. Once a type-II superconductor is cooled below its critical temperature, Kordyuk's model creates two images: the frozen image and the mobile image. For a magnet field-cooled with initial position $\boldsymbol{r_{FC}}$ and magnetic moment $\boldsymbol{m_{FC}}$, the frozen image position is $\boldsymbol{r_f}$ and magnetic moment $\boldsymbol{m_f}$, as shown in Figure 12. The frozen image remains static while the mobile image moves with its magnetic field source, reflecting in both position and orientation across the superconductor surface. $\boldsymbol{\rho_m}$ is the distance between the corresponding mobile image and magnet, $\boldsymbol{\rho_f}$ the frozen image to magnet. The following equations form the basis of the frozen-image model, maintaining the external magnetic field gradient in the presence of disturbances.

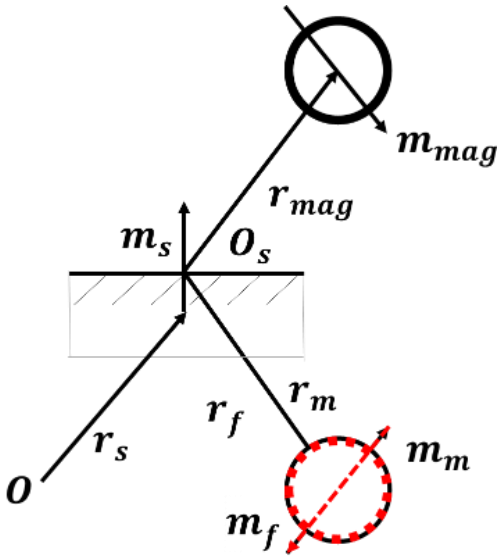

Figure 12: Geometric relationship of frozen image, mobile image, superconductor and magnet in equilibrium, in which $r_{mag} = r_{FC}$ and $m_{mag} = m_{FC}$ [2].

$$\boldsymbol{H_z(\rho - r_{FC}, m_{FC}) = H_z(\rho - r_f, -m_f)} \tag{3}$$

$$\boldsymbol{H_z(\rho - r_{mag}, m_{mag}) + H_z(\rho - r_m, -m_m) = 0} \tag{4}$$

The external magnetic field $\boldsymbol{H_z}$ of the permanent magnet is equivalent to the internal magnetic field of the frozen image within the superconductor upon the process of field-cooling a frozen image into the superconductor, as shown in Eq. (3). The magnetic field contribution $\boldsymbol{H_z}$ from both the magnet and mobile image sum to no net magnetic field disturbance, represented by

Eq. (4). These equations form the basis for dynamics derivations and carry a series of fundamental assumptions that are discussed below.

Mobile/Diamagnetic Image

All superconductors display the Meissner effect, which is the expulsion of magnetic flux. The magnetic source that creates the Meissner effect may be represented as an image within the superconductor that changes polarity and magnitude to always repel. That image, more specifically, follows the external magnetic source and reorients to the moment dipole to mirror the external magnetic source. The mobile image's magnetic-moment dipole depends on the permanent magnet's moment dipole and the orientation of the superconductor, given by Eq. (6). $\boldsymbol{m_{mag}}$ is the vector from Eq. (2) or Eq. (3) that represents the physical magnet's moment dipole. $\hat{\boldsymbol{m}}_{\boldsymbol{s}}$ is the unit direction normal to the surface of the superconductor, illustrated by Figure 11.b. The mobile image moves when the permanent magnet moves. The location of the magnetic field from the mobile image is dynamic. $\boldsymbol{r_{mag}}$ and $\boldsymbol{r_m}$ change in the expression for magnetic field and potential energy. The magnetic field of the magnet's mobile image from Figure 11.b is given by Eq. (7), where $\boldsymbol{\rho_m}$ is the distance from the mobile image to the permanent magnet. That distance is given by Eq. (8), where $\boldsymbol{r_m}$ is the location of the mobile image and $\boldsymbol{O_s}$ is a point on the superconductor surface. The mobile image's magnetic-moment dipole location and orientation are dependent on the superconductor's geometry.

In an ideal superconductor, the mobile image exactly compensates for a change in magnetic field, the source magnet. The ideal superconductor expels all disturbances, but for a real superconductor, the magnetic field may penetrate through the superconductor boundary, implying that the right side of Eq. (2) is nonzero. The mobile image is defined by the source magnet's state

and is affected by the same geometric parameters: relative geometry, the magnet source's relative position, and orientation. The source magnet may also generate a mobile image of differing strength upon approach and exit but does not permanently change the system, a manifestation of elastic magnetic hysteresis [101] [95] [102]. The source magnet may permanently change the embedded magnetic field after field-cooling in a process called flux creep or plastic magnetic hysteresis [18], [103] [104]. Analogously, Eq. (2) does not address these effects on the mobile image.

$$\boldsymbol{m_m} = \left(\underline{1} - 2\hat{\boldsymbol{m}}_s \otimes \hat{\boldsymbol{m}}_s\right)\boldsymbol{m_{mag}} \tag{6}$$

$$\boldsymbol{\rho_m} = \boldsymbol{r_{mag}} - \boldsymbol{r_m} \tag{7}$$

$$\boldsymbol{r_m} = \boldsymbol{r_{mag}} - \mathbf{2}\left(\left(\boldsymbol{r_{mag}} - \boldsymbol{O}_s\right) \cdot \hat{\boldsymbol{m}}_s\right)\hat{\boldsymbol{m}}_s \tag{8}$$

Frozen/Paramagnetic Image

The frozen image is an image specific to high-temperature or Type-II superconductors. Instead of expelling all magnetic flux like Type-I superconductors do, Type-II superconductors field-cool a magnetic field during a transition phase and expel external fields that differ from the embedded field. This property allows for the stable presence of a field, in this application, infinitesimal magnetic dipole. The frozen image is a consequence of the presence of an infinitesimal magnetic dipole *a priori* and *a posteriori* cryocooling, which embeds a field in the superconductor that enforces restoration to this initial state. To counter the mobile image's repulsion, the frozen image acts as an attractive infinitesimal magnetic dipole that stays in place and aligns magnetic-moment dipoles with the field-cooled magnet. The frozen image's magnetic-moment dipole depends on the magnet-moment dipole field-cooled onto the superconductor and the orientation of the superconductor, as shown in Eq. (9) and geometrically in Figure 11.c.

Equation (10) and (11) are analogous to the frozen-image distance vectors. Like the mobile image, the frozen image is dependent on the superconductor's geometry but, unlike the mobile image, does not move when the permanent magnet moves after field-cooling.

The frozen-image magnetic-moment dipole is defined by the field-cooled magnet's position and strength in which important geometric parameters are not included. Eq. (1) assumes the frozen-image dipole is of the same strength as the magnet dipole field-cooled to the superconductor, a one-to-one mapping. A comparable representation of the magnetization behavior is the percentage of total magnetic flux from the source dipole penetrating the volume of the superconductor. The relative size of the magnet and superconductor scales the percentage of flux captured in the superconductor [105]. The embedded magnetic field is agnostic to the location of the field-cooled magnet, which is valid for an infinite plane, but invalid for a superconductor of finite surface [106]. The magnet's location relative to the superconductor surface also determines the strength of the frozen image. Eq. (1) does not address any of these effects on the frozen image.

$$\boldsymbol{m_f} = \left(2\hat{\boldsymbol{m}}_s \otimes \hat{\boldsymbol{m}}_s - \underline{\mathbf{1}}\right)\boldsymbol{m_{mag}} \tag{9}$$

$$\boldsymbol{\rho_f} = \boldsymbol{r_{FC}} - \boldsymbol{r_f} \tag{10}$$

$$\boldsymbol{r_f} = \boldsymbol{r_{FC}} - 2\left((\boldsymbol{r_{FC}} - \boldsymbol{O_s}) \cdot \hat{\boldsymbol{m}}_s\right)\hat{\boldsymbol{m}}_s \tag{11}$$

Outside the fundamental physics, the explicit geometric expressions also carry underlying assumptions. Equations (6) to (11) formalize both images' magnetic-moment dipoles as a geometric function of position and orientation of both the source magnet and superconductor, depicted geometrically in Figure 12. Subscript $\boldsymbol{m}$ and $\boldsymbol{f}$ correspond to the mobile image and frozen image, respectively. The unit direction normal to the surface of the superconductor is $\hat{\boldsymbol{m}}_s$. The distance from the images to the source magnet are $\boldsymbol{\rho_f}$ and $\boldsymbol{\rho_m}$, where $\boldsymbol{r_f}$ and $\boldsymbol{r_m}$ are the location

of the image and $\boldsymbol{O_s}$ is an arbitrary point on the superconductor surface. This formulation assumes that the strength, orientation, and location of the frozen image map one-to-one with the field-cooled magnet and remain fixed. Many of the same assumptions from Eq. (1) apply to Eq. (6) and Eq. (9).

In these equations, the superconductor orientation and location relate explicitly to the image definition. The direction normal to the superconductor surface is $\hat{\boldsymbol{m}}_{\boldsymbol{s}}$ in Eq. (3) and (4). Kordyuk assumes that the superconductor plane is flat, without manufacturer defects, and of single domain [107], [108]. On an infinite-superconductor plane, $\boldsymbol{O_s}$ serves as a reference point that is arbitrarily placed. This reference point must be strategically placed on a finite surface of the superconductor due to the reference point's effect on representing total flux captured in the superconductor volume. The full geometric definition of the images is then used in the governing equations of motion.

c. *Villani's Magnetic-Dipole model*

Villani derived the force of a magnetic dipole $\boldsymbol{m_b}$ acting on another magnetic dipole $\boldsymbol{m_a}$ at distance $\boldsymbol{\rho}$, given by Eq. (12) in which the scalars are brought out front and all vectors are unit direction vectors [4]. The moment/torque of a magnetic dipole $\boldsymbol{m_b}$ acting on another magnetic dipole $\boldsymbol{m_a}$ at distance $\boldsymbol{\rho}$ is given by Eq. (13), also derived by Villani [5]. The total force from a flux-pinned interaction is the superposition of the mobile-image force and frozen-image force.

$$\boldsymbol{F_{ab}} = \frac{3\mu_0 m_a m_b}{4\pi\rho^4}\Big((\hat{\boldsymbol{\rho}} \times \hat{\boldsymbol{m}}_{\boldsymbol{a}}) \times \hat{\boldsymbol{m}}_{\boldsymbol{b}} + (\hat{\boldsymbol{\rho}} \times \hat{\boldsymbol{m}}_{\boldsymbol{b}}) \times \hat{\boldsymbol{m}}_{\boldsymbol{a}} - 2\hat{\boldsymbol{\rho}}(\hat{\boldsymbol{m}}_{\boldsymbol{a}} \cdot \hat{\boldsymbol{m}}_{\boldsymbol{b}}) + 5\hat{\boldsymbol{\rho}}\big((\hat{\boldsymbol{\rho}} \times \hat{\boldsymbol{m}}_{\boldsymbol{a}}) \cdot (\hat{\boldsymbol{\rho}} \times \hat{\boldsymbol{m}}_{\boldsymbol{b}})\big)\Big) \quad (12)$$

$$\boldsymbol{\tau_{ab}} = \frac{\mu_0 m_a m_b}{4\pi\rho^3}\big(3(\hat{\boldsymbol{m}}_{\boldsymbol{a}} \cdot \hat{\boldsymbol{\rho}})(\hat{\boldsymbol{m}}_{\boldsymbol{b}} \times \hat{\boldsymbol{\rho}}) + (\hat{\boldsymbol{m}}_{\boldsymbol{a}} \times \hat{\boldsymbol{m}}_{\boldsymbol{b}})\big) \quad (13)$$

For a system of *M* rigidly constrained magnets on a rigid body with each magnet flux-pinned to *N* fixed superconductors, each superconductor stores *M* frozen images. The system of

permanent magnets is influenced by each N^{th} superconductor's embedded images in which each superconductor holds M frozen images, totaling $M \times N$ frozen images. An equal number of mobile images pair with the frozen image counterparts, yielding a total $2 \times M \times N$ images that generate forces and torques. Assuming the magnets are rigidly mounted together, the summation of the forces on each magnet yields the total force on the rigid body at its center of mass.

A single flux-pinned interaction happens between magnet *i* and magnet *j*'s images in which magnet j produces a frozen and mobile image on superconductor k, given by (14) and shown in Figure 13. Magnet *j* produces frozen and mobile images on multiple superconductors, which all affect magnet *i*. The total contribution of magnet *j*'s images onto magnet *i* is the summation of all individual flux-pinned interactions between magnet *i* and *j* across all superconductors, given by (15). The total force on magnet *i* from all magnet images is the sum of all magnet *j* influences across all superconductors, given by (16). The total force on a rigid body is the summation of total force on each magnet *i*, given by (17).

The torque is similar to the force summation with an extra term attributed to force with a moment arm on magnet *i*, given by (18). The total torque on a rigid body is analogous to the total force equation but also includes a torque from each force displaced from the center of mass, given by (19). These two summation equations can be rearranged into a set of linear equations with the same

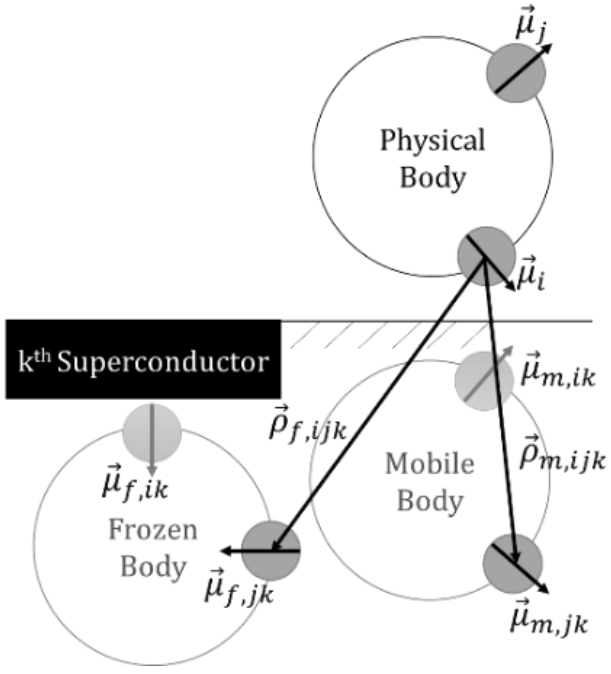

Figure 13: Frozen and mobile image from magnet j acting on magnet i across superconductor k

linearization techniques from the single-magnet single-superconductor case.

$$\boldsymbol{F_{ijk}} = \boldsymbol{F_{frozen}} + \boldsymbol{F_{mobile}} \tag{14}$$

$$\boldsymbol{F_{ij}} = \sum_{k=1}^{M} \left(\boldsymbol{F_{frozen}} + \boldsymbol{F_{mobile}}\right)_k \tag{15}$$

$$\boldsymbol{F_{i}} = \sum_{j=1}^{N} \sum_{k=1}^{M} \left(\left(\boldsymbol{F_{frozen}} + \boldsymbol{F_{mobile}}\right)_k\right)_j \tag{16}$$

$$\boldsymbol{F_{COM}} = \sum_{i=1}^{N} \sum_{j=1}^{N} \sum_{k=1}^{M} \left(\left(\left(\boldsymbol{F_{frozen}} + \boldsymbol{F_{mobile}}\right)_k\right)_j\right)_i \tag{17}$$

$$\boldsymbol{\tau_{i}} = \sum_{j=1}^{N} \sum_{k=1}^{M} \left(\left(\boldsymbol{\tau_{frozen}} + \boldsymbol{\tau_{mobile}}\right)_k\right)_j + \boldsymbol{\rho_i} \times \boldsymbol{F_i} \tag{18}$$

$$\boldsymbol{\tau_{COM}} = \sum_{i=1}^{N} \sum_{j=1}^{N} \sum_{k=1}^{M} \left(\left(\left(\boldsymbol{\tau_{frozen}} + \boldsymbol{\tau_{mobile}}\right)_k\right)_j\right)_i + \sum_{i=1}^{M} \boldsymbol{\rho_i} \times \boldsymbol{F_i} \tag{19}$$

d. *Rigid-Body Dynamics Model*

For the case of a single-magnet and single-superconductor, the magnet's dynamics are due to the forces and torques from the frozen and mobile image. In this single-magnet case, there are two magnet-moment dipoles exerting forces and torques on the magnet. The force and torque equations are given in Eq. (20) and (21). The translational dynamics of the flux-pinned magnet is a result of the force-balance equation, Eq. (23). Newton's linear-momentum balance, given by Eq. (24), in matrix form can be easily inserted into a state space form later. Euler's rigid-body equation, Eq. (25), propagates attitude dynamics. The linearized version of the rigid body equations is given by Eq. (26). Equation (27) simplifies to no longer include gyroscopic dynamics because the magnitude of angular velocity at equilibrium is 0. The orientation of the magnet may be represented by an Euler axis-angle, Eq. (28), and alternatively by a quaternion, Eq. (29). In this case, the Euler axis is the magnetic-moment dipole unit vector and the angle may be chosen to be π because the magnet is axisymmetric. Choosing π retains the most information about the magnetic-moment dipole pointing vector. Upon inspection, the fourth component of the quaternion

about equilibrium is always zero, thus no information is lost if the quaternion state vector is shortened to just the vector components, q_v. To propagate the attitude dynamics, there is a linear relationship between the quaternion and angular velocity that yields the quaternion derivative, given by Eq. (29). This set of equations fully defines the linearized dynamics of a rigid body.

$$\sum \boldsymbol{F} = \boldsymbol{F_f} + \boldsymbol{F_m} \tag{20}$$

$$\sum \boldsymbol{\tau} = \boldsymbol{\tau_f} + \boldsymbol{\tau_m} \tag{21}$$

$$\sum \boldsymbol{F} = M\ddot{\boldsymbol{r}} \tag{22}$$

$$\delta\ddot{\boldsymbol{r}} = M^{-1}\delta\boldsymbol{F_{tot}} \tag{23}$$

$$\boldsymbol{\tau} = I \cdot \dot{\boldsymbol{\omega}} + \boldsymbol{\omega} \times (I \cdot \boldsymbol{\omega}) \tag{24}$$

$$\delta\dot{\omega} = I^{-1}(\omega_e^{\times} I - (I\omega_e)^{\times})\delta\omega + I^{-1}\tau \tag{25}$$

$$\delta\dot{\omega} = I^{-1}\delta\tau \tag{26}$$

$$\delta\boldsymbol{m} = \theta\delta\hat{\boldsymbol{m}} \tag{27}$$

$$\delta q = \begin{bmatrix} \delta\hat{m}\sin\left(\frac{\theta}{2}\right) \\ \cos\left(\frac{\theta}{2}\right) \end{bmatrix} \tag{28}$$

$$\delta\dot{q}_v = \frac{1}{2} q_{ve} \times \delta\omega \tag{29}$$

II. Equilibria of General Flux-Pinned Interfaces

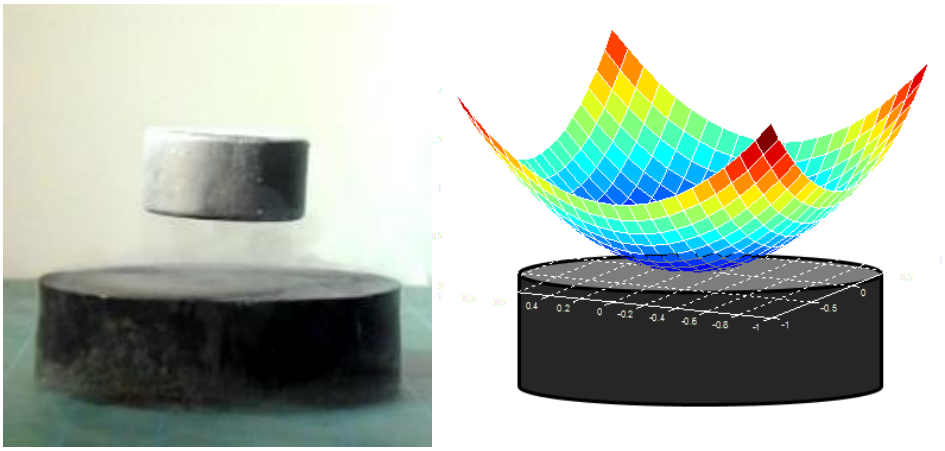

Figure 14: Left: cylindrical magnet in equilibrium position and attitude above superconductor; Right: conceptual magnetic potential well generated by superconductor mapped in two directions of translation

A physical magnet-superconductor system is stable through a flux-pinned joint in equilibrium, conceptualized by a magnetic potential well generated by the flux-pinned superconductor, depicted in Figure 14. A magnet in proximity to this potential well is driven to the minimum energy state, the equilibrium state. This section derives the potential energy for a magnetic dipole subject to an external magnetic field, resolves an expression for the location of equilibria, and the subsequent stability of these equilibria points.

a. Potential Energy Derivation

A magnet's potential energy topography of an external magnetic field affects the passive dynamics of the magnet of interest and provides insight into the stability of the system. The potential energy of the magnetic dipole $\boldsymbol{m_i}$ under the influence of *n* magnetic fields is given by Eq. (30), where $\boldsymbol{r_i}$ is the position of the magnetic-moment dipole of interest. $\boldsymbol{B_{tot}}$ is the summation of all external magnetic field sources acting on magnet *i*. U_i is the potential energy of the magnetic-moment dipole of interest at $\boldsymbol{r_i}$. Index *j* represent all permanent magnets, electromagnets, mobile images, and frozen images for $j \neq i$. Eq. (30) holds true for all the magnetic field sources except mobile image sources. The mobile image's potential energy is half of the general form for magnetic potential energy given in Eq. (30). The potential energy of the magnetic dipole $\boldsymbol{m_i}$ may also be expressed as a summation of individual potential energies given by Eq. (31), where $\sum_{j=1}^{n} U_j(\boldsymbol{r_{ij}})$ is the summation of all expressions for potential energy for the different magnetic sources, such as Eq. (32) for a permanent magnet or electromagnet, Eq. (33) for a mobile image, and Eq. (34) for a frozen image. All external magnetic fields must be accounted for in the general summation.

$$U_i(\boldsymbol{r_i}) = -\boldsymbol{m_i} \cdot \boldsymbol{B_{tot}}(\boldsymbol{\rho_{ij}}) = -\boldsymbol{m_i} \cdot \sum_{j=1}^{n} \boldsymbol{B_j}(\boldsymbol{\rho_{ij}}) \tag{30}$$

$$U_i(\boldsymbol{r_i}) = \sum_{j=1}^{n} U_j(\boldsymbol{r_{ij}}) = \sum_{jp=1}^{np} U_{jp}(\boldsymbol{r_{ijp}}) + \sum_{jm=1}^{nm} U_{jm}(\boldsymbol{r_{ijm}}) + \sum_{jf=1}^{nf} U_{jf}(\boldsymbol{r_{ijf}}) \quad (31)$$

$$U_{jp}(\boldsymbol{r_i}) = -\boldsymbol{m_i} \cdot \boldsymbol{B_p}(\boldsymbol{\rho_p}) \quad (32)$$

$$U_{jm}(\boldsymbol{r_i}) = -\boldsymbol{m_i} \cdot \frac{1}{2}\boldsymbol{B_m}(\boldsymbol{\rho_m}) \quad (33)$$

$$U_{iFC}(\boldsymbol{r}) = -\boldsymbol{m_i} \cdot \boldsymbol{B_{FC}}(\boldsymbol{\rho_f}) \quad (34)$$

b. Local Extrema of Potential Energy Topography

The local extrema are locations of relative stability or instability. The local extrema positions are calculated by taking the derivative of the potential energy topography with respect to location, given by Eq. (35). The derivative of the potential energy topography is given by Eq. (36). Since the magnetic-moment dipole does not change as a function of location, the expression simplifies to the expression in Eq. (37). The equilibrium position must be represented by three generalized coordinates, q_i. The critical points or local extrema are at the positions where the partial derivatives of U in all 3 dimensions are zero, given by Eq. (38). The local extrema locations exist at $\boldsymbol{r_e}$, the values that cause the partial derivatives to equal 0. The local extrema orientation is the orientation of the magnet during field cooling.

$$U(\boldsymbol{r}) = -\boldsymbol{m} \cdot \boldsymbol{B_{tot}}(\boldsymbol{r}) \quad (35)$$

$$\frac{dU(\boldsymbol{r})}{d\boldsymbol{r}} = -\frac{d\boldsymbol{m_i}}{d\boldsymbol{r}} \cdot \boldsymbol{B_{tot}}(\boldsymbol{r}) - \boldsymbol{m_i} \cdot \frac{d\boldsymbol{B_{tot}}(\boldsymbol{r})}{d\boldsymbol{r}} \quad (36)$$

$$\frac{dU(\boldsymbol{r})}{d\boldsymbol{r}} = -\boldsymbol{m_i} \cdot \frac{d\boldsymbol{B_{tot}}(\boldsymbol{r})}{d\boldsymbol{r}} \quad (37)$$

$$0 = \frac{\partial U(\boldsymbol{r})}{\partial q_i} \quad (38)$$

c. Concavity of Potential Energy Gradient

The concavity of the potential energy gradient reveals the stability of the flux-pinned system. The sign of second partial derivative of the potential energy function at that extremum location

determines concavity, whether the extrema is a minimum, maximum, or saddle point. $\frac{\partial U(\boldsymbol{r_e})}{\partial q_i}$ reveals the concavity of the topography where $\boldsymbol{r_e}$ is the equilibrium position. If all three derivatives are positive, the extrema are concave up and a local minimum. Such an equilibrium is stable. If all three derivatives are negative, the extrema are concave down and a local maximum. This would be considered an unstable equilibrium. If the three derivatives are not all negative or positive, the extremum is a saddle point in which it is stable in some directional disturbances but unstable in other directions.

III. Linearized Dynamics of General Flux-Pinned Interfaces

This section derives the six degree-of-freedom linear dynamics about an equilibrium for any magnet/superconductor configuration. Linearized dynamics are well-suited to predicting close-proximity maneuvers, provide insights into the character of the dynamic system, and are essential for linear control synthesis. Kordyuk's frozen-image model and Villani's magnetic-dipole model provides the nonlinear flux-pinning response to these magnetic forces and torques, which are then linearized. Comparing simulation results of the nonlinear and linear dynamics shows the extent of the linear model's applicability. Nevertheless, these simple models offer computational speed and physical intuition that a nonlinear model does not.

a. Single Flux-Pinned Magnet and Superconductor Interaction

The linearized dynamics for the simplest flux-pinned interface is derived. The dynamics are solely dependent on the magnetic field source's position and orientation, along with physical parameters specific to the system geometry. Each subsection describes the linearization process briefly before presenting the final linearized equation set.

Linearizing General Magnetic Dipole Force and Torque Equations

Villani derived the force of a magnetic dipole $\boldsymbol{m_b}$ acting on another magnetic dipole $\boldsymbol{m_a}$ at distance $\boldsymbol{\rho}$, reiterated in Eq. (39) in which the scalars are brought out front and all vectors are unit direction vectors [4]. The final linearized force equation relates the first order terms $\delta\boldsymbol{F_{ab}}$ to $\delta\boldsymbol{r}, \delta\boldsymbol{m_a}$, and $\delta\boldsymbol{m_b}$, all vectors denoting deviation from equilibrium. To linearize about $\boldsymbol{\rho_e}$, $\boldsymbol{m_{ae}}$, and $\boldsymbol{m_{be}}$, a first order Taylor expansion was taken of (39) by replacing $\boldsymbol{F_{ab}} = \boldsymbol{F_e} + \delta\boldsymbol{F_{ab}}$, $\boldsymbol{\rho} = \boldsymbol{\rho_e} + \delta\boldsymbol{r}$, $\boldsymbol{m_a} = \boldsymbol{m_{ae}} + \delta\boldsymbol{m_a}$, $\boldsymbol{m_b} = \boldsymbol{m_{be}} + \delta\boldsymbol{m_b}$. The equilibrium force is subtracted from both sides. The cross products and dot products are replaced with cross and transpose operators ($v\times$ to $v^{\times}, v\cdot$ to v^{T}), then rearranged to isolate the first order terms. To transform the linear equation to matrix form, notice that the quantities in front of $\delta\boldsymbol{r}, \delta\boldsymbol{m_a}$, and $\delta\boldsymbol{m_b}$ are 3x3 matrices. The final matrix expression for linearized force between two magnetic-moment dipoles is given in Eq. (40). The moment/torque of a magnetic dipole $\boldsymbol{m_b}$ acting on another magnetic dipole $\boldsymbol{m_a}$ at distance $\boldsymbol{\rho}$ is reiterated by Eq. (41), also derived by Villani [5]. The same process of linearization is applied to Villani's moment equation to yield Eq. (42). All intermediate steps are listed in Appendix II.

$$\boldsymbol{F_{ab}} = \frac{3\mu_0 m_a m_b}{4\pi\rho^4}\Big((\hat{\boldsymbol{\rho}}\times\hat{\boldsymbol{m}}_{\boldsymbol{a}})\times\hat{\boldsymbol{m}}_{\boldsymbol{b}} + (\hat{\boldsymbol{\rho}}\times\hat{\boldsymbol{m}}_{\boldsymbol{b}})\times\hat{\boldsymbol{m}}_{\boldsymbol{a}} - 2\hat{\boldsymbol{\rho}}(\hat{\boldsymbol{m}}_{\boldsymbol{a}}\cdot\hat{\boldsymbol{m}}_{\boldsymbol{b}}) + 5\hat{\boldsymbol{\rho}}\big((\hat{\boldsymbol{\rho}}\times\hat{\boldsymbol{m}}_{\boldsymbol{a}})\cdot(\hat{\boldsymbol{\rho}}\times\hat{\boldsymbol{m}}_{\boldsymbol{b}})\big)\Big) \quad (39)$$

$$\delta\boldsymbol{F_{ab}} = \frac{3\mu_0}{4\pi|\rho_e|^5}\begin{bmatrix} m_{be}^{\times}m_{ae}^{\times} + m_{ae}^{\times}m_{be}^{\times} - 2m_{ae}^{T}m_{be}\underline{1} - \frac{5}{|\rho_e|^2}(\rho_e(\rho_e^{\times}m_{be})^{T}m_{ae}^{\times} - \rho_e(\rho_e^{\times}m_{ae})^{T}m_{be}^{\times}) + \cdots \\ -\frac{5}{|\rho_e|^2}\Big((\rho_e^{\times}m_{ae})^{\times}m_{be} + (\rho_e^{\times}m_{be})^{\times}m_{ae} - 2(m_{ae}^{T}m_{be})\rho_e + \frac{5}{|\rho_e|^2}\big((\rho_e^{\times}m_{ae})^{T}(\rho_e^{\times}m_{be})\big)\rho_e^{T}\Big) \\ -m_{be}^{\times}\rho_e^{\times} + (\rho_e^{\times}m_{be})^{\times} - 2\rho_e m_{be}^{T} + \frac{5}{|\rho_e|^2}\rho_e(\rho_e^{\times}m_{be})^{T}\rho_e^{\times} \\ (\rho_e m_{ae})^{\times} - m_{ae}^{\times}\rho_e^{\times} - 2\rho_e m_{ae}^{T} + \frac{5}{|\rho_e|^2}\rho_e(\rho_e^{\times}m_{ae})^{T}\rho_e^{\times} \end{bmatrix}^{T}\begin{bmatrix}\delta\boldsymbol{r}\\ \delta\boldsymbol{m_a}\\ \delta\boldsymbol{m_b}\end{bmatrix}$$

(40)

$$\boldsymbol{\tau_{ab}} = \frac{\mu_0 m_a m_b}{4\pi\rho^3}\big(3(\hat{\boldsymbol{m}}_{\boldsymbol{a}}\cdot\hat{\boldsymbol{\rho}})(\hat{\boldsymbol{m}}_{\boldsymbol{b}}\times\hat{\boldsymbol{\rho}}) + (\hat{\boldsymbol{m}}_{\boldsymbol{a}}\times\hat{\boldsymbol{m}}_{\boldsymbol{b}})\big) \quad (41)$$

$$\delta\boldsymbol{\tau_{ab}} = \frac{\mu_0}{4\pi|\rho_e|^3}\begin{bmatrix} \frac{3}{|\rho_e|^2}\left(m_{ae}^T\rho_e m_{be}^\times + m_{be}^T\rho_e m_{ae}^\times - \left(\frac{3}{|\rho_e|^2}m_{ae}^T\rho_e m_{be}^\times\rho_e + m_{ae}^\times m_{be}\right)\rho_e^T\right) \\ \frac{3}{|\rho_e|^2}m_{be}^\times\rho_e\rho_e^T - m_{be}^\times \\ -\frac{3}{|\rho_e|^2}m_{ae}^\times\rho_e\rho_e^T - m_{ae}^\times \end{bmatrix}^T \begin{bmatrix} \delta\boldsymbol{r} \\ \delta\boldsymbol{m_a} \\ \delta\boldsymbol{m_b} \end{bmatrix} \quad (42)$$

Linearized Forces and Torques for Flux-Pinned Forces and Torques

The total force from a flux-pinned interaction is the superposition of the mobile-image force and frozen-image force. These images are magnetic field sources that impart linearized forces given by (40). The frozen-image force is found by substituting $\boldsymbol{m_{ae}}$ to $\boldsymbol{m_e}$ the magnet's equilibrium magnetic-moment dipole, and $\boldsymbol{m_{be}}$ to $\boldsymbol{m_{fe}}$ the frozen image's equilibrium magnetic-moment dipole into (40). The frozen image never changes in orientation, thus $\delta\boldsymbol{m_f} = 0$. The linearized force from the frozen image is given by (43). The mobile-image force, given by (16), is similarly found by substituting $\boldsymbol{m_{ae}}$ to $\boldsymbol{m_e}$ the magnet's equilibrium magnetic-moment dipole, and $\boldsymbol{m_{be}}$ to $\boldsymbol{m_{me}}$ the mobile image's equilibrium magnetic-moment dipole into (40). From Kordyuk's geometric interpretation of the frozen-image model, the mobile image reorients itself like a mirror image across the superconductors surface, where $\widehat{\boldsymbol{m}}_{\boldsymbol{s}}$ is the unit normal to the superconductor's surface given by Eq. (44). A direct relation from $\boldsymbol{m}$ to $\boldsymbol{m_m}$ is given by Eq. (44). This relationship reduces the number of independent state variables. The mobile-image force equation depends only on the magnet's orientation and position, given by (45). The forces from the mobile and frozen image are additive and may be combined to a final equation for force on the system, given by (46). The total force is dependent on the physical magnet's position and orientation, which constitutes the translational dynamic state of the flux-pinned interaction.

$$\delta \boldsymbol{F_f} = \frac{3\mu_0}{4\pi|\rho_e|^5}\begin{bmatrix} m_{fe}^{\times}m_e^{\times} + m_e^{\times}m_{fe}^{\times} - 2m_e^T m_{fe}\underline{1} - \frac{5}{|\rho_e|^2}\left(\rho_e\left(\rho_e^{\times}m_{fe}\right)^T m_e^{\times} - \rho_e(\rho_e^{\times}m_e)^T m_{fe}^{\times}\right) + \cdots \\ -\frac{5}{|\rho_e|^2}\left((\rho_e^{\times}m_e)^{\times}m_{fe} + \left(\rho_e^{\times}m_{fe}\right)^{\times}m_e - 2\left(m_e^T m_{fe}\right)\rho_e + \frac{5}{|\rho_e|^2}\left((\rho_e^{\times}m_e)^T\left(\rho_e^{\times}m_{fe}\right)\right)\rho_e^T\right) \\ -m_{fe}^{\times}\rho_e^{\times} + \left(\rho_e^{\times}m_{fe}\right)^{\times} - 2\rho_e m_{fe}^T + \frac{5}{|\rho_e|^2}\rho_e\left(\rho_e^{\times}m_{fe}\right)^T\rho_e^{\times} \end{bmatrix}^T \begin{bmatrix}\delta\boldsymbol{r}\\ \delta\boldsymbol{m}\end{bmatrix} \quad (43)$$

$$\boldsymbol{m_m} = \left(\underline{1} - 2\widehat{\boldsymbol{m}}_s\widehat{\boldsymbol{m}}_s^T\right)\mathbf{m} \quad (44)$$

$$\delta \boldsymbol{F_m} =$$

$$\frac{3\mu_0}{4\pi|\rho_e|^5}\begin{bmatrix} 2\widehat{m}_s\widehat{m}_s^T(m_{me}^{\times}m_e^{\times} + m_e^{\times}m_{me}^{\times} - 2m_e^T m_{me}\underline{1} - \frac{5}{|\rho_e|^2}(\rho_e(\rho_e^{\times}m_{me})^T m_e^{\times} - \rho_e(\rho_e^{\times}m_e)^T m_{me}^{\times}) + \cdots \\ -\frac{5}{|\rho_e|^2}\left((\rho_e^{\times}m_e)^{\times}m_{me} + (\rho_e^{\times}m_{me})^{\times}m_e - 2(m_e^T m_{me})\rho_e + \frac{5}{|\rho_e|^2}\left((\rho_e^{\times}m_e)^T(\rho_e^{\times}m_{me})\right)\rho_e^T\right) \\ -m_{me}^{\times}\rho_e^{\times} + (\rho_e^{\times}m_{me})^{\times} - 2\rho_e m_{me}^T + \frac{5}{|\rho_e|^2}\rho_e(\rho_e^{\times}m_{me})^T\rho_e^{\times} + \cdots \\ \left(\underline{1} - 2\widehat{m}_s\widehat{m}_s^T\right)\left((\rho_e m_e)^{\times} - m_e^{\times}\rho_e^{\times} - 2\rho_e m_e^T + \frac{5}{|\rho_e|^2}\rho_e(\rho_e^{\times}m_e)^T\rho_e^{\times}\right) \end{bmatrix}^T \begin{bmatrix}\delta\boldsymbol{r}\\ \delta\boldsymbol{m}\end{bmatrix} \quad (45)$$

$$\delta \boldsymbol{F_{tot}} =$$

$$\frac{3\mu_0}{4\pi|\rho_e|^5}\begin{bmatrix} m_{fe}^{\times}m_e^{\times} + m_e^{\times}m_{fe}^{\times} - 2m_e^T m_{fe}\underline{1} - \frac{5}{|\rho_e|^2}\left(\rho_e\left(\rho_e^{\times}m_{fe}\right)^T m_e^{\times} - \rho_e(\rho_e^{\times}m_e)^T m_{fe}^{\times}\right) + \cdots \\ -\frac{5}{|\rho_e|^2}\left((\rho_e^{\times}m_e)^{\times}m_{fe} + \left(\rho_e^{\times}m_{fe}\right)^{\times}m_e - 2\left(m_e^T m_{fe}\right)\rho_e + \frac{5}{|\rho_e|^2}\left((\rho_e^{\times}m_e)^T\left(\rho_e^{\times}m_{fe}\right)\right)\rho_e^T\right) + \cdots \\ 2\widehat{m}_s\widehat{m}_s^T(m_{me}^{\times}m_e^{\times} + m_e^{\times}m_{me}^{\times} - 2m_e^T m_{me}\underline{1} - \frac{5}{|\rho_e|^2}(\rho_e(\rho_e^{\times}m_{me})^T m_e^{\times} - \rho_e(\rho_e^{\times}m_e)^T m_{me}^{\times}) + \cdots \\ -\frac{5}{|\rho_e|^2}\left((\rho_e^{\times}m_e)^{\times}m_{me} + (\rho_e^{\times}m_{me})^{\times}m_e - 2(m_e^T m_{me})\rho_e + \frac{5}{|\rho_e|^2}\left((\rho_e^{\times}m_e)^T(\rho_e^{\times}m_{me})\right)\rho_e^T\right) \\ -m_{fe}^{\times}\rho_e^{\times} + \left(\rho_e^{\times}m_{fe}\right)^{\times} - 2\rho_e m_{fe}^T + \frac{5}{|\rho_e|^2}\rho_e\left(\rho_e^{\times}m_{fe}\right)^T\rho_e^{\times} + \cdots \\ -m_{me}^{\times}\rho_e^{\times} + (\rho_e^{\times}m_{me})^{\times} - 2\rho_e m_{me}^T + \frac{5}{|\rho_e|^2}\rho_e(\rho_e^{\times}m_{me})^T\rho_e^{\times} + \cdots \\ \left(\underline{1} - 2\widehat{m}_s\widehat{m}_s^T\right)\left((\rho_e m_e)^{\times} - m_e^{\times}\rho_e^{\times} - 2\rho_e m_e^T + \frac{5}{|\rho_e|^2}\rho_e(\rho_e^{\times}m_e)^T\rho_e^{\times}\right) \end{bmatrix}^T \begin{bmatrix}\delta\boldsymbol{r}\\ \delta\boldsymbol{m}\end{bmatrix} \quad (46)$$

The total torque from a flux-pinned interface is the sum of the combined frozen and mobile image effects. The frozen-image torque is found by substituting $\boldsymbol{m_{ae}}$ to $\boldsymbol{m_e}$ the magnet's equilibrium magnetic-moment dipole, and $\boldsymbol{m_{be}}$ to $\boldsymbol{m_{fe}}$ the frozen image's equilibrium magnetic-moment dipole. The orientation of the frozen image does not change so the state $\delta\boldsymbol{m_f}$ and the corresponding coefficient is excluded, given by Eq. (47). The same process is applied to the mobile image. Substituting (44) into the previous equation, the number of states needed to calculate $\delta\boldsymbol{m_m}$ reduce, given by Eq. (48). The total torque on the magnet is the sum of the torque from the mobile

and frozen image, given by Eq. (49). The total torque is solely dependent on the physical magnet's position and orientation, which constitutes the rotational dynamic state of the flux-pinned interaction.

$$\delta\boldsymbol{\tau_f} = \frac{\mu_0}{4\pi|\rho_e|^3}\begin{bmatrix} \frac{3}{|\rho_e|^2}\left(m_e^T\rho_e m_{fe}^{\times} + m_{fe}^T\rho_e m_e^{\times} - \left(\frac{3}{|\rho_e|^2}m_e^T\rho_e m_{fe}^{\times}\rho_e + m_e^{\times}m_{fe}\right)\rho_e^T\right) \\ \frac{3}{|\rho_e|^2}m_{fe}^{\times}\rho_e\rho_e^T - m_{fe}^{\times} \end{bmatrix}^T \begin{bmatrix}\delta\boldsymbol{r}\\ \delta\boldsymbol{m}\end{bmatrix} \tag{47}$$

$$\delta\boldsymbol{\tau_m} = \frac{\mu_0}{4\pi|\rho_e|^3}\begin{bmatrix} 2\hat{m}_s\hat{m}_s^T\left(\frac{3}{|\rho_e|^2}\left(m_e^T\rho_e m_{me}^{\times} + m_{me}^T\rho_e m_e^{\times} - \left(\frac{3}{|\rho_e|^2}m_e^T\rho_e m_{me}^{\times}\rho_e + m_e^{\times}m_{me}\right)\rho_e^T\right)\right) \\ \frac{3}{|\rho_e|^2}m_{me}^{\times}\rho_e\rho_e^T - m_{me}^{\times} + \left(2\hat{m}_s\hat{m}_s^T - \underline{1}\right)\left(\frac{3}{|\rho_e|^2}m_e^{\times}\rho_e\rho_e^T + m_e^{\times}\right) \end{bmatrix}^T \begin{bmatrix}\delta\boldsymbol{r}\\ \delta\boldsymbol{m}\end{bmatrix} \tag{48}$$

$$\delta\boldsymbol{\tau_{tot}} = \frac{\mu_0}{4\pi|\rho_e|^3}\begin{bmatrix} \frac{3}{|\rho_e|^2}\left(m_e^T\rho_e m_{fe}^{\times} + m_{fe}^T\rho_e m_e^{\times} - \left(\frac{3}{|\rho_e|^2}m_e^T\rho_e m_{fe}^{\times}\rho_e + m_e^{\times}m_{fe}\right)\rho_e^T\right) + \cdots \\ 2\hat{m}_s\hat{m}_s^T\left(\frac{3}{|\rho_e|^2}\left(m_e^T\rho_e m_{me}^{\times} + m_{me}^T\rho_e m_e^{\times} - \left(\frac{3}{|\rho_e|^2}m_e^T\rho_e m_{me}^{\times}\rho_e + m_e^{\times}m_{me}\right)\rho_e^T\right)\right) \\ \frac{3}{|\rho_e|^2}m_{fe}^{\times}\rho_e\rho_e^T - m_{fe}^{\times} + \frac{3}{|\rho_e|^2}m_{me}^{\times}\rho_e\rho_e^T - m_{me}^{\times} + \left(2\hat{m}_s\hat{m}_s^T - \underline{1}\right)\left(\frac{3}{|\rho_e|^2}m_e^{\times}\rho_e\rho_e^T + m_e^{\times}\right) \end{bmatrix}^T \begin{bmatrix}\delta\boldsymbol{r}\\ \delta\boldsymbol{m}\end{bmatrix} \tag{49}$$

State-Space Model

The single magnet flux-pinned system dynamics may be represented with a first-order system state-space matrix, given by Eq. (50). The state matrix has the form given in Eq. (51). Each entry in the state matrix is a block matrix of size corresponding to the state and resultant, where the following a_{ij} values are derived from or given by Eqs. (52) to (59). The matrix entries a_{ij} are block matrices of size 3x3 that are generated from the linearized forces and torques from Eq. (46) and (49). Notably, all states are in matrix form.

$$\begin{bmatrix}\delta\dot{r}\\ \delta\ddot{r}\\ \delta\dot{q}_v\\ \delta\dot{\omega}\end{bmatrix} = A\begin{bmatrix}\delta r\\ \delta\dot{r}\\ \delta q_v\\ \delta\omega\end{bmatrix} \tag{50}$$

$$\begin{bmatrix}\delta\dot{r}\\ \delta\ddot{r}\\ \delta\dot{q}_v\\ \delta\dot{\omega}\end{bmatrix} = \begin{bmatrix} 0 & \underline{1} & 0 & 0 \\ a_{21} & 0 & a_{23} & 0 \\ 0 & 0 & 0 & \frac{1}{2}q_{ve}^{\times} \\ a_{41} & 0 & a_{43} & 0 \end{bmatrix}\begin{bmatrix}\delta r\\ \delta\dot{r}\\ \delta q_v\\ \delta\omega\end{bmatrix} \tag{51}$$

$$\delta\dot{r} \;=\; \delta\dot{r} \tag{52}$$

$$\delta\dot{q}_v = \tfrac{1}{2} q_{ve} \times \delta\omega \tag{53}$$

$$\delta\ddot{r} \;=\; a_{21}\delta r \;+\; a_{23}\delta q_v \tag{54}$$

$$\delta\dot{\omega} \;=\; a_{41}\delta r \;+\; a_{43}\delta q_v \tag{55}$$

$$a_{21} = M^{-1}\frac{3\mu_0}{4\pi|\rho_e|^5}\begin{pmatrix} m_{fe}^{\times}m_e^{\times} + m_e^{\times}m_{fe}^{\times} - 2m_e^T m_{fe}\underline{1} - \frac{5}{|\rho_e|^2}\left(\rho_e\left(\rho_e^{\times}m_{fe}\right)^T m_e^{\times} - \rho_e(\rho_e^{\times}m_e)^T m_{fe}^{\times}\right) + \\ -\frac{5}{|\rho_e|^2}\left((\rho_e^{\times}m_e)^{\times}m_{fe} + \left(\rho_e^{\times}m_{fe}\right)^{\times}m_e - 2\left(m_e^T m_{fe}\right)\rho_e + \frac{5}{|\rho_e|^2}\left((\rho_e^{\times}m_e)^T\left(\rho_e^{\times}m_{fe}\right)\right)\rho_e^T\right) + \\ 2\hat{m}_s\hat{m}_s^T(m_{me}^{\times}m_e^{\times} + m_e^{\times}m_{me}^{\times} - 2m_e^T m_{me}\underline{1} - \frac{5}{|\rho_e|^2}(\rho_e(\rho_e^{\times}m_{me})^T m_e^{\times} - \rho_e(\rho_e^{\times}m_e)^T m_{me}^{\times}) \\ -\frac{5}{|\rho_e|^2}\left((\rho_e^{\times}m_e)^{\times}m_{me} + (\rho_e^{\times}m_{me})^{\times}m_e - 2(m_e^T m_{me})\rho_e + \frac{5}{|\rho_e|^2}\left((\rho_e^{\times}m_e)^T(\rho_e^{\times}m_{me})\right)\rho_e^T\right)\end{pmatrix} \tag{56}$$

$$a_{23} \;=\; M^{-1}\frac{3\mu_0|m_e|}{4\pi|\rho_e|^5}\begin{pmatrix} -m_{fe}^{\times}\rho_e^{\times} + \left(\rho_e^{\times}m_{fe}\right)^{\times} - 2\rho_e m_{fe}^T + \frac{5}{|\rho_e|^2}\rho_e\left(\rho_e^{\times}m_{fe}\right)^T\rho_e^{\times} + \\ -m_{me}^{\times}\rho_e^{\times} + (\rho_e^{\times}m_{me})^{\times} - 2\rho_e m_{me}^T + \frac{5}{|\rho_e|^2}\rho_e(\rho_e^{\times}m_{me})^T\rho_e^{\times} + \\ \left(\underline{1} - 2\hat{m}_s\hat{m}_s^T\right)\left((\rho_e m_e)^{\times} - m_e^{\times}\rho_e^{\times} - 2\rho_e m_e^T + \frac{5}{|\rho_e|^2}\rho_e(\rho_e^{\times}m_e)^T\rho_e^{\times}\right)\end{pmatrix} \tag{57}$$

$$a_{41} = I^{-1}\frac{\mu_0}{4\pi|\rho_e|^3}\begin{pmatrix} \frac{3}{|\rho_e|^2}\left(m_e^T\rho_e m_{fe}^{\times} + m_{fe}^T\rho_e m_e^{\times} - \left(\frac{3}{|\rho_e|^2}m_e^T\rho_e m_{fe}^{\times}\rho_e + m_e^{\times}m_{fe}\right)\rho_e^T\right) + \\ 2\hat{m}_s\hat{m}_s^T\left(\frac{3}{|\rho_e|^2}\left(m_e^T\rho_e m_{me}^{\times} + m_{me}^T\rho_e m_e^{\times} - \left(\frac{3}{|\rho_e|^2}m_e^T\rho_e m_{me}^{\times}\rho_e + m_e^{\times}m_{me}\right)\rho_e^T\right)\right)\end{pmatrix} \tag{58}$$

$$a_{43} = I^{-1}\frac{\mu_0|m_e|}{4\pi|\rho_e|^3}\left(\frac{3}{|\rho_e|^2}m_{fe}^{\times}\rho_e\rho_e^T - m_{fe}^{\times} + \frac{3}{|\rho_e|^2}m_{me}^{\times}\rho_e\rho_e^T - m_{me}^{\times} + \left(2\hat{m}_s\hat{m}_s^T - \underline{1}\right)\left(\frac{3}{|\rho_e|^2}m_e^{\times}\rho_e\rho_e^T + m_e^{\times}\right)\right) \tag{59}$$

b. Arbitrary Number of Magnets and Superconductors

The state space of the single-magnet-single-superconductor case has 12 state variables: translational position, translational velocity, quaternion vector, and angular velocity of the magnet. For the general case of a *M* magnet *N* superconductor interaction, the states include those 12 state variables for each magnet on the rigid body, $12M$ total states. The most general plant, given in Eq. (47), is a simplification of the multiple-magnet and multiple-superconductor plant to a matrix of block matrices, where $\delta s_i = [\delta r_i\ \delta\dot{r}_i\ \delta q_{vi}\ \delta\omega_i]^T$ and *Ai,j* is the linearized dynamics of magnet i due to magnet j's images.

$$\begin{bmatrix} \delta\dot{s}_1 \\ \vdots \\ \delta\dot{s}_M \end{bmatrix} = \begin{bmatrix} A_{1,1} & \cdots & A_{1,M} \\ \vdots & \ddots & \vdots \\ A_{M,1} & \cdots & A_{M,M} \end{bmatrix} \begin{bmatrix} \delta s_1 \\ \vdots \\ \delta s_M \end{bmatrix} \tag{60}$$

Four Jacobians provide the basis for the partitions in the $A_{i,j}$ matrix of Eq. (60): force and torque as a function of position and orientation. The single-magnet and single-superconductor plant is derived in this general form $A_{i,j}$, given by (61). The magnet images affecting the dynamics can be from any magnet's images embedded in any superconductor. Every interaction is pairwise and all block matrices are populated. The larger system variables are analogous to the single-magnet and single-superconductor variables in (50) to (59). The velocity of the magnet *i* is only the velocity of magnet *j*, when *i=j*. The quaternion derivative of magnet *i* is only propagated when magnet *j=i*. Any magnetic-moment dipole from an image is established from magnet *j* about superconductor *k*. Any magnetic-moment dipole from a magnet is established from magnet *i*. The distance vectors are calculated from magnet *j*'s images about superconductor *k* to magnet *i*. These equations constitute the entries of the linearized state matrix, forming the basis of a linearized flux-pinning dynamics model for magnet *i* from specific magnet j's images from superconductor *k*. $a_{21,ij}, a_{23,ij}, a_{41,ij}$, and $a_{43,ij}$ are expressions with summation over all *N* superconductors.

$$\begin{bmatrix} \delta\dot{r}_i \\ \delta\ddot{r}_i \\ \delta\dot{q}_{vi} \\ \delta\dot{\omega}_i \end{bmatrix} = A_{i,j} \begin{bmatrix} \delta r_j \\ \delta\dot{r}_j \\ \delta q_{vj} \\ \delta\omega_j \end{bmatrix} \quad \text{where} \quad A_{i,j} = \begin{bmatrix} 0 & a_{12,ij} & 0 & 0 \\ a_{21,ij} & 0 & a_{23,ij} & 0 \\ 0 & 0 & 0 & a_{34,ij} \\ a_{41,ij} & 0 & a_{43,ij} & 0 \end{bmatrix} \tag{61}$$

The output states of a rigid body about the center of mass are translational position, translational velocity, attitude, and angular velocity of the magnet. For the *M*-magnet-*N*-superconductor case, the input state includes the position, velocity, attitude, and angular velocity of every magnet *j,* where A_j represents the contribution to body dynamics from magnet *j*'s state,

given by Eq. (61). $a_{21,j}$, $a_{23,j}$, $a_{41,j}$, and $a_{43,j}$ are expressions with summation over all N superconductors and M magnets. An analogous operation would be to sum each $A_{i,j}$ block matrix along each column or ith index, resulting in A_j. These 3x3 block matrices form the basis of a linearized flux-pinning dynamics model for a rigid body with all M magnets.

$$\begin{bmatrix} \delta\dot{r}_{COM} \\ \delta\ddot{r}_{COM} \\ \delta\dot{q}_{vCOM} \\ \delta\dot{\omega}_{COM} \end{bmatrix} = [A_1 \quad \dots \quad A_M] \begin{bmatrix} \delta r_1 \\ \delta\dot{r}_1 \\ \delta q_{v1} \\ \delta\omega_1 \\ \vdots \\ \delta r_M \\ \delta\dot{r}_M \\ \delta q_{vM} \\ \delta\omega_M \end{bmatrix} \quad \text{where} \quad A_{i,j} = \begin{bmatrix} 0 & a_{12,ij} & 0 & 0 \\ a_{21,ij} & 0 & a_{23,ij} & 0 \\ 0 & 0 & 0 & a_{34,ij} \\ a_{41,ij} & 0 & a_{43,ij} & 0 \end{bmatrix} \tag{61}$$

c. Sensitivity and Comparison of Single-Magnet and Single-Superconductor Dynamics

To validate the linearized dynamics and investigate the dynamic sensitivity of each state, a simulation with the full nonlinear dynamic equations is compared to the linearized state space. The fully nonlinear simulation also offers a second method to validate the linear state space with a common software package. Dynamic characteristics of the linear state space are discussed, followed by a comparison of the nonlinear dynamic state timeseries and the derived linearized state space propagated dynamics to generate RMS error. Finally, the paper studies the sensitivity of force and torque by independently varying each state.

Defining System Parameters

The specific magnet chosen is that of strength 0.8815 Tesla and of diameter 0.75 in. If z represents the vertical height in Cartesian coordinate space, the magnet is field-cooled 1 cm above the superconductor. Both the superconductor and magnet are pointing directly upward. The position of the permanent magnet from an arbitrary origin on the superconductor surface is

represented by $\boldsymbol{r_1}$. The magnetic-moment dipole of the permanent magnet contains a field strength and a unit direction, represented by $\boldsymbol{m_1}$. The orientation of the superconductor is the surface normal unit vector, given by $\widehat{\boldsymbol{m}}_{\boldsymbol{s}}$. The mass matrix is the mass of the permanent magnet, multiplied by an identity matrix, given by *M*. *R* is the radius of the spherical magnetic-moment dipole. *I* is the inertia tensor of the spherical magnet.

Table 1: Single magnet and superconductor case study parameters

Distance [m]	Magnet-moment dipole [T]	Body Parameters
r_1 = [0; 0; 0.01]	m_1 = 0.8815[0; 0; 1]	$\widehat{m}_s$ = [0; 0; 1]
ρ_e = [0; 0; 0.02]	m_e = 0.8815[0; 0; 1]	M = 0.0272 kg
r_f = [0; 0; −0.01]	m_{fe} = 0.8815[0; 0; 1]	R = 0.009525m
r_m = [0; 0; −0.01]	m_{me} = 0.8815[0; 0; −1]	$I = 3.63 \times 10^{-5}$ kg-m^2

From these physical parameters, the image parameters are found. r_f is the position of the frozen image. r_m is the position of the mobile image. ρ_e is the position vector from the images to the permanent magnet when in equilibrium, which is also the field-cooled position. The equilibrium magnetic-moment dipole is equivalent to the field-cooled orientation of the permanent magnet m_e. The frozen image magnetic-moment dipole m_{fe} is the same orientation as the permanent magnet orientation when field-cooling. The mobile image magnetic-moment dipole m_{me} is the mirrored orientation as the permanent magnet orientation when field-cooling. Refer to Table 1 for a complete list of system parameter matrices. All code is online and available at: github.com/frankiezoo/SMSS Linear Dynamics.git

Linearizing a Nonlinear Simulation and Deriving Linearized Matrix

After building a nonlinear dynamics model of a single-magnet and single-superconductor, the model is linearized with the Linear Analysis Toolbox from Mathworks Simulink. The input perturbation states are the quaternion and the position of the permanent magnet. The output measurement is the force and torque. The state space produced from Simulink's linearization produces the expression in Eq. (62). The single-magnet and single-superconductor plant from Eq. (51) is modified to include the four Jacobians from Simulink's linearization process from Eq. (61), given by Eq. (63). The state matrix generated from the simulation is equivalent within machine precision to the linearized state matrix derived in the preceding sections.

$$J = \begin{bmatrix} \frac{\partial \boldsymbol{F}}{\partial \boldsymbol{r}} & \frac{\partial \boldsymbol{F}}{\partial \boldsymbol{q}} \\ \frac{\partial \boldsymbol{\tau}}{\partial \boldsymbol{r}} & \frac{\partial \boldsymbol{\tau}}{\partial \boldsymbol{q}} \end{bmatrix} \tag{62}$$

$$\begin{bmatrix} \delta\dot{r} \\ \delta\ddot{r} \\ \delta\dot{q}_v \\ \delta\dot{\omega} \end{bmatrix} = \begin{bmatrix} 0 & \underline{1} & 0 & 0 \\ M^{-1}\frac{\partial \boldsymbol{F}}{\partial \boldsymbol{r}} & 0 & M^{-1}|m_e|\frac{\partial \boldsymbol{F}}{\partial \boldsymbol{q}} & 0 \\ 0 & 0 & 0 & \frac{1}{2}q_{ve}^{\times} \\ I^{-1}\frac{\partial \boldsymbol{\tau}}{\partial \boldsymbol{r}} & 0 & I^{-1}|m_e|\frac{\partial \boldsymbol{\tau}}{\partial \boldsymbol{q}} & 0 \end{bmatrix} \begin{bmatrix} \delta r \\ \delta\dot{r} \\ \delta q_v \\ \delta\omega \end{bmatrix} \tag{63}$$

Modal Analysis of Linearized Flux-Pinned Model

Modal analysis of a dynamic system reveals stability and frequency information. The eigenvalues and eigenvectors are found with the linearized state-space matrix. The plant derived in the previous subsection has the following eigenpairs. The flux-pinned system is marginally stable because all eigenvalues have a 0-real component. The numerical values associated with each eigenpair manifest different properties in the physical system, shown in Table 2.

Table 2: Single magnet and superconductor eigenpairs

eigenpair	λ	mode	shape
1	108.5i	ω_y	$\dot{r}_x$
2	-108.5i	ω_y	$\dot{r}_x$
3	108.5i	ω_x	$\dot{r}_y$
4	-108.5i	ω_x	$\dot{r}_y$
5	37.4i	ω_x	ω_y
6	-37.4i	ω_x	ω_y
7	37.4i	ω_y	ω_x
8	-37.4i	ω_y	ω_x
9	146.4i	$\dot{r}_z$	r_z
10	-146.4i	$\dot{r}_z$	r_z
11	0	q_3	r_z
12	0	q_3	

The first 10 eigenvalues of the flux-pinned plant are all imaginary, which represent the spring-like nature of flux-pinned interfaces. Due to the axial symmetry of the magnet, the eigenvalues representing the x and y dynamics come in quadruplets. The eigenvectors with imaginary values must be paired with the conjugate eigenvector to manifest real physical dynamics. Intuitively, flux-pinned interfaces have stiffer translational joints than rotational joints. The modal analysis reveals the same conclusion, where the z translation has the highest stiffness, the x and y translation also relatively high, and the x and y rotation with the lowest stiffness.

The first four modes show a relation between rotation and translation about x and y. The rotation is the main modal shape but contributes to translation. This stiffness is rather high. The next four modes, 5 to 8, show a relation between the rotation about x and y. The rotation about one axis is the main modal shape, but the rotation about the other axis is also a significant modal. This

stiffness is the lowest of all modes. Modes 9 and 10 strictly reflects translation in the z direction. It has the highest stiffness of all the modes. The last modes have 0 eigenvalues because the dynamics of the system do not resist to any perturbation of these states. Any perturbation in q_3, or the magnetic strength of the magnet, results in translation in the z direction. Any perturbation in the rotation about the z axis, q_3, results in rotation about the z axis until another perturbation or energy dissipation is introduced.

Sensitivity of Linearized Dynamics due to State Variation

Although the linearized plant is nearly exact to machine precision error at equilibrium, the linear plant approximates nonlinear dynamics less accurately the further the system deviates from equilibrium. Below are sensitivity plots varying state variables and correlating error in force and torque calculations between the linearized equations and nonlinear equations. Translation and rotation in x and y are the same due to symmetry, shown in Figure 15, Figure 16, Figure 18, and Figure 19. There is no rotation in z because the magnet is axially symmetric. The most sensitive state is the translational displacement in the z direction, shown in Figure 17. The equilibrium separation distance from the superconductor surface is 1 cm, or 10^{-2} m. To retain below 5% error in force, displacements in z must be bound to 10^{-4} m. This requirement is much more stringent if the error threshold is 1%, decreasing the displacement bound down to 10^{-5} m. Perturbations in the x and y translational displacement may be as high as 1 m, or 10^{-3} m, yet still retain 5% RMS error in force.

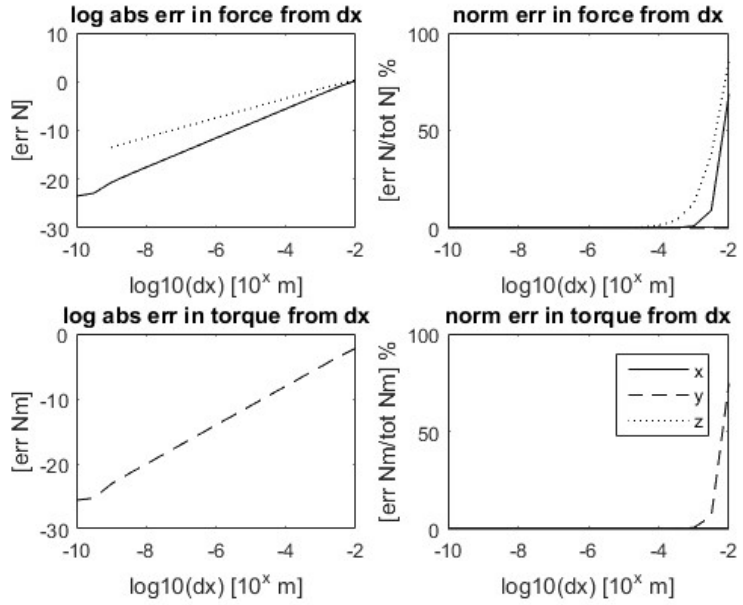

Figure 15: Error in force and torque between linearized and nonlinear model when varying x displacement

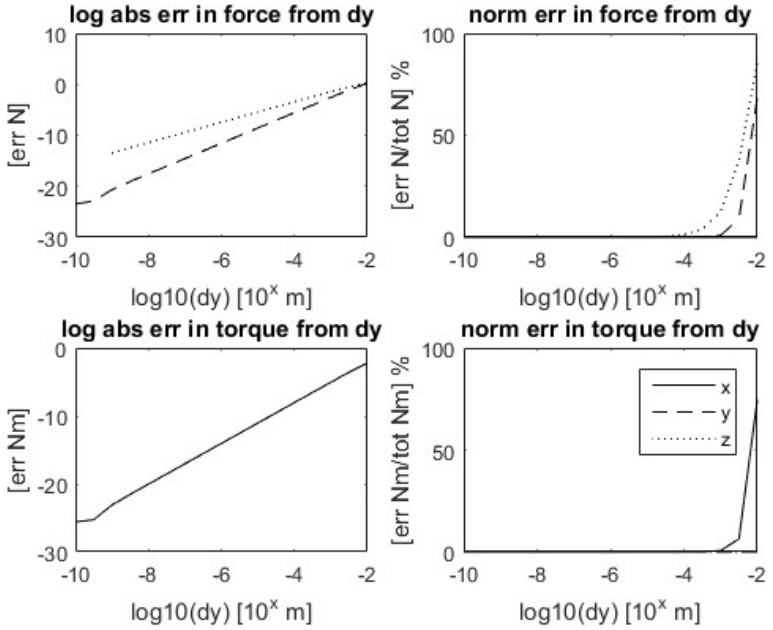

Figure 16: Error in force and torque between linearized and nonlinear model when varying y displacement

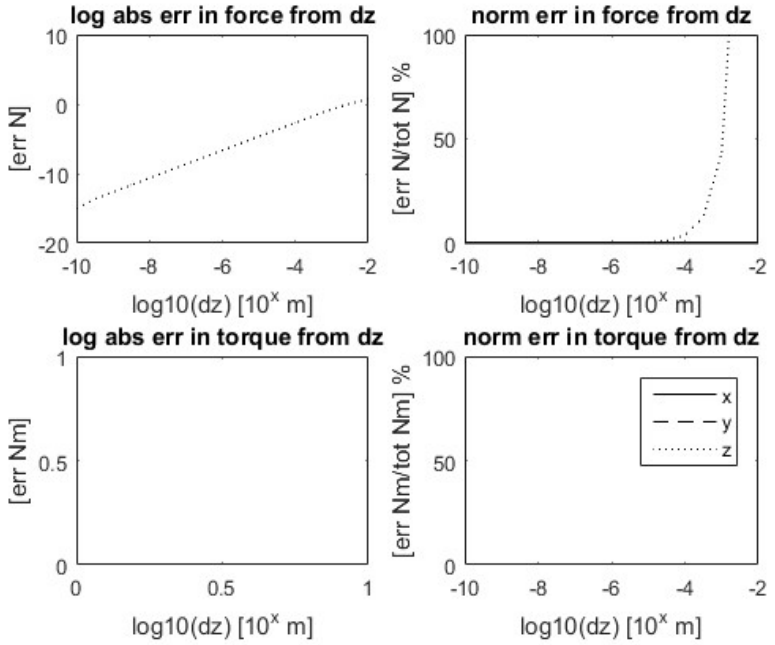

Figure 17: Error in force and torque between linearized and nonlinear model when varying z displacement

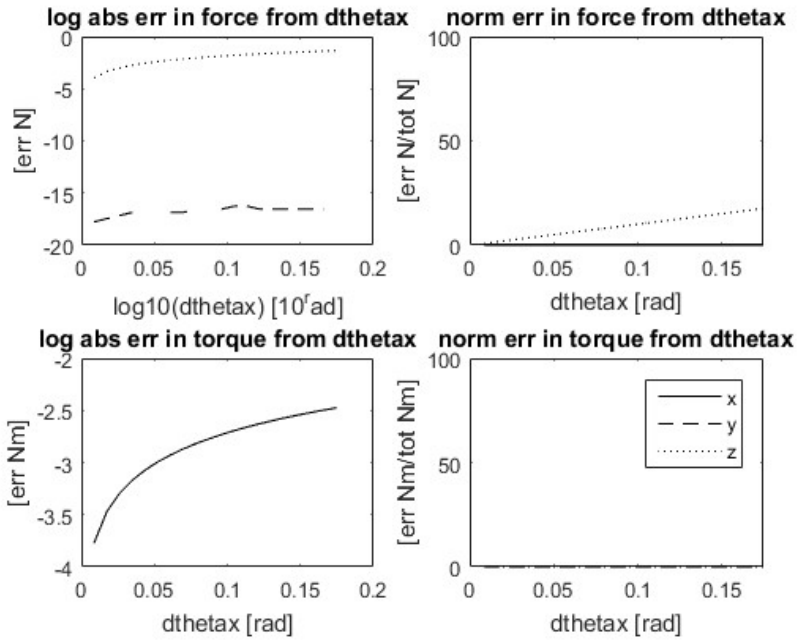

Figure 18: Error in force and torque between linearized and nonlinear model when varying x rotation

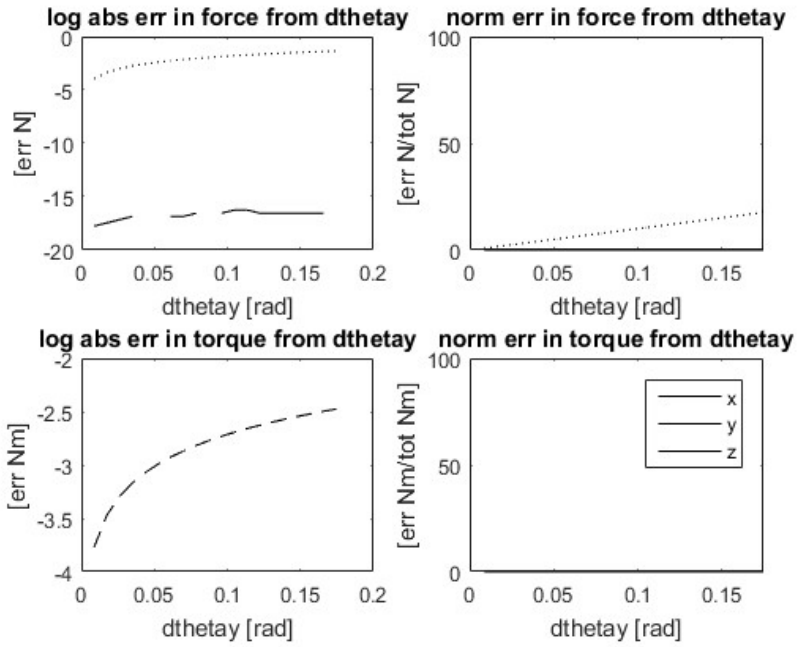

Figure 19: Error in force and torque between linearized and nonlinear model when varying y rotation

d. Contribution from Linearizing Dynamics

The general, linearized state-space equations derived here allow closed-form analytical characterization of a flux-pinned interface, along with the state matrix needed to formulate linear control algorithms. The results are an important step toward implementing six degree-of-freedom dynamic systems, such as docking, formation flying, autonomous assembly of multiple bodies, and non-contacting pointing platforms.

This model is expected to help characterize the passive dynamics of a flux-pinned system in all its degrees of freedom to permit the formulation of control algorithms. The linearized model accurately reflects the nonlinear dynamics within small displacements. Understanding the sensitivity of spatial perturbations informs the implementation of feedback control, for example in choosing the proper sensor resolution and predicting the expected excursions of the flux-pinned interface dynamics. Although the linearized equations are consistent with the fundamental physics,

Kordyuk's geometric mapping and Villani's dipole interactions represent limitations that may come into play for systems with nonlinear excursions and for which the dipole assumptions break down. A later section refines the basic nonlinear flux pinning model and parameterizing the nonlinearities in the dynamics model.

IV. Reduced Embedded Magnetic Field in Type-II Superconductor of Finite Dimension

This section maps the magnetic field within a type-II superconductor of finite dimension that is flux-pinned and demonstrates the need for a refined image-dipole model. The measured magnetic field within the superconductor is lower in magnitude than anticipated from the frozen-image model and changes shape dependent on location of the field-cooled image. The refined model more accurately bounds dynamic capabilities of flux-pinned bodies.

a. *Frozen-Image Model for Ideal Type-II Superconductors*

Kordyuk's frozen-image model provides an exact analytical solution for the case of a field-cooled magnetic dipole over a flat, hard, infinite-plane superconductor [93]. The total magnetic field generated by the superconductor from the frozen-image model is the sum of contributions from the frozen and the mobile images' strength, location, and orientation, given in Eq. (64). For an explicit derivation and definition of the flux-pinned dynamics model as well as a comprehensive list of physical parameters that affect the subsequent dynamics, refer to the previous and subsequent sections [109] and [94]. The analytical expressions for force and torque are essential for the equations of motion. The potential energy characterizes stability and offers intuition into the macroscopic dynamic behavior of the system. Ultimately, the magnetic field provides the fundamental basis for the physics, which then defines the dynamic behavior of the system.

$$\boldsymbol{B}(\boldsymbol{r}) \;=\; \boldsymbol{B_f}(\boldsymbol{r}-\boldsymbol{r_f},\boldsymbol{m_f}) \;+\; \boldsymbol{B_m}(\boldsymbol{r}-\boldsymbol{r_m},\boldsymbol{m_m}) \tag{64}$$

$$\boldsymbol{r_f} \;=\; \boldsymbol{r_{FC}} - 2\big((\boldsymbol{r_{FC}} - \boldsymbol{O_s})\cdot\hat{\boldsymbol{m}}_s\big)\hat{\boldsymbol{m}}_s \tag{65}$$

$$\boldsymbol{r_m} \;=\; \boldsymbol{r_{mag}} - 2\Big(\big(\boldsymbol{r_{mag}} - \boldsymbol{O_s}\big)\cdot\hat{\boldsymbol{m}}_s\Big)\hat{\boldsymbol{m}}_s \tag{66}$$

Kordyuk's model does not explicitly define the reference point, $\boldsymbol{O_s}$, on the superconductor surface because a point on an infinite plane may be arbitrarily defined, seen in Eq. (65) and (66). For a real superconductor of finite dimension, the amount of magnetic flux from the magnetic field source that penetrates the superconductor volume varies with distance from the superconductor surface. This distance is measured with respect to the reference point, which should be defined to yield a direct, straightforward relationship between distance and magnetic flux. With the advantage of symmetry, the simplest definition for the reference point is the center of the finite-superconductor surface.

b. *Finite-Plane Effect on Type-II Superconductors*

The frozen-image model, as applied to an ideal type-II superconductor and a perfect magnetic-dipole system, models only these ideal superconductors. This paper explores the change in the system dynamics of the flux-pinned interface for the practical case of finite-dimensioned superconductors. The finite-dimension effect is investigated by correlating experimentally measured magnetic fields of the superconductor with the Kordyuk's frozen-image model. The present study assesses the finite-dimension effect by characterizing a single-domain 56 mm diameter, 16 mm thick YBCO sample in the presence of a 0.75 inch diameter spherical, N42 Neodymium magnet with a surface field of 8815 Gauss. For uniformly-magnetized spheres, the magnetic-dipole representation is exact everywhere outside of the physical magnet sphere [110]. This study's approach to quantifying the finite-dimension effect centers on empirical data of the

flux-pinned magnetic fields generated by the shielding currents within the superconductor. The experiments were designed to isolate the finite-dimension effect on magnetic field flux pinning by varying only field-cooled positions.

A testbed, shown in Fig. 2, measures these resultant magnetic fields. The entire testbed consists of a three degree-of-freedom linear stage, three position sensors, three Hall sensors, one spherical permanent magnet, one cylindrical YBCO superconductor, and a liquid-nitrogen reservoir. The linear stage translates a permanent magnet and sensor package in three degrees-of-freedom. Three SICK ultrasonic sensors, with 0.0168 mm resolution and 3 – 35 cm range, measure the position of the Hall sensors and of the permanent magnet. All measurements are subject to position control resolution: x position within 0.1 mm, and y and z position within is 5 mm. Three programmable analog Hall sensors from Sensor Solutions M12-PAH-5VSB5, with a range from -1000 Gauss to 1000 Gauss, are aligned such that they are mutually perpendicular to measure the magnetic field in the three spatially orthogonal directions. The spherical magnet provides a magnetic field source during field cooling and a mobile-image dipole source during experiment. The liquid-nitrogen tank serves as a heat sink that maintains the temperature of the YBCO below a critical temperature of 88 K.

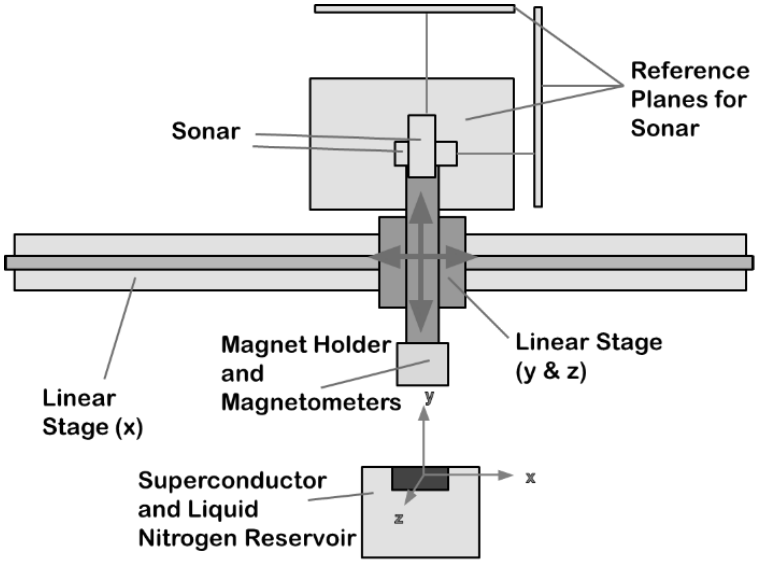

Figure 20: Top view of linear stage experiment testbed to spatially map magnetic flux of magnets and images within superconductors.

Two sets of experiments were conducted to investigate finite-dimension effects: the first set aimed to look only at the frozen image and the second to look at

both the frozen image and the mobile image together. Across all experiments, the magnet is field-cooled pointing normal to the superconductor surface and verified to align within 2.5 degrees. To isolate the frozen image, the magnet is field-cooled to the superconductor, and afterwards, the magnet is replaced with the three magnetometers. To measure both the frozen and mobile image, the magnet is field-cooled to the superconductor as before, then, the magnetometer is installed with the magnet on top of the magnetometer. After mapping the magnetic field, the measured magnetic field extrema locations are compared to extrema locations generated by the frozen-image model magnetic field, separated into three orthogonal (x, y, and z) components. For a magnet field-cooled directly above the center of the superconductor, a comparison of frozen image's magnetic field in the three spatial components is shown in Figure 21.

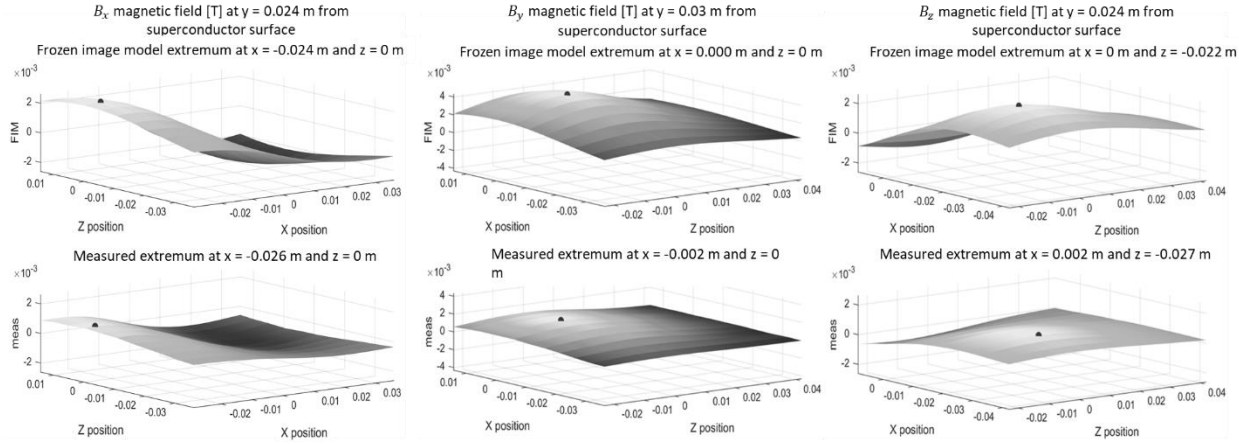

Figure 21: Topography of magnetic field components with marked extrema points of a centered field-cooled image

c. *Experiment Results*

Frozen-Image Model Magnitude Verification

The frozen-image model predicts magnetic field gradient or shape accurately for a magnet flux-pinned directly above the center of superconductor but severely overestimates the magnitude of strength of the image. Kordyuk's model does not capture the reduction in image strength as a magnet is field-cooled farther away from the reference point. The magnet field-cooled above the center of superconductor is the maximum magnetic flux observable, yet measurements for the surface normal component of magnetic field are 39% less than the frozen-image model predictions, shown in Figure 23. The percentage reduction of image magnetic field strength is consistent across all components of magnetic field within an average 4% standard deviation. The sole frozen image and combined images decrease in magnetic field penetration at the same rate[1], depicted in Figure 22. To implement this magnetic-field-strength reduction in a dynamic model, the image strength may be scaled by interpolating empirical values in a look-up table or with an approximation.

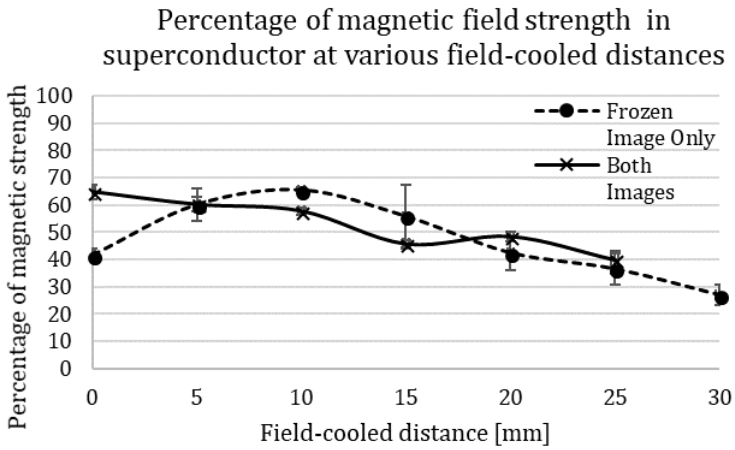

Figure 22: Average percentage of magnetic field captured within superconductor for a frozen image only and both images scenario. Error bars indicate variation in magnetic field components

[1] The frozen image experiment at 0 mm field-cooled distance is an outlier. A possible explanation is poor temperature control during the field-cooling process.

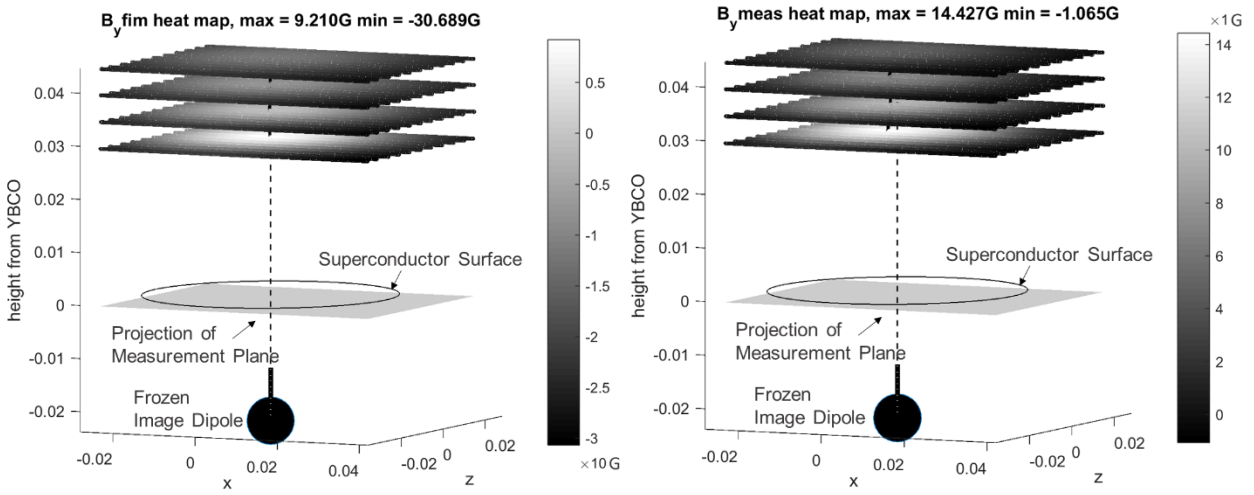

Figure 23: Comparison of frozen-image model prediction and measurements. Magnetic field represented in the form of heat map for surface normal (y) component of magnetic field

Frozen-Image Model Shape Verification

Implied in theory, the frozen-image model generates a symmetric potential well because an infinite plane superconductor captures equivalent magnetic flux in all directions. A physical superconductor of finite dimension also generates a symmetric potential well when the field-cooled image is centered. The difference lies in field-cooling the magnet away from the center of the superconductor, producing an asymmetrical imprint of magnetic field due to uneven flux distribution throughout the superconductor volume. The displacement between the predicted extrema location and measured extrema increase as the field-cooled location displaces farther from the center of the superconductor, shown by Figure 24.

The potential-well extrema locations are displaced from their expected locations, which is emphasized the farther the magnet is cooled from the center of the superconductor. The potential well extrema bias closer to the center of the superconductor, thus the magnetic field over the edge of the superconductor is only partially captured, shown in Figure 25. This clipping effect

contributes not only to the extrema location displacement, but also to the reduction in the magnitude of magnetic field captured in the superconductor.

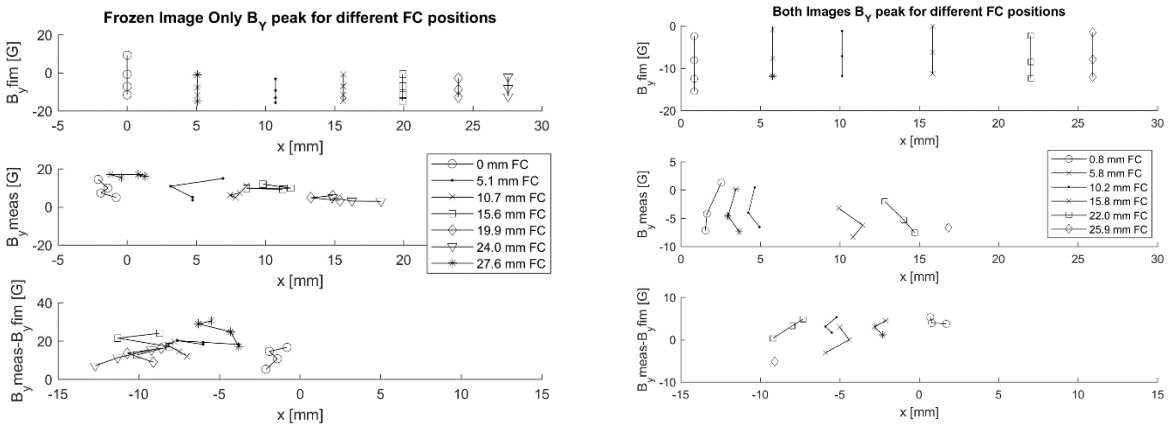

Figure 24: Left, comparison of frozen image extrema locations from frozen-image model (top), measurements (middle), and the difference (bottom) in extrema locations; right, comparison of both images

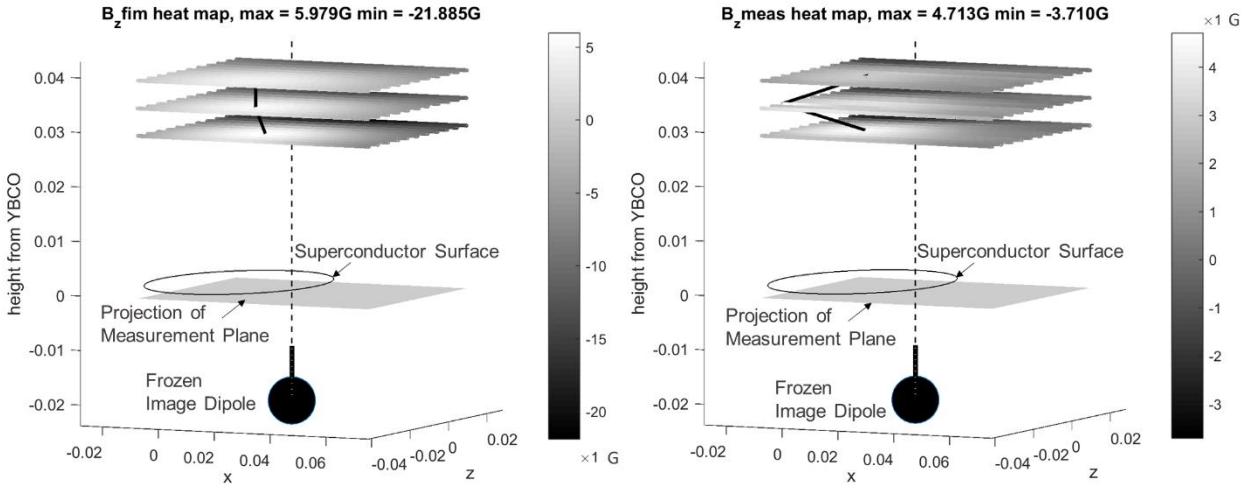

Figure 25: Magnetic field heat map of z component of magnetic field, for magnet field-cooled completely off superconductor surface area (30 mm FC distance over a 28 mm radius superconductor), showing clipped field

d. *Finite-Dimension Modification in Frozen-Image Model*

A scalar reduction in magnitude of magnetic field (c_F), given by Eq. (67), describes the reduction in magnetic field strength from finite-dimension effect by incorporating the position of the physical magnet ($\boldsymbol{r}$) and superconductor surface normal ($\hat{\boldsymbol{m}}_{\boldsymbol{s}}$). Lateral distance from the center of the superconductor (r_l) directly produces this reduction relationship in magnitude of magnetic field. The lateral distance is the projection of the location of the physical magnet onto the superconductor surface from the center of the superconductor ($\boldsymbol{O}_{\boldsymbol{s}}$), given by Eq. (68) and shown in Figure 26. The reduction scalar (c_F) may be interpolated from a look-up table of measured values or approximated, given by Eq. (69). c_{Fmax} is the percentage of magnetic field captured with the magnet located directly above the center of the superconductor and m_F is the rate of reduction, (c_F), as the magnet displaces farther from the center of the superconductor. The reduction scalar is bounded from 0 to c_{Fmax}. The physical configuration for these experiments yields numerical values $c_{Fmax} = 0.64$ and $m_F = 0.001$ but for different geometries of magnet and superconductor, these parameters may change. The authors suggest quantifying reduction for configurations specific to different systems.

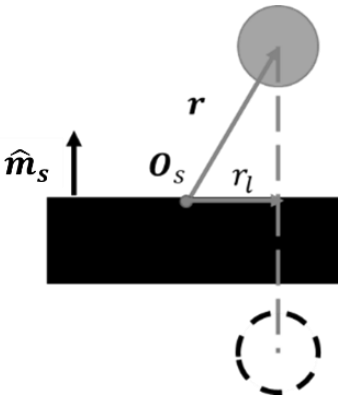

Figure 26: Parameter definition relevant for finite dimension modification

$$c_F = f(\boldsymbol{r}, \hat{\boldsymbol{m}}_{\boldsymbol{s}}) \tag{67}$$

$$r_l = |\boldsymbol{r} - (\boldsymbol{r} \cdot \hat{\boldsymbol{m}}_{\boldsymbol{s}})\hat{\boldsymbol{m}}_{\boldsymbol{s}}| \tag{68}$$

$$c_F = \max(c_{Fmax} - m_F * r_l,\ 0) \tag{69}$$

The general dynamics model includes the reduction scalar by modifying the expressions for the images' magnetic-moment dipoles, originally given by Eq. (65) and (66). Eq. (70) and (71) give the modified expressions in which the reduction scalars incorporate the relevant position

vectors. The frozen image magnetic-moment dipole scales with field-cooled position ($\boldsymbol{r_{FC}}$) and the mobile image with instantaneous magnet position ($\boldsymbol{r}$). The subsequent force and torque equations between the image and physical magnet do not change and are solved with the refined magnetic-moment dipole expressions.

$$\boldsymbol{m_f} = c_F(\boldsymbol{r_{FC}}, \hat{\boldsymbol{m}}_s)(2(\hat{\boldsymbol{m}}_s \cdot \boldsymbol{m_{FC}})\hat{\boldsymbol{m}}_s - \boldsymbol{m_{FC}}) \tag{70}$$

$$\boldsymbol{m_m} = c_F(\boldsymbol{r}, \hat{\boldsymbol{m}}_s)\left(\boldsymbol{m}_{\mathbf{mag}} - 2(\hat{\boldsymbol{m}}_s \cdot \boldsymbol{m_{FC}})\hat{\boldsymbol{m}}_s\right) \tag{71}$$

e. *Contribution from Investigating Finite-Dimension Effect*

From these experiments, a finite-dimension effect is clearly visible. Field-cooling a magnet farther away embeds less magnetic flux within the superconductor and modifies the shape of the magnetic field gradient over the edge of the superconductor. A reduction scalar is defined to modify the magnetic-moment dipoles of the weaker images. The reduction scalar implies a threshold distance of the magnet from the superconductor to generate a magnetic image. The frozen-image model may be used as a basis to simulate dynamics for any arbitrary configuration of magnets and superconductors, with a more accurate model including finite-dimension effects.

V. Flux-Pinned Dynamics Model Parameterization and Sensitivity Study

Although flux-pinning physics has been studied from a materials-science perspective and at the systems level, the sensitivities and implications of system-level designs on the dynamics need to be better understood, especially in interfaces with multiple magnets and superconductors. These interfaces have highly nonlinear, coupled dynamics that are influenced by physical parameters including strength of magnetic field sources, field-cooled position, and superconductor geometry. Kordyuk's frozen-image model successfully approximates the characteristics of flux-pinning dynamics but for this technology to be mature enough for spaceflight applications, its

physics must be represented in a high-fidelity predictive dynamics model that can inform design trade and analyses. Current closed-form dynamics models of the interactions express the basics of the interaction qualitatively but are too coarse to meet the needs of the design process. This section addresses that gap by offering parametric terms to improve the dynamics model, which may better simulate the behavior of a multiple-magnet-multiple-superconductor interface. The sensitivity of the general flux-pinned dynamics model is studied by varying the physical parameters and simulating the systems level dynamics. This work represents a critical step in the development of a model suited to spacecraft performance verification.

The field-cooled (FC) state has a significant effect on dynamic behavior and is only one of numerous critical design parameters. Firstly, the FC state initializes the natural equilibrium location for any magnet with the same properties as the field-cooling source. Multiple equilibria may exist for identical magnetic sources populating a single body−a concept utilized in this work. Secondly, the FC state also determines the stiffness of the interface by dictating the amount of captured magnetic flux in the superconductor that can respond to magnetic motion. Finally, the FC state determines the clearance distance between the two bodies moving relative to one another, which influences the amount of energy needed to force contact between them. Recent work describing parameter design to system level behavior, including but not limited to the FC state, can be found in reference [94].

The behavior of the interface after field cooling, under some simplifying assumptions, can be modeled by Kordyuk's frozen-image model and Villani's dipole equations [109]. The frozen-image model maps the magnetic field source to virtual images within the superconductor volume that interact with the source contactlessly [93]. The contactless nature of the interface implies that the mechanical interfacing/physical configuration do not directly influence the system's behavior;

rather, the magnetic field shape relative to the field-cooled magnetic source dominates the system behavior. The dynamics of the system is then primarily governed by an electrodynamical model derived by Villani et. al, which provides functions for force and torque given the spatial state and magnetic-moment dipoles of two sources [97] [96].

The governing equations of motion show that the force and torque relationships are highly nonlinear and coupled. The nonlinearity varies stiffness as a function of spatial displacement r with an inverse polynomial order. The nonlinearity in the direction normal to the superconductor face produces desirable behaviors by offering collision mitigation forces between spacecraft. As the spacecraft passes the equilibrium FC position and nears contact, the flux-pinned interface acts to repel the incoming spacecraft with an increasing resistance force. The coupling of the degrees of freedom results in the attitude affecting imparted forces, and the position affecting imparted torques, enabling energy transfer across degrees of freedom (DOF).

a. *Parameter Identification in Application*

This section reviews the assumptions from the frozen-image model in depth, surveys the supporting literature that extends the basic model, and offers a mathematical formulation to account for these effects in the dynamics model. The physical properties that affect the frozen-image model are temperature, material properties, manufacturing process, hysteresis, geometric and spatial relationships. All physical parameter effects are absorbed into a scaling factor modifying the strength of the frozen and mobile images. The parametric effects affect the expression and summation of force and torque but do not ultimately affect the governing equations of motion.

Temperature

Temperature affects flux-pinning interactions in three ways: maximum levitation stiffness, physics activation, and elastic hysteresis. Unlike Kordyuk's assumption of binary activation in superconductors, observations suggest the superconducting phenomenon is continuously activated. Chiang and Jiang both found that the colder the superconductor, the more levitation stiffness and less hysteresis are emphasized in the force curves [111], [112]. Although both investigators studied YBCO samples, the relationship between levitation force and temperature disagree, as seen in Figure 27. The discrepancy may lie in the samples. Chiang used superconductor samples on the scale of two to three millimeters with a magnet much larger than the superconductor (roughly four times the surface area), whereas Jiang used a superconductor 30 mm in diameter and a magnet slightly smaller than the superconductor. For the small superconductor samples, the hysteresis gaps are very evident and temperature variation does not taper off, but seemingly extends linearly. For the large superconductor samples, the temperature variation tends to taper off as the superconductor reaches 40 K and hysteresis affects the force path negligibly. A general trend may be drawn that colder temperatures offer stronger interactions, but a precise scaling factor cannot be extrapolated from these two studies. Intuitively, the variation in temperature scales the strength of the interaction.

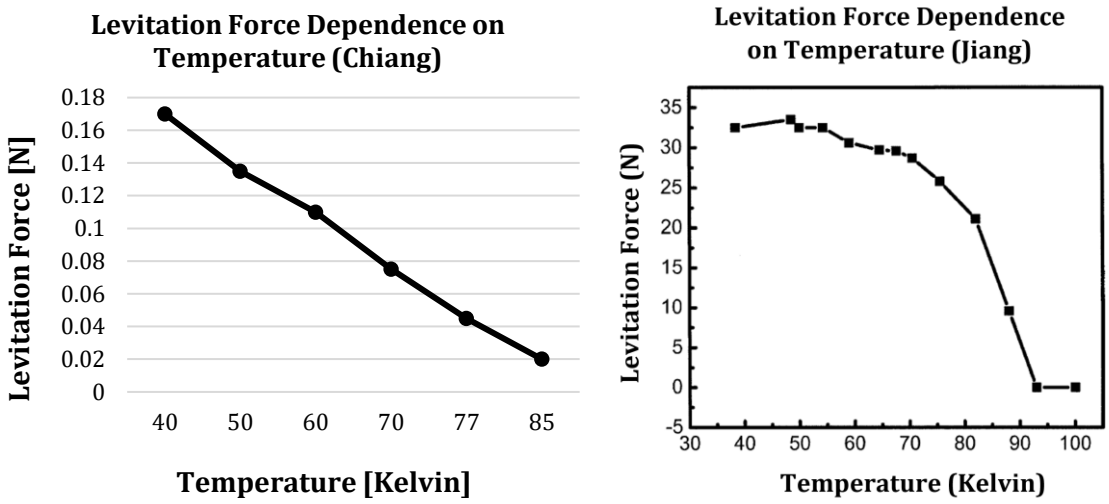

Figure 27: Comparison of Chiang and Jiang's results on levitation force and temperature relationship [111], [112].

To incorporate temperature variation into the dynamics model, the formulation for the mobile and frozen-image magnetic-moment dipoles include a scaling factor $c_t(T|T_{ref})$ given by Eq. (72) and (73). T is the temperature in which the superconductor operates and T_{ref} is the reference temperature in which the levitation force was measured, separated by the condition given operator '|'. c_t is greater than 1 when $T < T_{ref}$, less than 1 when $T > T_{ref}$, and equal to 1 when $T = T_{ref}$. $c_t(T|T_{ref})$ can be found through interpolation or extrapolation of the empirical dataset provided by Chiang or Jiang [111], [112], but due to the disagreement, the most accurate method to determine the scaling factor is to measure the temperature variation for each specific magnet and superconductor used in a given application.

$$\boldsymbol{m_m} = c_t(T|T_{ref})(\underline{1} - 2\hat{\boldsymbol{m}}_s \otimes \hat{\boldsymbol{m}}_s)(\boldsymbol{m_{mag}}) \tag{72}$$

$$\boldsymbol{m_f} = c_t(T|T_{ref})(2\hat{\boldsymbol{m}}_s \otimes \hat{\boldsymbol{m}}_s - \underline{1})(\boldsymbol{m_{FC}}) \tag{73}$$

Material Properties

The material properties of the superconductor vary the behavior of the flux-pinned interaction immensely, ranging from the elemental composition, manufacturing process, and crystalline structure. The elemental composition affects the critical temperature at which the superconductor is superconducting, its lower and upper critical field, and the critical current density [113]. Yttrium Barium Copper Oxide (YBCO) has been studied extensively due to its heritage, high critical temperature, and high critical magnetic fields. In addition, YBCO superconductor discs exhibit flux pinning above liquid nitrogen's boiling temperature, requiring only inexpensive and widely-accessible technology. YBCO also has no known material safety hazards [37]. When modeling the dynamics, the lower critical-magnetic-field bounds affect the interaction continuity. The higher critical-magnetic-field bounds affect the strength of the interaction. And finally, hysteresis affects the predictability of the system.

An intrinsic property of a superconductor is its elemental composition. Important energy parameters like critical temperature and thermodynamic critical field are defined by the material composition. At a microscopic level, the material affects the surface impedance at low fields, acting through intermediate-state tunneling in which a lower threshold of critical field must be surpassed to give rise to any electromagnetic interaction. The weak-tunnel coupling emphasizes anisotropy in different crystalline structures, such as copper, bismuth, or thallium planes [113]. For a YBCO sample structure (copper oxide planes) of specific temperature and geometry, the lower critical field is 0.1 T perpendicular to the plane and 0.02 T parallel to the plane [114]. The macroscopic geometry of the superconductor, such as surface area and volume shape, also play an important role in critical-field thresholds and caution must be used when implementing these thresholds.

The lower critical-field threshold effect is modeled as a discontinuous magnetic regime transitioning from no current excitation to current excitation. Treating the magnet as a singular dipole, the interaction is considered binary. Treating the magnet as a flux field, the interaction is better encapsulated as a continuous scaling of the dipole. B_a, the applied field, is the magnetic field penetrating the superconductor at its boundary. B_a is a function of the strength and orientation of the magnet dipole, the position with respect to the superconductor surface, and the superconductor surface normal. If B_a is above the minimum critical-threshold B_c, there exists a virtual magnetic image that interacts with the source magnet, given by Eq. (74) and (75). The ultimate effect of material properties manifest as a critical-field conditional that results in a binary interaction.

$$if\ B_a(\boldsymbol{m_{FC}}, \boldsymbol{r_{FC}}, \hat{\boldsymbol{m}}_s) > B_c,\quad then\ \boldsymbol{m_f} = \left(2\hat{\boldsymbol{m}}_s \otimes \hat{\boldsymbol{m}}_s - \underline{1}\right)\boldsymbol{m_{FC}} \tag{74}$$

$$if\ B_a(\boldsymbol{m_{mag}}, \boldsymbol{r_{mag}}, \hat{\boldsymbol{m}}_s) > B_c,\quad then\ \boldsymbol{m_m} = \left(\underline{1} - 2\hat{\boldsymbol{m}}_s \otimes \hat{\boldsymbol{m}}_s\right)\boldsymbol{m_{mag}} \tag{75}$$

Manufacturing Process

A bulk superconductor may be made in different ways, ranging from compressing grains into a mold or inducing melt–textured growth of a single crystal in an oven. Manufacturing processes define intrinsic properties of the superconductor. The internal structure and external geometry of the superconductor affect the strength and hysteretic behavior of the flux-pinning physics.

Regardless of the manufacturing method, every superconductor has defects in its composition: surface smoothness, cracks, and impurities between copper planes [113]. Chan [115] fabricated superconducting samples with YBCO various sizes of grains and epoxy without aligning the grains to investigate the effects on critical current density, levitation force, and

hysteresis. The larger-grained samples had a lower current density, larger maximum levitation stiffness, and larger gap in the hysteresis curve. Similarly, Yang [107] sliced a large YBCO sample into smaller components to investigate the effect of different grain sizes on levitation stiffness, while retaining the same grain orientation. The smaller components, when reassembled to resemble the original disc, did not provide the same amount of levitation stiffness. The stiffness linearly decreased as a function of number of cuts/parts. Yang [108] explores the specific consequences of cracks in the superconductor sample, showing that the larger the crack, the less levitation stiffness the superconductor provided. Single-domain superconductors offer maximum levitation stiffness.

Grain alignment of a single-domain superconductor affects the strength of interaction and presence of hysteresis. After the raw sample is grown, the sample may be cut in different geometries with intended surface area aligned along the grain. The largest measured levitation stiffness occurs when the magnetic vector field is perpendicular to the copper planes, with a monotonic reduction of levitation force as the magnetic field becomes parallel with the copper planes [116]–[118]. The hysteresis gap is also observed to be largest when the copper planes are perpendicular to the applied field. The levitation force may be scaled as a function of relative alignment between the superconductor surface and magnetic-moment dipole pole axis. Equation (76) characterizes this degradation, assuming the copper planes are parallel to the cut superconductor surface and the angle is zero when the moment dipole is aligned with the superconductor surface normal [117]. $\boldsymbol{m}$ is either image's magnetic-moment dipole, a value scaled down by a function of angle between the dipole and superconductor normal in Eq. (77). The maximum magnitude of magnetic-moment dipole m_0 is measured at $\theta = 0°$, and the minimum levitation force m_{90} is measured at $\theta = 90°$. The strength of the flux-pinned interaction is scaled

by the relative orientation between the magnetic-moment dipole and superconductor surface normal.

$$\boldsymbol{m} = c_g(\theta) m_0 \hat{\boldsymbol{m}} \tag{76}$$

$$c_g(\theta) = \cos^2\theta + \frac{m_{90}}{m_0}\sin^2\theta \tag{77}$$

The maximum levitation stiffness vs. distance reveals the strength and depth of the potential well of the magnetic system, but the shape of the potential is still left uncharacterized. The simplest dynamics model includes no hysteresis or negligible hysteresis, seen only in very cold flux-pinned interfaces [112]. At a higher temperature, the superconductor exhibits levitation whose force paths vary in elastic hysteresis and inelastic (or plastic) hysteresis. Both affect equilibrium position and orientation.

Hysteresis

Hysteresis stems from elastic instabilities in the flux-line lattice that dissipate energy [103]. At a microscopic level, the flux line changes to a different energy state and dissipates through tiny eddy currents in the current vortices. Hysteresis that occurs during relative magnet-superconductor movement can bring the system to a continuous range of stable equilibria positions and orientations [101]. Some hysteresis is not recoverable, and plastic deformation in the internal magnetic field permanently changes the dynamic behavior of the system [18], [103], [104]. For the recoverable or elastic hysteresis curves, Zhang [102] and Yang [95] have proposed modifications to the frozen-image model by including a vertical and horizontal movement image that even accounts for saturation within the superconducting material. The addition of the two scalable images accounts for the hysteresis gap.

Yang's full derivation is not repeated but the relevant additional image expressions are shown in Eq. (78) – (81) for insight. Eq. (78) is the vertical image expression as the magnet descends towards the superconductors, where h is the initial cooling position, h is vertical position, and h_0 is the lowest position. Eq. (79) is the counterpart vertical image expression for magnet ascension, where h_m is the highest position. Eq. (80) is the horizontal image expression as the magnet traverses farther from the center of the superconductor, where l is horizontal position. Eq. (81) is the counterpart horizontal image expression for a magnet moving closer to the field-cooled position, where l_m is the maximum horizontal displacement. All $a, b, c,$ and d terms are found by empirical data collected from the specific system of interest. The additional images influence the physical magnet in the same way as the frozen and mobile image, expressed with Villani's model. The additional image contributions are superimposed in the force and torque summations.

$$if\ \dot{h} < 0, \quad then\ \boldsymbol{m_v} = \big(-a_1(h - h_0) + a_2(h - h_0)\big)\hat{\boldsymbol{m}}_{\boldsymbol{v}} \tag{78}$$

$$if\ \dot{h} \geq 0, \quad then\ \boldsymbol{m_v} = \big(b1(h_m - h_0) - b_2(h_m - h)\big)\hat{\boldsymbol{m}}_{\boldsymbol{v}} \tag{79}$$

$$if\ sign(\dot{l}) = sign(l), \quad then\ \boldsymbol{m_h} = c_1 l\ \hat{\boldsymbol{m}}_{\boldsymbol{h}} \tag{80}$$

$$if\ sign(\dot{l}) \neq sign(l), \quad then\ \boldsymbol{m_h} = \big(d_1 l_m - d_2(l_m - l)\big)\hat{\boldsymbol{m}}_{\boldsymbol{h}} \tag{81}$$

Geometric and Spatial Relationship

Extrinsic factors, such as geometry and spatial relationships, affect the way the source magnet flux penetrates the superconductor geometry, which then modifies the stiffness of the interaction. For example, the geometric mapping from a spherical source magnet to either image differs from that of a flat magnet [98]. Superconducting samples with the largest surface area and thickness offer the most levitation force. Thickness does not increase levitation force linearly but diminishes in rate of influence [119]. The optimal magnet size is slightly smaller than that of the

superconductor; larger magnet diameters reduce the stiffness of the flux-pinned interaction [105]. The magnetic field shape of the source magnet affects the levitation force profiles, leading to stiffer interactions in which the gradient of the magnetic field changed drastically, like corners or sharp edges [120]. These higher-order effects are not accounted for in a dipole representation, and the magnetic-moment dipole equation must be modified for the magnet of interest.

The spatial relationship between the magnet and superconductor influences the flux penetration within the superconductor, related to the minimum critical field. Kordyuk assumes an infinite-plane superconductor but infinite geometries are nonphysical. A finite-dimension relationship requires a problem-specific formulation. As the equilibrium position of the source magnet moves farther from the center of the superconductor, the amount of flux penetrating the volume of the superconductor decreases, and thus, the stiffness of the interaction also decreases [106]. Even when the magnet is field-cooled directly above the center of the superconductor, the frozen image strength is only 64% of the frozen-image model anticipated strength. The strength of the images scale with distance from the center of the superconductor, given by Eq. (82) and (83). l, defined in Eq. (84), expresses the absolute distance from the center of the superconductor parallel to the surface of the superconductor and c_F, defined by Eq. (85), is a linear approximation of the degradation of strength as the magnet moves off the surface of the superconductor. c_D is found empirically where c_{max} is the portion of field captured in which the magnet is center above the superconductor and c_f is the reduction of field as a function of lateral distance l. Since the distance from the center of the superconductor is an important parameter in the flux-pinned system, Kordyuk's formulation of the distance vectors in Eq. (8) and (11) are modified to no longer use an arbitrary point as the reference origin O_s but to reference the center of the superconductor. The

resulting coefficient, c_F, reduces the strength of flux-pinned interaction as the physical magnet moves laterally farther from the superconductor.

$$\boldsymbol{m_m} = \left(\underline{1} - 2\hat{\boldsymbol{m}}_{\boldsymbol{s}} \otimes \hat{\boldsymbol{m}}_{\boldsymbol{s}}\right)\left(c_F\left(\boldsymbol{r_{mag}}\right)\boldsymbol{m_{mag}}\right) \tag{82}$$

$$\boldsymbol{m_f} = \left(2\hat{\boldsymbol{m}}_{\boldsymbol{s}} \otimes \hat{\boldsymbol{m}}_{\boldsymbol{s}} - \underline{1}\right)\left(c_F(\boldsymbol{r_{FC}})\boldsymbol{m_{FC}}\right) \tag{83}$$

$$l = |\boldsymbol{r} - (\boldsymbol{r} \cdot \hat{\boldsymbol{m}}_{\boldsymbol{s}})\hat{\boldsymbol{m}}_{\boldsymbol{s}}| \tag{84}$$

$$c_F \approx c_{Fmax} - c_f l \tag{85}$$

Summary

The physical properties of the magnet-superconductor system have significant consequences on the image expressions from Eq. (72) to (85). Reduction in magnetic field strength through temperature or geometric/spatial effects is embodied in scalar form, seen in Eq. (72) – (73), (76), and (82) – (83). The activation of flux-pinning physics in different material properties is represented by a conditional statement, seen in Eq. (74) – (75). The higher-order effects of hysteresis are captured in additional magnetic-moment images, seen in Eq. (78) – (81). The physical parameters solely modify the magnetic-moment dipole expressions for the frozen and mobile images. The superimposed effect of each parameter modification on the original magnetic-moment dipole expressions are given in the Eq. (86) and (87). The dynamic behavior of the interface follows the summation of all individual image expressions (and their modifications). The revised expression for force and torque are given in Eq. (88) to (90), where the additional effects of the vertical and horizontal images are explicitly incorporated. The present study investigates the sensitivity of stiffness, energy, force, and natural frequency to small discrepancies in knowledge or control of these parameters.

$$if\ B_a(\boldsymbol{m_{FC}}, \boldsymbol{r_{FC}}, \hat{\boldsymbol{m}}_{\boldsymbol{s}}) > B_c, \quad then\ \boldsymbol{m_f} = c_t\left(T|T_{ref}\right)c_g(\theta)c_D\left(\boldsymbol{r_{mag}}\right)\left(2\hat{\boldsymbol{m}}_{\boldsymbol{s}} \otimes \hat{\boldsymbol{m}}_{\boldsymbol{s}} - \underline{1}\right)\boldsymbol{m_{FC}} \tag{86}$$

$$if\ B_a(\boldsymbol{m_{mag}}, \boldsymbol{r_{mag}}, \hat{\boldsymbol{m}}_{\boldsymbol{s}}) > B_c, \quad then\ \boldsymbol{m_m} = c_t(T|T_{ref}) c_g(\theta) c_D(\boldsymbol{r_{mag}}) (\underline{1} - 2\hat{\boldsymbol{m}}_{\boldsymbol{s}} \otimes \hat{\boldsymbol{m}}_{\boldsymbol{s}}) \boldsymbol{m_{mag}} \quad (87)$$

$$\boldsymbol{F_i} = \sum_{j=1}^{N} \sum_{k=1}^{M} \left(\left(\boldsymbol{F_{frozen}} + \boldsymbol{F_{mobile}} + \boldsymbol{F_{vertical}} + \boldsymbol{F_{horizontal}} \right)_k \right)_j \quad (88)$$

$$\boldsymbol{F_{COM}} = \sum_{i=1}^{N} \sum_{j=1}^{N} \sum_{k=1}^{M} \left(\left(\left(\boldsymbol{F_{frozen}} + \boldsymbol{F_{mobile}} + \boldsymbol{F_{vertical}} + \boldsymbol{F_{horizontal}} \right)_k \right)_j \right)_i \quad (89)$$

$$\boldsymbol{\tau_{COM}} = \sum_{i=1}^{N} \sum_{j=1}^{N} \sum_{k=1}^{M} \left(\left(\left(\boldsymbol{\tau_{frozen}} + \boldsymbol{\tau_{mobile}} + \boldsymbol{\tau_{vertical}} + \boldsymbol{\tau_{horizontal}} \right)_k \right)_j \right)_i + \sum_{i=1}^{M} \boldsymbol{\rho_i} \times \boldsymbol{F_i} \quad (90)$$

b. *Parameterization in Design and Model Fidelity*

Physical Parameters Optimizing Performance

Design considerations at the systems level maximize stiffness in a practical flux-pinned interface. At a component level, the material properties of a superconductor dominate the operations and capabilities of flux-pinned interactions. The other side of the interface, the magnet, contributes to performance through its strength, size, and geometry. Other higher-level considerations include the relative size and location of the magnet and superconductor. These physical parameters are selectable during system design and may optimize stiffness, but they do not impact the accuracy and fidelity of the dynamics model.

The most influential characteristic of a superconductor is its material, specifically its critical current density. Many different materials have been investigated, including Niobium, Cuprate, and Magnesium based compositions [121]. YBCO material exhibits strong pinning effects in moderate fields with a critical temperature above that of liquid nitrogen. Thanks to its availability, YBCO bulk superconductors garner academic interest and are actively studied. Other materials have higher critical current densities but also require further cooling due to the lower critical temperatures. YBCO superconductors offer stiff joints for nanosatellites (~1-10 kg) while reducing the cooling power needed to activate flux-pinning physics.

The superconductor-bulk formation and fabrication impact the stiffness of flux-pinning physics within material bounds. Grown from a single crystal, a single-domain superconductor yields higher levitation stiffness and exhibits less hysteresis than a granular, epoxy-bonded superconductor. In the context of integrating superconductors on a spacecraft, any cracks or imperfections in the boundary of the superconductor reduce the efficacy of the joint so the superconductor disk should be protected from impact. The superconductor geometry and surface depend on the quality of cut and polish during manufacture. Grain alignment can be adjusted to maximize stiffness in a chosen direction in which the magnetic-moment dipole aligns with the superconductor surface normal.

When sizing the magnet and superconductor, the relative geometry and relative position of the magnet and superconductor determine the strength of the interaction. The flux-pinned interface is optimally stiff when both the diameter of the magnet and the superconductor are similar. Superconductor and magnet size are both bound by manufacturing capabilities of which superconductor size is more limiting. Although larger superconductor and magnet combinations increase the flux penetrating the superconducting volume, the strength of the interaction does not scale with mass.

The stiffest interaction is achieved through setting an optimal field-cooled orientation, aligning the magnetic-moment dipole perpendicular to the superconductor surface, and aligning the grain parallel to the surface. Field-cooled position depends on lateral and normal separation distance in which lateral movement is motion parallel to the superconductor plane and normal separation distance is movement perpendicular to the superconductor plane. In designing for field-cooled separation distance, adjusting this separation is a trade between stiffness and collision mitigation. Stiffness in a system with a dipole magnet pinned with the dipole perpendicular to the

superconductor surface, when measured along that perpendicular axis is proportional to the field-cooled distance to the 4th power. The closer distance also reduces the clearance between two spacecraft, which could make collisions more likely. A larger field-cooled distance decreases the stiffness but offers more clearance for a compliant arrest to occur. After the parameters are optimized for performance, the following parameters are studied for model fidelity.

Physical Parameters Affecting Model Fidelity

To inform system-level design on dynamics, different physical parameters are studied to evaluate the most dominant characteristics of the flux-pinned system. The dynamics model formulation is explicitly defined, but the physical parameters of the system are rarely exactly known. The important adjustable physical parameters are field-cooled rotation and position, magnet strength, and temperature coefficient, given by Eq. (91). There are some physical characteristics that are inherent to the system and should be optimized outside the context of dynamic modeling, such as the superconductor grain alignment, surface smoothness, and material composition. The state of interest s is the spacecraft's position $[\, x\ y\ z\,]$, velocity $[\, v_x\ v_y\ v_z\,]$, acceleration, quaternion $[\, q_x\ q_y\ q_z\ q_s\,]$, and angular velocity $[\, \omega_x\ \omega_y\ \omega_z\,]$, given by Eq. (92), which are ultimately propagated by force and torque on the system. Dynamic properties of the system include stiffness, natural frequencies and modes, and potential energy.

$$p = [\, \theta_{FC}\ x_{FC}\ z_{FC}\ B_0\ c_t\,]^{\mathrm{T}} \tag{91}$$

$$s = \left[\, x\ y\ z\ v_x\ v_y\ v_z\ q_x\ q_y\ q_z\ q_s\ \omega_x\ \omega_y\ \omega_z\,\right]^{\mathrm{T}} \tag{92}$$

The parameters are integrated into the dynamics model by injecting them into frozen-image model mapping and state equations. θ_{FC} is the angular displacement from the ideal field-cooled attitude and $[\, x_{FC}\ z_{FC}\,]$ is the position displacement from the ideal field-cooled position, which

causes a discrepancy in knowledge of superconductor location and orientation. [$\theta_{FC}\ x_{FC}\ z_{FC}$] affect the geometric mapping from source magnet to images, given by Eq. (6) to Eq. (11), and consequently the equilibrium position and orientation of the spacecraft. B_0 is the surface strength of the source magnet, which forms the magnetic-moment dipole of the source magnet and the consequential image mapping. c_t is the scalar coefficient that adjusts the strength of the images depending on the superconductor's temperature, given by Eq. (72) and (73).

These parameters are studied in the context of a single-magnet and single-superconductor system, then a multiple-magnet and multiple-superconductor system to emphasize the compounding effect and coupled nonlinear dynamics of certain parameters. The parameters operate under different length scales and to avoid unit specific sensitivity analysis, a related numerical parameter is offered with parameters perturbed by one percent.

c. *Sensitivity Study of Dynamics*

Single-Magnet and Single-Superconductor System

A common pairing of magnets and superconductors for studying flux-pinning dynamics involve Neodymium (NdFeB) permanent magnets and Yttrium Barium Copper Oxide (YBCO) bulk superconductors. All literature referenced in this paper is specific to YBCO material composition, and when relevant, NdFeB magnets. The magnet used in this study is a NdFeB, N42 grade, 0.75 inch diameter spherical magnet of 8815 Gauss manufacturer-specified maximum surface strength. The superconductor disk used in this study is a CAN melt–textured $YBa_2Cu_3O_{7-x}$, single–domain, 56 mm diameter 16 mm thick cylindrical superconductor disk [122]. The magnet is field-cooled at 2.55 cm with its centroid above the center of the superconductor surface and its

pole aligned with the superconductor surface normal. The direction convention for studying the single-magnet and single-superconductor (SMSS) system shown in Figure 28.

SMSS Variation of Physical Parameters

To study meaningful variations of physical parameters, relevant parameters are offered to reference for scale. Table 3 summarizes the physical parameters, reference parameters, numerical value of each reference parameter, and numerical value of each physical parameter perturbation. The critical-field-threshold conditional is assumed to be met and hysteresis is not analyzed. The parameters that encapsulate temperature, geometric and spatial relationship, and physical magnet field-strength are all represented explicitly or implicitly in Table 3. The misalignment of the magnet during field-cooling could be up to half the span of full reorientation due to symmetry, from and angle of 0° to 90°. The field-cooled-position radial displacement is with respect to the diameter of the superconductor and varies from 0 to 28 mm. The field-cooled-position height displacement is with respect to a chosen arbitrary field-cooling height 25.5 mm, from the center of the 19.1 mm diameter magnet to the center of the superconductor, from 9.5 to 41.5 mm. The magnetic field strength of the source magnet is with respect to the manufacturer specified surface field strength, from no strength (0 Gauss) to double the strength (17630 Gauss). Due to dissidence in current literature, temperature variation does not have an accurate model that relates temperature and levitation stiffness. Instead, the temperature variation is captured as a coefficient with respect to 1, from no flux pinning effect (0) to double the effect (2).

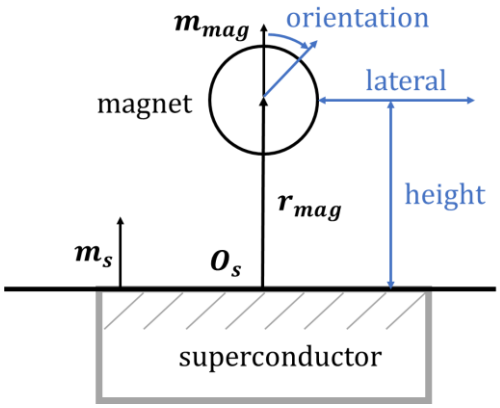

Figure 28: Direction convention for SMSS system.

Table 3: Summary of Physical Parameters with Relevant Reference Parameters for SMSS system.

Parameter to Vary	Relevant Parameter	Span of Relevant Parameter	Span of Variance
θ_{FC}	Pole to pole orientation	180 deg	[0 to 90] deg
x_{FC}	Diameter of superconductor	56 mm	[0 to 28] mm
z_{FC}	Separation distance/height	25.5 mm	[9.5 41.5] mm
B_0	Magnet surface field strength	8815 G	[0 17630] Gauss
c_t	Temperature coefficient	1	[0 2]

The following section investigates the dynamic response of the system as a result of perturbing these physical parameters. Appropriate metrics to characterize the performance of a flux-pinned interface include stiffness, depth of potential well, natural frequencies, and magnitude of attractive force. The stiffness is the resistance of motion away from equilibrium position or attitude. The potential energy is the energetic capability of the interface to capture a dynamic body and defines the sphere-of-influence across which the interface acts. Although natural frequency is directly related to stiffness, associating a realistic mass to a stiff joint yields physical intuition to system design. Magnitude of attractive force is a common metric to compare other physical phenomena acting on spacecraft. The sensitivity is represented as a series of plots across the entire span of each physical parameter with each dynamic response variable normalized to the reference response.

SMSS Sensitivity Results

By linearly varying the physical parameters across the entire span in Table 3, a relationship can be drawn from the magnet's dynamic response and the physical parameters. The following plots are separated by physical parameter. Each plot overlays the lateral stiffness k_l, normal stiffness k_h, rotational stiffness k_θ, potential energy U, and attractive force F normalized to the

reference response from the system described in SMSS Physical System. Noise stems from calculations perturbing the magnet state within machine precision error.

When the physical parameter is equivalent to the reference value, the dynamic response is equivalent to the reference response and the normalized reference response is always 1, with reference physical parameters given in Table 4 and reference responses given in Table 5. Table 5 also reports the angular velocity reference response in the lateral ω_l, normal ω_h, and rotational ω_θ directions, which is specific to the mass configuration but physically intuitive. Any normalized values below 1 imply that the reference dynamic model overestimates the actual system's dynamic response, and vice versa for normalized values above 1. Due to the nonlinear behavior of flux-pinned dynamics, some physical parameter variation is amplified despite minimal perturbation. Lateral displacement is the only parameter in which a 1% variation results in less than 1% variation in the consequent dynamic response. When varying the most sensitive physical parameter, field-cooled height, the normal stiffness of the flux-pinned interface changed by over 10%, as shown in Table 6.

Table 4: Reference Physical Parameters for SMSS system.

Reference Physical Parameter	Physical Parameter Numerical Value
θ_{FC}	0 degrees
x_{FC}	0 m
z_{FC}	0.016 m
B_0	8815 Gauss
c_t	1

Table 5: Reference Dynamic Response Parameters for SMSS system.

Reference Dynamic Response Parameter	Dynamic Response Numerical Value
k_l	29 N/m
k_h	58 N/m
k_θ	0.65 Nm/rad
U	-0.0109 J
F	1.29 N
ω_l	32.7 rad/sec
ω_h	46.5 rad/sec
ω_θ	4.9 rad/sec

The system accumulates error from least sensitive to most sensitive: field-cooled lateral displacement, field-cooled orientation, temperature, magnetic field strength, and field-cooled height. All dynamic response parameters decrease linearly with increasing lateral displacement, with the scalar drawn from experiments measuring magnetic field within a YBCO superconductor disk, as shown in Table 1Table 6.

Table 6 [106]. Note that the reference response already accounts for the 64% reduction. Varying the field-cooled orientation from perfectly aligned to perfectly misaligned orientation shows monotonic degradation in every dynamic response except for rotational stiffness, which is restored past 45 degrees, as shown in Figure 29. The lateral stiffness was least affected and rotational stiffness was the most affected by orientation perturbation. Normal stiffness, potential energy, and attractive force were similarly degraded by orientation. All dynamic response parameters increase linearly with increasing temperature coefficient, as shown in Figure 30. Temperature and lateral displacement are linear relationships that only affect the images, not the source magnet. All dynamic response parameters increase quadratically with increasing magnetic

field strength, not linearly due to magnetic field strength affecting both the source magnet and image strength, as shown in Figure 31. Field-cooled height affects all dynamic response parameters drastically, inversely proportional with z^4, as shown in Figure 32.

Table 6: Percent error in SMSS dynamic response from 1% variation of physical parameters.

		Δx	$\Delta\theta$	Δc	ΔB	Δz
+1% variation in parameter	lateral stiffness k_x % difference	-0.80	-0.01	2.00	4.19	-10.54
	height stiffness k_h % difference	-0.78	0.78	2.33	4.26	-9.69
	rotation stiffness k_θ % difference	-0.80	-1.58	2.00	4.19	-8.53
	potential energy U	-0.80	-0.01	2.00	4.19	-6.46
-1% variation in parameter	lateral stiffness k_x % difference	-0.80	-0.01	-2.00	-3.82	9.24
	height stiffness k_h % difference	-0.78	0.78	-2.33	-3.49	10.08
	rotation stiffness k_θ % difference	-0.80	-1.58	-2.00	-3.82	7.33
	potential energy U	-0.80	-0.01	-2.00	-3.82	5.44

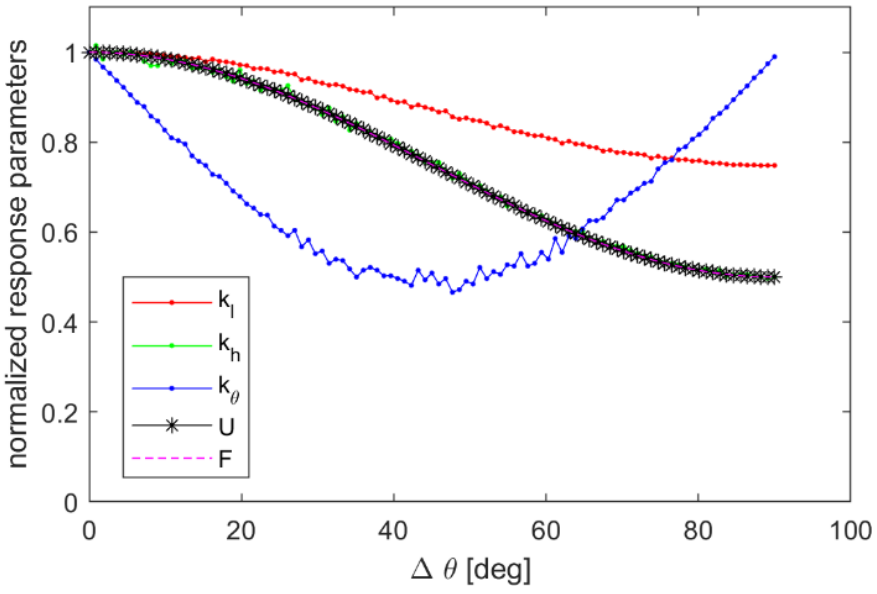

Figure 29: Dynamic response from field-cooled orientation variation.

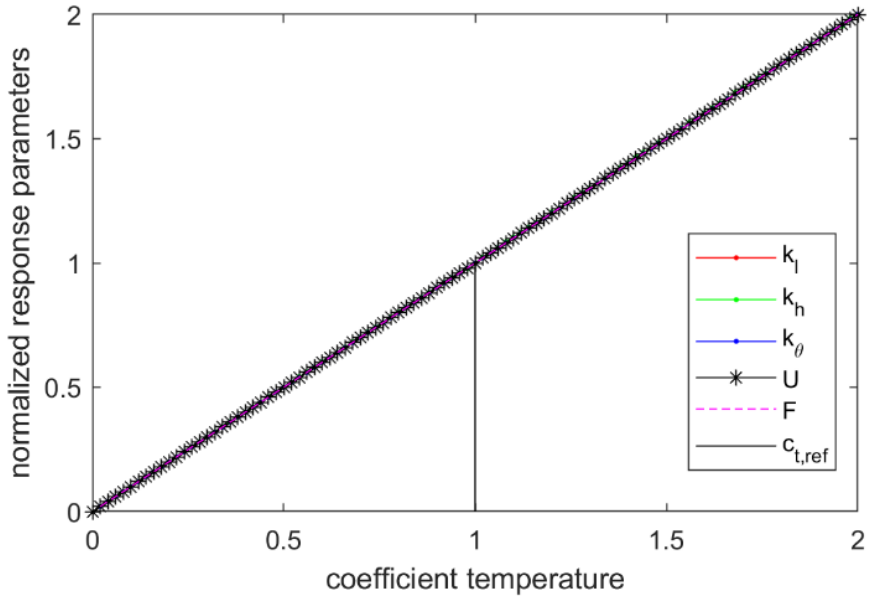

Figure 30: Dynamic response from coefficient of temperature variation.

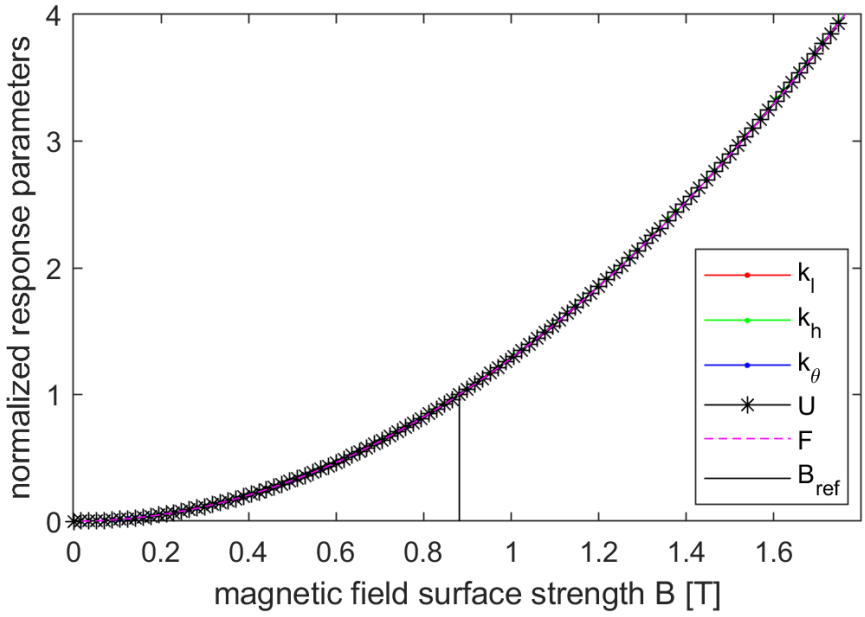

Figure 31: Dynamic response from field-cooled magnetic field strength variation.

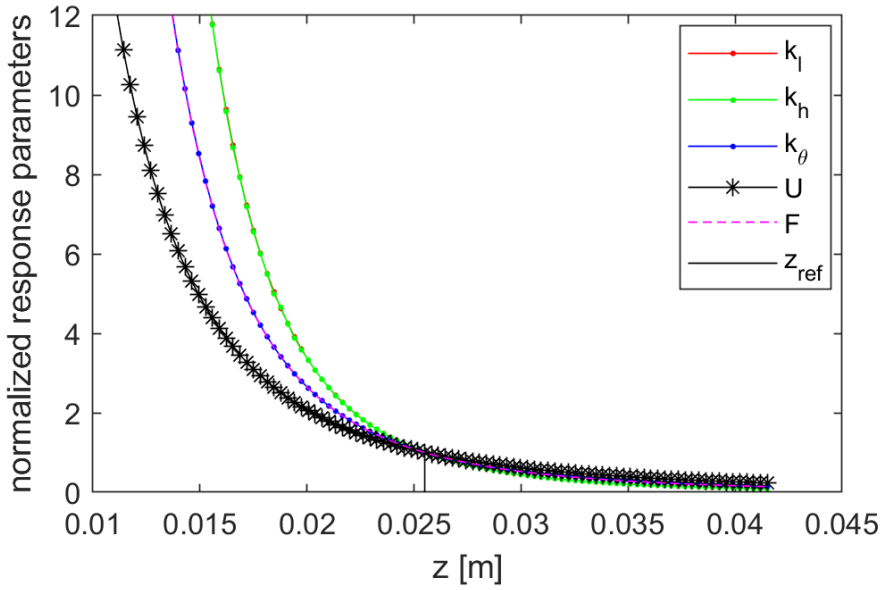

Figure 32: Dynamic response from field-cooled height displacement variation.

Multiple-Magnet and Multiple-Superconductor System

The multiple-magnet and multiple-superconductor (MMMS) interface uses the same components and physical parameters described in the SMSS Physical System section but involves three superconductors and twelve magnets. In a case studying two spacecraft for a docking application, the magnetic spacecraft has a mass of 2.1 kg, 20.3 cm diameter sphere with full range of motion and the superconducting spacecraft of significantly more volume and mass with no motion. The magnets are arranged in an icosahedron geometry, in which all magnets are pointing radially outward and equidistant from each neighboring magnet. The superconductors are placed so that any trio of the magnetic spacecraft's magnets are 2.55 cm radially inward in equilibrium position and pointed along the radial direction. This interface has been tested on a series of testbeds to study docking and capture dynamics, as shown in Figure 33 [22]. The same dynamic response parameters in lateral, normal, and rotational directions must be defined similarly to the single-magnet and single-superconductor system, shown in Figure 34.

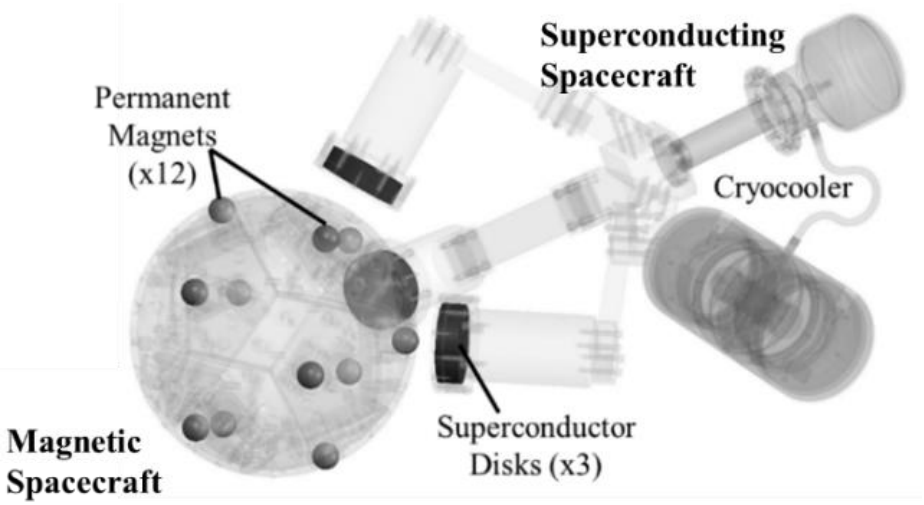

Figure 33: Multiple-magnet and multiple-superconductor flux-pinned interface of docking interface concept.

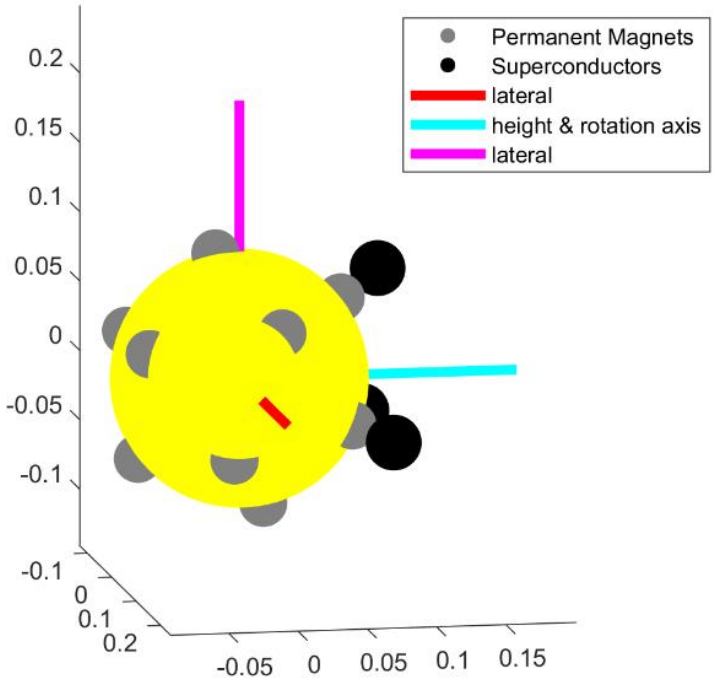

Figure 34: Direction convention for MMMS system.

MMMS Variation of Physical Parameters

Although the physical parameter symbols are analogous to the SMSS system, $\theta_{FC}, x_{FC}, z_{FC}$ represent slightly different physical parameters relating to the spacecraft, not an individual magnet.

θ_{FC} is the angular displacement between two equilibria rotated about the center of the superconductors. As the spacecraft rotates about this axis, the magnets move off the superconductor surface at 16.5 deg. The lateral separation distance, x_{FC}, between the magnetic spacecraft and the superconducting spacecraft spans from equilibrium position to physical interference between the two spacecraft bodies, symmetric in either direction. The lateral displacement never allows the magnet to move off the surface area of the superconductor because the two spacecraft surfaces interfere before the magnet moves too far in the lateral direction. The normal separation distance, magnetic field strength, and temperature coefficient cover the same spans. Table 7 lists all parameters and the corresponding span of variance.

Table 7: Summary of Physical Parameters with Relevant Reference Parameters for MMMS system.

Parameter to Vary	Relevant Parameter	Numerical Value of Relevant Parameter	Span of Variance
θ_{FC}	Angular displacement between spacecraft EQ orientation	16.5 deg	[0 16.5] deg
x_{FC}	Lateral separation distance	8.5 mm	[0 8.5] mm
z_{FC}	Normal separation distance	25.5 mm	[-16 16] mm
B_0	Magnet surface field strength	8815 G	[0 17630] Gauss
c_{temp}	Temperature coefficient	1	[0 2]

MMMS Sensitivity Results

By linearly varying the physical parameters across the entire span in Table 7, a relationship can be drawn from the spacecraft's dynamic response and the physical parameters. The reference physical parameters are given in Table 8 and the reference responses are given in Table 9. Unlike the SMSS system, the MMMS rotational and translational degrees of freedom are coupled due to the source magnet and superconductor orientations spanning $\mathbb{R}^3$. The MMMS system is stiffer than the SMSS system in the translational degrees of freedom, but less stiff in rotation. The

baseline rotational stiffness is very low and any modifications to the system, like translational perturbation, transfers stiffness in translation to stiffness in rotation. Any perturbation in the system is amplified in the dynamic response to different degrees, as shown in Table 10. The most sensitive dynamic response is rotational stiffness. The physical parameter causing the most drastic change in a single dynamic response parameter is field-cooled orientation, but the change in the other dynamic responses are minimal. The physical parameter that affected the most distributed change across the entire system is field-cooled height.

Table 8: Reference Physical Parameters for MMMS system.

Reference Physical Parameter	Physical Parameter Numerical Value
θ_{FC}	0 degrees
x_{FC}	0 m
z_{FC}	0.016 m
B_0	8815 Gauss
c_{temp}	1

Table 9: Reference Dynamic Response Parameters for MMMS system.

Reference Dynamic Response Parameter	Dynamic Response Numerical Value
k_l	65 N/m
k_h	89 N/m
k_θ	0.304 Nm/rad
U	0.0497 J
F	1.8137 N
ω_l	5.57 rad/sec
ω_h	6.53 rad/sec
ω_θ	0.38 rad/sec

The system manifests the most error in any single dynamic response from least sensitive to most sensitive: temperature, magnetic field strength, field-cooled height, field-cooled lateral displacement, and field-cooled orientation, as shown in Table 10. The system accumulates the most error across all dynamic responses, from least sensitive to most sensitive, in temperature, field-cooled lateral displacement, magnetic field strength, field-cooled height, and field-cooled orientation, as shown in Table 11. Temperature and magnetic field vary the MMMS system in the same way that they did in the SMSS system because these parameters are agnostic to specific geometries. Temperature and magnetic field affect all magnet-superconductor interactions equally, seen in Figure 35 and Figure 36. The other physical parameters require a specific geometry context to explain the change in dynamic response.

The geometry-specific parameters include field-cooled lateral displacement, height, and orientation. The lateral displacement, symmetric in the negative and positive directions, shifts one magnet-superconductor closer together in the surface normal direction. The opposite is true for the other magnet-superconductor pairs, which slides each magnet laterally across the corresponding superconductor surfaces. Although two of the three magnet-superconductor pair interactions are weaker, the closer magnet-superconductor more than compensates for the other reductions by increasing strength with z^3, increasing normal and lateral stiffness, seen in Figure 37. Rotational stiffness depends on the lateral stiffness of individual magnet-superconductor pairs and scales with less than a z^3 interaction. The field-cooled height for the spacecraft shifts every magnet superconductor pair equally, in a combination of normal and lateral direction motion with respect to each superconductor surface. The spacecraft dynamic responses are predictably stronger as the magnetic spacecraft is field-cooled closer to the superconducting spacecraft, seen in Figure 38. The MMMS system does not behave as dramatically to height variation as the SMSS system

because the individual magnets also move in the lateral direction along the superconductor surface, reducing the amount of flux penetrating each superconductor. At the reference field-cooled orientation, the magnet-superconductor pairs are aligned, but as the field-cooled orientation is perturbed, the magnet-superconductor pairs are misaligned, causing a reduction in lateral and height stiffness. The magnetic-moment dipoles begin to align with the superconductor surface tangent, contributing to an increase in rotational stiffness. With further angular displacement, the magnet is farther from the superconductor center in both lateral and normal distance, seen in Figure 39.

Table 10: Percent error in MMMS dynamic response from 1% variation in each physical parameter.

		Δx	$\Delta\theta$	Δc	ΔB	Δz
+1% variation in parameter	lateral stiffness k_x % difference	1.67	4.63	3.90	-1.46	-4.66
	height stiffness k_h % difference	2.87	6.09	7.06	4.14	-1.85
	rotation stiffness k_θ % difference	2.51	15.91	22.75	24.39	45.66
	potential energy U	2.00	2.00	2.63	-0.22	-0.47
	attractive force F	2.00	4.59	2.58	-0.22	-0.47
-1% variation in parameter	lateral stiffness k_x % difference	-2.37	-3.33	-4.72	-1.46	-4.66
	height stiffness k_h % difference	-1.21	-2.21	-5.35	4.14	-1.85
	rotation stiffness k_θ % difference	-0.75	-3.33	10.76	24.39	45.66
	potential energy U	-3.42	-2.00	-4.28	-0.22	-0.47
	attractive force F	-3.42	-2.00	-4.34	-0.22	-0.47

Table 11: Accumulated percent error in dynamic response from 1% variation in each physical parameter.

	Δx	$\Delta\theta$	Δc	ΔB	Δz
Accumulated percent error over all dynamic responses due to +1% variation in parameter	11.05	30.42	33.23	38.92	53.10
Accumulated percent error over all dynamic responses due to -1% variation in parameter	11.17	30.42	12.87	29.44	53.10

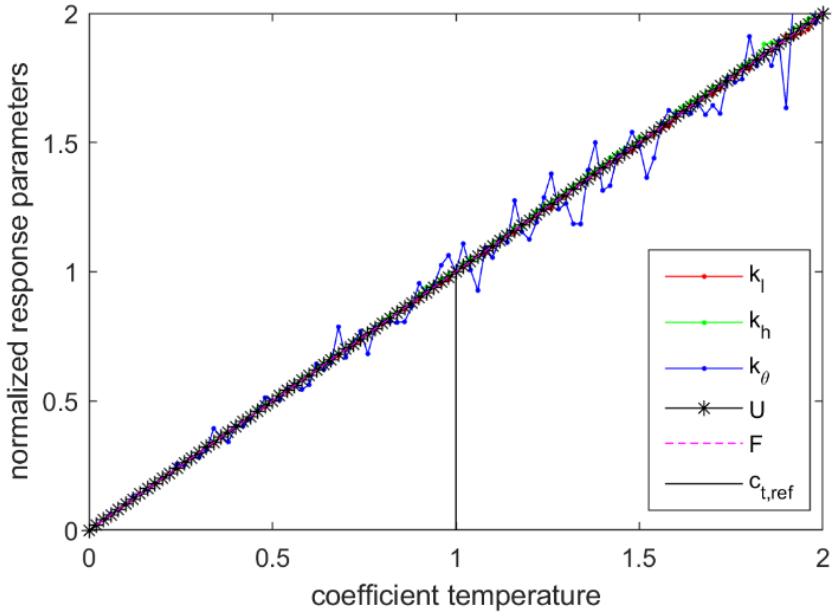

Figure 35: Dynamic response of system due to temperature coefficient variation.

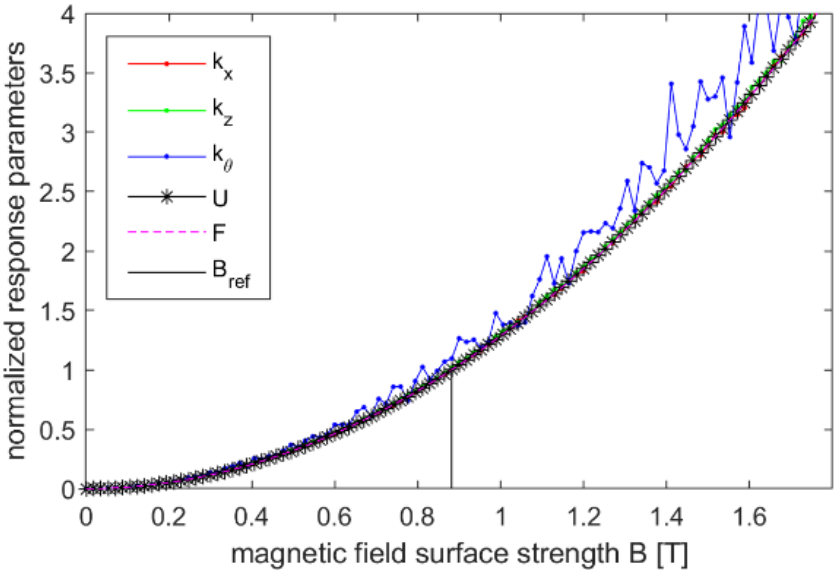

Figure 36: Dynamic response of system due to magnetic field strength variation.

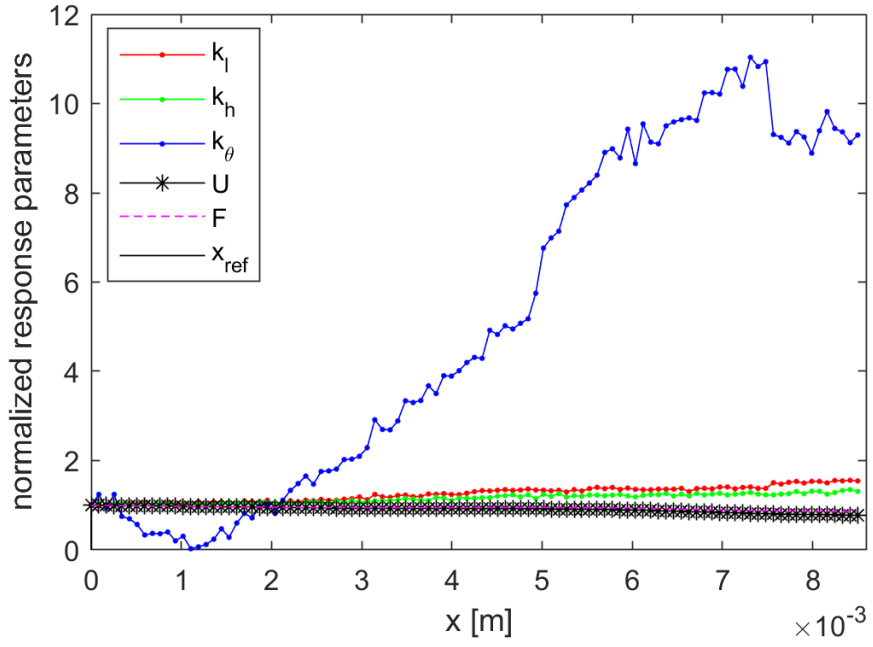

Figure 37: Dynamic response of system due to lateral displacement variation.

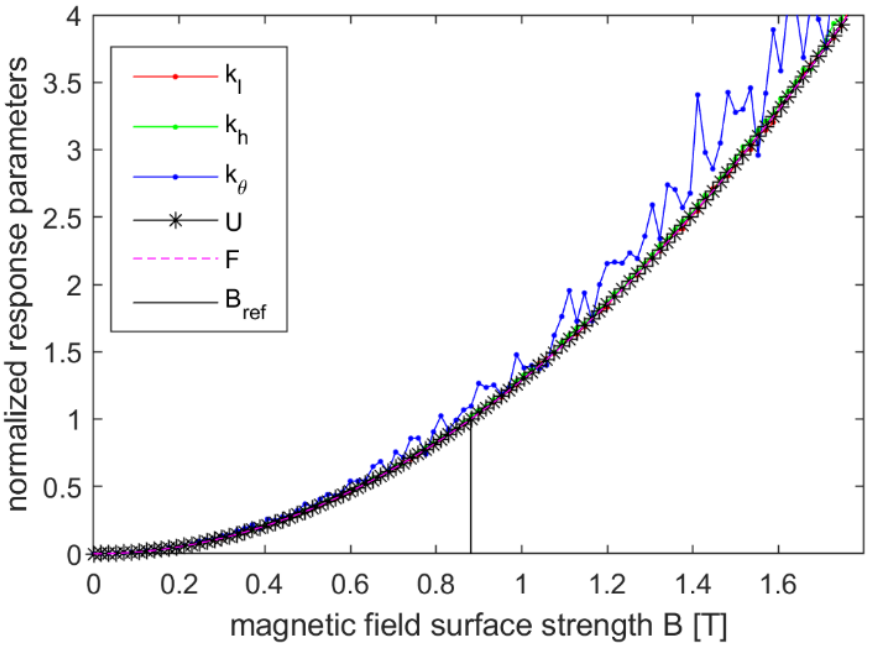

Figure 38: Dynamic response of system due to height variation.

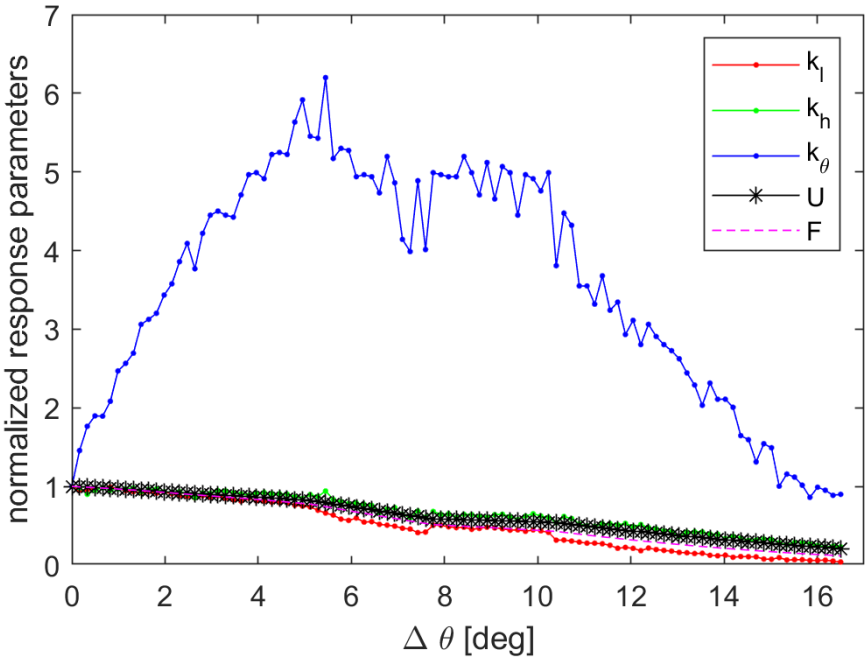

Figure 39: Dynamic response of system due to field-cooled angle displacement variation.

d. *Contribution from Parameterization Study*

In this section, many modifications are suggested to refine Kordyuk's frozen-image model, which is a less computationally intensive alternative to the critical state model. These modifications are based upon empirical data from that explain discrepancies between ideal and physical system. The refinements are expressed in analytical form and injected into a dynamics model simulating flux-pinned interface dynamics. Although the refinements add more computation, the order of computation of the refined model is on the order of $\sigma(16MN^2)$ vs. the baseline order of $\sigma(2MN^2)$, which is still significantly less intensive than the critical state model. Two systems, based on commercially available components, are described to form a baseline dynamic response for a single-magnet single- superconductor system and multiple-magnet-multiple-superconductor system. A sensitivity study is performed on each system to probe the effect of different physical parameters on the dynamic response of the system.

From the sensitivity study, system-level design considerations may be formed to target less error or emphasize certain dynamic responses. Some parameters are not geometry specific, like temperature and magnetic field strength, but all field-cooled parameters are geometry specific. In general, the field-cooled separation distance affects the system performance most significantly. When designing, integrating, or validating the specifications of a physical system, trade-offs are made weighing different dynamic characteristics, which are adjusted with knowledge of the consequences from each physical parameter. For example, interface stiffness is the resistance of the two bodies to separate for which higher stiffness implies a more robust joint. An implication of stiffness is also natural resonant frequency for which either the interface can excite unwanted vibration in the individual spacecraft or spacecraft components can excite the interface unstably. Realistically at the mass of small satellites and the strongest permanent magnets, the natural frequencies range from 10's of Hz to single Hz in magnitude, which must be considered for low and high frequency jitter. Outside control of system design, this sensitivity study informs technologists observing flux-pinning dynamics of potential sources and magnitudes of error from each physical parameter. In developing flux-pinned technology, this paper demonstrates the need to measure or control certain parameters with more precision to guarantee predictable dynamics below certain error bounds.

VI. Backwards Reachability of Flux-Pinned Docking Interface

a. *Problem Definition and Approach*

Given a poorly modeled dynamic system, is there guarantee that the system reaches a final state with some confidence (probability) with formal methods? Instead of simulating a timeseries from an initial value to validate reaching a final state, a backwards reachable set answers the same

question of reachability without exact state knowledge through time evolution. Further, a precomputed set of safe states is more computationally efficient than real-time sensing and evaluation, more informative for system design, and safer during operations. This section explores the generation of a viability kernel for a flux-pinned docking and capture application.

Dynamic Model and Uncertainty

The system model contains a rigid body with states: position, orientation, velocity, and angular velocity. The rigid body follows continuous, nonlinear, coupled dynamics that are propagated by nonlinear differential equations but may be represented in linearized state spaces for convenience [109]. The dynamics model has unknown residual effects, which may be modeled as stochastic, affine disturbances. There is no control input, thus all dynamics are driven by passive physics. The dynamics are Lyapunov stable, which is advantageous in calculating the viability kernel [23].

The dynamics model is highly nonlinear and coupled, encapsulated by Kordyuk's frozen-image model and Villani/Landecker's magnetic-dipole model [93], [96], [97]. For this magnet and superconductor configuration, there are a total of 864 interactions. Although the expressions for force and torque are explicit and of closed-form, the summation of forces and torques is not a tractable hand-calculation. The full, nonlinear dynamic propagation and linearization all occur with numerical analysis on computers. The linearization approximation is analyzed for accuracy and sensitivity in a previous paper [109].

Bridging theory to physical implementation, a physical manifestation of a flux-pinned interface is affected by parameters or states that are either not precisely known or controlled. The parameters and state sensitivities primarily affect the stiffness of the interface, discussed

extensively in the previous section [94]. The most sensitive parameter in a physical system is the orientation of the two spacecraft relative to each other.

Viability Kernel

$$Viab\,(V) \coloneqq s_0 \in S, \forall t, s_{s0}^{S}(t) \in V \tag{93}$$

The viability kernel of a safe set V is the set of all initial states in V for which the trajectories emanating from those states remain within V, defined formally in Eq. (93). A safe-state set and a final-state set must be defined to find the viability kernel. The viability kernel is then approximated by backwards recursion. For every timestep or spatial partition, a maximal reachable set is computed. The viability kernel is the intersection of all reachable sets and the safe set.

For a Lyapunov-stable dynamic system, a maximal reachable set emanating backwards always includes the current set, the definition of positive invariance. Another definitions guarantees that the system never exits the maximal reachable set propagating forward. Lyapunov stability simplifies the calculation of viability kernel because an intersection of backwards reachable sets does not need to be computed, simply the backwards reachable set. Further, if the dynamic system is Lyapunov stable and acts over finite distance, the maximal reachable set is closed and compact. The shape of the boundary is continuous and smooth. Although polytopes and zonotopes may be used to express the boundary, a polynomial more closely approximates the boundary.

Safe-State Set

The safe state is defined by the physical intersection between the magnetic spacecraft and the superconductor spacecraft. Assuming a specific separation distance between the OSA and

SROA in final configuration, the OSA may oscillate within a hemisphere with radius of the separation distance. If the OSA is farther away from SROA, the constraint is less restrictive, allowing movement within a conical volume.

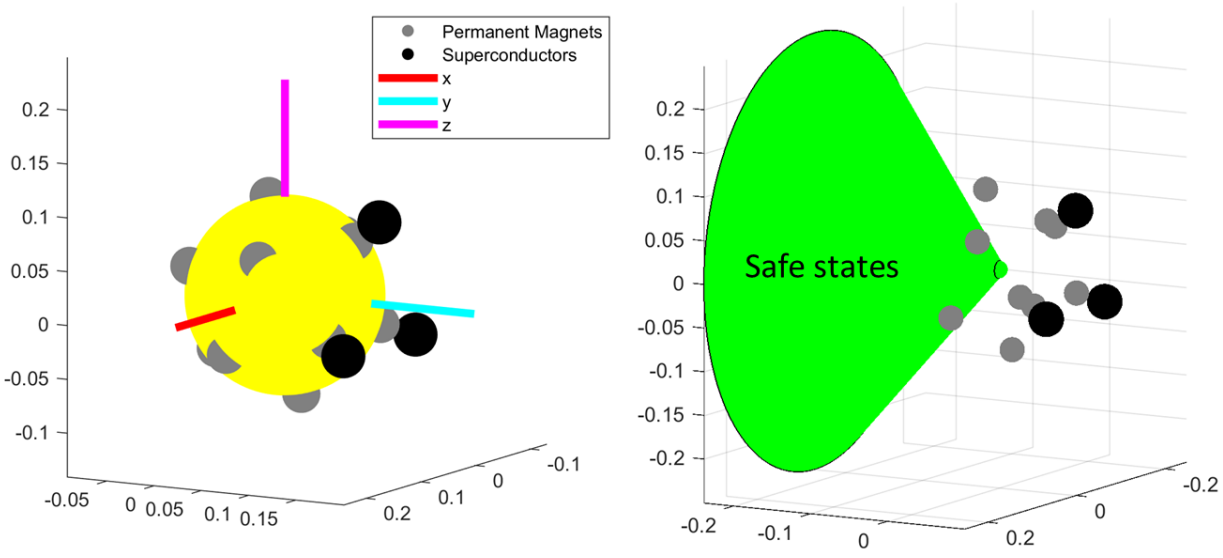

Figure 40: left, MATLAB representation of flux-pinned interface with attached coordinate system; right, safe set constrain in 3D position with respect to final configuration

Backwards Reachable Sets

There exists a boundary in dynamic state that separates two different behaviors: successful docking and escape. A mathematical analogy in differential equations is called the separatrix. For deterministic systems, the separatrix defines binary behavior. For probabilistic systems, boundaries/contours in phase space may be drawn to represent different degrees of certainty. The stricter the requirement for certainty, the smaller the set of acceptable conditions for successful capture. In the absence of control input, the maximal reachable set is the separatrix.

Physical Intuition

Some physical insights help in bounding states. If the system has more kinetic energy than potential energy, the system ejects out of the potential well. Conversely, if the system has more

potential energy than kinetic energy, the system is captured within the potential well. The separatrix is defined by the state boundary in which potential energy negates kinetic energy, or the total energy of the system is zero. The system must have no kinetic energy at the boundary of the safe state set, otherwise the two spacecraft occurs. The potential energy well is a closed and compact set. The boundary of the potential energy well ($U = 0$) is the most inclusive position and orientation state boundary. For any nonzero kinetic energy states, the system must at least lie within the potential energy well boundary. The equilibrium state is the global minimum location of the potential energy well.

b. *Methodology*

Viscosity Solution of Hamilton-Jacobi Equations

The viscosity solution of Hamilton-Jacobi equations yields an exact solution describing the reachability boundary but requires specific definition of formulation. The viscosity solution requires that the partial differential equation of interest is first order, which is not true of the flux-pinned dynamics. The system must also be formulated as Lagrangian or Hamiltonian mechanics, which requires an explicit representation of kinetic energy and potential energy. This formulation is not tractable as there are 864 interactions to sum over, although the solution yields an analytical solution.

Discretized Search Space

Given that the potential energy well is a closed, compact set, the system's potential energy boundaries may be found by incrementing through the safe-state space. The search is diffusive, starting at the global minimum of the potential energy well, the equilibrium state. The search is exhaustive and computationally intensive (exponential with number of states). The resolution of

the boundary maintains the resolution of the discretization. The boundary can only be underapproximated because of uncertainty between adjacent discretized states. The advantage lies in its comprehensiveness and inclusion of full nonlinear dynamics. There is no linearization needed, and therefore no approximation error.

Polynomialization

The nonlinear dynamics or energy boundaries may be approximated by a polynomial. If a closed-form analytical expression is available, a Taylor expansion is feasible. For expressions with an intractable amount of terms, numerical methods include curve fitting algorithms. In MATLAB, one such tool is cftool, but only handles up to three dimensions of data.

c. *Results*

The energy boundaries described are generated with a discretized search space and increment into higher degrees of freedom. The combinations of degrees of freedom are intuitively selected, considering system symmetry to reduce the total number of variables and coupling translational/rotational modes. The three cases studied are 2DOF radial distance and velocity, 4DOF radial/angular distance and radial/angular velocity, and 3DOF full position movement.

2DOF: Radial Distance and Radial Velocity

Starting in two degrees of freedom, the energy components are calculated as a function of radial distance and radial velocity (the direction toward and away from the orbiter). The components of energy and total energy [Joules] are plotted against distance [meters] and velocity [meters/sec]: $U(r)$ potential, $T(v)$ kinetic, $D(r,v)$ dissipative, and $E(r,v)$ total, Figure 41. The maximum straight-on distance for OS capture with no velocity is 8.2 cm away from the orbiter.

The maximum instantaneous velocity to ensure no collision with the orbiter in final state is 4.54 cm/s. The intermediate values do not follow a linear relationship due to the nonlinear nature of the dynamics, but more so an exponential or high polynomial decay. For successful capture, the OS' instantaneous state must lie within the zero-energy contour, which may be checked visually. For a more rigorous process, a polynomial may be fit to the zero-energy contour and checked at a continuum of states.

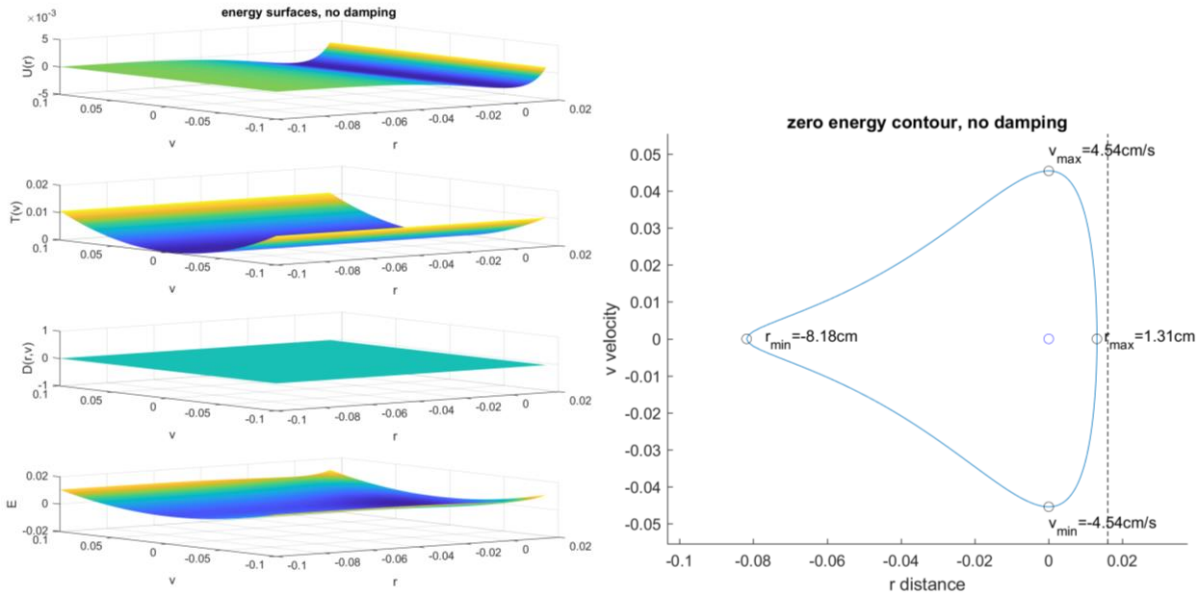

Figure 41: left, energy surfaces; right, zero-energy contour for 2DOF system

4DOF: Radial Distance, Radial Velocity, Angular Displacement, and Angular Velocity

Adding angular displacement and angular velocity into the allowable degrees of freedom, the zero-energy contours for each combination of two degrees of freedom while holding the other two degrees of freedom at equilibrium, shown in Figure 42. The zero-energy contours vary with an additional degree of freedom, showing a 3D boundary in Figure 43. The extrema values for the zero-energy contours are listed in Table 12.

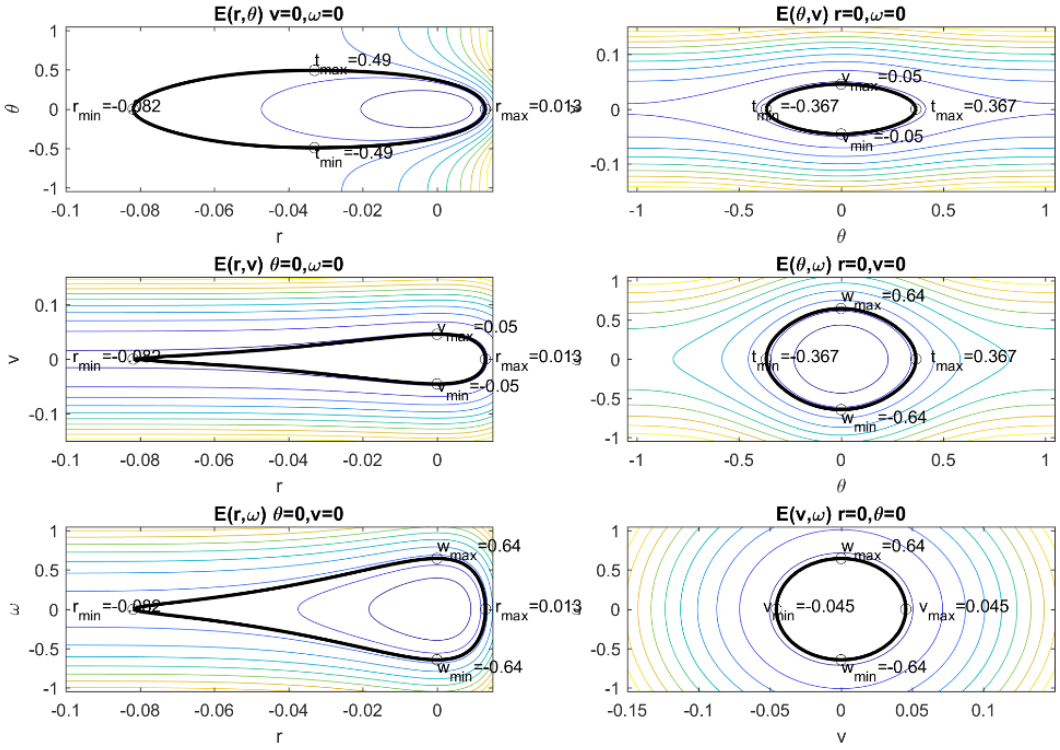

Figure 42: energy contours of each pair combination while holding the other two fixed for 4DOF system; zero-energy contour drawn with thick black, extrema labeled.

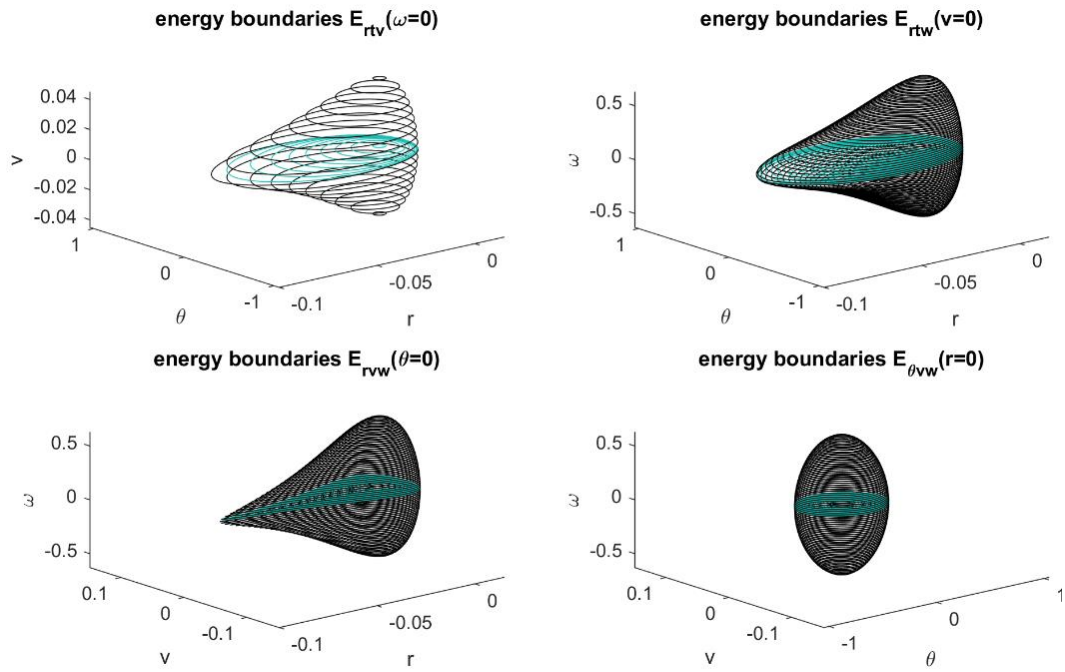

Figure 43: energy contours of each pair combination superimposed with another degree of freedom, displaying the boundary up to three degrees of freedom.

Table 12: extrema values of zero-energy contours of 4 DOF system

State	Min	Max	Units
r	-8.2	1.3	cm
v	-4.5	4.5	cm/s
θ	-21	21	deg
ω	-28	28	deg/s

3DOF: Full Position Movement

Instead of calculating the total energy at every state, extracting the potential energy at every position/ orientation from the full nonlinear simulation and then calculating acceptable kinetic energy reduces computation exponentially. Kinetic energy has a clear, straightforward relationship with the kinetic states: $T(\boldsymbol{v}, \boldsymbol{\omega}) = \frac{1}{2} M \boldsymbol{v}^{\boldsymbol{T}} \boldsymbol{v} + \frac{1}{2} \boldsymbol{\omega}^{\boldsymbol{T}} I \boldsymbol{\omega}$. The work space is discretized to 1 mm resolution, bounded by the safe set. X, Y, and Z position are incremented with nested for-loops, broken by an if-statement that checks if potential energy is non-positive (boundary condition). Figure 44 shows the resultant volume boundary and Table 13 lists the resultant extrema positions for each degree of freedom. The following process determines capture success with the 3DOF discretized potential energy volume: position state and kinetic states are measured, potential energy found with nearest-neighbor or 3D interpolation, and then kinetic energy checked against the extracted potential energy volume.

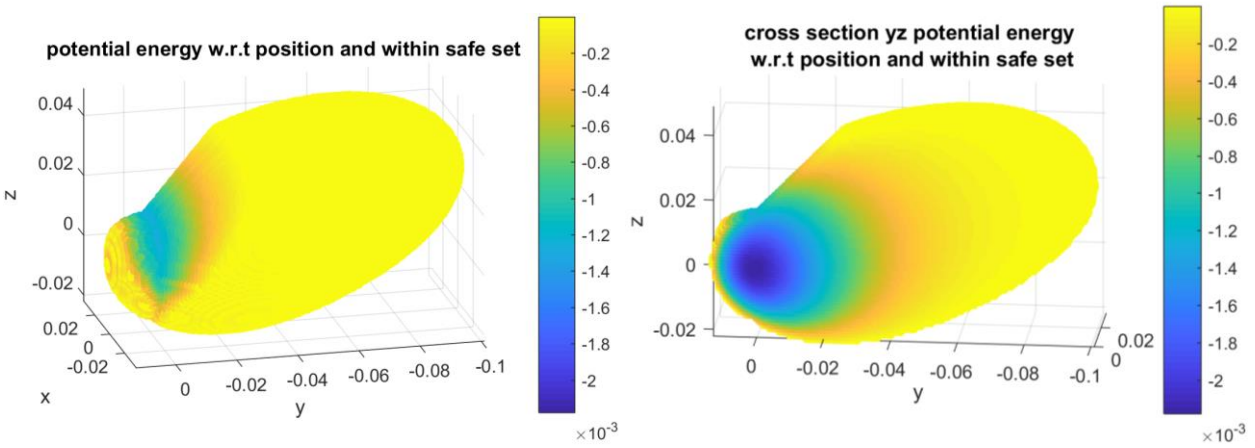

Figure 44: left, resultant volume of potential energy with respect to 3DOF position, color scaled by potential energy. right; yz cross section of volume

Table 13: extrema of potential energy volume with respect to 3DOF position

	$r(x\ extremum)$ [m]	$r(y\ extremum)$ [m]	$r(z\ extremum)$ [m]
minimum	(-0.035 -0.055 0.02)	(0 -0.101 0.027)	(0 -0.022 -0.022)
maximum	(0.035 -0.055 0.02)	(0 0.013 0)	(0 -0.067 0.049)

Polynomialization

Cftool is a polynomialization tool developed by Mathworks that fits the surfaces to a multivariable polynomial expression. The user defines the order of the polynomial, iteratively increasing the order of the polynomial until the fitted curve falls below an error threshold. The problem of overfitting is necessary to consider for applications involving prediction, but for this specific system, there exists only one configuration of interest. The best fit remains the best fit.

2DOF: Radial Distance and Radial Velocity

By extracting the data points from the zero-energy contour, a polynomial is fit to the two states. Figure 45 shows the resultant fit and polynomial coefficients are listed in Appendix II. The approximation error oscillates between overestimating and underestimating the relationship between the two states. To be conservative, the lower bound coefficients should be used to represent the maximal reachable boundary: $|v| \leq |f_l(r)|$ where v is the instantaneous velocity, f is the fitted polynomial with lower bounds, and r is the instantaneous distance. If the linear inequality is satisfied, the spacecraft is captured.

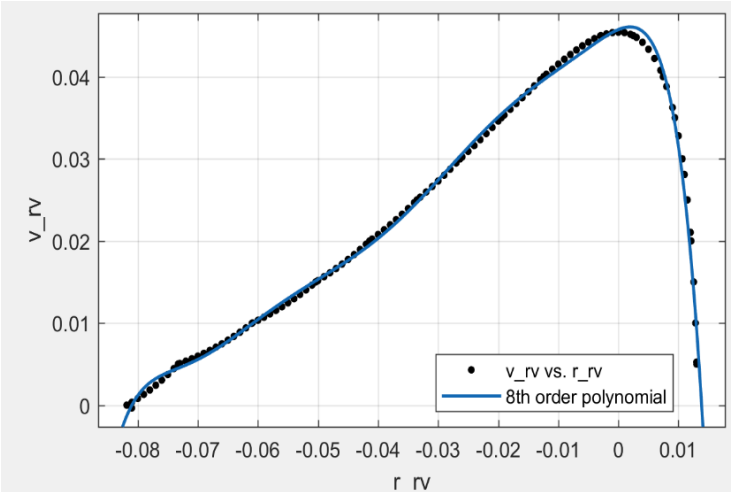

Figure 45: left, zero energy contour for 2DOF system, fit with cftool resulting in 8th order polynomial.

4DOF: Radial Distance and Radial Velocity

Extending the polynomialization methodology to four degrees of freedom, a multivariable polynomial expression is fit to surfaces, generated from zero-energy contours, taken from Figure 43. Cftool is limited to fit fourth-order polynomials for 3D surfaces, which does not capture all four dimensions and underfits the data points. To incorporate all four dimensions, every combination of three degree-of-freedom energy surfaces are fit, shown in Figure 46. One of the fitted energy surfaces is shown in Figure 47. The final four degree-of-freedom boundary must satisfy a combination of linear inequalities:

$$|v| \leq |f_{rtv}(r,\theta)| \qquad |\omega| \leq |f_{rv\omega}(r,v)|$$

$$|\omega| \leq |f_{rt\omega}(r,\theta)| \qquad |\omega| \leq |f_{\theta v\omega}(\theta,v)|$$

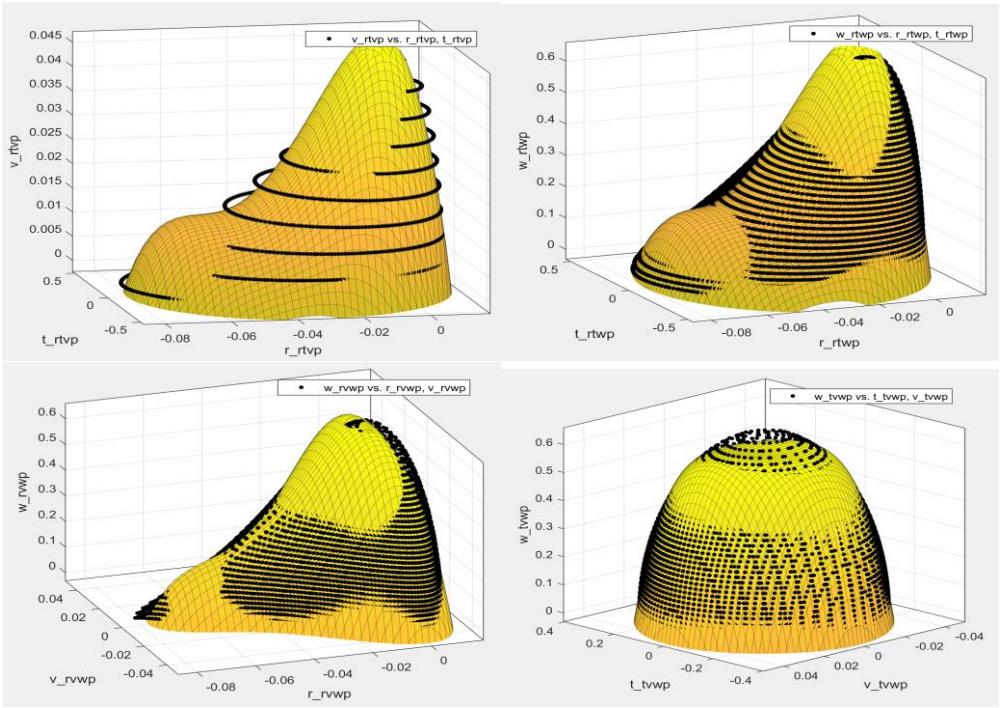

Figure 46: zero-energy and fitted surfaces for every combination of three states

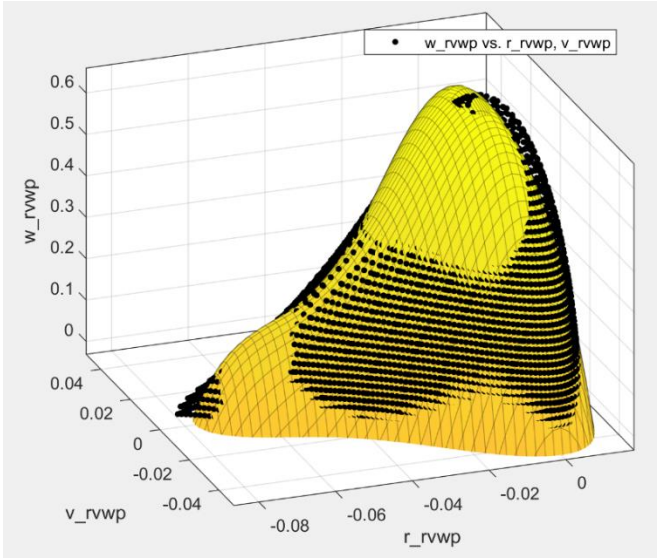

Figure 47: left, energy surface varying distance, velocity, and angular velocity.

3DOF: Full Position Movement

With the help of the boundary function, the surface data points of the volume are isolated. To fit the surface, the surface is divided into three sections, shown in Figure 48: the nearly hemispherical bowl section 1 ($y > 0$), the left approach surface section 2 ($y < 0, x > 0$), the right approach surface section 3 ($y < 0, x < 0$). Section 2 and 3 are symmetrical about the yz plane, or an even function with respect to x. Section 2 was fit with cftool, which yielded surprisingly close boundaries, shown in Figure 48. Still, as discussed before of the polynomial fit, the coefficients should be chosen to underapproximate the volume. The spacecraft position laying within this boundary is a necessary but insufficient verification for capture. To fully verify capture, the potential energy and kinetic for the full state must be calculated.

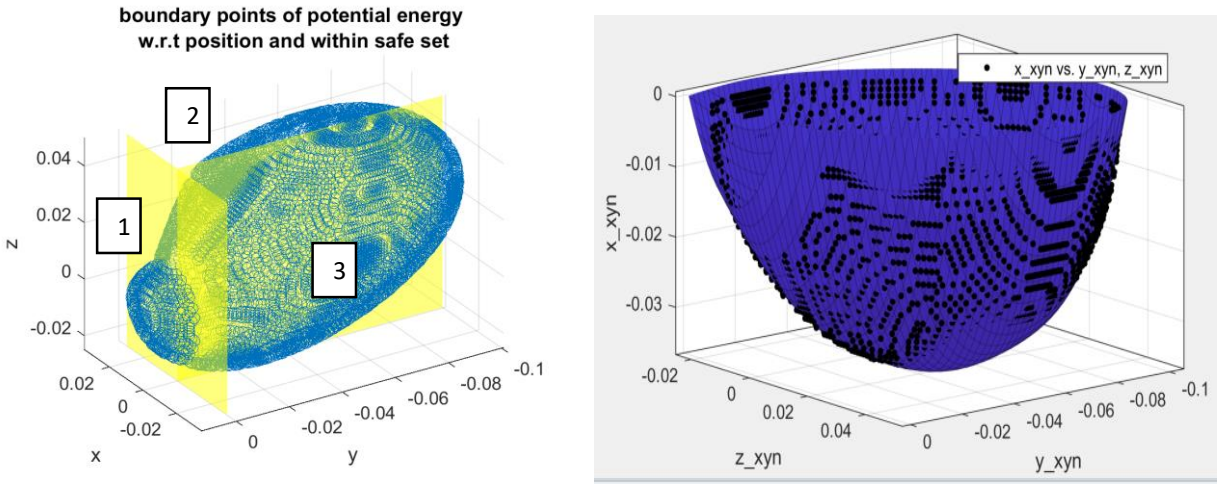

Figure 48: left, boundary data points of zero potential energy volume w.r.t position with planar separation. Right, section 2 evaluated with a fifth order multivariate polynomial x = f(y,z)

d. *Contribution from Backwards-Reachability Analysis*

The discretized energy volume utilizes the full nonlinear system upon each evaluation but is only exact to within the resolution of the discretization. Verifying that an instantaneous state lies within the volume is not straightforward for nearest-neighbor or n-dimensional interpolation,

especially near the boundary of the volume. Polynomialization offers a solution to straightforward verification but has approximation errors due quality of fit. More sophisticated or in-house generated algorithms could fit higher-order polynomials and/or highe- dimensional data sets. Future work includes generating a boundary with a Support Vector Machine, an arbitrarily high-dimensional classification algorithm that maximizes safety margin between safe and unsafe data points [123]. The boundary/maximal reachable set problem is significantly more tractable if total energy is decomposed into separate potential and kinetic energy volumes. The energies are decoupled, and kinetic energy is extremely straightforward to map from state to energy.

The larger contribution to this body of work is a different method to solve an initial value problem. Instead of generating timeseries for an initial state to then show the system is driven to equilibrium, backwards reachability offers a set of initial states that are known a priori to be driven to equilibrium. The intermediate analysis of calculating dynamic state between the initial condition and final condition may not be of interest and unnecessary. Instead, a direct mapping of initial state to capture success is more computationally efficient and informative.

CHAPTER 3: Hardware Maturation and Dynamic Experiments

Building test systems incorporating flux-pinned components contributes to hardware maturity by overcoming engineering challenges and dynamic model development through the collection of data. A system-design architecture resulted from 2015 in which a MATLAB simulation utilizing first principles validated that flux pinning feasibly captures and docks two spacecraft [22]. The simulation design formed the basis of a proof-of-concept hardware testbed, which successfully demonstrated capture and docking between two spacecraft analogues on ground, TRL 3. The proof-of-concept design evolved to a more rigorous, flight-traceable experiment design in which an extensive experiment campaign was conducted on ground, measuring with more precise sensors in 2016, TRL 4. Figure 49 and Figure 63 shows the increasing-fidelity planar-air-bearing capture and manipulation experiment testbeds, carried out with a roughly 1:1 scale OS analogue. To push forward into TRL 5, the ground-experiment test articles were reconfigured into two microgravity-experiment testbeds, which were flown in parabolic flights to simulate a relevant environment. This chapter details the motivation, design, implementation, and experimental results of each incrementally more mature testbed.

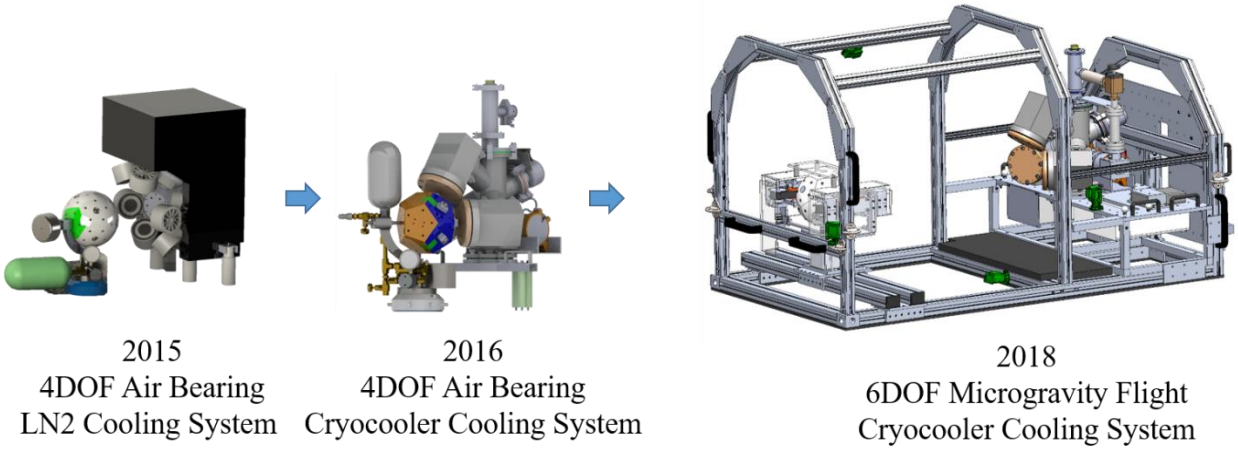

Figure 49: The hardware for the technology development has evolved from a liquid nitrogen bath to a cryocooler- and vacuum- based thermal system that operates in microgravity.

I. Proof-of-Concept Experiment

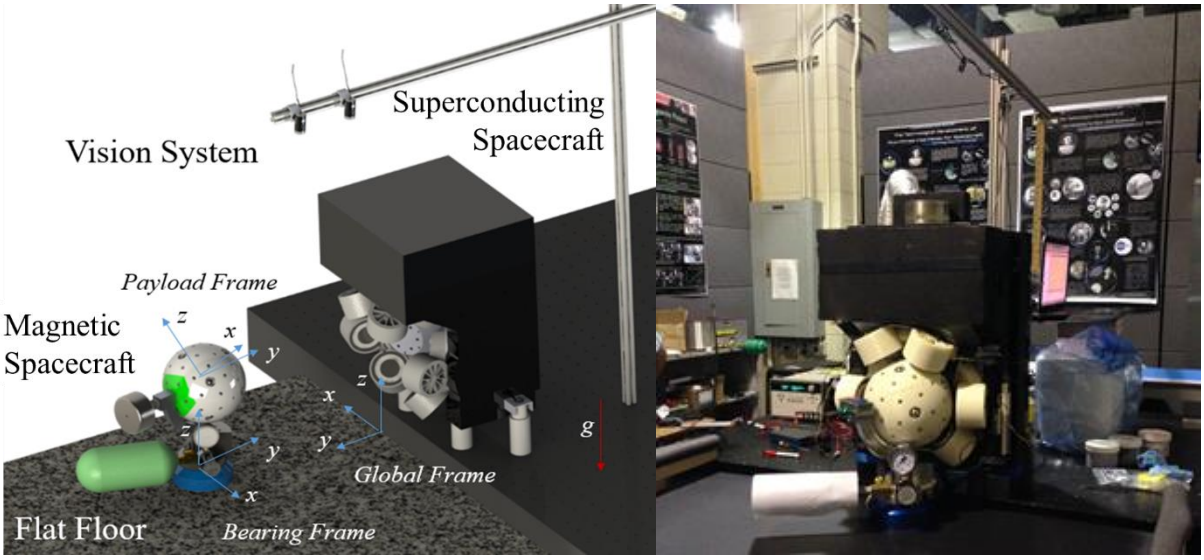

Figure 50: left, CAD rendering of entire testbed, illustrating placement of vision system, payload assembly, stationary spacecraft, and flat floor with three reference frames to describe dynamics. Right, the built testbed shown with the payload assembly in its equilibrium position.

A proof-of-concept experiment explores the feasibility of a flux-pinned docking interface with permanent magnets on one spacecraft and superconductor discs cooled by liquid nitrogen on the counterpart spacecraft, seen in Figure 50. This interface is the largest structure proposed and built incorporating flux-pinning multi-degree-of-freedom dynamics up to the year 2015. The reduced degree-of-freedom granite-flat-floor facility, developed by a partnership between Cornell University and NASA's JPL, was constructed to test the docking interface. The testbed is comprised of a planar air bearing, a granite testing surface, two mechanical ball bearings to provide the rotational fourth degree-of-freedom, a sensor package that can be mounted to the payload, and a webcam-based vision sensor system. The magnetic spacecraft, or OS analogue, afloat the planar air bearing was set at various initial positions, orientations, velocities, and angular rates to characterize the capture and docking capabilities of this flux-pinned interfaces. The sensor package transmitted IMU information about relative dynamics and the vision system offered global position

and attitude dynamics. Not only did this conceptual docking interface work, a series of experiments characterized clear measurable capabilities, such as sphere-of-influence and capture success for initial kinetic energy. The docking interface drew in the magnetic spacecraft up to 10 cm away from equilibrium position and accepted initial velocities up to 7 cm/s. The mechanical ball bearing on the floating spacecraft was locked for various initial conditions and captured at lower incoming velocities. The docking interface captured the floating spacecraft at a higher success rate for certain incoming path angles.

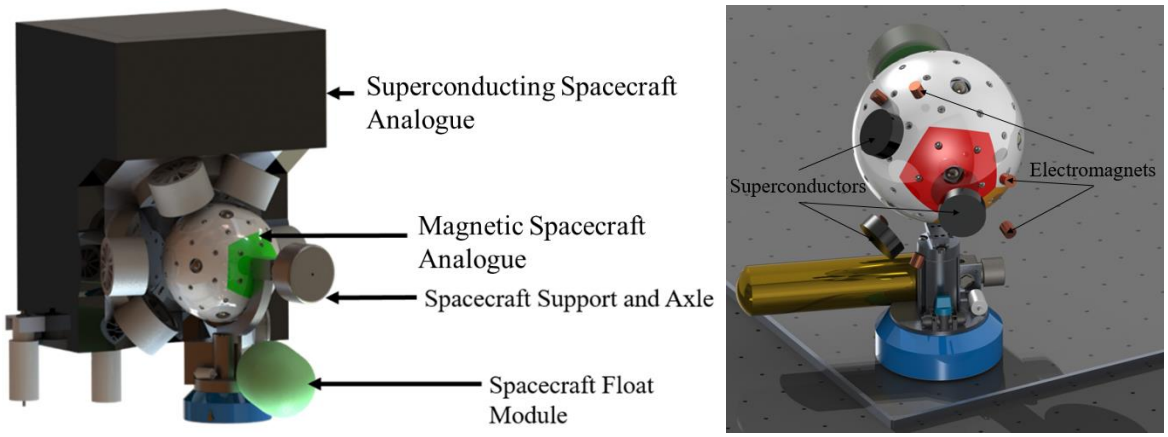

Figure 51: Left: CAD of 4 DOF testbed setup, courtesy of William Wilson and Ian McKinley
Right: CAD of 4 DOF testbed setup, with the thermal support system hidden to show superconductor and electromagnet placement

a. *Experiment Hardware*

The two test articles of interest are the superconducting spacecraft analogue, or SROA, and the magnetic spacecraft analogue, or OSA, pictured in Figure 51. The OSA structure takes the form of a hollow dodecahedron, which was 3D printed from ABS plastic. A dodecahedron structure eases in securely and accurately mounting permanent magnets for the flux-pinned interface, shown in Figure 52, while ensuring there would be several magnetically identical orientations of the spacecraft analog when rotated about the shaft. Mounted within the spacecraft analog, a sensor module includes an Epson G362 6-axis IMU, a Raspberry Pi microcontroller, a

battery, and a Wi-Fi transmitter. The rechargeable lithium ion battery pack has a capacity of 2900 mAh, which can last up to four hours during experiments. The mounting structure for the avionics was designed specifically to align one axis of the IMU with the shaft's axis of rotation. For translation, the OSA uses a New Way S1015001 flat air bearing, which is supplied with compressed air that is stored in an onboard Empire 68/4500 tank at 3000 psi. This full tank provides 30 minutes of float time before the pressure falls below 413.7 kPa (60 psi), the operating pressure of the air bearing. The tank is connected to a needle valve, pressure regulator, and filter to provide a constant supply of air.

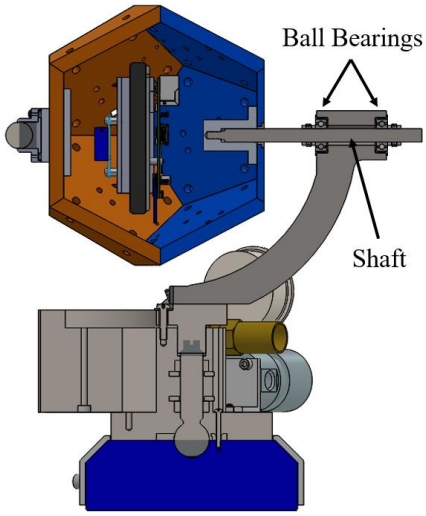

Figure 52: Cross section of the OS analogue, attached to the mechanical hardware of the mobile unit by a shaft which is free to rotate by two mechanical ball bearings

The superconducting spacecraft analogue, or SROA, is an aluminum structure that has three YBCO disks, 56 mm in diameter and 16 mm thick, that fit into designated panels. Liquid nitrogen is filled into the aluminum structure to cool the YBCOs by conduction below their critical temperature of 88K. 56 mm thick fiberglass disks are sandwiched between each YBCO and an aluminum cover to reduce conductive heat transfer to the environment, and to press the YBCO firmly against the wall separating it from the liquid nitrogen. To validate that the critical temperature of the YBCOs are not exceeded at any point during an experiment, thermocouples were connected to the faces of the SROA. The thermocouples are connected to a NI SCB-68A DAQ, which was selected because it includes features for cold-junction compensation.

The proof-of-concept testbed implements a global vision system to track translation and orientation of the OSA with respect to a static inertial frame. The vision system consists of two Microsoft LifeCam Studio USB cameras, capable of recording visual data up to 30 frames per second at 720 × 1280-pixel resolution. The cameras' combined field of regard is 1.5 m × 1 m and can resolve the position of marked targets to within 1 mm. There are three colored markers installed on the testbed: red, green, and blue. The red and blue markers are rigidly attached to the OSA at a fixed known distance, which establishes a conversion from pixel space to physical distance, shown in Figure 53. The red and blue marker positions yield 3DOF dynamic information: position and rigid body rotation about the air bearing. A green marker is rigidly mounted to a known static location to isolate measurement noise and offer a reference for the markers of the OSA.

The final component of testbed is the launching mechanism, which imparts initial translational and angular velocities on the OSA,

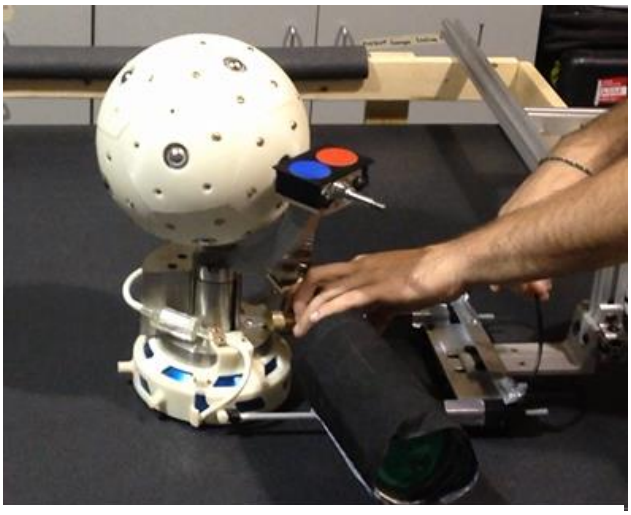

Figure 53: visual fiducials to track magnetic spacecraft analogue

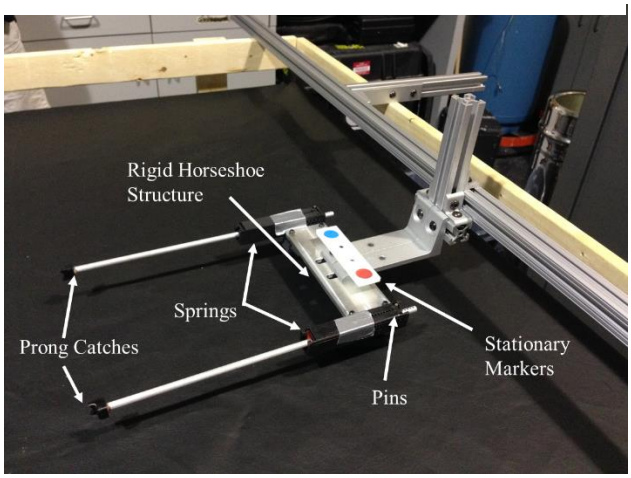

Figure 54: components of proof-of-concept testbed launch mechanism

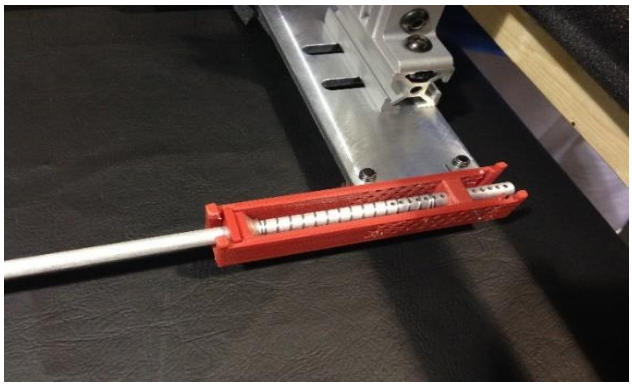

Figure 55: Spring boxes supply the force to impart an initial velocity on the air bearing

shown in Figure 54. The launch system uses two spring boxes, seen in Figure 55, a locking pin system, and two prongs. The two prongs push against knobs on the sides of the air bearing. The launch system is calibrated to correlate spring compression to imparted velocity, and it can generate speeds from 2 cm/s to 9 cm/s. The exact velocity is determined during data post-processing. The two springs can also be differentially compressed to impart an angular velocity up to 25 deg/s. Because both springs still push against the OSA in one direction, imparting an angular velocity also imparts a translational velocity, the relationship between which is determined empirically from Figure 56.

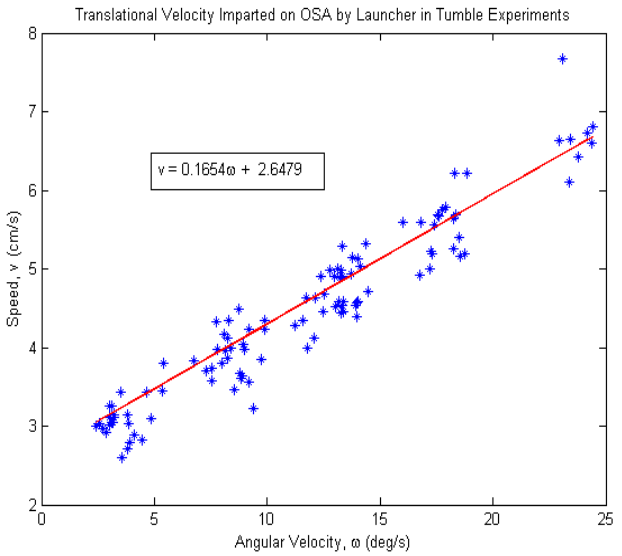

Figure 56: Translational velocity imparted on the magnetic spacecraft analogue is related to angular velocity for this launch system.

Testbed Characterization

The OSA's mass properties are carefully considered because of its critical role in simulating the payload's dynamic performance, and various external forces act on the unit, shown in Figure 57. The mass distribution of the

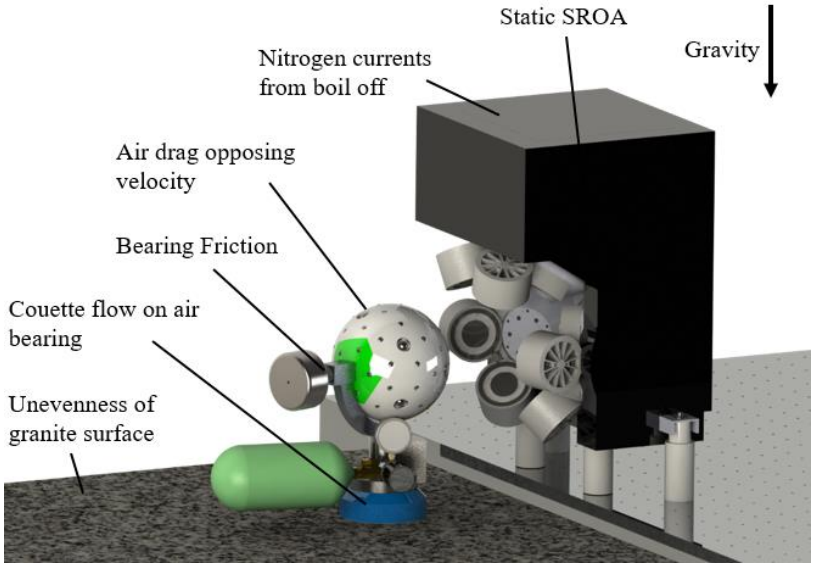

Figure 57: Summary of environmental effects and sources of error on the testbed.

spacecraft analog affects the observed dynamics of the system, especially in the presence of gravity, which would not otherwise be present in flight. A gravity-based torque generates pendulum-like motion on the spacecraft analogue, as captured in Figure 58. Additionally, the mass of air stored in the pressurized air tank decreases during operation, which influences the behavior of the system over time. The mass of a full tank is 300 grams greater than that of an empty tank, displacing the center of mass of the OSA by a maximum of 1-2 millimeters. Therefore, the OSA's total mass changes by 2% over the course of one tank charge, while the inertia about the air-bearing's normal direction changes by 3.4%. All center-of-mass locations are given in Table 14.

Table 14: The center of masses of the OSA without a spacecraft analog are given below for a full and empty air tank. The mass properties of the entire OSA with an example payload is also provided. All coordinates are with respect to the bearing frame.

Center of Mass of the OSA				
Configuration:	Empty Tank (no Payload)	Full Tank (no Payload)	Payload Only	OSA with Payload and Full Tank
Total Mass	13.20 kg	13.46 kg	1.14 kg	14.61 kg
X_{CG}	-1.13 mm	-2.05 mm	-1.76 mm	-2.03 mm
Y_{CG}	-10.64 mm	-12.24 mm	38.80 mm	-8.24 mm
Z_{CG}	130.79 mm	136.23 mm	266.05 mm	146.44 mm

Another consideration imposed by gravity is that there is an asymmetric downward load on the air bearing relative to its center of geometry. When this is the case, the separation distance between the air bearing and the floor is nonuniform, and an external lateral force is generated that must be accounted for. This lateral force was modeled with Couette Flow, where the average separation distance was estimated from the specifications of the New Way planar air bearing. The float height is approximately 25 microns given that the total wet mass of the system is 14.5 kg.

To isolate the flux-pinned dynamics of the system from external perturbations, friction is estimated between the air bearing and the flat floor, and for the shaft bearings. The kinetic friction from planar motion was characterized by measuring the deceleration of the OSA when released at a constant velocity. The deceleration was calculated from position data recorded by the vision system. After 30 trials, the kinetic friction coefficient was found to be 0.003 kg-m^2/s, with a standard deviation of 0.0037 kg-m^2/s. To measure friction in the ball bearing, the payload was spun up to an arbitrary angular velocity, and the change in angular velocity during coast down was measured by the IMU. The change in angular rate directly produces the coefficient of friction, C, to a first order approximation. 21 repeated trials yielded a bearing friction coefficient of C = 0.0023 kg-m^2/s and a standard deviation of 2.4121 × 10^{-4} kg-m^2/s.

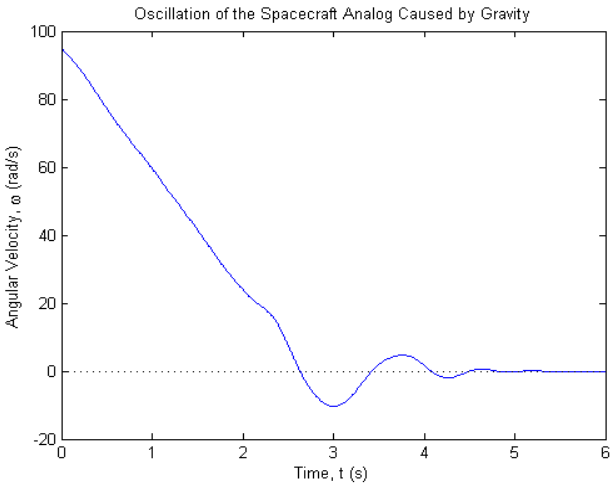

Figure 58: While characterizing the bearing friction, the spacecraft was given an initial angular velocity and allowed to decelerate to rest. When the center of mass of the payload is not aligned with the shaft, gravity causes oscillatory motion

Friction in the bearings can also stem from position misalignment between the two bearings along the rotating shaft. Two RBC Bearings evenly distribute the load of the shaft to limit misalignment. The bearings are tightly secured into two machined sockets in the mechanical hardware of the OSA to minimize misalignment. The shaft is made of 9.53 mm (3/8 in) diameter AISI 52100 Alloy Steel, which has a deflection of no more than 0.023 mm at its tip when subjected to a 11.18 N load, corresponding to a payload mass of 1.14 kg, 80.9 mm from the edge of the first bearing in the y axis of the payload frame. Finally, the topography of the granite surface across the

1.2 m square block was quantified with acceleration data, illustrated by Figure 59. The unilateral trend shows the consistency and flatness of the granite surface with the maximum height difference of 0.0034 m, a tilt of 0.17° from exact alignment.

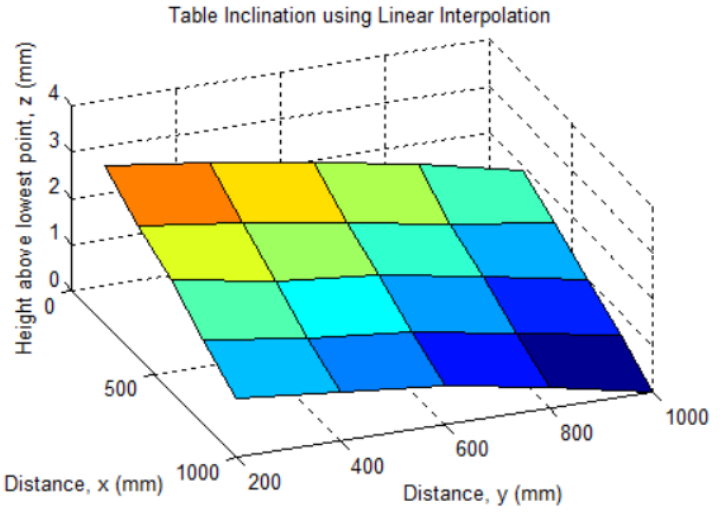

Figure 59: Inclination of the granite surface, showing unilateral slanting of 1.3 mm and 2 mm across each respective 1.2 m side.

b. *Experiment Campaign*

The FPI was field-cooled before the start of every test run. The OSA was placed so that three of the magnets on the spacecraft analog were 1 cm from each of the respective superconductors faces on the SROA. The aluminum structure was then filled with liquid nitrogen. The liquid nitrogen was refilled until the level of the liquid stabilized. A lid was installed to insulate the nitrogen and to prevent nitrogen vapor from obscuring the cameras. A duct and fan were used to direct vapor away from the testbed to limit the effect of vapor pushing against the OSA. Then, a pre-filled air tank was attached to the magnetic spacecraft's pressure system and the OSA was placed in a starting position on the granite floor. The temperature of each of the superconductors was confirmed to be below 88 K with thermocouples before continuing with the experiment.

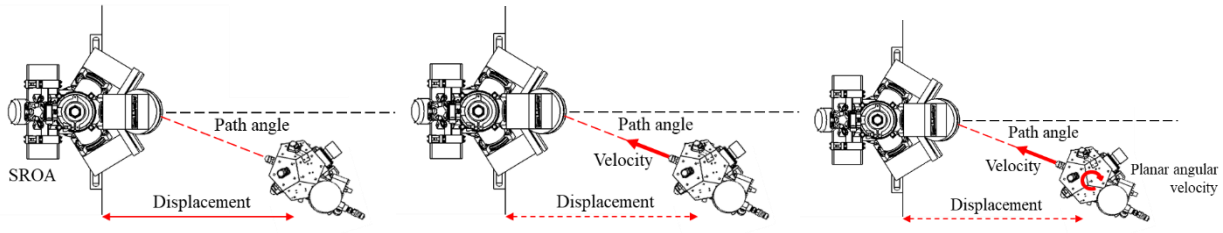

Figure 60: from left to right, sphere-of-influence experiment, capture experiment, and tumble experiment conducted on proof-of-concept testbed

Three types of experiments were performed: displacement, capture, and tumble tests, shown from a bird's eye view in Figure 60. For displacement tests, the OSA was displaced a set distance away from the magnet's field-cooled position. The OSA was then released by hand and allowed to be drawn into the FPI by forces related purely to magnetic flux-pinning. The dynamics of the experiment were observed for 30 seconds, correponding to the time scale at which the motion from electromagnetism would damp out. These tests were performed to observe the dynamics caused by flux-pinning with the goal of validating the feasibility of docking with this interface.

Next, a series of capture tests were performed by initializing conditions with the launch mechanism. These experiments aim to determine the maximum kinetic energy that the magnetic spaceraft analogue could approach the interface at and still be captured. The mechanism was placed outside the sphere-of-influence of the FPI and aimed direcltly in line with the FPI. Various initial velocities were imparted onto the OSA, and the dynamics of the OSA as it entered the interface were recorded. Initial velocities were tested up until when the OSA would consistantly escape the FPI, meaning that magnetic flux-pinning was unable to absorb the energy of the kinetic interaction. The launcher was also offset horizontally and directed at the FPI to examine the effect of path angle on the capture limits of the FPI.

Finally, a series of tumble tests were performed to evaulate the effect of angular velocity on the capture limits of the FPI. Again, the launcher imparted a series of angular velocities while

the OSA moved toward the FPI at zero path angle. The launcher was then offeset to investigate the role of path angle, given angular velocity.

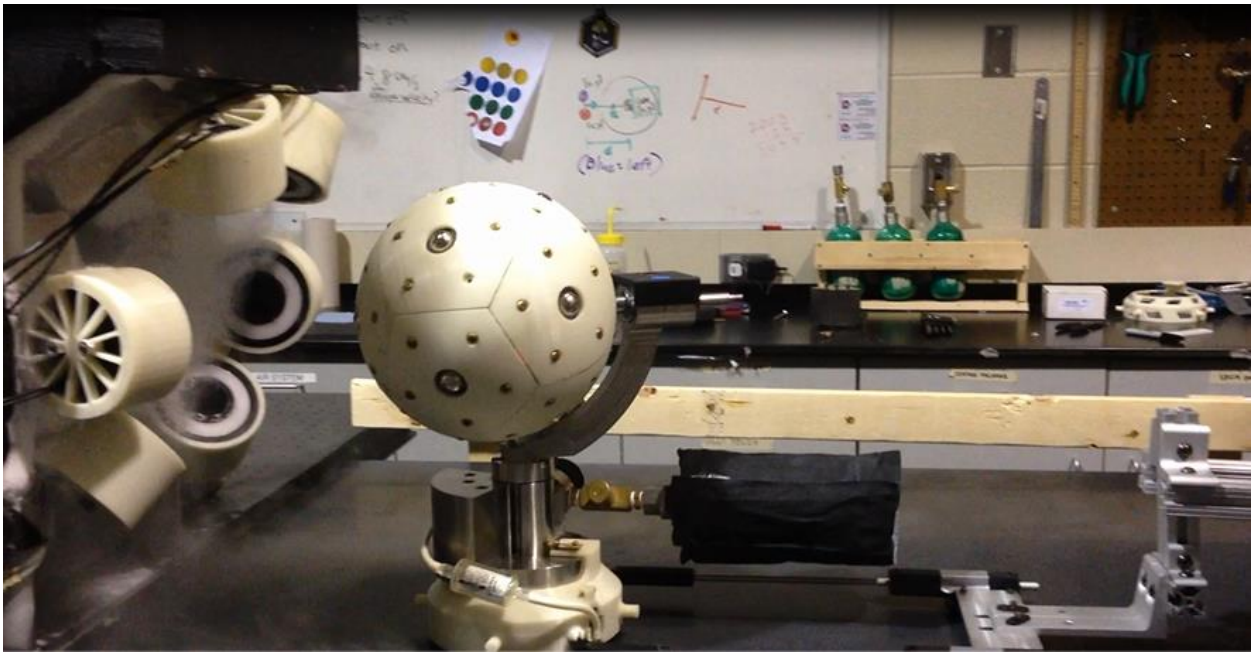

Figure 61: capture experiment conducted on proof-of-concept testbed

c. *Experiment Results*

From over 107 docking and capture tests, preliminary results reveal that flux-pinning interactions have influence up to 10 cm. Distances farther than 10 cm are overwhelmed by testbed forces. For the 4 degree-of-freedom capture tests, the maximum amount of kinetic energy the flux pinned superconductors could absorb is between 0.0796 J and 0.01498 J. The capture success at different initial kinetic conditions can be seen in Table 15 and sample timeseries of distance for capture experiments further illustrate capture performance in Figure 62. The maximum capture velocity extrapolated for a flight traceable system predicts up to 7 cm/s for successful capture. The proof-of-concept testbed not only proves flux-pinned capture is feasible but offers coarse capability results that informs a more rigorous experiment campaign, discussed in the next section.

Table 15: proof-of-concept capture experiment initial conditions and capture success

4 DOF Proof-of-Concept Results		# trials	# trials
Initial Energy [J]	Initial Direction	capture	escape
0.00315	0 deg	5	0
0.00796	0 deg	10	2
0.01498	0 deg	4	5
0.02419	0 deg	2	5

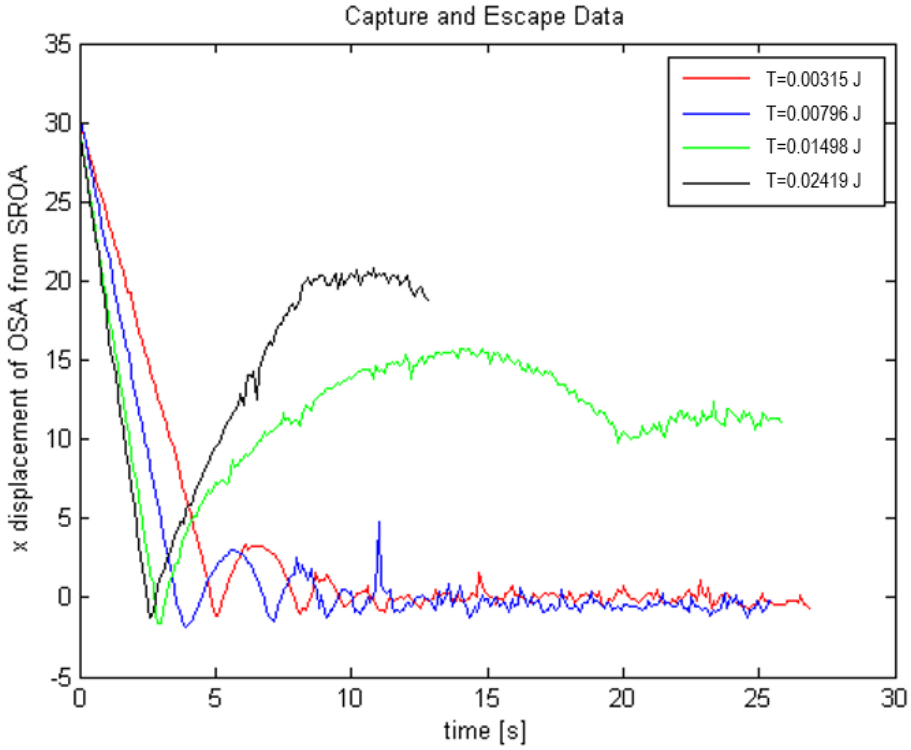

Figure 62: position data of sample-capture experiments, showing capture and escape behaviors at different energy levels

II. Capture and Docking Experiments in a Reduced Degree-of-Freedom Testbed

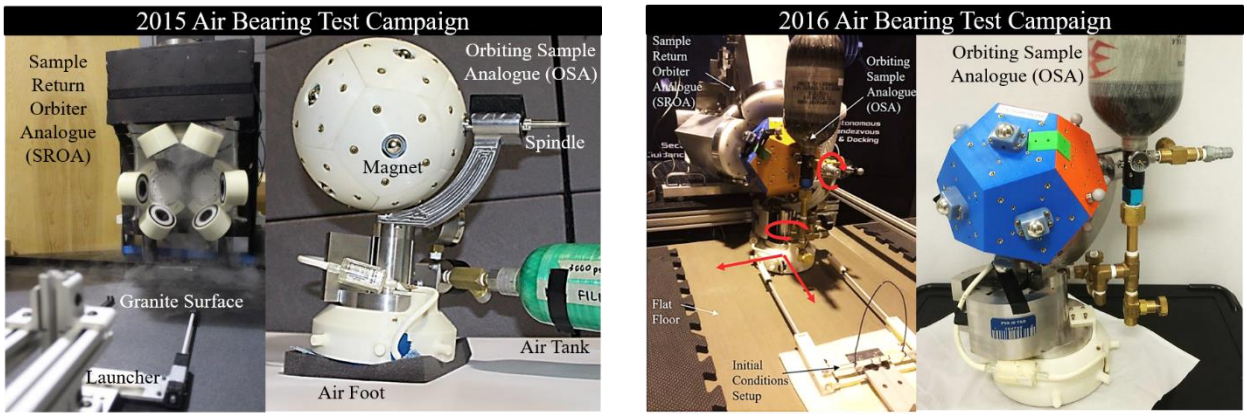

Figure 63: (a) and (b) Hardware components used in the 2015 air bearing testing at Cornell; (c) and (d) Hardware components used in the 2016 air bearing test campaign at JPL.

Beyond a proof-of-concept demonstration, a reduced degree-of-freedom dynamic testbed offers easy access and detailed characterization of a flux-pinned capture and docking interface. As a passive system, it is important to characterize the depth and shape of the potential well to bound the acceptable relative motion between two notional spacecraft to ensure a successful capture. An extensive series of ground experiments are designed to determine these bounds and offer insight to modify a dynamic simulation for deterministic, predictive capabilities. This section explains the specific air bearing test campaign objectives and design as well as the testbed hardware used to conduct the experiments. The results from these experiments are then described, especially as they relate to the sphere-of-influence, stiffness and damping of the interface, and capture threshold offered by this FPI design.

a. Experiment Setup and Operation

Test Campaign Objectives

To raise the technology readiness level of FPIs for sample capture, the size and shape of the field-cooled superconductors' potential well characterize the interface's performance. A concept of the magnetic potential well generated by the superconductors in the spacecraft analogue can be seen in Figure 65. This information provides the bounds on acceptable relative states (position, orientation, and linear/angular velocities) between an SRO and OS to ensure the FPI can

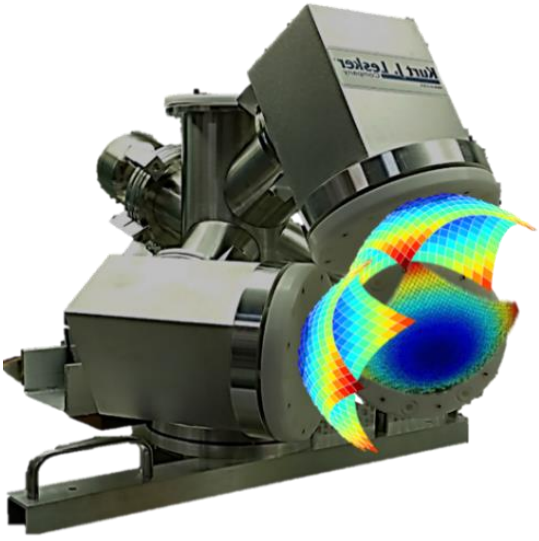

Figure 65: Magnetic potential wells above superconductor surfaces to conceptually depict interface potential well

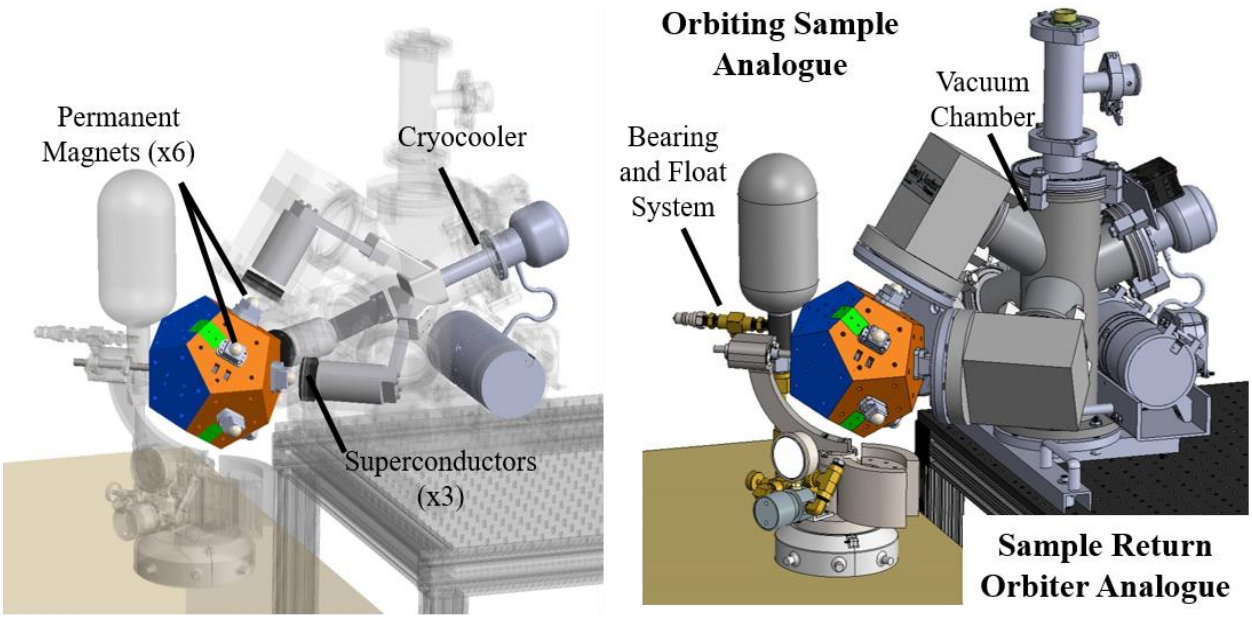

Figure 64: The key elements of the FPOS testbed, including elements that would be present in an orbital system (left), and elements included to support testing in a ground environment (right). Both analogues are based on conceptual mission hardware.

generate a successful capture. Thus, the flux-pinned interface for orbiting sample capture (FPOS) air-bearing testbed (shown in Figure 64) was created to directly measure these values, in addition to improving FPI modeling capabilities and establishing the reliability of ground test environments in evaluating these parameters for an FPI.

Testbed Hardware Description

The FPOS testbed is four degree-of-freedom system that uses a mechanical bearing mounted to a planar air bearing to simulate the motion of spacecraft under the influence of an FPI for sample capture. The testbed has two primary elements: the Orbiting Sample Analogue (OSA) and the Sample Return Orbiter Analogue (SROA), which are based on conceptual mission hardware. The OSA is a 1:1 scale of a conceptual OS (20.3 cm in diameter) that is mounted to a bearing and float system that provides two translational and two rotational degrees of freedom (shown in Figure 66). To ensure that the OSA can rotate freely on the mechanical spindle, only six of the permanent magnets are included on the icosahedron pattern, but the distance and relatively sharp decrease in influence as a function of distance suggests that this approximation should not have a significant effect on the field-cooled equilibrium interacting with the FPI. Although the OS interior contains surface samples, the OSA

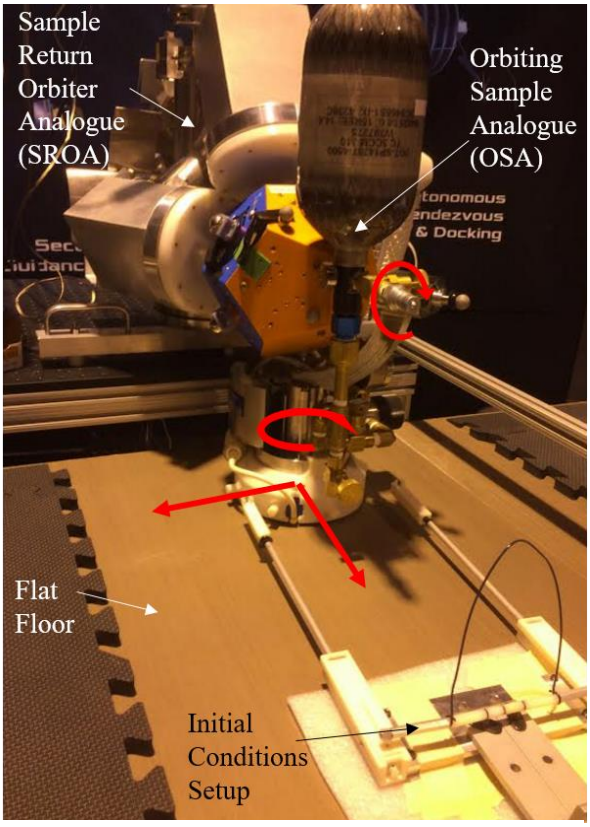

Figure 66: The major components of the FPOS testbed used to generate the results discussed in this work.

has an avionics and sensor package (which includes an Epson M-G362 inertial measuring unit (IMU)) to aid in modeling the dynamics on the testbed. The IMU sampled at 125 Hz with a dynamic range up to 150 deg/s and 3g with 32-bit resolution. This sensor package communicates with the testbed laptop via WiFi. The rotating sphere of the OSA is also prepared with markers identifiable by the testbed Vicon position sensor system.

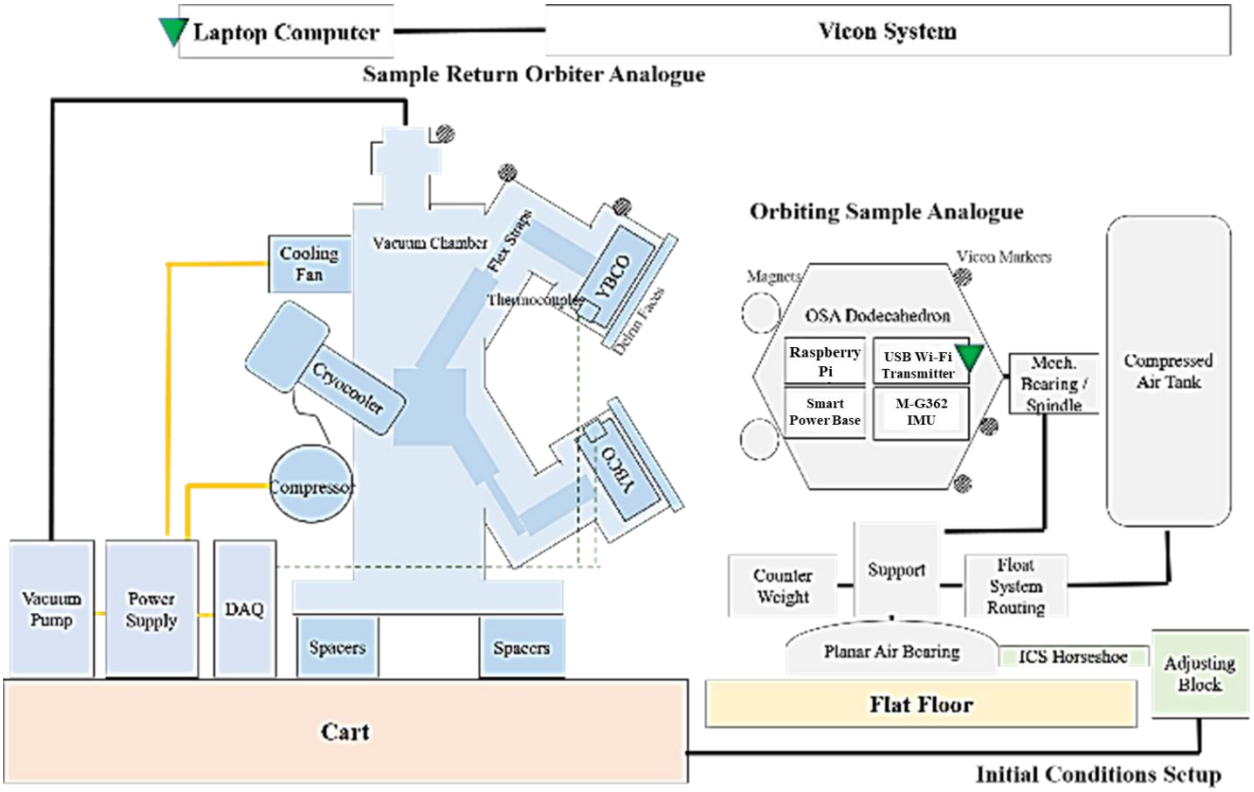

Figure 67: A schematic of the FPOS testbed elements.

The SROA, on the other hand, is stationary and includes the relevant flight-traceable thermal systems and three YBCO superconductor disks necessary to support the sample capture FPI design. The thermal design and modeling for this unit, which includes a vacuum chamber that surrounds the superconductor disks to support ground testing in an ambient thermal environment, is described by McKinley [124]. The significantly larger mass of the SRO relative to the OS means that a stationary SROA is a reasonable approximation of the dynamics of the flight system. The

SROA is also outfitted with thermal sensors to monitor the temperature of the superconducting disks and Vicon markers to provide a stationary point of reference in the data processing.

In addition to these main elements, the testbed also includes a Vicon sensor system, a laptop for data acquisition, a mechanism for imparting initial conditions on the OSA, and a leveled flat floor for performing the experiments. These elements are shown in the photograph in Figure 66 and the schematic shown in Figure 67**.** The Vicon sensor system includes five Bonita cameras and Tracker 1.3.1 software. The cameras and tracking system resolve position to within 0.2 mm with an approximate (but varying) update rate of 100 Hz. The laptop collects the video, Vicon data, and initializes the wireless avionics package on the OSA. The initial conditions setup is a set of spring-loaded arms mechanically attached to the SROA that can be adjusted to provide either stationary OSA initial conditions (static position or orientation relative to the SROA) or can be compressed and released to impart translational or angular momentum to the OSA. Finally, the FPOS testbed utilizes the JPL Formation Control Testbed (FCT) flat floor to leverage its finely leveled surface to minimize gravity bias and friction [125]. The flat floor is polished to within a thousandth of an inch across each panel and flattened with a state-of-the-art metrology system.

Table 16. Physical Parameters for the FPOS Testbed

Physical Parameter	**Value**	**Units**
OSA Mass	14.23	kg
Inertia about spindle	0.0044	kg m^2
Inertia about air bearing	0.062	kg m^2
Coefficient of kinetic friction in ball bearing	0.0023	--
Coefficient of kinetic friction between air bearing and floor	0.0019 L 0.0027 T	--
Center of rotation displacement along spindle	-7.27	mm
Center of rotation displacement away from spindle	-1.18	mm

System Dynamical and Mass Properties

The mass properties of the unit are necessary to model the OSA behavior and the forces acting on the OSA beyond those generated by the FPI, compiled in Table 16. The OSA has a diameter of 20.3 cm and a mass of 14.23 kg. The moment of inertia of the rotating icosahedron assembly about the mechanical bearing/spindle is 0.0044 kg m^2 and the moment of inertia about the whole assembly is 0.062 kg m^2 about the axis perpendicular to the flat floor.

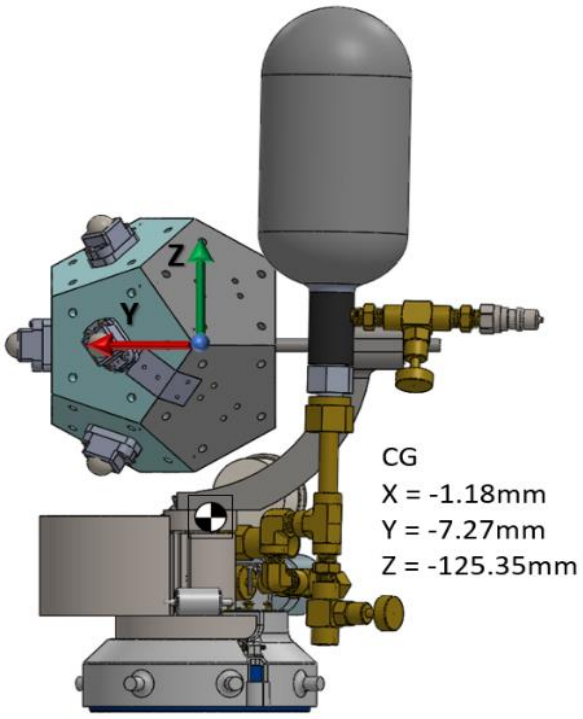

Figure 68: Center of gravity for the OSA relative to the geometric center of the dodecahedron assembly (shown at the origin of the coordinate axes).

The offset between the center of rotation and center of mass of the system causes torques to arise from the FPI forces acting on the OSA. Off-axis center of mass locations can also cause uneven loading of the bearing, which can also adversely affect the dynamics. To counteract these effects, the OSA was designed to have a center of mass as close as possible to the axis of rotation, and small trim masses were added on the icosahedron assembly until the rotating assembly did not exhibit any observable pendulum effects about its mechanical spindle. According to the CAD assembly, the offset of the center of mass of the icosahedron assembly was -1.18 mm from the shaft and was -7.27 mm from the system center of mass along the shaft in the direction of the icosahedron assembly, refer to Figure 68. During characterization testing, the center of mass of the system was too offset from the geometric center of the air bearing, which led to increased friction between the air bearing and the flat floor. The

OSA was redesigned to its current form to bring the center of mass to within 10 mm of the air bearing's center. The system center-of-mass displacement from the geometric center of the OSA is a consequence of counteracting gravity for a reduced friction environment. The additional system mass shifts the center of rotation away from the geometric center of the OSA and significantly reduces the natural frequency of the system. The supplemental experiment hardware obscures the dynamics solely from flux-pinned physics but allows reduced friction, accessible ground testing for this innovative technology.

Although designed to have limited impact on the dynamics, the mechanical and air bearings in the OSA inevitable do enact some dissipative forces on the assembly. The empirically determined kinetic coefficient of friction for the OSA mechanical bearing has an average of 0.0023 with a standard deviation of 2.4e-4. Air bearings also exhibit dissipation in the form of shear forces of the air between a moving plate and the static flat floor. The dissipative coefficient experimentally determined on this floor with a similar set of air bearings was established to be 0.0027 in the transverse direction (away from the SROA) and 0.0019 in the lateral direction (along the face of the SROA) [126]. The unique weave in the flat floor construction and the relatively low float height of these air bearings contributes to the directionality in the results. Air drag is considered negligible in this analysis.

Experiment Operation

With this hardware, a series of tests were carried out over the summer of 2016 to establish the FPI's sphere-of-influence, stiffness and damping, and capture energy threshold. Prior to every test campaign, the vacuum chamber was evacuated (a process of approximately 12 hours), and then the cryocooler was powered on to cool the superconductors from ambient temperature to 80 K (a process that took another 12 hours). During this cooling process, the superconductors were field-cooled with surrogate magnets temporarily mounted to the SROA face with plastic spacers as shown in Figure 69. The equilibrium was set where a magnet is centered 1.6 cm directly above the center of each superconductor disk. With the inclusion of the Delrin faces and other material between the superconductor disks and the magnets on the OSA, the available gap before an impact is 0.9 cm. These field-cooled positions were selected based on prior experience to achieve a compromise between stiffness of the interface and impact likelihood. The FPI can be re-optimized for different field-cooling configurations if necessitated by the specific concerns of the mission scenario.

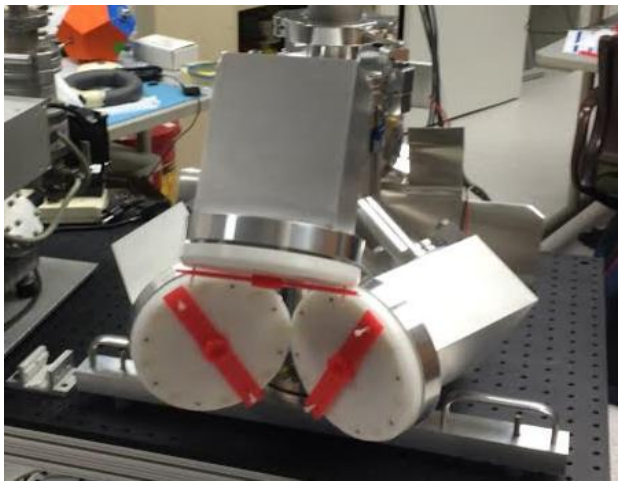

Figure 69: Magnet spacers mounted to the SROA Delrin faces in the location for field-cooling (magnets not shown).

Table 17. Experiment Initial Conditions and Configuration

	Primary Test Suite					Constrained DOF Comparison Test Suite			
Test Name	**Sphere of Influence Tests**	**Roll Stiffness and Damping Tests**	**Natural Mode Tests**	**Capture Tests**	**Tumble Tests**	**Sphere of Influence Tests**	**Natural Mode Tests**	**Capture Tests**	**Tumble Tests**
# Total Experiments Performed	120	72	180	105	180	40	12	50	70
# Trials for Each Initial Condition	3	9	3	3	3	1	1	2	2
# DOF	4	1	4	4	4	3	3	3	3
Translational Radial Distance from Equilibrium, r (cm)	1, 2, 4, 6, 8, 10, 12, 14	0	0, 1, 2	18	18	1, 2, 4, 6, 8, 10, 12, 14	0, 1, 2	18	18
Initial Path Angle (Angle Relative to Perpendicular Approach of Equilibrium), α (deg)	0, 5, 10, 15, 30	--	0	0, 5,10, 15, 30	0, 5,10, 15, 30	0, 5, 10, 15, 30	0	0, 5, 10, 15, 30	0, 5, 10, 15, 30
Initial Roll Angle (Rotation about Spindle), θ (deg)	0	5, 10, 15, 30	5, 10, 15, 30 (varied with 0 deg yaw)	0	0	0	0	0	0
Initial Yaw Angle (Rotation about Planar Air Bearing), φ (deg)	oriented to point to equilibrium, matched with path angle (0, 5, 10, 15, 30)	0	5, 10, 15, 30 (varied with 0 deg roll)	oriented to point to equilibrium, matched with path angle (0, 5, 10, 15, 30)	45 when <= 20 deg/s yaw angular velocity, 90 when > 20 deg/s yaw angular velocity	oriented to point to equilibrium, matched with path angle (0, 5, 10, 15, 30)	5, 10, 15, 30	oriented to point to equilibrium, matched with path angle (0, 5, 10, 15, 30)	45 when <= 20 deg/s yaw angular velocity, 90 when > 20 deg/s yaw angular velocity
Initial Translational Velocity, $\dot{r}$ (cm/s)	0	0	0	1, 2, 3, 4, 6, 8, 10	0.5, 1, 1.5, 2, 2.5, 3, 4, 5 (coupled to yaw angular velocities)	0	0	1, 2, 3, 4, 5	1, 2, 3, 4 (coupled 1:1 to yaw angular velocity, where higher translational velocities match higher yaw angular velocities)
Initial Angular Velocity About Roll $\dot{\theta}$ (deg/s)	0	0	0	0	0	--	--	--	--
Initial Angular Velocity About Yaw, $\dot{\varphi}$ (deg/s)	0	0	0	0	5,10,15,20,25,30 (coupled to translational velocities)	0	0	0	6, 12, 18, 24 (coupled 1:1 to initial translational velocity, where higher yaw angular velocities match higher translational velocities)

Once the superconductors are below their critical temperature, the plastic spacers are removed. The OSA was placed onto the flat floor and allowed to settle into an equilibrium with the SROA. This equilibrium was recorded by the Vicon system for later processing. The OSA was then pulled away from the equilibrium and rotated abruptly about its spindle to provide a timestamp-syncing maneuver distinguishable by the IMU and the Vicon system. The system was then placed at the appropriate initial conditions for the test, and three trials with the same initial conditions were recorded. The field-cooling solution was re-imprinted only four times throughout the test campaigns described here. Once the set of tests was complete, the data from the IMU was downloaded from the onboard card and processed to sync the timestamps with the Vicon system. These measurements were blended with a moving-average filter to establish the estimated state of the OSA. The accelerometer values were processed with a thresholding algorithm, and any time during the experiment where the IMU recorded a spike, a contact between the OSA and SROA is detected.

Experiment Types

There are five different types of tests discussed in this work: sphere-of-influence, roll stiffness and damping, natural mode, capture, and tumble. Three of these experiments are repetitions of the proof-of-concept experiment suite. The primary test suite consists of the data collected when the OSA had four degrees of freedom (apart from

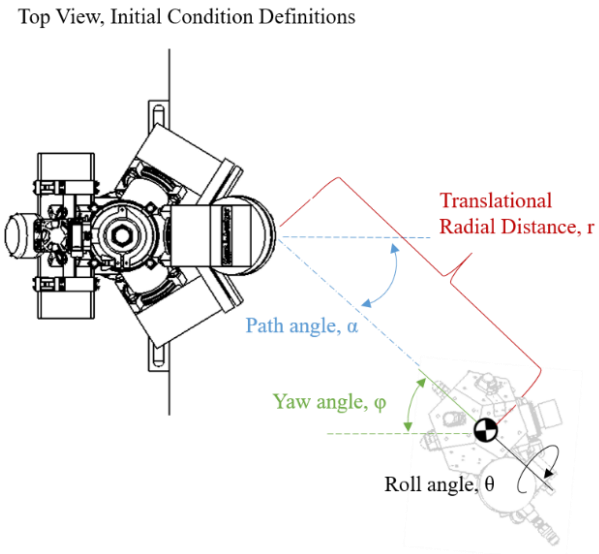

Figure 70: Schematic of the initial condition parameters under test, where zero corresponds to the initial conditions and the positive angle is shown.

the roll stiffness and damping tests, which only had one DOF). Some of these tests were also repeated in a DOF comparison suite where the roll degree of freedom about the spindle was immobilized to understand the sensitivity of the FPI to these non-flight-like constraints. The initial conditions and number of trials for each one of these experiments is shown in Table 17 and the parameters that were varied over the different runs are defined in the schematic in Figure 70.

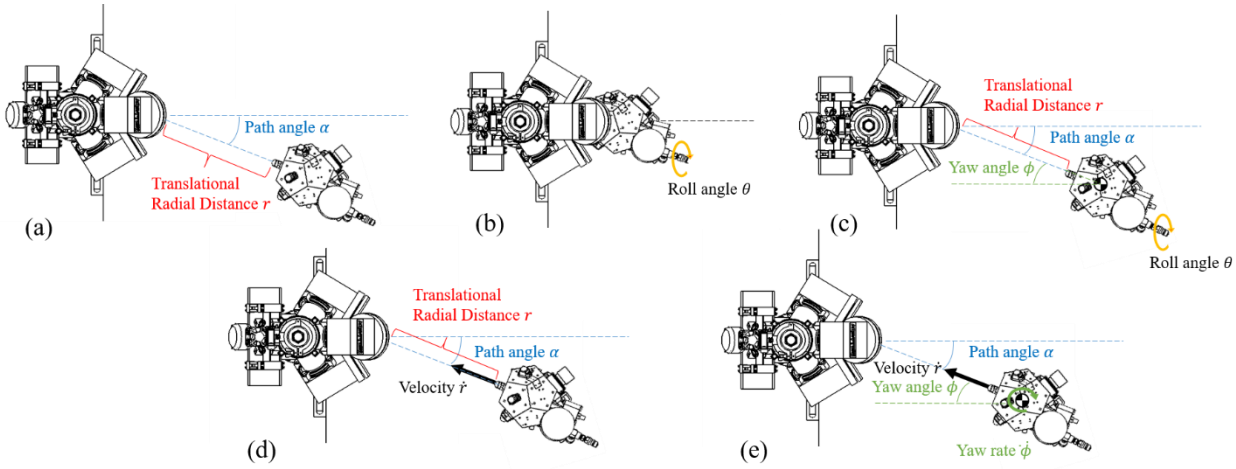

Figure 71: From the top left to bottom right, top-down views of the a) sphere of influence test b) roll stiffness and damping test, c) natural modes test, d) capture test, and e) tumble test

The sphere-of-influence tests are designed to understand reach of the FPI influence to pull the OSA into the potential well on this testbed. This information also provides insight into passive dynamics (such as the differences in capture time) for different capture distances and angles. This experiment, shown in Figure 71a, varied the path angle and translational displacement from the equilibrium, then released the OSA from a static state. The passive dynamics of the FPI captured the OSA if the environmental effects did not overwhelm the attractive forces from the FPI. The experiments end if the OSA exhibited no noticeable motion toward the SROA after 15 seconds, which may conservatively truncate the measured influence range.

The roll stiffness and damping tests in Figure 71b aim to determine if the frozen-image model [93] can be applied to this FPI to assess roll stiffness and to provide an empirical estimate

for damping, which the model does not predict. The frozen-image model predicts flux-pinning dynamics normal to the surface of the superconductor but the lateral and rotational dynamics are not as well characterized. Thus, to understand the full four-DOF rigid-body dynamics, these tests only left the roll degree-of-freedom unconstrained, with the system otherwise in its equilibrium. The OSA was then perturbed at different roll angles and allowed to naturally settle. Two different relative equilibria were tested (two different magnet trios 72 degrees apart) to investigate consistency across relative equilibria.

Natural-mode experiments, shown in Figure 71c, investigate the coupling effects of rotation on translational dynamics. By perturbing all degrees of freedom available to the experiment testbed, natural modes and frequencies are excited. These modes and frequencies are important in characterizing the stiffness and damping of the flux pinned interactions. In this experiment, every degree of freedom is displaced from the equilibrium position or orientation and held stationary, then released from a static state. The full four-DOF system testing examined the angular displacement about each axis separately.

Capture experiments, in Figure 71d, mimic a capture maneuver within the four-DOF constraints of the testbed. In this type of test, the OSA is launched at the stationary SROA with a specified initial velocity. These tests vary the initial translational velocity but do not include any angular velocity. The initial position is always 18 cm away in distance (because this is the distance on this testbed at which the FPI does not influence the OSA into the potential well without additional energy input). The entrance path angle was varied to test a cone of possible path angles. The ultimate goal of these experiments is to understand what kinetic energy thresholds generate capture successes.

The tumble experiments, shown in Figure 71e, build upon the capture experiments by adding angular velocity. This addition generates some of the most complicated dynamics but also simulates the most realistic flight scenarios. The OSA is launched at varying translational velocities, angular velocities, and path angles for the full four DOF. The yaw angular velocity and translational velocities are coupled because the difference in compressed spring lengths counted in pegs. These experiments directly inform the maximum capabilities of the flux pinned interface under more realistic dynamic conditions.

A subset of these tests was also conducted with the spindle locked in place, thus reducing the OSA dynamics to three degrees of freedom to evaluate how the interface capabilities change when fewer degrees of freedom are available to the system. Previous investigations show state sensitivity in dynamics and the coupled nature of state dynamics are integral to interface performance. The FPI's sensitivity to constrained degrees of freedom can guide decisions about the next steps in the technology development process and infer flux-pinned capabilities in spaceflight operations.

b. Experimental Results

Sphere-of-influence Experiments

The sphere-of-influence tests were designed to empirically determine the maximum range and shape of the potential well generated by the FPI in order to 1) evaluate where the attractive forces imparted by the FPI are dominated by environmental factors of this particular testbed and 2) characterize the passive dynamics of the system at a range of initial conditions, as seen in Figure 72. As shown in Figure 73, the OSA reliably captured for a radial distance from the equilibrium of less than 12 cm in the four DOF testbed but for distances past 14 cm, the OSA was very unlikely to capture. Thus, the radial range of influence for this FPI on the testbed

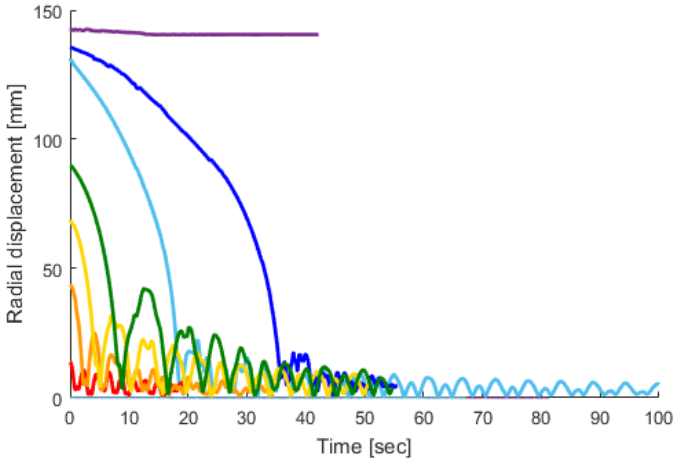

Figure 72: Time histories of radial displacement for different initial displacements, showing the dynamics of tests within the sphere of influence and a test that was not drawn in

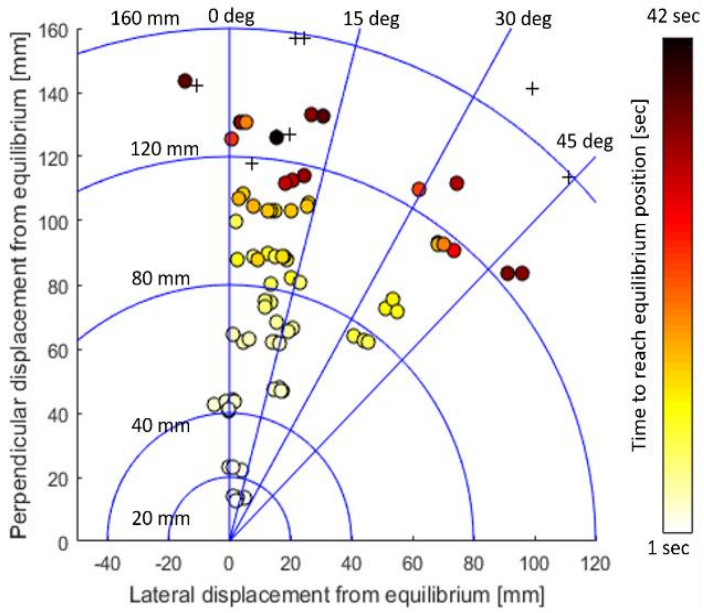

Figure 73: A plot of as-measured displacement from the equilibrium (shown at the origin) for both initial radial distances and path angles in the four DOF sphere of influence tests. The heat map illustrates the travel time of the OSA until it first passes through equilibrium position.

was between those numbers. A dynamic simulation of the OSA and SROA interaction predicts the magnitude of the FPI-generated forces acting on the OSA at 12 cm from the equilibrium at 0 deg path angle is approximately 5 mN [109]. The data show no apparent trends as a function of initial path angle – the influence of the FPI is a function of radial distance from equilibrium and independent of path angle up to 45 degrees. However, more data is needed to confirm this preliminary assessment, especially at smaller radial displacements.

When applied to a flight scenario, the sphere-of-influence of the same FPI is expected to be larger because the environmental forces that overwhelm the FPI attraction are significantly smaller. In LEO at 400 km altitude, for example, the dominant environmental force is atmospheric drag assuming the system has no net magnetic dipole interacting with Earth's magnetic field. The orbital OS described previously would generate approximately 0.0055 mN of drag force under these conditions. The equivalent sphere-of-influence for the LEO threshold force is 26 cm. In a Mars orbit, on the other hand, the dominant environmental force is solar radiation pressure, which would generate a force of approximately 0.0001 mN on a 20.3 cm OS. The equivalent sphere-of-influence for the Mars orbit threshold force is therefore conservatively 50 cm, although the directionality of the forces is an important element that may extend the FPI range beyond this value. Further, the sphere-of-influence of the interface may be adjusted to meet specifications by varying the strength of the magnets on both the field-cooling device and the target spacecraft.

Roll Stiffness and Damping

The roll stiffness and damping tests were performed to empirically characterize the dynamic properties of the roll axis of the FPI as measured independently of all other degrees of freedom in the FPI. The OSA under an angular displacement exhibits an underdamped oscillatory behavior, as shown in a representative trial with a small (5 deg) displacement and a large (30 deg) displacement in Figure 75. The motion of the OSA exhibits a natural frequency of about 1.66 Hz for small displacements (5 deg) and 0.88 Hz for large displacements (30 deg), when any nonlinearities are presumably more likely to be excited shown in Figure 76. The nonlinearity in the larger displacement experiments also smears the FFT peak across more frequencies, making the peak less distinct. This nonlinearity is much clearer when observing the peak frequency of the Fast Fourier Transform (FFT) plotted as a function of initial displacement roll angle for all the trials, as shown in Figure 74. The figure shows

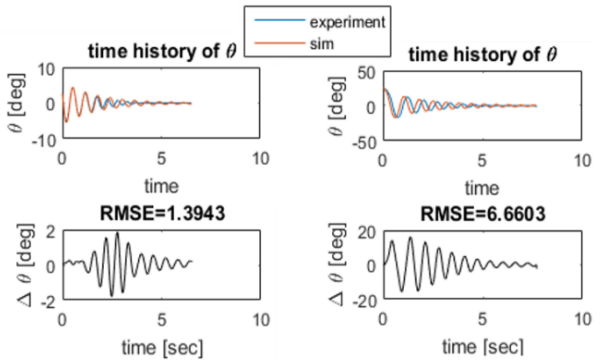

Figure 75: Time history and error between the time histories of a small angle (left) and large angle (right) displacement test, showing a comparison of the experiment vs simulation

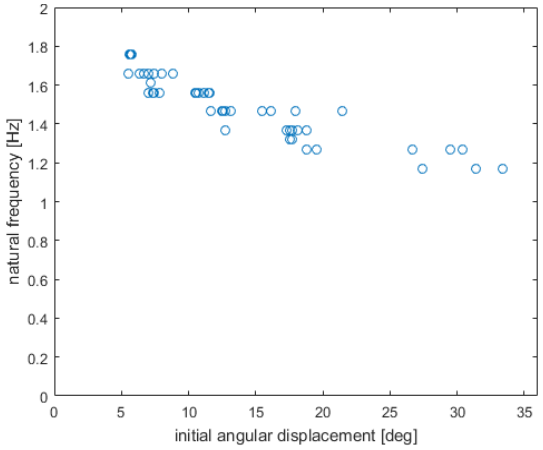

Figure 74: Dominant natural frequency is dependent on initial angular displacement due to nonlinear flux-pinning interactions for 1 DOF experiments

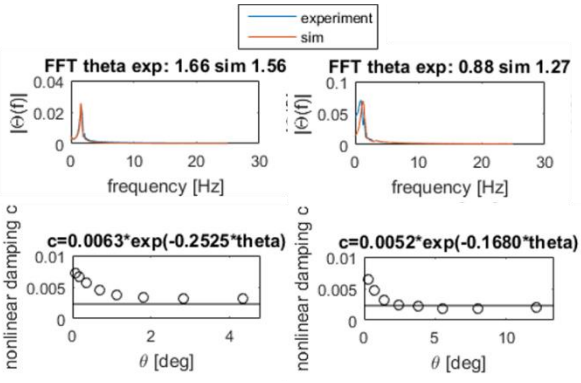

Figure 76: First row is a Fast Fourier transform of small angle and large angle displacement tests with nonlinear damping in the second row

that the fundamental frequency of the system can vary by as much as 0.6 Hz across the 30 degree initial condition spread.

The experimental data do not show a linear damping trend; rather, the damping coefficient calculated from logarithmic decrement shows a clear dependence on angular displacement and/or angular velocity. The damping close to the equilibrium orientation or absence of angular velocity has the highest damping, whereas the damping coefficient converges to the friction coefficient of the ball bearing (0.0023, shown as a line in the damping plot) as the magnet moves farther away from equilibrium. The FPI clearly exhibits additional damping beyond that produced by the friction in the bearing, which may be the effect of eddy-current damping between the permanent magnets and the aluminum SROA structure. When the displacement is within a degree of the equilibrium, the damping is over three times seen at larger displacements.

$$\tau_{FPI} = I\ddot{\theta} + c_1 e^{-c_2\dot{\theta}}\dot{\theta} \tag{94}$$

When this interaction is modelled with the previously mentioned dynamics model with an added nonlinear damping term that has been empirically determined by these tests, the equations of motion are given in Eq. (94). These results are also plotted in Figure 13 and Figure 14. Clearly, the small angular-displacement experiments better matched simulated dynamics; the natural frequency of the underdamped system was predicted to within 0.1 Hz (about 6% of the simulated value). The simulations of larger angular displacements (15 degrees and above), on the other hand, match the experimental data's general shape, but the natural frequencies differ by almost 0.4 Hz (or 30% of the simulated value). These results suggest that, even for this relatively simple, single-degree-of-freedom system, the damped advanced frozen-image model can be used to evaluate natural frequencies at small displacements about the roll equilibrium, but larger displacements

(where more of the nonlinearity is in effect) and any time history prediction requires modifications to the basic model to better match the observed motion.

Natural-Mode Experiments

Natural-mode experiments are the most rigorous and comprehensive experiments to investigate the coupled, passive dynamics of the interface by exciting all unconstrained natural modes and frequencies. The following data analysis includes only the experiments that do not experience collisions to obtain purely the flux-pinning dynamics without external contact forces. The observed dynamics from every experiment display coupled, underdamped oscillatory behavior in each degree of freedom, which is shown in Figure 77.

A comparison of simulation and measurements for each degree of freedom in both time domain and frequency domain is shown in Figure 77. The simulation is consistent with the simulation used in data analysis from previous subsection with environmental parameters from Table 16. The simulated time history is generated by extracting initial conditions from measurements, setting initial conditions for the simulation, and running the simulation open loop.

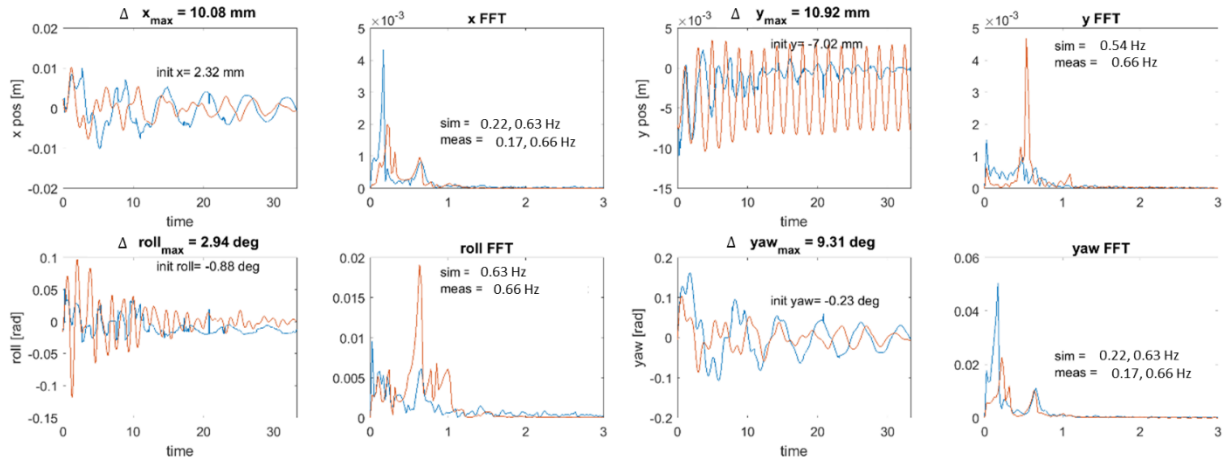

Figure 77: Time history and frequency spectrum of each degree of freedom side by side from one experiment run. Red is the simulated response and blue is the measured response.

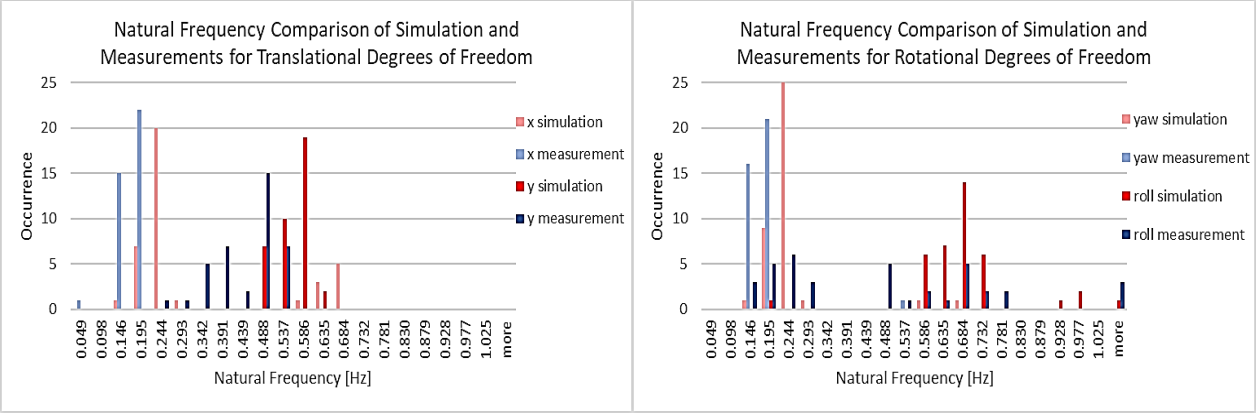

Figure 78: Left, histogram of natural frequencies for the translation degrees of freedom; right, histogram of natural frequencies for the rotation degrees of freedom

The simulated frequency spectra are generated with a fast Fourier transformation on the simulation time history. Coupled dynamics manifest as a beat pattern in the time histories and as subdominant frequency peaks in the frequency spectra. In all degrees of freedom, the simulation response is close in predicting dominant and secondary frequencies. The simulation overestimates amplitude response in the y and roll directions but underestimates amplitude in the x and yaw directions. The flux-pinned system in this reduced-DOF dynamic testbed displays four natural frequencies but not necessarily unique frequencies. In this geometric configuration, the x and yaw degrees of freedom are deeply coupled and oscillate at the same frequencies. Due to nonlinearity of the underlying physics, the natural frequencies are not consistently at the same frequency. The nonlinearity is explored by analyzing a wide range of initial conditions across all the degrees of freedom.

A broad range of initial conditions are tested to explore the nonlinearity of the flux-pinned system. Figure 78 and Figure 79 display natural

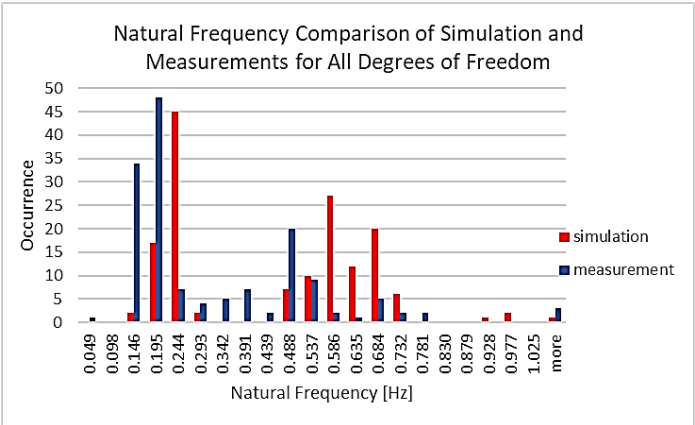

Figure 79: Histogram of natural frequencies for all degrees of freedom

frequencies from 38 distinct experiment runs and their corresponding simulated frequencies. Figure 78 separates translation and rotation degrees of freedom to show four natural frequencies, although not all unique frequencies. A dominant frequency for any degree of freedom is not consistently one frequency but a swath of frequencies, dependent on the initial conditions. Initial conditions starting farther away yield slower oscillations, or lower natural frequencies. The modal natural frequencies and corresponding stiffness of the many experiment runs are shown in Table 18. The simulation consistently overestimates the measured natural frequencies; the as-built flux-pinned interface is less stiff than the simulated interface. Although the simulation predicts natural frequencies close to the as-measured dynamics, modifications for a more predictive simulation should compensate for the reduced amplitude response and reduced stiffness of the actual interface.

Table 18: Measured and simulated natural frequencies with corresponding stiffness for each degree of freedom

degree of freedom	measurement frequency [Hz]	measured stiffness [N/m]	simulation frequency [Hz]	simulation stiffness [N/m]
x	0.195	3.40	0.244	5.32
y	0.488	21.29	0.586	30.70
roll	0.684	0.0129	0.684	0.0129
yaw	0.195	0.0148	0.244	0.0232

Capture and Tumble Experiments

The sphere-of-influence tests examined the case when the potential energy well created by the field-cooled magnetic field in the superconductors draws in the OSA from a state with no kinetic energy. The capture and tumble

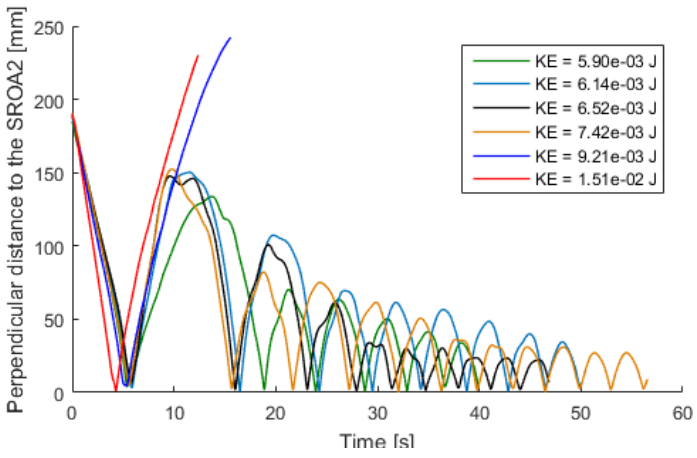

Figure 80: Time history of capture tests at 0 degrees with different initial kinetic energies

tests, on the other hand, were designed to characterize the bounds of rotational and translational kinetic energy that lead to capture, escape, and impacts in the FPI. If the kinetic energy of the OSA is larger than the potential well created by the FPI, the OSA escapes from the FPI (rather than being captured), as shown in Figure 80. Similarly, if the kinetic energy of the system can generate motion that exceeds the separation distance between the OSA and SROA, an impact occurs (which is undesirable for many sample capture scenarios). A capture without a collision is therefore the most desired sample capture outcome, and an escape with an impact is the least desired. These tests examined these kinetic energy thresholds.

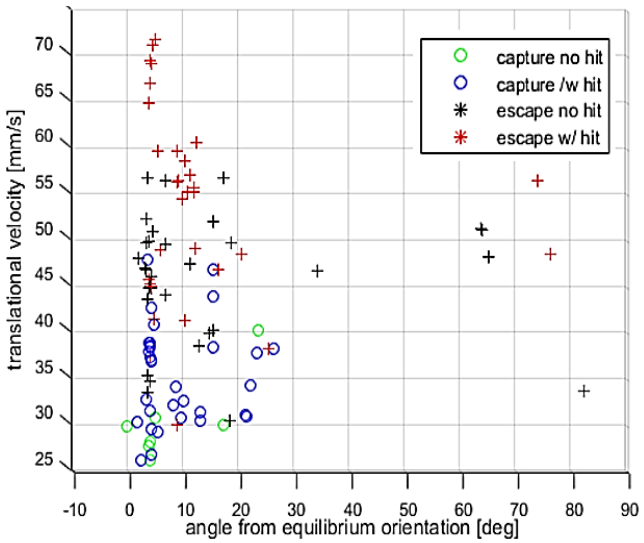

Figure 81: Scatter plot of 4DOF tumble tests with varying absolute angles from equilibrium and entrance angular velocities

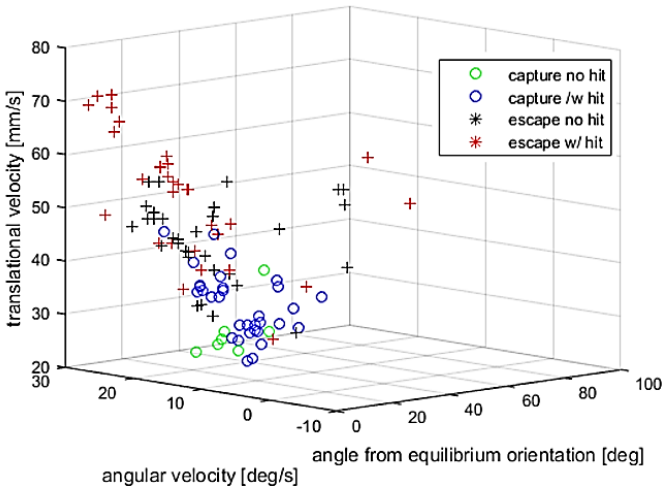

Figure 82: 3D scatter of 4 DOF tumble tests plot with varying absolute angles from equilibrium, entrance angular velocities, and translational velocities

The capture tests enter the potential energy well with only translational velocity. The OSA yaw angle matched the path angle when entering the sphere-of-influence to ensure that the potential energy well was stable (drawn in) vs. unstable (repulsed out), refer to Figure 82 and Figure 81. The tumble tests did not guarantee that the OSA entered the potential well with a stable orientation and added rotational kinetic energy. For a more direct computation of the energy in the

system, the system was placed outside of the range of the FPI attraction (as established by the sphere-of-influence tests) and given an initial velocity to enter the FPI's potential well.

Figure 83 shows the capture tests as a function of their path angle, translational and angular velocity, and final impact/capture state. Figure 84 is the same scatter plot but at a different perspective to highlight different observations. As expected, lower velocity tests capture more consistently than higher velocity tests. The system more likely captures and impacts than escaping without an impact. Reliable captures occur at angular velocities up to either 10 deg/s or 2 cm/s, corresponding to 0.01 J, marked by the orange arc in Figure 84. The capture scenarios with no collisions are a lower energy subset of the larger capture set, with preferential path angles at -10 degrees and 32 degrees, seen in Figure 83. Capture events with collisions occurred much more frequently when the path angle was near 0 deg, with a regime of escapes without collisions separating the lower energy captures with the higher energy captures, as shown

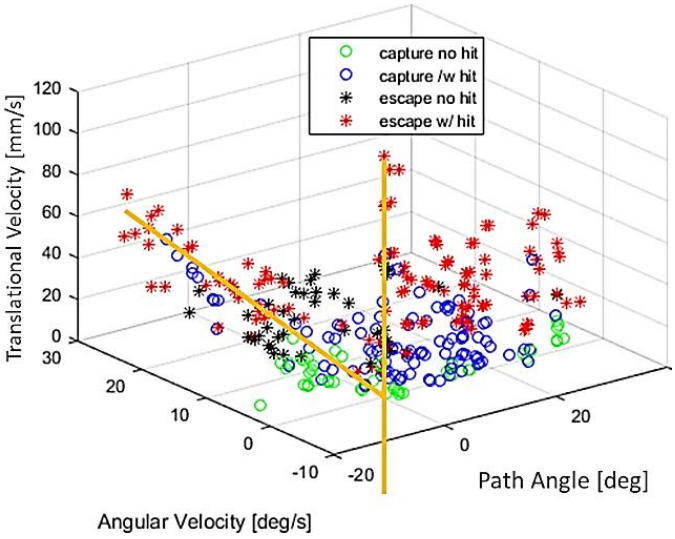

Figure 83: 3D scatter plot with parameters path angle, angular velocity, and translational velocity on the axes. Orange lines represent a path angle of 0 degrees

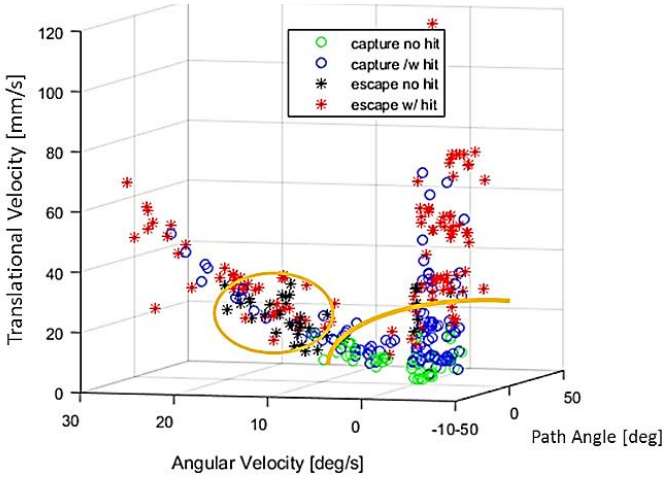

Figure 84: 3D scatter plot with parameters path angle, angular velocity, and translational velocity on the axes for 4 DOF capture and tumble tests. Orange circle includes the region of escapes with collisions and the orange arc bounds the angular velocity and translational velocity for reliable capture

by the straight orange lines in Figure 83. This pattern could be the result of the impacts absorbing the rotational kinetic energy of the OSA into an acceptable capture range. The largest occurrence of collision-free escapes occurs in a range of angular velocities between 10 deg/s and 20 deg/s, as seen by the orange circle in Figure 84.

The successful capture of tumble tests, shown in Figure 82, depended on angular velocity and the orientation of the OSA upon entering equilibrium position. As seen by the unstable equilibrium potential well (in Figure 85), despite being in equilibrium position, the orientation effects the shape/gradient of the potential well and could reject the OSA. The angle from equilibrium orientation is the combination of roll and yaw displacement, calculated with the differential quaternion. The angular velocity is measured before the OSA enters the potential well. The OSA is more likely to capture when entering the potential well in equilibrium orientation; although for slower velocities, the OSA can be farther skewed from equilibrium orientation and still capture, as shown in Figure 83. The implications for a flight mission are clear: lower relative velocities and angular rates generate more successful, non-impacting capture scenarios. If contact is unacceptable and the OS may experience larger energy states during capture, the state of the OS

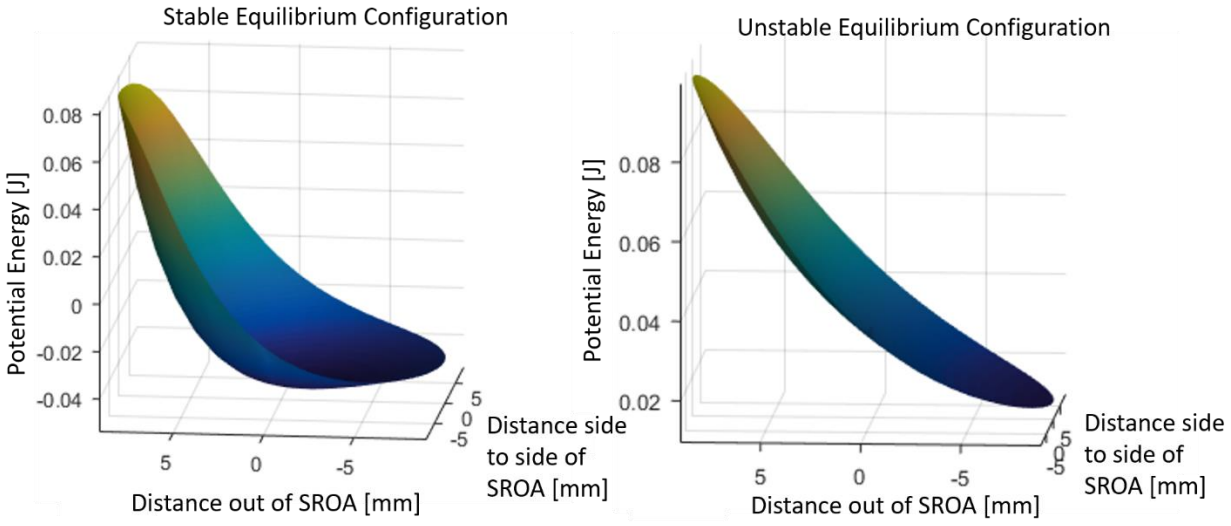

Figure 85: Comparison of a stable and unstable potential wells for different OSA configurations

may need to be estimated to ensure that the OS is within an acceptable range of attitude to guarantee capture.

Degree-of-Freedom Sensitivity

By locking the OSA's rotation about the spindle, the FPOS testbed limits the motion to three degrees of freedom. Selected tests and results were repeated in this configuration to investigate the sensitivity of FPI dynamic performance to the number of DOFs available. As can be seen in Figure 86 and Figure 87, the OSA consistently captures at much lower angular and translational velocities, with a corresponding kinetic energy threshold of 0.0025 J as compared to the 0.01 J of the four DOF system. The four DOF tests also showed more subtle

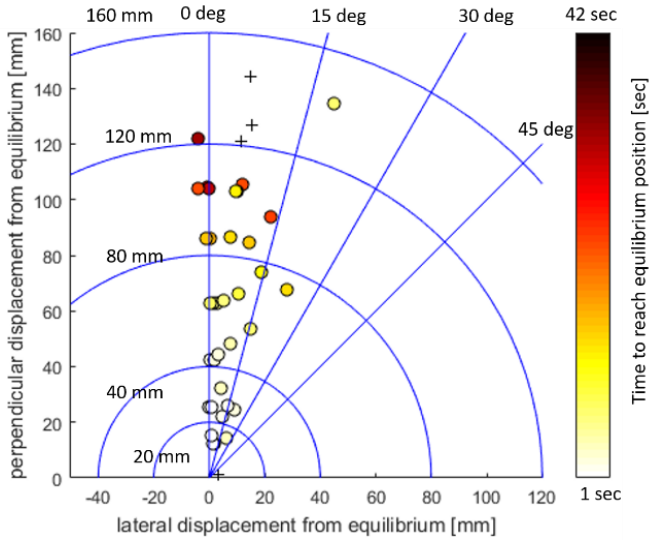

Figure 86: Sphere of influence for different initial displacements for 3DOF system

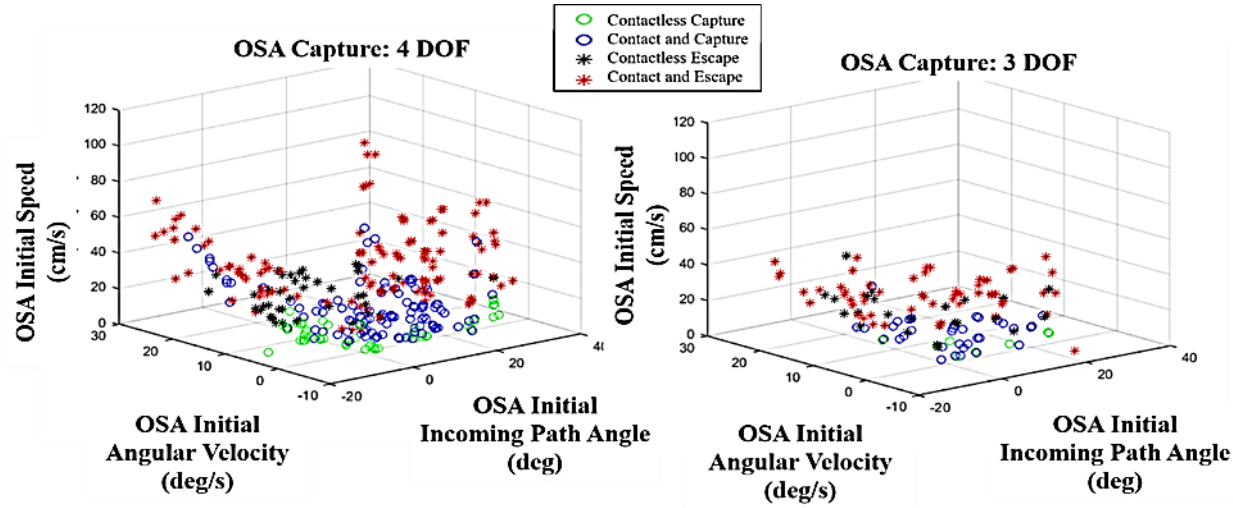

Figure 87: 3D scatter plots showing the reduction in capture range in a three DOF test (left) from a four DOF test (right, which is repeated for comparison)

effects of the parameters on the system capture state. For example, four DOF tests showed that for a zero-degree path angle, captures could be made at higher velocities, but this path angle preference does not appear in the three DOF data. Also, most three DOF experiments involved collisions. The reason for the reduced performance is likely because the nonlinear degrees of freedom in an FPI are also coupled. When one degree of freedom is constrained, the energy couples into the remaining degrees of freedom, causing the system to be more likely to exceed the energy thresholds in that degree of freedom. However, the sphere-of-influence (shown in Figure 86) are approximately the same (12 cm). Ultimately, the implications of this sensitivity to the number of degrees of freedom suggest that the best testing environment for an FPI is microgravity – where all six coupled degrees of freedom can be tested simultaneously – but that reduced degree-of-freedom testbeds can provide conservative, bounding estimates on performance that only improve as the system becomes more flight-like.

c. Contributions from a Reduced Degree-of-Freedom Testbed

Flux-pinned interfaces are a unique technology that offer several advantages to close-proximity spacecraft maneuvers, including potential sample capture scenarios. For the sample capture concept described in this work, the flux-pinned interface design has been shown to successfully capture an orbiting sample in a four degree-of-freedom ground testbed environment over a variety of conditions. Given the maturity of the cooling system and the 1:1 scale of the FPI dimensions in this testbed, the technology has achieved a system demonstration in a (conservative and bounding) laboratory dynamic environment and a relevant thermal environment.

The results of the test campaigns on the FPOS air-bearing testbed show that, for the test hardware, the sphere-of-influence of the FPI is generally independent of path angle and is about 12 cm in radial distance. Extrapolating from the ground testing environment, a flight-like interface

is expected to work at a range of 50 cm in orbit around Mars and operates best in a path angle of 0 degrees. The natural frequencies and stiffness of the test hardware is less stiff than a baseline dynamic simulation. The kinetic energy threshold for capture is approximately 0.01 J, which corresponds to a total relative translational velocity of up to 4.7 cm/sec or a total angular rate of 24 deg/sec between the spacecraft and the sample cache (but not both simultaneously). Achieving better relative approach angles (staying near the 0-degree path angle) may enable those relative bounds to loosen to 16.7 cm/sec or 47 deg/sec for a flight-like system.

Furthermore, the series of ground-based experiments shown in Figure 87 showed that the system's capture performance is degraded in the presence of fewer degrees of freedom: a three-degree-of-freedom system captures less consistently than a four-degree-of-freedom system with the same initial conditions [22]. Clearly, the range of successful capture is reduced with fewer degrees of freedom. Because of this high sensitivity to the test configuration, this variability must be further explored in a less constrained environment, which is the primary motivation for the SPECTRE 2 test campaign.

Ultimately, the FPI's full performance capabilities and dynamic subtleties are not able to be fully expressed in a constrained degree-of-freedom environment. These results likely underpredict the performance of a true flight-like system. When the FPOS testbed was constrained to three degrees of freedom, the capture energy threshold was reduced by 80 %. A full six degree-of-freedom experiment (whether on a microgravity plane flight [68] or a demonstration in low earth orbit) is the next step in maturing this technology. This information assists in the tuning of a predictive model for the dynamics that make it possible to consider FPIs on a potential flight sample-capture mission.

III. Capture and Docking Experiments in a Microgravity Testbed

Naturally, the next environment to build and test technology for spaceflight is a microgravity environment. The lowest altitude and lowest cost option to still achieve microgravity conditions is parabolic flight. Motivated by the degree-of-freedom sensitivity discovered in the ground tests, a microgravity environment fully allows the flux-pinned interface to express its nonlinear and coupled dynamics with no need to interpret the effect of constrained DOFs. NASA JPL spearheaded the efforts in chartering a commercial parabolic flight campaign with Zero-G not only for a flight experiment in 2017, but also a similar experiment in 2018. Because both testbeds are similarly designed, the testbed anatomy is thoroughly described in the first microgravity flight experiment section, and the second flight section only briefly discusses the difference between the two testbeds. This section walks through the microgravity experiment motivation, the first and second microgravity experiment setups, and the dynamic capabilities observed in the experiments.

a. Introduction and Motivation

To reach a level of maturity such that flux pinning technology can be used in a flight mission, designers require a parametric mapping to system behavior and a predictive, reliable dynamics model. Recent research efforts have focused on developing a parametric mapping and predictive dynamics model [20] [94]. Numerous previous ground testbeds explore the capabilities of flux-pinned interfaces for several close-proximity spacecraft applications [33] [34]. These testbeds collect dynamic data under a multitude of initial conditions to aid characterization and development of a more predictive dynamics model. Due to the highly nonlinear coupled dynamics of flux-pinning physics, ground testing cannot fully assess, and thus does not accurately predict, the capabilities of a flux-pinned interface in a six degree-of-freedom environment [22].

Observations made in a constrained-DOF environment under-predict the performance of the FPI for a space-based system because the energy that would normally be distributed across all DOF become concentrated into the remaining unconstrained DOF. Furthermore, the depth of the potential well generated from field-cooling a magnetic source is not of equal shape and depth in each DOF due to asymmetries in the magnetic field source. Thus, the maximum energy that the system can absorb to successfully execute a capture maneuver differs across DOF, of which 6DOF is most representative of spaceflight performance. A microgravity testbed enables the full expression of the coupled dynamics and better represents the capabilities in a spaceflight environment.

Parabolic flights enabled the collection of dynamic data from a flux-pinned interface. Although parabolic flights offer only short periods of microgravity environment, data collected from these experiments offer highly relevant insight into the dynamics of an FPI in a space system [31] [38]. Two experiment campaigns of similar build but of differing intention were flown in 2017 and 2018 with Zero Gravity Corporation. At a high level, both experiment testbeds are composed of the two test articles (magnetic and superconducting spacecraft), a free-floating frame to contain the experiment, a launching mechanism to set initial conditions, support equipment for the superconducting spacecraft, and a data acquisition system. Coined SPECTRE, the 2017 testbed aimed to demonstrate successful capture in a flight-traceable environment, microgravity, while also measuring relative dynamics of the two experimental spacecraft at different initial conditions. Armed with insight from the first flight, the 2018 testbed, fittingly named SPECTRE2, improved several aspects of the 2017 testbed, namely a consistent launching mechanism, stronger magnets, and a more aggressive set of initial conditions. This suite of efforts results in compelling

demonstrations and characterization that steadily increases the technology readiness level of FPIs towards spaceflight adoption and implementation.

b. First Microgravity Flight Experiment

For FPIs to be considered a viable option in an MSR trade study, the FPI technology must sufficiently mature to better estimate resource consumption such as mass and power, preferably from a proven flight-like demonstration. Similarly, it is essential to develop predictive models of the interaction and the resulting spacecraft dynamics. A microgravity flight demonstration of the capture and manipulation is the most effective method of improving the technology's maturity because the microgravity dynamic environment best captures the nonlinear coupled dynamics that an FPI with experience under flight conditions. In March 2017, SPECTRE 1 was flown on two microgravity flight days. A successful demonstration in this environment provides credence to the resource estimates for a flight FPI and provide critical data necessary for improving the dynamics model of flux pinning.

Several technical objectives for the first flight campaign include successful demonstration, data collection, and sufficient characterization across a spread of initial relative dynamic states. The first objective is to demonstrate successful capture in six degrees-of-freedom with a specific FPI design. Although previous ground experiments all signal that a flight system should capture, a physical demonstration is extremely compelling and validates the hardware implementation. The second objective is to record relative position, orientation, angular velocity, and acceleration between the OSA and SROA that enable researchers to characterize the properties of the FPI (such as stiffness and damping). These data provide the basis for updates to the dynamics model of the FPI. The last objective is to characterize a sufficient set of initial conditions to appropriately bound the range of influence and energy that results in a successful capture. Velocity initial conditions

span from 1 cm/s to 8 cm/s. Angular velocity initial conditions span from 0 deg/s to 40 deg/s. The testbed hardware and experiment operations were carefully designed to achieve these objectives.

Experiment System Description

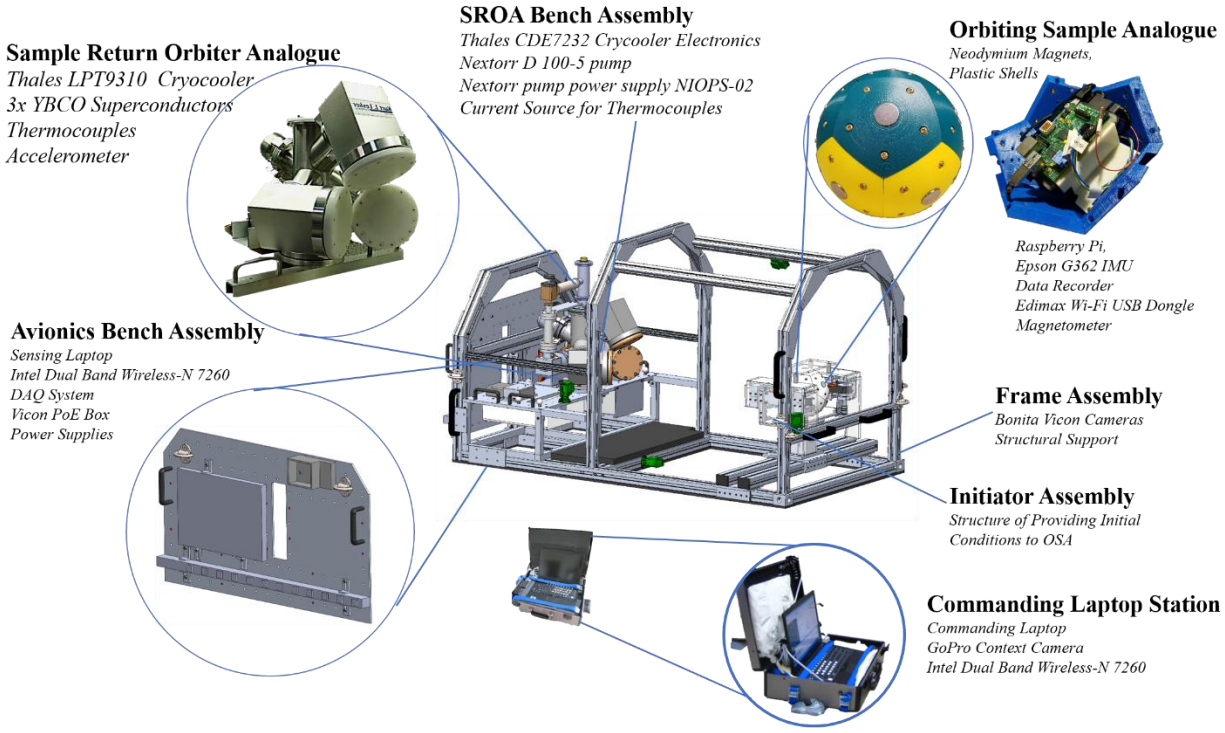

Figure 88: Diagram of key elements of the SPECTRE and SPECTRE2 testbeds hardware.

Figure 88 shows the high-level system layout for reference in discussing the experiment design and procedures. SPECTRE 2 consists of three main elements: the commanding laptop station (CLS), the orbiting sample analogue (OSA), and the integrated frame assembly (IFA). The IFA is broken into five different subassemblies: the Avionics Bench Assembly (ABA), the Sample Return Orbiter Analogue (SROA), the SROA Bench Assembly (SBA), the Initiator Assembly (IA), and the Frame Assembly (FA). These different subassemblies are shown in a model of the hardware shown in Figure 88 and the block diagram in Figure 89.

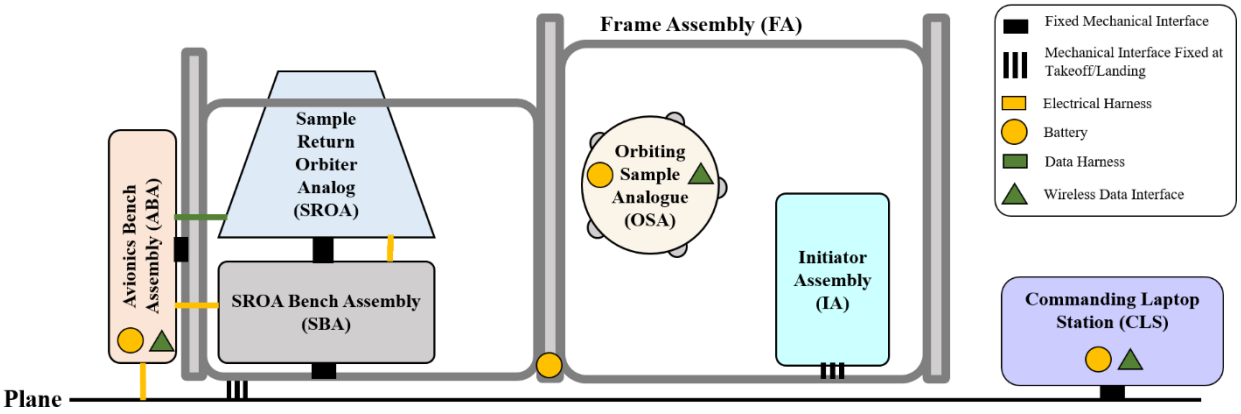

Figure 89: A block diagram of the SPECTRE hardware with major interfaces identified.

The CLS is a small briefcase-like structure that holds a standard laptop to the floor of the aircraft, which has (commercial-off-the-shelf (COTS)) batteries for its components and interacts with the ABA wirelessly. The primary purpose of the CLS is to allow the operator to make quick evaluations of the data being collected and to make notes in the experiment log for each parabola. The CLS also initiates the start of the data collection bursts via a wireless command to the ABA.

The OSA is an approximate to-scale representation of an orbiting sample cache, making it roughly the dimensions of a volleyball. The OSA has internal electronics that measure and record accelerations and rates and is also powered via an internal COTS battery. The OSA has a computing element (a Raspberry Pi), which manages its internal data collection. Some subset of the collected data is wirelessly transmitted to the ABA for monitoring during the flight. However, all of the data is stored on an internal SD card that is downloaded at the end of the flight. This unit is also populated with an array of eleven permanent magnets to form one part of the FPI. It is stored in a Zero-G pelican case during takeoff and landing and is free floating during the flight operations.

The Integrated Frame Assembly (consisting of the SROA, SBA, ABA, IA, and FA) is mounted to the aircraft during takeoff and landing but the restraints are removed for the experiment. The entire unit is free-floating during operations. This experiment design enables the

relative motion between the IFA and the OSA to be unperturbed by the variations in the flight deck dynamics. An element of the IFA, the SROA is the other half of the FPI and contains the Thales LPT9310 cryocooler, a custom designed vacuum chamber fabricated from a commercial contractor, the Nextorr D 100-5 pump, and superconductors in the experiment. It can be seen in the images of the 2016 ground test campaign shown in Figure 63c. It maintains the YBCO superconductors below their critical temperature of 88 K. All of the cryogenic temperatures are enclosed by the vacuum chamber to avoid any exposed cryogenic surfaces. The temperature of the superconductors and the cryocooler is monitored by a series of temperature sensors, and these data are recorded for subsequent processing and used real-time to monitor the health and safety of the system. This assembly is attached to the SBA, its companion bench assembly, which houses the Nextorr pump power supply NIOPS-02, the Thales CDE7232 cryocooler electronics, and the current source for the temperature sensors. The SBA (with the SROA attached) is a separate assembly that can be removed from the IFA during ground operations to facilitate the powering of the pump and cryocooler prior to the flight. During flight, however, its main powered elements are connected to the power strip on the ABA. The IFA is connected to the plane via a tether cable during the microgravity portions of the flight that limits its motion to a designated experiment area only.

The Avionics Bench Assembly has a laptop identical to the one in the CLS, a power strip, and a data acquisition card. The "sensing" laptop manages the collection of the temperature sensors and serves as a conduit for the data transmitted from the OSA via a wireless connection. As a result, it also generates the common timestamp for the data collection. Ultimately, this sensing computer is the source of the data displayed on the CLS. The sensing laptop and the inclinometer are powered by a battery, but all of the other avionics on the IFA are powered via a power strip

that connects to a power panel of the plane. During the free-float operations, the power cable is the only electrical link between the ground and the plane, and its low stiffness limit the transmission of disturbances along its path.

The Initiator Assembly, or launching mechanism, can be manipulated in between experiment sets and set in place with locking handles. The IA mechanism consists of two variable speed motors and belt assemblies to enable launching the OSA and controlling electronics. This design enables the initial conditions of the OSA to be imparted at the beginning of each parabola set, eliminating some of the uncertainty and operational difficulty with setting initial conditions. The total range of the IA assembly movement is 0.6m along the long axis of the IFA (toward the SROA), 0.75 m in the direction parallel to the SROA, and ± 30° in pitch. For takeoff and landing these components are locked in place with a through bolt, which is removed prior to the first parabola. The launching assembly is also powered down during takeoff and landing.

The last element in the IFA is the Frame Assembly (FA), which consists of the extruded aluminum structure inherited from a previous Mars Orbiting Sample Return project, seen in Figure

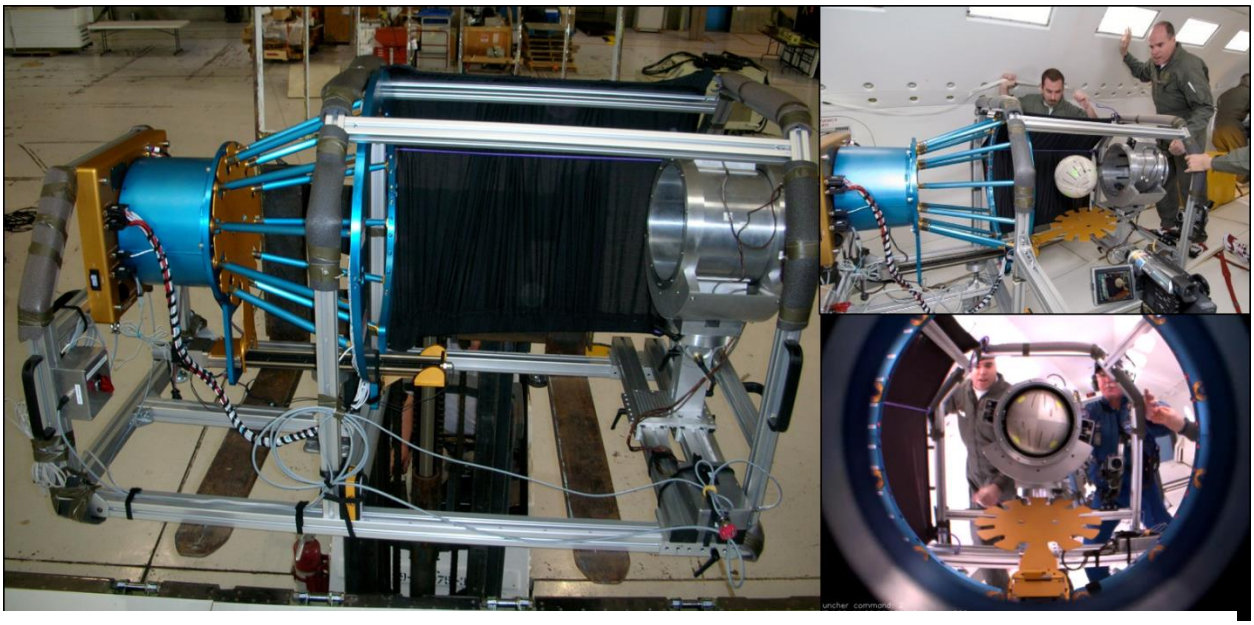

Figure 90: The SPHERES-MOSR hardware and experiment.

90. The aluminum frame provides the structure necessary to mount five GoPro cameras that collect video, which yield information on the position and velocity of the OSA [68]. The GoPro cameras are self-contained with their own internal batteries. Together, this hardware supports the flux-pinned interface sample capture experiment that forms the core of the technology maturation goals of SPECTRE 1 and 2. Table 19 compiles the volumetric and mass properties of each component of the Integrated Frame Assembly.

Table 19: SPECTRE 1 and 2 System Dynamical and Mass Properties

Assemblies	Dimensions	Mass (Weight)
Frame Assembly (FA) (including feet, and GoPro)	1.242 × 0.959 × 1.68 m (48.9 in × 37.8 in × 66.14 in)	68.7 kg (151.4 lbs)
> Feet (x4)	9.28 × 6.6R cm (3.65 × 2.60R in)	0.253 kg (0.558 lbs)
> GoPro Assemblies (x4)	5.9 × 4.1 × 3 cm (2.32 × 1.61 × 1.18 in)	0.162 kg (0.36 lbs)
Avionics Bench Assembly (ABA)	0.914 × 0.521 × 0.065 m (36 in × 20.5 in × 2.6 in)	11.94 kg (26.32 lbs)
Initiator Assembly (IA)	0.978 × 0.401 × 0.464 m (36 in × 15.7 in × 18.3 in)	23.32 kg (51.41 lbs)
SROA Bench Assembly (SBA) / Sample Return Orbiter Analog (SROA)	0.914 × 0.567 × 0.766 m (36 × 22.32 × 30.16 in)	60.10 kg (132.50 lbs)

Orbiting Sample Analogue (OSA)

The OSA, shown in Figure 91, is a custom-built analogue for the spherical orbiting cache that needs to be captured and returned to Earth in a conceptual Mars Sample Return scenario. The OSA incorporates surface-mounted Neodymium magnets and constitutes one half of the experimental flux-pinned interface. A sensor package is rigidly mounted inside the structural housing of the OSA, show in Figure 92, and offers dynamic data during microgravity tests. During flight, the spacecraft analogue free-floats and intercepts with the other half of the docking interface. This

Figure 91: Images of the (left) OSA CAD model, (center) OSA, and (right) OSA with a close-up of the switch.

interaction involves the dynamics of interest. After each experiment, the OSA must be secured and loaded back into the initiator assembly.

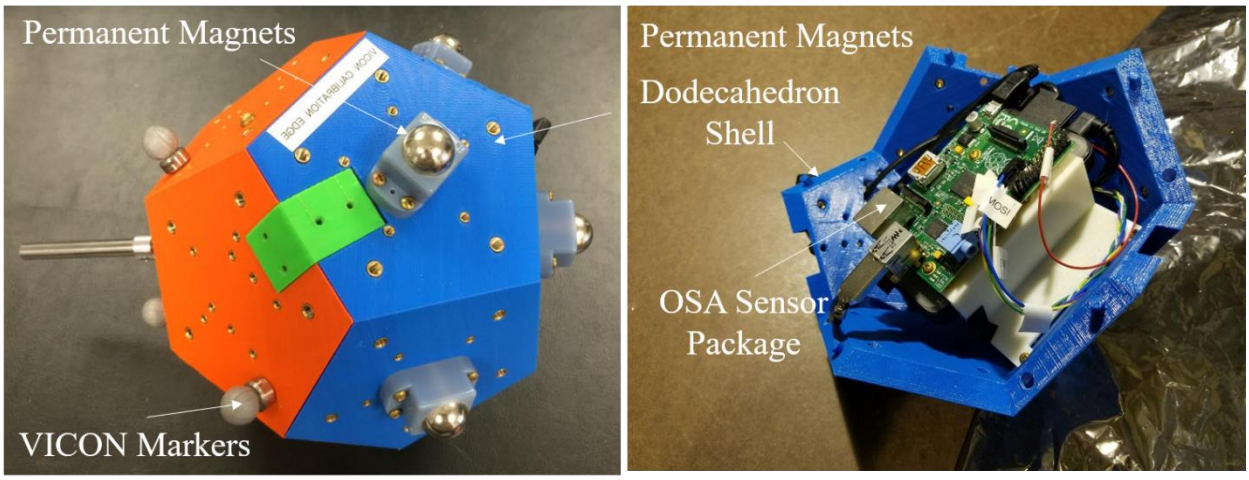

Figure 92: Images of the OSA at various stages of assembly.

Frame Assembly (FA)

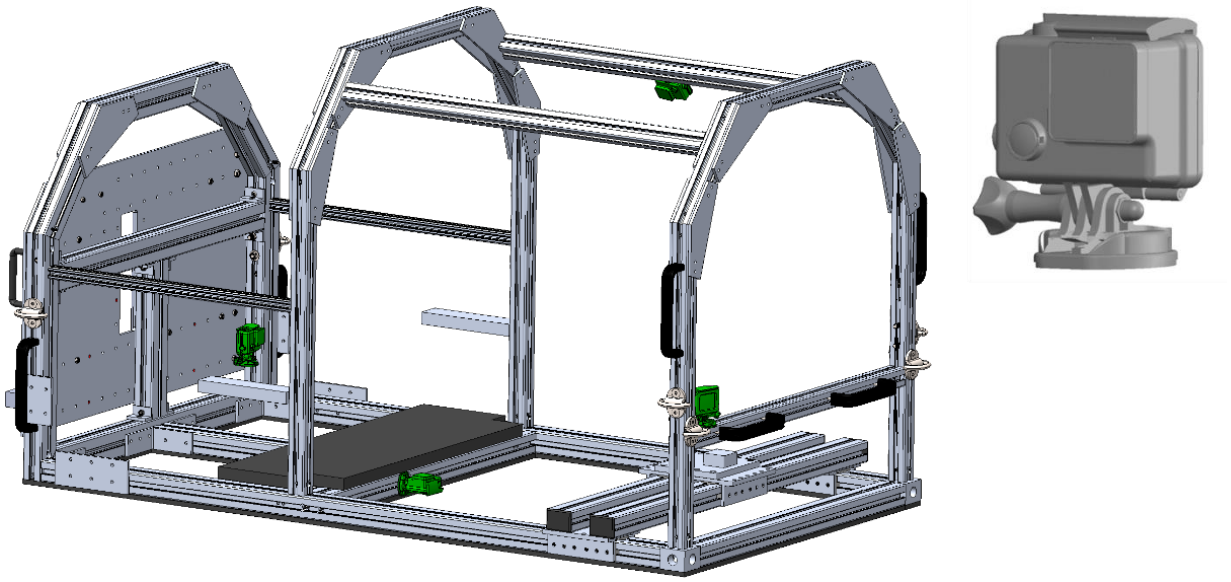

Figure 93: (left) Frame assembly in its ground configuration (shown with the IA attached), and (right) the GoPro assembly.

The frame assembly, shown in Figure 93, consists of the extruded aluminum structure that is heritage from the MOSR experiments, with the properties described in the table below, and a set of four GoPro cameras. The bounding volume of the FA is approximately the size of the integrated frame assembly because almost all the components fit within its volume. The FA serves as the base structure for mounting all the components in the system. It also houses most of the cargo strap rings used to attach the cargo straps during pre-flight operations [127]. The T-slotted aluminum structure is manufactured by Rexroth, which provides the material properties shown in Figure 93 for all their aluminum extrusions. The Rexroth specifications can be found in Figure 95.

	Metric	U.S. Equivalent
Material designation according to DIN (ISO) for Bosch profiles	**EN AW - Al MgSi**	**AW-6063-T66**
Material number according to DIN (ISO)	**3.3206.7**	**AW-6063-T66**
Tensile strength (expected)	$R_m = 245$ N/mm²	(35,530 lb./in.²)
0.2% proof stress (expected)	$R_{p0,2} = 195$ N/mm²	(28,280 lb./in²)
Elongation at rupture A_5 or A_{10}	$A_5 = 10\%$ $A_{10} = 8\%$	
Modulus of elasticity E	E = 70,000 N/mm²	(10×10^6 lb./in²)
Brinell hardness	75 HB	
Coefficient of linear expansion	$\alpha_{(-50°...+20°C)} = 21.8 \times 10^{-6}$1/K $\alpha_{(-58°...+68°F)} = 12.1 \times 10^{-6}$in/in/°F $\alpha_{(+20°...+100°C)} = 23.4 \times 10^{-6}$1/K $\alpha_{(+68°...+212°F)} = 13.0 \times 10^{-6}$in/in/°F	
Poisson's ratio	$\mu = 0.34$	
Anodizing process–layer thickness–layer hardness	E6/EV1-12µm - 300HV	R204-(.0003 in-300HV)

Figure 95: Rexroth material properties considered in mechanical design

Figure 94: Examples of joints on the frame with embedded pins and locking bolts.

The frame components consist of two cross-sections: the 40 × 40 and the 45 × 60 beams, and section-specific properties can be found in the Rexroth specifications document. The structural model used the detailed cross-section of these elements to perform the system-level analysis, adding fidelity to the results. The inherited T-slotted aluminum framing has a number of friction-

based joints, including a series of pin-and-bolt connections, where set screws fit into a notch in the pin (a few examples are shown in Figure 94, and an image of the assembled base of the heritage frame can be seen in Figure 96). Where these joints occur, the hardware is instead retrofitted with through-bolts and L-brackets, and gussets to secure all joints. Gussets further reinforce the angled joints of the MOSR heritage frame (one example shown in Figure 97). Each gusset plate has two parallel holes along each bar to join the angled pieces together and to resist external moments. The gussets provide a secure way to keep all joints together in addition to the embedded pins. The frame has also been retrofitted with a 1-inch-thick polyurethane foam sheeting to ensure the frame transitions from 0g to 2g gradually. The pad elevates the height of the base frame to allow easier manipulation of the IA rails. The pad also mitigates the hazards to experimenters as the frame lands back on the aircraft floor. Similarly, to ensure a soft landing for the OSA during acceleration profiles, a polyurethane foam pad has been added underneath the OSA equilibrium position to the FA. The OSA can land on the foam pad if the OSAM does not retrieve it prior to the transition back to 2g.

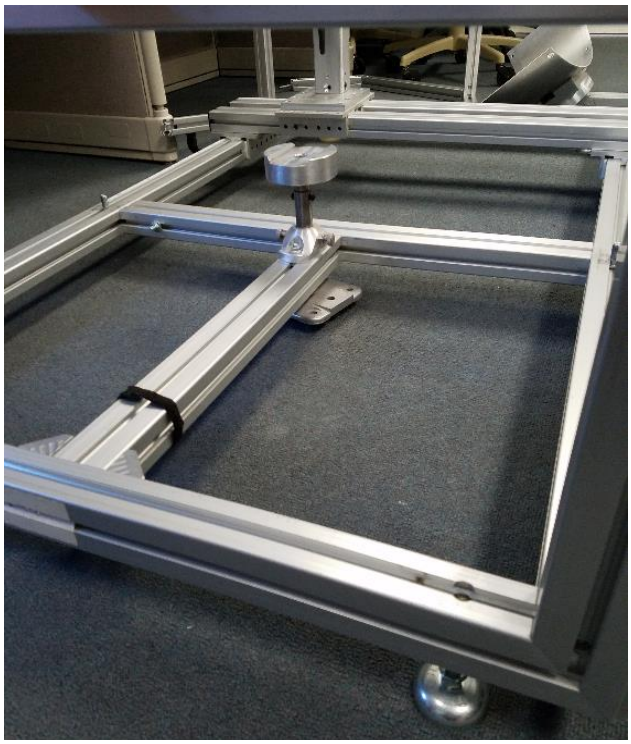

Figure 96: The base of the FA bolted together.

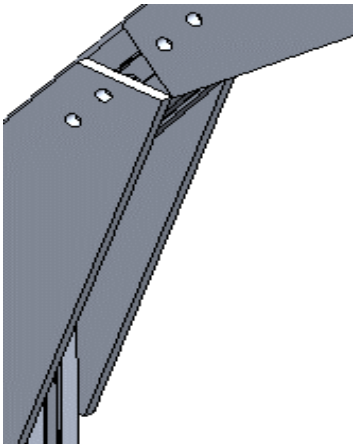

Figure 97. Gussets connect angled joints together securely.

Avionics Bench Assembly (ABA)

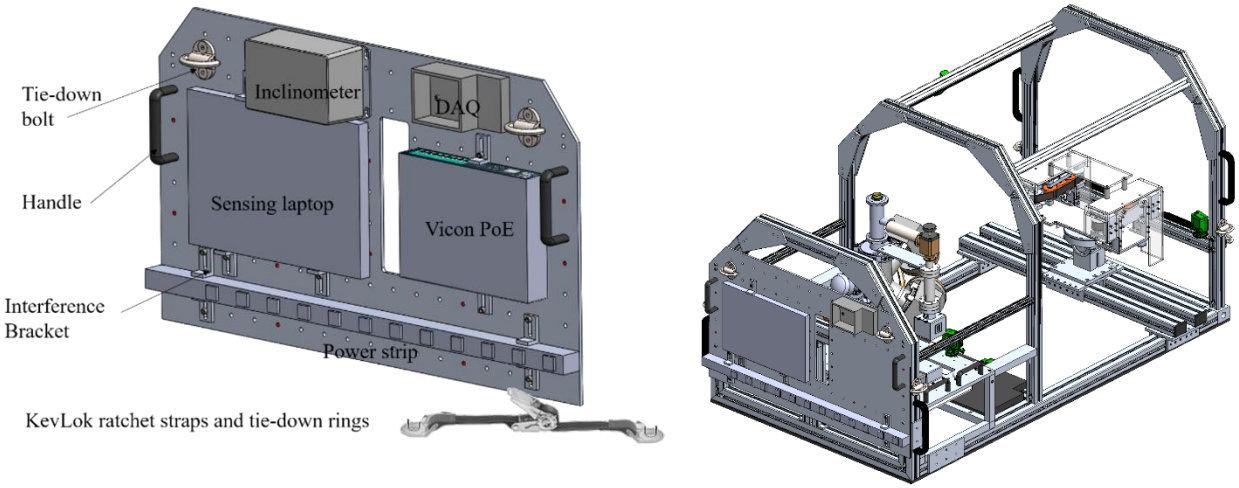

Figure 98: The Avionics Bench Assembly shown (left) in its ground handling configuration and (right) mounted to the IFA. POE box is not be used in SPECTRE 2.

The avionics bench assembly is an aluminum plate with two handles that mounts the NI DAQ input and output modules, and the Sensing Computer, as shown in Figure 98 and Figure 99. The NI DAQ system offers an interface between the Sensing Computer and the SROA thermocouples. The Sensing Computer stores all the telemetry. The sensing laptop is connected to the plate with Kevlok straps with steel fittings that bolt to the plate [128]. Each box is approximately 10 lbs, never exceeding the working load limit of each Kevlok strap of 330 lbs. This plate also houses the main power connection to the aircraft, which is an industrial power strip that has 12 outlets, is rated at 1800W, 120V, and features a 20A resettable circuit breaker to prevent circuit overloads [129]. The cable is 15 feet long and can be plugged into a 5-20P outlet. An adapter to wall power provides power during ground testing.

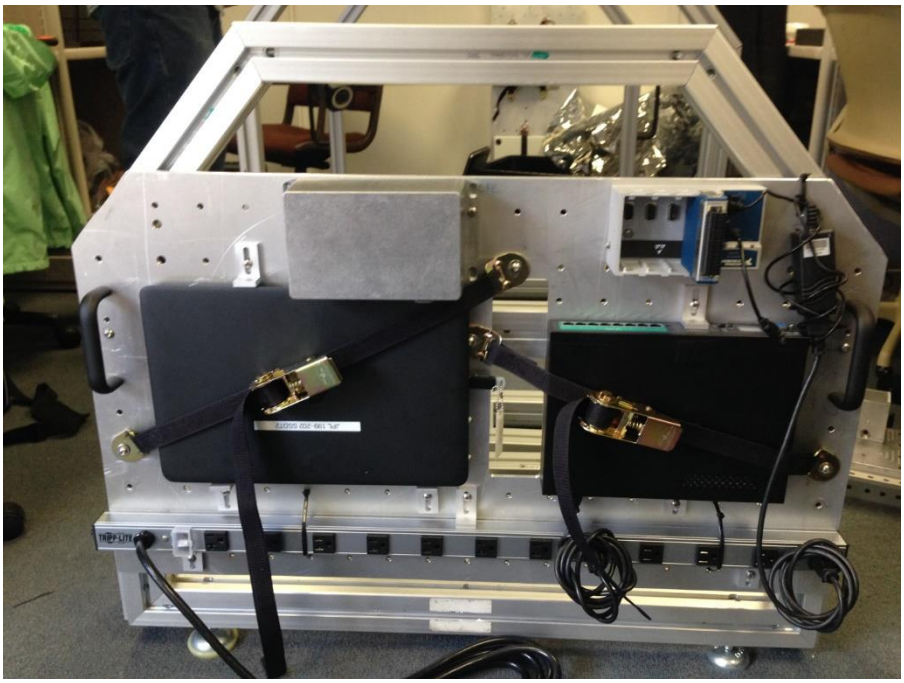

Figure 99: An image of the ABA (POE box not used in SPECTRE 2 flight).

Initiator Assembly (IA)

The initiator assembly, shown in Figure 100 and Figure 101, physically constrains the OSA to start at various displacements and path angles from the SROA. The IA is mounted to an aluminum platform that is free to rotate in yaw and pitch. The platform can slide on two sets of rails; one rail allows 1 DOF motion side to side relative to the SROA, the other allows 1 DOF motion toward and away from the SROA. All these degrees of freedom are locked out by a friction joint during operation, but they can be secured into takeoff/landing configuration with a quick-release pin. The quick-release bolt goes through two layers of extruded aluminum – on both the base frame and initiator assembly. The hoop and pegs on top of the cantilevered platform offer edge and point contacts to position the OSA. All components are rigidly constrained and passive (i.e., they do not have the ability to be actively controlled or powered). During 1g breaks in the

experiment phase of the flight, the platform may be repositioned and then locked again with the handles on the assembly to set up a different initial condition location.

The IA is set to specified initial displacements and angles by operators. Prior to the microgravity portion, the commanding laptop activates the IA via for a set speed on each of the two motors. During microgravity experiments, the OSA manager sets the OSA gently into the far end of the launcher and feed it into the rubber belts. After the OSA manager lets go, the launching mechanism draws the OSA in and dispenses it with a velocity and direction based on the speeds of the two belts. All moving parts are covered with plastic safety panels that prevent any flyer from accidentally touching any of the moving parts during the experiment.

Figure 100: Initiator assembly launching mechanism, including safety covers and motors.

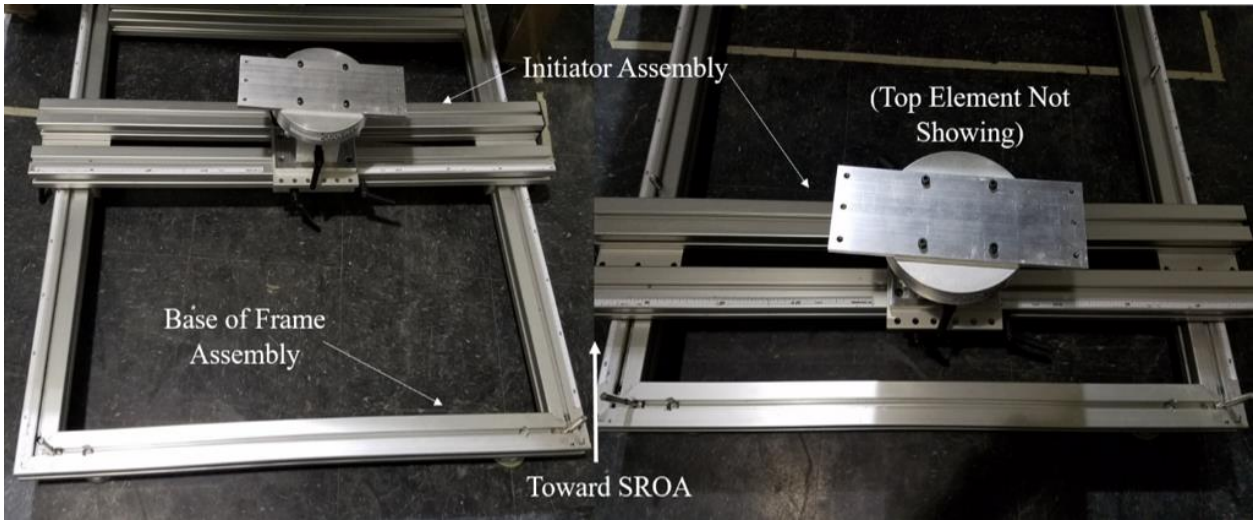

Figure 101: Initiator assembly attachment to base of frame.

Sample Return Orbiter Analogue (SROA)

The SROA, shown in Figure 102, is the other half of the docking interface, and includes the Yttrium Barium Copper Oxide (YBCO) CSYL-56 superconductor disks provided by Can

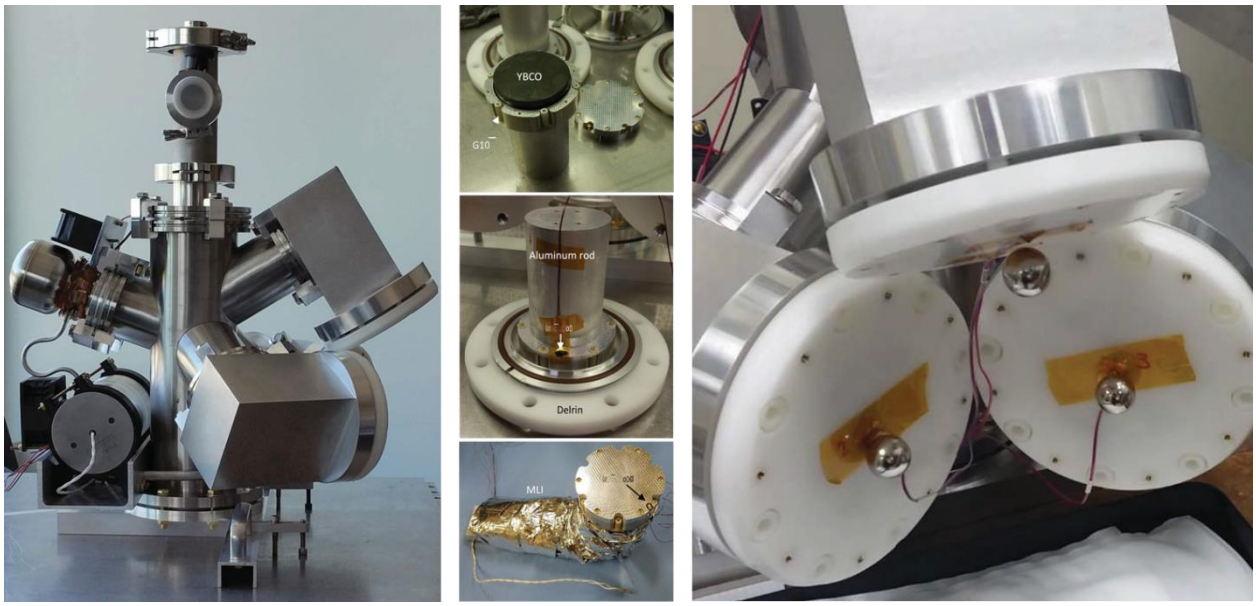

Figure 102: Images of the SROA assembly shown (left) assembled from the side, (center) in various stages of assembly, and (right) with levitating spherical magnets at the OSA equilibrium (these magnets are not the training magnets, which are bolted to the faces).

Superconductors and the peripheral equipment (shown in a lab environment in Figure 102) to keep the superconductors cold [122]. The peripheral equipment includes a customized commercial vacuum chamber that is mated together with full fusion vacuum welds, and a variety of fittings to support the switch from the ground turbo pump to the flight pump. A thorough description of the design and characterization is referenced here [130].

The flight pump is an ion pump that has no moving parts and is entirely passive. The ion pump requires only electrical power to operate and does not encounter performance issues related to the microgravity flights [131]. The Thales LPT9310 Cryocooler cools the superconductors to below the critical temperature (88K, 82K is the nominal operating temperature) [132]. Note, the cooled elements are thermally isolated and do not present a touch hazard for the experiment operators or aircraft crew. The cryocooler maintains that temperature with automated temperature controllers and thermal sensors in the system. Because the system must maintain the temperature of the superconductors throughout the flights, and the cooling process takes almost 12 hours from room temperature, it is important to keep the assembly powered continuously. The aircraft is not powered in between flights. The SROA must be transported on and off the aircraft between flight days, which is accomplished with the detachable SBA/SROA assembly.

SROA Bench Assembly (SBA)

The SBA, shown in Figure 103, is constructed of a welded aluminum frame that allows the mounting of an interface plate containing the SROA and supporting electronics boxes. The frame consists of 2.54cm^2 (1 in^2) solid aluminum 6061 beams welded together into a base structure. Aluminum rods bolt into this structure, which then mount to a 1.27 cm (0.5in) thick aluminum 6061 interface plate via bolts and brackets. This plate includes holes for mounting the SROA,

brackets to constrain the electronics boxes in several degrees of freedom, and strap attachment holes for Kevlok straps to constrain these boxes in the other degrees of freedom. Any electronics box mounting holes that exist are used as the primary method of attachment to the interface plate, but when there are none, Kevlok straps provide a reasonable alternative for securing the boxes to the rest of the SBA.

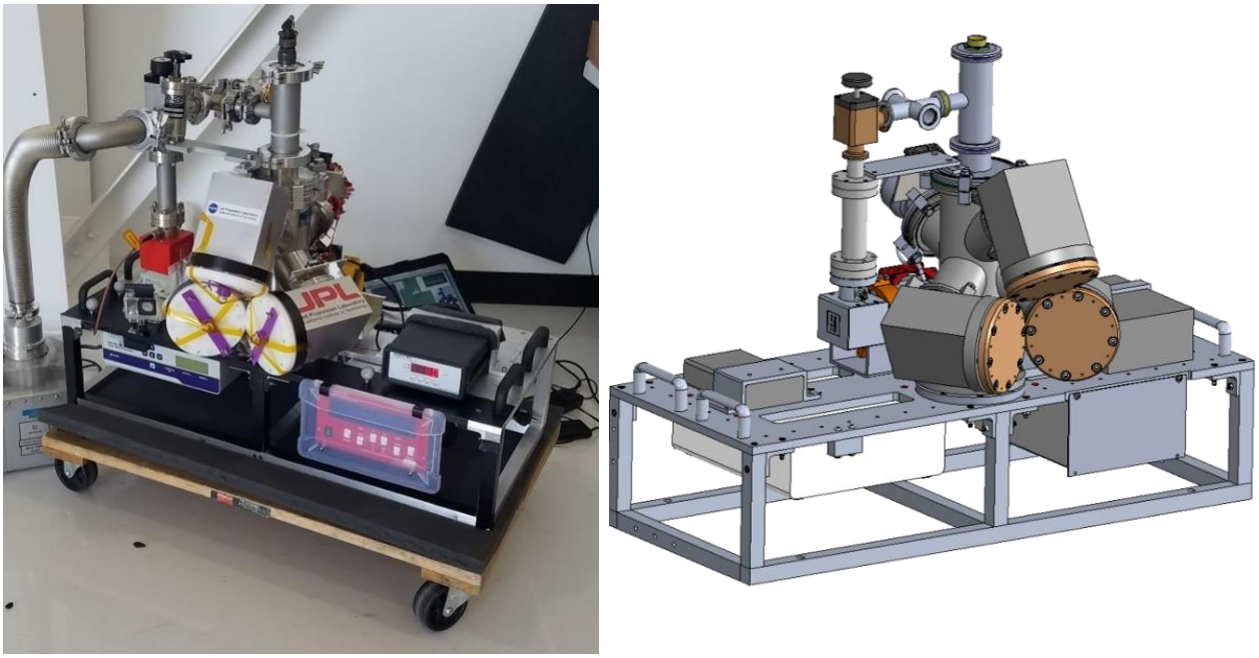

Figure 103: (left) The SBA/SROA assembly in the ground configuration and (right) the assembly in its loaded configuration.

The top surface of the interface plate accommodates the SROA assembly, the current source electronics box, and the temperature regulator electronics box. These boxes are mounted via brackets and bolts to the interface plate. On the bottom face of the SBA interface plate, three electronics assemblies are mounted. The Thales cryocoooler electronics box and the Getter pump electronics box are mounted with a combination of brackets, built-in mounting holes, and Kevlok straps.

The SBA includes removable wheels that can be mounted to the assembly to simplify transportation while it is not attached to the IFA. As shown Figure 103, four wheels can be attached

to the bottom of the welded aluminum frame to allow the SBA to roll. These wheels are attached on the ground and taken off only during integration of the SBA and the IFA on the plane, immediately before take-off. The wheels can be removed by removing the bolt from the top of the SBA frame and sliding the entire assembly directly onto the IFA. Similarly, during unloading of the SBA after the flight, the assembly are slid partially off the IFA, the wheels are installed two at a time, and the assembly is again ready for transport.

Commanding Laptop Station (CLS)

The commanding laptop (HP Elitebook 850) is secured into a heritage briefcase with cinching straps, which is bolted to the aircraft hull bolt pattern with two bolts passing through an aluminum plate that goes through the bottom of the case, as shown in Figure 104. The commanding laptop is strapped in to the briefcase and is embedded in a foam cutout to prevent motion during microgravity. The commanding laptop is connected to the local SPECTRE Wi-Fi network, where

(a) (b)

Figure 104: (left) The Commanding Laptop Station in its (a) stowed and (b) experiment configuration.

the screen of the sensing computer is broadcast to the commanding laptop. Thus, the CLS displays selected data from the experiment and houses a GUI for recording flight events. During the experiment, the CLS powered by its battery. The CLS also hosts a context GoPro camera, which is mounted to the front of the case with industrial Velcro (and stowed during takeoff and landing).

Experiment Operation

The timeline for the experiment can be broken down into several different segments, each of which is described in detail in this section. These segments and their approximate schedule can be found in Figure 105. The operations can be categorized into ground operations and flight operations. Ground operations include all activities that occur in the staging area/hangar, and flight operations are those that occur on the aircraft immediately prior to a flight up until landing. SPECTRE's equipment is delivered, assembled and tested in the staging area/hangar. The assembly of the hardware is not described in detail, as it is a perquisite for all subsequent activities described in this section. The relevant procedures for the Final Checkouts prior to a Test Readiness Review are in the Ground Operations section, including the critical vacuum pump-down and

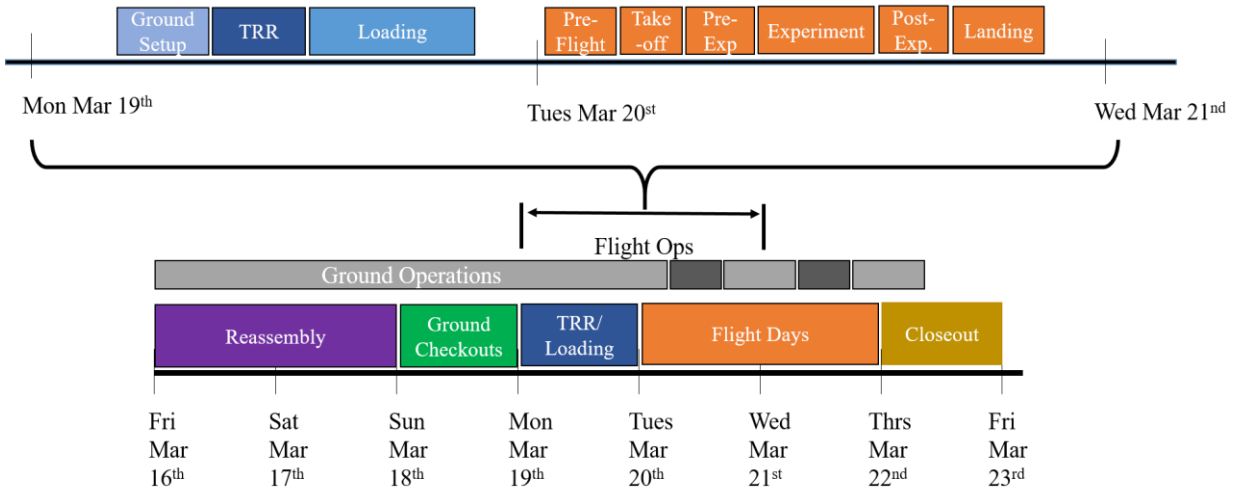

Figure 105: Timeline for ground and flight operations. Note that this schedule shows two flights at the beginning of the week, although the specific scheduling of the experiments is dependent on the Zero-G flight order. The sequence of events remain the same independent of flight days or number of flights.

cryocooler cool-down. This section also describes the process for disconnecting the equipment from the hangar power and transferring it to the plane power, and the consequences of off-nominal scenarios on the schedule. The process for loading the equipment to the plane via the cargo door is described in Pre-Flight Operations. Finally, ground operations after the flight are described in Post-Flight Operations.

Flight operations are repeated for each flight day. They occur when boarding the plane prior to the flight, as described in the Pre-Flight Section. The Flight Operations explain the take-off and landing configurations and procedures, including the setup at altitude prior to the first parabola. The next section, Experiments, describe the experiment configuration for the hardware and the procedures for performing the experiment.

Experimenter Role Definitions:

During each flight, every experimenter is assigned a specific role that remains unchanged for the duration of that flight. Each role has an associated responsibility for in-flight experiment work, as well as pre-experiment checkouts and post-experiment take downs. Experimenter roles include two frame managers, an OSA manager, an experiment manager, and a computer operator. If there are additional

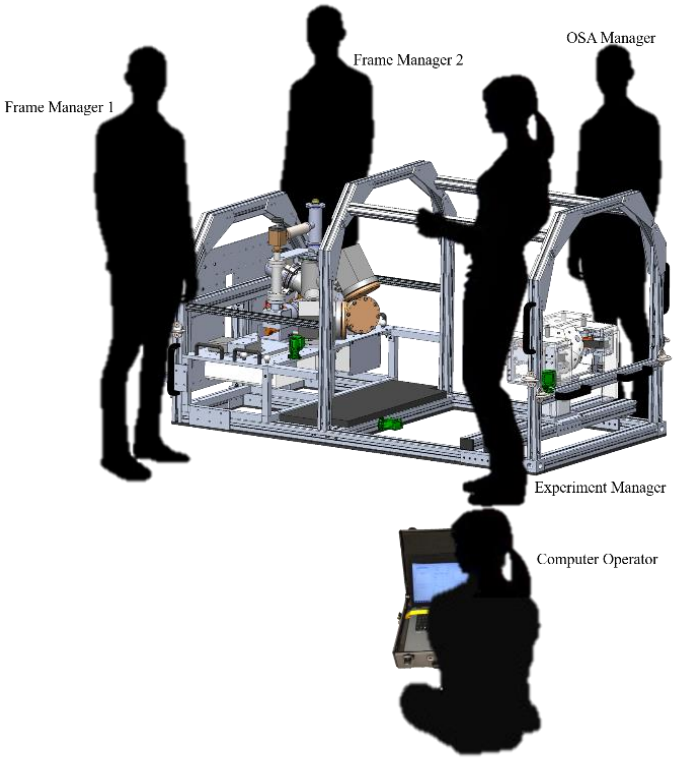

Figure 106: The notional arrangement of experimenters around the SPECTRE hardware.

experimenters onboard, one of them assists the management of the testbed frame as Frame Manager 3.

- Frame Managers (FM1, FM2): These two team members manage the position and orientation of the testbed frame during free-float experiments. The frame managers also ensure that the camera views are not occluded, nor the physical camera moved at any time. One manager simultaneously monitor for contact between the OSA and the SROA, communicating to the experiment manager the result of the OSA/SROA interaction.
- OSA Manager (OSAM): This team member is responsible for loading the OSA into the initiator mechanism before free-float experiments, monitoring the movement of the OSA during free-float experiments, and retrieving the OSA immediately after free-float experiments. The OS manager adjusts the initiator assembly along the rails and pivot to achieve the desired experiment initial conditions.
- Computer Operator (CO): This team member sits at the laptop to execute control sequences and manage data collection. The computer operator also monitors the health of the hardware/software through real time dynamic data collection, communicating to the experiment manager the quality of experiment data.
- Experiment Manager (EM): This team member monitors the entire experiment testbed and manage team members to conduct a meaningful campaign of experiments while maintaining safety of the team. The experiment manager makes executive decisions about the experiments to repeat or to modify a set of initial conditions.

Ground Operations

To ensure all systems are healthy and a successful experiment campaign follows, a series of checkout tests are conducted in the hangar. All procedures follow the reassembly of IFA. They may be repeated throughout ground operations as necessary provided the perquisites, timing, and configuration needs are met. The checkout procedures include SROA Pump and Cool-Down, Command/Sensing Computer Verification, all Battery Charge Verification, and all Sensor Verification. The detailed procedures are found in Table 60 to Table 66, found in the Appendix III.

Pre-Flight

Pre-Flight Configuration and Plan Summary:

Sometime between 2.0 hours and 0.5 hours prior to takeoff, the SBA/SROA needs to be removed from hangar power and transferred to the aircraft, where it is secured to the frame assembly and transferred to aircraft power, detailed in Appendix Table 67. The process of moving the SBA/SROA should limit the time the system is unpowered, because the system begins to warm. It is preferred that this unpowered time be limited to 15 minutes, but the system is still experiment-ready with a power outage of 30 minutes. The timing of the start of this process is constrained by

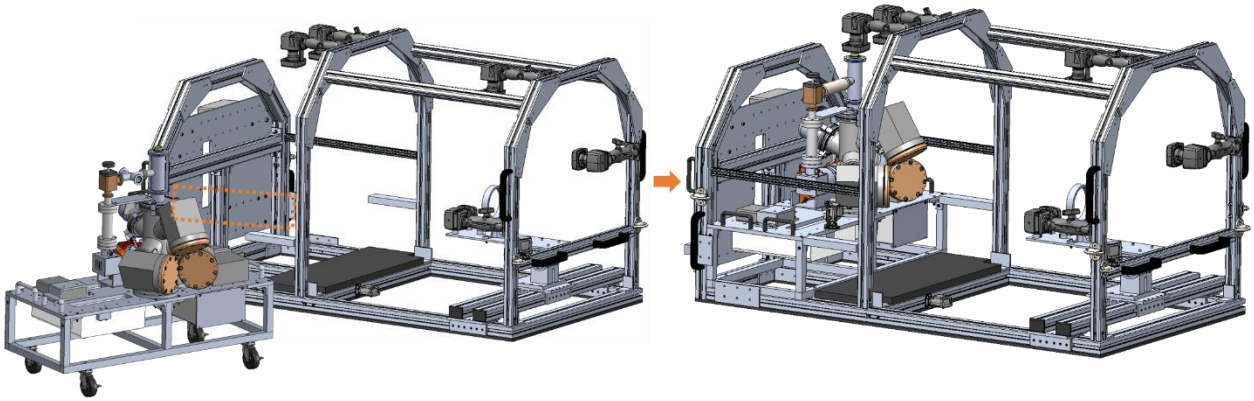

Figure 107: SBA installation onto the FA prior to flight.

power availability on the aircraft, the desire to limit the amount of time the system is on the getter ion pump, and the need to let the system re-cool after the move. During the pre-flight phase, the team should also ensure that all equipment and experimenters are ready for the experiment, listed in Appendix Table 68.

In-Flight

Pre-Experiment In-Flight Setup and Preparation:

After takeoff, the experimenters must convert the takeoff configuration to the experiment configuration. All experimenters must in sequence and collectively perform the Pre-Experiment In-Flight Setup, GoPro Calibration, and Checkout Procedures, detailed in Appendix Table 69 to Table 71. At this point, the testbed is properly set up to perform an experiment in the first microgravity parabola.

Experiments

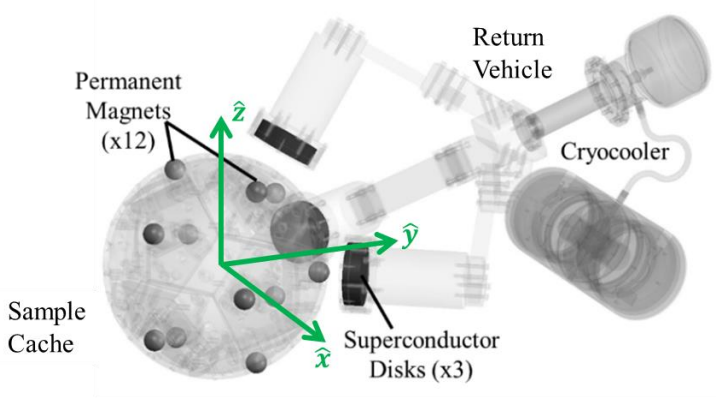

Figure 108: Multiple-magnet and multiple-superconductor flux-pinned docking interface concept with relative coordinate frame definition

The key hardware for the flux-pinned interface resides in the OSA and the SROA. The outside of the OSA has been populated with eleven evenly-spaced permanent Nickle-plated Neodymium magnets. The SROA, although outfitted with a variety of subsystems to support its

operation in a non-space environment, is fundamentally a set of three hockey-puck-sized YBCO disks and a cryocooler that removes heat via an enclosed thermal conduction path. A CAD rendering of the FPI in the system is shown in Figure 108.

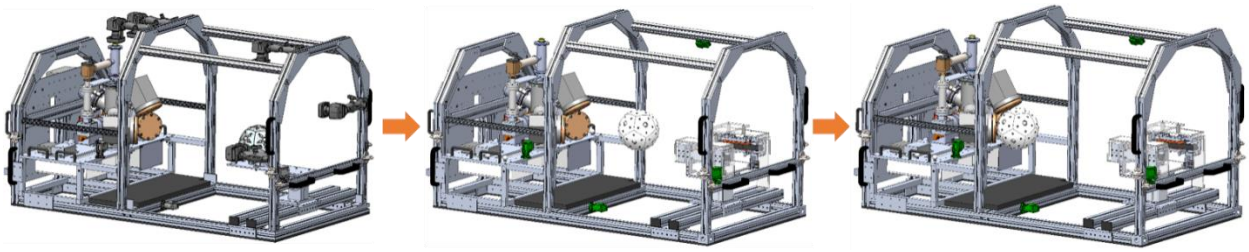

Figure 109: Operational sequence for each parabola.

Each experiment consists of the same basic steps visually sequenced in Figure 109:

1. Achieve IFA free float and stabilize out any transient disturbances
2. Launch the OSA with an initial velocity and spin, or manually place it in its initial starting location
3. Provide the appropriate initial rates or velocities to the OSA and release it to a free float
4. The OSA is drawn towards the SROA as it falls into the magnetic potential well of the FPI
5. Allow the dynamics of the OSA and IFA to remain unperturbed by experimenters or other constraints for the duration of microgravity while recording data and streaming it to the CLS
6. After the experiment the OSA is retrieved and returned to the IA for the next experiment.

Two types of experiments were conducted: capture experiments and equilibrium experiments, a sample seen in Figure 110. The capture experiments initialize the spacecraft analogues outside the magnetic potential well in the capture plane with a range of translational and angular velocities (energetic boundaries found in prior ground testing). The capture experiments aim to characterize the boundary between capture and no capture outcomes, identifying the range of initial conditions that lead to successful capture. The equilibrium experiments, on the other hand, initialize the relative state of the spacecraft analogues within their established magnetic potential well near the equilibrium state to characterize the near-equilibrium stiffness and damping effects.

Figure 110: SPECTRE 1 FPI

The starting initial positions range from at or very near equilibrium only a few millimeters apart, to ranges on the order of 30 centimeters from the equilibrium, and the initial path angle may vary by up to 30 degrees. The OSA always remains within the frame assembly so it can be viewed by the cameras. Starting velocities range from 120 mm/s to zero, or approximately 30 deg/s to zero. Each set of relevant initial conditions is tested three to five times each, and the maximum range of those conditions is established after the first flight day resolves initial questions about the OSA sphere-of-influence and performance improvement in the six degree-of-freedom environment.

Microgravity Experiment Procedure

In this experiment, there are two types of free-floating objects: the OSA and the IFA. The OSA is free-floating within the volume of the IFA; their relative motion is the key to the data collected in the experiment. The OSA is a small volleyball-sized object, and one of the five experimenters (the OSA manager) is tasked with the job of managing its motion to ensure it remains in the test area. The IFA, on the other hand, is bulkier and requires more hands to handle. An experimenter is positioned at each of the four corners of the equipment and together, these experimenters manage its motion. Two of the experimenters (the Frame Managers, or FMs) are tasked with maintaining its motion in flight, although the OSA manager and Experiment Manager are also able to help maneuver the OSA as necessary. The computer operator monitors the health of the thermal system, observes the dynamic data, and controls the belt speed of the launching mechanism. The experimenters are situated around the testbed as shown in Figure 106.

Each parabola follows the same essential steps; the only difference between each of the parabolas is the disturbance environment and initial conditions of the OSA. The OS initial conditions are changed by imparting different velocities on the OSA (where the OSA Manager taps the OSA toward the SROA) during a parabola, or by orienting the OSA differently in the IA. However, if the IA needs to change location, the change only occurs during a 1g break in the parabolas by unlocking the appropriate handle, sliding the IA to the correct location, and then locking it down again (the responsibility of the OSAM). During the parabolas, however, the repeating operations for the experiment are as follows, where time = 0 is when the aircraft achieves microgravity, given in Table 20.

Table 20: Experiment Parabola Assignment and Chronological Procedure

During Experiment Parabolas						
Time	**Gravity**	**FM1**	**FM2**	**OSAM**	**EM**	**CO**
-15s	2g				Call out experiment type	
-10s	2g	Hold IFA handles and brace in foot restraints	Turn off cryocooler fans, hold IFA handles and brace in foot restraints	Brace in foot restraints	Hold IFA handles and brace in foot restraints	Set initial conditions in GUI
-5s	2g to 0g	Guide IFA up away from walls and people	Guide IFA up away from walls and people	Load OSA into initiator assembly	Guide IFA up away from walls and people	Start recording OSA IMU data
0s	0g	Let go of IFA while imparting minimal forces	Let go of IFA while imparting minimal forces	Initialize OSA according to experiment plan (for example, by tapping the back)	Let go of IFA while imparting minimal forces	Monitor dynamics and returning data
0s to ~25s	0g	Maintain frame control – only touching it when necessary to prevent it from floating out of experiment area	Maintain frame control – only touching it when necessary to prevent it from floating out of experiment area	Maintain OSA control – only touching it when necessary to prevent it from floating out of the experiment area	Maintain frame control – only touching it when necessary to prevent it from floating out of experiment area	Monitor dynamics and returning data, noting major events such as frame disturbances and documenting key configurations
25s	0g to 2g	Use handles to guide IFA down towards floor landing location, move power harness out of landing area	Use handles to guide IFA down towards floor landing location, turn on cryocooler fans	Retrieve OSA and place back in IA for next parabola	Use handles to guide IFA down towards floor landing location	Stop recording and save data
30s	2g	Relay observations to EM and CO	Relay observations to EM and CO	Relay observations to EM and CO	Notify team of next parabola plan for initial conditions	Relay observations to EM

Data Collection

For each experiment, the key dynamics data come from the (identical) Epson inertial measurement units (IMU) on the OSA and the IFA, and GoPro cameras mounted on the IFA. The IMU data on the OSA is collected at 125 Hz for up to two hours. The command to collect this data is triggered by a wireless command from the CLS to the sensing computer on the ABA and then

relayed to the OSA. The data collection can be interrupted and restarted by the operator to trigger a software reset (a power reset can only be initiated with the power switch on the OSA). This relay is the only active element that is electronically commanded by the operators. The GoPro footage, on the other hand, is collected continuously at 30 frames per second (FPS) from the start of the experiment phase.

The GoPro cameras require an initial calibration with a printed chessboard pattern. This process involves moving the chessboard pattern such that over a series of frames the pattern cover the entire field of view of the camera. Camera calibration software then estimates the intrinsic parameters of the camera. The images from the camera is undistorted with the estimated intrinsic camera parameters. If the calibration is successful, then the straight lines in the image appear straight. If the calibration was unsuccessful, then new calibration footage is obtained, and the above process repeated until a successful calibration is achieved.

The system also collects data on the temperature of the system throughout the flight – from takeoff to the end of the flight. The collected measurements are the superconductor temperatures (3 silicon diodes), the cryocooler cold tip temperature (1 silicon diode) (this is used for closed loop temperature control with the Thales CDE7232), and the cryocooler temperatures (2 thermocouples). These sensors collect data at approximately 0.1 Hz and are used to evaluate the thermal validity of the experiments. If any of the temperature sensors indicate that superconductor is no longer cold enough to exhibit flux pinning behavior, then the experiment is invalid. This measurement also alerts the health of the SROA system from which a warming trend can be identified and corrected quickly (for example, by adjusting the fans around the cryocooler) before the experiment results are in jeopardy. Experiment events were recorded manually on the commanding computer experiment log from which issues, such as imperfect microgravity

conditions or accidentally perturbing the IFA during an experiment, can be quickly identified. A graphical user interface (GUI) on the CLS facilitated this data entry.

Figure 111: SPECTRE 1 Microgravity Experiment

In the SPECTRE testbed, there are three dynamics sensors each in their own reference frame: an IMU on the OSA, an IMU on the SROA, and the Vicon camera system. The OSA and frame assembly have independent Vicon frames attached to each body (VO and VF frame). The OSA IMU reference frame is rigidly attached to the OSA (IO). The SROA IMU reference frame is rigidly attached to the frame assembly (IF). The CAD frame is useful in mapping geometric relationships to each other (F). The simulation frame is the resultant frame that may be integrated into the dynamics model (S). Although some reference frames are aligned and static with respect to each other, other reference frame rotate with respect to each other and must make use of sensor measurements to rotate between reference frames, depicted in Figure 112.

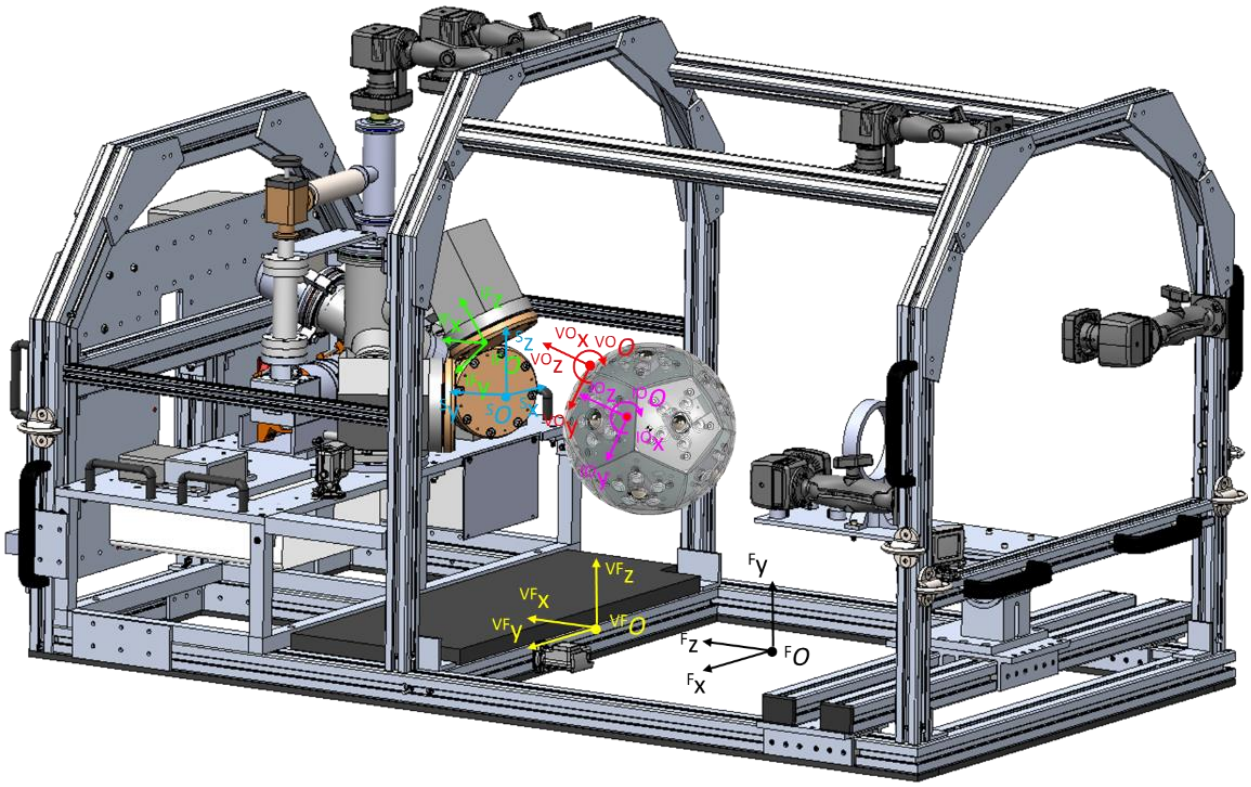

Figure 112: CAD of 2017 testbed with the six relevant reference frames attached to respective origins and coordinates axes

After the flight, the IMUs are characterized for bias and used to calculate center of mass offset within the OSA. IMUs must be calibrated in their own body frames prior to transforming into inertial reference frames. There are no static IMU calibration datasets. Biases are extracted from snippets from the experiments. For frame IMU acceleration bias characterization, the snippets taken out of the flight logs are during free float, when the angular velocity profile is constant to ensure there are no external disturbances. For frame IMU gyro bias characterization, the snippets taken out of the flight logs are during straight and level flight, when the acceleration profile is minimal (subject to airplane turbulence). For OSA IMU gyro bias characterization, the snippets taken out of the flight logs are during straight and level flight, when the acceleration profile is minimal (subject to airplane turbulence). For OSA IMU acceleration bias characterization, the snippets taken out of the flight logs are during free float, when the angular

velocity profile is constant to ensure there are no external disturbances or flux pinning influences (typically right after escaping). The OSA IMU is off center from the center of mass so an angular rate accelerates the IMU. The magnitude of acceleration is proportional to the magnitude of angular velocity, shown in Figure 113.

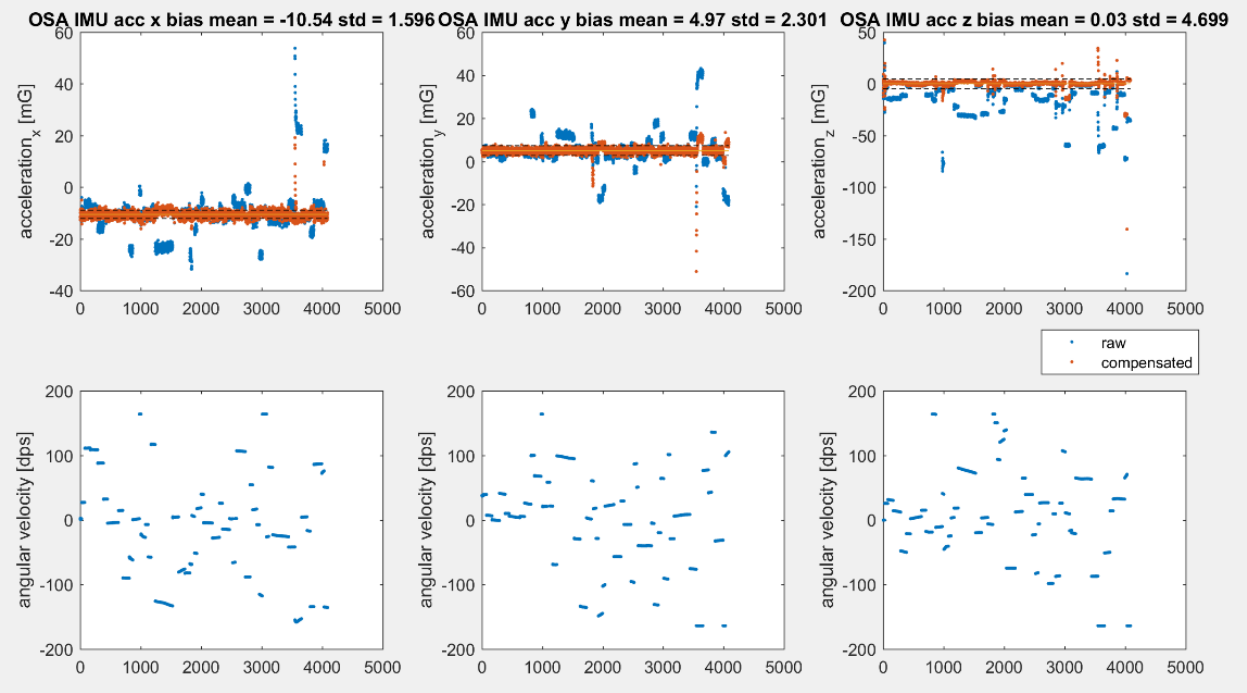

Figure 113: Comparison of raw acceleration data and acceleration compensated for off origin IMU

On top of origin and reference frame bookkeeping and IMU characterization, some geometric parameters are not precisely known. Two parameters that are integral to this experiment is the OSA field-cooled position and the OSA center of mass. The OSA field-cooled position is constrained to the mechanical assembly of the SROA but the summation of all the fabrication and integration errors mounting the SROA to the frame assembly obscures knowledge of where that position exactly is. This position must be estimated later in the process. The OSA center of mass does not exactly align with the center of geometry. The OSA center of mass was calculated by minimizing error the kinematic relation between the OSA centripetal acceleration from gyro data

and directly measured IMU acceleration, also represented in Figure 2. The optimizer calculated center of mass location within millimeter precision to the CAD generated location (0.5% error).

Video footage was collected from 6 different points of view, IMU data from the OSA and IFA, and Vicon global position and orientation data. After reviewing much of the video footage and dynamic profiles, the second day yielded 32 clean runs with up to 6 seconds of natural flux-pinning dynamics. These trials are priceless for maturing the predictive dynamics model of the flux pinned interface docking technology. A sample of the best microgravity in shown in Figure 114. Although the IMU data displays continuous, nonlinear, coupled dynamics, the Vicon position and attitude estimates fail intermittently and the sequential estimates are not always continuous. The faulty measurements from the Vicon system are due to a combination of false marker readings and camera displacement, which breaks the initial camera calibration. Unfortunately, there was not enough global dynamic information (position and orientation) gathered from the Vicon cameras in the 2017 microgravity flight experiment. A possible solution to salvage global position and attitude data is to process the GoPro video with computer vision scripts. A major consideration for the next microgravity flight was replacing the vision system with a more robust solution to guarantee global position and attitude data.

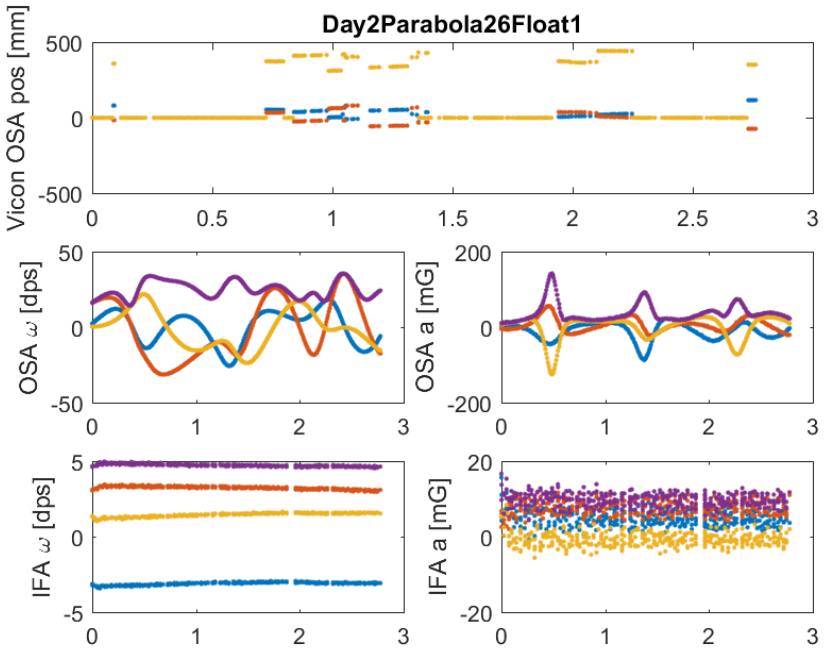

Figure 114: Experiment run with most consistent Vicon measurements from the second day of 2017 microgravity flights

Contribution of First Microgravity Experiment Campaign

From the conclusion of the March 2017 microgravity flights, the specific FPI design proved to capture and sustain equilibrium in six degrees of freedom. Over two flight days, the team attempted 97 experiment runs. A view of the experiment testbed and operators during an experiment is shown in Figure 111. 76 runs have observable flux-pinning dynamics, including trials with and without external forces and torques on experimental testbed. 32 runs of the observable runs have impeccably clean experiment environments in which no external forces and torques are observed. The average trial length was 2.7 sec with a standard deviation of 1 sec. 25 of the 32 runs showed the OSA captured with the FPI interface. The operational success of running experiments and length of experiment runtime significantly improved on the second day of testing, suggesting a learning curve associated with operating this experiment in microgravity.

The equilibrium tests examined the case when the potential energy well created by the field-cooled magnetic field in the superconductors draws in the OSA from a state with no kinetic energy. The capture/tumble tests, on the other hand, were designed to characterize the bounds of rotational and translational kinetic energy that lead to capture, escape, and impacts in the FPI. If the kinetic energy of the OSA is larger than the potential well created by the FPI, the OSA escapes from the FPI (rather than being captured). Similarly, if the kinetic energy of the system can generate motion that exceeds the separation distance between the OSA and SROA, an impact occurs, which is undesirable for many conceptual sample capture scenarios. A capture without a collision is therefore the most desired sample capture outcome, and an escape with an impact is the least desired. These tests examine these kinetic energy thresholds. As expected, lower velocity tests capture more consistently than higher velocity tests, and the system is more likely to capture and impact then escaping without an impact. Preliminary analysis shows successful capture for a velocity of at least 5.5 cm/s.

c. Second Microgravity Flight Experiment

Ultimately, the set of experiments in the 2017 microgravity flights did not express the full range of dynamic conditions expected in spaceflight operations. Position and attitude timeseries are essential to develop a dynamics model and that data was lacking from the 2017 experiments. A second microgravity flight was pursued in 2018 to conduct experiments in the unexplored dynamic range and collect precise, continuous dynamic data.

Testbed Design

For the microgravity experiments, the main test equipment consists of the orbiting sample analogue (OSA), seen in Figure 115 and sample return orbiter analogue (SROA), shown in Figure

65. The experiment testbed from the second flight is the same design as the first flight, despite a few modifications. A lesson learned from the first flight is that the useful experiment time in microgravity limits the lowest energy conditions and farther displacement conditions. To expand this acceptable energy range, stronger cylindrical magnets replaced the current spherical magnets. A custom launching mechanism was implemented to yield consistent kinetic energy initial conditions. The motion capture system changed from a Vicon system to the April tag system [133].

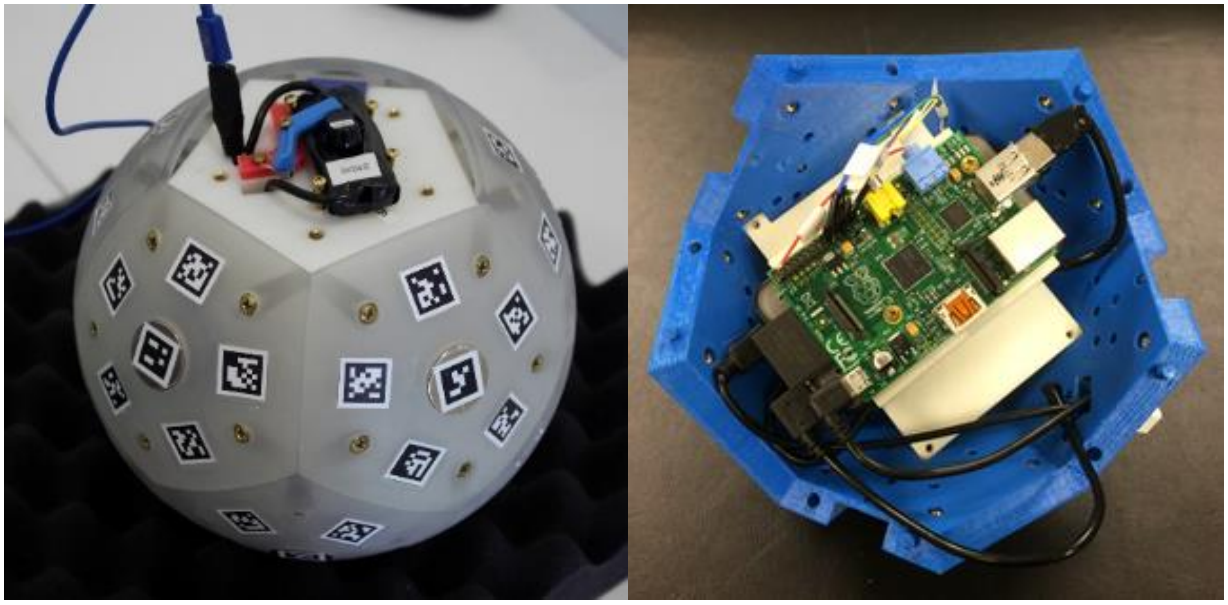

Figure 115: Left: surface of OSA populated with April tags. Right: sensor package inside OSA structure to support experiment

As with the OSA, the surface of the SROA has unique April tags and an IMU mounted close to the docking interface surface. The April tags offer static reference markers to generate the OSA's position and attitude relative to the SROA. The SROA IMU provides reference motion in the frame that the OSA's motion operates within. The dynamic sensors are circled and labeled in Figure 116.

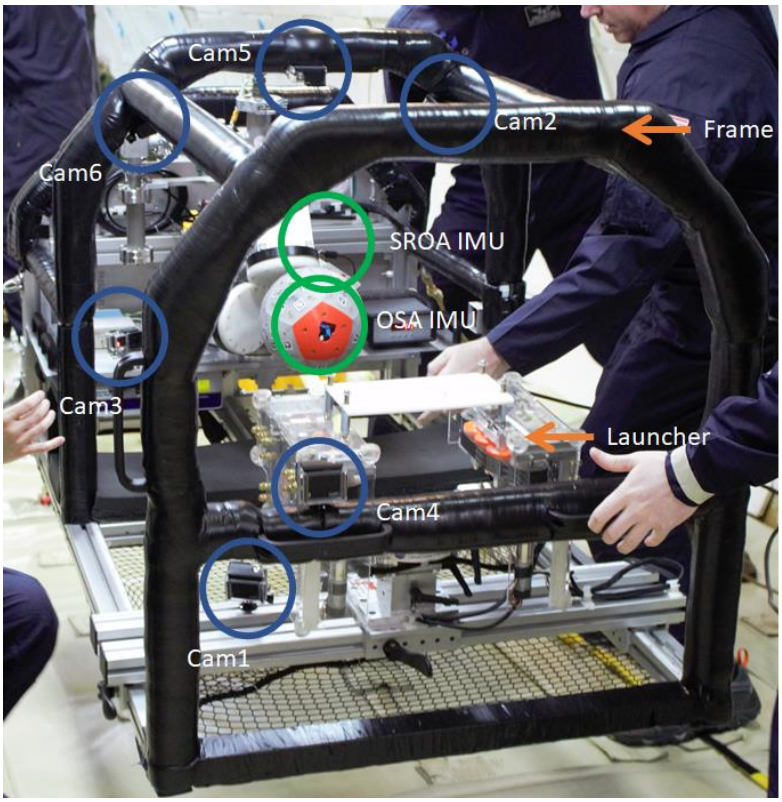

Figure 116: Dynamic sensors on experiment testbed; cameras circled in blue and IMU's in green

Experiment Campaign

The experiments conducted on the second microgravity flight mirror the same objectives as the 2017 microgravity flight, but the 2018 experiment investigated higher and more consistent initial kinetic conditions. The March 2018 microgravity aircraft flight campaign consisted of 50 parabolic maneuvers over the course of two days. Each parabola provides a microgravity environment for ~30 seconds in which dynamic data is collected continuously for the entire duration of the flight. At the start of each parabola, the IFA is positioned in the middle of the allocated aircraft experiment area, the OSA is positioned into its initial position, and the experimenters release the frame, as shown in Figure 117. Environmental factors during operation can lead to disturbances (such as contact with the aircraft or experimenters) on the OSA-SROA system. When such a contact is noted the experiment is reset with a new free-float trial in the same

parabola. Each trial is considered a separate experiment for this paper. This process is continued until the end of the free-float period and the experiment is placed on the aircraft deck to wait until the next microgravity phase.

Figure 117: Experiment setup for a capture experiment from a 2018 microgravity flight

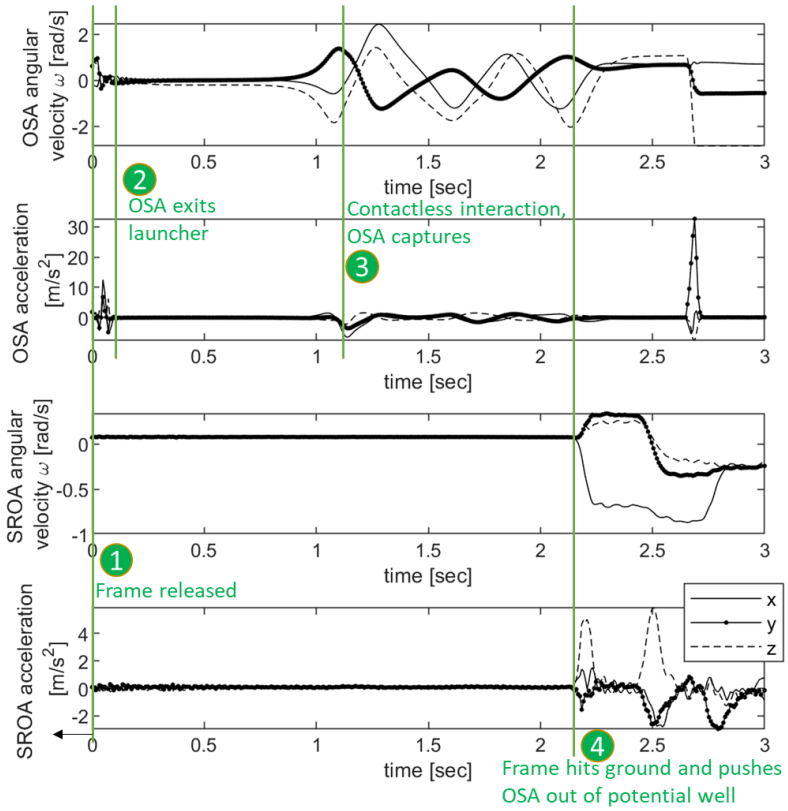

Figure 118: Sample of IMU data with sequential events labeled

A sample of IMU data from the experiment is detailed with reference events in Figure 118. Progressing in chronological order, the frame is first released with minimal motion (1). The frame's angular velocity is minimal, and acceleration is near zero. During release, the OSA rattles in the launcher seen in the OSA's IMU measurements prior to exiting the launcher. The OSA leaves the launcher, depicted by the smooth angular velocity and acceleration profiles (2). As the flux-pinned interface draws the OSA in, some translational momentum transfers to angular momentum and oscillates about the equilibrium state (3). When the frame contacts the airplane hull, external energy transfers and excites the OSA out of the potential well (4).

d. Dynamic Metrics

This subsection lists the relevant metrics that encapsulate the performance of the docking interface and the desired capabilities for a potential Mars Sample Return mission. This work aims to expand upon the past work by conducting tests in microgravity, enabling the full coupled and nonlinear dynamics to be captured. The resulting data is used to inform a more accurate mapping between dynamic conditions and capture performance. The dynamic state of interest for the rest of this subsection is the sample cache's dynamic state relative to return vehicle in the return vehicle's frame, where state includes position ($r_x\ r_y\ r_z$), attitude ($\theta_x\ \theta_y\ \theta_z$), translational velocity ($v_x\ v_y\ v_z$), and angular velocity ($\omega_x\ \omega_y\ \omega_z$), reiterated in Eq. (95). The $x\ y\ z$ convention follows Figure 108. All metrics forego analysis with any predictive dynamics model and are purely derived from sensor measurements collected during the second microgravity flight experiments. Each metric is described in more detail in this section.

$$s = [x\ \ y\ \ z\ \ v_x\ \ v_y\ \ v_z\ \ \theta_x\ \ \theta_y\ \ \theta_z\ \ \omega_x\ \ \omega_y\ \ \omega_z] \tag{95}$$

Each FPI docking design can be characterized by the following metrics:

1) maximum input energy resulting in successful capture,
2) contact/interaction imparted momentum change,
3) system damping (related to settling time), and
4) final system stiffness (related to deflections experienced given certain input disturbances).

Maximum Input Energy/Bounds on Initial State for Capture

The relative dynamic state of the spacecraft prior to entering the flux-pinned interface's potential well determines the capture outcome for a given FPI design. Position and attitude dictate

the alignment of the magnets with respect to the superconductors. This alignment determines the amount of attractive potential energy the system experiences when within the edge of the magnetic potential well. The translational velocity and angular velocity relate to the spacecraft's kinetic energy prior to entering the magnetic potential well. FPIs have a maximum input kinetic energy that result in capture of the system, related to the depth and shape of the potential well. If a system has more input energy than the FPI can absorb, the OS exits the potential well and does not successfully dock. Metrics that identify bounds for each of these states that results in a successful capture are important. The FPI design may be more sensitive to certain states than others (for example, having less tolerance to translational velocity than angular velocity). Mapping the spacecraft's dynamic state to capture performance yields bounds of dynamic state to guarantee a successful capture.

Imparted Momentum Change at the Interface

Each spacecraft experiences a change in momentum as a result of an FPI interaction. Any interaction, contactless or non-contactless, transfers momentum and energy from one spacecraft body to the other spacecraft body. The amount the momentum is changed is dependent on the initial state of the system. For scenarios in which the spacecraft do not contact, the spacecraft experiences momentum change from the flux-pinning physics in a smooth and continuous manner. For scenarios in which initial momentum of the system cannot be arrested contactlessly, the system experiences a contact between the OSA-SROA system that imparts an impulsive change in momentum, which can cause damage to either spacecraft. Characterizing this momentum change allow FPI designers to evaluate input conditions that guarantee contactless interaction if necessary and ensure hardware tolerance to the interaction forces and torques. Additioanly, characterizing

the momentum change allows a direct comparison of an FPI to a mechanical system that relies on these momenta changes during contact to bring the system to equilibrium.

System Damping

Once the FPI successfully executes a capture maneuver, the system settles towards its equilibrium state on a time scale determined by the system damping. A flux-pinned interface offers damping in the form of eddy-current damping and hysteresis loss in the superconducting current vortices. Hysteresis loss is due to the magnetic field inhomogeneity and is manifested through thermal dissipation [9]. Eddy-current damping is caused by the motion of magnets near a conductive surface and varies linearly with velocity [134]. Eddy-current damping can be used to manage the input energy of a potential tumbling sample cache prior to any docking attempt near the aluminum structure of the return vehicle or to settle to equilibrium after a successful capture. Quantifying the total damping parameter characterizes the dissipation of energy and settling time of this underdamped oscillator, which shape the time scales of the capture operation.

Final Interface Stiffness at Equilibrium

Once captured, the spacecraft system oscillates within the confines of the magnetic potential well until all energy is dissipated through damping. The oscillations stem from a virtually rigid joint with nonlinear stiffness [42] [135] [109]. Although the concept of stiffness is well-documented and investigated for FPIs, each configuration is unique and must be specifically characterized. This metric is critical in understanding the magnetic potential well that governs the system's passive dynamics. The derivation from Eq. (96) to (99) illustrates an explicit relationship between stiffness and potential energy. $\boldsymbol{\Delta s}$ is the change in dynamic state of the orbiting spacecraft with respect to the equilibrium state, $\boldsymbol{s}_e$. $k(\boldsymbol{s})$ is the stiffness of the interface as a function of state. $\boldsymbol{F}$ is the force between the two spacecraft, following Hooke's law for a linearized spring. U is the

potential energy as a function of state. For a general relationship between dynamic state to stiffness and potential energy, please refer to [94].

$$\boldsymbol{F} = k(\boldsymbol{s})\,\Delta\boldsymbol{s} \tag{96}$$

$$\boldsymbol{F} = \nabla U(\boldsymbol{s}) \tag{97}$$

$$k(\boldsymbol{s}_e)\Delta\boldsymbol{s} = \nabla U(\boldsymbol{s}_e) \tag{98}$$

$$k(\boldsymbol{s}_e) = \frac{\nabla U(\boldsymbol{s}_e)}{\partial \boldsymbol{s}} \tag{99}$$

The experimental results report the stiffness for each DOF at the equilibrium position and attitude. The oscillatory motion passes through or near equilibrium state at every period, thus the stiffness at this state generally represents the stiffness of the joint once the orbiting spacecraft is captured. Stiffness of the system determines the frequency of oscillations and the deflections the system exhibits when exposed to disturbance forces or torques.

e. Dynamics Capabilities

Maximum Input Energy/Bounds on Initial State for Capture

Over the 27 capture experiments conducted during the second microgravity flight, 15 experiments successfully captured and 12 did not capture on the time scales afforded by the experiment (~10 seconds). The outcome matrix with contact information for the 27 experiments is shown in Table 21, showing a breadth of capture outcomes used for analysis. During experimentation, the initial position of the OSA upon entering the flux pinning sphere-of-influence did not change. The initial attitude displacement from any equilibrium attitude varied by up to 72 degrees. Translational velocity and angular velocity varied within the bounds shown in Table 22, which shows that the set of experiments spanned the desired test range.

Table 21: Outcome matrix with capture success and contact information

Outcome Matrix Across 27 Experiments	Capture (Number of Trials)	No Capture (Number of Trials)
No Contact	8	3
Contact	7	9

Table 22: Bounds of OSA initial state across all capture experiments with desired capabilities

OSA Initial State	Imparted on Test System	Desired Test Capabilities
Translational Velocity [m/s]	[0.02 0.38]	[0.05 0.22]
Angular Velocity [rad/s]	[0.01 1.07]	[0.23 0.70]

Table 23: Bounds of OSA measured initial velocity across all capture experiments

	Measured Performance for the Test System		Estimated Performance for a Flight System		Required Range for Capture of a Flight System
Outcome as a Function of Translational Velocity	Capture	No Capture	Capture	No Capture	
No Contact [cm/s]	[1.7 22.3]	[18.0 22.9]	[0.7 10.0]	[8.1 10.3]	[2 10]
Contact [cm/s]	[11.1 28.5]	[12.7 38.3]	[4.9 12.7]	[5.7 17.1]	[2 10]

Table 24: Bounds of OSA measured initial angular velocity across all capture experiments

	Measured Performance for the Test System		Estimated Performance for a Flight System		Required Range for Capture of a Flight System
Outcome as a Function of Angular Velocity	Capture	No Capture	Capture	No Capture	
No Contact [RPM]	[1.2 10.2]	[2.7 5.0]	[0.5 4.6]	[1.2 2.2]	[1 3]
Contact [RPM]	[0.3 3.8]	[2.3 5.7]	[0.1 1.7]	[1.0 2.5]	[1 3]
No Contact [deg/s]	[7.2 61.2]	[16.0 29.8]	[3.2 27.4]	[7.1 13.3]	[6 18]
Contact [deg/s]	[1.6 22.9]	[13.9 34.0]	[0.7 10.2]	[6.2 15.2]	[6 18]

The observed capture outcome for the test system is shown in Figure 119 in which the experiment OSA captures up to 0.25 m/s and 0.22 rad/s simultaneously. All trials below these values captured. When the translational velocity and angular velocity states are separately evaluated, the OSA captures up to 0.28 m/s and up to 1.068 rad/s. Of the 15 trials that captured, the range of initial conditions in the experiment set are listed in detail in Table 23 and Table 24.

The estimates for a flight system are extrapolated from the data collected on the test system by scaling the mass of the OSA to match that of a notional OS while conserving energy. The extrapolated capture outcome for the 12.5 kg spaceflight OS is shown in Figure 120. When extended to a flight mass, this flux-pinned interface design can support the capture of a system where the OS is moving up to 0.11 m/s and 0.084 rad/s simultaneously relative to the SRO when contact dynamics are not in play. When the translational velocity and angular velocity states are separately evaluated, the OSA captures up to 0.13 m/s and up to 0.41 rad/s. 11 of 14 trials within the desired velocity bounds capture successfully but three trials did not capture at a low energy initial state within the desired capabilities range.

The duration of microgravity for one of these unsuccessful capture trials was not long enough for the system to allow capture past the initial interaction, although the system began to show restorative motion at the end of the trial, shown in Figure 121. There are two capture scenarios in which a contactless interaction from a low-energy state generates a no capture outcome. A closer study of this case should be conducted because it has clear implications for the efficacy of the flux-pinned system.

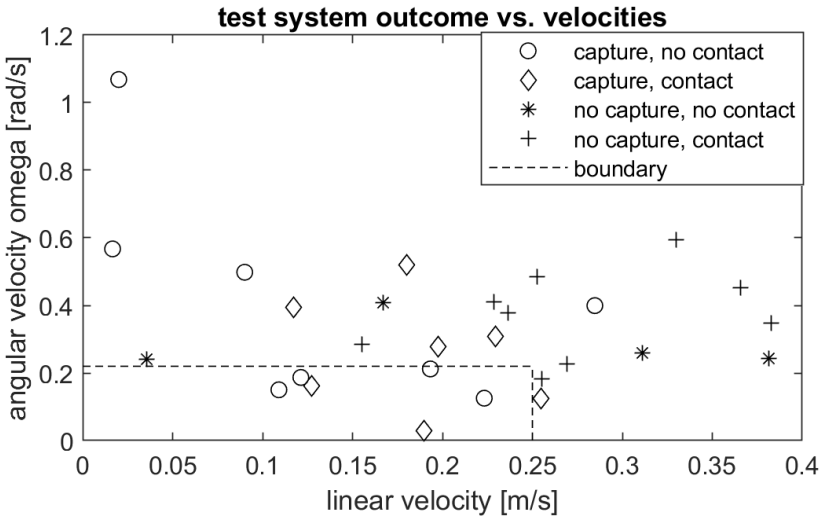

Figure 119: Observed capture outcome for test system

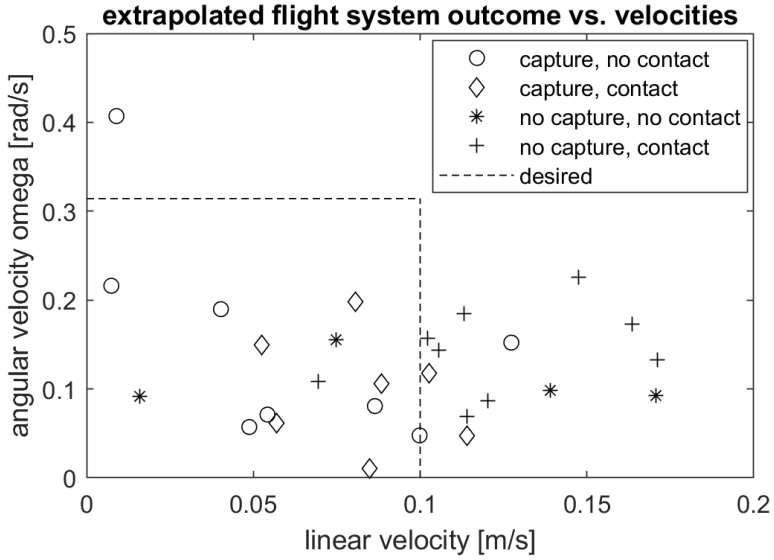

Figure 120: Most conservative, extrapolated capture outcome for spaceflight system

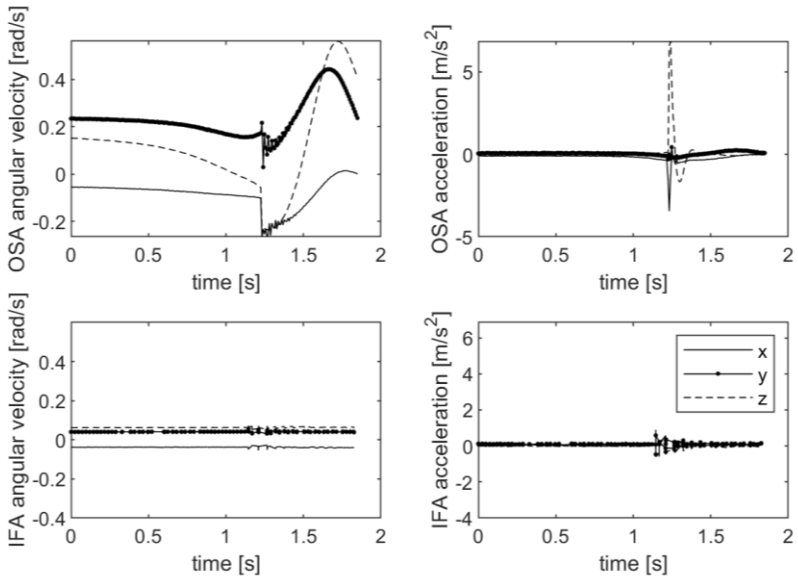

Figure 121: A trial in which the data implies restorative motion, but the experiment did not last long enough time to fully express capture

Total kinetic energy, T, is a more general metric to describe the docking interface's capabilities, shown in Eq. (100), where angular velocity is $\omega = [\omega_x\ \omega_y\ \omega_z]$ and translational velocity is $v = [v_x\ v_y\ v_z]$. Total kinetic energy, separated into capture outcomes, is depicted in Figure 122. Although components of energy are not depicted, rotational kinetic energy is significantly less than translational kinetic energy and constitutes up to 10% of the total energy of the system. Generally, lower total energy states are more likely to capture. From the wide distribution of energy states in each capture outcome, still there is not a clear direct mapping from energy to capture. To produce a comprehensive mapping, OSA attitude close to equilibrium must also be included in the mapping function.

$$T = \frac{1}{2}m\boldsymbol{v}^T\boldsymbol{v} + \frac{1}{2}\boldsymbol{\omega}^T I\boldsymbol{\omega} \tag{100}$$

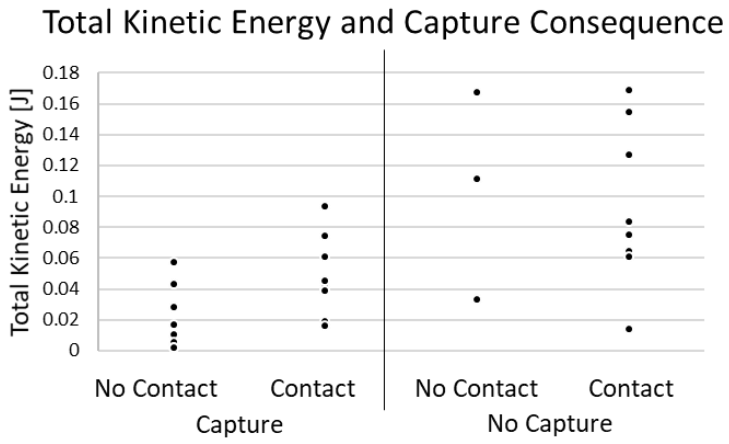

Figure 122: Total kinetic energy separated into capture and contact outcome

To complete the mapping function between state and capture outcome, position ($r = [r_x\ r_y\ r_z]$) and attitude ($\theta = [\theta_x\ \theta_y\ \theta_z]$) relates to potential energy with function f_U, seen in Eq. (101). Potential energy must be greater than kinetic energy to successfully capture, seen in Eq. (102), where $\delta_{capture}$ is 1 if a successful capture occurs and 0 otherwise. This task proves difficult as the potential energy is not directly observable and there currently does not exist an accurate analytical function mapping f_U. Instead, the kinetic energy measurements drive at discovering the depth and shape of the potential energy well indirectly by applying conservation of energy.

$$U = f_U(\boldsymbol{r}, \boldsymbol{\theta}) - f_U(\boldsymbol{r} = \infty) \tag{101}$$

$$\delta_{capture} = \begin{Bmatrix} 1 & if\ U > T \\ 0 & if\ U < T \end{Bmatrix} \tag{102}$$

Imparted Momentum Change at the Interface

Flux-pinned interfaces are distinct from other state-of-the-art capture systems because they increase the time over which the momentum exchange occurs between the two bodies. Without active control, FPIs eliminate or reduce the impulsive exchange characteristic of mechanical contact in a docking system. For the capture experiments, the first contact upon entering the

magnetic potential well measured forces up to 120 N whereas the first contactless interaction upon entrance measured forces up to 20 N, seen in Figure 123. The integrated momentum change across the entire time scale of the contactless interaction is comparable to the trials that contacted.

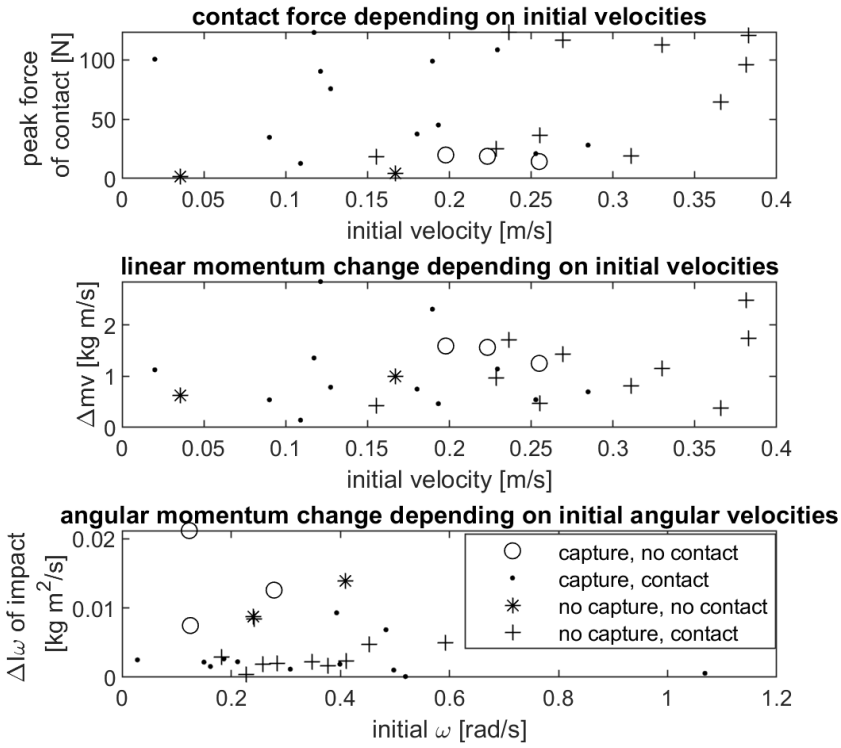

Figure 123: Contact force and angular momentum change with respect to initial velocities

Characteristics of momentum exchange and peak force are functions of the initial dynamic state and show trends with the resultant capture outcome, seen visually in Figure 123 and qualitatively in Table 25. The trends are specific to the experiments observed, with sample sizes explicitly stated under each classification in Table 25. The bounds in initial dynamic states are binned by capture outcome. For the ideal outcome of capturing without contact, the initial state held mid-range velocity and low-range angular velocity, which resulted in low peak force and mid to high exchange in both linear and angular momentum. For a successful capture with contact, the initial translational velocity ranges from low to mid energetic level whereas the angular velocity

ranges the entire spectrum, as capture outcome is more sensitive to translational velocity. The resultant peak force also varies from glancing contacts to high energy dissipating contacts, which reflects the linear momentum variance, but angular momentum exchange consistently remains minimal. The trials that did not capture contactlessly reflect similarities between the trials that did capture contactlessly. The initial states have low energy, but the difference is more allocation into initial angular velocity. For the least ideal outcome of not capturing upon first attempt and contacting, the subsequent interaction is very similar to the trials that did capture with contact but differ consistently in having more energetic initial states. Some of the variability in the results are a function of the difference in potential energy in the system caused by different initial attitudes.

Table 25: Different capture outcomes with initial velocities, peak force, and momenta exchange characterized with numerical ranges and qualitative ranges

	v_0 [m/s]	ω_0 [rad/s]	Peak Force [N]	Δmv [kg·m/s]	$\Delta I\omega$ [kg·m^2/s] $\times 10^{-3}$
Capture No Contact [n = 8]	[0.20 0.25] Mid	[0.12 0.28] Low	[14 20] Low	[1.3 1.6] Mid	[7.5 21] Mid - High
Capture Contact [n = 8]	[0.02 0.28] Low - Mid	[0.03 1.06] Low - High	[13 120] Low - High	[0.1 2.8] Low - High	[0.1 9.3] Low
No Capture No Contact [n = 3]	[0.036 0.17] Low	[0.24 0.40] Mid	[2 4.3] Low	[0.6 1] Low	[9 14] Mid - High
No Capture Contact [n = 9]	[0.16 0.38] Mid - High	[0.17 0.59] Mid - High	[18 123] Low - High	[0.37 2.5] Low - High	[0.4 8.5] Low - Mid

System Energy Damping Parameter

Once the system successfully captures, damping removes energy from the OSA until it settles to its equilibrium position and attitude. To clearly observe the damping effects, the OSA was placed near equilibrium for 23 experiments. The longest trial lasted up to 9 seconds and the

shortest, 2 seconds. The average trial lasted 4 seconds. Damping is visible in all the successfully captured experiments but especially visible in equilibrium data, seen in Figure 124. The damping parameter discussed in this section is derived from only the equilibrium tests because the capture tests do not present enough underdamped oscillations in each trial and show nonlinear dynamics.

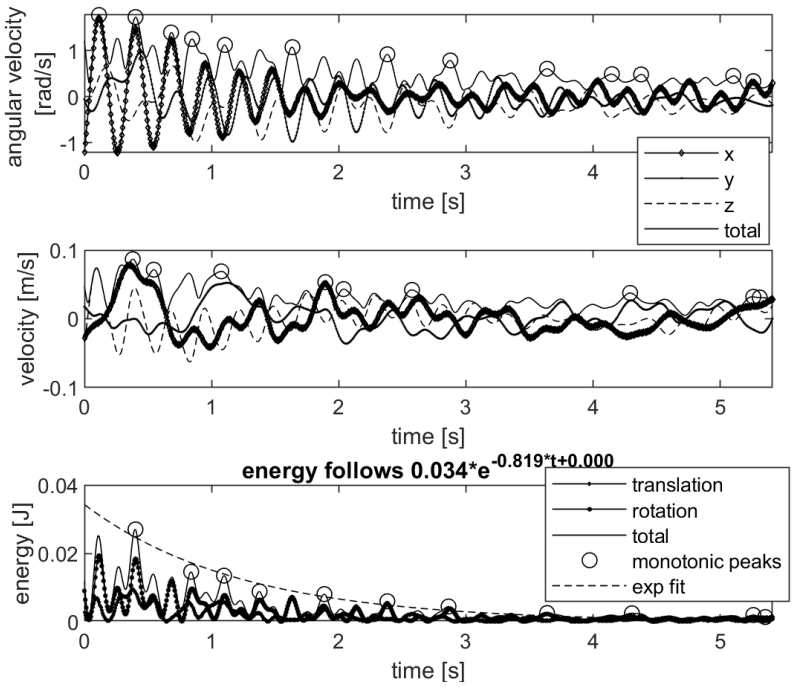

Figure 124: Sample IMU data from a single equilibrium trial, showing angular velocity, translational velocity, and energy with exponential fit

The two spacecraft bodies start very close to equilibrium and with small perturbations, where the nonlinear dynamics can be approximated as locally linear. The dynamics are coupled in all six degrees of freedom, which lead to coupling of damping and mass parameters between translational and rotational states. For simplicity, the damping parameter discussed here describes the dissipation of total kinetic energy over time, depicted in Figure 125. Total system kinetic energy absorbs the differing mass and state-dependent damping terms into one state over time. This damping term is specific to the current configuration and lacks generality to other flux-pinned interfaces but may offer an approximation for similar magnet-superconductor systems.

$$E(t) = Ae^{-\gamma t}\cos(\omega_d t + \phi) \quad (103)$$

While FPIs inherently represent nonlinear dynamics, framing FPI behavior with a linear approximation is convenient. By assuming linear damping and stiffness, the underdamped oscillations are represented by Eq. (103). $E(t)$ is the system energy over time. γ is a combination of damping coefficients and mass/inertia in all degrees of freedom that encapsulates total energy dissipation. $A, \omega_d,$ and ϕ, are constants specific to the configuration: amplitude response, damped frequency, and phase shift. Across the 23 equilibrium experiments, the best estimates of γ and its distribution are reported in Table 26 and Figure 125. The distribution of γ is skewed to smaller values, as the median value is significantly smaller than the mean value. The small normalized root mean square error shows that the exponential fit with a linear damping relationship is a good fit and consistent within each experiment trial. The wide distribution spread demonstrates that the damping parameter is inconsistent across all trials, illustrating that the damping depends on the system state. $1/\gamma$ is the time constant, τ_s, defining settling time of the system. The settling time to reach 2% of the initial energy state is listed in Table 26. The values in Table 7 represent estimates of wait time before moving onto the next operational phase.

Table 26: Characteristics of damping estimate distribution

	$\gamma \equiv 1/\tau_s$	2% settling time [s]
$E(\cdot)$	0.7355	7.06
$\sigma(\cdot)$	0.36	4.12
median	0.6815	5.87

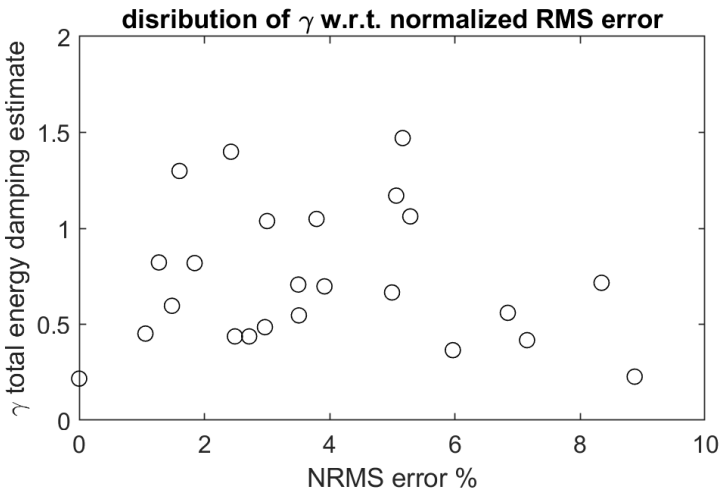

Figure 125: Damping estimate and associated normalized RMS error

System Damping and Stiffness in Each DOF

Deriving a stiffness value about the equilibrium provides insight into general dynamic behavior, such as natural frequencies. The stiffness of the interface changes with the direction and magnitude of the motion about the equilibrium – especially in motions normal to the face of the superconductors. The damping in each degree of freedom describes the dissipation of each state and differs from the previous section, which analyzes system energy damping.

A linearized state transition matrix that incorporates stiffness and damping matrices is shown in Eq. (104). K represents the stiffness matrix that is positive definite and C represents the damping matrix populated by nonnegative values along the diagonal. Δt is the time difference between the previous measurement and the next measurement, constant if the sensor samples uniformly. 1_3 are identity matrices of size 3 along each dimension and 0_3 is analogously a square matrix of zeros of dimension 3.

$$\begin{bmatrix} \boldsymbol{r} \\ \boldsymbol{\theta} \\ \boldsymbol{v} \\ \boldsymbol{\omega} \end{bmatrix}_{k+1} = \begin{bmatrix} 1_3 & 0_3 & \Delta t 1_3 & 0_3 \\ 0_3 & 1_3 & 0_3 & \Delta t 1_3 \\ -\frac{K_{rr}\Delta t}{M} & \frac{-K_{r\theta}\Delta t}{I} & 1_3 - \frac{C_{rr}\Delta t}{M} & 0_3 \\ -\frac{K_{\theta r}\Delta t}{M} & -\frac{K_{\theta\theta}\Delta t}{I} & 0_3 & 1_3 - \frac{C_{\theta\theta}\Delta t}{I} \end{bmatrix} \begin{bmatrix} \boldsymbol{r} \\ \boldsymbol{\theta} \\ \boldsymbol{v} \\ \boldsymbol{\omega} \end{bmatrix}_k \tag{104}$$

By utilizing IMU-generated velocity measurements, the K and C values that minimize error between propagated state and measured state are computed with the CVX convex optimizer. The positive definite and nonnegative constraints are encoded into this optimization. The state matrix assumes a linear propagation of stiffness and damping, an accurate assumption for states close to equilibria. The resulting linear relationship fits well; a sample of data shown in Figure 126 in which the measurements and propagated states are nearly indistinguishable. All state predictions fit within 2.5% normalized root-mean-squared error.

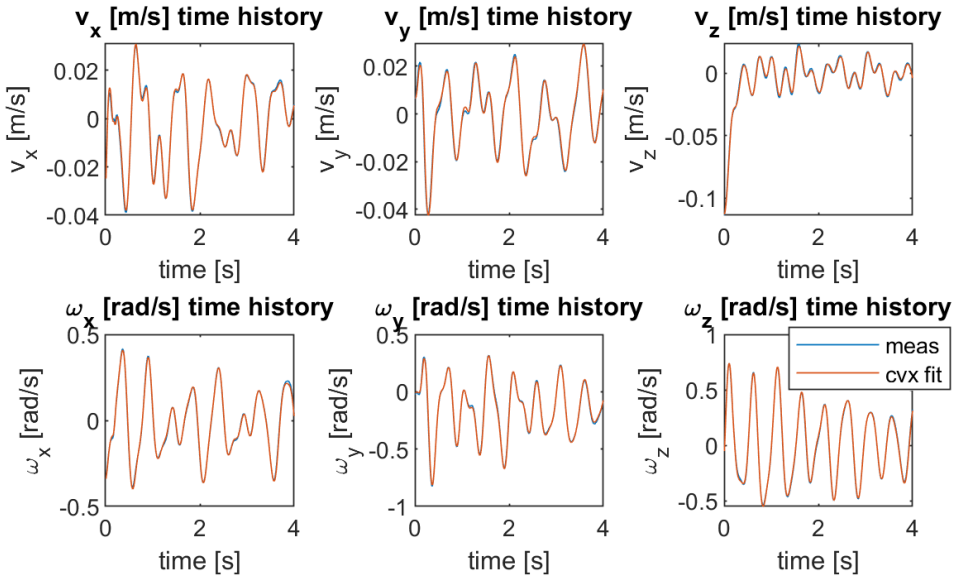

Figure 126: Comparison of measured and propagated velocity state from one experiment, fit with linear stiffness and damping

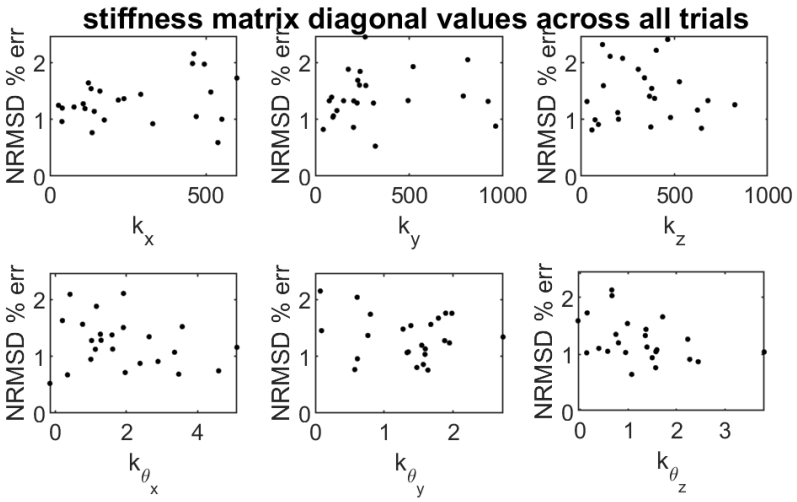

Figure 127: Stiffness matrix diagonal values across trials

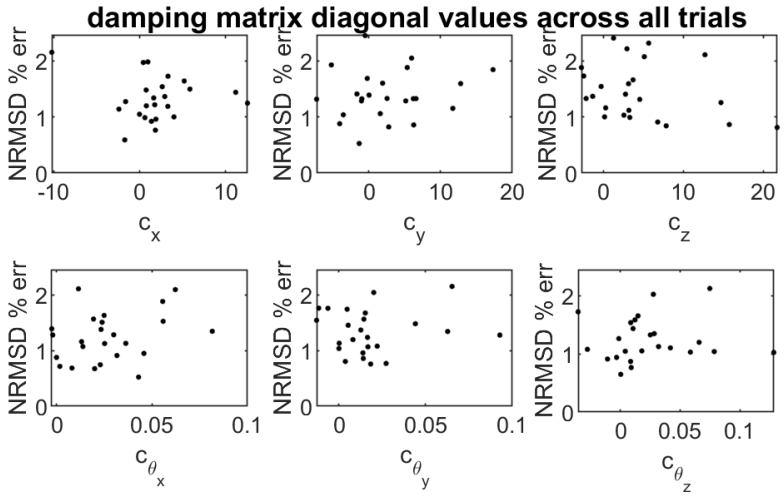

Figure 128: Damping matrix diagonal values across trials

The stiffness and damping parameters from all the trials plotted against the normalized root-mean-squared deviation (NRMSD) percent error are shown in Figure 128 and Figure 128. The distribution characteristics of stiffness and damping are listed in

Table 27 Table 27 and Table 28. The standard deviation for each of the stiffness and damping values are nearly as large as the expected value, revealing the inconsistency from trial to trial. Just like the energy analysis, the distribution spread demonstrates that the stiffness and

damping parameters are consistent within a trial and inconsistent across all trials. There is a relationship to initial state that is needed to fully describe the anticipated stiffness and damping.

Table 27: Stiffness values resulting from discrete state matrix fit

	K_x	K_y	K_z	K_{θ_x}	K_{θ_y}	K_{θ_z}
$E(\cdot)_{meas}$ [N-m]	554	262	108	1.57	0.92	0.88
$\sigma(\cdot)_{meas}$ [N-m]	265	176	109	1.34	0.81	0.73
median [N-m]	524	192	73	1.53	0.52	0.69

Table 28: Damping values resulting from discrete state matrix fit

	C_x	C_y	C_z	C_{θ_x}	C_{θ_y}	C_{θ_z}
$E(\cdot)_{meas}$ [kg m/s]	2.63	3.58	4.93	0.027	0.020	0.027
$\sigma(\cdot)_{meas}$ [kg m/s]	3.29	4.77	5.80	0.021	0.024	0.033
median [kg m/s]	1.71	1.72	3.17	0.024	0.014	0.014
2 % settling time ($E(C_s)$) [sec]	1.11	0.82	0.44	75	108	84

The damping parameter is magnitudes greater in the translational degrees of freedom than the rotational degrees of freedom. The position states take less than 2 seconds to settle within 2% of the initial state but the rotational modes take up to 2 minutes to damp out. The difference in translational vs rotational dissipation is clearly visible in the equilibrium tests. All trials lasted long enough to see the translational states settle but not long enough to observe the rotational modes settle significantly.

Contribution of Second Microgravity Experiment

The individual metrics that characterize the FPI describe the dynamic behavior throughout the entire docking maneuver. Initiating the capture operation to successfully capture, the flight system OS enters the magnetic potential well with relative motion up to 0.11 m/s and 0.084 rad/s

simultaneously. Upon successful capture, the OS experiences a peak force of either an impulsive contact, up to 120 N, or a contactless momentum exchange, up to 20 N. The total system kinetic energy dissipates to within 2% of initial magnitude within ~ 12 seconds. The system settles into equilibrium through underdamped oscillations, characterized by translational stiffness of 100 – 550 N·m and angular stiffness of 0.9 – 1.6 N·m. The last DOF to settle to within 2% of initial value is rotation about $\hat{\boldsymbol{y}}$, which settles after ~ 2 minutes. After the slowest mode dissipates, the docking maneuver is complete.

Discussion

A conceptual Mars Sample Return mission motivates the technology development a flux-pinned interface to perform docking and capture. The design of the experiment analogues is similar in mass and geometry of the mission concept and the experiment campaign reflects the initial conditions that the spacecraft would experience in spaceflight operations. The microgravity experiment campaign aimed at characterizing the capabilities of this system in five different dynamical metrics, such as energetic states to successfully capture, momentum exchange, rate of energy dissipation, and stiffness. This body of work matures and characterizes flux-pinning technology for consideration in the MSR concept but also aims to inform future technologists who wish to utilize flux-pinned interfaces for other use cases.

As designed and implemented in the experiments described in this work, this flux-pinned interface does not meet the desired capabilities specified by the most conservative MSR requirements. With a less stringent spaceflight OS mass requirement of 4.3 kg, the desired capability to successfully capture fulfills the initial velocity specifications. The observed performance of the OSA is farther from fulfilling the angular velocity requirement given that the

entrance attitude may be any orientation. If the entrance attitude is specified within smaller bounds, the FPI can produce better performance.

Upon successful capture, the reported damping parameters bound the settling time to under 2 minutes. After sufficient settling time, the OS is in equilibrium and remains in equilibrium with a certain stiffness. The stiffness of the interface offers two insights: the maximum external disturbance the FPI can tolerate and maintain the FPI with the OS and the necessary work required to detach the OS from the SRO. The stiffness values reported in the results are the expected spaceflight stiffness values if the magnetic image remains identical. Although the characterization is limited in the amount of states measured, these metrics represent approximate values. Either more testing is needed to empirically observe all states of interest or a more predictive, higher fidelity dynamics model must be developed to simulate states of interest.

FPIs are contactless, passive, and stabilizing but there are definitive limitations to these qualities. This paper aims to quantify the performance of FPIs for a sample return mission. The capture mechanism demonstrates capabilities that are not offered by conventional mechanisms at this mass and power specification. Additionally, flux-pinning offers unique advantages that should be considered for specific applications, but these limitations must be understood and designed around.

Future Work

Although the results revealed general insights into each metric, further work involves refining every mapping function by incorporating position and attitude information if applicable. The capture outcome boundary is unclear with only the velocity states, but by incorporating the position and attitude information, a boundary may be distinguished. By including attitude misalignment upon entrance, a boundary could be found to guarantee contactless interactions. For

the stiffness and damping analysis, the IMU measurements shall be transformed into the SROA relative frame as the OSA body measurements do not yield precise interface characteristics. As this paper addresses system level metrics, a large body of work remains in producing a predictable dynamics model from the same data set. To improve the predictive dynamics model, dynamic state measurements are generated by processing the GoPro video footage into global position and attitude data that may be directly compared to simulation output. The raw April tag position and attitude data has been processed for each camera. Currently, the raw measurement data is being verified to match transformations tied to various reference geometries, seen in Figure 129.

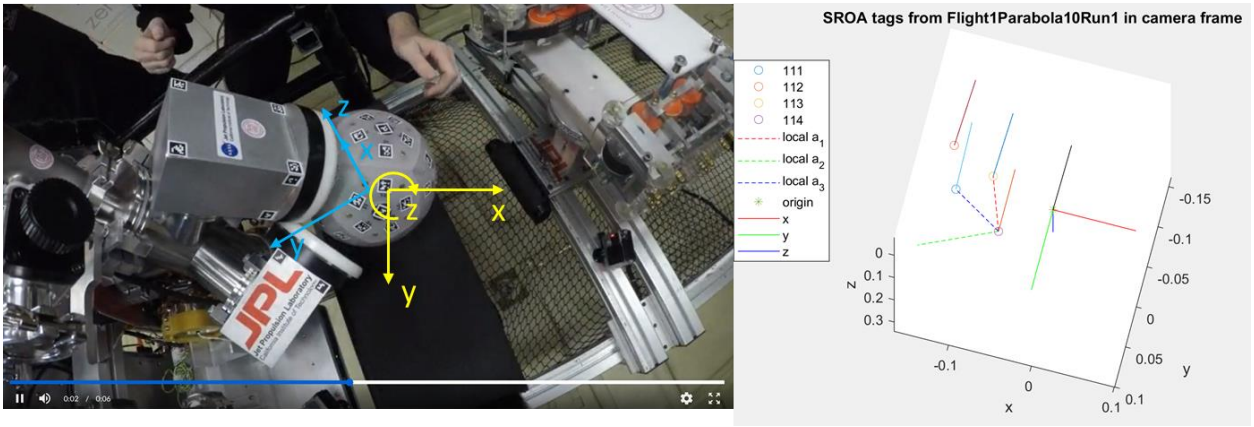

Figure 129: Comparison of tag data of reference geometry between GoPro visual and processed data in MATLAB

IV. Contribution of Experiment Testbeds across all Environments

As a result of the four experiment testbeds, the technological maturity of the interface hardware design increased from TRL 2 – TRL 5. The 2015 proof-of-concept testbed validated the system level design and implementation of the magnet-superconductor configuration and thermal cooling system, as well as offering coarse capture success related to initial kinetic energy and path angle. The 2016 laboratory experiment on ground expanded on and validated the system level design with a flight-traceable cryocooler thermal system. The capabilities of this system were

characterized with a more comprehensive experiment campaign, better dynamic sensors, and more finely controlled initial conditions. Although only expressive in 4 degrees of freedom, the laboratory experiment results are extrapolated to predict successful capture up to 5 cm/s and up to 50 cm in Mars orbit. In the first microgravity flight of 2017, successful capture was demonstrated at 5 cm/s, validating not only the hardware design and implementation but proving capture capabilities in the full 6 degrees of freedom. To design and observe desired capture capabilities up to 10 cm/s, the second microgravity flight of 2018 incorporated stronger magnets and more control over initial velocities from a launcher. This experiment campaign showed that the test articles consistently capture for initial conditions less than 24 cm/s and 2 rev/min but, when extrapolated to the spaceflight mass and inertia, did not fully meet the Mars Sample Return concept desired capabilities. From the dynamic data, the latest microgravity experiments revealed many characteristics of the interface, such as capture success related to energy, stiffness, damping, and collision force. To push the maturity of this docking interface to TRL 6, the predicted dynamics of the system must be representative of the observed dynamics of the hardware experiment: a system identification effort.

CHAPTER 4: System Identification

Flux-pinning technology maturation is currently held back by the relative immaturity of the predictive dynamics model compared to the system hardware development. Fortunately, the experiment testbeds offer a large dataset of dynamic measurements for a range of different degree-of-freedom environments and various physical parameters that can inform the predictive dynamics model. The current metric to gauge the accuracy of the dynamics model is normalized root-mean-squared error, NRMS. The goal is to achieve NRMS error below 5%, a requirement set by the NASA JPL Mars directorate. This chapter discusses different state error metrics, various system identification techniques, and the predictive state error from each technique.

I. Error Metrics

Evaluating the predictive capabilities of a dynamics model requires an error metric but choosing the proper error metric is not straightforward. The error metric represents the error between the measured timeseries data from dynamic experiments and an arbitrary, propagated predictive dynamics model. A more precise model minimizes error between the data and model but each objective function, the expression of error, has subtle implications for the true objectives the optimization problem is trying to minimize. A simple example is $L1$ minimization and $L2$ minimization, where the former objective promotes parameter sparsity and the latter objective promotes parameters of smaller magnitude. This section defines and lists the subsequent advantages and disadvantages of each error metric.

a. *Shooting-Method Metric*

Shooting method propagates the entire timeseries from a single state initialization, an initial value problem, defined in Eq. (105). e_k is the error between the k^{th} state s_k and the state

propagated k timesteps Δt forward from the initial measured state s_0 from a model $f()$. The state at timestep k calculated for all n timesteps in the timeseries. This metric implies analysis in the time domain, propagating and integrating derivatives of states from ODEs.

Matching the timeseries with only a single measurement is a very aggressive and, if successful, powerful approach to generating a predictive dynamics model. The resulting model offers insight into reachability and ultimately guarantees about successful capture. This error metric is most attractive for mission concept operations, as the requirement to initiate docking is a single relative state estimate to ascertain whether capture is successful or not. The disadvantage to this type of error is the integration of error, due to divergence or natural frequency discrepancies. Minimal stiffness or frequency error integrates to large time-domain error.

$$e_k = s_k - f(s_0, k\Delta t) \tag{105}$$

b. *Direct-Collocation Metric*

To borrow a term from trajectory optimization, direct collocation may be defined in Eq. (106). e_{k+1} is the error between the measured next state s_{k+1} and the state propagated one timestep Δt forward from a previous measured state s_k from a model $f()$. The state at timestep k is iteratively updated/initialized for all T timesteps in the timeseries. Matching each state in a timeseries is a more relaxed condition for model propagation. The prediction does not diverge due to integration, as only one timestep is ever integrated. Some disadvantages include susceptibility to measurement noise, the inability to guarantee capture farther into the time horizon, and sampling more frequently during mission operations.

$$e_{k+1} = s_{k+1} - f(s_k, \Delta t) \tag{106}$$

c. *Frequency Metrics*

Another approach to matching a timeseries to a predictive model lies in the frequency domain. Before any metric is evaluated, a Fast Fourier Transform, FFT, of the measurement timeseries and the shooting method predictive model timeseries are calculated. Two potential error metrics are then produced from the frequency spectra between the two timeseries: distribution of frequency and peak frequency comparison.

The distribution of frequency error metric is the integrated error in power spectra across all frequencies of interest between the measured and model propagated timeseries, shown in Eq. (107). e_k is the power difference at frequency k between the power curve, $P(\,)$, generated by the measured data, $P_k\big(x(t)\big)$, and the propagated shooting method timeseries, $P_k\big(f(x_0,t)\big)$. The advantage of this error metric is that it captures the importance of frequency spectra, which represents a physical characteristic of importance, stiffness. A frequency representation avoids the time integration of frequency difference in the time domain shooting error metric. The minimization of error in the frequency spectrum drives the model to match not only frequency and amplitude of natural modes at the peaks but also the continuous spread of frequencies around the peaks, which are manifestations of nonlinearities and damping in the system. A precaution to this method is that the integrated error in power spectrum does include noise in the frequency spectrum related to sampling rate and a peak from the FFT of noise in the measurement data.

$$e_k = P_k\big(x(t)\big) - P_k\big(f(x_0,t)\big) \tag{107}$$

$$e_k = p_k\left(P\big(x(t)\big)\right) - p_k\left(P\big(f(x_0,t)\big)\right) \tag{108}$$

Another frequency domain metric relaxes the effort of matching the entire power spectrum by instead matching only the top n peak frequencies in the spectrum, shown in Eq. (108). e_k is the

frequency difference between the k^{th} peak, p_k, generated from FFT power spectrum of the measured data and model shooting propagated timeseries. The peaks are found with MATLAB's peak function and sorted by decreasing power magnitude. The first peak is the most dominant in amplitude. The relaxation from spectrum matching to peak matching avoids integration error of the area under the power curve, instead, only accounting for distance in the frequency dimension. The advantage of peak matching is direct optimization of matching the natural frequencies of the system, instead of potentially fitting to unimportant frequencies, which do not appear in the peak finding function. The disadvantage of excluding the entire power spectrum and the amplitude at each frequency is neglecting the wealth of information embedded in that spread, such as amplitude response in the timeseries and the damping or nonlinearities expressed in the continuous power spectrum.

The disadvantage of these frequency error metrics is the inability to generate a prediction of state or capture success directly from this analysis. The frequency analysis only pertains to the characterization of the interface for experiment trials that have already captured. The predictive model may be refined in the frequency-domain error but ultimately needs to be validated with timeseries data to ensure unseen data from trials that did not capture are also well predicted.

d. *Normalized Root-Mean-Squared Error*

$$NRMS = \frac{\sqrt{\sum_{k=1}^{n} \frac{e_k^2}{n}}}{s_{max} - s_{min}} \tag{109}$$

Across all error metrics, the normalized root-mean-squared error, NRMS, of an experiment trial's timeseries is given in Eq. (109), x_{max} and x_{min} are the maximum and minimum measures states respectively. The time domain metrics interpret n as the total number of timesteps. The

number of timesteps n is determined by 2% settling time for each state. The frequency domain NRMS of an experiment trial's timeseries interprets n as the maximum frequency or number peaks to take into consideration. For a four degree-of-freedom system, there exists four natural modes and frequencies, which may or may not be distinct. Normalization across each trial avoids disproportionate representation for trials with larger initial conditions, weighing each trial approximately equally.

II. Methods

The methods for system identification branch in two different mindsets: analytical methods and numerical methods. Analytical methods involve a physics-based model, refining this model with model with mathematical expressions to capture higher-order effects, and parameter estimation to populate the expressions. The physics-based model and model refinements stem from fundamental principles and link to physical intuition, which is very attractive from a system design and safety perspective. Numerical methods generate approximate models from the data. There exist a multitude of different numerical methods of which only four methods are discussed here: neural networks, polynomial fit, sparse identification with a bag of functions, and symbolic regression with genetic algorithms.

a. *Analytical Methods*

The physics to dynamics model is thoroughly described in the Flux-Pinning Theoretical Dynamics Model section and the proper refinements are described in the Flux-Pinned Dynamics Model Parameterization and Sensitivity Study section. A later section focuses on the method of parameter estimation once the baseline simulation is created and the proper refinements are added to the baseline simulation. The experiment data used is primarily from the 1DOF and 4DOF

experiments from the 2016 laboratory testbed. The parameter estimation algorithms discussed is a nonlinear programming solver from the MATLAB library, fmincon.

The physics-simulated model is intuitive and interpretable, useful for design and sensitivity studies (if assumed error is acceptable). The physics-based model is also verifiable, as energy conservation and adherence to geometric constraints may be enforced or observed from the model. The potential disadvantage of these analytical models is the lack of precision if not all physical effects are represented in the model. The rigor required to investigate the fundamental physics is time-consuming, expensive, and possibly still insufficient to capture all relevant effects. Unknown unknowns are arguably difficult to anticipate. At some point, a numerical method is necessary to reach a threshold prediction error ("perfect is the enemy of good enough" [136]).

b. *Numerical Methods*

Numerical methods can approximate a dynamics model with little context of the physical system that generated the data. From timeseries data of dynamic states, the final product is either a discrete state transition mapping or a continuous state function, describing an ordinary differential equation. The discrete transition maps the dynamic state at timestep k to the next dynamic state at timestep $k+1$. The continuous function maps the dynamic state at timestep k to the derivatives of that state, which can then be integrated to produce the next dynamic state at timestep $k+1$. Both forms yield intuition into the system dynamics, although the continuous function may directly in the form of identifiable physical laws, like Newtonian mechanics. This section reviews four different numerical methods, ranging from a classical Taylor expansion to modern day machine learning techniques. Each technique has advantages and disadvantages of which the advantages from each technique is ideally incorporated into the final dynamics model. All numerical methods are subject to the quality of the data collected, no matter the technique.

Taylor Expansion Polynomial

Commonly, the first approach that engineers take when approximating a function is a Taylor expansion. The relationship between input and output is explicitly defined by varying degrees of monomials. Some domain knowledge may be included in the explicit structure, like linear inequalities. The coefficients in the expression structure are then estimated with a simple least-squares estimate or with a more involved convex programming solver. An advantage of this method is the ability to control system dynamic properties like stability, boundedness, and solution convergence in finite time. The resultant model is also verifiable with respect to conserving energy or adhering to geometric constraints. The precision of this approximation may be arbitrarily precise by incrementing the highest monomial degree, but at the risk of overfitting and polynomial instability. The Taylor expansion is easy to generate and retrain given good data, but the Taylor form is not easily interpretable or intuitive to design. Finally, the resultant model is system specific and very rarely can parameters from one Taylor expansion be transferred to training a separate system's data.

Sparse Identification with Bag of Functions

A bag of functions is an expansion of expressions, which could or could not include the polynomial expressions in the Taylor expansion. The bag of functions is a comprehensive user-defined library of expressions, ideally chosen to span all possible child expressions in the final approximation. Child expressions include monomials, exponentials, logistic, trigonometric, power functions, etc. Much like the Taylor expansion, domain knowledge may be included, and the coefficients of each child expression is estimated with least-squares or a convex programming solver. Sparse identification with a bag of functions is an adaptation from Brunton's system

identification in which a sparsity condition is applied iteratively upon coefficient estimation [137]. The sparsity condition may be thought of as a pruning process that gets rid of unnecessary terms, leaving only the dominant terms. On top of the advantages of the polynomial approximation, the bag of functions model may include less child expressions, as the non-monomial functions are more expressive and succinct. Like the polynomial, the bag of functions is system specific, but unlike the polynomial, the bag of functions can be very interpretable. Unlike the polynomial, the other functions in the library are basis dependent. Unless the user intuits the bases, the bag of functions needs more terms than necessary to represent the final model.

Symbolic Regression with Genetic Algorithms

Symbolic regression is a type of system identification aim to discover model structure to best fit a dataset, both in terms of accuracy and simplicity. Not only the parameters within a mathematical expression are searched, but the form of expressions is searched [138]. With the GPTIPS2 toolbox driven by a genetic algorithm, expressions are obtained that accurately represents the general structure of the true expression, although the parameters within may change [139]. An advantage to symbolic regression is that the form of the expression may be extended to other systems and the estimated parameters within the expression may change. This technique is the only numerical method that can extend to other systems, granted with the same underlying physics but differing physical parameters. Unfortunately, getting an interpretable expression out of thin air is idealistic and it is rare for genetic algorithms to yield the true expression.

Neural Networks

Neural networks are machine learning algorithms that use data to predict an output from an input, which can be used as an approximate dynamics model. Multilayer feedforward neural

networks are known and proven to be universal approximators, as long as the nonlinear transformation function is not polynomial [140], [141]. Neural networks are increasingly popular for their incredible ability to approximate nonlinear relationships without any context. A neural networks unfortunately cannot guarantee safety in the predictions. Predictions are only valid if the current state lies within bounds of state in experiments (in other words, invalid if propagating state outside of observed experiment conditions). Another disadvantage is that the parameters generated by the neural network are not interpretable or extensible to other systems.

III. Physical Model Refinement

The general methodology behind refining the spaceflight dynamics model is to work up from a limited amount of degrees of freedom on ground to the full 6DOF spaceflight system. Three sets of experiments offer dynamics ranging from pure rotation (1DOF), to coupled constrained dynamics (4DOF), to full degree-of-freedom dynamics (6DOF). The incremental progression in additional degrees of freedom also helps transfer knowledge about the system, such as physical parameter estimates. Several physical phenomena drawn from scientific literature help refine the frozen-image model from theory to implementation. Effects, such as finite-dimension superconductors, temperature dependence, and reduced magnetic field strength of images, must be incorporated into the dynamics model. A combination of different algorithms, error metrics, parameters, and datasets

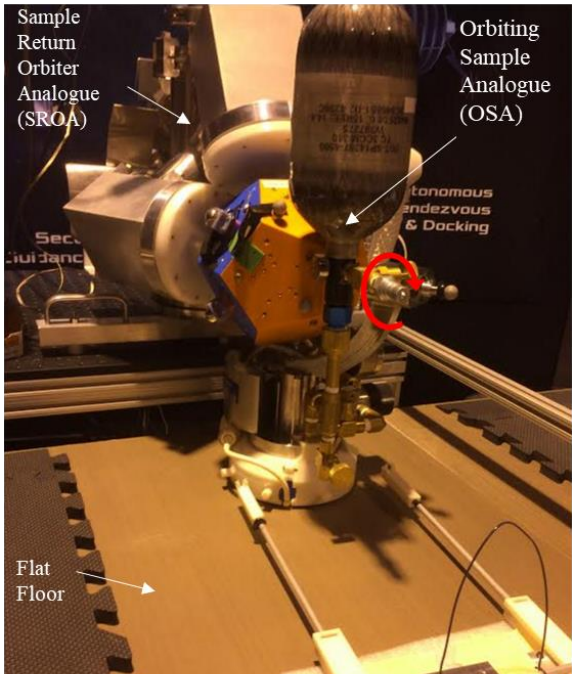

Figure 130: Capture and docking dxperiment in a reduced degree-of-freedom testbed measuring rotation due to flux pinning dynamics about mechanical spindle

were used to estimate the parameters and to validate the accuracy of the physics-based predictive dynamics model. Each of the following results describe the parameters and experiment effects included in the simulation setup, the experiment data used in the analysis, and the predictive performance of the model for a range of error metrics.

Described in the capture and docking experiments in a reduced degree-of-freedom testbed, the 1DOF flux-pinned dynamics were measured in a single rotational degree-of-freedom about a mechanical spindle, depicted by the red arrow in Figure 130, and the 4DOF in Figure 131. Measurements include position timeseries and attitude timeseries in quaternion form from the Vicon motion capture system, and angular velocity from an internally mounted IMU. The task is to define and incorporate relevant parameters into the baseline simulation, then estimate consistent values of these parameters to reduce error between simulated and measured state error.

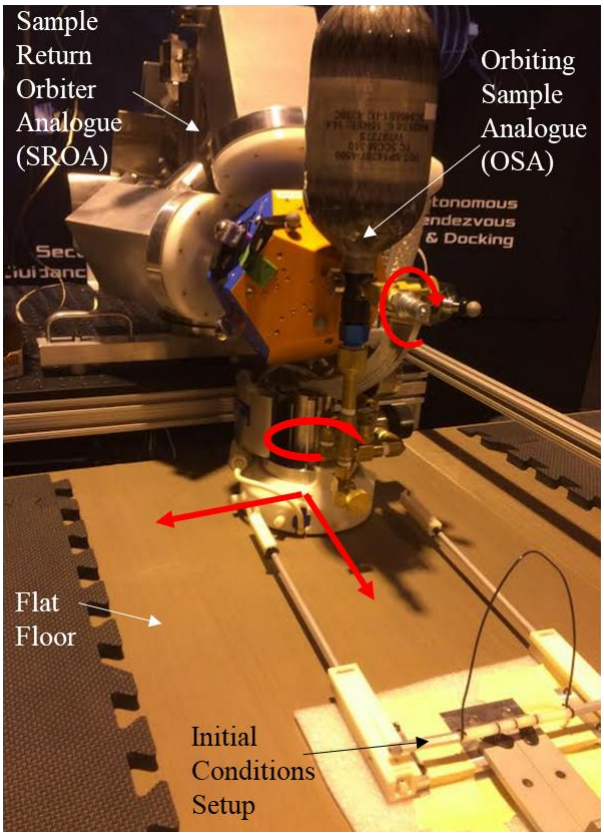

Figure 131: Capture and Docking Experiment in a Reduced Degree-of-Freedom Testbed measuring rotation due to flux pinning dynamics about mechanical spindle and planar air bearing

The parameters to be estimated are separable by two categories: environment-specific parameters and fundamental physical parameters. Environment-specific parameters are tied to the experiment testbed, not the test articles, and are ideally decoupled from the physics of interest. Examples include friction coefficient from the mechanical bearing and friction from the planar air bearing. Fundamental

physical parameters are factors inherent to the flux-pinning physics, like field-cooled position and orientation, eddy-current damping, temperature dependency, etc. In this testbed, the friction about measured degree-of-freedom is a combination of both friction from the mechanical spindle and eddy-current damping. The contribution of each friction source is not possible to separate and so remains as a single encompassing term. Each method described below reports the baseline simulation error to improve upon, the relevant parameters incorporated, the process to reduce prediction error, and the resulting error.

a. *Predicting Dynamics from 1 Degree-Of-Freedom Experiments*

Shooting Method Error

Across 55 trials with initial angular displacements ranging from 5 to 30 degrees, the baseline simulation error evaluated with the shooting method yielded a mean normalized RMS error of 31 % in the angular velocity prediction. The physical parameters incorporated into the simulation include the effect of a finite-dimensioned superconductor, damping, and temperature. An initial set of parameters and optimally estimated parameters are then compared to the baseline simulation prediction error.

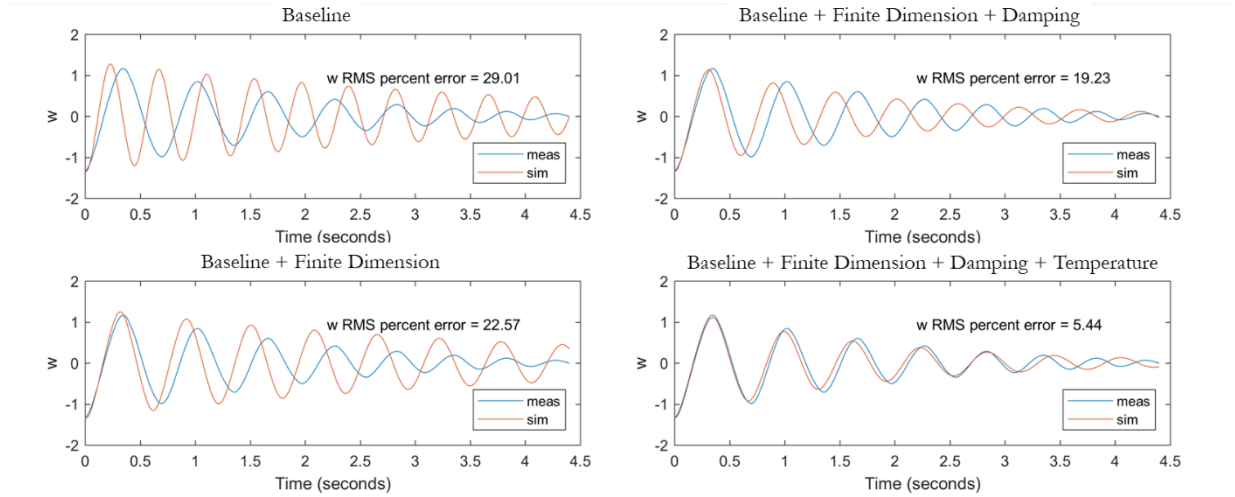

Figure 133: Progression of 1DOF angular velocity prediction with incremental optimal parameter estimates from shooting method

An initial set of parameters are injected into the refined simulation based on previous characterization, like the finite-dimension experiments, bearing-friction tests, and a coefficient-of-temperature fit by trial and error. Figure 133 shows the angular velocity timeseries comparison between the baseline simulation and measurement for a sample experiment trial on the top left. As the optimally estimated parameters are individually added into the baseline simulation, the simulated angular velocity profile begins to match the measured profile, reducing this sample to 5% RMS error. This trial shows the most significant improvement but

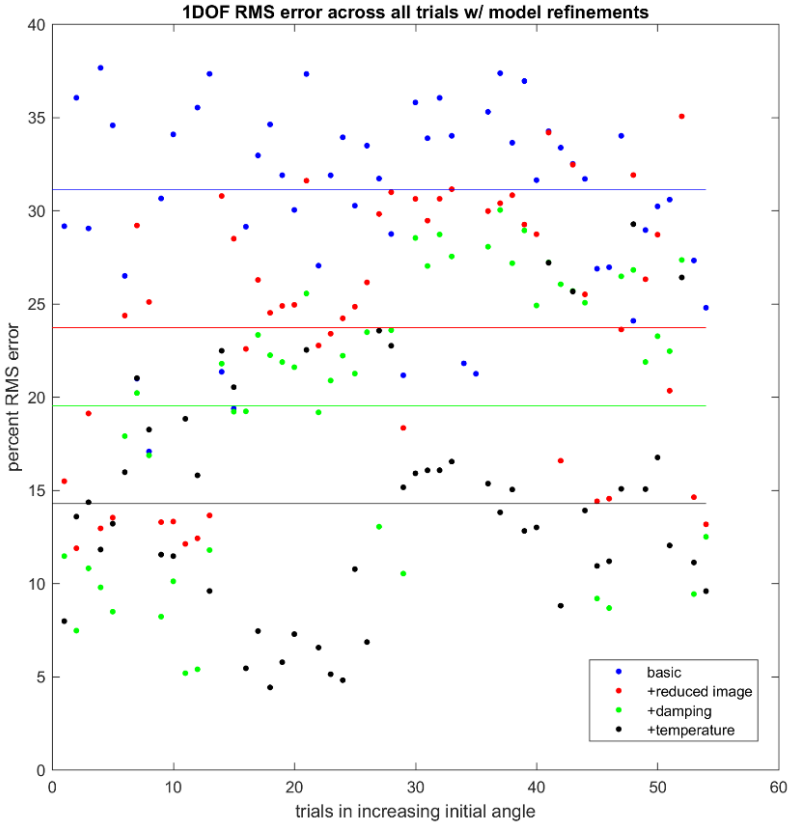

Figure 132: 1DOF RMS error across all experiment trials with shooting method, incrementally incorporating initial parameter estimates

even the most refined simulation, in the bottom right of Figure 133, the simulated angular velocity reveals an initial faster natural frequency then in the latter reveals a slower natural frequency.

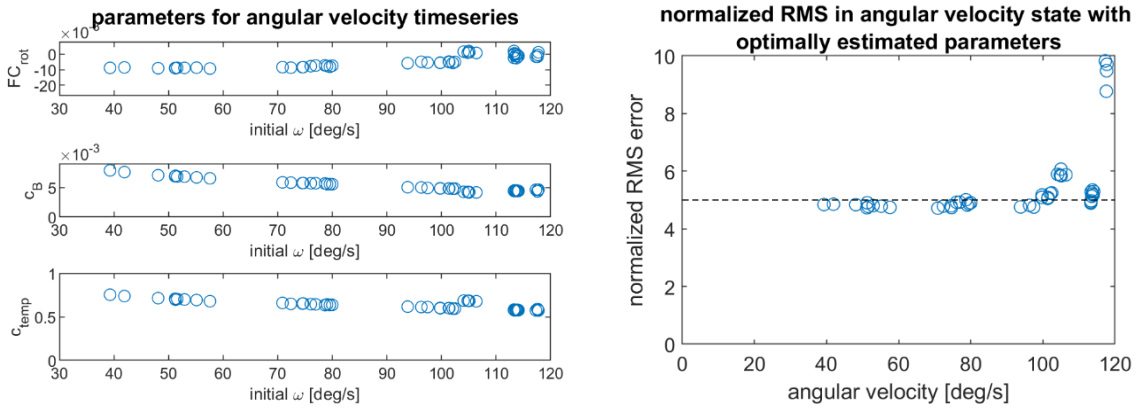

Figure 134: left, parameter spread over the initial angular velocity of each trial; right, normalized RMS error in angular rate with optimal parameters

The optimal parameters are then estimated by minimizing normalized RMS error propagated with the shooting method across all trials with the nonlinear programming solver, fmincon. The optimal parameter distribution and resultant RMS error are shown across all initial angular rates in Figure 134. General trends from the optimal parameters show consistent parameter estimates for all three parameters, given that the standard deviation across the estimates spanned 20 times smaller than the allowable parameter range. The field-cooled rotation displacement stays constant, which matches physical intuition that the hardware maintains the same bias throughout all experiment trials. The bearing friction and coefficient of temperature decrease in a linear fashion as the experiment initializes at larger angular displacements and angular rates. The dominant dynamics are captured through these parameter estimates, but the consistent parameter movement signal that there are subtle dynamics yet to be represented at a higher order than scalar or linear terms. This conclusion is further reiterated in the right plot in Figure 134. The refined dynamic simulation is less able to accurately predict timeseries at larger angular rates, a manifestation of more nonlinear behavior. Granted, the cluster of trials exhibiting error above 8 %

are due to measurement noise, seen in Figure 135. If these noisy trials are excluded, the mean RMS error reduces to 5.1%.

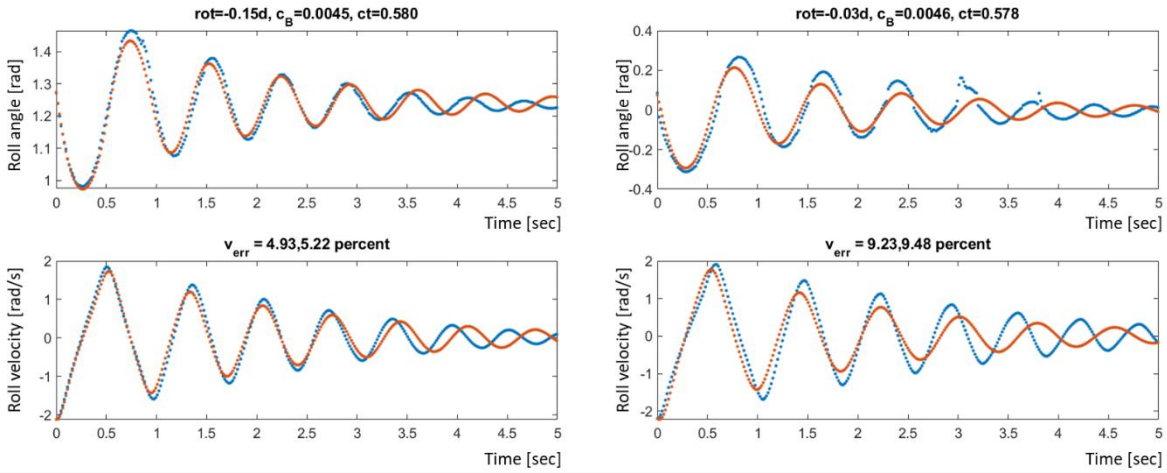

Figure 135: left, large nonlinear 1DOF dynamics with minimal measurement noise; right, similar initial conditions but clear and large measurement noise

Across all trials, the average reduction in prediction error from the initial parameters is 14% RMS error, seen in Figure 132. With the optimally estimated parameters, the prediction error reduces to 5.1 % RMS error across all, seen in Figure 134. The initial and optimal parameters with corresponding mean values are listed in Table 29. The optimal parameters nearly satisfy the targeted prediction 5% normalized RMS error.

Table 29: Percentage RMS error from incrementally incorporating physical parameter estimates in 1DOF experiments with shooting method

Model	Mean RMS error from Initial Value	Initial Value	Mean RMS error from Optimal Value	Optimal Value
Baseline	31 %			
+Finite Dimension	24 %	$0.64 - 0.001\, r_l$		
+Damping	20 %	0.0029		0.0053
+Temperature	14 %	0.835	5.1 %	0.6349

Direct Collocation Error

The mean normalized RMS error dropped to 2 % in angular velocity with no error above 8 % with the direct collocation error metric. The nonlinear programming solver used to minimize direct collocation error estimated slightly different parameters than the shooting method: damping, temperature, field-cooled position, and field-cooled rotation. All trials converged to the same values within machine precision, seen in Figure 136 and Table 30. After estimating the optimal parameters, the simulation error reduced the angular velocity error to 1.3 %. The baseline and optimally parameterized simulation are shown in Figure 137.

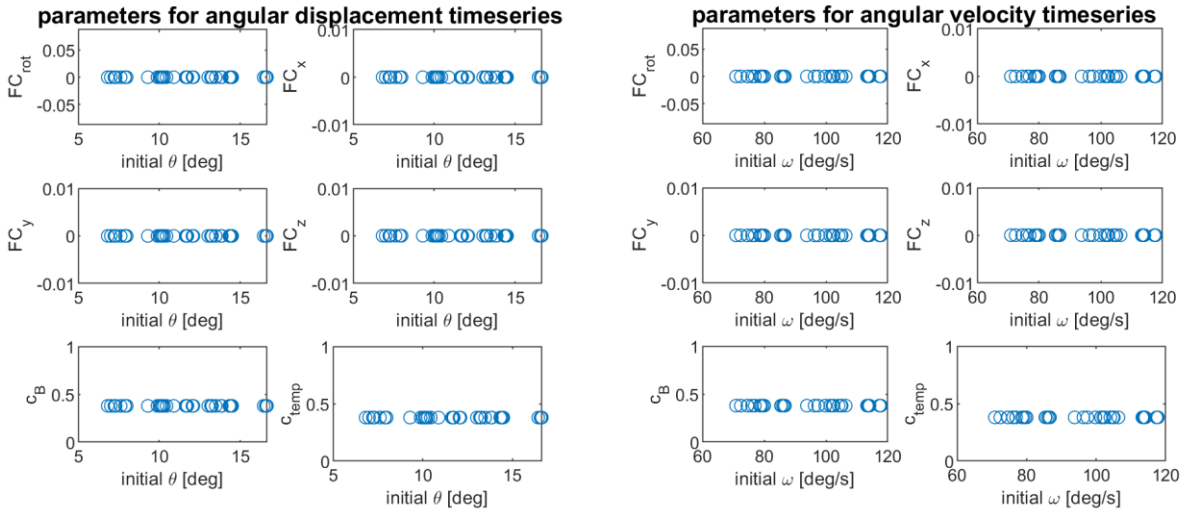

Figure 136: Optimal estimated parameters for various initial conditions of angular displacement (left) and angular velocity (right) minimizing direct collocation error

Table 30: With direct collocation, mean and standard deviation of estimated parameters across all 1DOF experiment trials

Parameter	E(optimal parameter)	σ(optimal parameter)
Field-cooled rotation offset	0	$\epsilon \cong 0$
Field-cooled x position offset	0	$\epsilon \cong 0$
Field-cooled y position offset	0	$\epsilon \cong 0$
Field-cooled z position offset	0	$\epsilon \cong 0$
Coefficient of friction about the bearing	0.38	$\epsilon \cong 0$
Coefficient of temperature	0.38	$\epsilon \cong 0$

Upon closer inspection, the error across trials can be separated into two sets, with trials above the median values having particularly bad noise in the data. Across all initial conditions with smooth timeseries data, the normalized root mean square error is consistently at 0.9% attitude and 1.5% angular velocity error. The higher error regime can be attributed to discontinuous, noisy data, seen in a side-by-side comparison of a trial with and without discontinuity at the same magnitude of initial perturbation, Figure 138.

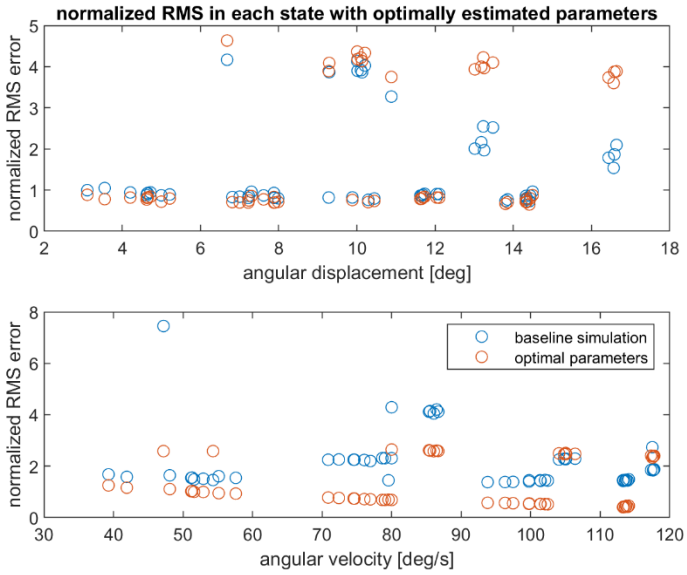

Figure 137: normalized RMS error of 1DOF experiments before and after estimating optimal parameters with direct collocation method

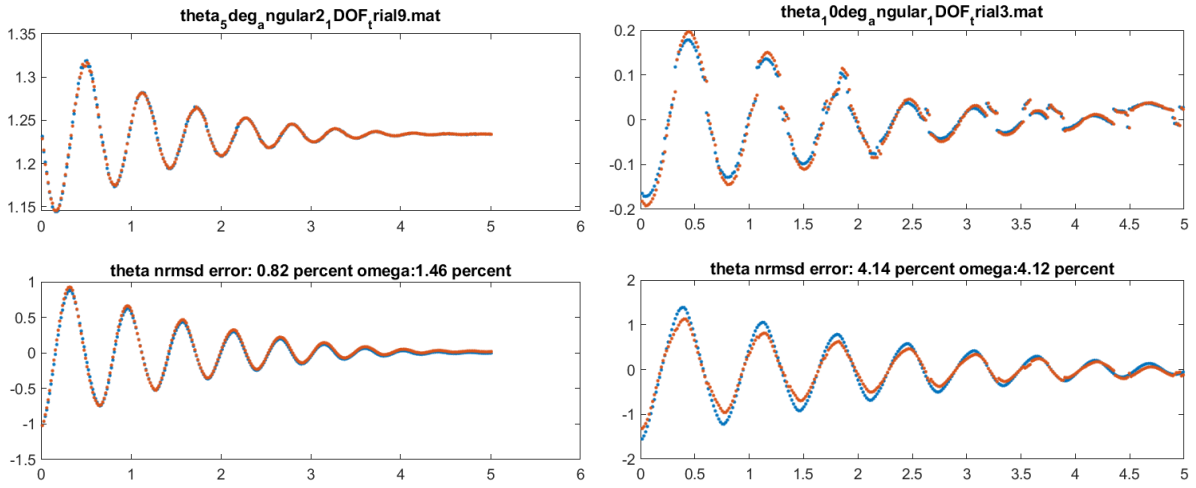

Figure 138: left, 1DOF smooth timeseries; right, 1DOF noisy timeseries. Both propagated with direct-collocation method but with dramatically different error

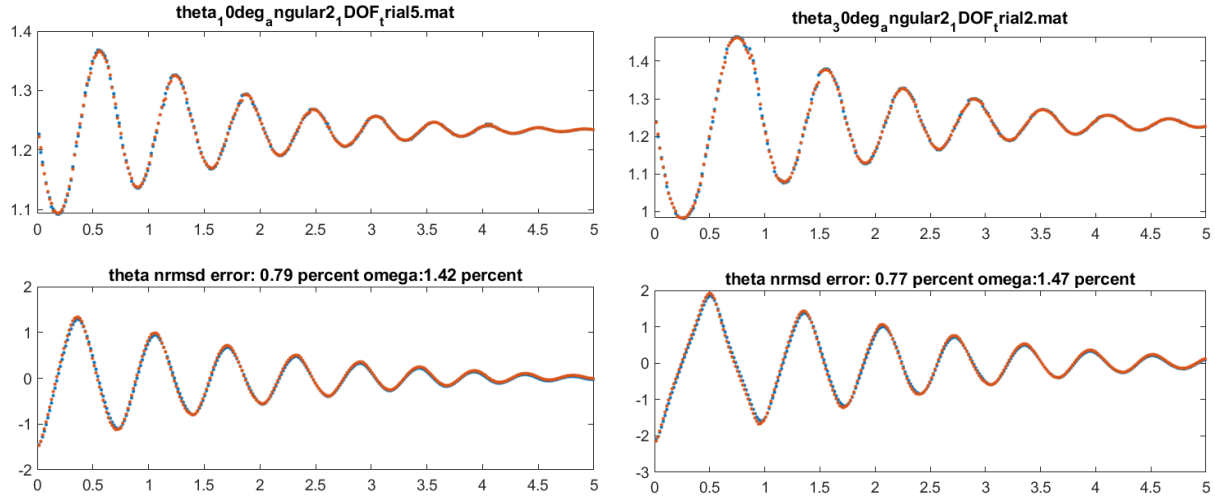

Figure 139: left, 1DOF timeseries initialized at a small displacement; right, initialized at a large displacement with nonlinearity accentuated. Simulation still performs well

For the trials absent of the discontinuities, the baseline and refined simulation both predict state with the direct-collocation method very well. The simulation predicts nonlinear behavior very well, as seen by the error variation with initial state in Figure 137 and in a comparison of two trials in Figure 139. Despite dramatically reducing the expected predictive error and reaching below the targeted 5% normalized RMS error, injecting the optimal parameters from the collocation error with the shooting error metric reveals terrible prediction, seen in Figure 140. Although the parameter estimates from the collocation metric are consistent and yield very low prediction error, the resulting parameters are invalidated with other metrics.

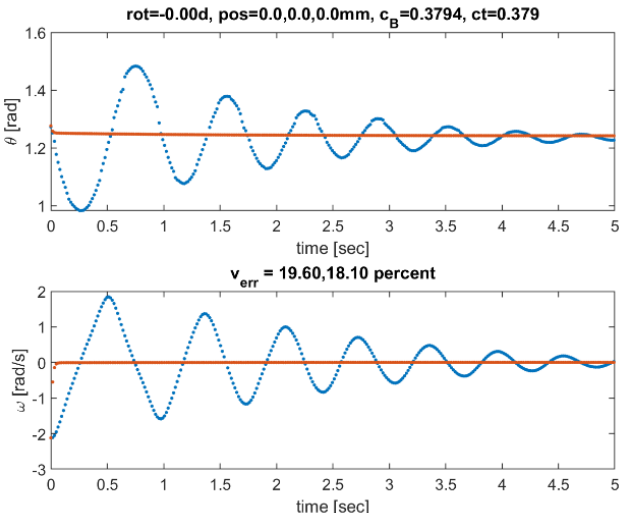

Figure 140: optimal parameters from the collocation error propagated with the shooting method, measurements in blue and simulation in red

Frequency Domain

Instead of comparing angular velocity timeseries, frequency-domain parameter estimation involved initializing user-defined parameters, simulating a timeseries, generating an FFT of the angular timeseries, and either differencing dominant peaks or the entire frequency spread. The selected parameters to vary are identical to the previous analyses: damping, coefficient of temperature, and field-cooled state. The natural frequency of the measured interaction typically lies between 1.3 Hz to 1.8 Hz. The power spectrum in consideration is only integrated to 5 Hz. Although the timeseries is misaligned due to a bias term, Figure 141 and Figure 142 show that the frequency-domain profiles are relatively well-matched. Both figures yield similar frequency profiles, albeit each sample is a result from a different frequency error minimization schema. The main visual distinctions are that the power spectra tails lie closer to the origin and the peak amplitudes are less in magnitude for the full spectrum analysis. The optimal parameters for the frequency peak matching are shown in Figure 143 and listed in Table 31.

Table 31: With frequency peak matching, mean and standard deviation of estimated parameters across all 1DOF experiment trials

Parameter	E(optimal parameter)	σ(optimal parameter)
Field-cooled rotation offset [deg]	0.00066	0.1031°
Field-cooled x position offset [mm]	0.029	0.082
Field-cooled y position offset [mm]	0.014	0.052
Field-cooled z position offset [mm]	0.014	0.40
Coefficient of friction about the bearing	0.0029	0.00003
Coefficient of temperature	0.83	0.025

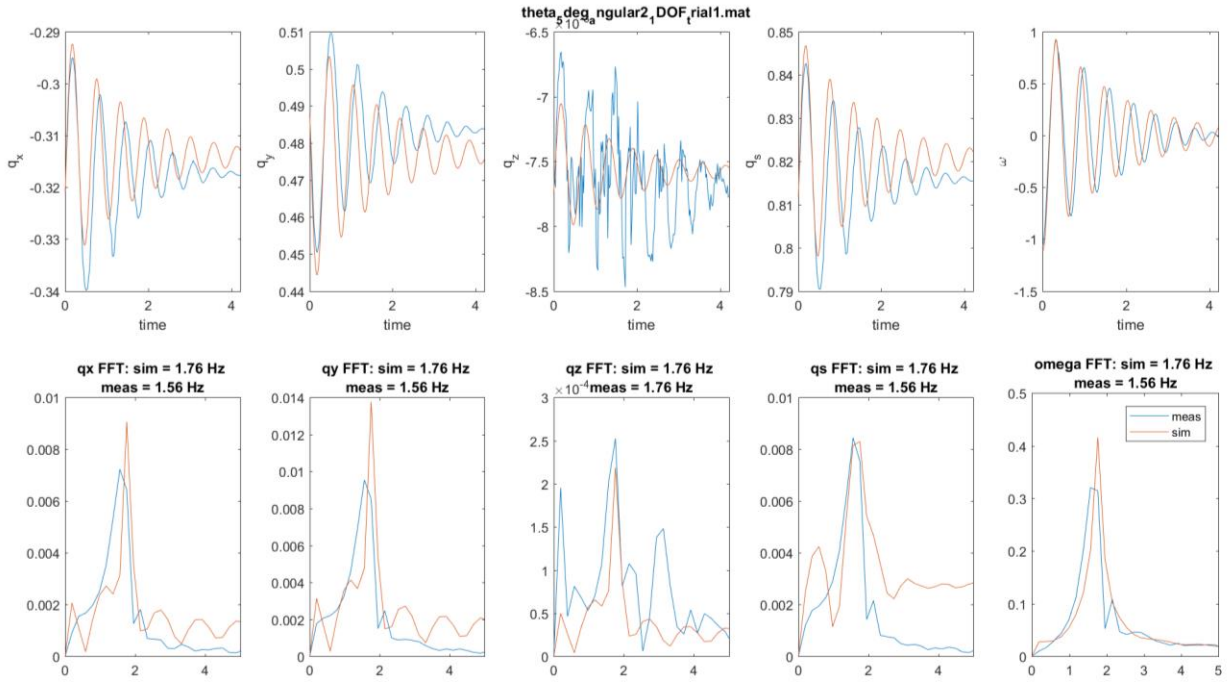

Figure 141: 1DOF experiment data sample with attitude and angular velocity timeseries on the top row and corresponding FFT on the bottom row, specifically minimizing difference in power spectra

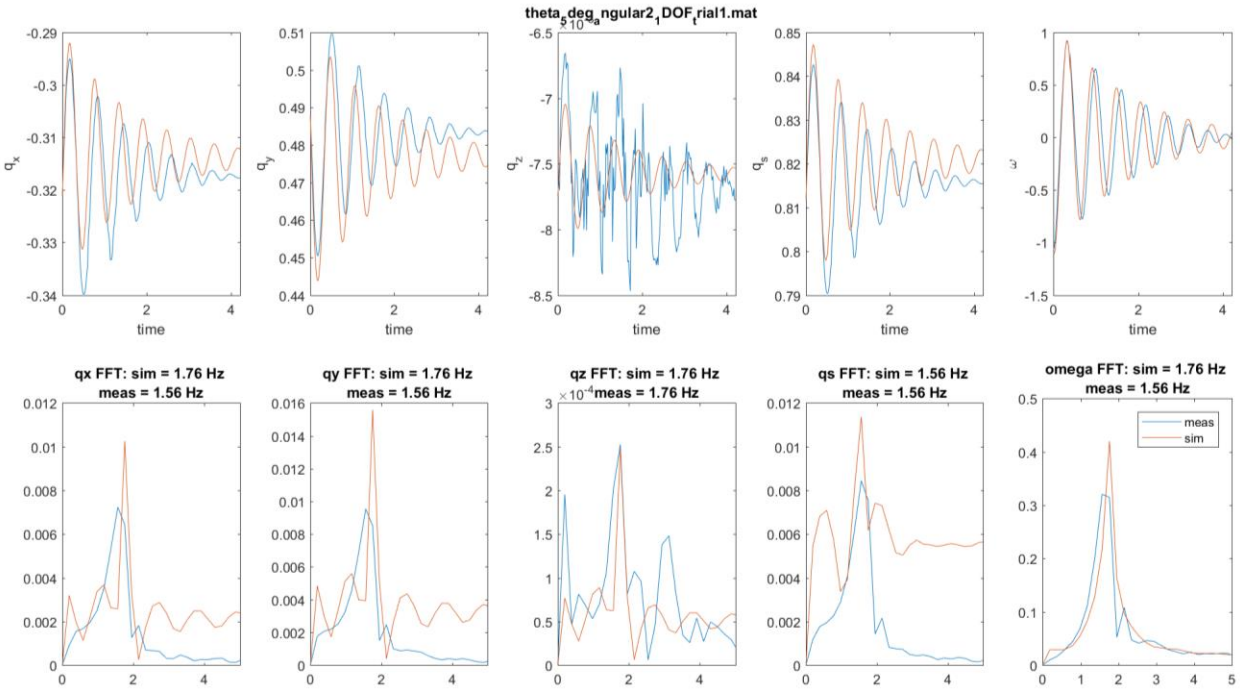

Figure 142: 1DOF experiment data sample with attitude and angular velocity timeseries on the top row and corresponding FFT on the bottom row, specifically minimizing difference in dominant peak

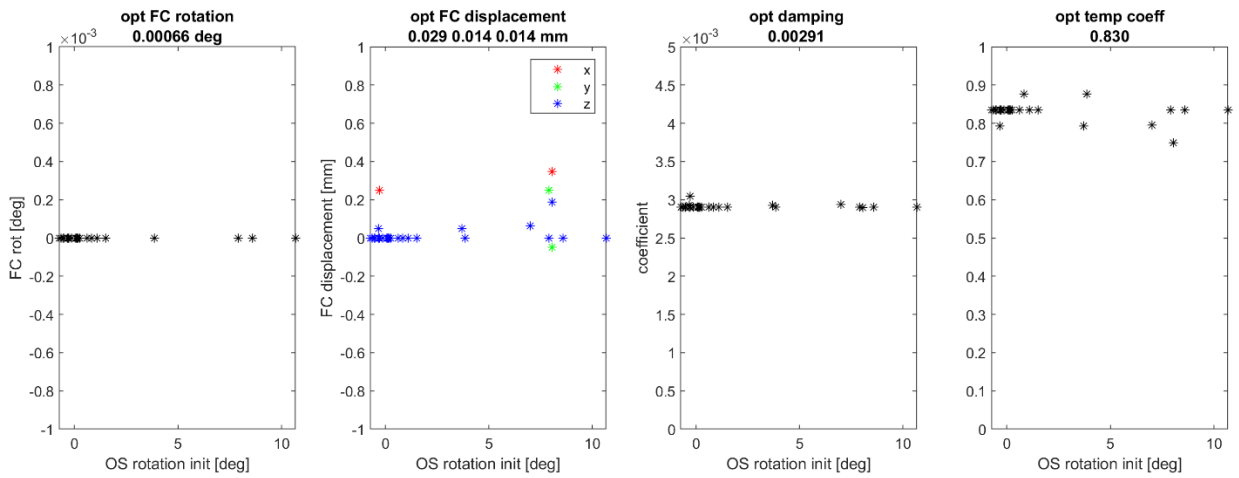

Figure 143: Optimal parameters as a result of frequency-domain peak matching for 1DOF experiment data

Summary across Methods

The optimal parameters from all methods are compiled in Table 32. Direct-collocation parameters most disagree with all other method results and cannot be validated with another propagation scheme. The initial parameter values are assumed to be close to the real values and offer a starting point for optimization, as each initial parameter was characterized individually in a scenario different from the fully integrated dynamic experiments. The frequency-peaks method minimizes the error in natural frequency, which emphasizes predicting accurate stiffness characteristics. Stiffness correlates to the strength of the interaction, which is tied to the coefficient of temperature. For that reason, the optimal coefficient-of-temperature value is taken from the frequency-peaks method. The frequency-peaks method neglects timeseries amplitude, a consequence of damping, whereas the shooting method emphasizes the state magnitude, relevant in finding state bias as well. For that reason, bias and damping are taken from the shooting method. Drawing from strengths of each method and consistency across all methods, the best parameters to incorporate in a predictive dynamics model moving up in degrees of freedom are given in the last column of Table 32.

Table 32: Parameters in refined predictive dynamics model, found from various methods, with green highlighted terms considered the best estimate across methods

Parameter	Initial Value	Shooting Method	Direct Collocation	Frequency Peaks	Best overall
Field-cooled rotation offset [deg]	0	-0.262	0	0.00066	-0.262
Field-cooled x position offset [mm]	0	-	0	0.029	0
Field-cooled y position offset [mm]	0	-	0	0.014	0
Field-cooled z position offset [mm]	0	-	0	0.014	0
Friction coefficient about the bearing	0.0023	0.0053	0.38	0.0029	0.0053
Coefficient of temperature	0.87	0.6349	0.38	0.83	0.83

b. *Predicting Dynamics from 4 Degree-Of-Freedom Experiments*

For this 4DOF system, the directly measurable states are: $s_{meas} = [r_x\ r_y\ \theta\ \phi\ \dot{\theta}\ \dot{\phi}]$ where r_x & r_y are planar position on the flat floor surface, θ is the angle about the ball bearing, ϕ is the angle about the air foot, and the associated derivatives. The position and attitude are measured from Vicon and the angular velocities are measured from an IMU gyroscope. The simulation incorporates coefficient of temperature, mechanical bearing friction, air bearing friction, and magnetic field strength of the magnets. Coefficient of temperature is assumed to be map magnetic source strength to image strength in a 1 to 1 ratio. All friction coefficients and the magnetic field strength of the magnetic source were empirically measured and reflected in the simulation initialization. These refinements incorporate physical parameters of the system to higher-order effects that would not otherwise be seen in the basic frozen-image model. Some effects not included are vertical/horizontal image and finite-dimension effects. The refined simulation does not include resultant dynamics from collisions, thus all trials in which the two spacecraft bodies contacted are omitted. Although the full experiment suite included capture and tumble experiments, most experiments with kinetic conditions collided. The following analyses focus on the trials from the sphere-of-influence and natural-modes experiments, which had near static initial

conditions and contained a significant number of trials in which the spacecraft did not contact. The initial refined simulation parameters are generated from isolated testbed characterization tests, listed in Table 33, and offer a baseline to improve upon with optimally estimated parameters.

Table 33: Initial parameters incorporated into 4DOF predictive dynamics model

Simulation Parameter	Initial Value	Optimal 1DOF Value
Coefficient of friction about the mechanical bearing	0.0023	0.0053
Friction of the air foot (rotational)	0.0177	0.0177
Friction of the air foot (translational)	0.0177	0.0177
Coefficient of temperature	1	0.83
Field-cooled rotation offset [deg]	0	0
Field-cooled x position offset [mm]	0	0
Field-cooled y position offset [mm]	0	0
Field-cooled z position offset [mm]	0	0

Shooting Method for Sphere-of-Influence Experiments

Simulating the 4DOF sphere-of-influence experiments with shooting-method propagation and the initial parameters in Table 33 is much less initially accurate than the 1DOF case with the addition of more degrees of freedom. The two extreme cases of this experiment are shown in Figure 144. Generally, the simulation overestimates the strength of the interaction, exhibiting larger amplitude responses (seen on the left) and ejection out of the magnetic potential well (seen on the right). The simulation also underestimates the damping between the planar air bearing and flat floor, which is investigated in the parameter estimation effort. The simulated timeseries approach instability between 2 – 4 cm distances. Due to the instability, the normalized RMS error across states reports nonsensical values. These initial parameter values and simulation clearly do not predict the measured dynamics well.

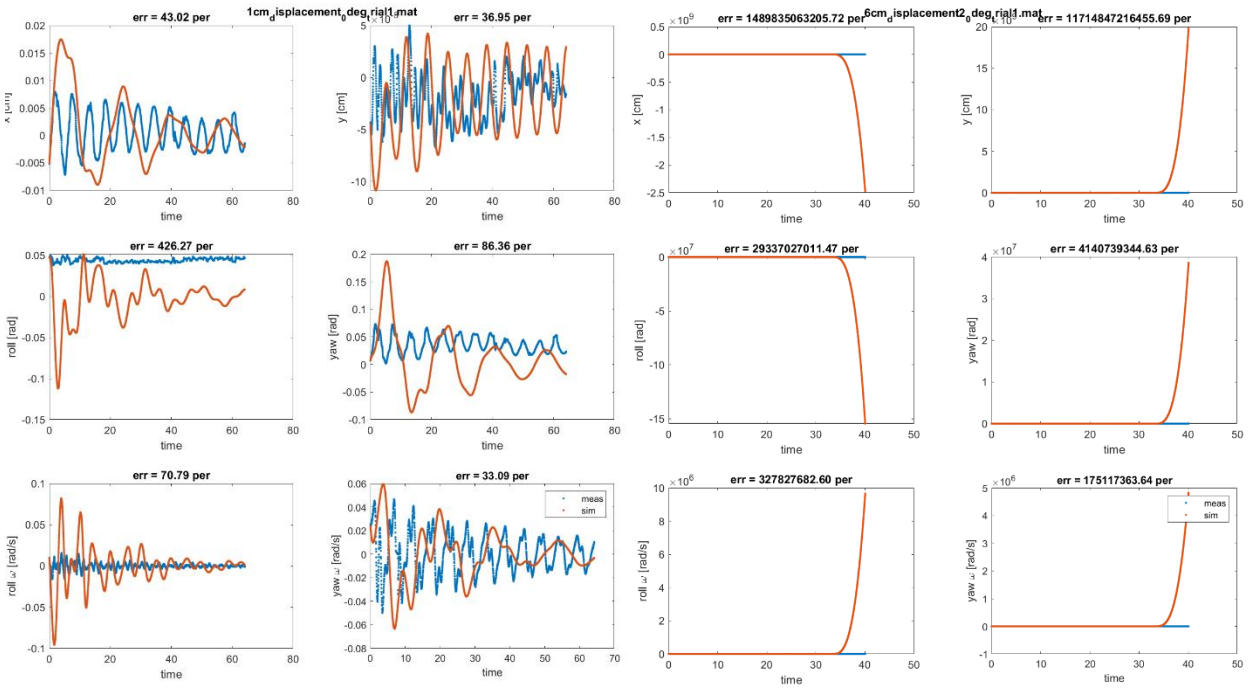

Figure 144: Sample timeseries of all six directly measured states comparing simulated dynamics of 4DOF sphere-of-influence experiment with initial parameters. Left plot displays experiment with the least initial displacement and right plot displays the most initial displacement

The prediction performance disparity between the 1DOF system simulation and 4DOF system simulation may be attributed to the degree of nonlinearity in the expressible dynamics. The 1DOF system is constrained to only move with the magnets nearly lateral to the surface of the superconductors, generating dominantly linear spring motion. In fact, the seed-generation analysis in the following symbolic regression section initially fits a linear underdamped spring expression to the 1DOF data with good initial approximation. Once the translational degrees-of-freedom are unconstrained in the 4DOF system, the flux-pinning nonlinear dynamics may be expressed fully and dominates the other less nonlinear state dynamics due to coupling. Estimating parameters in the 4DOF system is a much harder task than the 1DOF because of the nonlinear and coupled dynamics but is critical to prove the predictive capabilities moving toward a 6DOF spaceflight system.

Incorporating the optimal 1DOF parameters in Table 33 into the 4DOF refined simulation, the simulation state prediction yields less error and is unstable at a farther distance, between 4 – 6 cm. The 1DOF parameters reduce the state prediction error yet still displays overestimation of interface strength and instability at larger initial state displacements. The parameters must be further estimated with the 4DOF data to achieve the desired predictive capabilities.

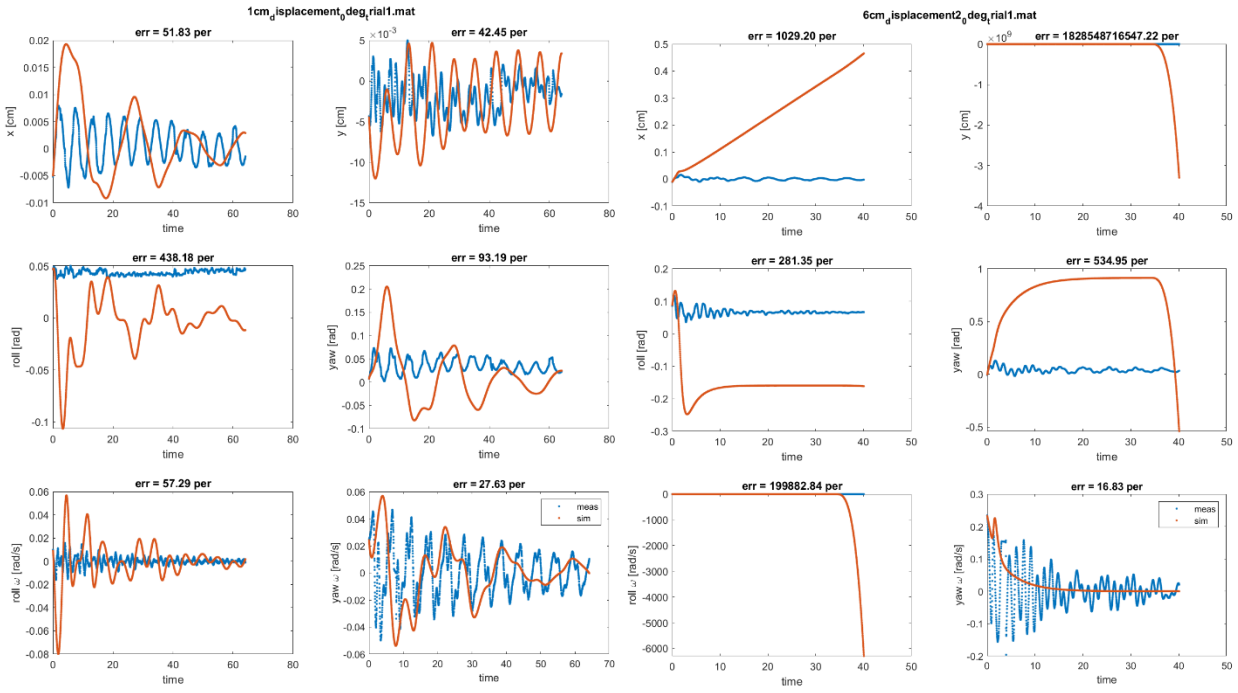

Figure 145: Sample timeseries of all six directly measured states comparing simulated dynamics of 4DOF sphere-of-influence experiment with optimal parameters from 1DOF experiments. Left plot displays experiment with the least initial displacement and right plot displays the most initial displacement

Direct-Collocation Method for Sphere-of-Influence Experiments

Over the 10 sphere-of-influence tests, the initial simulation error is bounded to 9 % across all measured states. Angular velocity in the roll direction showed the most discrepancy across all states, and translation in the normal direction (y direction) showed the least discrepancy. A driving source of error in the angular velocity measurement is bias in the IMU measurements, shown in the bottom row of plots in Figure 147. Excluding the trial with extraordinarily high IMU bias, the normalized RMS error is bounded to 3%, shown in Figure 147 and listed in Table 34.

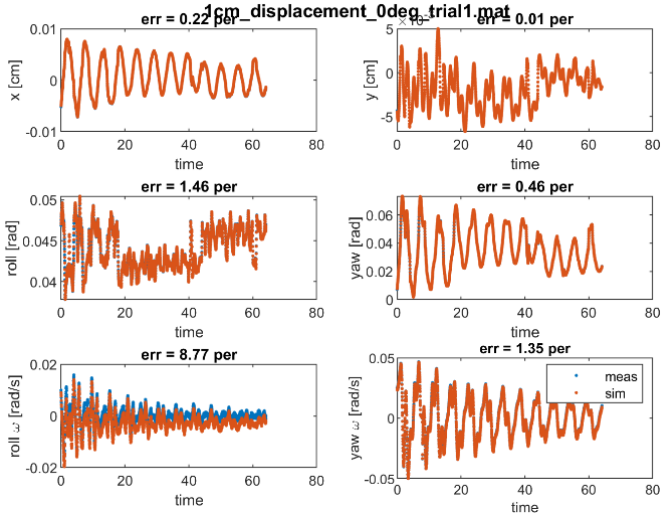

Figure 146: Sample of direct collocation propagated predictions for 4DOF sphere-of-influence experiment

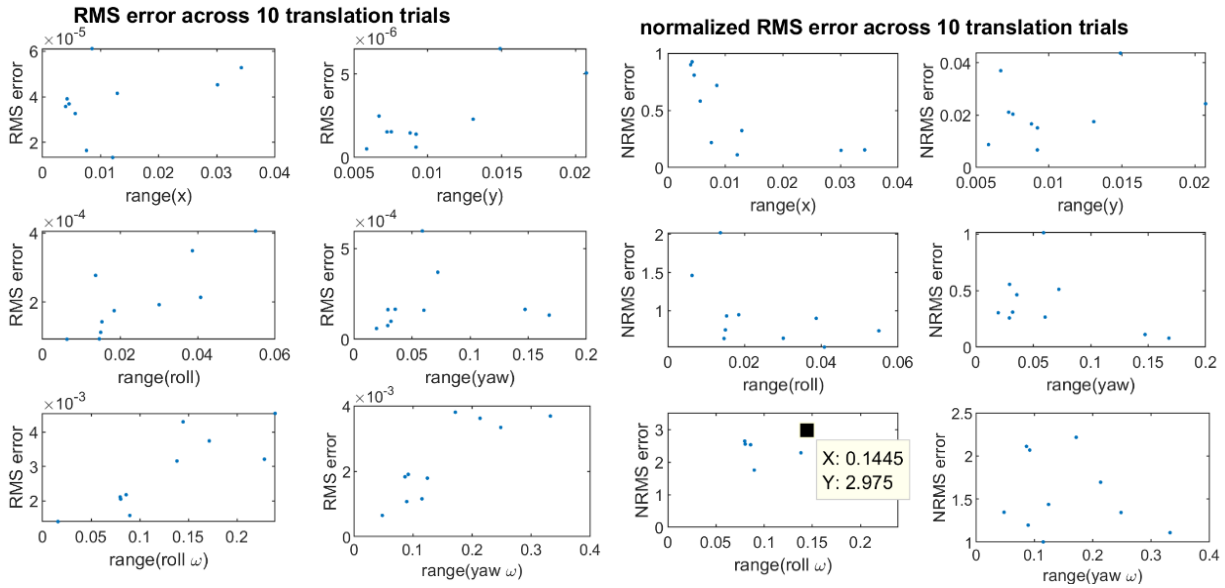

Figure 147: left, RMS error for 4DOF translation experiment trials in all directly measured degrees of freedom; right, normalized RMS error with largest state error labeled

Table 34: Initial refined simulation prediction RMS and normalized RMS error for each directly measured state across 4DOF sphere-of-influence experiments

State	x [mm]	**x %**	Y [mm]	**y %**	Roll [mrad]	**Roll %**	Yaw [mrad]	**Yaw %**	Roll rate [mrad/s]	**Roll rate %**	Yaw rate [mrad/s]	**Yaw rate %**
Median RMS	0.038	**0.45**	0.002	**0.019**	0.184	**0.825**	0.161	**0.307**	2.669	**2.410**	1.868	**1.392**
Mean RMS	0.038	**4.20**	0.002	**0.021**	0.205	**0.955**	0.198	**0.387**	2.828	**2.902**	2.285	**1.553**
std RMS	0.015	**0.33**	0.002	**0.012**	0.108	**0.457**	0.164	**0.27**	1.124	**2.115**	1.211	**0.443**
Upper bound 1σ RMS	0.052	**0.82**	0.004	**0.033**	0.313	**1.412**	0.362	**0.657**	3.952	**5.017**	3.496	**1.995**

Nearly all states (within rounding error) adhere to a target error of 5% normalized RMS error in each state. The exception to this prediction error requirement is the aforementioned outlier in roll rate bias. These translation tests are limited in number (only 10) and limited in range of state (up to 6 cm) but show that the physics model is sufficient to predict dynamics within the specified requirement and within the bounds of these initial states.

Direct-Collocation method for Natural-Mode experiments

Across the 103 natural-mode experiments, the initial simulation error is bounded to 16 % across all measured states. A sample of the natural-mode experiment data and a simulated response with direct collocation is shown in Figure 148. Framing the prediction performance of the simulation varies with the

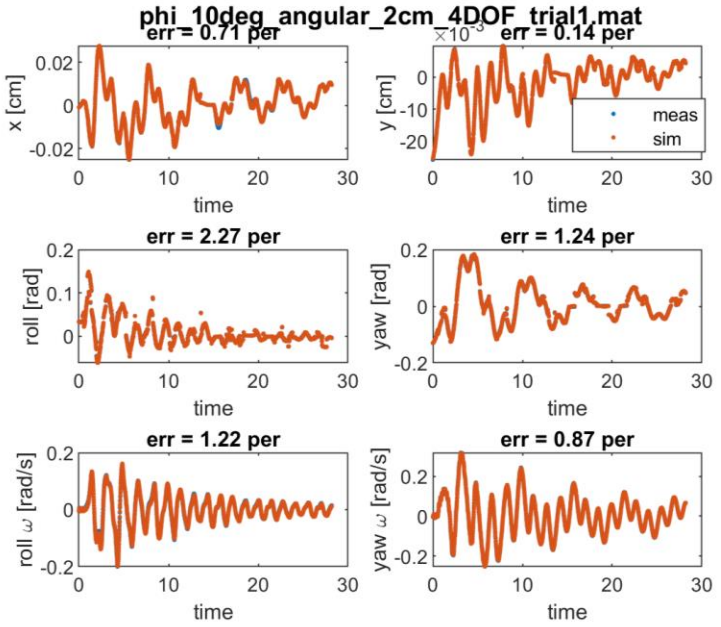

Figure 148: Sample of direct collocation propagated predictions for 4DOF natural mode experiment

consideration of RMS error or NRMS error, with all error values for each state listed in Table 35 and illustrated in Figure 149. For RMS error, translation in x shows a mean error up to 1 mm and translation in y up to 0.1 mm across various ranges of position. RMS error in the angular states is linearly proportional with the range of measured data within that trial, which seems reasonable if the simulation scales accordingly and normalization would better capture that scalar. For normalized RMS error, x position and roll data show an asymptote at the origin regardless of the absolute RMS error as the range of that state approaches zero. The normalized RMS error is very sensitive to noise for trials with very little range in motion, although the RMS error remains sensible, as the normalization doesn't account for the persistence of noise even as the range of state diminishes.

Table 35: Initial refined simulation prediction RMS and normalized RMS error for each directly measured state across 4DOF natural-mode experiments

State	x [mm]	**x %**	Y [mm]	**y %**	Roll [mrad]	**Roll %**	Yaw [mrad]	**Yaw %**	Roll rate [mrad/s]	**Roll rate %**	Yaw rate [mrad/s]	**Yaw rate %**
Median RMS	0.072	**0.627**	0.017	**0.18**	2.00	**2.33**	1.40	**1.16**	2.19	**1.18**	1.60	**0.92**
Mean RMS	0.171	**2.24**	0.024	**0.23**	2.13	**3.73**	1.39	**1.42**	4.36	**1.45**	1.87	**1.04**
std RMS	0.203	**4.20**	0.026	**0.18**	0.97	**9.28**	0.53	**1.06**	4.29	**1.22**	0.84	**0.65**
Upper bound 1σ RMS	0.4	**6.4**	0.05	**0.4**	3.1	**13**	1.9	**2.4**	8.8	**2.7**	2.7	**1.7**

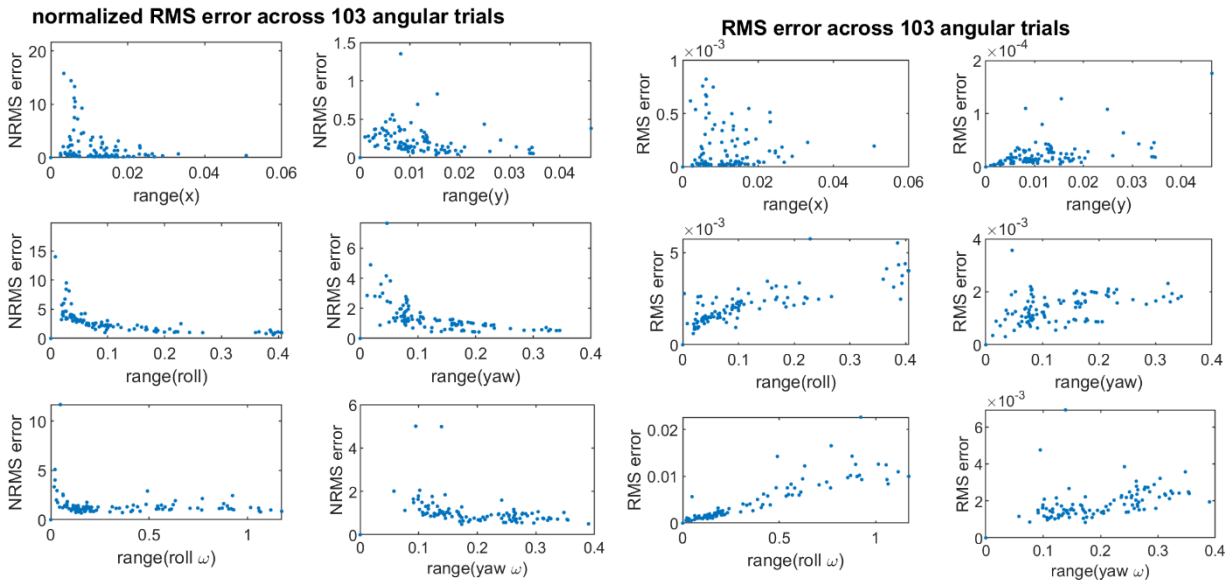

Figure 149: left, normalized RMS error for 4DOF angular experiment trials in all directly measured degrees of freedom; right, RMS error

The only state to adhere to a target error of 5% normalized RMS error is y position. The NRMS error of the other states are penalized very heavily if the range expressed in the timeseries is small; an unfair penalization for a system that expresses coupled dynamics. Looking at RMS error, both position state errors are bounded to 1 mm and angular resolution is bounded to 0.3 degrees even for large angle displacements up to 23 degrees. To fairly evaluate trials that accurately predict dynamics across most states but suffer from the minimal expression in a single state, the normalized RMS error is averaged across all six directly measurable states, seen in Table 36. The average normalized RMS error of all states per trial does reach the target error of 5% normalized RMS error across all experiment trials. The baseline simulation seems promising but still needs to be improved by incorporating the effect of physical parameters and estimating the values of the physical parameters.

Table 36: Initial refined simulation prediction normalized RMS error for each directly measured state across 4DOF natural-mode experiments with the averaged normalized RMS error across every state per trial

State	x %	y %	Roll %	Yaw %	Roll rate %	Yaw rate %	Avg. % across all states
Median RMS	**0.627**	**0.18**	**2.33**	**1.16**	**1.18**	**0.92**	**1.33**
Mean RMS	**2.24**	**0.23**	**3.73**	**1.42**	**1.45**	**1.04**	**1.47**
Standard deviation RMS	**4.20**	**0.18**	**9.28**	**1.06**	**1.22**	**0.65**	**0.92**
Upper bound 1σ RMS	**6.4**	**0.4**	**13**	**2.4**	**2.7**	**1.7**	**2.4**
Maximum RMS	**15.8**	**1.35**	**14**	**7.7**	**11.7**	**5**	**4**

Mixing Frequency and Time Domain for Sphere-of-Influence Experiments

The shooting-method and direct-collocation error metrics show immensely different predictive performance for the 4DOF refine dynamics simulation. Learning from the previous 1DOF analysis, the direct-collocation error minimization does not generalize well, as the resultant parameters showed poor performance with another propagation scheme. The shooting method integrated large frequency errors and the frequency-domain metric did not account for amplitude response. Instead, a new multi-objective function is defined that incorporates the shooting-method-propagated error metric and the frequency-spectra spread.

$$J(\boldsymbol{s}_{meas}(t), p) = \sum_{t=0}^{t_f} \frac{\sqrt{\left(s_{meas}(t) - s_{sim}(t, s_{meas}(t_0), p)\right)^2}}{n_t \ \text{range}(s_{meas})} * \sum_{f=0}^{f_f} \frac{\sqrt{\left(P(s_{meas}) - P\left(s_{sim}(s_{meas}(t_0), p)\right)\right)^2}}{n_f \ \text{range}(\text{P}(s_{meas}))} \quad (110)$$

J is the objective function the incorporates time-domain state error and frequency-domain spectra error, fully expressed in Eq. (110). The time-domain error matches the initial large motion while the frequency-domain error matches the small motion that happens at steady state. Expecting the time histories to match for long periods of time is unrealistic as small perturbations manifest into large state error as oscillations become directly out of phase. t represents time. t_f is the final time of interest for the objective function. The chosen time is 10 seconds, which completes about one full period of the slowest mode. p represents the physical parameters that affect the dynamic

behavior of the system. $s(t)$ is the dynamic state of interest over time, all relative to the equilibrium state. The simulation generated state over time takes in the initial state from measurements and physical parameters of the system. $s_{sim}(t, s_{meas}(t_0), p)$ implicitly encodes the analytical physics model and continuous system integration. n_t is the number of samples in the time history. f represents frequency. f_f is the final frequency of interest for the objective function. The chosen maximum frequency is 3 Hz, which is nearly always 3x greater than the fastest mode. $P(\cdot)$ is the fast Fourier transform of a time series

A sample of a translation experiment data with the optimal parameters is shown in Figure 150 with the resulting simulated time history and frequency spectrum. The dominant frequency peaks match up well, but the amplitude response doesn't match as well. The rotation θ proved to be a difficult state to match. While the other three degrees of freedom matched, the simulation overestimated the roll significantly. The cost was so significant for some trials that the optimization algorithm would flip to matching only the roll state at the expense of the three other states.

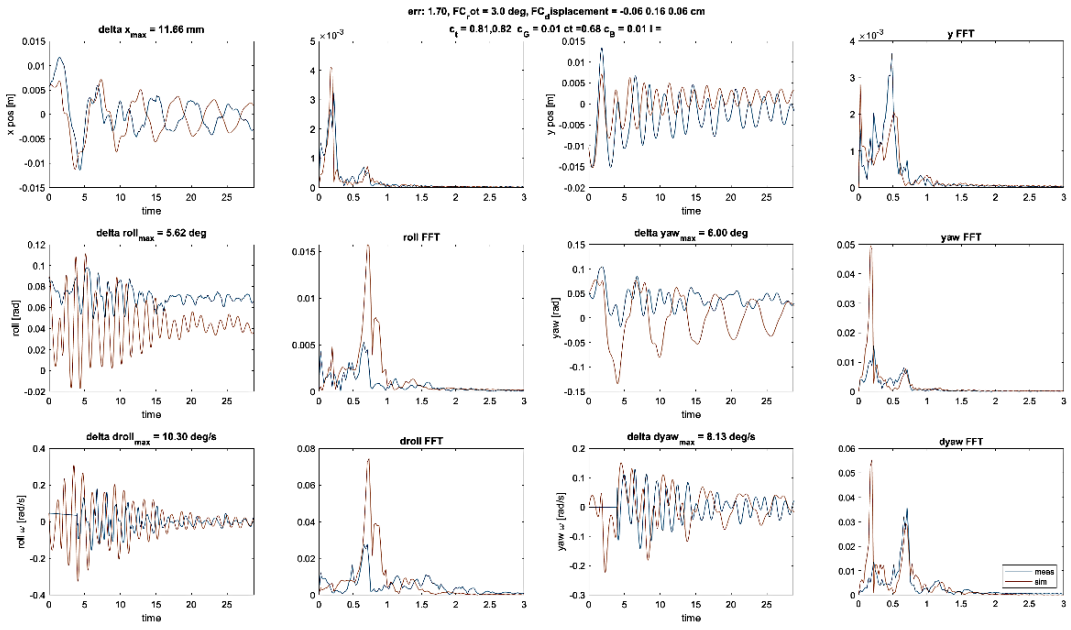

Figure 150: Sample of shooting method propagated predictions for 4DOF sphere-of-influence experiment with optimally estimated parameters from multi-objective function

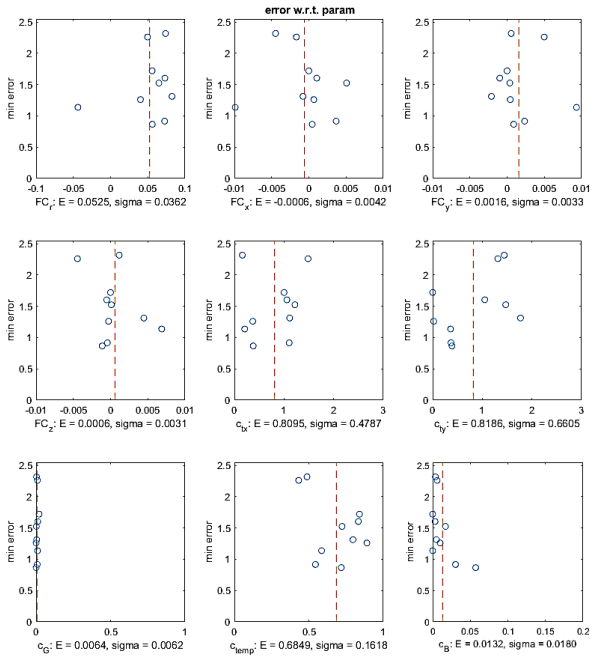

Figure 151: multi-objective error and optimal parameters generated from multi-objective function for 4DOF sphere-of-influence experiments

Table 37: optimal parameters generated from multi-objective function for 4DOF sphere-of-influence experiments, mean and standard deviations

Parameter	Mean	Std
θ_{FC}	0.052	0.036
x_{FC}	-0.0006	0.004
y_{FC}	0.0016	0.003
z_{FC}	0.0006	0.003
c_{tx}	0.81	0.48
c_{ty}	0.82	0.66
c_G	0.0064	0.0062
c_{temp}	0.68	0.16
c_B	0.013	0.018

The optimal parameters generated from the multi-objective function are shown in Figure 151 and listed in Table 37. The x limits represent the lower and upper bounds called in the fmincon function. The y limits are scaled to the maximum error. The values for field-cooled rotation are rather consistent with a single outlier. The standard deviation shows confidence within 2 degrees. Position seems nearly centered, which is ideal

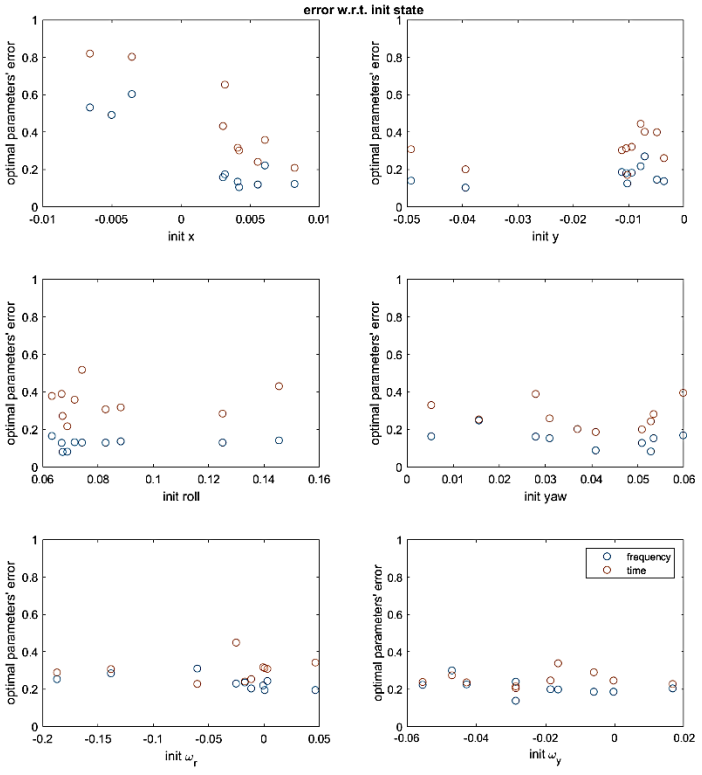

Figure 152: individual error metrics for each state when optimizing multi-objective function for 4DOF sphere-of-influence experiments

and suggests good control during field cooling. The standard deviation lays with 4 mm and none of the degrees of freedom are pushing against the bounds of the optimization constraints. The damping parameters, c_{tx} and c_{ty}, in the translation directions average to the same value, which is validating. The two friction terms are expected to match as they are from the same source. Unfortunately, the damping parameters are not centrally located; the damping is not consistent between different trials. The damping model may need a more extensive model, perhaps with higher order terms. The rotational damping parameter had a large search space and converged with very small margin to a small value consistent across all trials. The damping coefficient of the bearing also had generally the same values given a large search space, but the error margin is larger than the expected value. The expected value for coefficient of temperature is close to the experimental finite dimension coefficient, which is validating, but the standard deviation for these parameters estimate is large.

The refined simulation is not perfect but offers improved performance over the baseline frozen-image model. Predictions for the immediate subsequent state is quite accurate but the open loop integration for long periods of time diverge. The frequency spectra predict the measured natural frequencies, relevant for states close to equilibrium, but less can be said about the large motion nonlinearities. The optimizer tends to minimize frequency error more effectively than time history error, as seen in Figure 152, which is understandable from small errors compounding/propagating through the rest of time. This analytical model is rather predictive of close-proximity interactions. More work lies in the nonlinearities of states farther from equilibrium and understanding the overestimation of the roll θ state but this work would be immensely tedious. Instead of focusing more energy into the 4DOF data, 6DOF microgravity tests does not contain the physical friction that the 4DOF tests contain. The damping source from microgravity tests

isolate damping into eddy current and air drag effects. The full degrees of freedom are expressed, allowing all the coupled modes to be expressed.

c. *Predicting Dynamics from 6 Degree-Of-Freedom Experiments*

Of the Vicon data that was collected, the Vicon software did not resolve consistent position and attitude information. Without position and orientation data, a dynamics simulation does not have known initial conditions to propagate dynamics with the shooting method or with the direct-collocation method. Instead, initial position and attitude were estimated in the frequency domain by matching dominant natural frequencies measured from the IMU's gyroscope and accelerometer. A sample of microgravity data is shown in Figure 153.

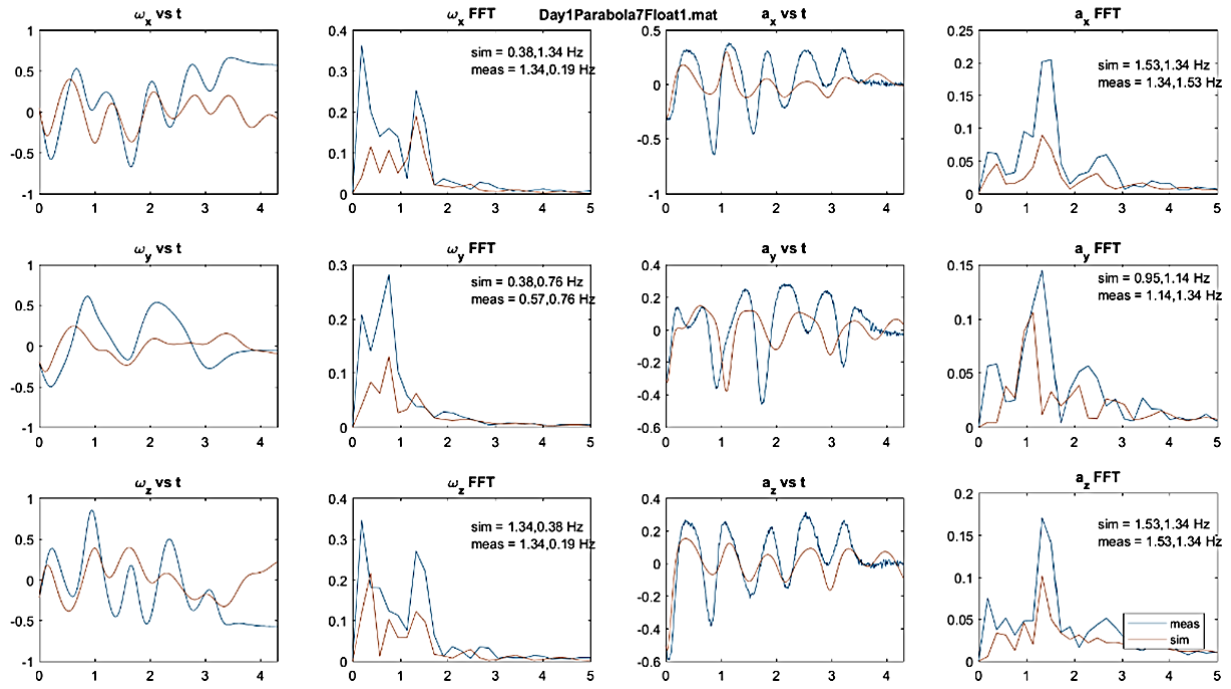

Figure 153: OSA IMU timeseries and frequency spectra comparison generated with estimated initial conditions

From a range of simulated initial conditions, a histogram compared the occurrence of 6DOF natural frequencies measured in the experiment and generated from the baseline simulation,

Figure 154. Coupled dynamics link common natural frequencies between rotation and translation modes so the histogram does not distinguish between different modes. Granted that the resolution of FFT is rather coarse and the simulated dynamic profile is not generated from measured initial conditions, the conclusions are purely at a high level. The measured dynamics generally have less stiff interactions (slower natural frequencies). Due to the symmetry of the OSA magnetic field source, four natural frequencies are predicted in system, reflected in the FFT analysis. Understanding that the 6DOF predictive dynamics model is of utmost importance, the April tag data from the GoPro video footage is incorporated into detailed analysis like the prior reduced DOF testbed experiment data.

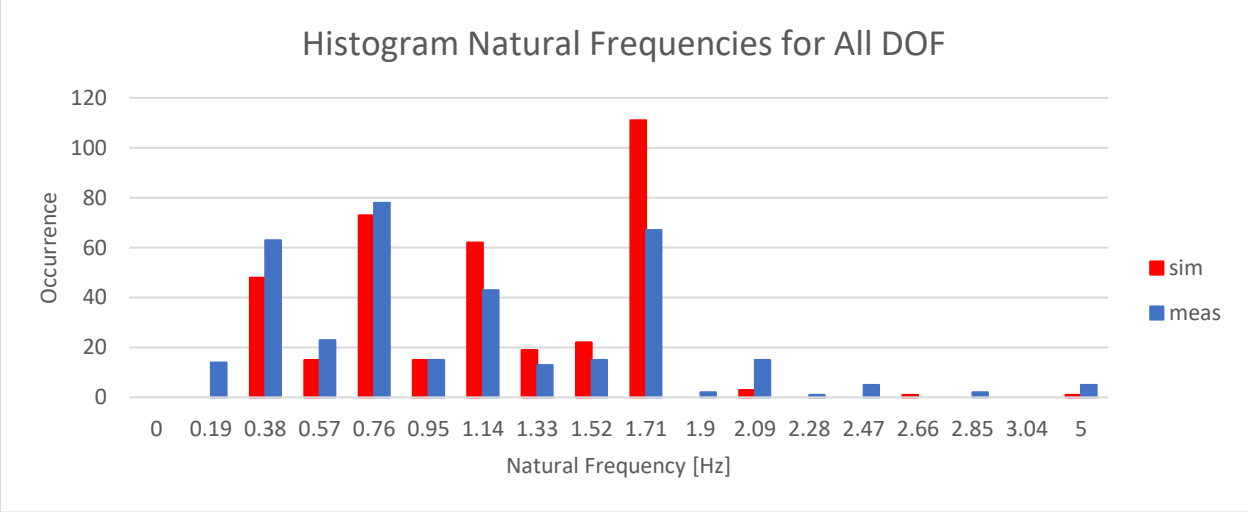

Figure 154: histogram of simulated and measured natural frequencies from the OSA IMU during the 2017 microgravity flight experiments

IV. Symbolic Regression with Genetic Algorithms

The symbolic regression analysis only focuses on the dataset for the 1DOF experiments, which includes 54 separate trials. Each individual trial is split into a training set and evaluation set by alternating each measurement in the timeseries. The symbolic regression algorithm only has access to the training set during the optimization process and is then evaluated on the evaluation

set for predictive accuracy. The independent variable is time with the dependent variables as angular displacement θ measured by Vicon and angular velocity ω measured by the internal IMU. The output expression is of the form $x = f(t)$ where x is the angle or angular velocity state. The metric to optimize is root mean square error, RMS, set at a threshold 1% the range of the state.

a. *Structure*

The symbolic regression toolbox is driven by genetic algorithm that represents mathematical expressions with binary expression trees. Through the analogy of gene evolution, these trees are mixed, mutated, and strategically selected so that each iteration's solutions are incrementally better solutions until an objective is met [142]. The GPTIPS2 toolbox diverges and improves capabilities from conventional genetic programs in its superposition of multiple binary expression trees, instead of a single, deep expression tree [143].

To search the space of mathematical expressions, a library of operators lays the foundation for a binary expression tree's nodes. For my configuration code, the library includes: the negative exponentiation $e^{-(\cdot)}$, regular exponentiation $e^{(\cdot)}$ elementwise division, multiplication, addition, subtraction, sinusoid $\sin(\cdot)$, quadratic $(\cdot)^2$, square root $\sqrt{(\cdot)}$, cubic $(\cdot)^3$, power $(\cdot)^{(\cdot)}$, negation $-(\cdot)$, absolute value $|(\cdot)|$, and logarithmic $\log(\cdot)$. Although some operators are specific incarnations of the more generic operators or a composition of other operators, the expanded set allows for quicker convergence as these specific operators occur frequently in physical expressions. The baseline algorithm does not have a particular model initialized as a consistent starting point, called a seed, but randomly initializes a set of binary expression trees.

b. *Hyperparameters*

The genetic algorithm has specific hyperparameters that are user-defined, such as population size, tournament size, pareto parameters, selection rate, and maximum number of genes. The algorithm is not guaranteed to converge so a termination criterion, timeout threshold, is also predefined. The hyperparameters that were held constant are listed in Table 38.

Table 38: Symbolic Regression Genetic Algorithm User-Defined Hyperparameters

Algorithm Hyperparameter	Numerical Value
Population Size	250
Number of Runs to Merge	2
Tournament Size	20
Pareto Parameter	0.3
Generational Selection Rate	0.3
Termination Timeout Criterion	1200 seconds

There are several features and modifications changed in the code package regarding sparsity, seeding, and termination criteria. Natural laws of physics are sparse and minimalistic in nature [144]. To give the algorithm a huge computational advantage, an expression similar to the real system, an underdamped linear spring, injected or seeded. The parameters within the expression were primed with estimated parameters from a nonlinear programming solver that minimizes RMS error. Finally, the default termination criterion is based upon run-time of which a threshold in RMS error was added. The next section offers a description of the seed generation and the section concludes with the symbolic regression results.

c. *Seed Generation*

An intermediate analysis, with the goal of seeding the genetic algorithm, is finding an approximate expression for the data in the form of a linear underdamped spring. The ordinary

differential equation solution is shown in Eq. (111), where A_0 is a scalar incorporating initial state, ζ is a damping ratio, ω_n and ω_d are natural and damped frequency respectively, ϕ is a phase shift, and b is the state bias. From the physics-based model, the true underlying motion is dictated by a nonlinear underdamped spring. A first order approximation is linear and the nonlinearities may be approximated as higher order terms in the ordinary differential equation solution. The direct extension for this strategy incorporates the first order approximation as the seed and the genetic algorithm then generates the higher order terms.

$$s(t) = A_0 e^{-\zeta \omega_n t} \sin(\omega_d t + \phi) + b \tag{111}$$

The form of the solution is static, but the parameters are estimated for each trial with MATLAB's nonlinear programming solver, fmincon. Each trial is evaluated separately for both the angular displacement and angular velocity measurements; a sample is shown in Figure 155. All data points in each timeseries are used in minimizing RMS error. The parameters are then compared across all trials to validate consistency and reveal any physical insight, shown in Figure 156.

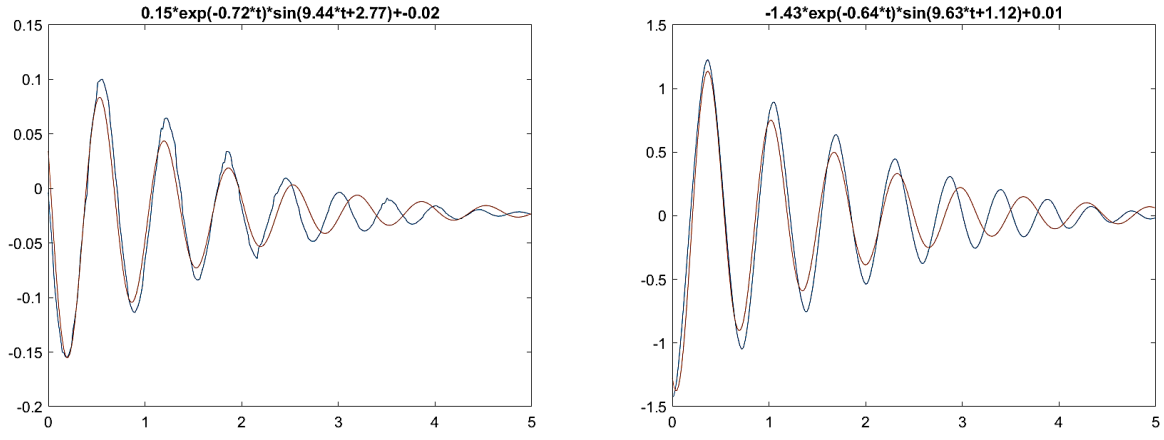

Figure 155: Sample of fmincon fitted expressions assuming a linear underdamped spring, angular displacement timeseries on left, angular velocity timeseries on right in which red is the simulation and blue is measurements

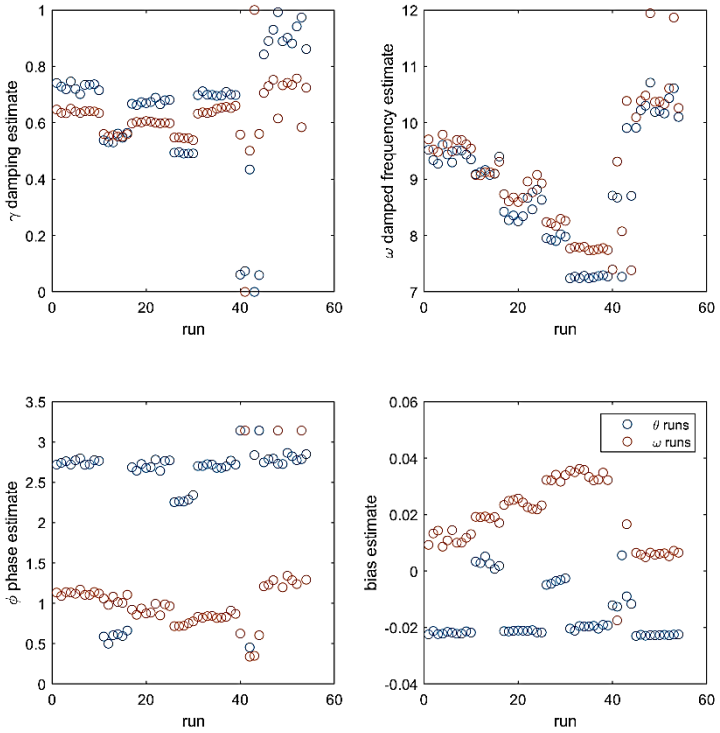

Figure 156: Estimated parameters from fmincon across all 1DOF experiments

Several high-level conclusions are drawn from the estimated parameters, reported in Table 39, where median values are reported to avoid the effect of outliers. By incorporating an inertia estimate of 0.004429 kg m^2 about the spindle, the stiffness and damping values are calculated. From Figure 156, estimates for damping and damped frequency are consistent across the angular displacement and angular velocity states, as they should because the two measured states represent the same degree of freedom. The phase estimates between the two measured states is predictably offset by $\frac{\pi}{2}$. The bias estimates differ dependent on the sensor measuring the particular state. The damping and frequency estimates noticeably vary across different experiment trials, which are broadly clustered in differing initial conditions. The variance is attributed to the nonlinearity of the underlying physics, where larger initial conditions manifest a more dominant nonlinearity.

Table 39: Median estimated parameters for the two measured states

	τ	ω_d	ζ	ω_n	k	c
θ dataset median	0.697	8.9441	0.0777	8.9712	0.3565	0.2779
ω dataset median	0.633	9.0743	0.0696	9.0964	0.3665	0.2541

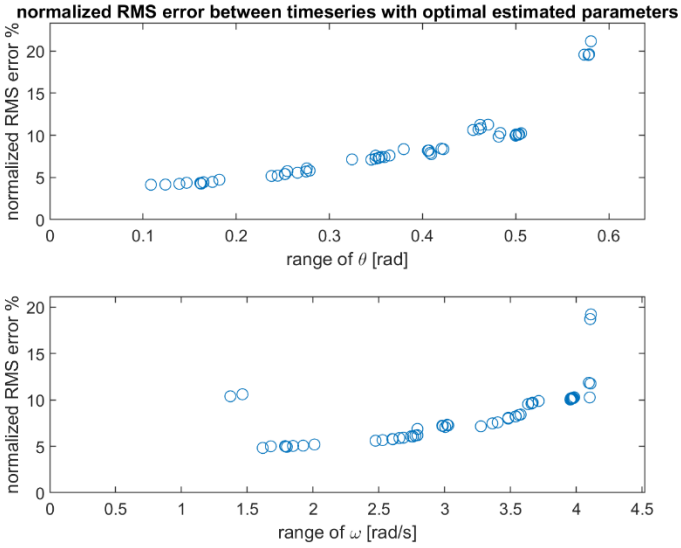

Figure 157: Normalized RMS error for each state with optimal estimated parameters

The normalized RMS error of a linear underdamped spring fit range from 4 % to 21 %, seen in Figure 157. The resultant normalized RMS error from a parameter estimated linear underdamped spring fit shows increasing error as the range of the state (initial condition) increases. Nonlinear dynamics are more significant in the larger displacements from equilibrium; thus, the linear fit is less accurate for these larger displacements.

d. *Prediction and Interpretability*

In the following analysis, two aspects of the algorithm changed: maximum number of genes and the decision to seed or not seed the algorithm. The maximum number of genes, or maximum tree depth, varied between 1, 2, 4, and 10, which is analogous to the increasing complexity of the mathematical expression. If the genetic algorithm is to be seeded, the seed is the ODE solution to the linear underdamped spring with the optimal parameters generated from

fmincon. Additionally, a strict sparsity condition is imparted on each expression in which subexpressions that do not change the overall RMS error significantly are excluded. The results from each combination of algorithm hyperparameters is shown in Figure 158.

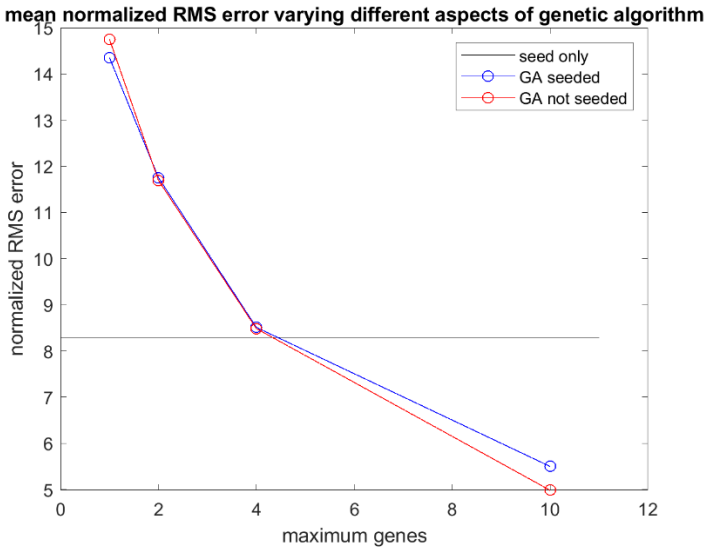

Figure 158: mean normalized RMS error varying number of genes and seeding

The genetic algorithm must perform better than the first order approximation to justify this method. From Figure 158, the output RMS error is shown not to differ greatly from initializing the algorithm with or without a seed. Intuitively, the runs that are seeded should perform at least as well as the baseline seed alone, but the algorithm may abandon the seed immediately as it does not adhere to the user-defined maximum gene requirement. The maximum number of genes greatly effects the predictive and expressive ability of the expression approximating the data, where 1-2 genes is not as expressive enough as the baseline first order approximation, 4 genes is comparable to the baseline, and 10 genes is more expressive than the baseline. Although adding more genes decreases the evaluation error, the resultant mathematical expression is at risk of overfitting the data, whereas the smaller number of genes are certainly underfitting. Enforcing a sparsity condition promotes a minimalistic representation of the output expression.

A closer look at the resultant mathematical expressions from each combination of hyperparameters yield intuition to the model tradeoff between accuracy and interpretability, dispersed between Figure 159 and Figure 162. Each figure is organized in the following fashion. Each row separates approximation for the angular displacement timeseries and the angular velocity timeseries. The first column is an overlaid timeseries plot of the real data, the genetic algorithm's full output expression, each subexpression, and a post-algorithm sparsity requirement on the genetic algorithm full output expression. The overlaid timeseries gives a quick indication of approximation accuracy between the real data and the GA output, the dominance of child subexpressions from the GA output, and the effect of a sparsity condition on the GA output. The second column is the normalized RMS error of the GA output if a selected child subexpression were to be excluded and the title RMS value represents the entire expression accuracy. This comparison indirectly shows the significance of this subexpression in the overall expression and for expressions that contribute less than 1% RMS error, the sparsity condition disposes of this subexpression. The third column is similar as each child subexpression of the GA output is evaluated individually and the dominant expression produces the least amount of disagreement with the real data, with the dominant expression's RMS error shown in the title. Ideally, the dominant subexpression forms the first-order approximation and the remaining subexpressions capture the higher-order effects, with the addition of each subexpression asymptotically decreasing the error in approximation.

None of the results from any combination of hyperparameters from the genetic algorithm yield mathematical expressions that were sufficiently accurate, interpretable, or consistent across all trials. The true expression should persist consistently across all trials as the dominant expression with the changing terms expressing noise. The results with 1 maximum gene have huge variability

in the form of the dominant expression, inconsistent even between the two states of the same experiment run, instilling very little trust in the validity of the resultant expression. The GA subexpressions are more human interpretable, and the GA bias term matches the bias estimate from the fmincon results, but the overall accuracy does not fulfill the target 5% RMS error. The results with 10 maximum genes have huge variability in the composition of child expressions, not only subexpressions in the overall expression within a single experiment but also across each experiment. Although the GA output approximates to RMS error below 5%, the lack of consistency does not demonstrate results grounded in a physical system that generated the data but is more likely a conglomeration of random expressions that happen to approximate the data well, the trap of a local well in a high-dimensional space. In conclusion, genetic algorithms geared towards symbolic regression can approximate this dataset well but does not offer the physical insight to produce a trustworthy analytical model.

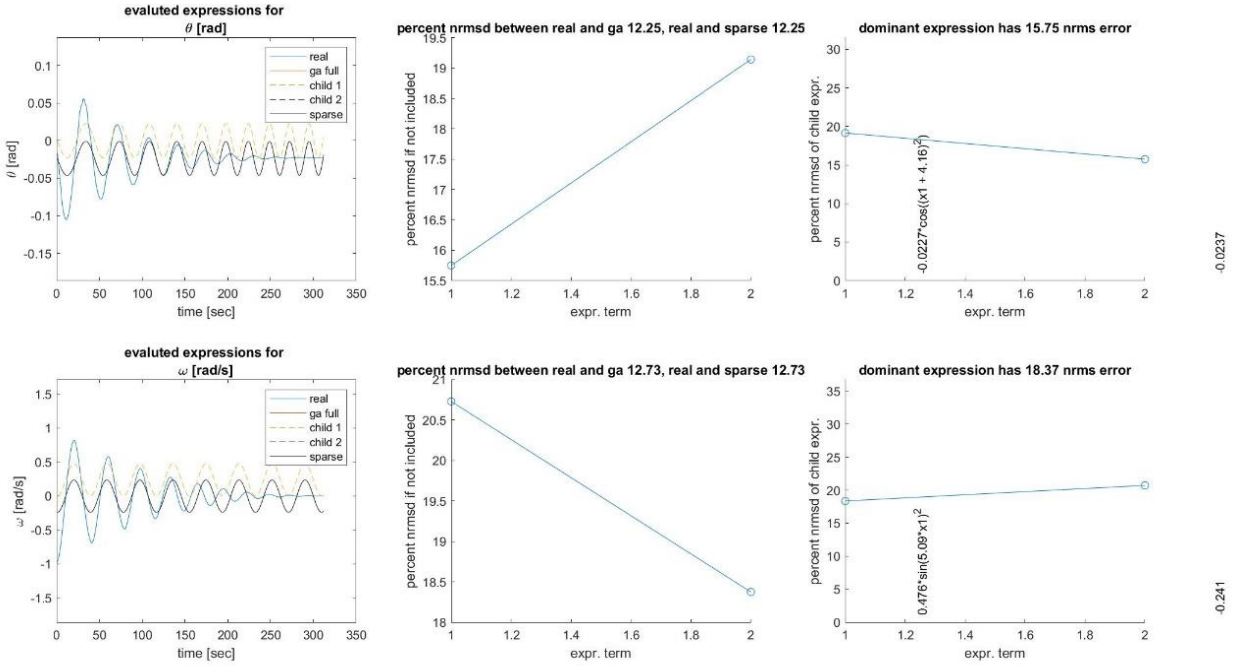

Figure 159: Sample output expression, resultant error, and dominance of subexpressions for a genetic algorithm run with 1 gene and no seeding

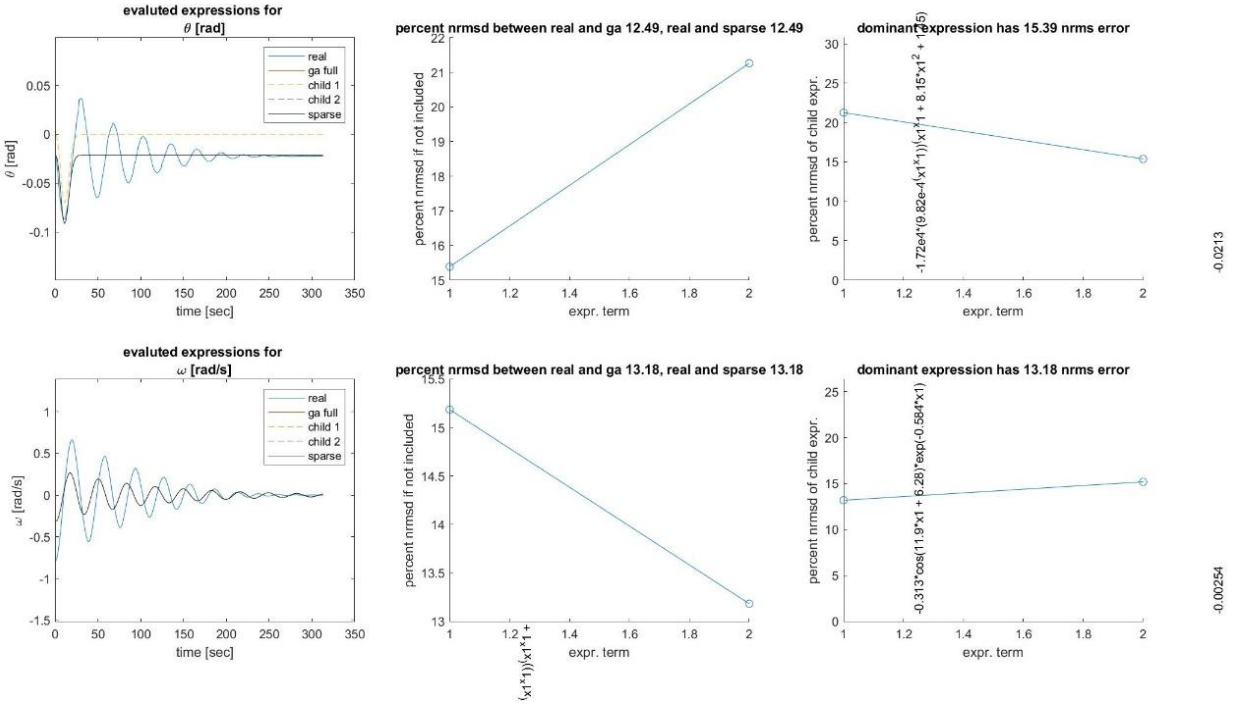

Figure 160: Sample output expression, resultant error, and dominance of subexpressions for a genetic algorithm run with 1 gene and seeding

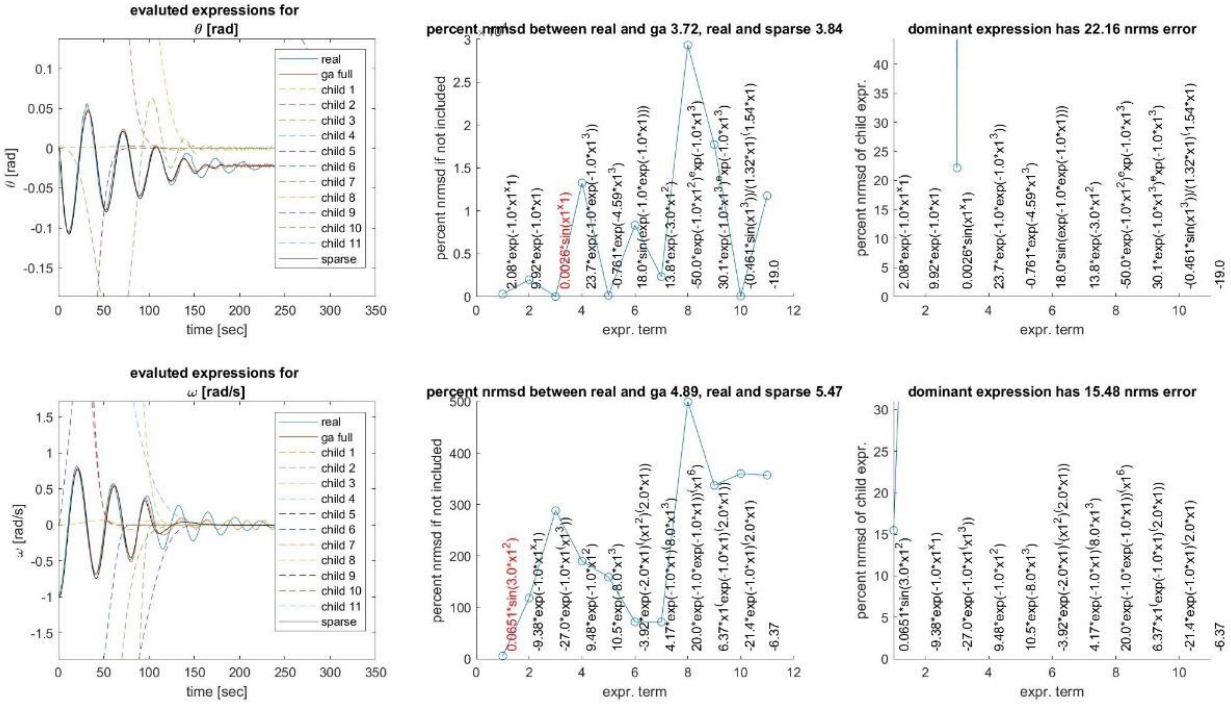

Figure 161: Sample output expression, resultant error, and dominance of subexpressions for a genetic algorithm run with 10 genes and no seeding

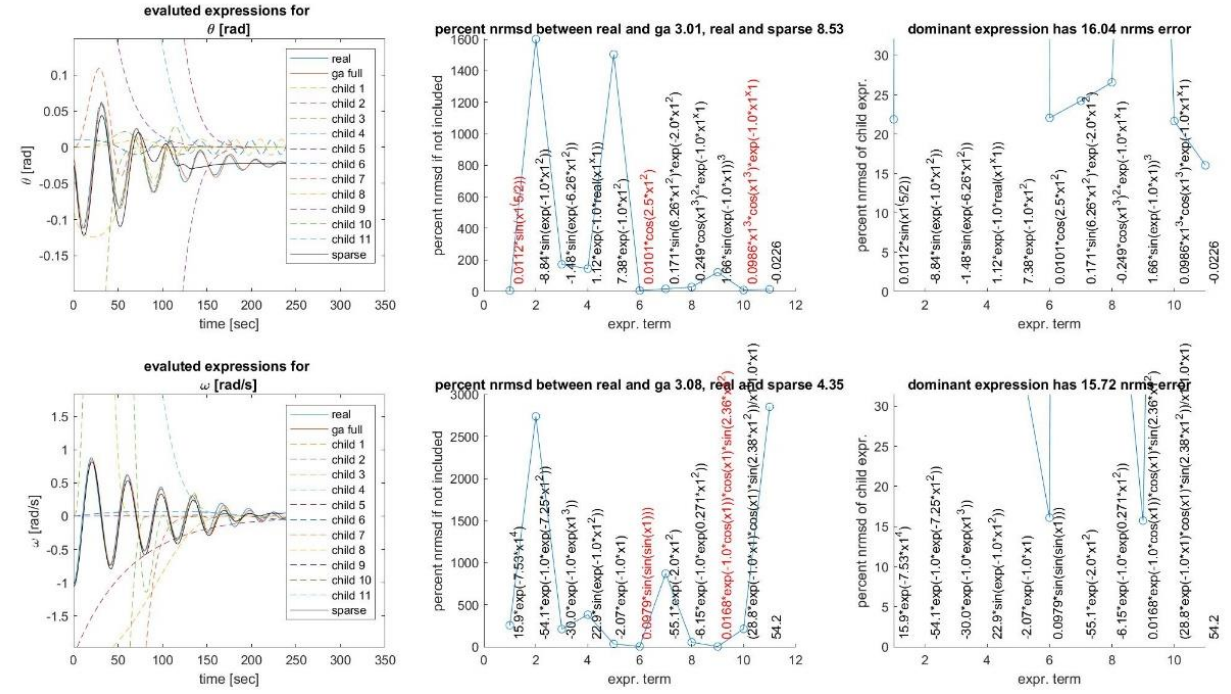

Figure 162: Sample output expression, resultant error, and dominance of subexpressions for a genetic algorithm run with 10 genes and seeding

V. Neural Network Function Approximation

The neural-network structure used in this body of work is a fully-connected feedforward neural network. This structure predates to 1958 when Rosenblatt created the basic unit of the artificial neural network, the perceptron [145]. Many basic perceptron units stacked together created a layer of neurons, and stacking layers creates a neural network. The neural network's ability to approximate nonlinear mappings and to learn these mappings directly from data make them a very popular technique for a variety of applications, including dynamic state prediction. The dynamics of a flux-pinned system is extremely nonlinear and coupled but the state transition is still well-behaved in the sense that the dynamics are deterministic and continuous. The MATLAB neural-network toolbox and data collected from the reduced DOF testbed create approximate models to completely replace the dynamics model or to compensate for the error in a simulation prediction.

The neural network replacing the simulation in its role as the dynamics model is given in Eq. (112) and the error-compensation model metric is given in Eq. (113). The input and output pairs are state at k and next state at $k+1, (s_k, s_{k+1})$. The neural network tries to minimize direct-collocation propagated error. e_{k+1} is the error between the measured next state s_{k+1} and the state propagated from a previous measured state s_k from a neural network f_{NN}. To reiterate the direct-collocation equation from the error metric section, the function $f(\cdot)$ is specifically labeled as the neural network mapping predicting the next state.

$$e_{k+1} = s_{k+1} - f_{NN}(s_k) \tag{112}$$

$$e_{k+1} = s_{k+1} - \left(f_{sim}(s_k) + \Delta f_{NN}(s_k)\right) \tag{113}$$

The data used in training the neural network uses evenly sampled measurements. The dataset is separated into training and evaluation sets by alternating every other time step in every timeseries due to achieve uniform sampling. The 50/50 dataset split differs from the convention of an 80/20 training evaluation split, which results in less training data for the neural network to learn a mapping. But as the results show, the neural network shows terrific prediction performance despite this handicap. To address a concern related to neural network approximation regarding overfitting, the approximate models not only minimize least-squares loss but also use the minimal representation (by minimizing the number of necessary parameters).

a. *Predicting Dynamics from 1DOF Experiments*

Full Model Approximation

With measurements of attitude and angular rate accumulated from the 1DOF experiments, a single-hidden-layer neural network of varying numbers of neurons were trained on the same dataset. The training error, reported in normalized RMS error, from a single neuron in the only hidden layer of the neural network immediately reports RMS error less than 5%, seen in Figure 163. To ensure consistent performance, the neural network was initialized, trained, and evaluated five different times in which mean and standard deviation curves represent that distribution. The sensitivity figure also shows little improvement in error beyond 2 neurons. To avoid overfitting, the neural network to

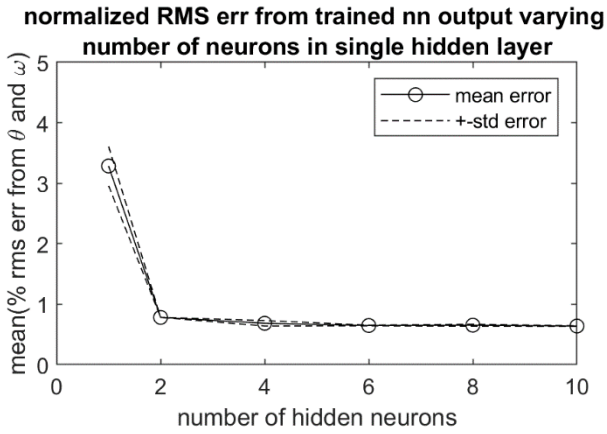

Figure 163: sensitivity analysis of normalized RMS error with respect to number of neurons in 1DOF experiment dataset

proceed forward in this analysis only contains the minimal number of parameters associated with 2 neurons.

After training a neural network with 2 neurons, the evaluation error, prediction error of unseen inputs, yield a mean normalized RMS error of 2.6% averaged between all predictions in both states. The simulation performs with 1.4% RMS error. A comparison of the NN predictions and physics-based model predictions overlaid on the target measurements is shown in the right plot in Figure 164, with the mean RMS error % of each trial separated by state in the left plot. The results indicate that the neural network does not perform as well as the physics-based simulation in predicting attitude, θ, but performs better than the simulation in predicting angular velocity. This result is a misleading as the measured attitude data is discontinuous and the NN is correctly compensating for the discontinuities through smoothing. The NN-generated attitude time histories seem more accurate to a physical model and the measurements seem worse than the NN predictions based on user intuition, despite hard data. For the neural network to achieve less prediction error than the physics model, the next method compensates for error in the physics model prediction, which guarantees better performance if the neural network learns anything in the right direction.

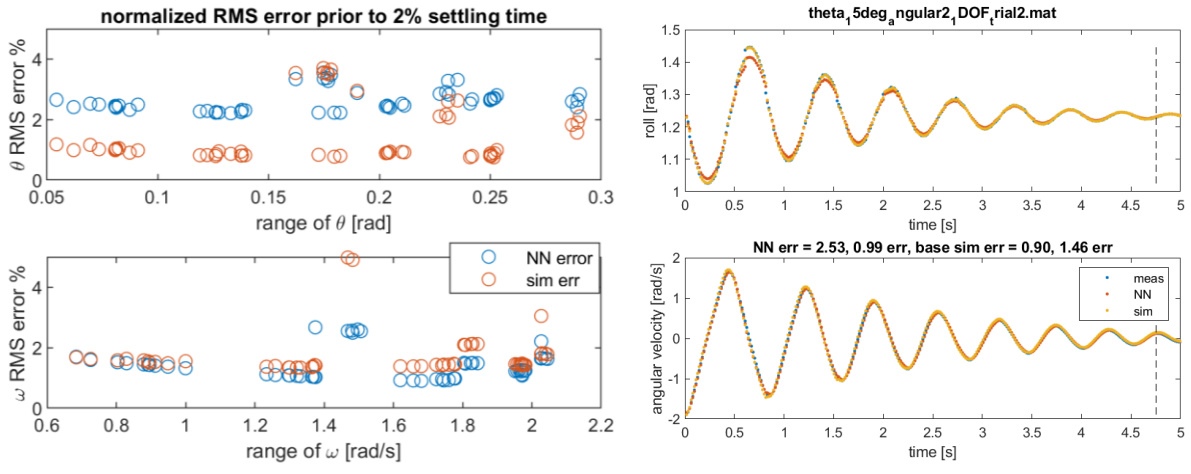

Figure 164: left, normalized RMS error approximating entire 1DOF model with 2 neurons across all experiment trials; right, sample of measured 1DOF data, simulation prediction, and NN prediction

Error-Model Compensation

Instead of replacing the physics-based simulation with a neural net completely, the physics model composes a dominant portion of the prediction and the neural network compensates for the remaining error. From the previous section, the simulation error is bound to 6% NRMS across all trials and bound to 2% error averaged across all trials. The neural network should only do better in conjunction with the simulation than just the simulation itself. The input and output pairs are state at k and error at state at k+1 (s_k, e_{k+1}). The neural network tries to minimize an error metric of interest given in Eq. (114). e_{k+1} is the error between the measured next state s_{k+1} and the state propagated from a previous measured state s_k from a simulation f_{sim}, shown in Eq. (115). δ_{k+1} is the error between the simulation and measurements that the neural network wants to represent.

$$\delta_{k+1} = \left(e_{k+1} - g_{NN}(s_k)\right) \tag{114}$$

$$e_{k+1} = s_{k+1} - f_{sim}(s_k) \tag{115}$$

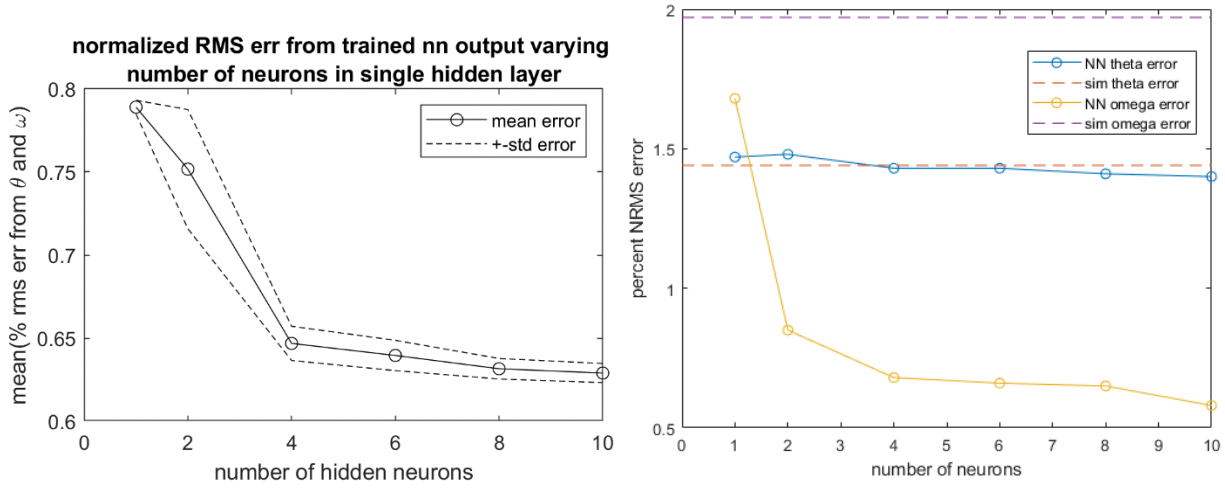

Figure 165: left, combined normalized RMS error approximating 1DOF error model for various numbers of neurons in the hidden layer; right, comparison of baseline-simulation error and NN-compensated error of each state for various number of neurons

Following much of the same process in the previous analysis, multiple single-layer neural networks were trained with various number of neurons in the hidden layer, shown in the left plot of Figure 165. During training, 4 neurons is the minimal representation, as it improves prediction error the most before diminishing returns. Note that the error model requires more neurons than the full-model approximation. The neural network must be more expressive to compensate for the error model because higher-order effects are more dominant. The right plot of Figure 165 separates the attitude state error from the angular rate state error, showing that the error compensation lies mostly in the angular rate state, but the neural network can't reduce attitude error. Figure 166 reiterates and further affirms that the attitude state rarely improves in each of the individual timeseries, but consistently improves in the angular rate timeseries.

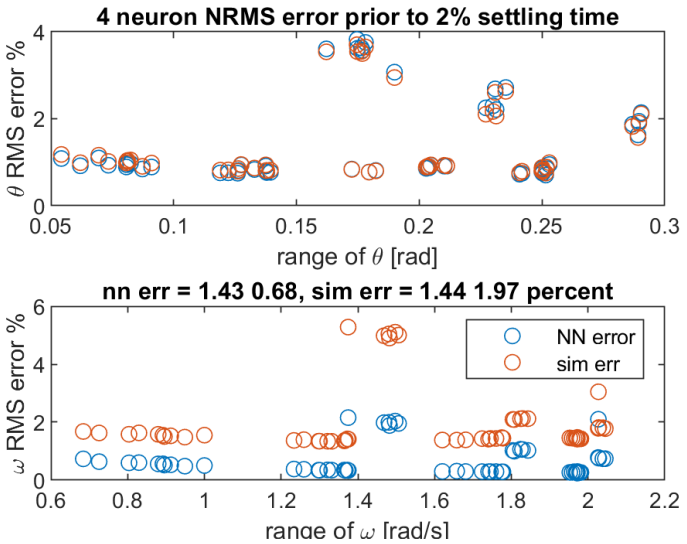

Figure 166: normalized RMS error approximating error 1DOF model with 4 neurons across all experiment trials

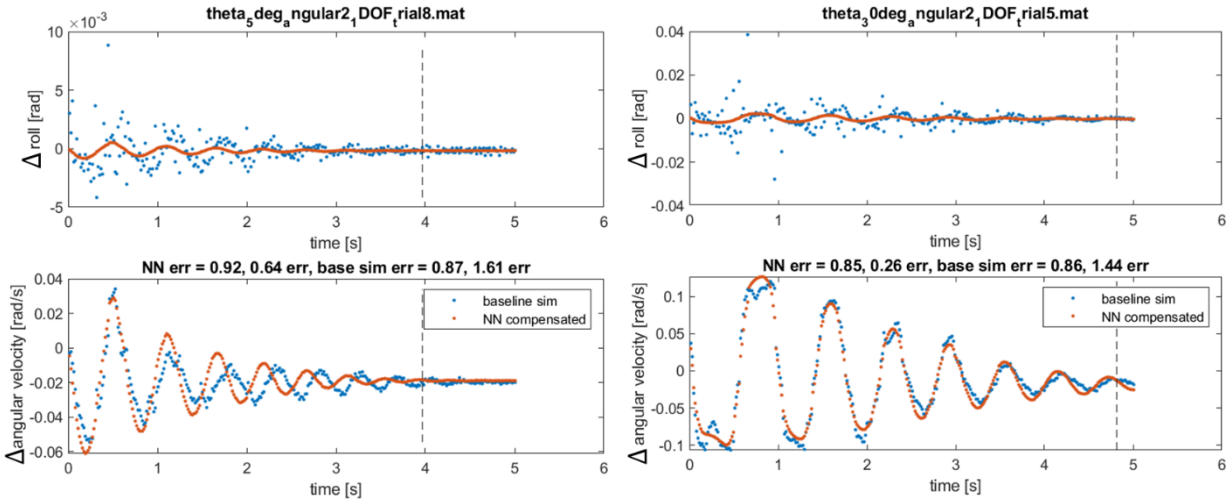

Figure 167: samples of baseline simulation error and NN compensated error of each state in 1DOF experiment trials. Left, small angle displacement. Right, large angle displacement

Upon closer look at the error timeseries plots in the individual trials, there are regimes of higher-order effects that are not captured. Two samples are shown in Figure 167. For large angles, the frequency is matched but the simulation doesn't not capture the sharpness of interactions in the measurements. For small angles, the neural network does not capture the correct frequency. The attitude data, collected by the Vicon system, is very noisy and neural network is trying to fit a trend to the noisiness. The NRMS error is not easily reduced due to noise. Overall, the neural network successfully deciphers an error mapping and can reduce the angular velocity state estimate to half the error value from the physics-based simulation.

b. *Predicting Dynamics from 4DOF Experiments*

Full-Model Approximation

The same neural network structure is extended to approximate the entire dynamics model of a 4DOF system in which nonlinear dynamics are more prevalent and states are coupled. The input states include the six directly measurable states: x and y position, roll and yaw attitude, and roll and yaw rates. First, the sensitivity analysis of normalized RMS error across all states is plotted against number of neurons, with a further breakdown of RMS error over each trial in the translation experiment dataset (n = 10), shown in Figure 168. The minimal representation for this neural network and this dataset is 6 neurons, notably larger than the 1DOF NN. As a result, the mean

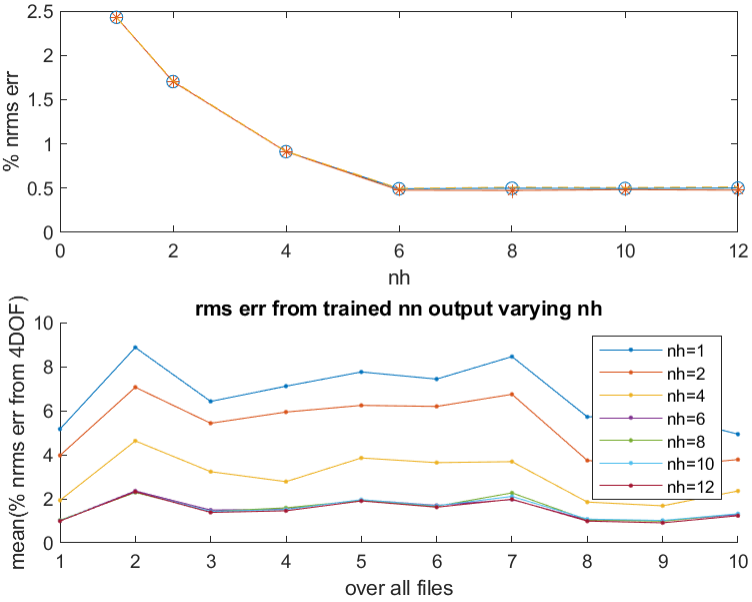

Figure 168: top, combined normalized RMS training error approximating entire 4DOF model for various numbers of neurons in the hidden layer; bottom, normalized RMS evaluation error with various numbers of neurons across each experiment trial

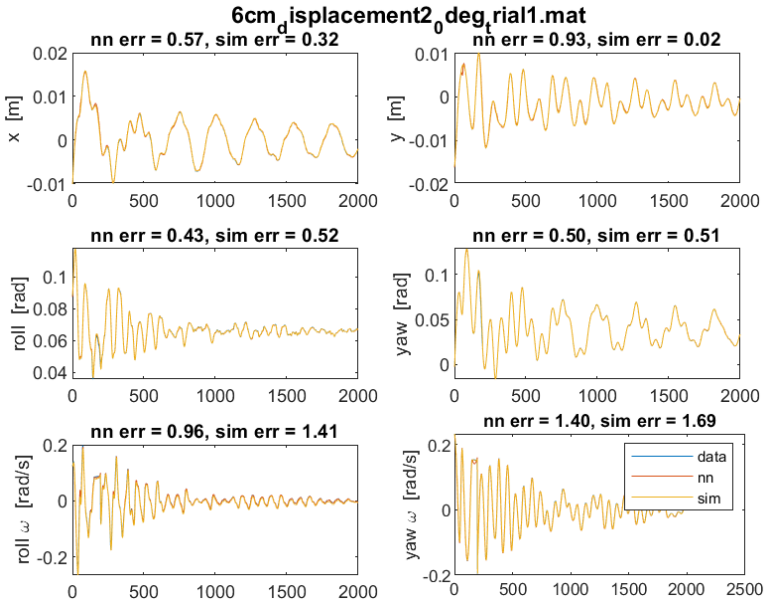

Figure 169: Sample of 4DOF translation experiment timeseries for each state, overlaid with trained NN and physics-based simulation predictions

evaluation error across all states is 1.05%, compared to the 1.03% simulation error. The approximate NN and simulation predict dynamic state with nearly the same performance; a sample of timeseries data for each state is overlaid with the NN and physics-based timeseries prediction in Figure 169.

Although the translation and angular experiments are both carried out on the same system, the approximate model for the angular dataset differs in performance from the translation approximate model performance, seen in Figure 170. The solid line is the per trial prediction error and the dashed line is the mean prediction error across all trials.

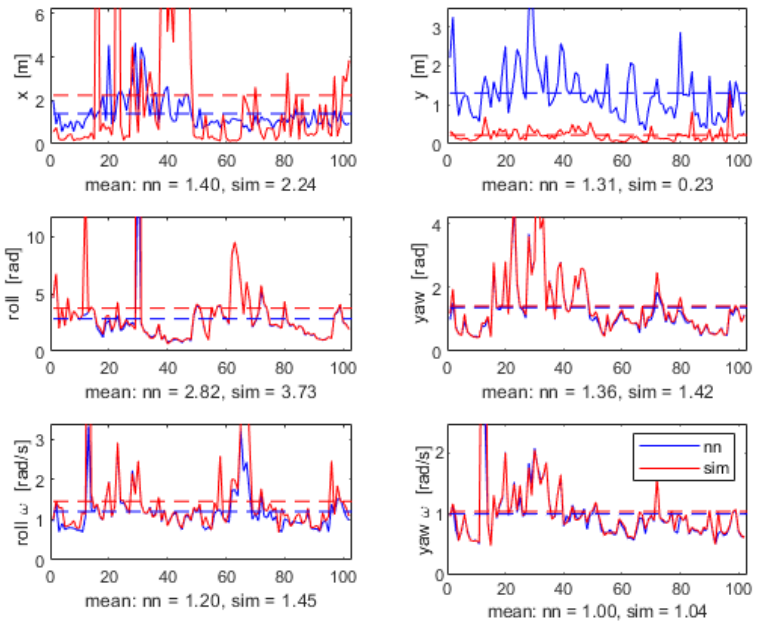

Figure 170: RMS evaluation error across each 4DOF natural mode experiment trial comparing NN and physics-based simulation prediction error

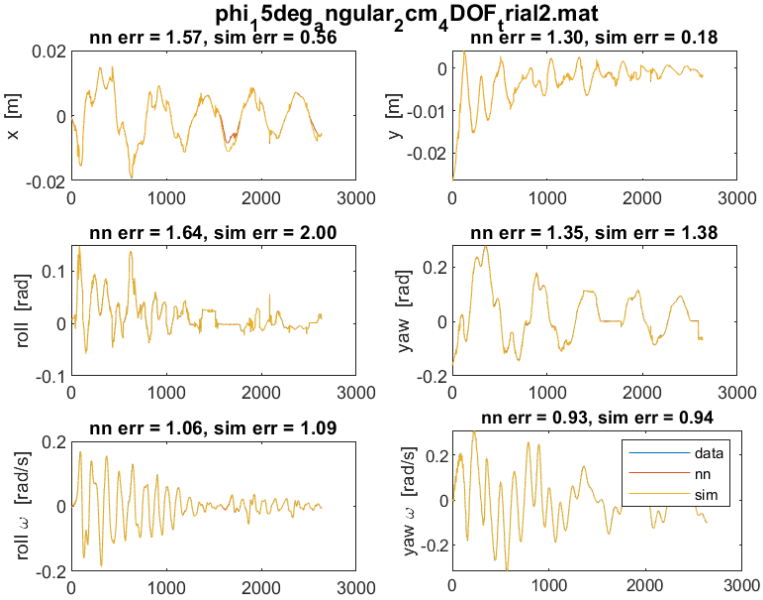

Figure 171: Sample of 4DOF angular experiment timeseries for each state, overlaid with trained NN and physics-based simulation predictions

The NN and physics-based simulation perform similarly for the rotation states but tradeoff performance in the two translation states. The NN performs much worse than the physics-based simulation in the y position timeseries, which coincides with the most nonlinear state. Another reason for a larger discrepancy in performance for translational degrees of freedom could be the lack of velocity states, whereas the rotational degrees of freedom have both attitude and rate data. By reducing overall state error across the six measured states, the dataset emphasizes the rotational degrees of freedom. The neural network performs more consistently than the physics-based simulation, as seen by the x state distribution in error, bounding error to below 5%. Much like the 1DOF analysis, the neural network is extended to compensate for the physics-based error to get prediction performance at least as good as the physics-based model.

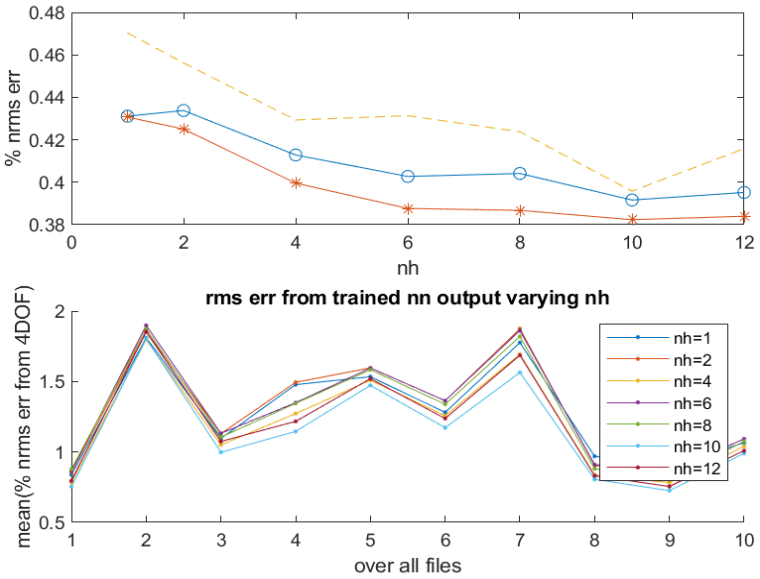

Figure 172: top, combined normalized RMS training error approximating 4DOF error model for various numbers of neurons in the hidden layer; bottom, normalized RMS evaluation error with various numbers of neurons across each experiment trial

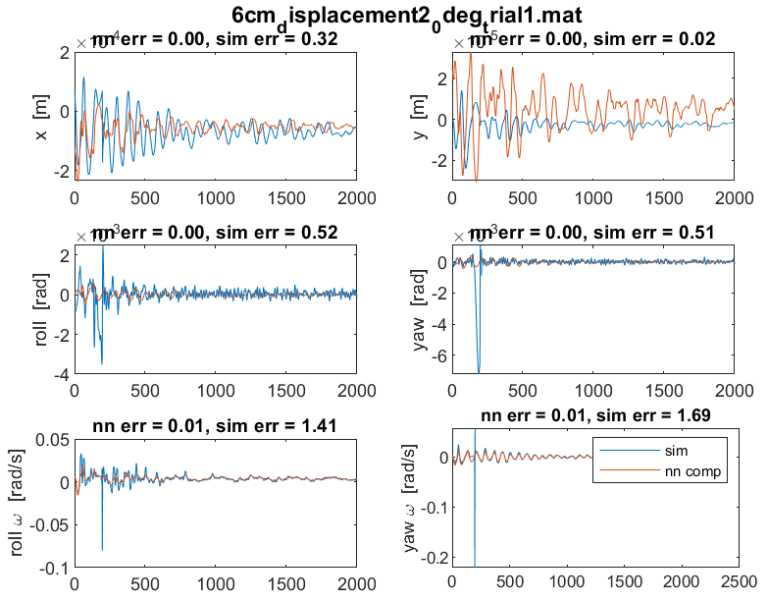

Figure 173: Sample of 4DOF translation experiment timeseries physics-based error, overlaid with NN predicted error

Error Model Compensation

The error-compensation sensitivity analysis in Figure 173 shows reduction in prediction error until 10 neurons before progress tapers. By training a single-layer neural network with 10 neurons to fit to state error in the 4DOF translation tests, every single state prediction improved from a mean normalized RMS error of 1.05% in the simulation to 0.006% after NN-error compensation. In each state, the neural network fits to the physics-based error very well, shown in Figure 172, while not overfitting to measurement noise.

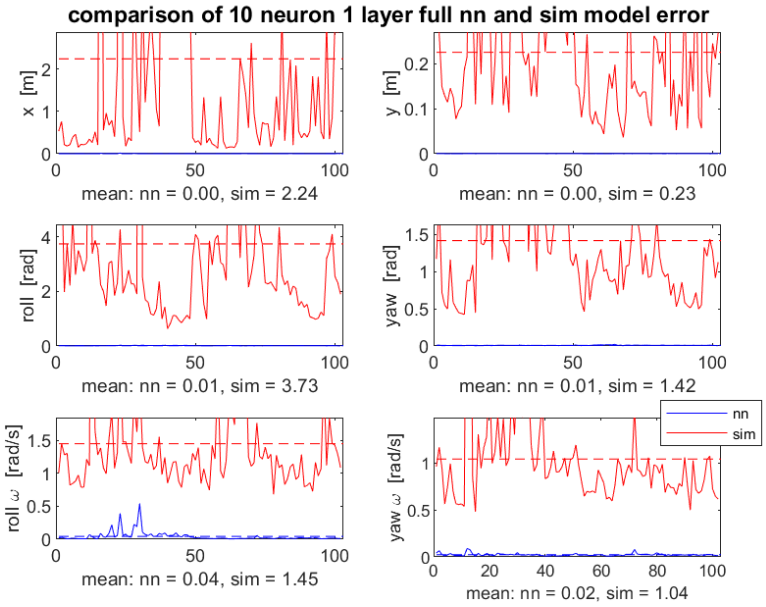

Figure 174: RMS evaluation error across each 4DOF natural mode experiment trial comparing original physics-based simulation prediction error and NN error compensated with physics-based error model

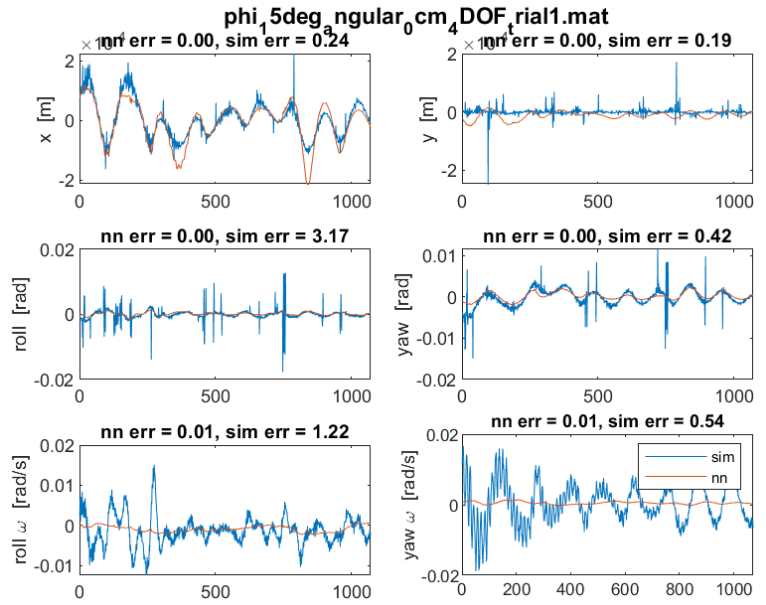

Figure 175: Sample of 4DOF translation experiment timeseries physics-based error, overlaid with NN predicted error

The same trends are seen after training the same neural network structure with the natural-mode experiment data, a reduction from 1.7% RMS error to 0.015% RMS error. Without exception, the neural network guarantees better prediction performance across

all trials, across all states, shown in Figure 174. A sample of angular data in Figure 175 shows the neural network's effort to compensate for most of the physics-based error but rejection of noise, especially x position, roll, and yaw. The angular rate error exhibits higher-order behavior that isn't captured in the neural network compensation.

Overall, the hybrid approach of combining a physics-simulated prediction and a neural-network error prediction performs much better than either individual method approximating the entire dynamics model. Despite the neural network's ability to approximate the dynamics model very well with little to no context, aerospace engineers are timid to adopt neural network predictions for high-risk applications due to lack of safety. This is a driving motivation for the research effort in the next section.

VI. Contribution of System Identification Across All Methods

As a result of a slew of different system identification methods, flux-pinning physics is more understood, better characterized, and is shown to predict within target requirements for certain error metrics with specific methods. As the 1DOF experiments covered the most methods and was extensively characterized, Table 40 reports the different methods, mean normalized RMS error, advantages, and disadvantages from the most analytical method at the top and the most numerical method at the bottom. Although the polynomial and sparse bag-of-functions methods were not described in depth, the resultant 12^{th} order polynomial and previously mentioned bag-of-function library results are also included in Table 40. The 1DOF results indicate that the refined frozen-image model nearly achieves the desired predictive capabilities and with it, carries the advantages of interpretability, extensibility, and verifiability. The neural network results far surpass the refined frozen-image model, and all other representations, in predictive performance but lacks exactly the advantages an analytical model provides. The disadvantages translate to not

safe, not interpretable, and not extensible. Despite the extraordinary predictive capabilities of neural networks, the trade-off in verification, safety, and extrapolation is too great to sacrifice.

Table 40: Summary of different system identification methods, resultant prediction performance for 1DOF data, advantages, and disadvantages of that representation

Dynamics Model Representation	**mean NRMS error from 1DOF experiment data**	**Advantages**	**Disadvantages**
Baseline Frozen-image model	30 %	• Fundamental	• Not precise enough
Refined Frozen-image model	5 %	• Descriptive and interpretable • Intuition into design • Verifiable (conserves energy, adheres to geometry constraints)	• Still not precise enough • Many parameters to estimate
Polynomial Approximator	11 %	• Descriptive and possibly interpretable • Verifiable (conserves energy, adheres to geometry constraints) • Easy to generate and retrain model given good data	• More work to derive design intuition • System specific
Sparse Identification Function Approximator	11 %	• Descriptive and very interpretable • Verifiable (conserves energy, adheres to geometry constraints) • Easy to generate and retrain model given good data	• System specific • Error in choice of bases manifests as many terms
Symbolic Regression	5 %	• Nearly achieved predictive capabilities • Human interpretable expressions	• System specific • Not verifiable
Neural Network Approximator	2 %	• Achieved predictive capabilities! • Very easy to generate and retrain model given good data	• Not interpretable or intuitive • Not verifiable • System specific

The 4DOF methods include the refined frozen-image model, the neural network, and a hybrid combination of both. The same conclusions may be made from the 1DOF results but emphasized. The physics-based simulation propagated with the shooting method is inaccurate and

does not achieve the prediction performance requirement. There exist fundamental higher-order and state coupling effects that are not captured in the proposed dynamics model refinements. Future work includes a more comprehensive and optimally-proven parameter estimation technique, as the fmincon analysis does not guarantee optimality and did not include an accurate measurement noise model. The physics-based simulation propagated with the collocation method is nearly accurate enough to predict 4DOF dynamics and augmented with a neural network to compensate for error, yields precise predictions that fulfill target requirements. The disadvantages still exist in that the neural network is a jumble of parameters, is specific to the exact system from which the data was generated, and could give nonsensical and possibly dangerous predictions for unseen inputs. The next contribution attempts to attack the problem of safety by extracting information out of the neural network by mapping the NN parameters into polynomial form.

CHAPTER 5: Extending Machine Learning Techniques for Aerospace Applications

Current mentalities driving spacecraft design put immense weight in ensuring safety and verification in systems. Machine learning applications on Earth show super-human capabilities on tasks but generally focus on low risk operations, an exception being autonomous driving cars. Neural networks, as seen by the previous system identification analysis, immediately predict state better than a user-driven, user-defined physics-based model with very little context and magnitudes less time in development. Lack of interpretability, extensibility, and safety are disadvantages holding this method back from adoption for spaceflight applications. By overcoming these shortcomings, the payoff is a step closer to true autonomous operations. This chapter is separated into two portions in which the first section reformulates neural networks into polynomial form to address safety and verification. The latter part of this chapter investigates the feasibility of autonomous planetary-surface exploration with genetic algorithms in which real-time system-identification highly benefits mobility performance.

I. Taylor Expansion of a Neural Network

This contribution approximates a neural network into a polynomial from which safety criteria/verification may be formed and domain knowledge in physical constraints and energy conservation may be applied. The approximation aims to be a straightforward mapping, executes in real-time, requires minimal data storage, and limits overfitting through the polynomial expression power. As neural networks are universal approximators, the derivation assumes that the general NN structure approximates the system mapping well [140]. The final form of the approximation is a system of linear equations with polynomial state from which semi-algebraic constraints may be applied to offer safety to the dynamics system. Related work comes from

Ferrari, in which neural-network parameter solutions are constrained to offer safety in dynamic systems [146]. This section details the derivation of the proposed polynomial approximation of the neural network and algorithm performance approximating various dynamic state transitions.

a. *Taylor Expansion for a Vector Function in Vector Domain*

Given the training pairs $(\boldsymbol{x}, \boldsymbol{y})$, a neural network predicts $\hat{\boldsymbol{y}}$ with a mapping $f_{NN}(W, \boldsymbol{b}, \boldsymbol{x})$, given in Eq. (116). The learned parameters are W and $\boldsymbol{b}$ in the neural network. The input $\boldsymbol{x}$ is of size m, $\boldsymbol{x} \in \mathbb{R}^{m\times 1}$, and output $\boldsymbol{y}$ is of size n, $\boldsymbol{y} \in \mathbb{R}^{n\times 1}$. The order of polynomial is defined ahead of time if the NN structure is known [147]. The goal is to find coefficients of a polynomial expression that minimizes the objective function given in Eq. (117).

$$(\boldsymbol{x}, \boldsymbol{y}) \to \hat{\boldsymbol{y}} = \mathrm{f}_{NN}(W, \boldsymbol{b}, \boldsymbol{x}) \tag{116}$$

$$J^* = \underset{a}{\operatorname{argmin}} \|f_{NN}(\boldsymbol{x}) - p(\boldsymbol{x},\, a)\|_2 \tag{117}$$

To interpret and verify this otherwise black box, a derivation shows the process to approximate the neural network with a polynomial. First, a Taylor expansion for a vector function must be derived in vector domain. The expansion includes various dimensions of tensors and redundant multinomial cross terms. An important contribution is reforming the tensor derivatives into matrix form and the tensor states into vector form, which results in matrix manipulability and computation savings. Next, the general derivatives of a neural network are derived in tensor form. The two efforts stitched together achieve the final polynomial coefficients in the polynomial expression. To validate the method and offer context for other methods, the last section offers a comparison of model fidelity and computation to other numerical system identification methods.

Given a vector input $\boldsymbol{x} \in \mathbb{R}^{m\times 1}$ and the output $\boldsymbol{y} \in \mathbb{R}^{n\times 1}$, a function f maps the input state to the output state $f(\boldsymbol{x})$: $\mathbb{R}^{m\times 1} \to \mathbb{R}^{n\times 1}$. Assume this function $f(\cdot)$ is a continuous vectorial

function with continuous partial derivatives of their components, $\boldsymbol{x}$. Taking notation and drawing foundation from Granados's paper [148], there are two relevant operations to manipulate tensors: $\otimes$ is the outer product and $\odot$ is the inner product. The vectorial series is then defined with Jacobian terms and exponentiated state vector terms in Eq. (118), where the expansion is expressed in a summation over n Jacobian terms and the remainder expressed in $\boldsymbol{R_n(x)}$. The summation expanded into the first few terms is given in Eq. (119). For simplicity, the expansion is about the zero-state, dropping $\boldsymbol{x_0}$ from the exponentiated state and simplifying the lower dimension terms, given in Eq. (120).

$$\boldsymbol{f(x)} = \sum_{k=0}^{n} \frac{J_f^k(\boldsymbol{x_0})}{k!} \odot (\boldsymbol{x} - \boldsymbol{x_0})^{k\otimes} + \boldsymbol{R_n(x)} \tag{118}$$

$$\boldsymbol{f(x)} = J_f^0(\boldsymbol{x_0}) \odot (\boldsymbol{x} - \boldsymbol{x_0})^{0\otimes} + J_f^1(\boldsymbol{x_0}) \odot (\boldsymbol{x} - \boldsymbol{x_0})^{1\otimes} + \frac{1}{2!} J_f^2(\boldsymbol{x_0}) \odot (\boldsymbol{x} - \boldsymbol{x_0})^{2\otimes} + \cdots + \boldsymbol{R_n(x)} \tag{119}$$

$$\boldsymbol{f(x)} = \boldsymbol{f(x_0)} + J_f^1(\boldsymbol{x_0})\boldsymbol{x} + \frac{1}{2!} J_f^2(\boldsymbol{x_0}) \odot \boldsymbol{x}^{2\otimes} + \cdots + \boldsymbol{R_n(x)} \tag{120}$$

The derivative structure of the first three terms contain various dimensions of tensors but all have distinct names due to their commonality. $\boldsymbol{f(x_0)}$ is a vector or a 1st-order tensor. $J_f^1(\boldsymbol{x_0})$, a 2nd-order tensor is often called a matrix. All tensors of higher orders carry generic labels, like $J_f^2(\boldsymbol{x_0})$ is a 3rd-order tensor. Further expansion of the vector series of the first few terms into individual terms in the arrays is given in Eq. (121). Although this vectorial series is elegant and possible to derive a closed-form expression for the original function, the subsequent derivative terms incrementally increase in dimension, which is not easily captured in a linear equation that can be solved with a single pseudoinverse.

$$\boldsymbol{f}(\boldsymbol{x}) = \begin{bmatrix} f_1(\boldsymbol{x_0}) \\ f_2(\boldsymbol{x_0}) \\ \vdots \\ f_n(\boldsymbol{x_0}) \end{bmatrix} + \begin{bmatrix} \frac{\partial f_1}{\partial x_1} & \frac{\partial f_1}{\partial x_2} & \cdots & \frac{\partial f_1}{\partial x_m} \\ \frac{\partial f_2}{\partial x_1} & \frac{\partial f_2}{\partial x_2} & \cdots & \frac{\partial f_2}{\partial x_m} \\ \vdots & \vdots & \ddots & \vdots \\ \frac{\partial f_n}{\partial x_1} & \frac{\partial f_n}{\partial x_2} & \cdots & \frac{\partial f_n}{\partial x_m} \end{bmatrix} \odot \begin{bmatrix} x_1 \\ x_2 \\ \vdots \\ x_m \end{bmatrix} \dots$$

$$+ \frac{1}{2!} \begin{bmatrix} \begin{bmatrix} \frac{\partial^2 f_1}{\partial x_1^2} & \frac{\partial^2 f_1}{\partial x_2 \partial x_1} & \cdots & \frac{\partial^2 f_1}{\partial x_m \partial x_1} \\ \frac{\partial^2 f_2}{\partial x_1^2} & \frac{\partial^2 f_2}{\partial^2 x_2 \partial x_1} & \cdots & \frac{\partial^2 f_2}{\partial x_m \partial x_1} \\ \vdots & \vdots & \ddots & \vdots \\ \frac{\partial^2 f_n}{\partial x_1^2} & \frac{\partial^2 f_n}{\partial x_2 \partial x_1} & \cdots & \frac{\partial^2 f_n}{\partial x_m \partial x_1} \end{bmatrix}, \cdots, \begin{bmatrix} \frac{\partial^2 f_1}{\partial x_1 \partial x_m} & \frac{\partial^2 f_1}{\partial x_2 \partial x_m} & \cdots & \frac{\partial^2 f_1}{\partial x_m^2} \\ \frac{\partial^2 f_2}{\partial x_1 \partial x_m} & \frac{\partial^2 f_2}{\partial x_2 \partial x_m} & \cdots & \frac{\partial^2 f_2}{\partial x_m^2} \\ \vdots & \vdots & \ddots & \vdots \\ \frac{\partial^2 f_n}{\partial x_1 \partial x_m} & \frac{\partial^2 f_n}{\partial x_2 \partial x_m} & \cdots & \frac{\partial^2 f_n}{\partial x_m^2} \end{bmatrix} \end{bmatrix} \odot \begin{bmatrix} x_1^2 & x_1 x_2 & \cdots & x_1 x_m \\ x_2 x_1 & x_2^2 & \cdots & x_2 x_m \\ \vdots & \vdots & \ddots & \vdots \\ x_m x_1 & x_m x_2 & \cdots & x_m^2 \end{bmatrix} + \cdots + \boldsymbol{R_n}(\boldsymbol{x}) \quad (121)$$

The tensor equation that approximates the original function may be collapsed into a set of linear equations, given in Eq. (122). In this equation, redundant state terms are summed in the same equation, highlighted. The multinomial cross terms are redundant as the tensors are symmetric. A reformulated matrix equation of the tensor equation yields the same set of linear equations yet reduces the number of total state terms and is in a more convenient representation, given in Eq. (123). The augmented state vector now contains scalar coefficients that represent the number of redundant terms, which can be separated into a new coefficient vector. There are significant computation cost savings in condensing these redundant terms, especially for the number of states in spacecraft dynamics and for taking more than two derivatives.

$$\boldsymbol{f}(\boldsymbol{x}) = \begin{bmatrix} f_1(\boldsymbol{x_0}) + \left(\frac{\partial f_1}{\partial x_1} x_1 + \frac{\partial f_1}{\partial x_2} x_2 + \cdots + \frac{\partial f_1}{\partial x_m} x_m\right) + \cdots \\ \ldots + \frac{1}{2!}\left[\left(\frac{\partial^2 f_1}{\partial x_1^2} x_1^2 + \frac{\partial^2 f_1}{\partial x_2 \partial x_1} x_2 x_1 + \cdots + \frac{\partial^2 f_1}{\partial x_m \partial x_1} x_m x_1\right) + \cdots + \left(\frac{\partial^2 f_1}{\partial x_1 \partial x_m} x_1 x_m + \frac{\partial^2 f_1}{\partial x_2 \partial x_m} x_2 x_m + \cdots + \frac{\partial^2 f_1}{\partial x_m^2} x_m^2\right)\right] + \cdots + R_1(\boldsymbol{x}) \\ f_2(\boldsymbol{x_0}) + \left(\frac{\partial f_2}{\partial x_1} x_1 + \frac{\partial f_2}{\partial x_2} x_2 + \cdots + \frac{\partial f_2}{\partial x_m} x_m\right) + \cdots \\ \ldots + \frac{1}{2!}\left[\left(\frac{\partial^2 f_2}{\partial x_1^2} x_1^2 + \frac{\partial^2 f_2}{\partial x_2 \partial x_1} x_2 x_1 + \cdots + \frac{\partial^2 f_2}{\partial x_m \partial x_1} x_m x_1\right) + \cdots + \left(\frac{\partial^2 f_2}{\partial x_1 \partial x_m} x_1 x_m + \frac{\partial^2 f_2}{\partial x_2 \partial x_m} x_2 x_m + \cdots + \frac{\partial^2 f_2}{\partial x_m^2} x_m^2\right)\right] + \cdots + R_2(\boldsymbol{x}) \\ \vdots \\ f_n(\boldsymbol{x_0}) + \left(\frac{\partial f_n}{\partial x_1} x_1 + \frac{\partial f_n}{\partial x_2} x_2 + \cdots + \frac{\partial f_n}{\partial x_m} x_m\right) + \cdots \\ \ldots + \frac{1}{2!}\left[\left(\frac{\partial^2 f_n}{\partial x_1^2} x_1^2 + \frac{\partial^2 f_n}{\partial x_2 \partial x_1} x_2 x_1 + \cdots + \frac{\partial^2 f_n}{\partial x_m \partial x_1} x_m x_1\right) + \cdots + \left(\frac{\partial^2 f_n}{\partial x_1 \partial x_m} x_1 x_m + \frac{\partial^2 f_n}{\partial x_2 \partial x_m} x_2 x_m + \cdots + \frac{\partial^2 f_n}{\partial x_m^2} x_m^2\right)\right] + \cdots + R_n(\boldsymbol{x}) \end{bmatrix} \quad (122)$$

$$\boldsymbol{f}(\boldsymbol{x}) = \begin{bmatrix} f_1(\boldsymbol{x_0}) & \frac{\partial f_1}{\partial x_1} & \frac{\partial f_1}{\partial x_2} & \cdots & \frac{\partial f_1}{\partial x_m} & \frac{\partial^2 f_1}{\partial x_1^2} & \frac{\partial^2 f_1}{\partial x_1 \partial x_2} & \cdots & \frac{\partial^2 f_1}{\partial x_1 \partial x_m} & \frac{\partial^2 f_1}{\partial x_2^2} & \frac{\partial^2 f_1}{\partial x_2 \partial x_3} & \cdots & \frac{\partial^2 f_1}{\partial x_2 \partial x_m} & \cdots & \frac{\partial^2 f_1}{\partial x_m^2} & \cdots & R_1(\boldsymbol{x}) \\ f_2(\boldsymbol{x_0}) & \frac{\partial f_2}{\partial x_1} & \frac{\partial f_2}{\partial x_2} & \cdots & \frac{\partial f_2}{\partial x_m} & \frac{\partial^2 f_2}{\partial x_1^2} & \frac{\partial^2 f_2}{\partial x_1 \partial x_2} & \cdots & \frac{\partial^2 f_2}{\partial x_1 \partial x_m} & \frac{\partial^2 f_2}{\partial x_2^2} & \frac{\partial^2 f_2}{\partial x_2 \partial x_3} & \cdots & \frac{\partial^2 f_2}{\partial x_2 \partial x_m} & \cdots & \frac{\partial^2 f_2}{\partial x_m^2} & \cdots & R_2(\boldsymbol{x}) \\ & & & & & & & & \vdots & & & & & & & & \\ f_n(\boldsymbol{x_0}) & \frac{\partial f_n}{\partial x_1} & \frac{\partial f_n}{\partial x_2} & \cdots & \frac{\partial f_n}{\partial x_m} & \frac{\partial^2 f_n}{\partial x_1^2} & \frac{\partial^2 f_n}{\partial x_1 \partial x_2} & \cdots & \frac{\partial^2 f_n}{\partial x_1 \partial x_m} & \frac{\partial^2 f_n}{\partial x_2^2} & \frac{\partial^2 f_n}{\partial x_2 \partial x_3} & \cdots & \frac{\partial^2 f_n}{\partial x_2 \partial x_m} & \cdots & \frac{\partial^2 f_n}{\partial x_m^2} & \cdots & R_n(\boldsymbol{x}) \end{bmatrix}$$

$$\cdot \begin{bmatrix} 1 & x_1 & x_2 & \cdots & x_m & \frac{1}{2!}x_1^2 & \frac{2}{2!}x_1 x_2 & \cdots & \frac{2}{2!}x_1 x_m & \frac{1}{2!}x_2^2 & \frac{2}{2!}x_2 x_3 & \cdots & \frac{2}{2!}x_2 x_m & \cdots & \frac{1}{2!}x_m^2 & \cdots & 1 \end{bmatrix}^T \quad (118)$$

Unfurling and keeping all terms in the state tensors falsely inflates the number of unknowns a set of equations needs to solve for. By grouping redundant multinomial cross terms together into a coefficient vector, the vector of unknowns contains only the unique states and accurately reflects the number of unknowns. Defining this new coefficient vector is necessary to reform the exponentiated states into a state vector and in the process reveals the reduction in computation. Referencing Hildebrand's lecture notes covering multinomial coefficients, the general solution for the multinomial coefficient is given in Eq. (124), where $a(\cdot)$ is the combinatorial function of choosing d states out of m total number of states to choose from. For consistency, d is associated with the order of the exponentiated state term $\boldsymbol{x}^{\otimes d}$, which is tied to the d^{th} derivative and Jacobian term in the Taylor expansion. m is still the number of states in the input $\boldsymbol{x}$. d_i is the order of each individual state in the multinomial state and must adhere to Eq. (125). As an example, equations (126) to (127) explicitly lists the unique states in the 3rd-order state $\boldsymbol{x}^{\otimes 3}$ and each multinomial states' coefficient.

$$a(d; < d_1, d_2, \dots, d_m >) = \frac{1}{d!}\frac{d}{d_1!\, d_2! \dots d_m!} \quad (124)$$

$$d = d_1 + d_2 + \cdots + d_m \quad (125)$$

$$\tilde{\boldsymbol{x}}^{\otimes 3} = \begin{bmatrix} x_1^3 & x_1^2 x_2 & \cdots & x_1^2 x_m & x_1 x_2^2 & \cdots & x_1 x_2 x_m & \cdots & x_1 x_m^2 & x_2^3 & x_2^2 x_3 & \cdots & x_2^2 x_m & x_2 x_3^2 & \cdots & x_m^3 \end{bmatrix} \quad (126)$$

$$\boldsymbol{a}^3 = \frac{1}{3!}\begin{bmatrix} \binom{3}{3} & \binom{3}{2,1} & \cdots & \binom{3}{2,1} & \binom{3}{1,2} & \cdots & \binom{3}{1,1,1} & \cdots & \binom{3}{2,1} & \binom{3}{3} & \binom{3}{2,1} & \cdots & \binom{3}{2,1} & \binom{3}{1,2} & \cdots & \binom{3}{3} \end{bmatrix}$$

$$= \frac{1}{3!}\begin{bmatrix} 1 & 3 & \cdots & 3 & 3 & \cdots & 6 & \cdots & 3 & 1 & 3 & \cdots & 3 & 3 & \cdots & 1 \end{bmatrix} \quad (127)$$

The unique multinomial state vector is $\tilde{\boldsymbol{x}}^{\otimes d}$ and $\boldsymbol{a}^d$ is the multinomial coefficient vector. The length of $\tilde{\boldsymbol{x}}^{\otimes d}$ and $\boldsymbol{a}^d$ follows Eq. (127) and the corresponding number of states for a full expansion vs. compacting to unique terms is listed in in Table 41. The reduction can be seen to approach 100% for large states and 0% for scalar domain. The real reduction rate falls somewhere beneath the $m = \infty$ bounding curve and the $m = 1$ origin. To consider whether this reduced projection is worth deriving, the minimum number of states and derivatives to yield a significant computation reduction of 25% is already achieved at $m = 2$ states and $d = 2$ derivatives. For the spacecraft application of interest, the 6DOF dynamics already include 12 states and if an approximation includes up to the Hessian (low-order approximation), the computational savings are already 45%. Condensing cross-terms is important for any real application of interest.

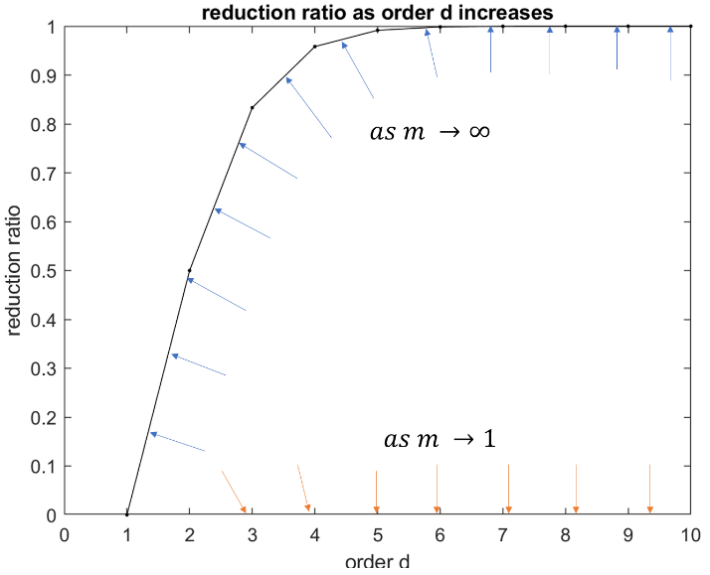

Figure 176: reduction ratio between number of reductions and number of full terms

$$n_d = \prod_{i=1}^{d} \frac{m+i-1}{i} \tag{122}$$

Table 41: progression of derivative order, number of tensor terms, unique combinations, and reduction ratio

Order	# full tensor terms	# unique terms	# reductions in state	Reduction ratio between # reductions and # full terms	Maximum reduction ratio
1	m	m	0	0	0
2	m^2	$\frac{m(m+1)}{2}$	$\frac{m^2-m}{2}$	$\frac{1}{2}-\frac{1}{2m}$	$\frac{1}{2}$
3	m^3	$\frac{m(m+1)(m+2)}{3!}$	$\frac{5m^3}{6}-\frac{3m^2}{6}-\frac{2m}{6}$	$\frac{5}{6}-\frac{3}{6m}-\frac{2}{6m^2}$	$\frac{5}{6}$
4	m^4	$\frac{m(m+1)(m+2)(m+3)}{4!}$	$\frac{23m^4}{24}-\frac{6m^3}{24}-\frac{11m^2}{24}-\frac{6m}{24}$	$\frac{23}{24}-\frac{6}{24m}-\frac{11}{24m^2}-\frac{6}{24m^3}$	$\frac{23}{24}$
⋮	⋮	⋮	⋮	⋮	⋮
d	m^d	$\prod_{i=1}^{d}\frac{m+i-1}{i}$			$\frac{d!-1}{d!}$

Knowing that the compact formulation of the multinomial state reduces computation significantly, a framework must be derived such that the tensor derivatives and states in the Taylor expansion can be reshaped into unique multinomial expansion terms in matrix form. The two components involved in each term of the tensor Taylor series is the Jacobian tensor and state. Those tensor components need to be mapped to three components in each term of the matrix Taylor series: the multinomial state vector, multinomial coefficient vector, and the Jacobian matrix. The dimension of each derivative tensor, state tensor, subsequent derivative matrix, multinomial state vector, and multinomial coefficient vector can be found in Table 42. Note that the 0th and 1st order derivative terms are not collapsed as they are already reduced to their unique terms.

Table 42: ascending order of derivative with associated tensor representation, dimension of tensor, state representation, and dimension of state

Order of derivative	Derivative tensor	Dimension of tensor	State	Dimension of state	Derivative matrix	Dimension of matrix	Multinomial state and coefficient vector	Dimension of multinomial state and coefficient vector
0	$\boldsymbol{f}(\boldsymbol{x_0})$	$\mathbb{R}^{n\times 1}$						
1	$J_f^1(\boldsymbol{x_0})$	$\mathbb{R}^{n\times m}$	$\boldsymbol{x}$	$\mathbb{R}^{m\times 1}$				
2	$J_f^2(\boldsymbol{x_0})$	$\mathbb{R}^{n\times m\times m}$	$\boldsymbol{x}^{\otimes \boldsymbol{2}}$	$\mathbb{R}^{m\times m\times 1}$	$\tilde{J}_f^2(\boldsymbol{x_0})$	$\mathbb{R}^{n\times\frac{m(m+1)}{2}}$	$\tilde{\boldsymbol{x}}^{\otimes \boldsymbol{2}}, \boldsymbol{a^2}$	$\mathbb{R}^{\frac{m(m+1)}{2}\times 1}$
⋮	⋮	⋮	⋮	⋮	⋮	⋮	⋮	⋮
d	$J_f^d(\boldsymbol{x_0})$	$\mathbb{R}^{n\times m\times\ldots\times m}$	$\boldsymbol{x}^{\otimes \boldsymbol{d}}$	$\mathbb{R}^{m\times\ldots\times m\times 1}$	$\tilde{J}_f^d(\boldsymbol{x_0})$	$\mathbb{R}^{n\times\prod_{i=1}^{d}\frac{m+i-1}{i}}$	$\tilde{\boldsymbol{x}}^{\otimes \boldsymbol{d}}, \boldsymbol{a^d}$	$\mathbb{R}^{\prod_{i=1}^{d}\frac{m+i-1}{i}\times 1}$

The process of projecting the higher dimensioned tensors to lower dimensioned matrices and vectors involves mapping the indices of each higher dimension to a single dimension. The multinomial state vector structure is defined first in Table 43, where j is the vector term index and $i_1, i_2, \dots, i_d$ are the individual tensor dimension indices. Note that for the $d \geq m$, i_1 to i_{d-m+1} does not increment in index but stays at index 1 as dummy dimensions. The multinomial coefficient vector structure is defined in Table 44, where the j index aligns with the state j index. The Jacobian mapping follows the multinomial state vector mapping with the first dimension always carried over, given in Table 45. These tables generalize to any order of terms in the Taylor expansion.

Table 43: tensor to vector mapping of multinomial state for ascending order terms

Multinomial state vector term	Equivalent state tensor term	State composition	Index mapping
$\tilde{\boldsymbol{x}}^{\otimes 2}(j)$	$\boldsymbol{x}^{\otimes 2}(i_1, i_2)$	$x_{i_1} x_{i_2}$	$j = i_1 + \frac{i_2(i_2-1)}{2}$ for $i_2 = 1{:}\,m$, for $i_1 = 1{:}\,i_2$
$\tilde{\boldsymbol{x}}^{\otimes 3}(j)$	$\boldsymbol{x}^{\otimes 3}(i_1, i_2, i_3)$	$x_{i_1} x_{i_2} x_{i_3}$	$j = i_1 + \frac{i_2(i_2-1)}{2} + \frac{(i_3+1)i_3(i_3-1)}{3 \cdot 2}$ for $i_3 = 1{:}\,m$, for $i_2 = 1{:}\,i_3$, for $i_1 = 1{:}\,i_2$
$\tilde{\boldsymbol{x}}^{\otimes 4}(j)$	$\boldsymbol{x}^{\otimes 4}(i_1, i_2, i_3, i_4)$	$x_{i_1} x_{i_2} x_{i_3} x_{i_4}$	$j = i_1 + \frac{i_2(i_2-1)}{2} + \frac{(i_3+1)i_3(i_3-1)}{3 \cdot 2} + \frac{(i_4+2)(i_4+1)i_4(i_4-1)}{4 \cdot 3 \cdot 2}$ for $i_4 = 1{:}\,m$, for $i_3 = 1{:}\,i_4$, for $i_2 = 1{:}\,i_3$, for $i_1 = 1{:}\,i_2$
$\vdots$	$\vdots$	$\vdots$	$\vdots$
$\tilde{\boldsymbol{x}}^{\otimes d}(j)$	$\boldsymbol{x}^{\otimes d}(i_1, i_2, \dots, i_d)$	$x_{i_1} x_{i_2} \dots x_{i_d}$	$j = i_1 + \frac{i_2(i_2-1)}{2} + \cdots + \prod_{k=1}^{d} \frac{i_d + k - 2}{k}$ for $i_d = 1{:}\,m$, for $i_{d-1} = 1{:}\,i_d, \dots,$ for $i_1 = 1{:}\,i_2$

Table 44: multinomial coefficient vector values and indices for ascending order terms

Multinomial coefficient vector term	Corresponding state composition	Multinomial coefficient value
$\boldsymbol{a}^2(j)$	$x_{i_1} x_{i_2}$	$= \frac{1}{2!}\binom{2}{1,1} = 2$ if $i_1 \neq i_2$ $= \frac{1}{2!}\binom{2}{0,2} = 1$ if $i_1 = i_2$
$\vdots$	$\vdots$	$\vdots$
$\boldsymbol{a}^d(j)$	$x_{i_1} x_{i_2} \dots x_{i_d}$	$= \frac{1}{d!}\binom{d}{n_1, n_2, \dots, n_m}$ for $n_1 = \mathcal{O}(x_1) \in x_{i_1} x_{i_2} \dots x_{i_d}, \dots, n_m = \mathcal{O}(x_m) \in x_{i_1} x_{i_2} \dots x_{i_d}$

Table 45: tensor to matrix mapping of derivative term for ascending order terms

Multinomial state vector term	Equivalent state tensor term	State composition	Index mapping
$J_f^2(:,j)$	$\tilde{J}_f^2(:,i_1,i_2)$	$x_{i_1}x_{i_2}$	$j = i_1 + \frac{i_2(i_2-1)}{2}$ for $i_2 = 1{:}\,m$, for $i_1 = 1{:}\,i_2$
⋮	⋮	⋮	⋮
$J_f^d(:,j)$	$\tilde{J}_f^2(:,i_1,i_2,\dots,i_d)$	$x_{i_1}x_{i_2}\dots x_{i_d}$	$j = i_1 + \frac{i_2(i_2-1)}{2} + \cdots + \prod_{k=1}^{d}\frac{i_d+k-2}{k}$ for $i_d = 1{:}\,m$, for $i_{d-1} = 1{:}\,i_d, \dots,$ for $i_1 = 1{:}\,i_2$

Taylor Expansion Validation

A vector function in vector domain with a toy-case polynomial is approximated to validate the above method. If the original functions are polynomials, the approximation process should generate the exact original polynomial. The Rosenbrock and sphere function are defined in Eq. (128) & (129) in which the input state $\boldsymbol{x} = [x_1\ x_2]$. The functions have tensor derivatives and are in vector domain, which is a meaningful test to validate this contribution. The desired product is in a form given in Eq. (130). The expected coefficients with the fully expanded multinomial state to the 4th order are given in Eq. (131).

$$sphere{:}\, f_1(\boldsymbol{x}) = y_1 = x_1^2 + x_2^2 \tag{128}$$

$$Rosenbrock{:}\, f_2(\boldsymbol{x}) = (1 - x_1)^2 + 100(x_2 - x_1^2)^2 \tag{129}$$

$$\boldsymbol{f}(\boldsymbol{x}) = \begin{bmatrix} f_1(\boldsymbol{x}) \\ f_2(\boldsymbol{x}) \end{bmatrix} = [\boldsymbol{a_0} \quad A_1 \quad A_2 \quad A_3 \quad A_4] \begin{bmatrix} 1 \\ \boldsymbol{x} \\ \tilde{\boldsymbol{x}}^{\otimes 2} \\ \tilde{\boldsymbol{x}}^{\otimes 3} \\ \tilde{\boldsymbol{x}}^{\otimes 4} \end{bmatrix} \tag{130}$$

$$\boldsymbol{f}(\boldsymbol{x}) = \begin{bmatrix} 0 & 0 & 0 & 1 & 0 & 1 & 0 & 0 & 0 & 0 & 0 & 0 & 0 & 0 & 0 \\ 1 & -2 & 0 & 1 & 0 & 100 & 0 & -200 & 0 & 0 & 100 & 0 & 0 & 0 & 0 \end{bmatrix} \cdot [1 \quad x_1 \quad x_2 \quad x_1^2 \quad x_1x_2 \quad x_2^2 \quad x_1^3 \quad x_1^2x_2 \quad x_1x_2^2 \quad x_2^3 \quad x_1^4 \quad x_1^3x_2 \quad x_1^2x_2^2 \quad x_1x_2^3 \quad x_2^4]^T \tag{131}$$

To find the expected Taylor expansion in Eq. (130), the original sphere and Rosenbrock function tensor derivatives must be derived and mapped to the A_i matrices in Eq. (130). Eq. (132)

is the sphere function's Taylor expansion, with the associated derivatives in Eqs. (133) to (136). Equivalently, Eq. (137) is the Rosenbrock function's Taylor expansion, with the associated derivatives in Eqs. (138) to (142). All polynomial coefficients exactly match the expected product, validating this section's derivation.

$$f_1(\boldsymbol{x}) = f_1(\mathbf{0}) + J_1^1(\mathbf{0})\boldsymbol{x} + \frac{1}{2!}J_1^2(\mathbf{0})\tilde{\boldsymbol{x}}^{\otimes 2} + \frac{1}{3!}J_1^3(\mathbf{0})\tilde{\boldsymbol{x}}^{\otimes 3} + \frac{1}{4!}J_1^4(\mathbf{0})\tilde{\boldsymbol{x}}^{\otimes 4} \tag{132}$$

$$f_1(\mathbf{0}) = \boldsymbol{a_0} = 0^2 + 0^2 = 0 \tag{133}$$

$$J_1^1(\mathbf{0}) = [\nabla f_1(\boldsymbol{x})]^T|_{\boldsymbol{x}=\mathbf{0}} = \begin{bmatrix}\frac{\partial f_1}{\partial x_1} & \frac{\partial f_1}{\partial x_2}\end{bmatrix}|_{\boldsymbol{x}=\mathbf{0}} = [j_1^1 \quad j_2^1]|_{\boldsymbol{x}=\mathbf{0}} = [2x_1 \quad 2x_2]|_{\boldsymbol{x}=\mathbf{0}} = [0 \quad 0] = A_1 \tag{134}$$

$$J_1^2(\mathbf{0}) = [\nabla J_1^1]^T|_{\boldsymbol{x}=\mathbf{0}} = \begin{bmatrix}\frac{\partial j_1^1}{\partial x_1} & \frac{\partial j_2^1}{\partial x_1} \\ \frac{\partial j_1^1}{\partial x_2} & \frac{\partial j_2^1}{\partial x_2}\end{bmatrix}^T|_{\boldsymbol{x}=\mathbf{0}} = \begin{bmatrix} j_{11}^2 & j_{12}^2 \\ j_{21}^2 & j_{22}^2\end{bmatrix}|_{\boldsymbol{x}=\mathbf{0}} = \begin{bmatrix}2 & 0 \\ 0 & 2\end{bmatrix} \rightarrow A_2 = \frac{1}{2}[j_{11}^2 \quad 2j_{12}^2 \quad j_{22}^2] = [1 \quad 0 \quad 1] \tag{135}$$

$$J_1^3 = J_1^4 = 0 \tag{136}$$

$$f_2(\boldsymbol{x}) = f_2(\mathbf{0}) + J_2^1(\mathbf{0})\boldsymbol{x} + \frac{1}{2!}J_2^2(\mathbf{0})\tilde{\boldsymbol{x}}^{\otimes 2} + \frac{1}{3!}J_2^3(\mathbf{0})\tilde{\boldsymbol{x}}^{\otimes 3} + \frac{1}{4!}J_2^4(\mathbf{0})\tilde{\boldsymbol{x}}^{\otimes 4} \tag{137}$$

$$f_2(\mathbf{0}) = \boldsymbol{a_0} = 1 - 2(0) + 0^2 + 100(0)^2 - 200(0)^2(0) + 100(0)^4 = 1 \tag{138}$$

$$J_2^1(\mathbf{0}) = [\nabla f_2(\boldsymbol{x})]^T|_{\boldsymbol{x}=\mathbf{0}} = \begin{bmatrix}\frac{\partial f_2}{\partial x_1} & \frac{\partial f_2}{\partial x_2}\end{bmatrix}|_{\boldsymbol{x}=\mathbf{0}} = [j_1^1 \quad j_2^1]|_{\boldsymbol{x}=\mathbf{0}} =$$
$$[-2 + 2x_1 - 400x_1x_2 + 400x_1^3 \quad 200x_2 - 200x_1^2]|_{\boldsymbol{x}=\mathbf{0}} = [-2 \quad 0] = A_1 \tag{139}$$

$$J_2^2(\mathbf{0}) = [\nabla J_2^1]^T|_{\boldsymbol{x}=\mathbf{0}} = \begin{bmatrix}\frac{\partial j_1^1}{\partial x_1} & \frac{\partial j_2^1}{\partial x_1} \\ \frac{\partial j_1^1}{\partial x_2} & \frac{\partial j_2^1}{\partial x_2}\end{bmatrix}^T|_{\boldsymbol{x}=\mathbf{0}} = \begin{bmatrix} j_{11}^2 & j_{12}^2 \\ j_{21}^2 & j_{22}^2\end{bmatrix}|_{\boldsymbol{x}=\mathbf{0}} = \begin{bmatrix}2 - 400x_2 + 1200x_1^2 & -400x_1 \\ -400x_1 & 200\end{bmatrix} = \begin{bmatrix}2 & 0 \\ 0 & 200\end{bmatrix}$$
$$\rightarrow A_2 = \frac{1}{2}[j_{11}^2 \quad 2j_{12}^2 \quad j_{22}^2] = [1 \quad 0 \quad 100] \tag{140}$$

$$J_2^3(\mathbf{0}) = [\nabla J_2^2]^T|_{\boldsymbol{x}=\mathbf{0}} = \begin{bmatrix}\begin{bmatrix}\frac{\partial j_{11}^2}{\partial x_1} & \frac{\partial j_{12}^2}{\partial x_1} \\ \frac{\partial j_{21}^1}{\partial x_1} & \frac{\partial j_{22}^1}{\partial x_1}\end{bmatrix} & \begin{bmatrix}\frac{\partial j_{11}^2}{\partial x_2} & \frac{\partial j_{12}^2}{\partial x_2} \\ \frac{\partial j_{21}^1}{\partial x_2} & \frac{\partial j_{22}^1}{\partial x_2}\end{bmatrix}\end{bmatrix}^T|_{\boldsymbol{x}=\mathbf{0}} = \begin{bmatrix}\begin{bmatrix} j_{111}^3 & j_{121}^3 \\ j_{211}^3 & j_{221}^3\end{bmatrix} & \begin{bmatrix} j_{112}^3 & j_{122}^3 \\ j_{212}^3 & j_{222}^3\end{bmatrix}\end{bmatrix}^T|_{\boldsymbol{x}=\mathbf{0}}$$
$$= \begin{bmatrix}\begin{bmatrix}2400x_1 & -400 \\ -400 & 0\end{bmatrix} & \begin{bmatrix}-400 & 0 \\ 0 & 0\end{bmatrix}\end{bmatrix}^T \rightarrow A_3 = \frac{1}{3!}[j_{111}^3 \quad 3j_{112}^3 \quad 3j_{122}^3 \quad j_{222}^3] = [0 \quad -200 \quad 0 \quad 0] \tag{141}$$

$$J_2^4(\mathbf{0}) = [\nabla J_2^3]^T|_{\boldsymbol{x}=\mathbf{0}} = \begin{bmatrix}\begin{bmatrix}\frac{\partial j_{111}^3}{\partial x_1} & \frac{\partial j_{121}^3}{\partial x_1}\\ \frac{\partial j_{211}^3}{\partial x_1} & \frac{\partial j_{221}^3}{\partial x_1}\end{bmatrix} & \begin{bmatrix}\frac{\partial j_{112}^3}{\partial x_1} & \frac{\partial j_{122}^3}{\partial x_1}\\ \frac{\partial j_{212}^3}{\partial x_1} & \frac{\partial j_{222}^3}{\partial x_1}\end{bmatrix}\\ \begin{bmatrix}\frac{\partial j_{111}^2}{\partial x_2} & \frac{\partial j_{121}^2}{\partial x_2}\\ \frac{\partial j_{211}^1}{\partial x_2} & \frac{\partial j_{221}^1}{\partial x_2}\end{bmatrix} & \begin{bmatrix}\frac{\partial j_{112}^2}{\partial x_2} & \frac{\partial j_{122}^2}{\partial x_2}\\ \frac{\partial j_{212}^1}{\partial x_2} & \frac{\partial j_{222}^1}{\partial x_2}\end{bmatrix}\end{bmatrix}^T|_{\boldsymbol{x}=\mathbf{0}} = \begin{bmatrix}\begin{bmatrix}j_{1111}^4 & j_{1211}^4\\ j_{2111}^4 & j_{2211}^4\end{bmatrix} & \begin{bmatrix}j_{1112}^4 & j_{1212}^4\\ j_{2112}^4 & j_{2212}^4\end{bmatrix}\\ \begin{bmatrix}j_{1121}^4 & j_{1221}^4\\ j_{2121}^4 & j_{2221}^4\end{bmatrix} & \begin{bmatrix}j_{1122}^4 & j_{1222}^4\\ j_{2122}^4 & j_{2222}^4\end{bmatrix}\end{bmatrix}^T|_{\boldsymbol{x}=\mathbf{0}}$$

$$= \begin{bmatrix}\begin{bmatrix}2400 & 0\\ 0 & 0\end{bmatrix} & \begin{bmatrix}0 & 0\\ 0 & 0\end{bmatrix}\\ \begin{bmatrix}0 & 0\\ 0 & 0\end{bmatrix} & \begin{bmatrix}0 & 0\\ 0 & 0\end{bmatrix}\end{bmatrix}^T$$

$$\rightarrow A_4 = \frac{1}{4!}[j_{1111}^4 \quad 4j_{1112}^4 \quad 6j_{1122}^4 \quad 4j_{1222}^1 \quad j_{2222}^4] = \frac{1}{24}[2400 \quad 0 \quad 0 \quad 0 \quad 0] = [100 \quad 0 \quad 0 \quad 0 \quad 0] \quad (142)$$

b. *Tensor Derivatives of an Artificial Neural Network*

Assume the structure of the neural network is of single layer with k number of neurons in the hidden layer, depicted in Figure 177. The output from the hidden layer, $\boldsymbol{z}$, is a nonlinear transformation of the input, $\boldsymbol{x}$, and a weight and bias matrix, W^I and $\boldsymbol{b^I}$, given in Eq. (143). $\boldsymbol{x}$ is of size $\mathbb{R}^{m\times 1}$. $\boldsymbol{z}$ is of size $\mathbb{R}^{k\times 1}$. $\boldsymbol{y}$ is of size $\mathbb{R}^{n\times 1}$. The output from the entire network, $\hat{\boldsymbol{y}}$, is a nonlinear transformation of the intermediate output, $\boldsymbol{z}$, and a weight and bias matrix, W^O and $\boldsymbol{b^O}$, given in Eq. (144). Assume the nonlinear transformation $\sigma(\cdot)$ is the tansig function, given in Eq. (145). Typically, the output layer is linear and there is no transformation function. The explicit transformation from input to output is given in Eq. (146).

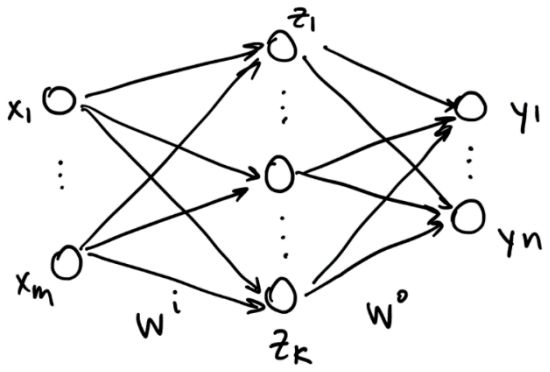

Figure 177: single layer neural network with hidden layer explicitly defined

$$\boldsymbol{z} = \sigma(W^I, \boldsymbol{b^I}, \boldsymbol{x}) \quad (143)$$

$$\hat{\boldsymbol{y}} = \sigma(W^O, \boldsymbol{b^O}, \boldsymbol{z}) \tag{144}$$

$$\sigma(s) = \frac{2}{1 + e^{-2s}} - 1 \tag{145}$$

$$\hat{\boldsymbol{y}} = f_{NN}(\boldsymbol{x}) = W^O\big(\sigma(W^I\boldsymbol{x} + \boldsymbol{b^I})\big) + \boldsymbol{b^0} \tag{146}$$

With this structure, the goal is to find the general derivatives of this function, $f_{NN}(\cdot)$, in tensor form with respect to the input state, $\boldsymbol{x}$. The derivative of function f_{NN} of order d is represented as J_f^d, a Jacobian, and is composed of the trained NN parameters: $W^O, \boldsymbol{b^O}, W^I, \boldsymbol{b^I}$. Ascending derivative orders of Jacobians grow in dimension, as discussed in the previous subsection. The first derivative is a 2nd order tensor can be formulated as a matrix, where $\odot$ is the Hadamard product and $\mathbf{1}_{\boldsymbol{m}}^{\boldsymbol{T}}$ is a vector of ones of length m, given in Eq. (147). The second derivative is a 3rd order tensor must be formulated as a tensor, where $1_{n\times m}$ is a matrix of ones of dimension $n \times m$, given in Eq. (148). The expression $\left(W^O_{\{n,1,k\}} \odot W^I_{\{1,m,k\}}\right)_{\{n,m,k\}}$ demonstrates ambiguity in matrix notation for tensor manipulation as the $\odot$ operator is overloaded and could either mean Hadamard product or a tensor contraction. At this point, the general derivatives are represented in index and summation notation for clarity.

$$J_f^1(\boldsymbol{x}) = \nabla f_{NN}(\boldsymbol{x}) = W^{\mathrm{O}}\big(W^{\mathrm{I}} \odot (1 - \sigma(W^I\boldsymbol{x} + \boldsymbol{b^I})^2 \mathbf{1}_{\boldsymbol{m}}^T)\big) \tag{147}$$

$$J_f^2(\boldsymbol{x_m}) = \left[\nabla J_f^1\right]^T = -2\left[\left(W^O_{\{n,1,k\}} \odot W^I_{\{1,m,k\}}\right)_{\{n,m,k\}} \odot \left(1_{n\times m} \otimes \sigma(W^I\boldsymbol{x} + \boldsymbol{b^I})\right)\right][W^I \odot (1 - \sigma(W^I\boldsymbol{x} + \boldsymbol{b^I})^2)] \tag{148}$$

To set up the index notation, the input, output, and hidden state vectors are represented by each of their components. $\hat{\boldsymbol{y}}$ is composed of scalars y_j for the indices $j = 1,2,\dots,n$. $\boldsymbol{x}$ is composed of scalars x_i for the indices $i = 1,2,\dots,m$. $\boldsymbol{z}$ is composed of scalars z_l for the indices $l = 1,2,\dots,k$. The neural-network parameters are expressed with the same indices as the vectors: $w^O_{jl}, b^O_j, w^I_{li}, b^I_l$. The expression mapping the input to the output in index and summation notation is given in Eq.

(149). The goal then is to find general derivatives of the function f_j with respect to the input x_i of order d: $\frac{\partial^d f_j}{\partial x_{i_1} \cdots \partial x_{i_d}}$.

$$\hat{y}_j = f_j(x_i) = \sum_l w_{jl}^O \sigma\left(\sum_i w_{li}^I x_i + b_l^I\right) + b_j^O \tag{149}$$

The general derivatives are derived primarily with the chain rule and product rule. All derivative expressions are composed of only four different forms, given by Eq. (150) to Eq. (153) for an arbitrary index i_q. The partial derivatives at a higher order, given in Eq. (154) and Eq. (155), are nilpotent, a useful property. The first tensor derivative to the fifth tensor derivative are given in Eq. (156) to Eq. (160) and only grows in number of terms. The expressions in Eq. (159) and Eq. (160) do not explicitly list the derivative in terms of the network parameters, only in terms of the partial derivative expressions, as the resultant full expression is too long. The recursive relationship to derive the immediate higher order derivative is given in Eq. (161).

$$\frac{\partial f_j}{\partial z_l} = w_{jl}^O \tag{150}$$

$$\frac{\partial z_l}{\partial x_{i_q}} = w_{li_q}^I \left[1 - z_l \left(\sum_{i_q} w_{li_q}^I x_{i_q} + b_l^I\right)^2\right] \tag{151}$$

$$\frac{\partial}{\partial \sigma_l}\left(\frac{\partial z_l}{\partial x_{i_q}}\right) = w_{li_q}^I \left[-2\sigma_l \left(\sum_{i_q} w_{li_q}^I x_{i_q} + b_l^I\right)\right] \tag{152}$$

$$\frac{\partial^2}{\partial z_l^2}\left(\frac{\partial z_l}{\partial x_{i_q}}\right) = w_{li_q}^I(-2) \tag{153}$$

$$\frac{\partial^2 f_j}{\partial z_l^2} = 0 \tag{154}$$

$$\frac{\partial^3}{\partial z_l^3}\left(\frac{\partial z_l}{\partial x_{i_q}}\right) = 0 \tag{155}$$

$$J^1_{ji_1} = \frac{\partial f_j}{\partial x_{i_1}} = \sum_l \frac{\partial f_j}{\partial z_l}\frac{\partial z_l}{\partial x_{i_1}} = \sum_l w^O_{jl} w^I_{li_1}\left[1-\sigma_l\left(\sum_{i_1} w^I_{li_1} x_{i_1} + b^I_l\right)^2\right] \quad (156)$$

$$J^2_{ji_1i_2} = \frac{\partial}{\partial x_{i_2}}\left(\frac{\partial f_j}{\partial x_{i_1}}\right) = \sum_l \frac{\partial f_j}{\partial z_l}\left[\frac{\partial}{\partial z_l}\left(\frac{\partial z_l}{\partial x_{i_1}}\right)\right]\frac{\partial z_l}{\partial x_{i_2}} = \sum_l w^O_{jl} w^I_{li_1} w^I_{li_2}\left[-2\sigma\left(\sum_{i_1} w^I_{li_1} x_{i_1} + b^I_l\right)\right]\left[1-\sigma_l\left(\sum_{i_2} w^I_{li_2} x_{i_2} + b^I_l\right)^2\right] \quad (157)$$

$$J^3_{ji_1i_2i_3} = \frac{\partial}{\partial x_{i_3}}\left(\frac{\partial}{\partial x_{i_2}}\left(\frac{\partial f_j}{\partial x_{i_1}}\right)\right) = \sum_l \frac{\partial f_j}{\partial z_l}\left[\frac{\partial^2}{\partial z_l^2}\left(\frac{\partial z_l}{\partial x_{i_1}}\right)\frac{\partial z_l}{\partial x_{i_2}} + \frac{\partial}{\partial z_l}\left(\frac{\partial z_l}{\partial x_{i_1}}\right)\frac{\partial}{\partial z_l}\left(\frac{\partial z_l}{\partial x_{i_2}}\right)\right]\frac{\partial z_l}{\partial x_{i_3}}$$
$$= \sum_l -2w^O_{jl} w^I_{li_1} w^I_{li_2} w^I_{li_3}\left[1-\sigma_l\left(\sum_{i_2} w^I_{li_2} x_{i_2} + b^I_l\right)^2 - 2\sigma_l\left(\sum_{i_1} w^I_{li_1} x_{i_1} + b^I_l\right)\sigma_l\left(\sum_{i_1} w^I_{li_1} x_{i_1} + b^I_l\right)\right]\left[1-\sigma_l\left(\sum_{i_3} w^I_{li_3} x_{i_3} + b^I_l\right)^2\right] \quad (158)$$

$$J^4_{ji_1i_2i_3i_4} = \frac{\partial}{\partial x_{i_4}}\left(\frac{\partial}{\partial x_{i_3}}\left(\frac{\partial}{\partial x_{i_2}}\left(\frac{\partial f_j}{\partial x_{i_1}}\right)\right)\right)$$
$$= \sum_l \frac{\partial f_j}{\partial z_l}\left\{\left[2\frac{\partial^2}{\partial z_l^2}\left(\frac{\partial z_l}{\partial x_{i_1}}\right)\frac{\partial}{\partial z_l}\left(\frac{\partial z_l}{\partial x_{i_2}}\right) + \frac{\partial}{\partial z_l}\left(\frac{\partial z_l}{\partial x_{i_1}}\right)\frac{\partial^2}{\partial z_l^2}\left(\frac{\partial z_l}{\partial x_{i_2}}\right)\right]\frac{\partial z_l}{\partial x_{i_3}} + \left[\frac{\partial^2}{\partial z_l^2}\left(\frac{\partial z_l}{\partial x_{i_1}}\right)\frac{\partial z_l}{\partial x_{i_2}} + \frac{\partial}{\partial z_l}\left(\frac{\partial z_l}{\partial x_{i_1}}\right)\frac{\partial}{\partial z_l}\left(\frac{\partial z_l}{\partial x_{i_2}}\right)\right]\frac{\partial}{\partial z_l}\left(\frac{\partial z_l}{\partial x_{i_3}}\right)\right\}\frac{\partial z_l}{\partial x_{i_4}} \quad (159)$$

$$J^5_{ji_1i_2i_3i_4i_5} = \frac{\partial}{\partial x_{i_5}}\left(\frac{\partial}{\partial x_{i_4}}\left(\frac{\partial}{\partial x_{i_3}}\left(\frac{\partial}{\partial x_{i_2}}\left(\frac{\partial f_j}{\partial x_{i_1}}\right)\right)\right)\right) =$$

$$\sum_l \frac{\partial f_j}{\partial z_l}\left\{\begin{array}{c}\left[\begin{array}{c} 3\frac{\partial^2}{\partial z_l^2}\left(\frac{\partial z_l}{\partial x_{i_1}}\right)\frac{\partial^2}{\partial^2 z_l}\left(\frac{\partial z_l}{\partial x_{i_2}}\right)\frac{\partial z_l}{\partial x_{i_3}} + 4\frac{\partial^2}{\partial z_l^2}\left(\frac{\partial z_l}{\partial x_{i_1}}\right)\frac{\partial}{\partial z_l}\left(\frac{\partial z_l}{\partial x_{i_2}}\right)\frac{\partial}{\partial z_l}\left(\frac{\partial z_l}{\partial x_{i_3}}\right) \\ +2\frac{\partial}{\partial z_l}\left(\frac{\partial z_l}{\partial x_{i_1}}\right)\frac{\partial^2}{\partial z_l^2}\left(\frac{\partial z_l}{\partial x_{i_2}}\right)\frac{\partial}{\partial z_l}\left(\frac{\partial z_l}{\partial x_{i_3}}\right) + \frac{\partial^2}{\partial z_l^2}\left(\frac{\partial z_l}{\partial x_{i_1}}\right)\frac{\partial z_l}{\partial x_{i_2}}\frac{\partial^2}{\partial^2 z_l}\left(\frac{\partial z_l}{\partial x_{i_3}}\right) + \frac{\partial}{\partial z_l}\left(\frac{\partial z_l}{\partial x_{i_1}}\right)\frac{\partial}{\partial z_l}\left(\frac{\partial z_l}{\partial x_{i_2}}\right)\frac{\partial^2}{\partial z_l^2}\left(\frac{\partial z_l}{\partial x_{i_3}}\right) \end{array}\right]\frac{\partial z_l}{\partial x_{i_4}} \\ +\left[\begin{array}{c} 2\frac{\partial^2}{\partial z_l^2}\left(\frac{\partial z_l}{\partial x_{i_1}}\right)\frac{\partial}{\partial z_l}\left(\frac{\partial z_l}{\partial x_{i_2}}\right)\frac{\partial z_l}{\partial x_{i_3}} + \frac{\partial}{\partial z_l}\left(\frac{\partial z_l}{\partial x_{i_1}}\right)\frac{\partial^2}{\partial z_l^2}\left(\frac{\partial z_l}{\partial x_{i_2}}\right)\frac{\partial z_l}{\partial x_{i_3}} \\ +\frac{\partial^2}{\partial z_l^2}\left(\frac{\partial z_l}{\partial x_{i_1}}\right)\frac{\partial z_l}{\partial x_{i_2}}\frac{\partial}{\partial z_l}\left(\frac{\partial z_l}{\partial x_{i_3}}\right) + \frac{\partial}{\partial z_l}\left(\frac{\partial z_l}{\partial x_{i_1}}\right)\frac{\partial}{\partial z_l}\left(\frac{\partial z_l}{\partial x_{i_2}}\right)\frac{\partial}{\partial z_l}\left(\frac{\partial z_l}{\partial x_{i_3}}\right) \end{array}\right]\frac{\partial}{\partial z_l}\left(\frac{\partial z_l}{\partial x_{i_4}}\right)\end{array}\right\}\frac{\partial z_l}{\partial x_{i_5}} \quad (160)$$

$$J^{d+1}_f = \frac{\partial J^d}{\partial z_l}\frac{\partial z_l}{\partial x_{i_{d+1}}} \quad (161)$$

c. *Taylor Approximation of Artificial Neural Network in Polynomial Form*

The previous section lays the foundation for a Taylor approximation of a single-layer neural network. The derivatives from Eq. (156) to (160) populate the expression given in Eq. (162), where A^d is the polynomial-coefficient tensor by evaluating the derivatives J^d_f at $x_i = 0$. The polynomial-coefficient tensors are given in Eq. (163) to Eq. (168). Note that b^O_j only appears in A^O_j. The higher orders of polynomial coefficients can be derived from lower orders of polynomial coefficients, given in Eq. (169). This result is important as the polynomial-coefficient tensor can

be derived without the entire partial derivative expression, vastly simplifying the coefficient tensor calculation.

$$f_j(x_i) = A_j^0 + \sum_{i_1} A_{ji_1}^1 a_{i_1}^1 x_{i_1} + \sum_{i_1}\sum_{i_2} A_{ji_1i_2}^2 a_{i_1i_2}^2 x_{i_1i_2}^{\otimes 2} + \cdots + \sum_{i_1} \cdots \sum_{i_d} A_{ji_1\cdots i_d}^d a_{i_1\cdots i_d}^d x_{i_1\cdots i_d}^{\otimes d} \tag{162}$$

$$A_j^0 = \sum_l w_{jl}^O \sigma(b_l^I) + b_j^O \tag{163}$$

$$A_{ji_1}^1 = \sum_l w_{jl}^O w_{li_1}^I (1 - \sigma(b_l^I)^2) \tag{164}$$

$$A_{ji_1i_2}^2 = \sum_l -2w_{jl}^O w_{li_1}^I w_{li_2}^I (\sigma(b_l^I) - \sigma(b_l^I)^3) \tag{165}$$

$$A_{ji_1i_2i_3}^3 = \sum_l -2w_{jl}^O w_{li_1}^I w_{li_2}^I w_{li_3}^I (1 - 4\sigma(b_l^I)^2 - 3\sigma(b_l^I)^3) \tag{166}$$

$$A_{ji_1i_2i_3i_4}^4 = \sum_l 8w_{jl}^O w_{li_1}^I w_{li_2}^I w_{li_3}^I w_{li_4}^I (2\sigma(b_l^I) - 5\sigma(b_l^I)^3 + 3\sigma(b_l^I)^5) \tag{167}$$

$$A_{ji_1i_2i_3i_4i_5}^5 = \sum_l 8w_{jl}^O w_{li_1}^I w_{li_2}^I w_{li_3}^I w_{li_4}^I w_{li_5}^I (2 - 17\sigma(b_l^I)^2 + 30\sigma(b_l^I)^4 - 15\sigma(b_l^I)^6) \tag{168}$$

$$A_{ji_1\cdots i_d}^d = \frac{\partial A_{ji_1\cdots i_{d-1}}^{d-1}}{\partial z} w_{li_d}^I (1 - \sigma_l(b_l^I)^2) \tag{169}$$

d. *Comparison of Model Fidelity to Other Numerical System-Identification Methods*

In this subsection, SINDy, symbolic regression (SR), single-layer neural network, and the NN's proposed Taylor expansion are compared to find analytical solutions of dynamic models. SINDy, Sparse Identification of Nonlinear Dynamics, is a newly developed method introduced by E. Kaiser et al. from University of Washington in Seattle in which data is approximated by a library of candidate expressions with a threshold value sparsity condition [137]. This analysis incorporated the SINDy solver to not only generate an expression from a comprehensive library of functions but also an expression based only on strictly polynomial terms. The symbolic regression algorithm draws from an open source MATLAB package GPTIPS2 created by Dominic

Searson from Synoptic Technologies Ltd., UK [139]. The neural network is created and trained through MATLAB's neural network toolbox. The proposed Taylor expansion with the NN parameters is coded in MATLAB. All methods, excluding the neural network, can generate an analytical solution to nonlinear systems but differ in performance. Metrics to evaluate performance of each method are efficiency, accuracy and complexity. This section discusses the method of comparison, metrics to evaluate performance, and subsequent results of the system identification methods.

Method

Several dynamic models are used to measure efficiency and accuracy of each system identification method. Each algorithm is trained with the same pairwise input and output data to a predict a state for the systems listed in Table 46. The input output data pairs are of form $< \boldsymbol{s_k}, \boldsymbol{s_{k+1}} >$ in which the input is state vector at time k and the output is of time $k+1$. The 1DOF underdamped linear spring-mass-damper system has a linear transition matrix from previous state to next state, constituting the simplest dynamic system to identify. The 1DOF flux-pinned system is much like the 1DOF linear spring but the stiffness of the spring is nonlinear and governed by a differential equation, given in Table 46. The spring-pendulum demonstrates nonlinearity and coupling of dynamics. In both the flux-pinned system and spring-pendulum case, the differential equations of motion propagate the state to generate data. The system-identification methods do not generate expressions for acceleration but generate a mapping from previous state to next state, implicitly integrating the double derivative. All methods, excluding the neural network, adhere to a sparse matrix solution representing linear combinations of nonlinear input terms in the form of Eq. (170). Nonlinear terms are from a selected expression library and the input state represented

by $h_i(\boldsymbol{s_k})$ in which the library includes monomial states of varying degree and $\boldsymbol{s_k}$ represents the state vector at time k.

$$\hat{\boldsymbol{s}}_{\boldsymbol{k+1}} = M \begin{bmatrix} h_1(\boldsymbol{s_k}) \\ \vdots \\ h_k(\boldsymbol{s_k}) \end{bmatrix} \tag{170}$$

Table 46: Dynamic systems for system identification comparison

System	Governing Equations of Motion
1 DOF Spring (discrete)	$\begin{bmatrix} x_{k+1} \\ v_{k+1} \end{bmatrix} = \begin{bmatrix} 0.9995 & 0.01 \\ -0.0999 & 0.9985 \end{bmatrix} \begin{bmatrix} x_k \\ v_k \end{bmatrix}$
1 DOF Flux-Pinned System	$\ddot{x} = \frac{-3\mu_0}{2\pi(x+a)^4}$
Spring Pendulum*	$\ddot{x} = -5\left(\sqrt{x^2+y^2}-1\right)\frac{x}{\sqrt{x^2+y^2}}$ $\ddot{y} = -5\left(\sqrt{x^2+y^2}-1\right)\frac{y}{\sqrt{x^2+y^2}} - 10$

Metrics of Evaluation

Metrics for evaluation are computation time, state error (mean squared error), coefficient error, length of solution, and coefficient stability, given in Table 47. The state error is of mean squared error form of the algorithm's state prediction and the true state. Coefficient error refers to a coefficient vector $\boldsymbol{c}$ of length m, geared toward polynomial solutions. Parameter stability refers to the learned parameters, relevant for all methods. The length of solution refers to the length of nonlinear terms in Eq. (170) or the number of $h(\boldsymbol{s})$.

Table 47: Metrics for evaluating system identification methods on dynamic systems

Metrics	Measurement	Definition/Equation
Computing time	Efficiency	Time cost to run calculation
State error (mean squared error or squared RMS error)	Accuracy	$MSE = \frac{1}{n}\sum_{i=1}^{n}(\boldsymbol{s_k} - \hat{\boldsymbol{s}}_{\boldsymbol{k}})^2$
Coefficient error	Accuracy / Correctness	MSE of coefficients (if in polynomial form) $CE = \frac{1}{m}\sum_{i=1}^{m}(c_i - \hat{c_i})^2$ Marked as N/A if not in polynomial form
Parameter stability	Accuracy / Complexity	Largest parameter divided by smallest coefficient $PS = \frac{\max(\boldsymbol{p})}{\min(\boldsymbol{p})}$
Length of solution	Accuracy / Complexity	Number of nonlinear terms in solution

Results

Computation in FLOPS

To illustrate one of the advantages of the neural-network-derived polynomial over a data-derived polynomial, the general number of FLOPS each polynomial derivation is compared. The relevant parameters to reiterate are dimension of input (m), dimension of output (n), number of neurons (k), number of training points (t), and order of polynomial approximation (d). There exist certain conditions in which either method of deriving the polynomial is advantageous. Unlimited computation, time, and access to data allows direct polynomial computation, which is the limit of polynomial model fidelity. In a situation where data and computation are limited due to download rate or processor limits, a neural-network approximation offers a compact representation of the information embedded in the data, although some model fidelity may be sacrificed. FLOPS reveal computational efficiency of either method for certain conditions of data size and state size.

For the data-derived polynomial, the expression for the polynomial coefficients that minimize linear-least-squared error is given in Eq. (171). The input and output matrices, Y and X, are the input-output vector pairs but concatenated to incorporate all training points, given in Eqs. (172) & (173). The exponentiated state $\boldsymbol{x}^{\otimes d}$ is of dimension $\sum_{i=1}^{d}\prod_{i=1}^{d}\frac{m+i-1}{i}$ of which the dominant size is approximately $\frac{m^d}{d!}$ for simplicity. The solution for the polynomial coefficients A is given in Eq. (174). The sequence of operations that contribute to FLOPS are three matrix multiplication operations and a single matrix inversion. The order of FLOPS assuming the dimension of output is significantly less than the number of training points, $n \ll t$, is $\mathcal{O}\left(\frac{m^d}{d!}\left(2t+\frac{m^{2d}}{d!}\right)\right)$, which is notably absent of the number of neurons. Although the polynomial approximation is most accurate with the largest dataset available t and highest order of polynomial d, a subset of data and a lower order of polynomial can dramatically decrease computation. The relative relationship between the effect of data size and the multinomial state inversion computation shows that data size dominates if $2t > \frac{m^{2d}}{d!}$, a computational trade-off when optimizing for algorithm speed.

$$Y = AX^{\otimes d} \tag{171}$$

$$Y = [\boldsymbol{y}(1) \quad \boldsymbol{y}(2) \quad \cdots \quad \boldsymbol{y}(t)] \in \mathbb{R}^{n\times t} \tag{172}$$

$$X^{\otimes d} = [\boldsymbol{x}^{\otimes \boldsymbol{d}}(1) \quad \boldsymbol{x}^{\otimes \boldsymbol{d}}(2) \quad \cdots \quad \boldsymbol{x}^{\otimes \boldsymbol{d}}(t)] \in \mathbb{R}^{\sim\frac{m^d}{d!}\times t} \tag{173}$$

$$A = YX^{\otimes d}\left(X^{\otimes d}X^{\otimes d^T}\right)^{-1} \tag{174}$$

For the NN-derived polynomial, the total number of FLOPS is the summation of the neural network training process and the polynomial coefficient derivation. The FLOPS needed to train a neural network is of order $\mathcal{O}(nmkt)$, which is dependent on number of connections in the neural

network and size of training data. The polynomial coefficients are derived directly from the NN parameters, which are reiterated in Table 48. The polynomial-coefficient expressions are generally proportional to the number of terms in the order of polynomial-coefficient tensor, as shown in Table 48. The order of FLOPS that dominates the overall polynomial-expression FLOPS is the largest term, $\mathcal{O}(nkm^d)$, which is notably independent of the size of training data. The total number of FLOPS from NN training to polynomial generation necessitates FLOPS on the order of $\mathcal{O}\left(nk(mt + m^d)\right)$. The training process needs more computation than conversion to polynomial form if $t > m^{d-1}$, which should generally be the case or held as a constraint for the polynomial order.

Table 48: FLOPS calculation for various orders of polynomial-coefficient tensors derived from the neural network

order	Coefficient tensor expression	FLOPS
0	$A_j^0 = \sum_l w_{jl}^O \sigma(b_l^I) + b_j^O$	$\mathcal{O}(nk)$
1	$A_{ji_1}^1 = \sum_l w_{jl}^O w_{li_1}^I (1 - \sigma(b_l^I)^2)$	$\mathcal{O}(nkm)$
2	$A_{ji_1i_2}^2 = \sum_l -2w_{jl}^O w_{li_1}^I w_{li_2}^I (\sigma(b_l^I) - \sigma(b_l^I)^3)$	$\mathcal{O}(nkm^2)$
⋮	⋮	⋮
d	$A_{ji_1\cdots i_d}^d = \frac{\partial A_{ji_1\cdots i_{d-1}}^{d-1}}{\partial z} w_{li_d}^I (1 - \sigma_l(b_l^I)^2)$	$\mathcal{O}(nkm^d)$

To compare the two methods of deriving a polynomial, the neural-network-derived polynomial is less computationally costly if $nk < \frac{1}{d!}(t + m^d)$. This inequality shows that the NN polynomial grows linearly with the dimension of state output and number of neurons whereas the polynomial from data grows linearly with data and exponentially with dimension of state input

and polynomial order. Typically, the output and neuron dimensions are much smaller than the size of training data and certainly smaller than an exponential combination of input size and polynomial order. If training data is limited or the order of polynomial is small, the neural network method is inappropriate and excessive, whereas the linear-least-squares approximation is much more appropriate.

Model Fidelity and Other Metrics

For each dynamic system, Table 49 to Table 51 report the performance of all five system-identification methods for each dynamic system. Wherever an ϵ is listed in the tables, ϵ denotes an immensely small value within machine precision. The computation time for the NN-Polynomial expansion does not include the NN training time, only the time to transform the NN parameters into polynomial coefficients. Across all metrics and all dynamic systems, a different system identification method carries various advantages and disadvantages.

The best method to approximate the 1DOF linear spring system is the strict polynomial, with performance across all methods shown in Table 49. The proposed NN-poly approximation method performance in each state's timeseries and across increasing polynomial degrees is shown in Figure 178. As expected, increasing the order of polynomial approximation yields less state error, although not much performance is gained past the second order approximation. The small error bars for each degree signals that the final solution from each NN random initialization does not vary much. SINDy's polynomial expression yields the correct result within machine precision, takes a minimal amount of time to compute, and has least state error. SINDy does not generate unnecessary terms with coefficients of negligible magnitude. The NN-polynomial conversion is comparable in computation but includes much more state error. This straightforward test case is best solved with the simplest solver, the direct polynomial solution; even a least squares solution

is sufficient. This system does not need a complex, expressive system identification method due to the simplicity of its linear form.

Table 49: 1 DOF spring evaluation of performance for all system identification methods

Metrics	Polynomial	SINDy	SR	NN	NN-Poly
Computing time	0.288 sec.	0.475 sec.	223.052 sec.	3.627 sec.	0.372 sec.
State Error (MSE)	ϵ (x) ϵ (v)	ϵ (x) ϵ (v)	ϵ (x) ϵ (v)	1.07×10^{-8} (x) 1.46×10^{-8} (v)	1.07×10^{-5} (x) 1.46×10^{-5} (v)
Coefficient Error (CE)	0.0060 (x) 0.0060 (v)	0.0060 (x) 0.0060 (v)	5.45×10^{-10} (x) 2.24×10^{-11} (v)	0.000 (x) 0.000 (v)	0.000 (x) 0.000 (v)
Parameter stability	99.95 (x) 9.950 (v)	99.95 (x) 9.950 (v)	1.99×10^{16} (x) 4.44×10^{13} (v)	99.95 (x) 9.995 (v)	99.95 (x) 9.995 (v)
Length of solution	2 (x) 2 (v)	2 (x) 2 (v)	12 (x) 10 (v)	2 neurons	2 (x) 2 (v)

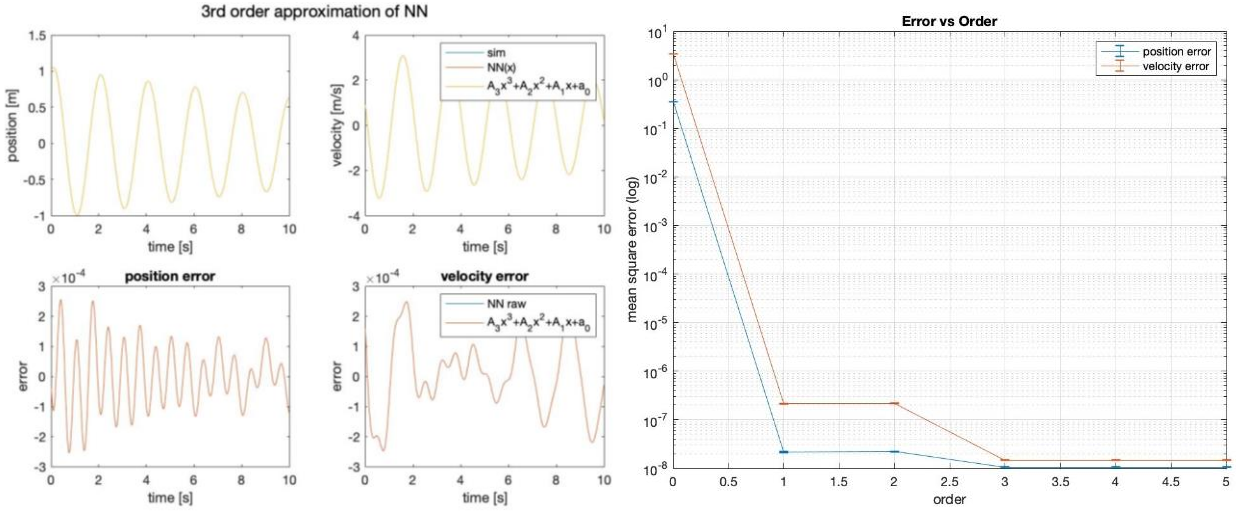

Figure 178: left, 3rd order NN-poly approximation of 1DOF linear system and error as difference of each state; right, MSE error of position and velocity state across different orders of approximation

The best methods to approximate the 1 DOF flux-pinned system are NN and NN-Poly, with performance reported in Table 50. Unlike the linear system approximation, the proposed NN-Poly approximation varies from the NN parameter initialization and does not converge to a steady state error until the fourth order, seen in Figure 179. The sole NN and NN-Poly approximate the data with the least state error, generate a minimal representation, and yield the most stable

parameters of all methods. Although the NN-poly method does require 2.5 × more time than the SINDy and strict polynomial method, the NN-poly method contains 10 × less state error, magnitudes more stable parameters, and 5 to 10 × less parameters in length of solution. SINDy, polynomial, and symbolic regression do not sufficiently express this magnitude of nonlinearity in a dynamic system and require the expressive power of a neural network. Subsequently, the NN-poly retains the same value of state error from the NN, demonstrating the accuracy of transformation from a NN form to polynomial form, while also offering a form from which to apply domain knowledge and safety guarantees.

Table 50: 1 DOF flux-pinned system evaluation of performance for all system identification methods

Metrics	Polynomial	SINDy	SR	NN	NN-Poly
Computing time	0.076 sec.	0.063 sec.	242.1 sec.	1.359 sec.	0.196 sec.
State Error (MSE)	1.90×10^{-3} (x) 9.0×10^{-4} (v)	1.90×10^{-3} (x) 9.0×10^{-4} (v)	6.30×10^{-3} (x) 1.03×10^{-2} (v)	1.30×10^{-4} (x) 1.12×10^{-4} (v)	1.30×10^{-4} (x) 1.12×10^{-4} (v)
Parameter stability	5.78×10^{4} (x) 2.81×10^{3} (v)	5.39×10^{4} (x) 1.61×10^{5} (v)	6.76×10^{3} (v) 3.41×10^{4} (v)	67.8 (x) 574.0 (v)	94.8 (x) 579.4 (v)
Length of solution	15 (x) 15 (v)	19 (x) 19 (v)	11 (x) 11 (v)	2 neurons	2 (x) 2 (v)

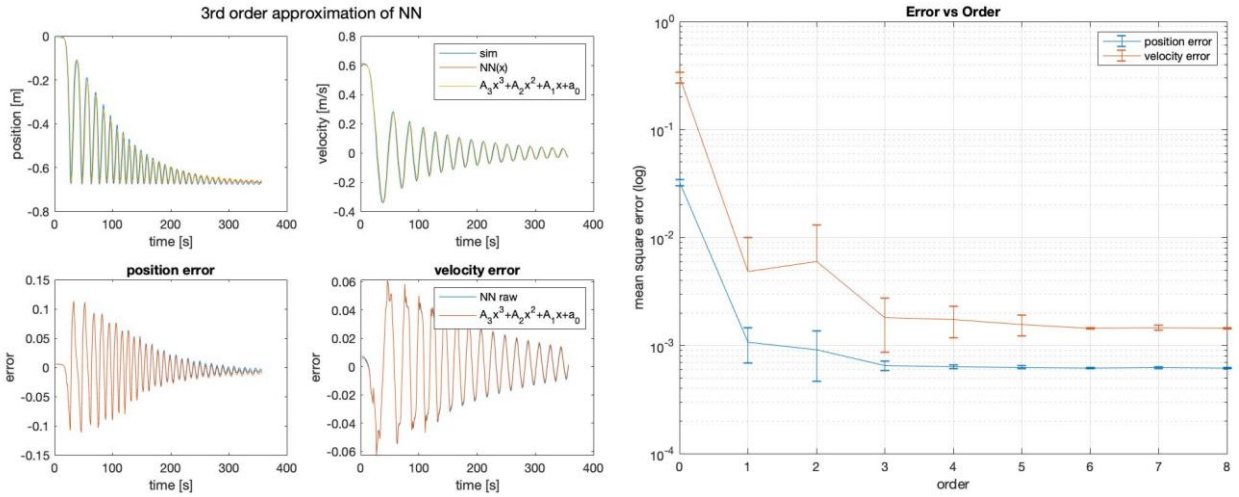

Figure 179: left, 3rd order NN-poly approximation of 1DOF flux-pinned nonlinear system and error as difference of each state; right, MSE error of position and velocity state across different orders of approximation

For the 2DOF system, SINDY, NN and NN-Poly all predict well, seen in Table 51. The third order NN-poly approximation for each state is shown in Figure 180. The NN-Poly MSE error decreases with increasing polynomial degree and does not converge until after the fourth order, seen in Figure 181. The NN and NN-Poly predict the 2DOF system with less terms, while SINDy generates least state error. Each method has comparable parameter stability and computation time. This coupled and slightly nonlinear dynamic system straddles the boundary in deciding which system identification method to use.

Table 51: 2 DOF spring pendulum system evaluation of performance for all system identification methods

Metrics	Polynomial	SINDy	SR	NN	NN-Poly
Computing time	0.293 sec.	0.329 sec.	258.041 sec.	3.577 sec.	0.355 sec.
State Error (MSE)	5×10^{-4} (x) 3.5×10^{-3} (y)	0.0006(x) 0.0037(y)	0.0046(x) 0.0037(y)	0.0030(x) 0.0162(y)	0.0032(x) 0.0170(y)
Parameter stability	6.616×10^{3} (x) 8.620×10^{3} (y)	3.772×10^{3} (x) 7.180×10^{3} (y)	1.055×10^{21} (x) 1.561×10^{3} (y)	7.644×10^{3} (x) 1.338×10^{3} (y)	8.076×10^{3} (x) 1.437×10^{3} (y)
Length of solution	15 (x) 15 (y)	15 (x) 15 (y)	11 (x) 14 (y)	4 neurons	4 (x) 4 (y)

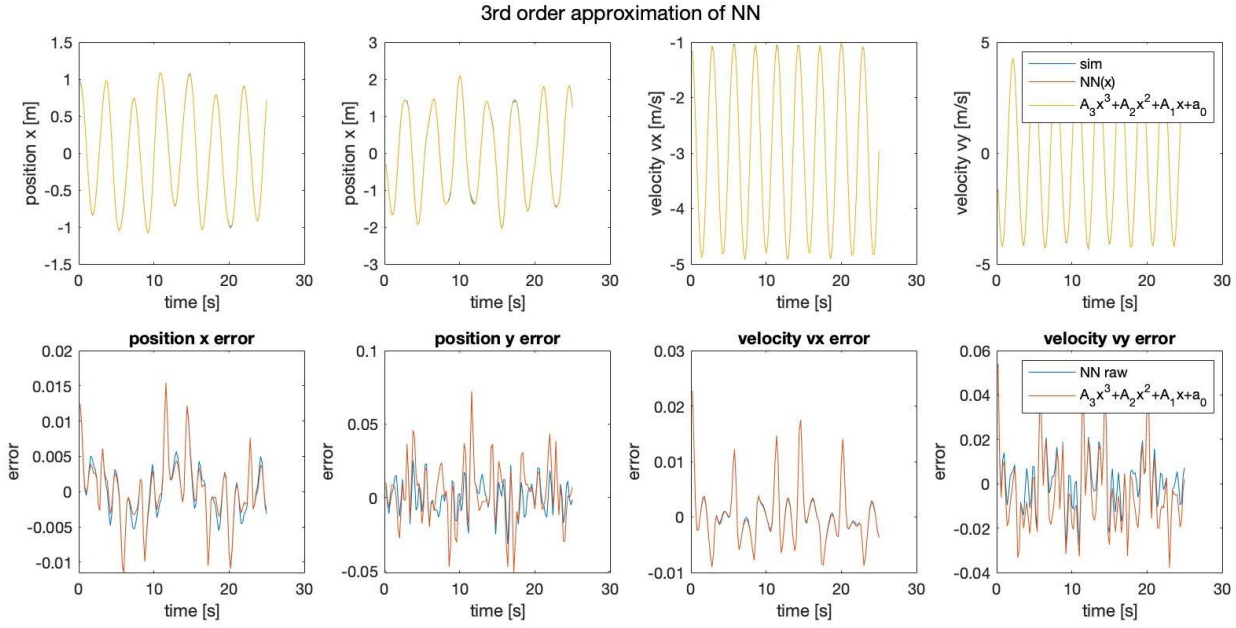

Figure 180: 3rd order NN-poly approximation of 2DOF nonlinear coupled spring-pendulum system and error as difference of each state

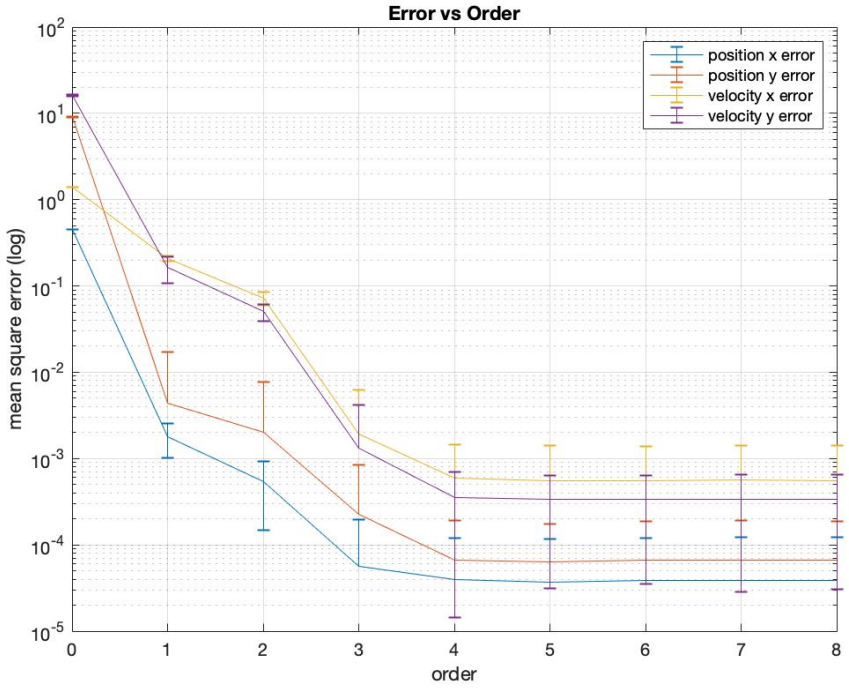

Figure 181: 2DOF spring-pendulum individual MSE error of position and velocity state across different orders of NN-poly approximation

No method is the best method for all systems. SINDy is fast and accurate when the true expression can be composed of the candidate expressions specified in the library. SINDy depends heavily on human intuition and algorithm setup, including tuning the hyperparameter enforcing sparsity. SINDY is more computationally efficient for systems in which users have good intuition of expression form describing the nonlinear systems. SR is slow but requires no prerequisites. Symbolic regression generates a more accurate solution than SINDy when handling systems in which a complex expression is the final answer and researchers have no intuition of the form. The expressions generated by symbolic regression consistently have unstable coefficients, leading to dangerous predictions in the presence of noise or for states outside the training data. Pointedly, SINDy and SR do not guarantee the true expression. SINDy can result in low accuracy solutions due to limited expressiveness of the expression library and symbolic regression tends to overfit due to arbitrary complexity of expression construction. NN and NN-Poly do not need much human intuition in the first place, and their computing time is much less than SR. The NN-Poly method

computation time is comparable to SINDy prior to any algorithm runtime optimization. Less prerequisites are necessary when using NN or NN-Poly methods. However, to generate best estimation while avoiding overfitting, general knowledge of neural networks should be understood by users, such as number of layers and number of neurons in a selected layer. The accuracy of NN and NN-Poly cannot be guaranteed if hyperparameters of neural networks are not tuned well. The NN and NN-Poly method is most effective in the nonlinear dynamic system, the author's suggested use case. A comprehensive table of advantages and disadvantages for each method is summarized in Table 52 and Table 53. In Table 53, positive characterization is represented by '+'. Human dependency describes the involvement of user intuition, in which '+' implies minimal domain knowledge from users.

Table 52: Qualitative advantages and disadvantages of all system identification methods

Method	Advantages	Limitations
Strict Polynomial	- Fast - No domain knowledge or context needed	- True analytical solution rarely guaranteed
Sparse Identification of Nonlinear Dynamics	- Fast - Less data required - Domain knowledge easily incorporated into solution set	- True analytical solution not guaranteed - Solution dependent on selected library of expressions - Ambiguous sparsity condition selection
Symbolic regression with genetic algorithms	- No domain knowledge or context needed	- Uncertain convergence on true expression -Slow - Large memory requirements when processing
Single-layer neural network	-no *a priori* knowledge required; very little domain knowledge or context needed - universal approximator - compact representation	- Poor safety guarantees for state predictions outside training data - Form not interpretable
Polynomial from NN	- Form enables verification and safety - Derived from compact representation	- Limited expression due to polynomial form - Unless original expression in polynomial form, correct analytical solution not guaranteed

Table 53: Rubric of algorithm and solution characteristics across all system identification methods

	Polynomial	SINDy	SR	NN	Poly
Computing speed	+	+	-	+	+
Data amount required	+	+	-	+	+
Accuracy	0	0	0	0	0
Human dependency*	0	-	+	0	0
Correctness	0	0	0	0	0
Complexity	0	0	+	0	0

e. *Contribution from Taylor Approximation of Artificial Neural Network*

A neural network predicts nonlinear, coupled system dynamics incredibly well with minimal context and compactly map input-output pairs in a minimal representation. A NN-polynomial mapping avoids the need to download an immense amount of data and fit a polynomial directly to a large dataset by exploiting the compactness of the NN. A polynomial addresses some limitations of the neural network by making the prediction mapping of more understandable form, as polynomial form has a long history of analysis and mathematical literature, including safety verification and guarantees. This work's major contribution is offering a form to which semi-algebraic constraints, such polynomial inequality and equality constraints, may be incorporated in the final predictive function solution. These semi-algebraic constraints represent the application of domain knowledge, such as conservation of energy in the form of quadratic rates, and safety constraints, such as linear inequalities that bound specific state values. The results of this effort show comparable prediction and computation performance between SINDy and the proposed method for linear systems but great improvement in the proposed method for highly nonlinear systems. Further future work also includes approximation of more complex systems, in increasing degrees of freedom, in the degree of nonlinearity, and in the coupling of states.

II. Genetic Algorithms to Autonomously Learn and Control Robotic Exploration in an Extreme, Unknown Environment

Exploring and traversing extreme terrain with surface robots is difficult, but highly desirable for many applications, including exploration of planetary surfaces, search and rescue, among others. For these applications, to ensure the robot can predictably locomote, the interaction between the terrain and vehicle, terramechanics, must be incorporated into the model of the robot's locomotion. Modeling terramechanic effects is difficult and may be impossible in situations where the terrain is not known *a priori*. For these reasons, learning a terramechanics model online is desirable to increase the predictability of the robot's motion. A problem with previous implementations of learning algorithms is that the terramechanics model and corresponding generated control policies are not easily interpretable or extensible. If the models were of interpretable form, designers could use the learned models to inform vehicle and/or control design changes to refine the robot architecture for future applications. This section explores a new method for learning a terramechanics model and a control policy with a model-based genetic algorithm. The proposed method yields an interpretable model, which can be analyzed with pre-existing analysis methods. The paper provides simulation results that show for a practical application, the genetic algorithm performance is approximately equal to the performance of a state-of-the-art neural network approach, which does not provide an easily interpretable model.

a. Introduction and Background

Exploring environments with extreme terrain is difficult for robotic systems. However, for many applications, such as search-and-rescue missions and planetary exploration, effectively exploring extreme terrain is crucial. One aspect that complicates exploration of extreme terrain is

that the dynamics interaction between the robot and terrain, the terramechanics, are often not known accurately *a priori*. When traversing extreme terrain, not accurately modeling the terramechanics inhibits the capability of robotic system to predictably locomote. As the terrain becomes more extreme or as the robot's motion becomes more agile, the adverse effect of poorly modeled terramechanics is even more significant because difficult-to-model nonlinearities and discontinuities from the environment's forces affect the body more significantly. Thus, to traverse extreme terrain effectively and predictability, the terramechanic effects must be incorporated into the control system of the robot. To incorporate terramechanic effects into the control system when the terramechanics are not known *a priori,* the terramechanics must be learned online.

Many methods have been used in past research to develop terramechanics models online. A promising method is to use reinforcement learning to efficiently learn a general relationship between the dynamics of the body and the environment, which includes the terramechanic effects. Learning a black-box model with neural networks (NNs) has been shown to increase the ability of the robot to traverse an unknown environment effectively, but is difficult to interpret by designers [149], [150], [151], [152], [153]. For many practical applications, users need transparency to better understand and refine robotic systems. For example, if the learned dynamic interaction between the robot and environment yields a reduced proportional relationship between expected acceleration and wheel speed, viscous drag can be identified. With a learned dynamic relationship, scientists may induce physical traits of the environment, which contributes two-fold to the planetary-science field. If the learned controller is in standard nonlinear control form, the model can be analyzed during or after operation with standard analysis techniques, informing control design and/or vehicle design improvements for future missions.

In this section, a proposed control system that learns an interpretable model of the terramechanics online and computes an optimal controller that enables accurate trajectory tracking. Specifically, this paper proposes a genetic learning algorithm (GA), which learns a model of the terramechanics along with an optimal controller in standard nonlinear control form. In simulation, the controller is implemented on a vehicle with Ackerman steering, enabling the vehicle to accurately track a trajectory through an environment with unknown terramechanics. The simulation results show that the proposed control, with a genetic algorithm, enables the vehicle to track a trajectory with approximately the same performance as a state-of-the-art NN, while also offering an interpretable terramechanics model stemming from fundamental physics.

Modeling terramechanics is a large and active field of study. Past research has explored how to model motion through extreme terrains like sand, mud, ice, and how to incorporate terramechanics to create controllers that track trajectories effectively [154], [155], [156]. However, these methods assume that the terramechanics are known *a priori,* which as discussed before, is not always the case, especially for applications of space exploration. Due to the inaccessibility of space and technological immaturity of reinforcement learning algorithms, previous work draws from the robotics community that focus on predominantly ground experiments.

For cases where the terramechanics are not known accurately *a priori,* methods for learning the terramechanics and controls have been proposed previously. For example, unsupervised learning has been used to classify the sliding events of discrete rovers, which enables more accurate tracking of trajectories [157]. Reinforcement learning with neural networks has also been applied to learning terramechanics models and controllers for autonomous robots, including drifting, walking on extreme terrain, traversing over obstacles, among others [149], [150], [151], [152],

[153]. However, none of these methods output an easily interpretable model of the terramechanics or controller, which makes analysis of the resulting model difficult.

Genetic algorithms have been used to effectively locomote robots in a variety of environments both aquatic and terrestrial [158], [159]. This previous work focuses on the morphology of the robot that best achieves locomotion, not learning a dynamics model. To address system identification, another divergent line of research learns a symbolic expression of a dynamics model with control input that most disagrees with candidate physical models in a controlled environment [138], [160]. Implementing control input with the most disagreement risks of immobilization for an extraplanetary rover operating outside the confines of a controlled laboratory environment. Aerospace applications desire robustness in autonomous operations, which involve guarantees and predictive confidence.

b. Learning Algorithm Design

To enable exploration of extreme terrain and learn an interpretable model, a two-part controller is proposed. The first part of the controller is a genetic algorithm, which learns a dynamic model, including terramechanic effects, and a controller in the form of an adaptive, linear gain matrix. The second part of the controller is a baseline controller, which uses the commonly employed pure-pursuit method, to roughly track the trajectory such that the learning controller can gather enough data to learn a dynamics model and a control policy. The baseline controller could be removed if the learning algorithm was trained with a dynamic simulation. However, the training is only as accurate as the modeled system structure. Thus, to accurately train the learning algorithm, an accurate model of the system would need to be developed, which is difficult and potentially impossible for unknown terrains. The dynamic model's static structure offers limitations in behavior that could offer safety in the form of guarantees.

Reinforcement Learner Specification & Design

The proposed learning method uses a genetic algorithm evolving a multivariable, nonlinear model approximation. To achieve efficient computation and to ensure the structure is interpretable, the genetic algorithm assumes a static model structure. The parameters in the structure are evolved, or estimated, to provide a candidate physics model and create a control policy.

Implementation

Many methods exist for implementing genetic algorithms. A basic genetic algorithm includes population initialization, fitness evaluation, reproduction, crossover, and mutation [142]. The important characteristics of a genetic algorithm are chromosome specification, evolution parameters, and fitness functions. The chosen method for the proposed controller is discussed below.

Two populations describe candidates for the dynamic model parameters and optimal control policy parameters. Parameters are analogously called chromosomes in the context of genetic algorithms. For unknown terramechanics, length of the chromosome for the dynamic parameters is determined by the complexity of the chosen terramechanics model, given in Eq. (175). The dynamics model needs a dynamic parameter chromosome string, θ_d, defined by a number m_d parameters in which each component is p_1 to p_{m_d}. These parameters represent necessary coefficients in the dynamics model expression, like scalars and biases, capturing a number of physical effects, like static or sliding friction. For the optimal control population, the chromosome length is dependent on the complexity of the chosen control policy. The control policy needs a control parameter chromosome string, θ_K, defined by a number n_d parameters in which each component is k_1 to k_{n_d} , given in Eq. (176). The components resemble gain matrix

values but reshaped into vector form, instead of the original matrix dimension. Each population evolves, guided by user-defined fitness metrics.

$$\theta_d = [p_1 \ \dots p_{m_d}] \tag{175}$$

$$\theta_K = [k_1 \dots k_{n_d}] \tag{176}$$

The two metrics for fitness evaluation of each population are prediction error Q and tracking error C. The prediction error is the squared difference between measured and predicted states. The predication error is dotted with a weight vector w_s, shown in Eq. (178). Given the measured state of the m^{th} previous timestep s_{k-m} and the current timestep s_k, the prediction error is the error between the current measurement s_k and the propagated state from the previous measurement $\hat{s}_k$. To propagate the vehicle's next dynamic states, each population member's dynamic parameters $\theta_{d,i}$ and the optimal actions taken since $k-m$ timesteps ago a^*_{k-m}, are injected into the prescribed dynamics model including terramechanics $f(\cdot)$,given in Eq. (177) and visually depicted in Figure 182. The fittest dynamic parameters are those that accurately reflect the physical system. w_s can be modified depending on what portions of the predicated state the designer is more concerned about predicting accurately.

$$\hat{s}_{k,i} = f(\theta_{d,i}, s_{k-m}, a^*_{k-m}) \tag{177}$$

$$Q_i = w_s \cdot \left|(s_k - \hat{s}_{k,i})\right|^2 \tag{178}$$

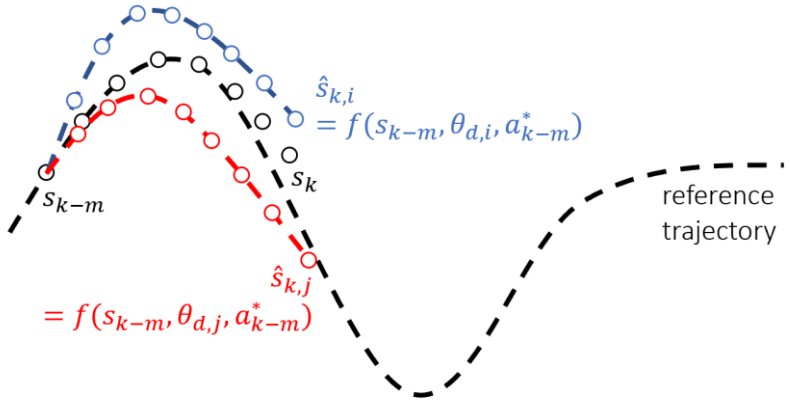

Figure 182: Propagation of vehicle state with optimal actions a^*_{k-m} and two population member's dynamic parameters $\theta_{d,i}$ and $\theta_{d,j}$

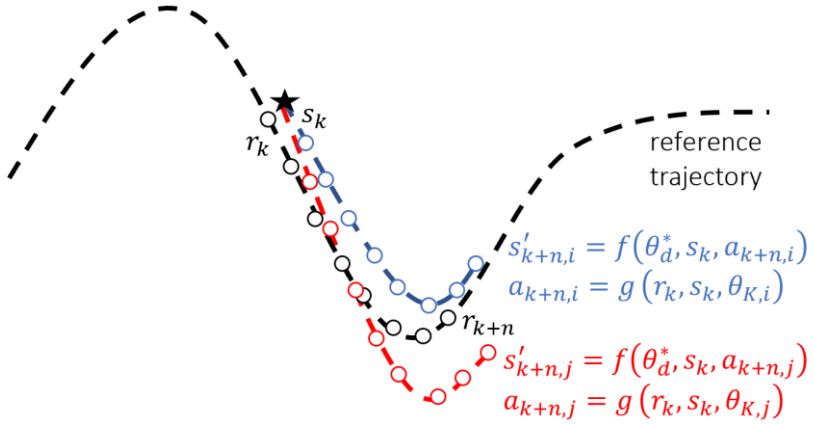

Figure 183: Propagation of vehicle state with optimal dynamic parameters θ^*_d and two population member's control parameters $a_{k+n,i}$ and $a_{k+n,j}$

Tracking error is the sum of error between the next to n projected trajectory waypoints and velocities to the projected state s'_{k+n}, propagating a simulation with the optimal dynamic parameters θ^*_d, the prescribed dynamics model including terramechanics $f(\cdot)$, and candidate control actions $a_{k+n,i}$, given in Eq. (179) and visually depicted in Figure 183. The selected control policy $g(\cdot)$ generates candidate control actions from the state s_k, a reference state r_k, and the candidate control parameters $\theta_{K,i}$ evolving in the genetic algorithm, given in Eq. (180). The final control fitness function is a weighted sum of squared error between the reference and projected

states and squared weighted penalty of gain values, shown in Eq. (181). The squared weighted penalty of gain values is included to ensure the gains do not become so large that the system becomes unstable. The fittest control parameters drive the system to the desired trajectory and velocity. The two populations are sorted from the most fit members to the least fit members. From these two ranked populations, the next generation of each population is created with reproduction, crossover, and mutation.

$$s'_{k+n,i} = f\left(\theta_d^*, s_k, a_{k+n,i}\right) \tag{174}$$

$$a_{k+n,i} = g\left(r_k, s_k, \theta_{K,i}\right) \tag{175}$$

$$C_i = w_r \cdot \left|\left(r_{k+n} - s'_{k+n,i}\right)\right|^2 + w_k \cdot \left|\theta_{K,i}\right|^2 \tag{176}$$

The next generation is produced from the ranked population with probabilistic sampling. Parents are sampled from the ranked population with a standard Gaussian distribution of which the fittest individuals are selected most often. With a crossover rate C_r, children are reproduced from the parent population by crossover from the two parental chromosomes. Every child's resultant chromosome is additionally mutated. Only the top C_f members of the previous generation survive into the next generation. Finally, C_n members enter the new generation to ensure the optimization process is adapting with the system, described in the next subsection.

The genetic algorithm progresses by reentering a loop to evaluate this new generation, which continues the evolution process. Allowing the system to implement the learned control input from the very start of the learning process could potentially be dangerous as the dynamics model has not been validated rigorously with enough measurements. The learner accumulates measurements and refines both the dynamics model parameters and control policy parameters until reaching a certain prediction and tracking error threshold, ensuring that the next state does not

stray far from the reference state. Once that threshold is met, the learned control policy is run in the system's forefront.

The learned dynamics model and control policy adapt as information is gathered, differing from a system in which a dynamics model and control policy are specified *a priori*. The latter system does not have the opportunity to update, likely resulting in suboptimal trajectory tracking. The learned system offers two main advantages: accuracy and adaptability. The dynamics model incorporates the approximate terramechanics of the current terrain, likely offering more accurate trajectory tracking compared to a terramechanics model specified *a priori*. Additionally, the adaptive nature of the dynamics model extends to terrains with different properties, such as ice, steep slopes, and mud, thus unexpected terrain can be effectively traversed.

Underdetermined System Identification

Domain knowledge is critical to form a minimal formalization both in structure and parameters. A comprehensive model precisely characterizes a system but requires more system parameters, which increases evaluation computation and convergence time. Machine learning techniques leverage quick iteration and immense computation power by implementing a minimum description of the system [161].

The implemented dynamics model and control policy as proposed both suffer from being underdetermined. Consequently, the dynamic parameter and control parameter populations are at risk of prematurely converging to a local well. The dynamics model intentionally does not fully capture the system's terramechanics behavior but instead simplifies the model to reduce computation time in the algorithm. The control policy has a consistent, nonlinear mapping from

state to input due to complex, unmodeled hardware effects but may be characterized locally in a linear mapping.

A new member is injected into the population at every generation to ensure that the genetic algorithm populations adapt locally with the system state. The dynamic parameter population receives a randomly generated member from the entire parameter space to guarantee a globally-scoped search. The control parameter population receives an inverse model mapping representative of the system within the immediate past timestep horizon of h, a local approximation. The inverse model is generated from vectors of previous control inputs A_k, corresponding state error E_k, and relevant system parameters P_k, given in Eq. (182) and Eq. (183). The newest control parameter member $\theta_{K,l}$ is the linear least squared error local approximation of the nonlinear control model, given in Eq. (184). The constant presence of this local approximation offers the genetic algorithm to adapt with the time-varying system if the evolved solutions do not track as well.

$$A_k = \begin{bmatrix} a_{k-h-1} \\ \vdots \\ a_{k-1} \end{bmatrix} \tag{182}$$

$$E_k = \begin{bmatrix} r_{k-h} - s_{k-h} \\ \vdots \\ r_k - s_k \end{bmatrix} \tag{183}$$

$$\theta_{K,l} = [E_k \quad P_k]^{\dagger} A_k \tag{184}$$

Baseline Controller

To enable the GA to learn effectively, the baseline controller is used to coarsely to track the trajectory. The baseline controller is broken up into two sections: the velocity-tracking controller and the path-tracking controller. The velocity-tracking controller attempts to track the desired velocity profile of the trajectory. The velocity-tracking base controller is a proportional

controller, as shown in Eq. (185), where V_d is the desired velocity in the $\hat{b}_1$ direction of the car as described in Appendix IV, V is the current velocity of the car, K_p is a user-defined gain that is tuned on the physical system, and C_V is the commanded wheel speed. The value of K_p does not need to be fine-tuned, because after the learner gathers an appropriate amount of data, poor tuning no longer affects the performance of the vehicle.

$$C_v = K_p\left(V_d - \boldsymbol{V} \cdot \hat{b}_1\right) \tag{185}$$

The path-tracking controller attempts to track the path of the trajectory. The path-tracking base controller is a pure-pursuit controller. Pure-pursuit controllers are a common control strategy to enable a robot with Ackerman steering to track paths. The equation describing the pure-pursuit controller is shown in Eq. (186), where L is the length between the front wheels and the real wheels, L_d is a look-ahead gain, α is the path intersection angle, and ϕ is the computed steering angle, as discussed in [162].

$$\phi = \tan^{-1}\left(\frac{2L\sin(a)}{L_d}\right) \tag{186}$$

c. Experiment

An experiment is run to determine if the proposed genetic learning algorithm control meets two main goals. The first goal is to verify if the GA can learn a dynamics model and controller in standard form when applied to a practical application. The second goal is to determine if the performance of the GA is approximately the same as a state-of-the-art NN approach. The two methods are anticipated to produce approximately equal tracking performance. The performance metrics are error in trajectory tracking, convergence time, and algorithm computation time at every timestep. The metric used to determine how accurately a trajectory is tracked is shown in Eq. (187),

where $\boldsymbol{r}^{T/b}$ is the distance to the nearest portion of the trajectory from the car, T_c is the time of convergence, and T_f is the time to complete ten laps. The computation time at each timestep is measured with the algorithm environment's stopwatch timer.

$$J = \int_{T_c}^{T_f} \left|\boldsymbol{r}^{T/b}\right| dt + \int_{T_c}^{T_f} \left(V_d - \boldsymbol{V} \cdot \hat{b}_1\right) dt \tag{187}$$

The convergence time is how long it takes for the controller to converge to the trajectory and continue to track the trajectory accurately and repeatedly. Convergence time is determined by user intuition. To test the genetic algorithm, a simulation of an Ackerman steering vehicle on a low friction inclined surface is used. The simulation is designed to mimic extreme terrains comprised of surfaces that are inclined and/or do not perfectly constrain the wheel's motion, such as sandy inclines or fine loose rubble, among others. The terramechanics of sand or fine loose rubble are different from a slippery incline and are more complicated. However, a slippery slope acts as a simplified test to understand the potential performance of the controller. The dynamics that are implemented into the simulation are derived below in Appendix IV. To increase the validity of the simulation, noise is added to all states and an estimator is used to determine the state of the vehicle from only position orientation and time measurements. The noise is specified in Table 54, along with the parameters for the simulation environment and vehicle.

Table 54: Parameters for the environment and vehicle

Parameter	Value
Dynamic parameter μ_s lateral wheel slip friction	5
Dynamic parameter μ_w forward wheel slip friction	1
Trajectory sloped surface angle δ	30°
Vehicle mass	1 kg
Vehicle wheel radius	0.10 m
Distance from vehicle center of mass to center of rear wheel axle	0.16 m
Measurement sampling time and control update rate	0.2 sec
Measurement Gaussian position noise (1σ)	1.3e-4 m
Measurement Gaussian rotation noise (1σ)	0.83e-4 rad

Test Procedure

To test the car, a predefined closed trajectory is specified for the RC car to track on the slippery slope. The trajectory remains constant throughout the test. Each controller is tested with the same starting configuration, which is consistently displaced from the reference trajectory. The car is commanded to track the trajectory, which is done at first with the baseline controller. Once the learned controller converges to a solution that meets a user-defined performance criterion, the trajectory is tracked with the learned controller. The desired tracking velocity is 0.2 m/s. The trajectory is shown in Figure 184.

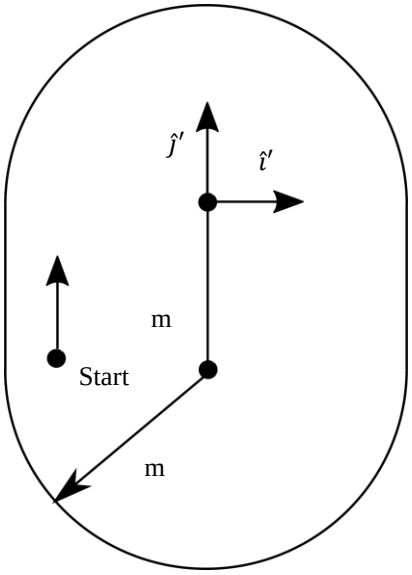

Figure 184: Trajectory for the car to track

Genetic Algorithm Implementation

The dynamic model used for the GA is described below in the Appendix IV. From that derivation, the dynamic model parameter population members have chromosome of length two: friction coefficients, μ_s and μ_w, describing lateral wheel slip and wheel slip in the direction of wheel velocity. The form of the controller is a time-varying gain matrix. The action a at every timestep is given by Eq. (188), where ϕ is the steering angle and ω_w is the rotation rate of the wheels. The control gain matrix is populated with the parameters in the control parameter chromosome, given by Eq. (189). The gain matrix maps the path intersection angle, error in velocity, and the estimated slope of the surface δ to the control actions a, given in Eq. (190). The fitness functions for each population are shown in Eq. (180) and (187) of which the specific weight matrices the remaining parameters for the GA are shown in Table 55.

$$a = [\phi \ \omega_w]' \tag{188}$$

$$K = \begin{bmatrix} \theta_{K,1} & \theta_{K,2} & \theta_{K,3} \\ \theta_{K,4} & \theta_{K,5} & \theta_{K,6} \end{bmatrix} \tag{189}$$

$$a = K[\alpha \ \Delta V \ \delta] \tag{190}$$

Table 55: Hyperparameters for evolution process

Parameter	Value
Steps compared for dynamics evaluation (n)	1
Steps compared for control evaluation (m)	2
Crossover Rate (C_r)	.67
Size of dynamic population	8
Size of control population	8
Number of breeders (C_f)	3
Number of new members (C_n)	1

Weight of prediction vector w_s	[10^3 10^3 0 0 180/pi 0]
Weight of tracking vector w_r	[1 1 0.01 0 0 0]
Weight control gain vector w_K	[0 10^{-7} 0 0 0 10^{-7} 0]

Implementation of Neural Network for Comparison

The genetic algorithm is compared to a supervised neural network controller. The idea of neural network controller was first introduced by Demetri Psaltis et al. [163] in which an architecture is proposed for a general learning process. The idea was further developed by Tomochika el al. [149] in which a neural network tracks a trajectory with unstructured uncertainty. This supervised neural network approach builds on the referenced work. In this approach, the neural network is used as a function approximator to the cost function, more formally described in Eq. (191), where s stands for the state and a stands for the action. In this problem, to simplify the learning process, the state of vehicle is chosen as follows in Eq. (192), where φ is the angle between the body of the vehicle and the tangent of the target trajectory, d is the shortest distance from the vehicle to the trajectory, and ρ is the angle between the body of the vehicle and the original point of axes. The cost value describes how well the vehicle near the desired trajectory. Given the state value, the cost value of this state is explicitly defined in Eq. (193).

$$\hat{f}(s,a) \approx C(s,a) \tag{191}$$

$$s = [\varphi \;\; d \;\; \rho] \tag{192}$$

$$C = d^2 + k \cdot \rho^2 \tag{193}$$

The learning process consists of two stages. On the first stage, vehicle is controlled to do a random walk strategy to fully explore the target environment. In this process, all states, actions, and cost values are collected as training data. A neural network with three layers uses these data

to train and form a function approximator. After the first stage in the learning process, a cost function is learned, which could be used to develop a control strategy. At each state, a unique action could be selected to minimize the cost value based on the neural network. However, this process is time-consuming. Then, during the second learning stage, another neural network is used to directly describe the control strategy. The input of this neural network is the state and the output of the neural network is the action, given in Eq. (194).

$$a = \hat{g}(s) \tag{194}$$

Training data in this learning process is generated by running the first neural network. After the second learning process, the neural network is ready to be used as a controller. This neural network controller doesn't use any dynamic model information and therefore is a model-free method, compared with the genetic algorithm. Due to limited space and time of training, the vehicle is subject to easily crash into the wall in the first learning stage. To address this problem, the first learning stage is implemented on the simulator.

d. Results

Both the learned controller and trained neural network tracked the desired trajectory better than the baseline controller, as shown in Figure 185. The tracking error integrated across ten laps after convergence is shown in Table 56 and the component error time history is depicted in Figure 186 and Figure 187. The total computation time to finish ten laps including the time to converge is shown in Table 57. The average computation time, along with a standard deviation, is reported in Table 58 with the computation at every timestep depicted in Figure 188. The convergence time for both methods are reported in Table 59 and depicted in Figure 189.

Table 56: Total tracking error comparison across ten laps

	Baseline	Learner	Neural Network
$J(r)$ [m]	648	34	78
$J(V)$ [m/s]	1393	44	23
J_{tot}	2041	78	101

Table 57: Total computation time comparison over ten laps

	Baseline	Learner	Neural Network
time	348.7 s	1244.1 s	869 s

Table 58: Average computation time comparison on a dell Xenon desktop in MatLab

	Baseline	Learner	Neural Network
mean	35 ms	330 ms	341 ms
std	15.4 ms	123 ms	26 ms

Table 59: Convergence time comparison

	Baseline	Learner	Neural Network
control	NA	217 s	200 s
dynamics	NA	40 – 130 s	NA

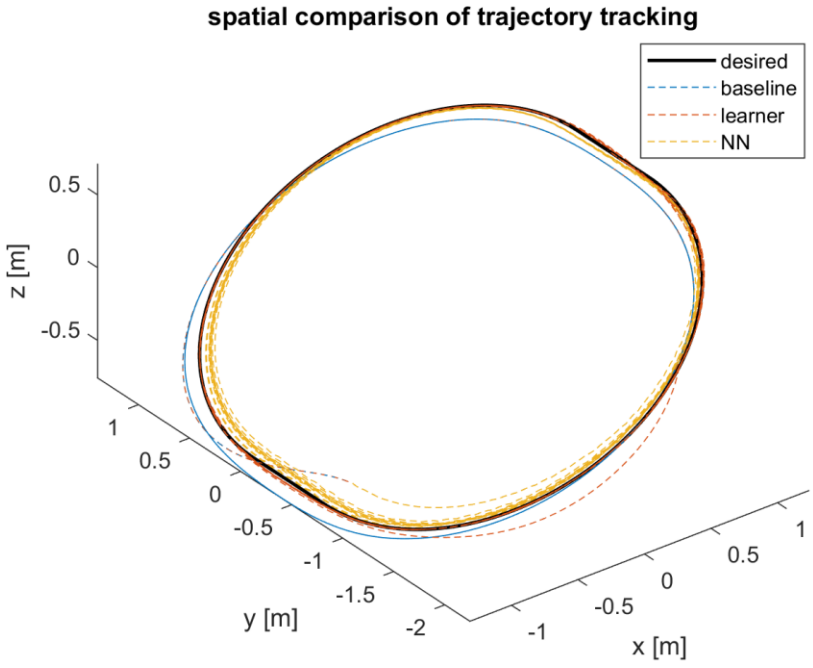

Figure 185: Trajectory comparison of baseline, learner, and neural network overlaid on desired trajectory

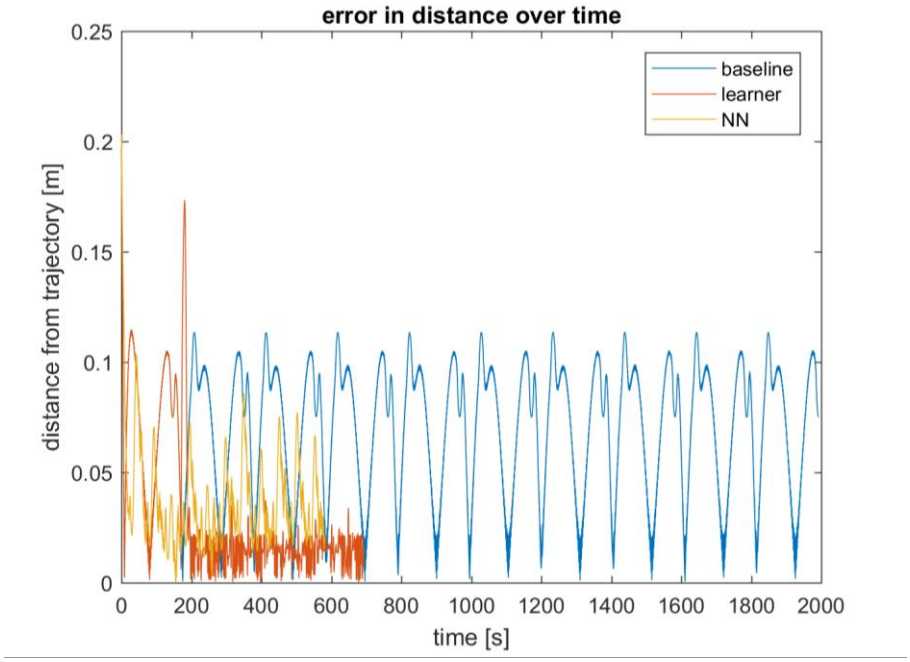

Figure 186: Time history of distance error comparison between baseline, real-time learner, and supervised neural network

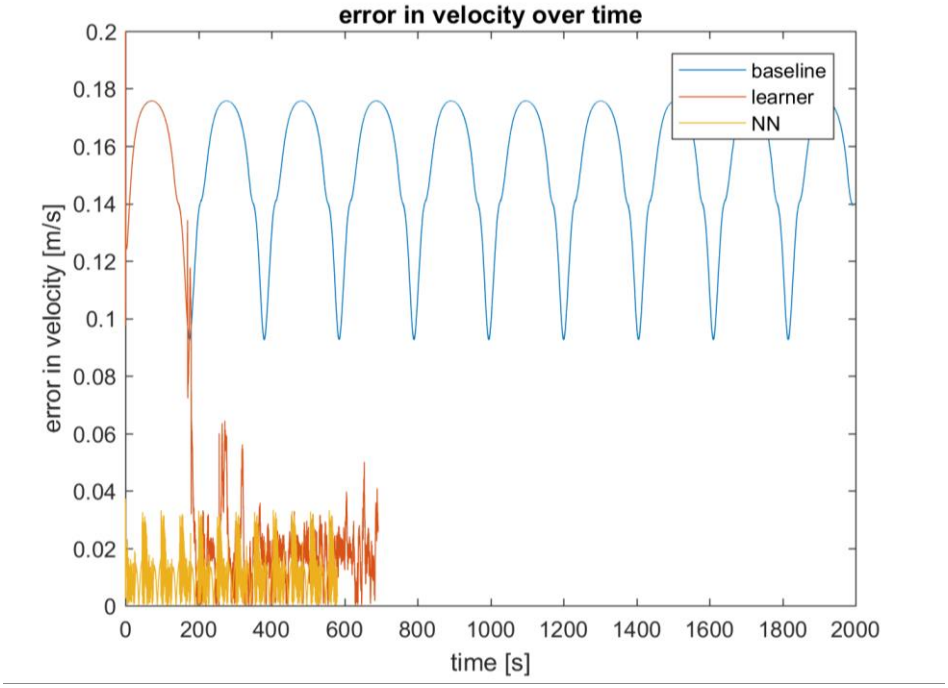

Figure 187: Time history of velocity error comparison between baseline, real-time learner, and supervised neural network

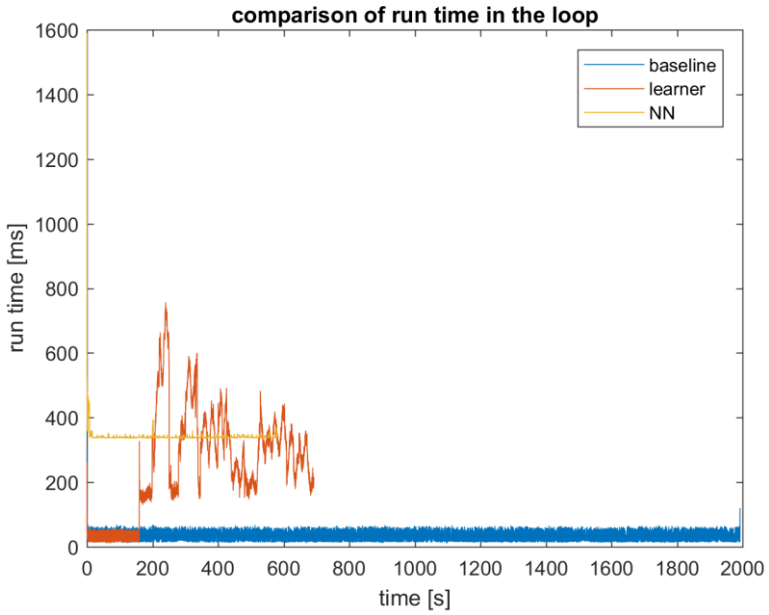

Figure 188: Comparison of computation per evaluation loop over time

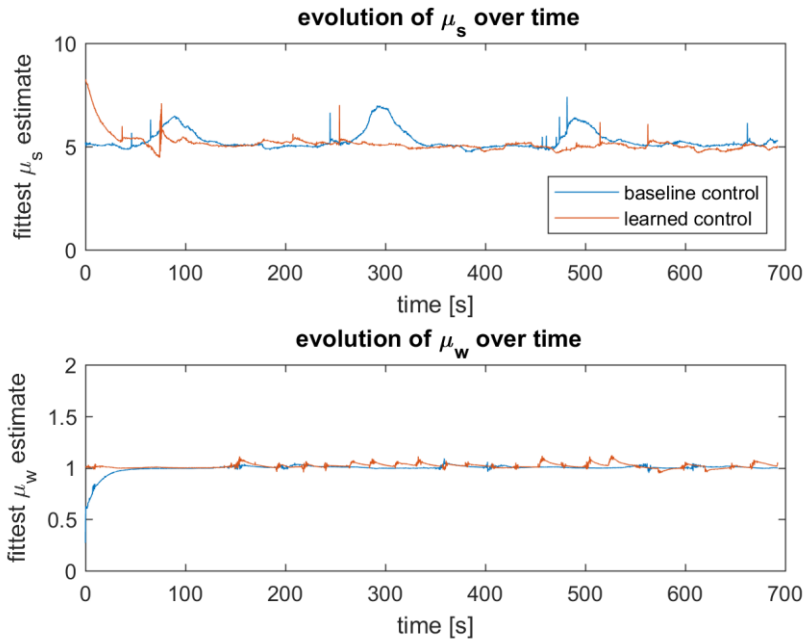

Figure 189: Evolution of dynamic parameters over time

From Figure 189, the GA converges to the real μ values with very little error. The noise that is seen in the estimate is due to the added noise in the measurements. The error for the controller also converges to an approximately steady value. Again, the variations are due to the

injected noise. From Table 58, the average computation time is relatively small, making it possible to implement this method onto physical systems. From these results, the GA is capable of learning dynamics parameters for the simulated RC car, which supports the hypothesis that the method can be implemented on a practical system.

Also, from the results above the GA performs similarly to the NN in tracking error, average computation time, and convergence time. There are no appreciable differences in the reported performance metrics between the two methods, which supports the initial hypothesis. The GA has similar performance to the state-of-the-art NN approaches, while providing an interpretable model.

Limitations

One major limitation of the proposed learned method is model bias due to underfitting, which results from some dynamic terms being excluded in the model structure. Model bias is caused by assuming a model structure that does not sufficiently describe the system. The model bias can be reduced by enabling the model structure to change. For example, the friction can be represented as a common friction model summed with a polynomial with varying order and coefficients. Enabling the GA to vary the order and coefficients enables more complicated friction models to be approximated. Similarly, polynomials can also be used to incorporate more complex dynamic effects or control methods.

Another limitation of the work is that the method proposed likely does not perform well when the dynamic parameters or optimal control parameters vary rapidly with time because the GA likely does not converge on rapidly changing parameters. For the simulation, the time varying effects of the control parameters were slow, on the order of a lap, and the true dynamic parameters were constant. The GA could continuously update the parameters. However, for other applications,

like drifting, this method may not work because the controller may not be able to converge to a solution fast enough to give accurate control and dynamic parameters. This lag may be solved by making the computation time faster and the convergence time faster. The last major limitation is that user intuition is needed to determine the underlying structure of the models. If the underlying structure is selected poorly, the performance of the method may be greatly reduced. Thus, care must be taken to ensure that the underlying structure reflects the actual physics.

e. Contribution of Genetic Algorithm Development for Autonomy

In this section, a new method learns a terramechanics model and an optimal controller with a genetic algorithm. Unlike methods used in the past research for learning terramechanics and optimal control models, the proposed method creates an interpretable model, which can be used to inform design changes of the vehicle or controller but also derive scientific conclusions. Simulation results show that for a practical system, the proposed method performs approximately equal to a state-of-the-art NN approach, while having the benefit of producing an interpretable model. The simulation results also suggest the computation time is low enough such that the method can be implemented on a physical system with limited computational capability.

CHAPTER 6: Conclusion

The accumulation of effort has resulted in progress in several different fronts, in dynamics theory, system design, hardware maturity, and system identification for flux-pinned interfaces. The beginning of this research started with a big picture question of how to utilize unexploited physical phenomena for spacecraft dynamics. Flux pinning displays fascinating properties, such as contactless, compliant, and passive behavior. Initially discovered in 1988, the field of superconductivity is only a few decades old and the application of superconductivity to spacecraft systems began with Mason Peck approximately a decade ago. Although there are many applications for space systems, the focus of this work is not in breadth of all applications but depth in a single application, docking and capture of two close-proximity spacecraft.

The Mars Sample Return mission concept motivates and drives the structure and scope of the docking and capture problem. From the mission requirements, mass, power, and physical geometry of the target spacecraft dictate the system design that incorporates the flux pinning technology, such as the spherical nature of the spacecraft outer surface and utilization of permanent magnets due to lack of power. The expected initial dynamic state for the capture and docking sequence drive the design and desired performance of the developing flux-pinned interface, such as arbitrary entrance attitude led to a symmetric configuration of magnets and the increase in magnetic field strength to meet initial entrance velocity requirements. A baseline simulation of the conceptual system's dynamics validate that this design could capture and dock two relative motion spacecraft. The concept design passed rigorous review internally at Cornell and externally from JPL, beginning hardware design to overcome significant engineering challenges like an enabling thermal design and detailed model development that predicts the experiment measured dynamic states.

A major contribution to this body of work is the dynamic model development. Previous work ties together Kordyuk's Frozen-image model and Villani's magnetic-dipole model to form the electromagnetic basis of the overall dynamics model, converting magnet-superconductor dynamic state into force-torque onto a rigid body. Newton and Euler's rigid-body dynamics form the remainder of the dynamics model, converting force-torque into derivatives of position-attitude. An integrator closes the loop by connecting derivatives of state to the next state. This baseline physics-based dynamics model is complex, nonlinear and coupled in nature, and assumes physically unrealizable aspects of a system that limit the dynamic model's predictive power. Still, the analytical model offers tremendous insight, which led to a derivation of a general dynamics model incorporating an arbitrary amount and configuration of magnets and superconductors. From this derivation, the equilibria states and a potential energy topography follow. From the potential energy landscape, the minimum energy state determines the equilibrium, the concavity dictates the stability, and the shape guides the manner of the subsequent dynamics. By taking advantage of the potential energy landscape, a method is proposed to calculate backwards reachability of a flux-pinned interface given an instantaneous measurement of dynamic state. Another important analysis derived from the full nonlinear model is a linearization in state matrix form, which reveals instantaneous stability from eigenvalue decomposition, sensitivity of the dynamics from corresponding states, and offers a structure to apply control theory.

Efforts to reconcile the baseline dynamic model assumptions with reality lie in two domains: basic science experiments and literature review. The basic science question explored the amount of magnetic flux pinned in a finite dimension superconductor, rectifying Kordyuk's major assumption of an infinite plan superconductor. The literature review aimed to comprehensively compile all parameters that affect control or knowledge of the flux-pinned interaction, which

includes but is not limited to superconductor temperature, material properties, manufacturing process, and geometry. The parameters are linked to mathematical expressions that modify the physics-based dynamic model. These parameters then need to be estimated to fit the observed data generated from a suite of experiments.

Two major contributions result from the extensive testbed effort: data collection for dynamic model development and technological maturity of a flux-pinned hardware system. Each testbed lifted the maturity of the hardware system from TRL 3 to TRL 5. In chronological order, a proof-of-concept, liquid nitrogen, ground testbed moved to a laboratory, cryocooler, ground testbed and ended with two microgravity testbeds. To get data of a real flux-pinned system, these testbeds span three different dynamically expressive environments: 1DOF, 4DOF, and 6DOF. The single degree of freedom is offered by a mechanical bearing, which allows for rotation about an equilibrium orientation. The guaranteed contactless interaction in the 1DOF experiments minimize external interactions and simplify flux-pinning dynamics by excluding coupled dynamics. The four degree of freedom system is the mechanical bearing mounted onto a planar air bearing, which offers an additional two degrees of translation and one degree of rotation. The 4DOF testbed specifically aimed to investigate the effect of coupled dynamics while still enabling easy and continued access on a ground testbed. To express the full degrees of freedom that spacecraft encounter, a microgravity testbed was built and flown in parabolic flights to measure 6DOF dynamics. All nonlinearities and coupled dynamics appear in this flight-traceable, representative environment. The combination of the dynamic model development and experiment data contribute to a more predictive dynamics model of the flux-pinned spacecraft.

The barrier to entry to adopt this technology for a spaceflight mission is a dynamics model that accurately predicts the relative state of the two spacecraft within 5% RMS error. The predictive

dynamics model offers insight into the behavior of the system when deployed in space, to ensure safety or guarantees about the performance of the system. To develop a dynamics model from the experiment data, error metrics are offered to explicitly evaluate the model performance. Each metric is discussed as how the metric embodies the objective and targets the right characteristics of the optimal dynamics model. Analytical and numerical methods minimize the error metrics in different ways and generate different types of models. The physics-based model gives tremendous intuition as to the relationship between physical parameters and resulting dynamics but also does not capture all higher-order effects observed in the experiment data. Numerical methods predict the dynamic relationship between input and output state much better than the physics-based model but are not interpretable and do not guarantee safe predictions when extrapolating for conditions or systems that the algorithm did not previously train. Of the numerical methods, neural networks and symbolic regression with genetic algorithms are explored in depth, as neural networks are universal approximators and symbolic regression generate interpretable mathematical expressions. Each method emphasizes different advantages and disadvantages, but not one model carries all the advantages of being physically intuitive, interpretable, high-fidelity, and highly accurate.

Neural networks were the most successful numerical method in reducing prediction error for the real experiment data but lack safety, extensibility, and interpretability. These features are critical for mission critical operations, such as aerospace applications in which expensive missions in distant environments must function autonomously. Neural networks update very quickly and approximate extremely well, but to close the gap in safety and verification, theoretical developments aim to approximate a neural network with a polynomial. The polynomial form offers more understood behavior compared to a neural network, especially for instances where inputs lie outside the bounds of the training data. Polynomials may also be structured with domain

knowledge, incorporated as constraints in the solver. An extension of this work aims for real-time system identification that guarantees safe and sensible predictions.

Flux-pinned technology is a promising, versatile, and unique interface that enables many applications in space. Adoption of this technology is held back by the technological maturity, which can be overcome with a high-fidelity predictive dynamics model. Future work lies in finishing the system identification problem by either transferring results from numerical methods to the physics-based model or deriving theoretical proofs of safety in with certain numerical methods. Through the theoretical work, the overall technology would transition from TRL 5 to 6. At which point, a spaceflight demonstration would move the hardware development to TRL 7. The goal is to develop technology that further enables space exploration and scientific discovery.

REFERENCES

[1] S. Earnshaw, "{On the nature of the molecular forces which regulate the constitution of the luminiferous ether}," *Trans. Camb. Phil. Soc*, vol. 7, pp. 97–112, 1842.

[2] L. C. Davis, E. M. Logothetis, and R. E. Soltis, "Stability of magnets levitated above superconductors," *Journal of Applied Physics*, vol. 64, no. 8, pp. 4212–4218, Oct. 1988.

[3] R. Williams and J. R. Matey, "Equilibrium of a magnet floating above a superconducting disk," *Appl. Phys. Lett.*, vol. 52, no. 9, pp. 751–753, Feb. 1988.

[4] M. Sjöström, "Hysteresis Modelling of High Temperature Superconductors," p. 147.

[5] P. M. Grant and T. P. Sheahen, "Cost Projections for High Temperature Superconductors," p. 6.

[6] D. Castelvecchi, "First hint of near-room-temperature superconductor tantalizes physicists," *Nature*, vol. 565, p. 12, Dec. 2018.

[7] P. Seidel, *Applied Superconductivity: Handbook on Devices and Applications*. John Wiley & Sons, 2015.

[8] J. R. Hull, "Superconducting bearings," *Supercond. Sci. Technol.*, vol. 13, no. 2, p. R1, 2000.

[9] Y. Sakurai, T. Matsumura, H. Kataza, S. Utsunomiya, and R. Yamamoto, "Estimation of the Heat Dissipation and the Rotor Temperature of Superconducting Magnetic Bearing Below 10 K," *IEEE Transactions on Applied Superconductivity*, vol. 27, no. 4, pp. 1–4, Jun. 2017.

[10] B. R. Weinberger, L. Lynds, and J. R. Hull, "Magnetic bearings using high-temperature superconductors: some practical considerations," *Supercond. Sci. Technol.*, vol. 3, no. 7, p. 381, 1990.

[11] B. Bolund, H. Bernhoff, and M. Leijon, "Flywheel energy and power storage systems," *Renewable and Sustainable Energy Reviews*, vol. 11, no. 2, pp. 235–258, Feb. 2007.

[12] "Designs and analyses of flywheel energy storage systems using high-Tc superconductor bearings | Request PDF." [Online]. Available: https://www.researchgate.net/publication/232363150_Designs_and_analyses_of_flywheel_energy_storage_systems_using_high-Tc_superconductor_bearings. [Accessed: 20-Mar-2019].

[13] A. Takamori, A. Araya, Y. Otake, K. Ishidoshiro, and M. Ando, "Research and Development Status of a New Rotational Seismometer Based on the Flux Pinning Effect of a

SuperconductorR&D Status of a New Rotational Seismometer Based on the Flux Pinning Effect of a Superconductor," *Bulletin of the Seismological Society of America*, vol. 99, no. 2B, pp. 1174–1180, May 2009.

[14] A. Gharabegian, "Maglev—A super fast train," *The Journal of the Acoustical Society of America*, vol. 108, no. 5, pp. 2527–2527, Nov. 2000.

[15] "Beijing Maglev." [Online]. Available: https://www.maglev.net/news/beijing-maglev/. [Accessed: 18-Mar-2019].

[16] B. Corporation, *Maglev: How they're Getting Trains off the Ground*. Bonnier Corporation, 1973.

[17] H. Fujimoto, H. Kamijo, T. Higuchi, Y. Nakamura, K. Nagashima, and M. M. and, "Preliminary study of a superconducting bulk magnet for the Maglev train," *IEEE Transactions on Applied Superconductivity*, vol. 9, no. 2, pp. 301–304, Jun. 1999.

[18] E. H. Brandt, "Rigid levitation and suspension of high-temperature superconductors by magnets," *American Journal of Physics*, vol. 58, no. 1, pp. 43–49, Jan. 1990.

[19] J. P. Shoer and M. A. Peck, "Flux-Pinned Interfaces for the Assembly, Manipulation, and Reconfiguration of Modular Space Systems," *J of Astronaut Sci*, vol. 57, no. 3, pp. 667–688, Jul. 2009.

[20] L. Jones, W. Wilson, and M. Peck, "Design Parameters and Validation for a Non-Contacting Flux-Pinned Docking Interface," in *AIAA SPACE 2010 Conference & Exposition*, American Institute of Aeronautics and Astronautics.

[21] L. Jones and M. Peck, "Control Strategies Utilizing the Physics of Flux-Pinned Interfaces for Spacecraft," in *AIAA Guidance, Navigation, and Control Conference*, American Institute of Aeronautics and Astronautics.

[22] F. Zhu, L. Jones-Wilson, and M. Peck, "Capturing and Docking Spacecraft with Flux Pinned Interfaces," presented at the International Astronautical Congress, Guadalajara, Mexico, 2016.

[23] L. Jones and M. Peck, "Stability and Control of a Flux-Pinned Docking Interface for Spacecraft," in *AIAA Guidance, Navigation, and Control Conference*, American Institute of Aeronautics and Astronautics.

[24] J. Shoer and M. Peck, “Simulation of Multibody Spacecraft Reconfiguration through Sequential Dynamic Equilibria,” in *AIAA Guidance, Navigation, and Control Conference*, American Institute of Aeronautics and Astronautics.

[25] J. Shoer and M. Peck, “A Flux-Pinned Magnet-Superconductor Pair for Close-Proximity Station Keeping and Self-Assembly of Spacecraft,” in *AIAA Guidance, Navigation and Control Conference and Exhibit*, Hilton Head, South Carolina, 2007.

[26] J. Shoer and M. Peck, “Reconfigurable Spacecraft as Kinematic Mechanisms Based on Flux-Pinning Interactions | Journal of Spacecraft and Rockets,” *Journal of Spacecraft and Rockets*, vol. 46, no. 2, pp. 466–469, 2009.

[27] J. Gersh, “Architecting the Very-Large-Aperture Flux-Pinned Space Telescope: A Scalable, Modular Optical Array with High Agility and Passively Stable Orbital Dynamics,” in *AIAA/AAS Astrodynamics Specialist Conference and Exhibit*, American Institute of Aeronautics and Astronautics.

[28] L. Jones, “Prospects and Challenges of Particulate Solar Sail Propulsion,” in *AIAA/AAS Astrodynamics Specialist Conference and Exhibit*, American Institute of Aeronautics and Astronautics.

[29] M. C. Norman and M. A. Peck, “Simplified Model of a Flux-Pinned Spacecraft Formation,” *Journal of Guidance, Control, and Dynamics*, vol. 33, no. 3, pp. 814–822, 2010.

[30] W. Wilson, J. Shoer, and M. Peck, “Demonstration of a Magnetic Locking Flux-Pinned Revolute Joint for Use on CubeSat-Standard Spacecraft,” in *AIAA Guidance, Navigation, and Control Conference*, American Institute of Aeronautics and Astronautics.

[31] J. Shoer, W. Wilson, L. Jones, M. Knobel, and M. Peck, “Microgravity Demonstrations of Flux Pinning for Station-Keeping and Reconfiguration of CubeSat-Sized Spacecraft | Journal of Spacecraft and Rockets,” *Journal of Spacecraft and Rockets*, vol. 47, no. 6, pp. 1066–1069, 2010.

[32] M. C. Norman and M. A. Peck, “Stationkeeping of a Flux-Pinned Satellite Network,” *Journal of Guidance, Control, and Dynamics*, vol. 33, no. 5, pp. 1683–1687, 2010.

[33] M. C. Sorgenfrei, L. L. Jones, S. S. Joshi, and M. A. Peck, “Testbed Validation of Location-Scheduled Control of a Reconfigurable Flux-Pinned Spacecraft Formation,” *Journal of Spacecraft and Rockets*, vol. 50, no. 6, pp. 1235–1247, 2013.

[34] W. Wilson, L. Jones, and M. Peck, "A Multimodule Planar Air Bearing Testbed for CubeSat-Scale Spacecraft," *Journal of Dynamic Systems, Measurement and Control*, vol. 135, no. 4, 2013.

[35] W. Wilson and M. Peck, "An Air-Levitated Testbed for Flux-pinning interactions at the Nanosatellite Scale," in *AIAA Modeling and Simulation Technologies Conference*, American Institute of Aeronautics and Astronautics.

[36] L. Jones, W. Wilson, J. Gersh, J. Shoer, and M. Peck, "Fight Validation of a Multi-Degree-of-Freedom Spacecraft Model," presented at the AIAA Guidance, Navigation, and Control Conference, Portland, OR, 2011.

[37] L. Jones, "The Dynamics And Control Of Flux-Pinned Space Systems: Theory And Experiment," Cornell, Ithaca, NY, 2012.

[38] L. Jones, W. Wilson, J. Gorsuch, J. Shoer, and M. Peck, "Flight Validation of a Multi-Degree-of-Freedom Flux-Pinning Spacecraft Model," in *AIAA Guidance, Navigation, and Control Conference*, Portland, Oregon, 2011.

[39] W. J. Yang, M. Ye, J. Xu, T. Zhang, H. B. Tang, and Y. Liu, "Dynamic Force Characteristics in a Superconducting Interface Module," *IEEE Transactions on Applied Superconductivity*, vol. 25, no. 3, pp. 1–4, Jun. 2015.

[40] M. R. James and S. A. Maloy, "The performance of high-temperature superconductors in space radiation environments," *IEEE Transactions on Applied Superconductivity*, vol. 13, no. 2, pp. 1600–1603, Jun. 2003.

[41] R. R. S. Romanofsky, "Prospects and progress of high Tc superconductivity for space applications," 1991.

[42] Y. Lu, M. Zhang, and D. Gao, "Connection stiffness and dynamical docking process of flux pinned spacecraft modules," *Journal of Applied Physics*, vol. 115, no. 6, p. 063904, Feb. 2014.

[43] Y. Lu, M. Zhang, and D. Gao, "Axial Force and Passive Stability of a Flux Pinned Space System," *J Supercond Nov Magn*, vol. 25, no. 7, pp. 2323–2329, Oct. 2012.

[44] W. Yang, J. Xu, L. Yu, and Y. Liu, "Experimental investigation of mechanical characteristics in superconducting interfaces for self-assembly of spacecraft modules," *Physica C: Superconductivity*, vol. 483, pp. 173–177, Dec. 2012.

[45] Y. Lu, M. Zhang, and D. Gao, “Lateral Force and Lateral Connection Stiffness of Flux Pinned Docking Interface,” *J Supercond Nov Magn*, vol. 26, no. 10, pp. 3027–3036, Oct. 2013.

[46] Y. Lu, F. K. Gao, D. Gao, and M. L. Zhang, “Design and Simulation Experiment Study on Reconfigurable Spacecraft Base on Flux Pinned Interface,” *Applied Mechanics and Materials*, 2013. [Online]. Available: https://www.scientific.net/AMM.303-306.1706. [Accessed: 20-Mar-2019].

[47] M. Zhang *et al.*, “The Demonstrations of Flux Pinning for Space Docking of CubeSat Sized Spacecraft in Simulated Microgravity Conditions,” *IEEE Transactions on Applied Superconductivity*, vol. 29, no. 6, pp. 1–16, Sep. 2019.

[48] M. Zhang, Y. Han, X. Guo, C. Zhao, and F. Deng, “The connection characteristics of flux pinned docking interface,” *Journal of Applied Physics*, vol. 121, no. 11, p. 113907, Mar. 2017.

[49] M. Zhang, L. Zhou, and Y. Lu, “Controllability of Flux-Pinned Docking Interface,” *IEEE Transactions on Applied Superconductivity*, vol. 25, no. 4, pp. 1–7, Aug. 2015.

[50] and and T. L. W. and, “Superconductor-magnet bearings with inherent stability and velocity-independent drag torque,” in *1999 IEEE/ASME International Conference on Advanced Intelligent Mechatronics (Cat. No.99TH8399)*, 1999, pp. 806–811.

[51] “A micro high-temperature superconductor-magnet flywheels with dual function of energy storage and attitude control,” in *2002 IEEE SENSORS*, 2002, vol. 2, pp. 757–762 vol.2.

[52] “Microsatellite combined attitude/energy systems,” *IEEE Aerospace and Electronic Systems Magazine*, vol. 19, no. 4, pp. 27–32, Apr. 2004.

[53] and and T. L. Wilson, “High-temperature superconductor-magnet momentum wheel for micro satellite,” in *2001 IEEE Aerospace Conference Proceedings (Cat. No.01TH8542)*, 2001, vol. 5, pp. 2463–2468 vol.5.

[54] J. Tang, J. Fang, and W. Wen, “Superconducting Magnetic Bearings and Active Magnetic Bearings in Attitude Control and Energy Storage Flywheel for Spacecraft,” *IEEE Transactions on Applied Superconductivity*, vol. 22, no. 6, pp. 5702109–5702109, Dec. 2012.

[55] E. A. Kervendal, D. R. Kirk, and R. B. Meinke, “Spacecraft Radiation Shielding Using Ultralightweight Superconducting Magnets,” *Journal of Spacecraft and Rockets*, vol. 46, no. 5, pp. 982–988, Sep. 2009.

[56] G. V. Gettliffe, “High-temperature superconductors as electromagnetic deployment and support structures in spacecraft,” Thesis, Massachusetts Institute of Technology, 2012.

[57] Z. Wen, Y. Liu, W. Yang, and M. Qiu, “Vibration measurements and analyses for a magnet–superconductor levitated system,” *J. Phys. D: Appl. Phys.*, vol. 40, no. 23, pp. 7281–7286, Nov. 2007.

[58] T. Shibata and S. Sakai, “Passive Micro Vibration Isolator Utilizing Flux Pinning Effect for Satellites,” *J. Phys.: Conf. Ser.*, vol. 744, p. 012009, Sep. 2016.

[59] T. Shibata and S. Sakai, “Design Method for The Micro Vibration Isolator Using Flux Pinning Effect for Satellites,” in *AIAA/AAS Astrodynamics Specialist Conference*, Long Beach, California, 2016.

[60] D. S. McKay *et al.*, “Search for Past Life on Mars: Possible Relic Biogenic Activity in Martian Meteorite ALH84001,” *Science*, vol. 273, no. 5277, pp. 924–930, Aug. 1996.

[61] J. P. Grotzinger *et al.*, “Mars Science Laboratory Mission and Science Investigation,” *Space Sci Rev*, vol. 170, no. 1, pp. 5–56, Sep. 2012.

[62] J. A. Crisp, M. Adler, J. R. Matijevic, S. W. Squyres, R. E. Arvidson, and D. M. Kass, “Mars Exploration Rover mission,” *Journal of Geophysical Research: Planets*, vol. 108, no. E12, 2003.

[63] “Lunar Rocks and Soils from Apollo Missions.” [Online]. Available: https://curator.jsc.nasa.gov/lunar/. [Accessed: 21-Mar-2019].

[64] P. Lucey *et al.*, “Understanding the Lunar Surface and Space-Moon Interactions,” *Reviews in Mineralogy and Geochemistry*, vol. 60, no. 1, pp. 83–219, Jan. 2006.

[65] J. J. Barnes *et al.*, “The origin of water in the primitive Moon as revealed by the lunar highlands samples,” *Earth and Planetary Science Letters*, vol. 390, pp. 244–252, Mar. 2014.

[66] “Origin of the Soviet Mars sample-return project.” [Online]. Available: http://www.russianspaceweb.com/5m-origin.html. [Accessed: 20-Mar-2019].

[67] “Groundbreaking Sample Return from Mars: The Next Giant Leap in Understanding the Red Planet.” .

[68] R. P. Kornfeld, J. C. Parrish, and S. Sell, “Mars Sample Return: Testing the Last Meter of Rendezvous and Sample Capture,” *Journal of Spacecraft and Rockets*, vol. 44, no. 3, pp. 692–702, 2007.

[69] R. Mattingly and L. May, “Mars Sample Return as a campaign,” in *2011 Aerospace Conference*, 2011, pp. 1–13.

[70] “Planetary Science Decadal Survey: 2013-2022,” *Solar System Exploration: NASA Science*. [Online]. Available: https://solarsystem.nasa.gov/resources/552/planetary-science-decadal-survey-2013-2022. [Accessed: 21-Mar-2019].

[71] J. F. Mustard *et al.*, “Report of the Mars 2020 Science Definition Team,” p. 205.

[72] A. Merlo, J. Larranaga, and P. Falkner, “SAMPLE FETCHING ROVER (SFR) FOR MSR,” p. 10.

[73] E. Klein *et al.*, “The Mobile MAV concept for Mars Sample Return,” in *2014 IEEE Aerospace Conference*, 2014, pp. 1–9.

[74] P. Younse, J. Strable, M. Dolci, P. Ohta, K. Lalla, and E. Olds, “An Orbiting Sample Capture and Orientation System Architecture for Potential Mars Sample Return,” presented at the IEEE Aerospace 2018, Big Sky, Montana, 2018.

[75] “Survey of orbital dynamics and control of space rendezvous - ScienceDirect.” [Online]. Available: https://www.sciencedirect.com/science/article/pii/S1000936113001787. [Accessed: 14-Mar-2019].

[76] “Spektr of Failure.” [Online]. Available: https://sma.nasa.gov/news/safety-messages/safety-message-item/spektr-of-failure. [Accessed: 14-Mar-2019].

[77] “A Survey of Teleoperator Rendezvous and Docking Technology--《Manned Spaceflight》2011年02期.” [Online]. Available: http://en.cnki.com.cn/Article_en/CJFDTOTAL-ZRHT201102010.htm. [Accessed: 14-Mar-2019].

[78] J. L. Goodman, “History of Space Shuttle Rendezvous and Proximity Operations,” *Journal of Spacecraft and Rockets*, vol. 43, no. 5, pp. 944–959, 2006.

[79] M. Hiltz, C. Rice, K. Boyle, R. Allison, and M. D. Space, “CANADARM: 20 YEARS OF MISSION SUCCESS THROUGH ADAPTATION,” p. 8.

[80] P. Singla, K. Subbarao, and J. L. Junkins, “Adaptive Output Feedback Control for Spacecraft Rendezvous and Docking Under Measurement Uncertainty,” *Journal of Guidance, Control, and Dynamics*, vol. 29, no. 4, pp. 892–902, 2006.

[81] Y. Wang and H. Ji, "Integrated relative position and attitude control for spacecraft rendezvous with ISS and finite-time convergence," *Aerospace Science and Technology*, vol. 85, pp. 234–245, Feb. 2019.

[82] J. Davis, J. Doebbler, J. Junkins, and J. Valasek, "Mobile Robotic System for Ground-Testing of Multi-Spacecraft Proximity Operations," in *AIAA Modeling and Simulation Technologies Conference and Exhibit*, American Institute of Aeronautics and Astronautics.

[83] B. J. S. Naasz, "Satellite Servicing's Autonomous Rendezvous and Docking Testbed on the International Space Station," presented at the 34th Annual AAS Rocky Mountain Section Guidance and Control Conference, Breckenridge, CO, United States, 2011.

[84] D. Miller *et al.*, "SPHERES: A Testbed For Long Duration Satellite Formation Flying In Micro-Gravity Conditions," p. 13.

[85] A. S. Otero, A. Chen, D. W. Miller, and M. Hilstad, "SPHERES: Development of an ISS Laboratory for formation flight and docking research," in *Proceedings, IEEE Aerospace Conference*, 2002, vol. 1, pp. 1–1.

[86] S. Stamm and P. Motaghedi, "Orbital express capture system: concept to reality," in *Spacecraft Platforms and Infrastructure*, 2004, vol. 5419, pp. 78–92.

[87] M. Romano and P. Oppenheimer, "Spacecraft docking interface mechanism," US8006937B1, 30-Aug-2011.

[88] J. Pei *et al.*, "Autonomous Rendezvous and Docking of Two 3U Cubesats Using a Novel Permanent-Magnet Docking Mechanism," in *54th AIAA Aerospace Sciences Meeting*, American Institute of Aeronautics and Astronautics.

[89] W. F. Barker, "Magnetic docking probe for soft docking of space vehicles," US4381092A, 26-Apr-1983.

[90] T. Mai, "Technology Readiness Level," *NASA*, 06-May-2015. [Online]. Available: http://www.nasa.gov/directorates/heo/scan/engineering/technology/txt_accordion1.html. [Accessed: 11-Mar-2019].

[91] C. Navau, N. Del-Valle, and A. Sanchez, "Macroscopic Modeling of Magnetization and Levitation of Hard Type-II Superconductors: The Critical-State Model," *IEEE Transactions on Applied Superconductivity*, vol. 23, no. 1, p. 8201023, 2013.

[92] A. Sanchez and C. Navau, "Critical-current density from magnetization loops of finite high-T c superconductors," *Supercond. Sci. Technol.*, vol. 14, no. 7, p. 444, 2001.

[93] A. A. Kordyuk, “Magnetic levitation for hard superconductors,” *Journal of Applied Physics*, vol. 83, no. 1, pp. 610–612, Jan. 1998.

[94] F. Zhu, L. Jones-Wilson, and M. Peck, “Flux-Pinned Dynamics Model Parameterization and Sensitivity Study,” presented at the IEEE Aerospace Conference, Big Sky, Montana, 2018.

[95] Y. Yang and X. Zheng, “Method for solution of the interaction between superconductor and permanent magnet,” *Journal of Applied Physics*, vol. 101, no. 11, p. 113922, Jun. 2007.

[96] K. W. Yung, P. B. Landecker, and D. D. Villani, “An Analytic Solution for the Force Between Two Magnetic Dipoles,” *Physical Separation in Science and Engineering*, 1998.

[97] P. B. Landecker, D. D. Villani, and K. W. Yung, “An Analytic Solution for the Torque Between Two Magnetic Dipoles,” *Physical Separation in Science and Engineering*, 1999.

[98] M. K. Alqadi, F. Y. Alzoubi, H. M. Al-khateeb, and N. Y. Ayoub, “Interaction between a point magnetic dipole and a high-temperature superconducting sphere,” *Physica B: Condensed Matter*, vol. 404, no. 12, pp. 1781–1784, Jun. 2009.

[99] A. Cansiz, J. R. Hull, and Ö. Gundogdu, “Translational and rotational dynamic analysis of a superconducting levitation system,” *Supercond. Sci. Technol.*, vol. 18, no. 7, p. 990, 2005.

[100] T. Sugiura, H. Ura, and K. Kuroda, “Magnetic stiffness of a coupled high-Tc superconducting levitation system - ScienceDirect,” *Physica C: Superconductivity*, vol. 392, pp. 648–653, 2003.

[101] C. Navau, A. Sanchez, E. Pardo, and D.-X. Chen, “Equilibrium positions due to different cooling processes in superconducting levitation systems,” *Supercond. Sci. Technol.*, vol. 17, no. 7, p. 828, 2004.

[102] X.-Y. Zhang, Y.-H. Zhou, and J. Zhou, “Modeling of symmetrical levitation force under different field cooling processes,” *Physica C: Superconductivity*, vol. 468, no. 5, pp. 401–404, Mar. 2008.

[103] E. H. Brandt, “Friction in levitated superconductors,” *Appl. Phys. Lett.*, vol. 53, no. 16, pp. 1554–1556, Oct. 1988.

[104] X.-Y. Zhang, Y.-H. Zhou, and J. Zhou, “Effects of magnetic history on the levitation characteristics in a superconducting levitation system,” *Physica C: Superconductivity and its Applications*, vol. 468, no. 14, pp. 1013–1016, Jul. 2008.

[105] H. Teshima, M. Sawamura, M. Morita, and M. Tsuchimoto, “Levitation forces of a single-grained Y-Ba-Cu-O bulk superconductor of 48 mm in diameter,” *Cryogenics*, vol. 37, no. 9, pp. 505–509, 1997.

[106] F. Zhu, M. Peck, and L. Jones-Wilson, “Reduced Embedded Magnetic Field in Type-II Superconductor of Finite Dimension,” *In submission*.

[107] W. M. Yang *et al.*, “Identification of the effect of grain size on levitation force of well-textured YBCO bulk superconductors,” *Cryogenics*, vol. 42, no. 10, pp. 589–592, Oct. 2002.

[108] W. M. Yang *et al.*, “Effect of perimeters of induced shielding current loops on levitation force in melt grown single-domain YBa2Cu3O7−x bulk,” *Appl. Phys. Lett.*, vol. 79, no. 13, pp. 2043–2045, Sep. 2001.

[109] F. Zhu and M. Peck, “Linearized Dynamics of General Flux-Pinned Interfaces,” *IEEE Transactions on Applied Superconductivity*, vol. 28, no. 8, pp. 1–10, Dec. 2018.

[110] B. F. Edwards, D. M. Riffe, J.-Y. Ji, and W. A. Booth, “Interactions between uniformly magnetized spheres,” *American Journal of Physics*, vol. 85, no. 2, pp. 130–134, Jan. 2017.

[111] C. H. Chiang, C. W. Yang, P. L. Hsieh, and W. C. Chan, “Levitation Force Measurement at Different Temperatures for YBCO Superconductor,” *Journal of Low Temperature Physics*, vol. 131, no. 3–4, pp. 743–746, May 2003.

[112] H. Jiang *et al.*, “The magnetic levitation performance of YBaCuO bulk at different temperature,” *Physica C: Superconductivity*, vol. 378–381, no. Part 1, pp. 869–872, Oct. 2002.

[113] J. Halbritter, “Granular superconductors and their intrinsic and extrinsic surface impedance,” *J Supercond*, vol. 8, no. 6, pp. 691–703, Dec. 1995.

[114] R. Liang, P. Dosanjh, D. A. Bonn, W. N. Hardy, and A. J. Berlinsky, “Lower critical fields in an ellipsoid-shaped ${\mathrm{YBa}}_{2}$${\mathrm{Cu}}_{3}$${\mathrm{O}}_{6.95}$ single crystal,” *Phys. Rev. B*, vol. 50, no. 6, pp. 4212–4215, Aug. 1994.

[115] W. C. Chan, C. Y. Wang, and J. J. Lee, “Grain size effect on magnetic levitation of YBCO superconducting samples,” *Physica C: Superconductivity*, vol. 282–287, no. Part 3, pp. 1455–1456, Aug. 1997.

[116] W. M. Yang *et al.*, “The grain-alignment and its effect on the levitation force of melt processed YBCO single-domained bulk superconductors,” *Physica C: Superconductivity*, vol. 307, no. 3, pp. 271–276, Oct. 1998.

[117] W. M. Yang *et al.*, “The effect of the grain alignment on the levitation force in single domain YBa2Cu3Oy bulk superconductors,” *Physica C: Superconductivity*, vol. 319, no. 3, pp. 164–168, Jun. 1999.

[118] W. M. Yang *et al.*, “The effect of different field cooling processes on the levitation force and attractive force of single-domain YBa 2 Cu 3 O 7− x bulk,” *Supercond. Sci. Technol.*, vol. 15, no. 10, p. 1410, 2002.

[119] Z. Ren *et al.*, “Influence of shape and thickness on the levitation force of YBaCuO bulk HTS over a NdFeB guideway,” *Physica C: Superconductivity*, vol. 384, no. 1, pp. 159–162, Jan. 2003.

[120] W. M. Yang *et al.*, “The effect of magnet configurations on the levitation force of melt processed YBCO bulk superconductors,” *Physica C: Superconductivity*, vol. 354, no. 1, pp. 5–12, May 2001.

[121] P. Chaddah, “Critical current densities in superconducting materials,” *Sadhana*, vol. 28, no. 1–2, pp. 273–282, Feb. 2003.

[122] “Levitation bulk,” *CAN SUPERCONDUCTORS*. [Online]. Available: http://www.can-superconductors.com/levitation-bulk.html. [Accessed: 04-Feb-2018].

[123] B. Scholkopf and A. J. Smola, *Learning with Kernels: Support Vector Machines, Regularization, Optimization, and Beyond*. Cambridge, MA, USA: MIT Press, 2001.

[124] I. McKinley and L. Jones-Wilson, “A Flight-Traceable Cryogenic Thermal System for use in a Sample-Capture Flux-Pinned Interface,” *In submission*.

[125] H. C. Schubert and J. P. How, “Space construction: an experimental testbed to develop enabling technologies,” in *Telemanipulator and Telepresence Technologies IV*, 1997, vol. 3206, pp. 179–189.

[126] D. Sternberg, C. Pong, N. Filipe, S. Mohan, S. Johnson, and L. Jones-Wilson, “JPL Small Satellite Dynamics Validation: Validated Models for Predicting On-Orbit Performance,” *Journal of Guidance, Navigation, and Control*, 2017.

[127] “Tie-Down Ring.” [Online]. Available: https://www.mcmaster.com/. [Accessed: 19-Mar-2019].

[128] "Tie Down." [Online]. Available: https://www.mcmaster.com/. [Accessed: 19-Mar-2019].

[129] "12 Outlet 10 15A 2 20A Vertical Power Strip 120V 20A 15 ft Cord 5 20P 36 in (PS361220) | Tripp Lite," *Tripp Lite Website*. [Online]. Available: https://www.tripplite.com/12-outlet-10-15a-2-20a-vertical-power-strip-120v-20a-15-ft-cord-5-20p-36-in~PS361220. [Accessed: 19-Mar-2019].

[130] I. McKinley, C. Hummel, and J.-W. Jones-Wilson Laura, "A Flight-Traceable Cryogenic Thermal System for Use in a Sample-Capture Flux-Pinned Interface," presented at the IEEE Aerospace 2019, Big Sky, Montana, 2019.

[131] "SAES Getter," *SAES Getter*. [Online]. Available: https://www.saesgetters.com/sites/default/files/NEXTorr%20D.pdf. [Accessed: 19-Mar-2019].

[132] "LPT93105000 mW / 24 mm slip-on," *Thales Cryogenics*. .

[133] E. Olson, "AprilTag: A robust and flexible visual fiducial system," in *2011 IEEE International Conference on Robotics and Automation*, 2011, pp. 3400–3407.

[134] "(4) Magnetic braking: Simple theory and experiment | Request PDF," *ResearchGate*. [Online]. Available: https://www.researchgate.net/publication/252850785_Magnetic_braking_Simple_theory_and_experiment. [Accessed: 07-Sep-2018].

[135] J. Shoer and M. Peck, "Stiffness Of A Flux-Pinned Virtual Structure For Modular Spacecraft," *Journal of the British Interplanetary Society*, vol. 62, pp. 57–65, 2009.

[136] "Perfect is the Enemy of Good Enough," *U.S. Naval Institute*, 01-Oct-1988. [Online]. Available: https://www.usni.org/magazines/proceedings/1988/october/perfect-enemy-good-enough. [Accessed: 25-Mar-2019].

[137] E. Kaiser, J. N. Kutz, and S. L. Brunton, "Sparse identification of nonlinear dynamics for model predictive control in the low-data limit," Nov. 2017.

[138] M. Schmidt and H. Lipson, "Distilling Free-Form Natural Laws from Experimental Data," *Science*, vol. 324, no. 5923, pp. 81–85, Apr. 2009.

[139] D. P. Searson, "GPTIPS 2: An Open-Source Software Platform for Symbolic Data Mining," in *Handbook of Genetic Programming Applications*, A. H. Gandomi, A. H. Alavi, and C. Ryan, Eds. Cham: Springer International Publishing, 2015, pp. 551–573.

[140] K. Hornik, M. Stinchcombe, and H. White, “Multilayer feedforward networks are universal approximators,” *Neural Networks*, vol. 2, no. 5, pp. 359–366, Jan. 1989.

[141] A. Pinkus, “Approximation theory of the MLP model in neural networks,” *Acta Numerica*, vol. 8, p. 143, Jan. 1999.

[142] D. E. Goldberg, *Genetic Algorithms in Search, Optimization and Machine Learning*, 1st ed. Boston, MA, USA: Addison-Wesley Longman Publishing Co., Inc., 1989.

[143] A. H. Gandomi and A. H. Alavi, “A new multi-gene genetic programming approach to non-linear system modeling. Part II: geotechnical and earthquake engineering problems,” *Neural Comput & Applic*, vol. 21, no. 1, pp. 189–201, Feb. 2012.

[144] H. W. Lin, M. Tegmark, and D. Rolnick, “Why does deep and cheap learning work so well?,” *Journal of Statistical Physics*, vol. 168, no. 6, pp. 1223–1247, Sep. 2017.

[145] F. Rosenblatt, “The perceptron: A probabilistic model for information storage and organization in the brain,” *Psychological Review*, vol. 65, no. 6, pp. 386–408, 1958.

[146] S. Ferrari, K. Rudd, and G. D. Muro, “A Constrained Backpropagation Approach to Function Approximation and Approximate Dynamic Programming,” in *Reinforcement Learning and Approximate Dynamic Programming for Feedback Control*, John Wiley & Sons, Ltd, 2013, pp. 162–181.

[147] D. Rolnick and M. Tegmark, “The power of deeper networks for expressing natural functions,” *arXiv:1705.05502 [cs, stat]*, May 2017.

[148] “(PDF) Taylor Series For Multi-Variable Functions,” *ResearchGate*. [Online]. Available: https://www.researchgate.net/publication/286625914_Taylor_Series_For_Multi-Variable_Functions. [Accessed: 11-Jan-2019].

[149] T. Ozaki, T. Suzuki, T. Furuhashi, S. Okuma, and Y. Uchikawa, “Trajectory control of robotic manipulators using neural networks,” *IEEE Transactions on Industrial Electronics*, vol. 38, no. 3, pp. 195–202, Jun. 1991.

[150] H. Gao, X. Song, L. Ding, K. Xia, N. Li, and Z. Deng, “Adaptive motion control of wheeled mobile robot with unknown slippage,” *International Journal of Control*, vol. 87, no. 8, pp. 1513–1522, Aug. 2014.

[151] X. B. Peng, G. Berseth, and M. van de Panne, “Dynamic Terrain Traversal Skills Using Reinforcement Learning,” *ACM Trans. Graph.*, vol. 34, no. 4, pp. 80:1–80:11, Jul. 2015.

[152] I. Vincent and Q. Sun, “A combined reactive and reinforcement learning controller for an autonomous tracked vehicle,” *Robotics and Autonomous Systems*, vol. 60, no. 4, pp. 599–608, Apr. 2012.

[153] M. Cutler and J. P. How, “Autonomous drifting using simulation-aided reinforcement learning,” in *2016 IEEE International Conference on Robotics and Automation (ICRA)*, 2016, pp. 5442–5448.

[154] B.-S. Chang and W. J. Baker, “Soil parameters to predict the performance of off-road vehicles,” *Journal of Terramechanics*, vol. 9, no. 2, pp. 13–31, Jan. 1973.

[155] G. Ishigami, A. Miwa, K. Nagatani, and K. Yoshida, “Terramechanics-based model for steering maneuver of planetary exploration rovers on loose soil,” *J. Field Robotics*, vol. 24, no. 3, pp. 233–250, Mar. 2007.

[156] D. Savitski *et al.*, “Improvement of traction performance and off-road mobility for a vehicle with four individual electric motors: Driving over icy road,” *Journal of Terramechanics*, vol. 69, pp. 33–43, Feb. 2017.

[157] M.-R. Bouguelia, R. Gonzalez, K. Iagnemma, and S. Byttner, “Unsupervised classification of slip events for planetary exploration rovers,” *Journal of Terramechanics*, vol. 73, pp. 95–106, Oct. 2017.

[158] J. Bongard and H. Lipson, “Evolved Machines Shed Light on Robustness and Resilience,” *Proceedings of the IEEE*, vol. 102, no. 5, pp. 899–914, May 2014.

[159] F. Corucci, N. Cheney, F. Giorgio-Serchi, J. Bongard, and C. Laschi, “Evolving Soft Locomotion in Aquatic and Terrestrial Environments: Effects of Material Properties and Environmental Transitions,” *Soft Robotics*, vol. 5, no. 4, pp. 475–495, Aug. 2018.

[160] J. C. Bongard and H. Lipson, “Nonlinear System Identification Using Coevolution of Models and Tests,” *IEEE Transactions on Evolutionary Computation*, vol. 9, no. 4, pp. 361–384, Aug. 2005.

[161] J. Rissanen, “Modeling by shortest data description,” *Automatica*, vol. 14, no. 5, pp. 465–471, Sep. 1978.

[162] R. C. Conlter, *Implementation of the Pure Pursuit Path ’hcking Algorithm*. 1992.

[163] D. Psaltis, A. Sideris, and A. A. Yamamura, “A multilayered neural network controller,” *IEEE Control Systems Magazine*, vol. 8, no. 2, pp. 17–21, Apr. 1988.

[164] “Rosetta enters hibernation - ScienceDirect.” [Online]. Available: https://www.sciencedirect.com/science/article/pii/S0094576512001695. [Accessed: 02-Feb-2019].

[165] D. Y. Kusnierkiewicz, C. B. Hersman, Y. Guo, S. Kubota, and J. McDevitt, “A description of the Pluto-bound New Horizons spacecraft,” *Acta Astronautica*, vol. 57, no. 2, pp. 135–144, Jul. 2005.

[166] R. Srianand, P. Petitjean, and C. Ledoux, “The cosmic microwave background radiation temperature at a redshift of 2.34,” *Nature*, vol. 408, no. 6815, pp. 931–935, Dec. 2000.

APPENDIX

I. CryoSat: A Cryogenic Mission to the Interstellar Medium

a. *Motivation and Challenges*

A completely cryogenic spacecraft does not yet exist. Conventional spacecraft adhere to a thermal architecture that separates cold components and warm components. The most stringent cold thermal requirements depend on the science instruments or payload, typically below 100 degrees Kelvin. The electronics and batteries function within a warm thermal range, typically between 273 to 313 degrees Kelvin. To compensate for the thermal dissonance, the spacecraft expends a significant portion of power not only to heat the avionics, but also cool the payload and reallocate the heat produced from the cooling system. In the event that the entire spacecraft falls below a certain temperature, the spacecraft typically hibernates with heaters running continuously until the spacecraft arrives at its destination [164], [165]. Consequently, the deep space science missions do not utilize the travel to destinations because the power budget is allocated to heaters instead of science instruments. This thermal regulation is incredibly inefficient and does not effectively utilize the sparse power available in outer space, especially deep space.

Propulsion, power generation, and C&DH (command and data handling) are the major technological hurdles in deep space travel. Deep space is naturally cold, with the black body temperature of the background radiation at 3 degrees Kelvin [166]. A spacecraft traveling through deep space with no active heating elements naturally resides in cryo-temperature environments. As a spacecraft moves farther from a central star, the intensity of power absorbed as heat and power generation decreases with distance squared. A cryogenic spacecraft follows this natural reduction of power with a highly efficient power architecture, thermally resilient structure, and

avionics systems. The only regenerative resource is power and thus to optimize for functionality over an indefinite mission lifetime, reduced mass solutions are ideal at the sacrifice of power consumption.

The goal of this work is to offer a spacecraft platform that functions continuously through cryogenic environments: interstellar space, prolonged station keeping in eclipse, and extreme planetary environments. Principal investigators may then implant their payload with a specified size, weight, and power to hitch a ride through deep space. This technological survey follows a spacecraft subsystem breakdown. Each subsystem includes a short introduction, a range of traceable technologies, design considerations involved with technology selection, and a final recommendation. The paper concludes with a cohesive spacecraft design based on each subsystem's final recommendations. The main text of this body of work was written by Hailee Hettrick and David Levine under the author's guidance. To access the full text, please contact the author at frankiezoo@gmail.com.

b. *Contribution from Cryogenic Spacecraft Concept Study*

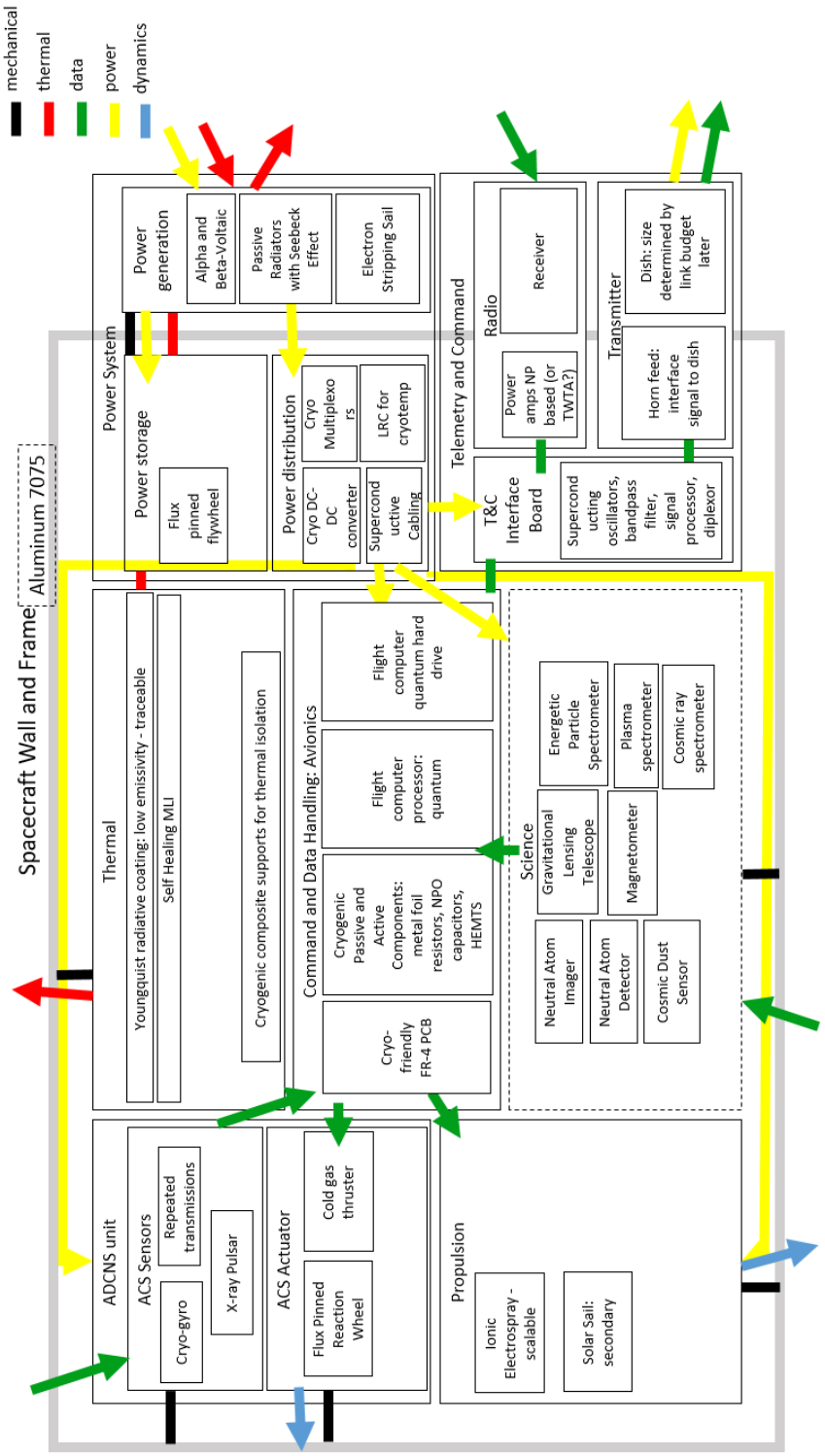

Figure 190: Block diagram of recommended technologies viable for a cryogenic spacecraft mission.

Some spacecraft subsystems require a large quantity of development and evaluation before a cryogenic spacecraft can embark on an interstellar mission. Figure 19 graphically depicts the different technologies within subsystems and the interactions between subsystems. Although this conglomeration of technologies represents a feasible path forward with existing traceable technologies, innovative industry-changing inventions could formulate a drastically different grouping of technologies. The most challenging technology gaps lie in power generation, propulsion, and C&DH, but low technology readiness level (TRL) advancements are made in each field. A discussion of the final constituents for the proposed cryogenic spacecraft follows.

Starting with power generation, continued development of an electron collector, or a particle-based betavoltaic device rely upon collector material performance (over time) after high energy collisions with free radicals, and the determination of the ISM's particle distribution for the purposes of path planning. A heat-based, thermoelectric method for power generation rely upon the location of heat producers and the spacecraft's heating area. These generation mechanisms have been developed in concept, but further assessment is necessary to select a particle or heat-based technique for a mission. A superconducting flywheel can store power successfully in cryotemperatures, but further testing is required to quantify the effect of resistive power loss due to the flywheel stator over the course of a multi-year mission. Longevity testing of these components at cryotemperatures ensure the power system's functionality in the ISM. The cryogenic power electronics necessary for such a mission have already been developed. However, the specific characteristics of cryogenic circuitry developed with these components should be compared to identical power circuitry operating at room temperature. This test enables the selection of components best suited to take advantage of the cryogenic environment.

The thermal subsystem has also been developed in theory alone, as the utilization of Youngquist's thermal coating and low-thermal conductivity structural supports should prevent heating via radiation and convection, respectively. Nevertheless, further testing of Youngquist's coating in a simulated deep space environment with infrared radiation sources is necessary to determine its viability. Passive cooling could be achieved via cryogenic radiators, but further development is necessary to scale down such devices to minimize spacecraft mass.

The structures subsystem can be comprised of contemporary materials such as aluminum-7075, although multifunctional supports (tensile straps) made of composite material could also provide additional thermal stability. Finally, a cryogenic spacecraft's science mission could employ scientific instruments proposed for the Innovative Interstellar Explorer (IIE) spacecraft. Nonetheless, more advanced science operations like a precursor mission for Project Breakthrough Starshot or a gravitational lensing telescope, require further development to ensure complete functionality with the rest of the cryogenic spacecraft architecture.

The ionic electrospray thruster solution would require further development since there are no proposals for a larger device than that for a CubeSat, which is insufficient for this application. Additionally, the measured and estimated velocities for both solar sail technology and the electrospray thruster are too slow with respect to the expected lifetime of the other components of the spacecraft. It is worth noting that Breakthrough Starshot is researching and developing the propulsive technology required for a spacecraft to travel at 20% the speed of light in order to make interstellar missions feasible. The focused technology of this effort is solar sail technology, which is in agreement with this design's final recommendation of advancing the capabilities of solar sails as the propulsive device for a cryogenic and interstellar spacecraft.

Thus, the recommended actuators of the GNC subsystem for the cryogenic spacecraft are the flux-pinned reaction wheel and cold gas thrusters. The flux-pinned reaction wheel, which allows for fine attitude control, requires a cryogenic environment for operation, which is naturally provided by the nature of this mission. Additionally, the flux-pinned reaction wheel has superior performance to the standard reaction wheel in that it endures less friction, therefore requiring less power to maintain the same torque as its mechanical bearing counterpart. The cold gas thruster does not produce excess heat like other state-of-the-art thrusters and allows for coarse attitude control. Employing these two actuators allows for redundancy in this experimental mission.

The recommended sensors for the cryogenic spacecraft mission are the cryogenic gyroscope, transmission pinging, and an x-ray pulsar detector. Recommendation for the cryogenic gyroscope comes with the caveat that the operation temperature would need to be around 77 K rather than the 2 K employed for the Gravity Probe B mission. While the cryogenic gyroscope provides absolute rotational knowledge, absolute position knowledge is necessary, as well. The transmission pinging method described previously is used for several deep space probes and is a solution for this mission as the method has high fidelity and no additional equipment is required. The telemetry and command subsystem is a spacecraft necessity. Lastly, an x-ray pulsar detector, a novel means for interstellar navigation, allows for absolute position knowledge based on detection of known x-ray pulsars, much like how a star tracker works for determining position based on a star catalog. Therefore, the combination of these sensors permit obtaining absolute attitude and position knowledge even in interstellar travel.

An on-board computer that utilizes a quantum hard drive and a quantum processor are recommended for a cryogenic spacecraft's command and data handling subsystem. While this

technology is still in its early stages, there exists a suitable quantity of interest and research that represents a promising future for quantum computers and their applicability to spacecraft.

II. Flux-Pinning Dynamics Supplemental Material

a. *Linearization of Flux-Pinning Dynamics*

Linearizing Villani's Force Equation Intermediate Steps

Linearize about $\boldsymbol{\rho_e}, \boldsymbol{m_{ae}}$, and $\boldsymbol{m_{be}}$. Take Eq. (39) and substitute $\boldsymbol{\rho}$ with $\boldsymbol{\rho_e} + \delta\boldsymbol{r}$, $\boldsymbol{m_a}$ with $\boldsymbol{m_{ae}} + \delta\boldsymbol{m_a}$, and $\boldsymbol{m_b}$ with $\boldsymbol{m_{be}} + \delta\boldsymbol{m_b}$:

$$F_{ab,e} =$$

$$\frac{3\mu_0}{4\pi|\rho_e+\delta r|^5}\begin{pmatrix}\big((\rho_e+\delta r)\times(m_{ae}+\delta m_a)\big)\times(m_{be}\times\delta m_b)+\big((\rho_e+\delta r)\times(m_{be}+\delta m_b)\big)\times(m_{ae}\times\delta m_a)\\ -2(\rho_e+\delta r)\big((m_{ae}+\delta m_a)\cdot(m_{be}+\delta m_b)\big)+5\frac{\rho_e+\delta r}{|\rho_e+\delta r|^2}\big((\rho_e+\delta r)\times(m_{ae}+\delta m_a)\big)\cdot\big((\rho_e+\delta r)\times(m_{be}+\delta m_b)\big)\end{pmatrix}-$$

$$\frac{5\cdot3\mu_0}{4\pi|\rho_e+\delta r|^7}\begin{pmatrix}\big((\rho_e+\delta r)\times(m_{ae}+\delta m_a)\big)\times(m_{be}\times\delta m_b)+\big((\rho_e+\delta r)\times(m_{be}+\delta m_b)\big)\times(m_{ae}\times\delta m_a)\\ -2(\rho_e+\delta r)\big((m_{ae}+\delta m_a)\cdot(m_{be}+\delta m_b)\big)+5\frac{\rho_e+\delta r}{|\rho_e+\delta r|^2}\big((\rho_e+\delta r)\times(m_{ae}+\delta m_a)\big)\cdot\big((\rho_e+\delta r)\times(m_{be}+\delta m_b)\big)\end{pmatrix}$$

(195)

The linearized equation of force is the expanded form of Eq. (195) subtracted by the expanded form of Eq. (39), with only the first order terms:

$$\delta F_{ab} = \frac{3\mu_0}{4\pi|\rho_e|^5}\begin{pmatrix}(\delta r\times m_{ae})\times m_{be}+(\rho_e\times\delta m_a)\times m_{be}+(\rho_e\times m_{ae})\times\delta m_b+(\delta r\times m_{be})\times m_{ae}+\\ (\rho_e\times\delta m_b)\times m_{ae}+\times\delta m_a-2((m_{be}\cdot\delta m_a)\rho_e+(m_{ae}\cdot\delta m_b)\rho_e+(m_{ae}\cdot m_{be})\delta r\end{pmatrix}+$$

$$\frac{5\rho_e}{|\rho_e|^2}\big((\rho_e\times\delta m_a)\cdot(\rho_e\times m_{be})+(\delta r\times m_{ae})\cdot(\rho_e\times m_{be})+(\rho_e\times m_{ae})\cdot(\rho_e\times\delta m_b)\big)+\frac{-5\cdot3\mu_0}{4\pi|\rho_e|^7}\Bigg((\rho_e\times m_{ae})\times$$

$$m_{be}+(\rho_e\times m_{be})\times m_{ae}-2\rho_e(m_{ae}\cdot m_{be})+\frac{5\rho_e}{|\rho_e|^2}\big((\rho_e\times m_{ae})\cdot(\rho_e\times m_{be})\big)\Bigg) \quad (196)$$

With cross matrices instead of cross products and some reordering:

$$\delta \boldsymbol{F_{ab}} =$$

$$\frac{3\mu_0}{4\pi|\rho_e|^5}\begin{pmatrix} m_{be}^{\times}m_{ae}^{\times}\delta r - m_{be}^{\times}\rho_e^{\times}\delta m_a + (\rho_e^{\times}m_{ae})^{\times}\delta m_b + m_{ae}^{\times}m_{be}^{\times}\delta r - m_{ae}^{\times}\rho_e^{\times}\delta m_b + (\rho_e^{\times}m_{be})^{\times}\delta m_a \\ -2\left(\rho_e m_{be}^T\delta m_a + \rho_e m_{ae}^T\delta m_b + m_{ae}^T m_{be}\underline{1}\delta r\right) \\ +\frac{5}{|\rho_e|^2}(\rho_e(\rho_e^{\times}m_{be})^T\rho_e^{\times}\delta m_a + \rho_e(\rho_e^{\times}m_{ae})^T\rho_e^{\times}\delta m_b - \rho_e(\rho_e^{\times}m_{be})^T m_{ae}^{\times}\delta r - \rho_e(\rho_e^{\times}m_{ae})^T m_{be}^{\times}\delta r) \end{pmatrix} +$$

$$\frac{-5\cdot 3\mu_0}{4\pi|\rho_e|^7}\left((\rho_e^{\times}m_{ae})^{\times}m_{be} + (\rho_e^{\times}m_{be})^{\times}m_{ae} - 2(m_{ae}^T m_{be})\rho_e + \frac{5}{|\rho_e|^2}\left((\rho_e^{\times}m_{ae})^T(\rho_e^{\times}m_{ae})\right)\rho_e^T\right)\delta r \tag{197}$$

By factoring into the following variables, $\delta \boldsymbol{r}, \delta \boldsymbol{m_a}, \delta \boldsymbol{m_b}$:

$$\delta \boldsymbol{F_{ab}} = \begin{pmatrix} \frac{3\mu_0}{4\pi|\rho_e|^5}\left(m_{be}^{\times}m_{ae}^{\times} + m_{ae}^{\times}m_{be}^{\times} - 2m_{ae}^T m_{be}\underline{1} - \frac{5}{|\rho_e|^2}(\rho_e(\rho_e^{\times}m_{be})^T m_{ae}^{\times} - \rho_e(\rho_e^{\times}m_{ae})^T m_{be}^{\times})\right) \\ -\frac{15\mu_0}{4\pi|\rho_e|^7}\left((\rho_e^{\times}m_{ae})^{\times}m_{be} + (\rho_e^{\times}m_{be})^{\times}m_{ae} - 2(m_{ae}^T m_{be})\rho_e + \frac{5}{|\rho_e|^2}\left((\rho_e^{\times}m_{ae})^T(\rho_e^{\times}m_{ae})\right)\rho_e^T\right) \end{pmatrix}\delta r$$

$$+\left(\frac{3\mu_0}{4\pi|\rho_e|^5}\left(-m_{be}^{\times}\rho_e^{\times} + (\rho_e^{\times}m_{be})^{\times} - 2\rho_e m_{be}^T + \frac{5}{|\rho_e|^2}\rho_e(\rho_e^{\times}m_{be})^T\rho_e^{\times}\right)\right)\delta m_a +$$

$$\left(\frac{3\mu_0}{4\pi|\rho_e|^5}\left((\rho_e^{\times}m_{ae})^{\times} - m_{ae}^{\times}\rho_e^{\times} - 2\rho_e m_{ae}^T + \frac{5}{|\rho_e|^2}\rho_e(\rho_e^{\times}m_{ae})^T\rho_e^{\times}\right)\right)\delta m_b \tag{198}$$

<u>Linearizing Villani's Moment Equation Intermediate Steps</u>

Linearize about $\boldsymbol{\rho_e}, \boldsymbol{m_{ae}}$, and $\boldsymbol{m_{be}}$. Take Eq. (41) and substitute $\boldsymbol{\rho}$ with $\boldsymbol{\rho_e} + \delta \boldsymbol{r}, \boldsymbol{m_a}$ with $\boldsymbol{m_{ae}} + \delta \boldsymbol{m_a}$, and $\boldsymbol{m_b}$ with $\boldsymbol{m_{be}} + \delta \boldsymbol{m_b}$:

$$\boldsymbol{\tau_{ab,e}} = \frac{\mu_0}{4\pi|\rho_e+\delta r|^3}\begin{pmatrix} \frac{3}{|\rho_e+\delta r|^2}\left((m_{ae}+\delta m_a)\cdot(\rho_e+\delta r)\right)\left((m_{be}+\delta m_b)\times(\rho_e+\delta r)\right) + \\ \left((m_{ae}+\delta m_a)\times(m_{be}+\delta m_b)\right) \end{pmatrix} \tag{199}$$

The linearized equation of force is the expanded form of Eq. (199) subtracted by the expanded form of Eq. (41), with only the first order terms:

$$\boldsymbol{\tau_{ab,e}}$$

$$= \frac{\mu_0}{4\pi|\rho_e|^3}\begin{pmatrix} \frac{3}{|\rho_e|^2}\left((m_{ae}\cdot\rho_e)(\delta m_b\times\rho_e) + (m_{ae}\cdot\rho_e)(m_{be}\times\delta r) + (m_{ae}\cdot\delta r)(m_{be}\times\rho_e) + (\delta m_a\cdot\rho_e)(m_{be}\times\rho_e)\right) \\ +(m_{ae}\times\delta m_b) + (\,\delta m_a\times m_{be})) \end{pmatrix}$$

$$-\frac{3\mu_0}{4\pi|\rho_e|^5}\left(\frac{3}{|\rho_e|^2}(m_{ae}\cdot\rho_e)(m_{be}\times\rho_e)+m_{ae}\times m_{be}\right)\rho_e^T\,\delta r \tag{200}$$

With cross matrices instead of cross products and some reordering:

$$\delta\boldsymbol{\tau_{ab}}=\frac{\mu_0}{4\pi|\rho_e|^3}\left(\frac{3}{|\rho_e|^2}(-m_{ae}^T\rho_e^\times\delta m_b+m_{ae}^T\rho_e m_{be}^\times\delta r+m_{be}^T\rho_e m_{ae}^\times\delta r+m_{be}^\times\rho_e\rho_e^T\delta m_a)+m_{ae}^\times\delta m_a\right)$$
$$-\frac{3\mu_0}{4\pi|\rho_e|^5}\left(\frac{3}{|\rho_e|^2}m_{ae}^T\rho_e m_{be}^\times\rho_e+m_{ae}^\times m_{be}\right)\rho_e^T\delta r \tag{201}$$

Grouping like terms together:

$$\delta\boldsymbol{\tau_{ab}}=\frac{\mu_0}{4\pi|\rho_e|^3}\left(\frac{3}{|\rho_e|^2}\left(m_{ae}^T\rho_e m_{be}^\times+m_{be}^T\rho_e m_{ae}^\times-\left(\frac{3}{|\rho_e|^2}m_{ae}^T\rho_e m_{be}^\times\rho_e+m_{ae}^\times m_{be}\right)\rho_e^T\right)\right)\delta r+$$
$$\left(\frac{3}{|\rho_e|^2}m_{be}^\times\rho_e\rho_e^T-m_{be}^\times\right)\delta m_a+\left(\frac{-3}{|\rho_e|^2}m_{ae}^\times\rho_e\rho_e^T-m_{ae}^\times\right)\delta m_b \tag{202}$$

b. *Backwards-Reachability Polynomial Fits*

Linear model Poly8 associated with Figure 45:

$$f(r)=p_1r^8+p_2r^7+p_3r^6+p_4r^5+p_5r^4+p_6r^3+p_7r^2+p_8r+p_9$$

Coefficients (with 95% confidence bounds):

p1 = -5.401e+09 (-6.722e+09, -4.079e+09)

p2 = -1.643e+09 (-2.004e+09, -1.282e+09)

p3 = -1.992e+08 (-2.37e+08, -1.613e+08)

p4 = -1.219e+07 (-1.406e+07, -1.032e+07)

p5 = -3.932e+05 (-4.344e+05, -3.519e+05)

p6 = -6471 (-6865, -6078)

p7 = -54.38 (-63.28, -45.47)

p8 = 0.2987 (0.2228, 0.3745)

p9 = 0.04574 (0.04523, 0.04626)

Linear model Poly44 associated with Figure 47:

f(x,y) = p00 + p10*x + p01*y + p20*x^2 + p11*x*y + p02*y^2 + p30*x^3 + p21*x^2*y + p12*x*y^2 + p03*y^3 + p40*x^4 + 1*x^3*y + p22*x^2*y^2 + p13*x*y^3 + p04*y^4

Coefficients (with 95% confidence bounds):

p00 = 0.6386 (0.632, 0.6453)

p10 = -13.32 (-13.62, -13.02)

p01 = -0.04633 (-0.2582, 0.1655)

p20 = -1355 (-1384, -1326)

p11 = -0.576 (-17.26, 16.11)

p02 = -106.1 (-118.8, -93.33)

p30 = -2.669e+04 (-2.742e+04, -2.596e+04)

p21 = 40.55 (-650.8, 731.9)

p12 = 6105 (5745, 6465)

p03 = 21.46 (-110.4, 153.4)

p40 = -1.66e+05 (-1.715e+05, -1.606e+05)

p31 = 702.8 (-9217, 1.062e+04)

p22 = -1.31e+05 (-1.501e+05, -1.12e+05)

p13 = -187.3 (-1.23e+04, 1.193e+04)

p04 = -8.631e+04 (-9.214e+04, -8.047e+04)

III. Microgravity Experiment Procedures

Ground Operations

Table 60: SROA Pump and Cool-Down Checkout Procedure

Name	**SROA Pump and Cool-Down**
Pre-requisites	SROA and SBA assembled
Timing	24 hours prior to flux pinning operations or checkout
Configuration	Training Magnets in place, hangar pump connected to vacuum chamber, Auber temperature control box in place.
Steps	1. Start data acquisition system 2. Turn on turbo pump 3. Monitor pressure until vacuum chamber reaches 10^{-4} Torr 4. Turn on ventilation fans 5. Turn on cryocooler 6. Monitor temperature until temperature set-point (~80 K) is reached 7. Verify telemetry on cooler drive electronics display (expect 1044 mV sensor reading and ~100 W of cooler input power)

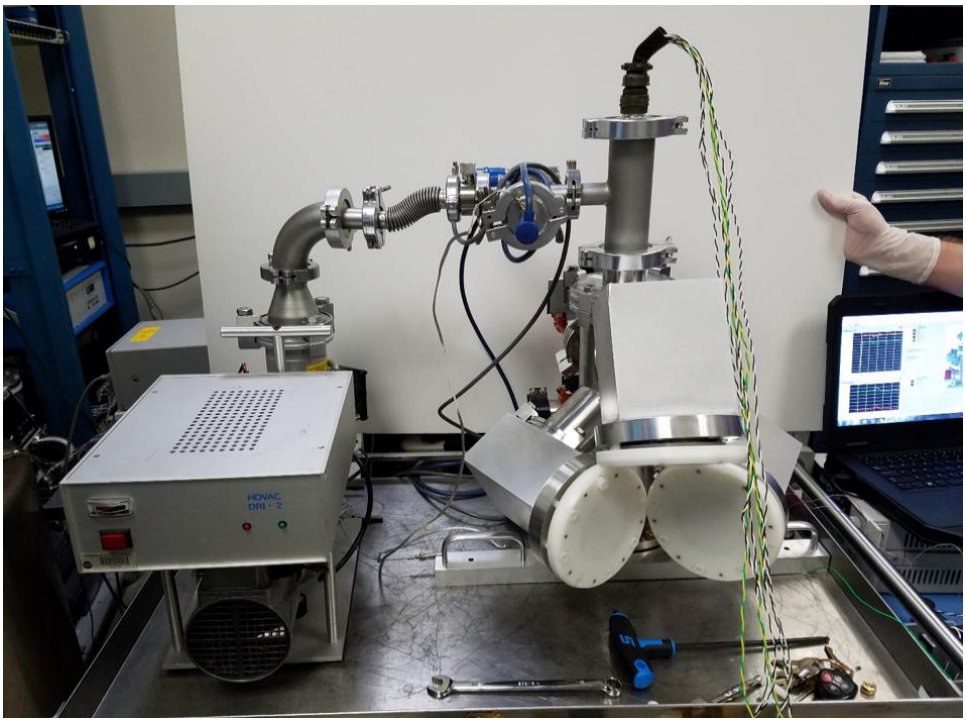

Figure 191. The SROA ground configuration looks similar to the lab setup shown here.

Notes: After a power interrupt, the vacuum pump with resume operation, but the cryocooler with default to “off.” Thus, during ground operations, a small power interrupt during the pump-down portion of the procedure (T-24 to T-12 hours to flux pinning operations) has no effect on experimental readiness, even if the system is unmonitored. However, a power interrupt during the cryocooler cool-down portion of the procedure (T-12 hours to flux pinning operations) leads to experimental delays unless the cryocooler is being actively monitored and the cryocooler is manually reset when the power resumes. The 12-hour requirement comes from cooling the system from room temperature to its nominal experiment temperature (82K at the YBCO superconductors).

Table 61: Commanding/Sensing Computer Connection Verification Checkout Procedure

Name	**Commanding/Sensing Computer Connection Verification**
Pre-requisites	None
Timing	Prior to aircraft loading
Configuration	No special requirements
Steps	1. Power on the Sensing computer and the Commanding computer 2. Once the OSA is turned on, connect the Sensing computer for the ad-hoc wireless network "FPOS". 3. Start the program TightVNC Server on the Sensing computer for screen sharing. 4. Connect the commanding computer to "FPOS", and begin screen sharing between the two computers with TightVNC Viewer. 5. Verify that the GUI may be commanded from the commanding computer

Table 62: OSA Battery Recharging Checkout Procedure

Name	**OSA Battery Recharging**
Pre-requisites	None
Timing	Prior to aircraft loading, as necessary
Configuration	Have LiPo Battery Emergency Burn Bag on hand; OSA can be disassembled, partially assembled, or fully assembled,
Steps	1. Ensure the OSA is powered off 2. Connect the USB cable to the outlet in the OSA 3. Connect the Apple USB charger to a wall outlet 4. Connect the USB cable to the USB outlet on the Apple USB charger 5. Disconnect after all LEDs are on. This step takes roughly 4 - 6 hours from a completely discharged state

Table 63: GoPro Battery Recharging Checkout Procedure

Name	**GoPro Battery Recharging**
Pre-requisites	None
Timing	Prior to aircraft loading, as necessary
Configuration	Have LiPo Battery Emergency Burn Bag on hand

Steps	1. Power the camera and Wi-Fi (if applicable) off. 2. Connect the camera to the USB port on the computer. 3. If possible use a USB port on the back of the computer. 4. Alternatively, you can connect it to a USB wall charger that outputs 5V and 1A. 5. The front red LED on the camera should turn on to indicate that it is charging. 6. Leave the camera powered off and charging until the front LED has turned off. Once the front LED turns off, the battery is fully charged. This step can take up to 4 hours if the computer is used and up to 2 hours if a USB wall charger is used.

Table 64: Laptop Battery Recharging Checkout Procedure

Name	**Laptop Battery Recharging**
Pre-requisites	None
Timing	Prior to aircraft loading, as necessary
Configuration	Have LiPo Battery Emergency Burn Bag on hand
Steps	1. Connect laptop power cable to wall power 2. Connect laptop to laptop power cable 3. Confirm charging on laptop power indicator 4. Disconnect when laptop indicates full charge

Table 65: OSA Sensor Package Verification Checkout Procedure

Name	**OSA Sensor Package Verification**
Pre-requisites	None
Timing	Prior to aircraft loading
Configuration	Sensing Computer and Commanding Computer available
Steps	1. Power on the OSA 2. Connect to the OSA Raspberry Pi ad-hoc network "FPOS" through the Sensing computer 3. With PuTTY, establish an SSH connection between the Raspberry Pi and Sensing Computer 4. Start recording dynamic data 5. Move the OSA in all six degrees of freedom 6. Graphically verify that the OSA sensors detected all six degrees of freedom motion

	7. With WinSCP, transfer all extra files from the OSA SD card over to the Sensing Computer local drive

Table 66: Systems Data Acquisition Verification Checkout Procedure

Name	**Systems Data Acquisition Verification**
Pre-requisites	All previous ground operations procedures.
Timing	Prior to aircraft loading
Configuration	Flight configuration, fully assembled
Steps	1. Open GUI on MATLAB with Commanding Computer 2. Move OSA in all six degrees of freedom 3. Check IMU gyroscope and accelerometer real-time plots 4. Check SROA pressure and temperature real-time plots 5. Tap the SROA face with a finger and look for contact detection in GUI 6. Ensure that all telemetry is recorded on the local drive

Pre-Flight Configuration and Plan Summary:

Table 67: SBA/SROA Loading Process

Name	**SBA/SROA Loading Process**
Pre-requisites	IFA loaded onto aircraft, aircraft is powered and that power is available to the power panels for experiments, access to the plane is provided
Timing	Initiate between 2 hours to 30 minutes before takeoff, at least 12 hours after cryocooler was first turned on
Configuration	SBA/SROA assembled, with wheels attached, in ground operations configuration; training magnets installed; IFA assembled and attached to aircraft
Steps	1. Remove necessary tools from toolbox and log them out 2. On the aircraft on the IFA, remove the reinforcing aluminum cross-beam that is facing the center of the aircraft (the beam interferes with the SBA/SROA assembly during mounting procedure) 3. Return to hangar 4. Open the getter pump valve 5. Close the turbo pump valve 6. Turn off the turbo pump

	7. Disconnect the KF connection between the turbo pump and the SROA 8. Turn off the cryocooler 9. Unplug the SBA/SROA from the hangar power 10. Wheel the SBA/SRPA to the aircraft 11. Lift the SBA/SROA up the aircraft stairs ensuring that at least the minimum number of required people participate in the lift 12. Roll the SBA/SROA to the previously-loaded IFA in the proper orientation, as shown in Figure 107. 13. Slightly lift the side of the SBA that faces the close wall of the aircraft and remove the two caster wheels on that side 14. Slide the SBA on to the IFA 15. Slightly lift the side of the SBA facing the center of the aircraft and remove the remaining two wheels. 16. Slide the SBA into the IFA. 17. Connect the six power lines from the SBA/SROA to the ABA: Current source, DAQ, Cooling Fans, cooler electronics, pressure gauge, ion pump, Auber temperature controller 18. Connect the ABA to the aircraft wall power 19. Turn on the ABA power supply 20. Turn on the cryocooler 21. Connect the ion pump cable to the getter/ion pump 22. Turn on the ion pump 23. Bolt SBA to the IFA for takeoff configuration 24. Reinstall the reinforcing aluminum cross-beam to the IFA 25. Confirm cargo straps remain taut and that power is on 26. Remove assembly tools and caster wheels from the aircraft 27. Return tools to toolbox and log them in

Table 68: Pre-Flight Checklist

Name	**Pre-Flight Checklist**
Pre-requisites	SBA/SROA is loaded
Timing	After the pre-flight briefing and at least 10 minutes prior to experimenter loading and takeoff
Configuration	Takeoff configuration

Steps	1. Ensure all tools are in the team toolbox, except for those listed as flight tools. 2. Ensure that the flight tools are on the aircraft in their takeoff configuration and secure 3. Ensure that the equipment in stowage is in place and secure 4. Ensure that all the GoPros/ hand-held cameras are fully charged 5. Ensure that all the laptops are fully charged 6. Ensure that all the SD cards are empty and installed 7. Ensure that the commanding computer, sensing computer, and OSA can connect on the network 8. Ensure that the CLS is closed and latched, with the commanding computer inside 9. Ensure the temperature sensors and pressure sensors are reading nominal outputs 10. Ensure that the cooling fans are operating 11. Ensure that experimenters have taken anti-nausea medication if they choose to

Pre-Experiment In-Flight Setup and Preparation:

Table 69: Pre-Experiment In-Flight Setup Checklist

Name	**Pre-Experiment In-Flight Setup Checklist**
Pre-requisites	1-g environment, experimenters can leave seating area and enter experimental area
Timing	After takeoff, prior to experiment and first parabola
Configuration	Takeoff configuration
Steps	1. Retrieve tools and equipment from the stowage containers 2. Confirm connections on Wi-Fi: a. Open the CLS and sign in to the commanding computer b. Open the sensing computer and sign in c. Turn on the OSA

	d. Perform Commanding/Sensing Computer Connection Verification Procedure e. Perform OSA Sensor Package Verification Procedure 3. Confirm SROA functionality a. Verify pressure and temperature readings are nominal b. Photograph starting configuration/readings c. Verify that the DAQ is reading and recording data d. Remove training magnets e. Use training magnets to confirm flux pinning field-cooling on each superconductor f. Stow training magnets and any tools 4. Set up the IA: a. Disconnect the T-pins from the IA and store b. Position the IA to the experiment configuration and secure c. Photograph the configuration 5. Set up the camera systems: a. Turn on all GoPro cameras and start recording b. Perform the camera calibration procedure 6. Prepare for free floating a. Remove cargo straps from the IFA b. Stow cargo straps c. Adjust foot straps and knee straps to fit the experimenter d. Place OSA in experiment area

Table 70: GoPro Calibration Procedure

Name	**GoPro Calibration Procedure**
Pre-requisites	IFA assembled and GoPro cameras mounted
Timing	After In-Flight Setup Checklist
Configuration	Experiment configuration
Steps	1. Wave calibration tool across entire capture volume 2. Stow calibration tool.

Table 71: Pre-Experiment In-Flight Checkout Assignments

Pre-Experiment In-Flight Checkout Assignments

FM1 Frame, Cargo Straps	**FM2** GoPro, SROA and Vacuum Configuration	**OSAM** OSA Configuration, IA Configuration	**EM** Sensing Laptop, ABA Checkouts	**CO** CLS, Telemetry Checkouts, Commanding Laptop
Unstrap frame from aircraft floor, stow straps	Confirm power state of IFA	Power OSA on in stowage container	Unstrap sensing laptop from its Kevlok straps	Unlatch and open CLS, open commanding laptop, turn on CLS GoPro
Calibrate GoPros	Turn on all GoPro cameras and start recording	Move IA to the initial experiment conditions, secure and document	Connect to FPOS network, connect to CLS with VNC Server, tell CO	Connect to network, load GUI, pull up experiment plan
	Check pressure and temperature readings, support telemetry checkouts	Retrieve OSA from stowage and stow IA locking pins	Secure Sensing Laptop on ABA	Coordinate with EM to setup sensing laptop
	Remove training magnets, confirm flux pinning, stow training magnets	Support calibrations and telemetry checkouts	Support telemetry checkouts	
		Load OSA into initiator assembly		Testbed telemetry and command checkouts (OSA IMU, frame IMU, and DAQ)

Off-Nominal Scenarios:

In the worst off-nominal cases, the microgravity experiment can be made safe but the data is lost. This section lists some off-nominal scenarios that could be encountered on the flight, and the steps that are taken to mitigate them.

Table 72: Wi-Fi Network Outage

Scenario	**Wi-Fi Network Outage**

Description	The commanding wi-fi network is not automatically initiated by the OSA on startup, or otherwise stops transmitting during flight.
Likelihood	Low
Consequence	If corrected: No problems after corrected. If not corrected: Data collection onboard the OSA cannot be initiated in-flight, sensing computer must be operated manually, potentially introducing external dynamics to the experiment. No real-time remote confirmation of data quality.
Troubleshooting / Correcting Steps	1. Check OSA wired connections to confirm that the Raspberry Pi is on. 2a. If yes: power cycle the OSA. 2b. If no: The battery is depleted, continue running experiments without data collection from the OSA.
Mitigation if not Correctable	Operate the sensing computer directly.

Table 73: Wi-Fi Network Interference, Zero-G Requires Network Shutdown

Scenario	**Wi-Fi Network Interference, Zero-G Requires Network Shutdown**
Description	Occurs if Zero-G finds that the commanding Wi-Fi network interferes with their operations.
Likelihood	Low
Consequence	The experiment must be conducted without the commanding Wi-Fi network. The sensing computer must be operated manually, possibly introducing external dynamics to the experiment. Data collection onboard the OSA cannot be initiated in-flight. No real-time remote confirmation of data quality.
Troubleshooting / Correcting Steps	1. Remove the Wi-Fi dongle from the OSA. 2. Connect the commanding laptop to the Raspberry Pi on the OSA with an Ethernet cable. 3. Initiate data collection on the OSA for the duration of the flight. 4. Disconnect the commanding computer from the OSA.
Mitigation if not Correctable	Data can be collected for the entire duration of the flight, and then separated into individual parabolas in post-processing.

Table 74: Component Not Connecting to Wi-Fi Network

Scenario	**Component Not Connecting to Wi-Fi Network**
Description	Either the sensing computer or commanding computer cannot find or does not connect to the commanding Wi-Fi network.
Likelihood	Low

Consequence	If corrected: No problems after corrected. If not corrected: The sensing computer and commanding computer have to be handled simultaneously by two individuals, potentially introducing external dynamics to the experiment.
Troubleshooting / Correcting Steps	1. Power cycle the sensing and commanding computers.
Mitigation if not Correctable	If the sensing computer cannot connect, initiate data collection on the OSA directly from the commanding computer, and operate the sensing computer manually. If the commanding computer cannot connect, operate the sensing computer manually.

Table 75: Data Collection Restart Required

Scenario	**Data Collection Restart Required**
Description	There is an error in data transmission that requires a restart of the sensors.
Likelihood	Medium
Consequence	If corrected: No problems after corrected. If not corrected: Experiments cannot resume until the data run is restarted, losing valuable time in microgravity.
Troubleshooting / Correcting Steps	1. Press Ctrl-C into the command window of the Raspberry Pi from the sensing computer to safely halt the OSA IMU and/or Frame IMU if still running. 2. Press "Start" on the GUI to restart all sensors and begin a new data collection run.
Mitigation if not Correctable	If problem persists, set the OSA to collect data continuously for 1 minute increments and manually run at the beginning of each parabola. The collection time on the OSA can be remotely reconfigured from the sensing computer.

Table 76: OSA Battery Fully Depleted

Scenario	**OSA Battery Fully Depleted**
Description	The OSA loses power because its battery is depleted.
Likelihood	Low
Consequence	If corrected: No problems after corrected. If not corrected: The commanding Wi-Fi network stops broadcasting.
Troubleshooting / Correcting Steps	1. Continue experiments without OSA acceleration and angular velocity data for remaining experiment runs.
Mitigation if not Correctable	Operate the sensing computer directly.

Table 77: Frame is Bumped During Experiment

Scenario	Frame is Bumped During Experiment
Description	The frame is bumped, causing the SROA to move relative to the OSA and introducing external dynamics to the experiment.
Likelihood	High
Consequence	If corrected: No problems after corrected. If not corrected: The frame must be held in place until the next parabola.
Troubleshooting / Correcting Steps	1. Operators secure the frame and hold it stationary. 2. Reset the OSA 3. Operators slowly release the frame. 4. Restart another experiment.
Mitigation if not Correctable	The experiment must be restarted on the next flight parabola.

Table 78: OSA Escapes Outside of Frame Volume

Scenario	OSA Escapes Outside of Frame Volume
Description	The OSA may collide with the SROA and rebound with enough kinetic energy to escape the effects of flux-pinning, moving towards the outside of the frame.
Likelihood	Medium
Consequence	If corrected: No problems after corrected. If not corrected: The OSA must be retrieved by an experimenter and returned to the frame.
Troubleshooting / Correcting Steps	1. Operator grabs the OSA before it leaves the frame. 2. Reset the OSA. 3. Restart another experiment.
Mitigation if not Correctable	Rerun experiment on the next flight parabola.

Table 79: High Cabin Temperature

Scenario	High Cabin Temperature
Description	The cabin temperature is >80°F
Likelihood	Low
Consequence	If corrected: No problems after corrected If not corrected: Cryocooler overheats and turns off
Troubleshooting / Correcting Steps	1. Wait until the over-temp protection turns the cryocooler electronics back on 2. Increase the maximum voltage to the cooler from 0 to 28 Vrms

	3. If the cooler overheats again, repeat steps 1 and 2 as necessary
Mitigation if not Correctable	The cooler is repeatedly turned on until the superconductor temperatures rise to above 90 K

Table 80: Rising Vacuum Pressure

Scenario	**Rising Vacuum Pressure**
Description	The vacuum pressure is rising
Likelihood	Low
Consequence	If corrected: No problems after corrected If not corrected: Cold surfaces in vacuum condense gases
Troubleshooting / Correcting Steps	1. Check the operation of the ion pump 2. If it's off, turn it on
Mitigation if not Correctable	Turn the cryocooler off when pressure exceeds 10^{-4} Torr

Table 81: Rising Superconductor Temperature

Scenario	**Rising Superconductor Temperature**
Description	The superconductor temperatures are rising
Likelihood	Low
Consequence	If corrected: No problems after corrected, unless superconductors reach 88 K at any point during the troubleshoot in which case the pinning effect is lost If not corrected: Flux pinning is lost at 88 K
Troubleshooting / Correcting Steps	1. Check the temperature of the other YBCO disks and coldtip 2. If they are as expected, ignore faulty sensor 3. Check cryocooler coldtip temperature 4. If this sensor is faulty, change to open loop cooler operation
Mitigation if not Correctable	Turn the cryocooler off when superconductor temperature exceeds 88 K

Table 82: Cooling Fan Failure

Scenario	**Cooling Fan Failure**
Description	The cooling fans shut off
Likelihood	Low
Consequence	If corrected: No problems after corrected If not corrected: The cryocooler overheats

Troubleshooting / Correcting Steps	1. Power cycle the cooling fans 2. Switch to backup 12 V DC power supply
Mitigation if not Correctable	The cooler overheats and shuts down. It can be power cycled repeatedly until superconductor temperatures exceed 90 K.

IV. Machine Learning Applications Supplemental Material

a. *Vehicle Dynamics Model Derivation*

The author acknowledges Sawyer Elliott for the following derivation and resides here for reference to the larger body of work.

Dynamics Model

A dynamics model of the vehicle is derived to enable coarse tuning of the baseline controller, enable pre-training for the NN learning algorithm, and provide a method for evaluating each population of the genetic algorithm. The dynamics are derived for the RC car described above in Chapter 5 but could be modified to represent a full-sized car or other vehicles.

Simplifications

For the derivation of the dynamics model, seven simplifications are made:

1. The vehicle and the surface are assumed to be rigid bodies.
2. The commands for rear wheel speed and steering angle are assumed to be implemented instantaneously, thus are quasi-static parameters.
3. The wheels are assumed to have zero inertia.
4. The car is assumed to only have two wheels: one in the front of the car and one in the back. By assuming only one wheel in the front, there is no need to encode the kinematics of the

Ackerman steering into the model, simplifying the derivation. Simplifying the model to have two wheels necessitates the unit vector $\hat{b}_2$ shown in Figure 192 to be constrained to be parallel with the surface, constraining the car to be upright.

5. The only contact points between the car and surface considered are the two points where the wheels contact the surface.
6. Both wheels are constrained to stay in contact with the surface at all times.

The friction between each wheel and the surface is assumed to be a combination of coulomb friction and viscous friction with a single μ value as shown in Eq. (203), where V is the difference in velocity between the wheel and the surface that the wheel is in contact with and F_N is the magnitude of the normal force due to contact between the wheel and the surface.

$$F_f = -\mu\big(V + F_N \text{sign}(V)\big) \tag{203}$$

Figure 192 and Figure 193 show the simplified model of the RC car. The seven simplifications above reduce the computational intensiveness of evaluating the equations of motion, enabling the GA to be implemented onto a system with limited computational capability. However, the simplified model does not accurately model the dynamics of the car on all terrains. For applications with more complex vehicle dynamics or terrain, the designer must decide on a proper model fidelity such that the dynamics accurately represent their system while remaining computationally tractable.

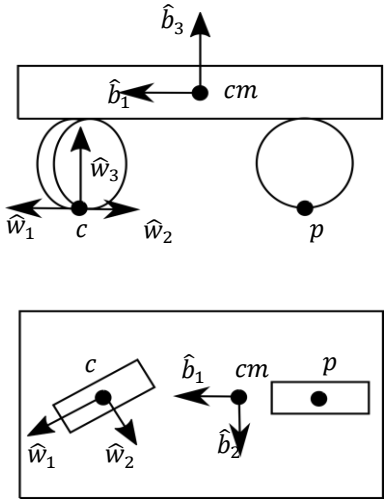

Figure 192: The point *cm* represents the center of mass of the car, including the wheels. The points *p* and *c* represent the points on the rear and front wheels that are in contact with the surface. The unit vectors $\hat{w}_i$ represent the coordinate system associated with the front wheel-fixed frame of reference, W. The unit vectors $\hat{b}_i$ represent the coordinate system associated with the body-fixed frame of reference, B.

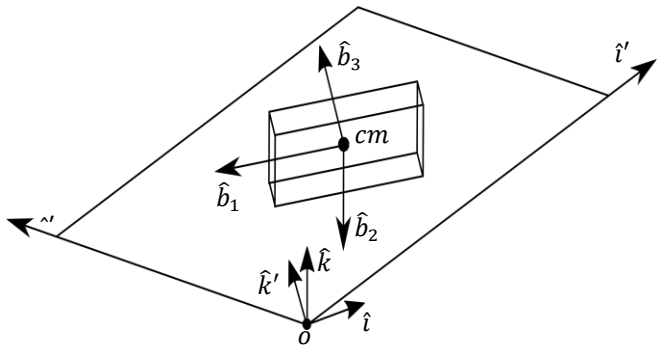

Figure 193: The unit vectors $\hat{\imath}$, $\hat{\jmath}$, and $\hat{k}$ represent the coordinate system for an inertially-fixed frame of reference, N, which is not aligned with the plane. The unit vectors $\hat{\imath}'$, $\hat{\jmath}'$, and $\hat{k}'$ represent the coordinate system associated with an inertially-fixed frame of reference, N′, which is aligned with the plane. For the derivation shown, $\hat{\jmath}$ and $\hat{\jmath}'$ are equal. For arbitrary orientations of the slope, $\hat{\jmath}$ and $\hat{\jmath}'$ may not be equal.

Derivation

Nomenclature

For the derivation, the following nomenclature is used. Not all symbols in each equation are described below, but an example of each symbol is provided. The vector $\boldsymbol{r}^{p/o}$ is a vector

spanning from point o to point p. The vector $\frac{^{\mathrm{N}}\mathrm{d}}{\mathrm{d}t}\boldsymbol{r}^{p/o}$ is the derivative of $\boldsymbol{r}^{p/o}$ with respect to the inertially-fixed frame, N. The vector $\frac{^{\mathrm{N}}\mathrm{d}^2}{\mathrm{d}t^2}\boldsymbol{r}^{p/o}$ is the derivative of $\frac{^{\mathrm{N}}\mathrm{d}}{\mathrm{d}t}\boldsymbol{r}^{p/o}$ with respect to the inertially-fixed frame, N. The vector $\boldsymbol{\omega}^{\mathrm{W/B}}$ is the rotation rate of frame W with respect to B. The dyadic $\underline{\boldsymbol{I}}$ is the vehicle's inertia dyadic about its center of mass. The scalar m is the mass of the vehicle and $\boldsymbol{g}$ is the gravity vector.

Equations of Motion

The equations of motion are derived by first determining the equations for the rate of change of the system's angular and linear momenta with respect to the inertially-fixed frame, N. The derivative of the angular momentum of the vehicle with respect to the inertially-fixed frame, N, about point o is shown in Eq. (204).

$$\frac{^{\mathrm{N}}\mathrm{d}}{\mathrm{d}t}\boldsymbol{H} = \boldsymbol{r}^{cm/o} \times m\frac{^{\mathrm{N}}\mathrm{d}^2}{\mathrm{d}t^2}\boldsymbol{r}^{cm/o} + \underline{\boldsymbol{I}} \cdot \frac{^{\mathrm{N}}\mathrm{d}}{\mathrm{d}t}\boldsymbol{\omega}^{\mathrm{B/N}} + \boldsymbol{\omega}^{\mathrm{B/N}} \times \left(\underline{\boldsymbol{I}} \cdot \boldsymbol{\omega}^{\mathrm{B/N}}\right) \tag{204}$$

The derivative of linear momentum of the car with respect to the inertially-fixed frame is shown in Eq. (205).

$$\frac{^{\mathrm{N}}\mathrm{d}}{\mathrm{d}t}\boldsymbol{L} = m\frac{^{\mathrm{N}}\mathrm{d}^2}{\mathrm{d}t^2}\boldsymbol{r}^{cm/o} \tag{205}$$

Next, equations are derived for the forces and moments acting on the vehicle. There is a total of three forces acting on the body: one contact force at each wheel, and the force due to gravity acting at the system's center of mass. The contact forces at point p and c are each separated into three orthogonal forces: 1) forces normal to the surface acting in the $\hat{b}_3$ direction, denoted as $\boldsymbol{F}_{p_{b_3}}$ and $\boldsymbol{F}_{c_{b_3}}$; 2) friction forces due to the commanded rotation rate of the wheels in the $\hat{b}_1$ and

$\hat{w}_1$ directions, denoted as $\boldsymbol{F}_{p_{b_1}}$ and $\boldsymbol{F}_{c_{w_1}}$; 3) frictions forces due to the sideways slipping of the wheels in the $\hat{b}_2$ and $\hat{w}_2$ directions, denoted as $\boldsymbol{F}_{p_{b_2}}$ and $\boldsymbol{F}_{c_{w_2}}$. The equations describing the friction forces $\boldsymbol{F}_{p_{b_1}}$, $\boldsymbol{F}_{c_{w_1}}$, $\boldsymbol{F}_{p_{b_2}}$, $\boldsymbol{F}_{c_{w_2}}$ are shown in the Eqs. (206) to Eq. (213), where r_w is the radius of the front and rear wheels, and ω_w is the rate of rotation of the front and rear wheels about the $\hat{w}_2$ and $\hat{b}_2$ axes, respectively.

$$\boldsymbol{F}_{p_{b_1}} = \mu_w \left(\Delta V_{p_{b_1}} + \left| \boldsymbol{F}_{p_{b_3}} \right| \operatorname{sign}\left(\Delta V_{p_{b_1}} \right) \right) \hat{b}_1 \tag{206}$$

$$\Delta V_{p_{b_1}} = r_w \omega_w - \frac{^{\mathrm{N}}\mathrm{d}}{\mathrm{d}t} \boldsymbol{r}^{p/o} \cdot \hat{b}_1 \tag{207}$$

$$\boldsymbol{F}_{c_{w_1}} = \mu_w \left(\Delta V_{c_{w_1}} + \left| \boldsymbol{F}_{c_{b_3}} \right| \operatorname{sign}\left(\Delta V_{c_{w_1}} \right) \right) \hat{w}_1 \tag{208}$$

$$\Delta V_{c_{w_1}} = r_w \omega_w - \frac{^{\mathrm{N}}\mathrm{d}}{\mathrm{d}t} \boldsymbol{r}^{c/o} \cdot \hat{w}_1 \tag{209}$$

$$\boldsymbol{F}_{p_{b_2}} = -\mu_s \left(\Delta V_{p_{b_2}} + \left| \boldsymbol{F}_{p_{b_3}} \right| \operatorname{sign}\left(\Delta V_{p_{b_2}} \right) \right) \hat{b}_2 \tag{210}$$

$$\Delta V_{p_{b_2}} = \frac{^{\mathrm{N}}\mathrm{d}}{\mathrm{d}t} \boldsymbol{r}^{p/o} \cdot \hat{b}_2 \tag{211}$$

$$\boldsymbol{F}_{c_{w_2}} = -\mu_s \left(\Delta V_{c_{w_2}} + \left| \boldsymbol{F}_{c_{b_3}} \right| \operatorname{sign}\left(\Delta V_{c_{w_2}} \right) \right) \hat{w}_2 \tag{212}$$

$$\Delta V_{c_{w_2}} = \frac{^{\mathrm{N}}\mathrm{d}}{\mathrm{d}t} \boldsymbol{r}^{c/o} \cdot \hat{w}_2 \tag{213}$$

The sum of all forces acting on the vehicle is shown in Eq. (214).

$$\boldsymbol{F}_T = \boldsymbol{F}_{p_{b_1}} + \boldsymbol{F}_{p_{b_2}} + \boldsymbol{F}_{p_{b_3}} + \boldsymbol{F}_{c_{w_1}} + \boldsymbol{F}_{c_{w_2}} + \boldsymbol{F}_{c_{b_3}} + m\boldsymbol{g} \tag{214}$$

The sum of all moments acting on the vehicle about point o is shown in Eq. (215).

$$\boldsymbol{M}_T = \boldsymbol{r}^{p/o} \times \boldsymbol{F}_{p_{b_1}} + \boldsymbol{r}^{p/o} \times \boldsymbol{F}_{p_{b_2}} + \boldsymbol{r}^{p/o} \times \boldsymbol{F}_{p_{b_3}} + \boldsymbol{r}^{c/o} \times \boldsymbol{F}_{c_{w_1}} + \boldsymbol{r}^{c/o} \times \boldsymbol{F}_{c_{w_2}} + \boldsymbol{r}^{c/o} \times \boldsymbol{F}_{c_{b_3}} + \boldsymbol{r}^{cm/o} \times m\boldsymbol{g} \tag{215}$$

The conservation of angular and linear momenta yield Eqs. (216) to (217).

$$\frac{^{\mathrm{N}}\mathrm{d}}{\mathrm{d}t}\boldsymbol{L} = \boldsymbol{F}_T \tag{216}$$

$$\frac{^{\mathrm{N}}\mathrm{d}}{\mathrm{d}t}\boldsymbol{H} = \boldsymbol{M}_T \tag{217}$$

The unconstrained vehicle has six degrees of freedom. However, the vehicle is constrained to not fall over, restricting the vehicle to five degrees of freedom: the rotation of the vehicle about $\hat{b}_2$ and $\hat{b}_3$, and the translation of the vehicle in the $\hat{b}_1$, $\hat{b}_2$, and $\hat{b}_3$ directions. The vehicle is further constrained to three degrees of freedom, the vehicle's rotation about $\hat{b}_3$, and the vehicle's translation in the $\hat{b}_1$ and $\hat{b}_2$ directions, by constraining points p and c to remain in contact the surface. The three constraints in conjunction with Eqs. (216) and (217) enable the equations of motion of the remaining three degrees of freedom to be derived. For brevity, the equations are not shown.